Active Volcanoes of the World

Volker Jörg Dietrich
Evangelos Lagios *Editors*

Nisyros Volcano

The Kos - Yali - Nisyros Volcanic Field

Springer

Active Volcanoes of the World

More information about this series at http://www.springer.com/series/10081

Volker Jörg Dietrich · Evangelos Lagios
Editors

Nisyros Volcano

The Kos - Yali - Nisyros Volcanic Field

Springer

Editors
Volker Jörg Dietrich
ETH Zurich
Zürich
Switzerland

Evangelos Lagios
National and Kapodistrian University of Athens
Athens
Greece

ISSN 2195-3589 ISSN 2195-7029 (electronic)
Active Volcanoes of the World
ISBN 978-3-319-55458-7 ISBN 978-3-319-55460-0 (eBook)
DOI 10.1007/978-3-319-55460-0

Library of Congress Control Number: 2017935401

Printed on acid-free paper

This Springer imprint is published by Springer Nature
The registered company is Springer International Publishing AG
The registered company address is: Gewerbestrasse 11, 6330 Cham, Switzerland

Foreword

Nisyros Volcano, which is located in the southeastern part of the Aegean Volcanic Arc, was formed during the Pliocene–Pleistocene age. The entire island is a stratovolcano with conical shaped area of approximately 42 km^2 and a base diameter of about 8 km. The most characteristic feature is an almost circular caldera with a diameter of 3.8 km and an average depth of 250 m, which was created in the central part of the island at least 24,000 years ago, after intense explosive activity. Since then, the volcanic activity remains in a dormant stage with high geodynamic activity and a large hydrothermal system being expressed in thermal springs and fumaroles. The most recent hydrothermal eruptions took place in 1871–1873 and 1887 that left large explosion crater holes behind.

Today, the post-volcanic activity of the volcano continues with gaseous emanation from fumaroles of 96–100 °C and is also manifested in several hot springs around the island at sea level, with their temperature ranging from 30 to 60 °C, while the most important ones are located in Loutra, Pali, and Avlaki. A total of ten hydrothermal craters exist inside the caldera, of which the largest and most impressive one worldwide is Stefanos Crater, which has a circular shape and a diameter of about 300 m.

The seismic activity is characterized as moderate to low, of tectonic and volcanic origin, respectively. However, substantial tectonic earthquakes in 1933 led to the destruction of the Emborios Village. A period of seismic unrest in 1996–1997 led an international team of earth scientists to initiate a proper study and monitoring of the Nisyros Volcano, including the volcanic area between Kos and Tilos islands, within the framework of the *GEOWARN* EU project. All their research results are incorporated in the present e-book.

The volcanic centers of Nisyros Island, the neighboring volcanic island of Yali and the islets of Strongyli, Pachia, and Pergusa, represent a perfect outdoor research and educational physical laboratory, an “open book of nature” that I had the privilege of studying for many years.

With this e-book, a detailed record of the individual characteristics of the Nisyros Volcano is given within twelf (12) chapters and electronic supplementary material, as well as an epilogue on the history of the island of Nisyros. It shows the present-day state of the art of a multi-disciplinary earth-science research. It constitutes the outcome of an approach by at least 27 distinguished researchers from Greece, Switzerland, Germany, and Italy to provide a compilation of all different available data. Important is the

description of the volcanic, geological, petrological, geochemical, geophysical, geodetic, and oceanographic parameters that focus to determine the history and geodynamic evolution of the volcano in space and time. Displayed and recorded are the issues related to the risk of natural phenomena, in particular those resulting from the volcanic activity that suggest specific ways to afront them. The new 1:15,000 scale "*Geological Map of the Island of Nisyros (Dodecanese Archipelago)*" and the associated cross sections as electronic supplementary material of Chap. 3 represent a comprehensive compilation of all previously published maps.

Particular reference is made in the direction of sustainable development with reference to alternative forms of tourism and thermal-spring exploitation. Also, data for upgrading the physical environment and cultural heritage, promotion of the built environment, and the promotion of geo-tourism promotional measures are given. Visitors to the island appreciate the endless and wonderful natural landscape dotted with colorful volcanic and rock formations. In addition, numerous historical, mythological, and folklore traditions refer to the giant *Polyvotis* trapped in the bowels of the volcano.

I think the e-book is a manual that will substantially contribute to the understanding of Nisyros Volcano and the associated complex volcanic phenomena in the southern Dodecanese region. This will greatly help in the deepening of new research activities using specialized technologies and the utilization of new scientific knowledge.

February 2017

Dr. Konstantinos G. Kyriakopoulos
Professor of Volcanology and Petrology
National and Kapodistrian University of Athens
Athens, Greece

Acknowledgements

The editors would like to thank Konstantinos Kyriakopoulos (Athens) for writing the foreword and revising Chaps. 3 and 4. W. d'Alessandro (Palermo), O. Bachmann (Zurich), M. Bohnhoff (Potsdam), J. Fiebig (Frankfurt am Main), E. Gartzos (Athens), K. Hartofilis (Nisyros and Athens), M. Schnabel (Hamburg), F. Tassi (Florence), and P. Ulmer (Zurich) are thanked for their detailed and constructive comments. Their reviews substantially improved the manuscript.

All chapters highly profited from multi-parametric data achieved during the multi-disciplinary EC project GEOWARN 2000–2003. The results of this project enabled the construction of a highly accurate digital topographic map of Nisyros Island by Lorenz Hurni and his team from the Institute of Cartography and Geoinformation (ETH Zurich, Switzerland) in cooperation with the first precise IKONOS satellite images in 2000 used by E. Lagios and S. Vassilopoulou (Laboratory of Remote Sensing, Department of Geophysics and Geothermy, National and Kapodistrian University of Athens, Greece). The work provided the basis for the geological, volcanological, and geophysical studies. As a result, detailed geological mapping could be carried out by Master and Ph.D. students from the Universities of Lausanne, Berne and Zurich (Switzerland). A compilation of all previously published maps and data is represented in the enclosed new 1:15,000 scale Geological Map of the Island of Nisyros (Dodecanese Archipelago) and the cross sections. The comprehensive digital work and design was done in countless hours by Andreas Baumeler (DIGIKARTO) Zurich.

The oceanographic research (swath bathymetry, ocean bottom topography, submersible exploration and sampling; active and passive OBS seismic work) could only be done with the help of the captain and crew of the Research Vessel R/V AEGAEO from the Hellenic Centre for Marine Research HCMR (Athens, Greece).

Several colleagues, who have contributed to the multi-parametric research efforts in Nisyros between 2000 and 2015, are gratefully acknowledged: N. Coppo, R. Carniel, A. Ganas, H. Kinvig, L. Martin, E. Partington, H. Rymer, A. Winson, and L. Wooller. I. Koulakov is thanked for providing the LOTOS code. The Institute of Geodynamics (National Observatory Athens) contributed with the installation of the Hellenic Unified Seismological Network (HUSN), Tobias Schorr (Nature Discovery Tours), and

Barry Hankey (Aartworld) with several beautiful photographs. Gregor Zographos finalized with great patience all figures in Chaps. 2–5.

Konstantinos Haritos, Lefteris, and Sideris Kontojannis are only a few persons of many Nisyrian inhabitants who provided local infrastructure and helping with sampling.

Those researchers who have particularly inspired our thinking of the geology, petrology and gas chemistry of Nisyros are also acknowledged here, especially A. Büttner, St. Caliro, J.C. Hunziker, L. Francalanci, L. Marini, C. Principe, Th. Rehren, L. Vanderkluysen, A.C.M. Volentik, J. Varekamp, and G. Vougioukalakis.

Institutional support for the editors and authors is greatly acknowledged, in particular from the EC project GEOWARN 2000–2003, as well as funding from the Institutes of Cartography and Geoinformation, Geochemistry and Petrology (ETH Zurich), research facilities of the University of Hamburg, Hellenic Centre for Marine Research (Athens), and GeoPro GmbH Hamburg, research grants of the National and Kapodistrian University of Athens (NKUA-S.A.R.G.), the Swiss National Science Foundation (PMPDP2 158309 to SH), the Royal Society (URF to JG), the NERC (NE/E007961/1), and the EC (FP7 Grant 282759: “VUELCO”).

Contents

About the Editors

Volker Jörg Dietrich Emeritus professor at the *Institute of Geochemistry and petrology (Swiss Federal Istitute of Technology, ETH-Zurich, Switzerland)* born 1940 in Berlin (Germany) with studies in: Technical University Berlin, (1952 bachelor); ETH-Zurich; (1964 master, 1969 Ph.D.). Visiting professor at State University of New York, Albany (1972/73), University of Washington, Seattle (1978); 1983–2005 teaching and research at the ETH-Zurich: Magmatic petrology, volcanology and applied mineralogy. 45 years of research on alpine tectonics, mapping in the Alps, Himalaya, Cameroon and Greece, specialising in geodynamic, magmatic and volcanic processes, as well as in volcanic hazard studies and risk evaluation (resulting in over 240 publications and 6 geological maps); 1992–2003 work European EC-RTD projects: SANTORINI VOLCANO LABORATORY as contractor; GEOWARN—Geo-spatial warning systems—Nisyros volcano (Greece) as scientific coordinator. In Switzerland and Germany he joined geological hazard and risk related pilot studies. For ten years he was Swiss Delegate of the IAVCEI (Internat. Assoc. of Volcanology and Chemistry of the Earth Interior), since 1974 board member and from 1992 to 2010 president of the Foundation "Vulkaninstitut Immanuel Friedländer" and board member of the Swiss Federal Geotechnical Commission, where he acted as president and active member from 1996 to 2008. E-mail: volker.dietrich@erdw.ethz.ch

Prof. Dr. Evangelos Lagios has studied Physics (B.Sc.) at the *National and Kapodistrian University of Athens* (NKUA), Hellas, and Geophysics (Ph.D.) at the *Edinburgh University* (UK). He is Director in the *Department of Geophysics and Geothermy* and the Laboratories of *Remote Sensing and Applied Geophysics* of the *NKUA* with teaching and research in various disciplines of Applied Geophysics and Space Application techniques. He has worked in Scotland and Greece, and especially along the Hellenic Arc implementing both gravity and long-period Magnetotellurics. He has carried out extensive geothermal exploration along the islands of the Hellenic Volcanic Arc in the Aegean Sea initiating the Audio-Magnetotelluric method in the '80s. He worked on various geodynamic problems at the most seismically active areas of Greece contributing to the earthquake prediction research, together with volcano-hazard monitoring assessments in Santorini and Nisyros volcanoes, applying Microgravimetry, Satellite Geodesy and Radar Interferometric techniques. He has been a board member of Greek and

international scientific committees and member in various societies of Earth sciences. He has published more than 180 research articles, and is currently involved in research of space-application techniques [GNSS, conventional DInSAR and Permanent Scatterers Interferometry (PSI)], as well as in archaeology and in real-time transfer of geophysical data using satellite technologies. E-maill: lagios@geol.uoa.gr

Geography, Nature and Habitation of Nisyros Volcano

1

Volker Jörg Dietrich

Abstract

This chapter outlines the general aspects of the unique geographical situation of the small island of Nisyros in the southeast Aegean Sea as a dormant, conical shaped and caldera bearing stratovolcano. Nisyros is located between the islands of Kos and Tilos within a prehistoric volcanic field that generated the largest volcanic eruption in the eastern Mediterranean (Kos Plateau Tuff), which devastated the entire Dodecanese area 161,000 years ago. The island benefits largely from its volcanic features, the nutrient-rich volcanic soil giving rise to all-year-round lush herbaceous vegetation and hosting a large variety of plants and animals. It profits since historical times from several thermal springs at sea level aligned in major fault zones. The northern and eastern slopes of Nisyros volcano as well as its neighbouring island Yali are covered with voluminous pumice deposits, which are mined on a large scale. The active hydrothermal system in the southern part of the caldera floor has been explorated for geothermal energy, but the initiative was abandoned due to high-risk performance and continuous micro seismicity. In 1996 and 1997 seismic activity started with earthquakes of magnitudes up to 5.5 and with hypocentres down to 10 km depth, damaging many houses in the major town of Mandraki. Tourism is today the major economy of the island. Daily, hundred of tourists visit the impressive hydrothermal explosion craters at the caldera floor, attracted by its fuming fumaroles and mud pools.

1.1 Introduction

The island of Nisyros is one of the smaller islands of the Southern Sporades, or Dodecanese islands in the eastern Aegean Sea. Its shape is almost circular with and a total width of 8.5 km,

V.J. Dietrich (✉)
Institute of Geochemistry and Petrology,
Swiss Federal Institute of Technology, ETH Zurich,
ETH-Zentrum, 8092 Zürich, Switzerland
e-mail: volker.dietrich@erdw.ethz.ch

V.J. Dietrich and E. Lagios (eds.), *Nisyros Volcano*, Active Volcanoes of the World,
DOI 10.1007/978-3-319-55460-0_1

Fig. 1.1 The Dodecanes islands and Anatolian peninsulas. *Photo* Google Earth

a coastal circumpherence of about 25 km, covering an area of 42 km^2, actually resembling a pentagon. The geographic position is Lat. 36°35′; Long. 27°10′, situated 9 nautical miles (16.7 km) east of the coast of the Datça Peninsula of Turkey, 10 miles (18.5 km) south of the island Kos; and 8 miles (14.8 km) northwest of the island of Tilos (Fig. 1.1). Nisyros is surrounded by the small island of Yali (the ancient Cisseris), the islets of Kondelioussa (the ancient Antilegoussa), Pergoussa, Strongyli and Pachia.

The island represents a pre-historic dormant volcano with a central caldera diameter of approximately 2.8 km, which is surrounded by volcanic domes and thick lavas averaging about 550 m with a maximum height of Profitis Ilias mountain at 698 m (Figs. 1.2 and 1.3). The last volcanice eruption dates back at least 24,000 years leaving a still active hydrothermal system behind (Chap. 3.5). Neither prehistoric signs nor historical reports exist about volcanic activity on Nisyros Island and in the Kos-Yali-Nisyros volcanic field. Only in the Greek mythology the battle between Poseidon and the Giant Polyvotis gives an allegoric hint of an ancient volcanic eruption (Chap. 12).

Approaching from the sea (Fig. 1.4), Nisyros appears as a green island, which rises abruptly out of the sea with terraced fields that reach as high as the tallest peak. The precipitation during the short rainy winter months seems to compensate the long and dry summer and fall season.

Fig. 1.2 The volcanic island of Nisyros with the caldera rim, the hydrothermal field and the villages of Mandraki, Loutra, Pali, Emborios and Nikia; thermal springs, idle pumice quarries and and geothermal wells Nis-1 and Nis-2. *Photo* Google Earth

Fig. 1.3 The volcanic island of Nisyros with the central caldera, the central hydrothermal crater field and the highest peak Profitis Ilias 698 m seen from south. In the *foreground* the village of Nikia with terraced fields, in the *background right* the islands of Yali and Kos. *Copyright note Photo* C. de Vries (Economakis and de Vries 2001)

Fig. 1.4 Nisyros Island approaching from north with Profitis Illias 698 m and the port of Mandraki (*right*). *Photo* V. Dietrich

Enough moisture is retained in the rich volcanic soil, ashes and pumice to provide the necessary humidity. The prevailing north winds can reach stormy conditions, even in summer time whereas southern winds tend to be smooth or rise to gale forces in wintertime.

The vegetation of the island consists mainly of Mediterranean evergreen sclerophyllous shrubs and phrygana communities with scattered trees of terebinth (Fig. 1.5, *Pistacia palaestina*) and oaks (Petanidou et al. 2008). Although the steep, cone shaped volcanic island lacks natural

Fig. 1.5 Typical Nisyrian mountainous slope covered with sclerophyllous shrubs and small trees of red blooming terebinth (*Pistacia palaestina*) during springtime. *Photo* V. Dietrich

springs and other substantial sources of drinkable water, the inhabitants built cisterns to store sufficient rainwater to last for at least a year and make fields exceptionally productive. Therefore, mainly step terraces fields, which cover approximately 58% of the island surface, were carved on the slopes of a volcano's cone, across a wide range of slope gradients and with exposure to the sea at many positions (i.e., on the outer slopes of the cone) and shelter from the sea with terraces inside the caldera walls. The agricultural terraced land uses on Nisyros were a characteristic mixed cultivation of cereals (mainly barley, and a lesser amounts of wheat), viniculture, as well as trees of terebinths, figs, almonds, and olives.

The nutrient-rich volcanic soil, combined with the island's geographical location on the eastern migrating bird zone, caused the development of the unique flora and fauna of 450 recorded plant species (i.e. the rare bellflower Campanula nisyria), 85 bird species (i.e. the partridge Alectoris chukar with the local name "Perdika", the owl Athena noctual and the ugly Phalacrocorax Carbo and Aristotelis with the local name "Kalikatsou") and 7 reptile species (i.e the lizard Agamo stelio with the local name "Kourkoutavlos", which is known only from Nisyros and the neighbouring turkish coast), as well as the monk seal Monachus around the southern coasts.

Four white-washed stone villages have been built on the north and east side along the shore and in the hills: Mandraki as the island's capital town with a little commercial and ferry harbour, Loutra with a small fishing harbour, and Pali with its beautiful little yacht harbour. Two little mountain villages are plastered close to the highest points of the caldera wall to be protected from pirates, Nikia in the south and Emborios in the north with respect to the caldera.

This idyllic look of the volcano is the result of habitation during the past two hundred years. During the past 3000 years the island was mainly covered with scrub and wild trees such as oak and terebinths and a few small villages, fortifications, and watch towers, which were built either from refugees or naval outposts during intermittent military and naval conflicts or after major natural catastrophes.

Since the beginning of seafaring the 700 m high Nisyros volcanic island had become an outstanding landmark for maritime traffic in the north-south direction on the west coast of Asia Minor from the Sea of Marmara to Rhodes, the exit to the coasts of southern Asia Minor, Cyprus, and Levante. In addition, most of the traffic from the west: Italy, the Greek mainland, the Peloponnese, and the Cycladic islands had to pass by. This situation became very important since Greek-Roman times and led to the

Fig. 1.6 Stormy day with northerly winds at Pali yacht harbour. In the *background* the abondoned spa complex of "Hippocrates". On February 6, 1941 the entire northern coast of the island was devastated by a storm and all houses along the waterfront were partly destroyed. *Photo* V. Dietrich

fortification of Paleokastro and watchtowers in several high outlook points on the island.

Strategically even exceptional was the inaccessibility of the island for large ships since these ancient times. They could only land in a few open bays under difficult circumstances, due to missing shelter and dangerous anchoring grounds, as well as the lack of water supply for crews, soldiers and slaves. To keep a small naval fleet permanently moored in the water somewhere close to the shore was impossible. The only place for anchoring on shallow sandy ground and shelter from northerly heavy winds was in the open southerly bay of Yali Island three nautical miles away from Mandraki (Fig. 1.6).

In contrast, the island was perfectly suitable for refugees. Small groups reaching its shores and small inlets with tiny boats could easily hide in the wilderness of the inaccessible mountains, not being followed and attacked by their enemies. They collected rainwater inside carved stones and lived in volcanic caves, especially in those digged into the soft pumice. Consecutively cultivation terraces were built on the slopes to hold the fertile volcanic soil and to grow agricultural products. This might have been already the case in the early history, i.e. during early Neolithic and Minoan times after the devastation of the Cycladic islands, Crete and the Eastern Mediterranean through the volcanic eruption of Santorini and its accompanied tsunami. The small Cycladic and Minoan boats and sailing galleys only needed shallow beeches to be pulled securely on land. In addition, many refugees may have come later to resort from the Philistinians, Persian invaders and Pirates or after total earthquake and tsunami destruction of Kos, 142 AD and 551 AD. Several hidden small monasteries and churches in the mountains are witnesses of the early Christian and Byzantine periods.

However, Nisyros volcano did not provide only a secure place of refuge, fertile soil in the mountains and hot springs along its shores, it terrified the inhabitants during all times with unpredictable disastrous earthquakes and unexplainable huge explosions in the middle of the island inside the caldera. The list of strong earthquakes >6 magnitudes on the Richter scale on Nisyros and neighboring islands is long and will be discussed in the following Chap. 2. According to some reports the largest hydrothermal explosion that left the 300 m wide Stefanos Crater behind, occurred during the strong earthquake shortly before 1420. 1871–1973 Megalos Polyvotis and Flegethron craters were formed, 1887 Mikros Polyvotis. During

April 23, 1933 a major earthquake south of Kos destroyed 80% of the mountain village of Emborios, which led to a total exodus of the inhabitants. During the past eighty years several strong earthquakes occurred causing local damages.

The population of the island during historical time is unknown. A first estimate appeared after the Greek Revolution 1821 with c. 3300 inhabitants. The number progressively increased to a maximum of c. 5000 people between 1910 and 1912. Since then, the population decreased with major drops during and after the 1st and 2nd World Wars, in particular 1918–1922 and 1950–1974 to c. 1000. During the past 40 years the permanent inhabitant number went up from 779 (1991, review in Petanidou et al. (2008) to ca. 1200 (2012).

Despite the emigration waves after the first and second world wars due to starvation and unemployment the Nisyrians remained patriots to their beautiful island founding communities in Attika (Greek mainland), Kos, Rhodes, United States of America (New York), Canada and Australia. In 1961 they established in Athens the Nisyrian Studies Society, who issued annual periodica "NISIRIAKA" focusing on the history, tradition and folklore of Nisyros.

1.2 The Benefits of the Volcano: Industry, Thermal Springs, Spas and Tourism

The main good effect that Nisyros volcano has on the environment is to provide nutrients to the surrounding soil. The volcanic ash, which is able to alter quickly and get mixed into the soil, contains many chemical elements that are beneficial to plants. The broken volcanic rocks offer a great variety of construction material used since ancient times; e.g. the well-known production of millstones (Fig. 1.7).

In addition, the voluminous pumice deposits have become precious industrial mineral resources in modern times. On a general scale, volcanic

Fig. 1.7 Millstone exhibition in the "Liotridia" ("oil pressing") hotel, a former olive oil pressing establishment at the waterfront in Mandraki. The millstone dish and barrel are carved out of andesite lava from idle quarries at the seaside east of Mandraki; in *background* a *grey* rhyodacite millstone. *Copyright note Photo* N. A. Mastrogianni ((tel. 0030 210 8831313–0030 22410 35 603). ΤΑ ΛΙΟΤΡΙΔΙΑ ΤΗΣ ΝΙΣΙΡΟΥ (Athens 2005) in Greek. Κωστα Νιχητα Καραλη, Γερανιου 7, Athens 105 52

gases are the source of all the water and the atmosphere that makes our planet unique. The hot underground gases and deep geothermal fluids are responsible for the thermal spring waters that represent mixtures with meteoric and seawater. From medieval to modern times the industry of sulfur exploitation flourished in the hydrothermal crater field supplied constantly by the fumarolic acxtivity.

Nisyros, as a small island in the Dodecanese archipelago are nowadays highly accessible with easy and fast transportation and thus offers many modern aspects of tourism.

1.2.1 Thermal Springs and Spas

Many reports exist since Roman times about the usage of thermal springs on Nisyros Island (Chap. 5). The main localities are shown on Fig. 1.2. The idea to exploit the thermal springs was given by a Nisyrian in 1870, who suffered from psoriasis and was healed by the unique properties of the thermal spring waters of Loutra ("Public bath", Chap. 5) with up to 45 °C. The healing properties of the thermal waters are suitable for arthritis, rheumatism, skin diseseases, inflammation of the gallbladder, graval and traumas. The most important and very hot spring since Roman times, the "Thermini spring" east of Pali, was turned into the impressive spa "Hippocrates" in 1889 by the doctor Pantaleon Pandelides (Fig. 1.8). Its operation stopped in 1928 and reopened again in 1932 for one year. All waters were taken from the original spring of the homonymous chapel of Panagia Thermiani (Fig. 12.11), which remains today only with stagnant waters. However, there seems to be still a large potential of thermal waters appearing as dispers influx at shallow sealevel.

A third thermal bath, Avlaki existed at the south coast profiting from rather hot thermal waters of 60 °C. It was also built next to a lava flow entering the sea supporting the construction of a little harbour (Fig. 3.35, Chap. 3) in the first decades of the 20th century. Although the location is a good shelter for northerly strong winds, it is completely exposed to the open Aegean sea and episodic southerly gales, which damage the lava cliffs with full power of house size waves.

Today only pittoresk ruins of the original bath remain.

Fig. 1.8 The spa "Hippocrates" bulit in 1889 by the doctor Pantaleon Pandelides and operating with intermissions until 1933, the death of Pandelides and earthquake of Kos; average temparatures 45 °C. Old postcard

1.2.2 Pumice Mining on Nisyros and Yali

Pumice originally used as polishing, abrasive and exfoliating applications due to its composition of siliceous glassy shards. The Romans discovered the amazing improvements in longevity and performance imparted to concrete by the addition of fine-grained pumice (nowadays the "alkali-silica-reaction"), which has become recently a major application again, besides additives as light-weight aggregates in concrete, filtration media, water purification, insulation media, soil conditioner, insecticide carrier and blast mitigation. After World War II, exploitation of pumice started in the northern slopes between Loutra and Pali (Fig. 1.9). A few years later the pumice quarries were abandoned due to impurities (e.g. xenolithic minerals and rocks) and lack of shelter of the coastal loading station from northerly storms.

Since 1952 the municipality of Nisyros profits from the commercially mined large and homogeneous pumice deposits and perlite on the neighbouring island Yali (Hartofilis 2013). According to "LAVA Mining & Quarrying S.A." the largest Greek pumice deposit (Fig. 1.10) contains more than 120 million tons, which are mainly exported to Europe, the USA, the Middle East and Asia. On the basis of annual mining of approximately 1 million tons the deposit will last up to the year of 2100.

Perlite is volcanic rhyolitic glass that has incorporated 2–5% water. It expands rapidly when heated. Thus, perlite is used mostly as aggregate in plaster and concrete, especially in precast walls.

Fig. 1.9 The idle pumice quarries in the northern slopes of Nisyros Island between Loura (*west* to the *right*) and Cape Akrotiri (*east* to the *left*). *Photo* V. Dietrich

Fig. 1.10 Pumice mining activity on Yali Island; in *background* obsidian lava flows and perlite mining; situation 2010. *Photo* V. Dietrich

1.2.3 Geothermal Energy of Nisyros Volcano

Exploration of geothermal energy in a 10 MW power plant with a prospection of 5 drill holes, and with a possibly extended capacity of 50 MW was proposed by the Public Power Corporation S.A. [PPC, Δημόσια Επιχείρηση Ηλεκτρισμού A.E. (DEI)] at the locality of Ag. Irini on the southern slopes of Nisyros Island (Koutroupis 1983, 1992). Geothermal drilling started in 1983 within the caldera at the southern part of the Lakki plain north of the hydrothermal explosion craters with the well Nis-1 by Geotermica Italiana and continued in 1984 with the well Nis-2 (Figs. 1.2, 1.11 and 1.12).

All activities had to be stopped due to overheating of 340 °C and overpressure at 1816 m depth on drilling equipment and steam production installations in Nis-1, as well as to boiling effects and pipe blocking with salt deposits (Fig. 1.11).

Although geothermal power plants in high-energy (high-enthalpy) geothermal areas can produce directly high electrical energy and work successfully in many areas of the world, drilling into an active volcanic system and exploiting continuous hot brine waters during the power plant operation might cause earthquake activity and might trigger unforeseen major hydrothermal explosions. Nisyros is a dormant volcano within a high geodynamic environment. Although no eruption occurred since prehistoric time no prediction can be made, how long the volcano will remain quiescent! The 1996–1998 seismic crisis with significant damages in the town of Mandraki demonstrated this unpredictable situation and initiated a period of intensive awareness, volcano monitoring and scientific research (i.e. the European Geowarn project). All the geological, volcanological, petrological, geochemical and geophysical results, including a new compiled geological map in the scale of 1:15,000, are subject of the following chapters.

Fig. 1.11 Nis-2 geothermal well 1983/84 in the Lakki plain. *Photo* in Aggelidis et al. (1990)

Fig. 1.12 The abandoned Nis-2 well 2004. *Photo* V. Dietrich

1.2.4 Tourism

Since the early eighties tourism started slowly on the island in connection with the growing tourism in all Dodecanese islands and in particular turning the small air field of Kos into an international airport. Nowadays Nisyros has become a saisonal vacation island with a steady season from April to October, offering its natural beauty, unspoiled black sandy beaches, the impressive caldera with its fumaroles in the world-wide unique hydrothermal explosive craters (Fig. 1.13) and traditionally restored pittoresque mountain villages, churches and monasteries.

During the summer months hundreds of daily tourists visiting the island, mainly approaching from Kos with little ferry boats. In addition, fast catamaran ferries connecting Nisyros daily with Kos, Rhodes and all Dodekanese islands as well twice weakly large ferries to Athens.

An outstanding feature is the small yacht harbour of Pali, which has become a pearl in the Dodecanese islands (Fig. 1.14). It is known for its good shelter all year round, even during heavy winter storms.

On the contrary, the Nisyrians keep their strong presence in the cultural tradition, which is expressed in numerous festivals. Almost all religious festivals organised in the island are visitor attractions, taking place in redecorated monasteries and are organized by the inhabitants of Mandraki and the three villages of Pali, Emborios and Nikia.

Fig. 1.13 Daily tourist groups visiting the bottom of Stefanos Crater with its fumarolic vents and mud pools. During the summer months the bottom is very dry and hard, whereas during winter, early spring and late fall the conditions of the floor can vary from mud to an internal lake. At these stages the situation of instability of the ground as well as breakdown of mud pools will become very hazardous. Then the entrance to the floor will be closed for public. *Photo* Barry's Ramblings

Fig. 1.14 The yacht harbor of Pali at the northern coast of Nisyros. *Photo* V. Dietrich

References

Aggelidis Z, Pavlidis S, Dikianidou D, Balaktsi M (1990) Nisyros, an active volcano. Association of towns and villages with mineral springs and spas. University Studio Press, Thessaloniki, p 36

Economakis R, de Vries C (2001) Nisyros, history and architcture of an Aegean Island. Publishing House Melissa, Athens, p 199

Hartofilis JD (2013) Yali von Nisyros. Nisyriaka 20:173–188

Koutroupis N (1983) Geothermal exploration in the Island of Nisyros. Nisyros 1 geothermal well. In: Strub AS, Ungemach P (eds) Proceedings of the third international seminar on the results of the EC geothermal energy research. Reidel, Dordrecht, pp 440–446

Koutroupis N (1992) Update of geothermal energy development in Greece. Geothermics 21:881–890

Petanidou Th, Kizos Th, Soulakellis N (2008) Socioeconomic dimensions of changes in the agricultural landscape of the Mediterranean Basin: a case study of the abandonment of cultivation terraces on Nisyros Island, Greece. Environ Manage 41:250–266

Geodynamics and Volcanism in the Kos-Yali-Nisyros Volcanic Field

2

Paraskevi Nomikou, Dimitrios Papanikolaou and Volker Jörg Dietrich

Abstract

This chapter encompasses a short review on the general aspects of the geodynamics in the southeast Aegean region, in the context of the plate convergence between the African plate and the Anatolian and Aegean microplates. Southeast-ward subduction of oceanic lithosphere and crust of a remnant Thethys ocean beneath the microplates are responsible for the generation of magmatism and volcanism during the past 5 million years. This formed the South Aegean Volcanic Arc and in particular the Kos-Yali-Nisyros-Tilos volcanic field in the southeast corner. The chapter mostly deals with the description of morphotectonic structures, obtained from a combination of onshore and offshore data, generated during numerous cruises since the European GEOWARN project seventeen years ago. The cruises focussed on a precise bathymetric exploration to determine the seafloor morphology with its young sedimentary cover, submarine volcanic features and fault zones within the different basins,

Electronic supplementary material The online version of this chapter (doi:10.1007/978-3-319-55460-0_2) contains supplementary material, which is available to authorized users.

P. Nomikou · D. Papanikolaou
Faculty of Geology and Geoenvironment,
National & Kapodistrian University of Athens,
157 84 Athens, Greece
e-mail: evinom@geol.uoa.gr

D. Papanikolaou
e-mail: dpapan@geol.uoa.gr

V.J. Dietrich (✉)
Institute of Geochemistry and Petrology,
Swiss Federal Institute of Technology, ETH Zurich,
ETH-Zentrum, 8092 Zürich, Switzerland
e-mail: volker.dietrich@erdw.ethz.ch

V.J. Dietrich and E. Lagios (eds.), *Nisyros Volcano*, Active Volcanoes of the World,
DOI 10.1007/978-3-319-55460-0_2

troughs and horsts. Geological outlines and maps are given for all volcanic eruptive centers: Kos Island and the distribution of the 161,000 years old Kos Plateau Tuff, Nisyros Volcano, Yali Island, Strongyli Volcano, Avyssos submarine crater, the volcanic islet Pergousa and Pachia and the Kondelioussa islet.

2.1 Introduction: Aegean Magmatism and Volcanism as Result of Cenozoic Plate Motions

The Kos-Yali-Nisyros Volcanic Field (Fig. 2.1) comprises the eastern sector of the South Aegean Volcanic Arc (SAVA). The arc is regarded as a magmatic expression of the ongoing north-eastward-directed subduction of the African plate beneath the Aegean-Anatolian microplate, which started around 5 Ma at the beginning of Pliocene (McKenzie 1972; Le Pichon and Angelier 1979; Papanikolaou 1993; Jackson 1993, 1994). All volcanic centers are located above a 38° dipping Benioff zone in the depth range of 130–150 km (Makropoulos and Burton 1984).

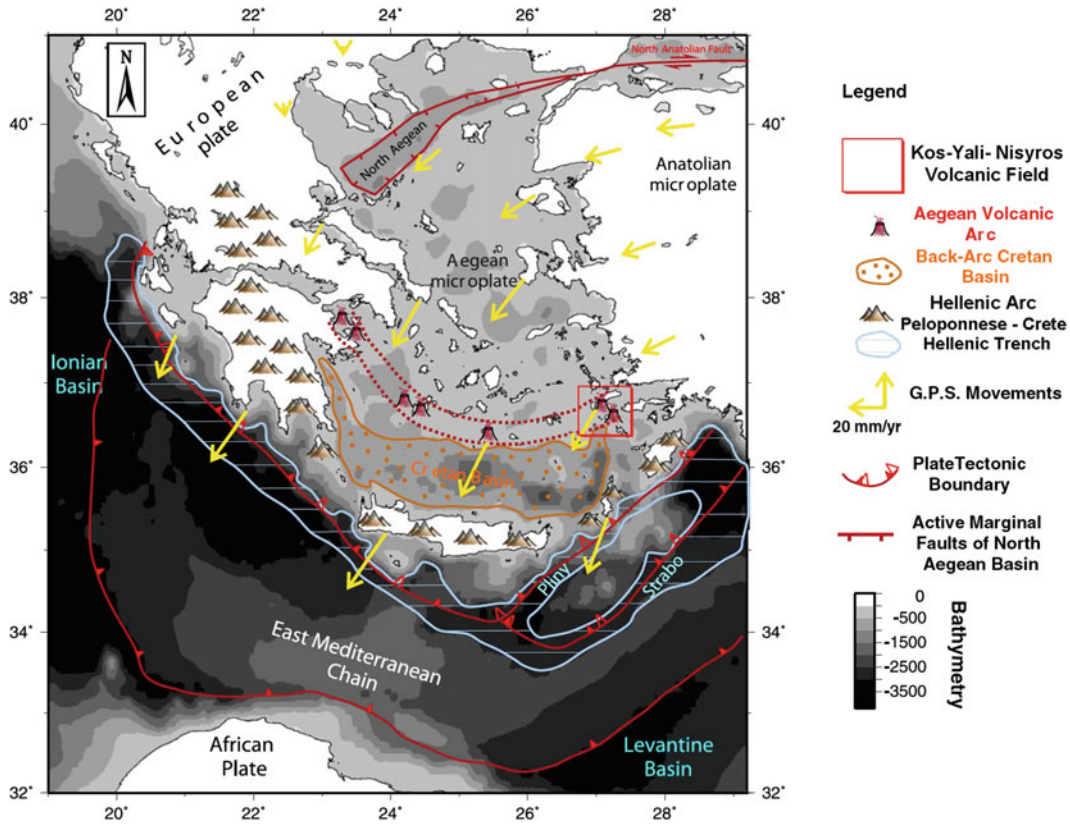

Fig. 2.1 Simplified map of the present day geodynamic structure of the Hellenic arc, showing the modern South Aegean Volcanic Arc developed behind the Hellenic trench, the Peloponnese-Crete island arc and the Cretan back-arc basin after Nomikou and Papanikolaou (2010b; Nomikou et al. 2013a). Note that the African plate to the south is subducting beneath the Eurasian plate to the north along the red lines just to the south of Crete. *Yellow arrows* indicate relative motions of approximately 35 mm/year of the Aegean-Anatolian microplate towards the African plate

The early continent/continent collision of the Aegean-Anatolian microplate (South Aegean, Menderes, Bey Daglan) began during Middle to Late Eocene and continuing into Lower Oligocene (Robertson and Dixon 1984; Collins et al. 1998). Synchronous anticlockwise rotational (northeast- to northward directed) movement of the Adriatic-Apulian promontory led to its subduction beneath the Aegean-Anatolian microplate. Continuation into Early Miocene caused compression and crustal thickening in the Hellenides, as well as extension in the external realm in northern Greece. As result of subduction and extension, magmatic activity occurred throughout the extensional realm from Middle Eocene to Late Miocene (Innocenti et al. 1981; Fytikas et al. 1984; Pe-Piper et al. 1994; for extensive review see Pe-Piper and Piper 2002).

Subduction of the south-eastern Mediterranean oceanic crust synchronously coupled with extensional magmatism during Miocene in the central and south-eastern Aegean, manifested by numerous granitic intrusions and adjacent volcanics in several Cycladic and Dodecanese islands and in the Bodrum peninsula (Anatolian coast). At about 5 Ma the spatial distribution of magmatism and volcanism shifted southward and westward and led to the development of the South Aegean volcanic arc. At this time the "consolidation" of the central Aegean block took place due to lithospheric strike-slip movements, which are expressed by the propagation of the "North Anatolian Fault" reaching the northeastern Aegean realm. South-westward motion of the Aegean block with up to 35 mm/year (Jackson 1994) and westward motion of the Anatolian block with about 20 mm/year accompanied by vertical displacements initiated strong lithospheric deformation (Fig. 2.1). The differential convergence rates between the north-eastward directed subduction of oceanic crust and African plate relative to the different blocks of the Eurasian lithosphere may have caused rapid extension, thinning of the continental Aegean back-arc region and thus, induced an adiabatic upwelling mantle.

2.2 The South Aegean Volcanic Arc

The volcanic islands of the South Aegean Sea, Aegina, Methana, Poros, Milos, Santorini, Kolombo, Yali Nisyros, and Kos define a volcanic island arc, which extends over a distance of approximately 600 km from Corinth in the Saronic Gulf bordering Attica and the Peloponnese to the islands of Kos and Nisyros near the Turkish coast (Fig. 2.1). In general, the volcanic rocks of the South Aegean volcanic arc belong to the calc-alkaline and high-K calc-alkaline (mainly of Pliocene age) series. Tholeiitic basalts occur in the Santorini islands.

Two different magmato-volcanic environments can be distinguished within the South Aegean volcanic arc, differing in age, magma types, volumes, volcanic edifices, and spatial distribution. The volcanic centers seem to be aligned by large fracture zones, trending E–W to NW–SE for the western part including Susaki, Poros, Methana, and Aegina (Dietrich et al. 1991; Hurni et al. 1995) and mainly NE-SW for the central and eastern parts of the arc including Milos, Santorini, Yali, Kos and Nisyros (Francalanci et al. 2005; Pe-Piper and Piper 2005). The volcanic activity started around 4.7 Ma and continued until present with the active but dormant volcanoes Methana, Santorini, Kolombo, and Nisyros. The western volcanic centers developed mainly as monogenic structures along fissures, plugs and domes whereas in the central and eastern volcanic islands composite volcanoes with caldera structures were formed.

The eastern sector of the island arc, including the islands of Kos, Yali and Nisyros, seems to be geodynamically very active, since it comprises the largest volumes of volcanic products, which were emitted during the past 161,000 years and is at present a tectonically active region (McKenzie, 1972; Drakopoulos and Delibasis 1982; LePichon 1982; Fytikas et al. 1984; Jackson 1994; Smith et al. 1996).

The magmatic processes started in Late Miocene and continued throughout 15 million years leading to the present day situation on the island

of Nisyros (Burri et al. 1967; Pe and Piper 1972; Fytikas et al. 1976, 1984; Innocenti et al. 1981; Pe-Piper and Piper 2002). In this respect, all volcanic and plutonic phases in the eastern Aegean islands from Mytilini through Chios, Samos, Izmir, Furni, Patmos, Bodrum and Kos down to Nisyros can be explained. The largest eruption, however occurred 161,000 years ago, which led to the largest eruption in the Eastern Mediterranean emitting more than 100 km^3 of pyroclastic material, the Kos Plateau tuff, which devastated an area of more than 3000 km^2 (Keller 1969; Stadlbauer 1988; Keller et al. 1990; Allen and Cas 1998a). Deposits occur on Kalymnos, on the peninsula of Datça and Tilos. The center of this catastrophic eruption was probably located north to northeast of Yali. Several hundreds of cubic kilometres of magmas were emplaced along the NE striking Kos-Tilos horst-graben system from the upper mantle into low crustal levels.

As the result of such a voluminous magma deficit in the underground a caldera of a diameter of 15–20 km must have been formed (Fig. 2.2), now covered with volcano-sedimentary products from younger eruptions and debris with an average thickness of 10 km. During the time span of 161,000 years the volcanic edifices of Nisyros, Yali, Pergousa, Pachia and Strongyli have grown in its inferred central part.

Nisyros and the surrounding islets have been formed during the Late Pleistocene-Holocene within an ENE-WSW trending neotectonic graben. The island of Nisyros is mainly composed of Quaternary calc-alkaline volcanic rocks which are represented by alternating lava flows, pyroclastic layers and viscous lava domes, formed during several cycles from 160 to 25 ka. The dominant feature on the island is a truncated cone with a base diameter of 8 km and a central caldera of 4 km in diameter (Di Paola 1974; Papanikolaou et al. 1991; Volentik et al. 2005). The Yali and Strongyli volcanic islands, located north of Nisyros, along with the submarine volcano of Avyssos, are prominent features in the area, bounded by NE-SW normal faults (Wagner et al. 1976; Allen and Cas 2001; Nomikou and Papanikolaou 2010a).

Figure 2.2 shows a magmato-tectonic model to demonstrate the close relationship between magmatism/volcanism, seismicity and structural

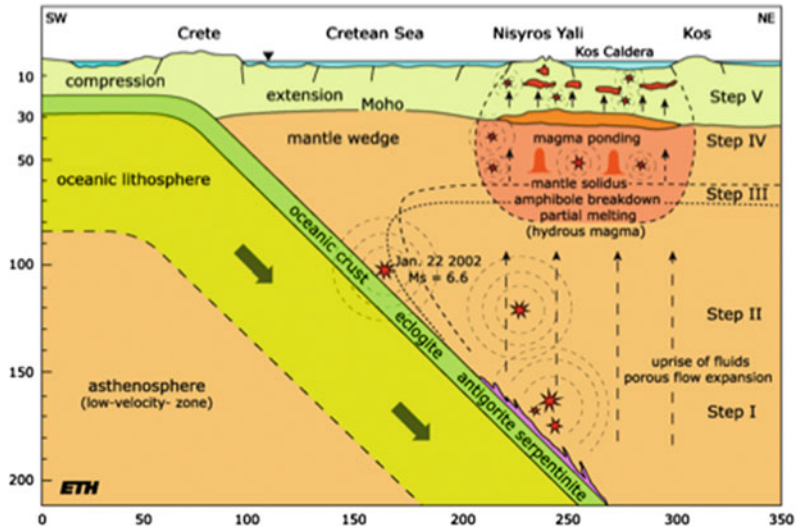

Fig. 2.2 The Magmato-Tectonic model of the eastern sector of the Aegean volcanic arc in a SW-NE cross-section from Crete to Kos. Depth and position of the subduction zone is inferred from the spatial distribution of deep earthquakes (Drakopoulos and Delimbasis 1982; Makropoulos and Burton 1984; Makropoulos et al. 1989). The encircled area marks the agglomeration of seismic activity in the Kos-Yali-Nisyros volcanic field. *Source* GEOWARN (2003)

configuration in the eastern sector of the Aegean volcanic arc. The increase of geodynamic activity can only be understood if the processes of magma generation, emplacement, fluid behaviour and tectonic environment are known. Magma generation and emplacement have been subdivided into five steps and linked to seismic activity and crustal deformation. For this reason, the volcanic islands of Milos, Santorini, Kos and Nisyros are dominated by large composite volcanoes with summit calderas and hydrothermal systems. Pyroclastic rocks of rhyodacitic to rhyolitic composition are predominant. This is an expression of the existence of relatively large, shallow crustal magma chambers allowing further crystal fractionation and crustal contamination, finally leading to highly explosive activity and Plinian eruptions.

The base of the central and eastern volcanic arc rests on normal and partially thinned continental crust (Makris 1977) and underwent several stages of deformation and metamorphism during the Alpine orogeny from Cretaceous to late Tertiary (Smith 1971). Thus, structural configuration of the continental crust can be regarded as a pile of nappes of the Hellenides, part of the "Alpine Orogen". The islands of Milos, Santorini and Nisyros show today a pronounced extensional lithospheric stress field, which favours upwelling of the asthenosphere, partial melting of peridotitic mantle rocks, uprise of primitive basaltic melts through a 25–30 km thick crust and the generation of shallow magma chambers.

2.3 The Kos-Yali-Nisyros-Volcanic Field

The Kos-Yali-Nisyros Volcanic Field (Figs. 2.1 and 2.3) covers the most complex eastern part of the Alpine-Hellenide orogen, which structurally merges into the nappe pile of the Taurides of SW Turkey. Since Late Miocene the entire area has been dissected by major tectonic lineaments such as "Horst-Graben systems" bordered by NE-SW and WNW-ESE faults, along which uplift, down-faulting and strike-slip movements occurred.

Normal faulting occurred along a NW-SE (at Miocene time probably N-S) lineament which extended in the Dodecanese Islands from Chios through Furni, the west of Patmos southeastward into the island of Rhodes and led to formation of the Antimachia graben. Extensional movements, directed towards SW, downdropped basement blocks along listric faults. Strong uplift and erosion of the "Menderes metamorphic complex" the "Cine sub-massif" and the "Bey Daglari unit" generated several E-W trending Neogene basins (e.g. "horst-graben" systems from North to South): Gediz graben, Küçük Menderes graben, the Büyük Menderes graben, and the Kerme Körfezi graben, the eastern extension of the East Kos Basin. The eastern boundary of the Hellenic arc is defined by the sinistral Rhodes Transform Fault, implying a dominant extension regime Lower Miocene (Müeller and Kahle 1993).

Synchronously, calc-alkaline magmas derived by partial melting of sub-continental mantle above down-going Cenozoic oceanic lithosphere segregated and accumulated beneath the collided Hellenic nappe piles and Lycian Taurides thrust sheets at the mantle/crust boundary.

The intersection of the N-S (at present NW-SE) and E-W "horst-graben" systems in the eastern Aegean Sea led to pronounced centers of weakness in the stress pattern of the rigid crust. Changes of the crustal stress field due to extensional, rotational and strike-slip movements at different crustal levels ("stockwerks" of nappe piles) favoured the migration of the deep magmas to upper crustal levels.

These processes started in Late Miocene and continued throughout 15 million years leading to the present day situation on the island of Nisyros (Burri et al. 1967; Pe and Piper 1972; Fytikas et al. 1976, 1984; Innocenti et al. 1981; Pe-Piper and Piper 2002). In this respect, all volcanic and plutonic phases in the eastern Aegean islands from Mytilini through Chios, Samos, Izmir, Furni, Patmos, Bodrum and Kos down to Nisyros can be explained. At present the Kos-Yali-Nisyros-Tilos volcanic field still is a region of high tectonic unrest (Drakopoulos and Delibasis 1982; Jarigge 1978; Makropoulos and Burton 1984; Papadopoulos 1984; Papadopoulos et al. 1986; Smith et al. 1996).

2.3.1 Morphotectonic Structures, a Combination of Onshore/Offshore Data

The neotectonic (post Plio- and Pleistocene) structures of the Kos-Yali-Nisyros volcanic field are demonstrated by the outcrops of the "Alpine basement". These pre-Miocene sedimentary and intrusive rocks are found in uplifted blocks—neotectonic horsts separated by the recent and actual marine basins where subsidence has prevailed during the last few millions of years. The Alpine basement in the submarine area occurs at great depths below the sea floor covered by thick post-Alpine sediments.

Thus, the submarine area between Kos and Tilos islands constitutes a regional neotectonic horst-graben system, which extends from the Datça peninsula in the coastal area of Minor Asia towards SW (Figs. 2.3 and 2.4). In addition, an intermediate Kondelioussa horst exists dividing the basins on both sides of Nisyros. Nisyros and surrounding islets represent the volcanic structures that have intruded within this regional graben as was confirmed by geothermal drillings (Geotermica Italiana 1983, 1984), which

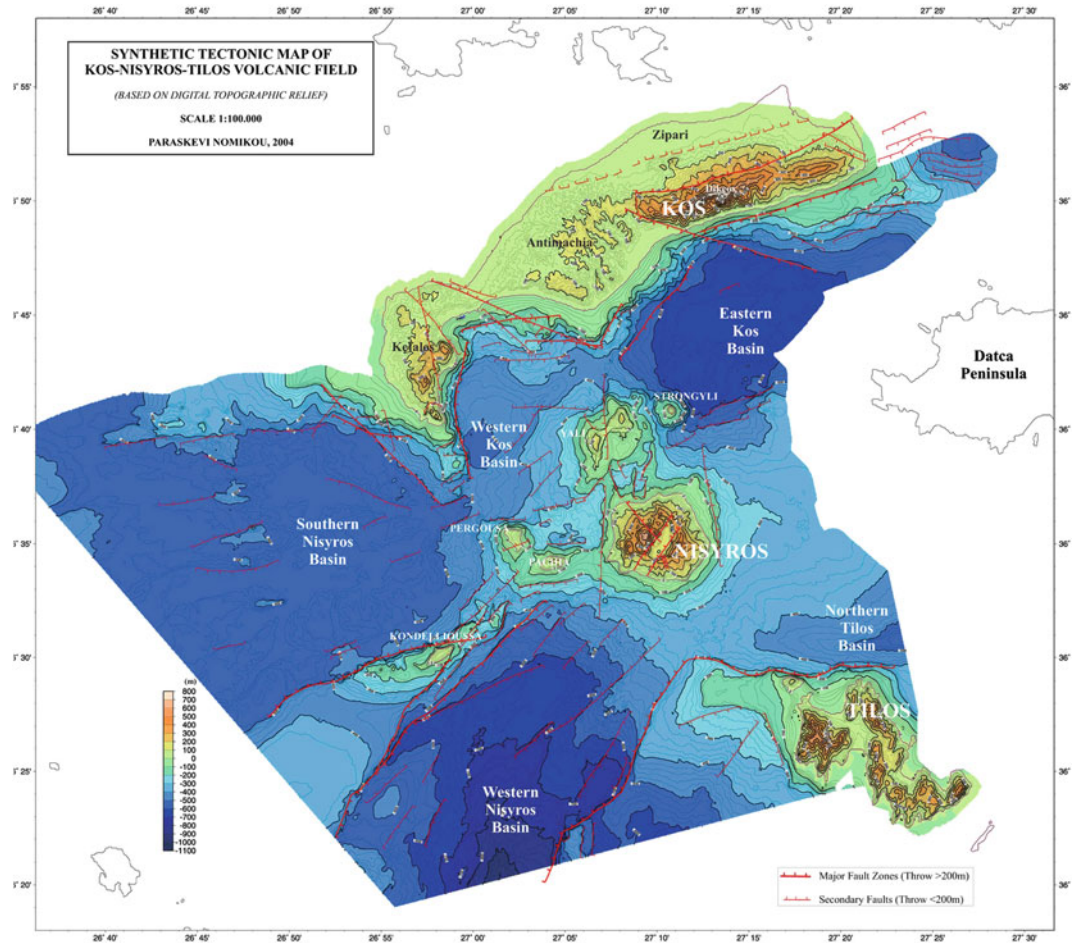

Fig. 2.3 Synthetic tectonic map of Kos-Yali-Nisyros volcanic field based on data obtained from multi-beam bathymetric surveys and combined with onshore hypsometric data (Electronic Supplementary Material Appendix). *1* Eastern Kos Basin, *2* Western Kos Basin, *3* Western Nisyros Basin, *4* Southern Nisyros Basin, *5* Tilos Basin, *6* Pachia-Pergousa Basin, *7* Yali-Nisyros Basin. *Source* Nomikou (2004), Nomikou et al. (2004), Nomikou and Papanikolaou (2010b)

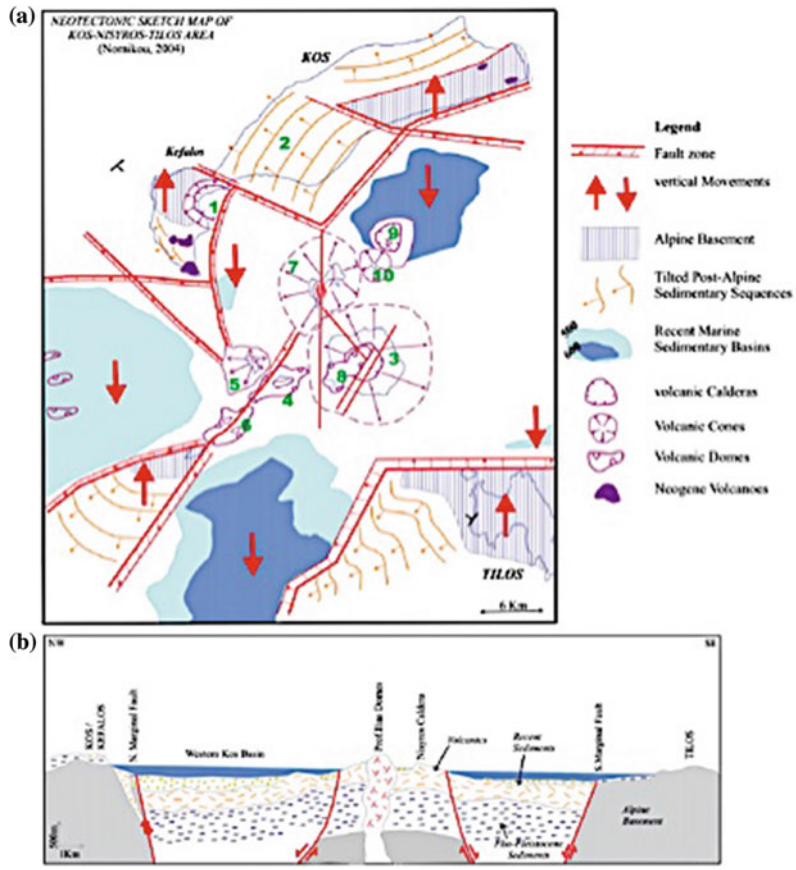

Fig. 2.4 **a** Interpretative neotectonic sketch map of Kos-Yali-Nisyros-Tilos volcanic field with distinction of the volcanic centers group (modified after Papanikolaou and Nomikou 2001; Nomikou 2004; Nomikou et al. 2013a). *1* Kefalos (500 ka), *2* Kos Plateau Tuff (161 ka) 3–10: late pleistocene-holocene volcanoes, *3* Nisyros stratovolcano, *4* Pachia, *5* Pergousa, *6* East Kondelioussa, *7* Yali, *8* Prophitis Ilias, *9* Avyssos, *10* Strongyli; **b** schematic tectonic profile from Kos/Kefalos Peninsula to Tilos. The intermediate uplift of the Nisyros volcanic area in the form of a minor horst is shown within the neotectonic graben structure

encountered Alpine basement rocks at 1800 m depth.

A morphotectonic map of the area of Kos-Nisyros-Tilos can be transformed to a neotectonic sketch map (Fig. 2.4a, b) characterized by the distinction of neotectonic blocks bordered by major faults. Each neotectonic block is characterised by its morphology, which is different across its tectonic margins from that of the neighbouring blocks. The difference may comprise the intensity of the relief, expressed by the slope gradients and/or the relief orientation, and its average elevation either positive or negative. Additionally, each neotectonic block may present a different tectono-stratigraphy referring to the Alpine formations and/or the post-Alpine sediments and eventual volcanic formations. The general dip of the strata and of the volcanic products may indicate the nature of vertical and/or tilt motions during or after the deposition of each geological formation.

Kos Island constitutes a synthetic tectonic mega-horst of ENE-WSW direction including three successive multi-blocks: Kefalos multi-block (1) in the west divided in Kefalos Peninsula, Western Kefalos and Southern Kefalos, Antimachia block (2) in the middle and Dikeos multi-block (3) in the east divided in Dikeos Mt. (3a) and Zipari block (3b) (Fig. 2.5). All these blocks constitute the Kos mega-horst bordering from the north the successive

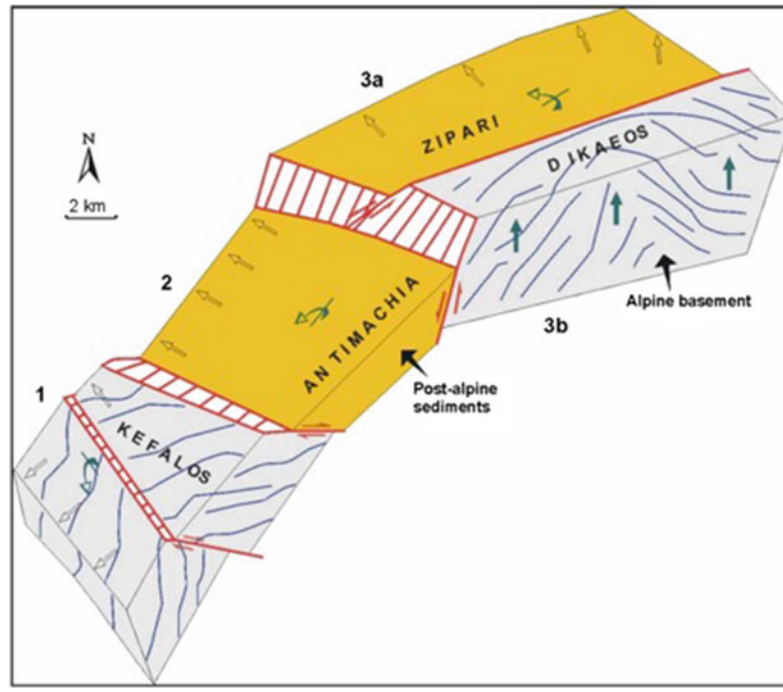

Fig. 2.5 Neotectonic blocks of Kos: *1* Kefalos, *2* Antimachia, *3a* Zipari, *3b* Dikeos (Papanikolaou and Nomikou 1998; Nomikou 2004)

grabens/basins of blocks 4, 5 and 6. However, the tectonic horsts showing relative uplift from all surrounding blocks are only blocks 1a of Kefalos peninsula and 3a of Dikeos mountain.

The Antimachia tectonic block (2) in Fig. 2.5 comprises outcrops only of Neogene and Quaternary sediments observed below the widespread Upper Pleistocene volcanic breccia and pumice of the "Kos Plateau Tuff" which forms the planar surface of the Antimachia plateau and is characterized as a tectonic graben between the adjacent tectonic horsts of Kefalos (1) and Dikeos (3b). However, it presents an important uplift relative to the submarine tectonic grabens (Fig. 2.5) of the Western Kos Basin and the Eastern Kos Basin (Fig. 2.3). This relative uplift is confirmed by the occurrence of marine Pleistocene sediments on the Antimachia plateau at altitudes around 100–120 m. The lack of outcrops of Alpine formations and of Miocene continental deposits (known from the adjacent horsts of Kefalos and Dikeos) imply a relative subsidence of more than 1000 m with respect to Dikeos and more than 600 m with respect to Kefalos. The tectonic throw between Antimachia block and Zipari block is only a few hundred meters. The post-Alpine sedimentary formations below the Kos Plateau Tuff are tilted to the NW by 10–15° around an ENE-WSW axis.

The tectonic block of Zipari (3a) comprises thick alluvial sediments observed all along the northern coast of Kos and Neogene continental sediments tilted towards the north. Small outcrops of Alpine rocks belonging to the Prophitis Ilias/Pindos tectonic unit occur in the hills of Zipari block. Thus, there is strong subsidence in relation to the tectonic horst of Dikeos (3a) and a relative uplift in relation to the tectonic block of Antimachia (2).

The two marginal tectonic blocks of Kefalos are subsided areas of the Kefalos Peninsula horst but they are uplifted blocks in relation to the Western Nisyros Basin. The tectonic block of Kos-Knidos channel also presents subsidence in relation to the tectonic horst of Dikeos (3a) and uplift in relation to the tectonic graben of the Eastern Kos Basin.

The Tilos horst (Fig. 2.4a, b) is made of Mesozoic "Alpine formations" covered by post-Alpine sediments occurring on the submarine plateau developed towards the southwest of Northern Tilos Island. The sediments of this

plateau look very similar in the lithoseismic profiles with those occurring over the neighbouring plateau of Kondelioussa and show the same tilt towards the SW. The tectonic margins of Tilos horst are made by a NE-SW oriented fault towards the Southern Nisyros Basin and another fault of EW direction towards the Northern Tilos Basin. Both faults produce an asymmetry of the basins with the deepest subhorizontal parts reaching the margins of Tilos horst. The fault throw is more than 1 km as the depths of the basins (about 600 m in Northern Tilos and more than 1000 m in Southern Nisyros) and the minimum thickness of the sediments (more than 600 m detected on the airgun profiles) imply.

2.3.2 Submarine Volcano-Sedimentary Basins

Five submarine basins (Fig. 2.3) can be distinguished within the regional graben of the Kos-Tilos area. The detailed "swath bathymetric map" permitted the delineation of the following five main marine basins in the circum-volcanic area of Nisyros (Fig. 2.3): (1) Eastern Kos Basin, (2) Western Kos Basin, (3) Western Nisyros Basin, (4) Southern Nisyros Basin and (5) Tilos Basin. Additionally, two smaller basins occur within the shallow-water intra volcanic area of Nisyros: (6) Pachia-Pergousa Basin and (7) Yali-Nisyros Basin. The intermediate horst of Kondelioussa and its northeastward volcanic prolongation of Nisyros and surrounding islets separate three basins (1, 2 and 5) along the northern sub-graben and another two basins (3 and 4) along the southern sub-graben.

2.3.2.1 Eastern Kos Basin

The Eastern Kos Basin (Fig. 2.6), representing a main block of a tectonic graben, is bordered to the north by the steep southern slopes of Dikeos Mountain whereas towards the south it is separated from the Tilos Basin by the rise connecting Nisyros Island with the Datça peninsula. To the east it continues into the basin developed north of Datça peninsula and south of eastern Kos. To the west it is bordered from the Western Kos Basin by the Yali-Kos rise and to the southwest by the very steep volcanic cone of Strongyli islet, which emerges to 120 m altitude from a depth of 600 m. The general orientation of the basin is ENE-WSW, parallel to the orientation of Kos Island. This orientation is due to a major neotectonic fault running parallel to the coast of Kos for more than 20 km, which has subsided the Eastern Kos Basin with respect to the Dikeos mountain with a throw more than 700 m. A number of submarine canyons have been detected from shallow depths of about 150 m to approximately 500 m where the morphological slopes become very shallow and grade to the sub horizontal basinal part at depths around 650 m. More than 600 m of Neogene sediments have been detected below the sea floor.

The irregular morphology of the southern basinal area is unique in this basin with a possible submarine caldera occurring immediately northeast of the base of the Strongyli volcanic cone (Figs. 2.6, 2.41 and 2.42). This submarine volcanic structure was named "Avyssos Crater" because of the great depth of its base around 680 m. The volcanic nature was verified by the analysis of the lithoseismic air-gun profiles showing only very few meters of sediments overlying volcanic formations.

Two representative lithoseismic profiles reveal the neotectonic structure of the Kos-Yali-Nisyros-Tilos volcanic field (Figs. 2.7 and 2.8).

The N-S profile starts from the southern slopes of the Dikeos Mt. on Kos island, showing the northern marginal fault zone and continues through the well-stratified marine and lacustrine sediments and intercalated volcano-sedimentary sequences (e.g. the Kos unidentified incoherent unit, KIU), which is, interpreted as the 161 ka Kos Plateau Tuff deposits (Pe-Piper et al. 2005) of the Eastern Kos Basin and the Eastern Nisyros Rise up to the Tilos marginal fault zone in the south.

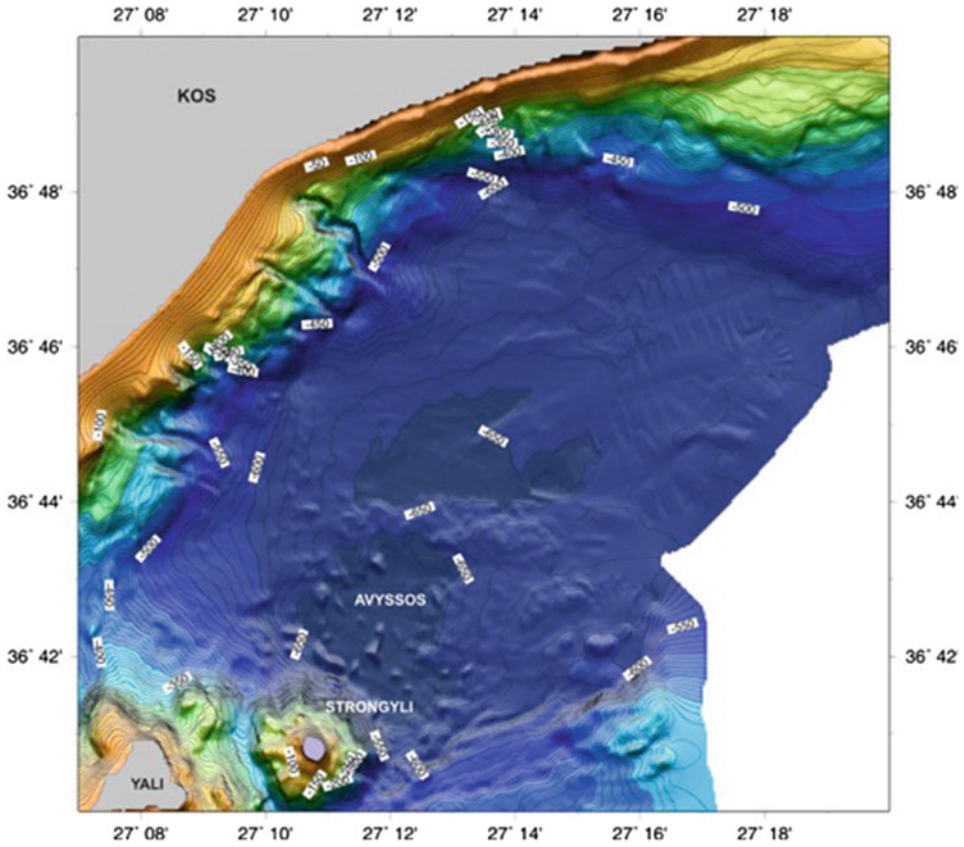

Fig. 2.6 Detailed bathymetric map of the Eastern Kos Basin using 10 m isobaths. Note the canyons along the northwestern margin and the submarine caldera of "Avyssos" to the northeast of Strongyli islet (Nomikou 2004; Nomikou and Papanikolaou 2010a)

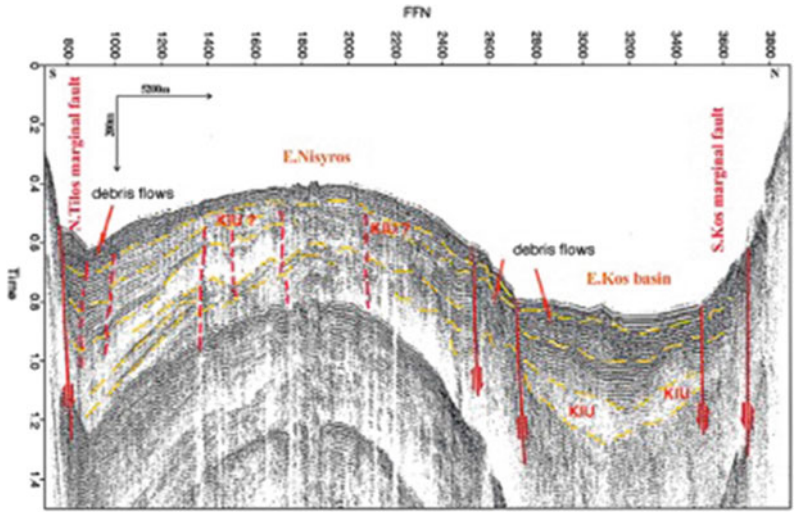

Fig. 2.7 Representative air-gun S-N profile between Kos and Tilos island through the volcano-sedimentary sequences and intercalated volcanics of the Eastern Kos Basin and the Eastern Nisyros Rise indicating steep marginal NE-SW trending faults (modified after Papanikolaou and Nomikou 2001); *KIU* Kos unidentified incoherent unit interpreted as 161 ka Kos Plateau tuff deposits (Papanikolaou and Nomikou 2001; Nomikou 2004)

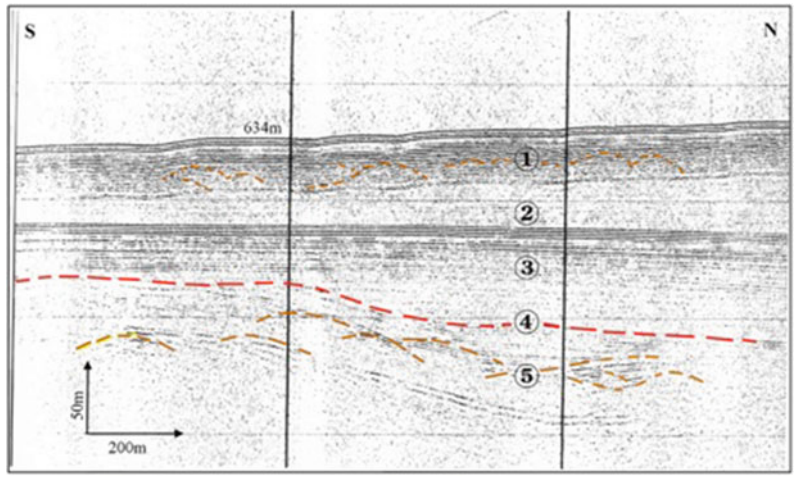

Fig. 2.8 Representative air-gun N-S profile through the large deep sedimentary Western Kos Basin between Kos and Yali, showing several hundred meters of thick flat-lying sediments (numbers 1–3); modified after Nomikou (2004)

2.3.2.2 Western Kos Basin

The Western Kos Basin is bordered to the west by the peninsula of Kefalos and to the north by the southwestern coast of the Antimachia plateau of central Kos (Figs. 2.3, 2.4 and 2.5). Yali islet occurs to the east and Pergousa and Pachia islets to the south. It comprises a volcano-sedimentary sequence of more than 500 m thickness (Fig. 2.8) below its average depth of 520 m and opens towards Eastern Kos Basin to the east, Western Nisyros Basin to the west and Pachia-Pergousa Basin to the south. The continental slopes are abrupt in almost all directions but the western margin towards Kefalos Peninsula is particularly steep and forms an N-S zone of morphological discontinuity.

The deepest part of the basin lies adjacent to the western margin with smooth morphological slopes within the rest of the basinal area, which accumulates radially the sediments towards this subsiding zone. The western margin is controlled by a neotectonic fault of N-S direction, which produces uplift of the western fault-block of the Kefalos Peninsula and subsidence of the eastern fault-block of the Western Kos Basin. The maximum depth of the basin is 530 m and only a small horizontal area can be observed around it of about 1 km^2 area. The southeastern and southern slopes of the basin are reflecting the geometry of the lower part of the volcanic cones of the Yali and Pergousa volcanoes. At the northwestern part of the basin is observed half of the Kefalos volcanic structure of Middle Pleistocene age (0.5 Ma), with some preserved onshore (Dalabakis and Vougioukalakis 1993) and the rest flowing offshore towards the south. Along the northern slopes of the basin the continental shelf of Kos is observed down to the depth of 150 m. Immediately, below the edge of the continental shelf there is a graduated arc-shaped form of a large landslide, exhibiting a type of radial flow to the south with a morphology of arcuate terraces reaching the depths of 400–450 m. The toe of the sliding mass to the south is confined by the base of the northwestern part of the Yali volcanic cone.

The lithoseismic N-S profiles through the Western Kos Basin (Fig. 2.8) revealed the existence of two major discontinuities, which define successive progradational sedimentary sequences (Papanikolaou and Nomikou 1998). The sequences show vertical displacements up to 100 m due to normal faulting:

- The upper seismic sequence is characterized by parallel seismic reflections with continuous, intense and relatively low-amplitude reflectors, which can be interpreted as relatively coarse-grained sediments reaching 50 m thickness (Fig. 2.8, No. 1).

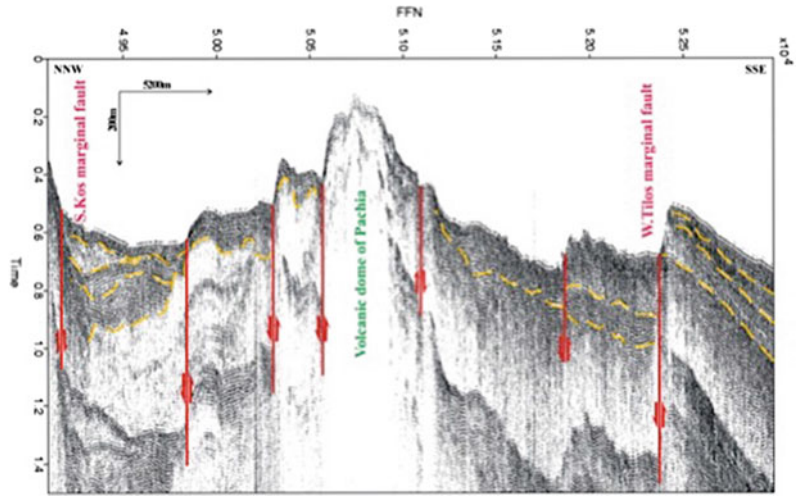

Fig. 2.9 Representative air-gun NNW-SSE profile between the southern marginal fault of Kefalos peninsula and marginal fault zone of Tilos through the volcano-sedimentary sequence of the western Kos basin, the Pachia volcanic edifice, and the volcano-sedimentary sequence of the southern Nisyros Basin; strongly elevated; modified after Nomikou (2004)

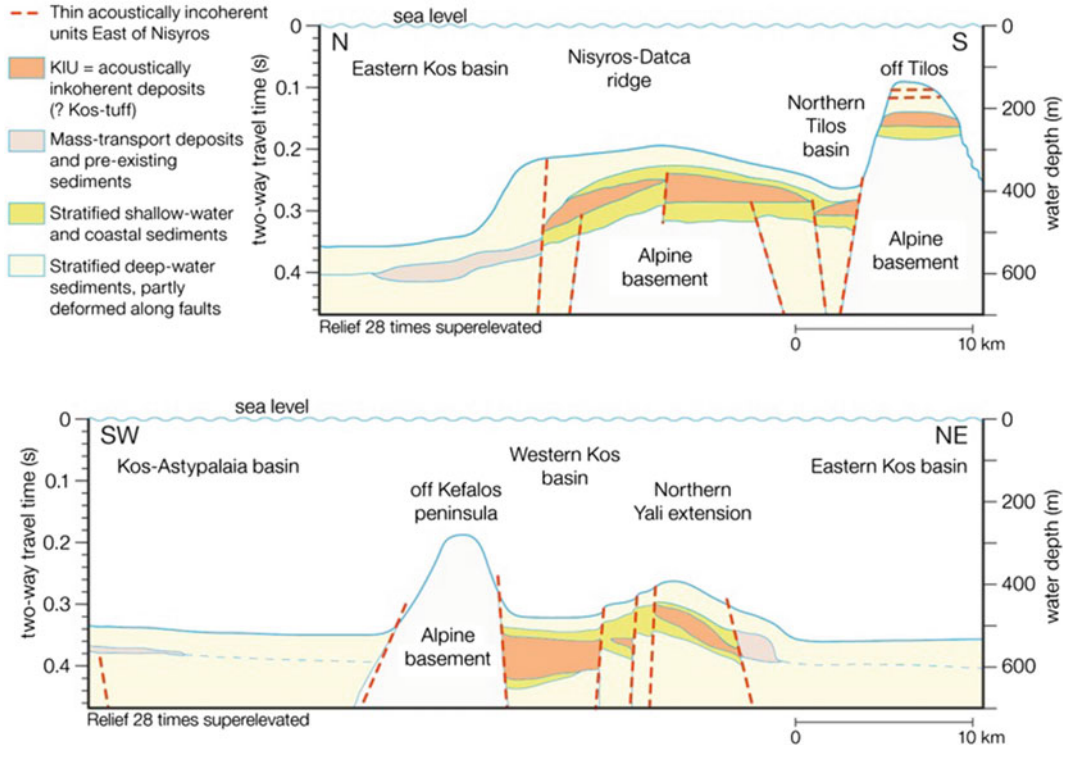

Fig. 2.10 An interpretative composite cross-section through the sub-seafloor volcano-sedimentary sequences of the west and east Kos basins between the peninsula of Kefalos and Tilos; modified after Pe-Piper et al. (2005)

- The lower seismic sequence (Fig. 2.8, No. 2 and 3) consists of a few weak, discontinuous, subparallel reflectors or reflection free-areas, suggesting fine grained sediment deposition from a relatively quiet environment with a thickness of not more than 200 m.
- A sequence of deformed reflectors (hyperbolic and bulged forms, Nos. 4 and 5, Fig. 2.8) which appear either below the second sequence or emerge from beneath them in some areas between Nisyros and Yali and especially near the island of Strongyli. These reflections may represent volcanic features and possibly volcanic domes. There are no sediments in this region. The volcanic domes emerge from 150 m depth with steep slopes (dip 35–40%).

The NNW-SSE profile between the Kefalos Peninsula and Tilos (Fig. 2.9) shows complex neotectonic structures in the volcano-sedimentary sequence of the western Kos Basin, the pre-Pleistocene Pachia volcanic lavas, dome south of Nisyros and in the volcano-sedimentary sequence of the southern Nisyros Basin, due to volcanic intrusions and eruptive phases combined with major vertical tectonic displacements (Fig. 2.10).

2.3.2.3 Western Nisyros Basin

The Western Nisyros Basin (Figs. 2.3 and 2.4) is bounded by the Kondelioussa tectonic block towards the south and the Western Kefalos Platform (Fig. 2.5) towards the north. Its average depth is 550 m and the volcano-sedimentary thickness below its sea bottom exceeds 600 m. The basinal area is rather flat with maximum depth around 600 m (Fig. 2.11). Its southern margin is characterized by abrupt breaks in slope with steep morphological slopes >20% observed

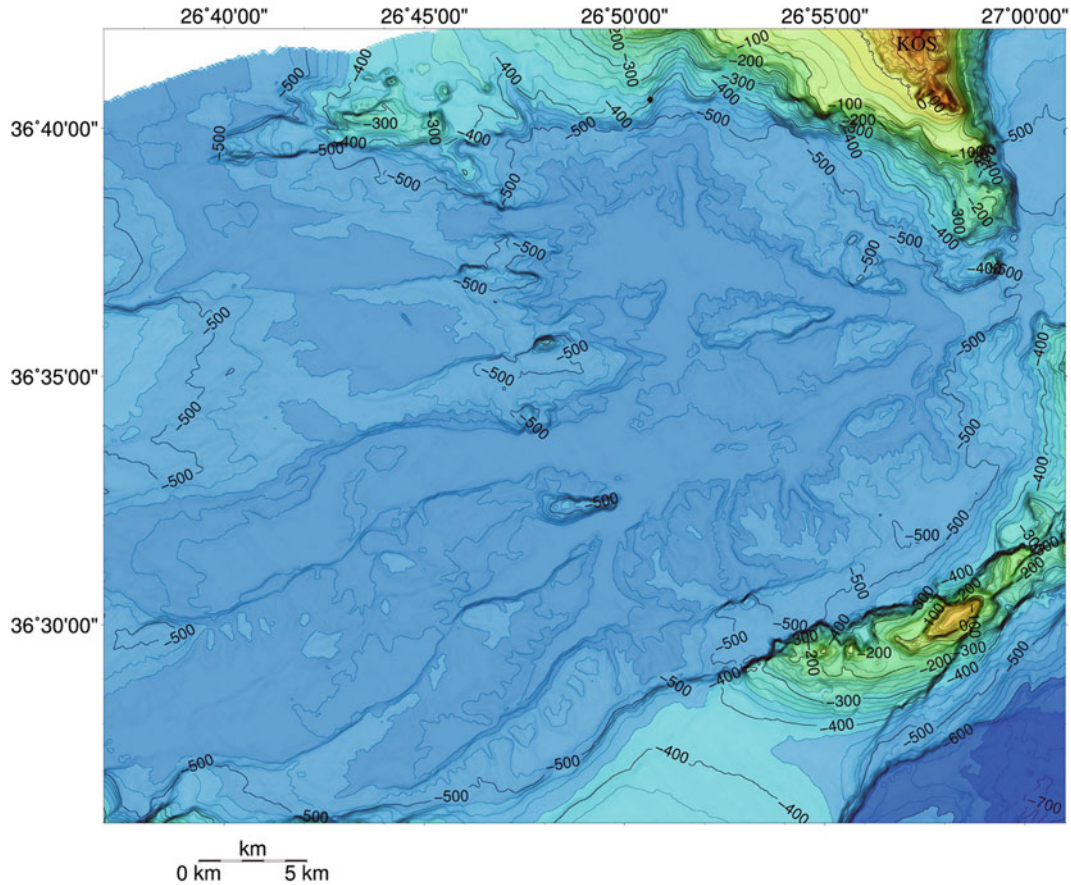

Fig. 2.11 Bathymetric map of the Western Nisyros Basin using 5 m isobaths. Note the alternation of submarine channels and ridges in the ENE-WSW direction, the latter being interpreted as volcanic intrusions (Nomikou 2004; Nomikou and Papanikolaou 2010a)

between 500 and 200 m of depth. The basin ends towards the west in the area between the islands of Syrna and Astypalaia. The overall length of the basin is 40–45 km in the ENE-WSW direction and its width is about 15–20 km. The basinal morphology is characterized by a number of flat-floored elongate basins of ENE-WSW direction alternating with parallel ridges, which, according to the air-gun profiles, are interpreted as volcanic intrusions (Nomikou 2004). The northern tectonic boundary of the basin is formed by two intersecting faults of E-W and NW-SE direction separating the tectonic graben from the intermediate marginal blocks and the Kefalos block. This steep morphology is controlled by major fault zone of ENE-WSW direction (Nomikou 2004) separating the uplifted tectonic horst of Kondelioussa islet to the south, which is made of Mesozoic carbonate rocks, from the subsided basinal area to the north.

2.3.2.4 Southern Nisyros Basin

The Southern Nisyros Basin (Figs. 2.3 and 2.12) constitutes the northern end of the large Karpathos basin extending towards the south-southwest, which comprises the eastern segment of the Cretan Basin, which reaches depths of more than 2000 m. The basin is delimited between two major fault zones of NE-SW direction (Nomikou 2004) that have caused subsidence of several hundreds of metres. The two fault zones form the parallel margins of the basin in the NE-SW direction and are characterised by steep slopes. Both marginal faults have produced a strong subsidence of the basin between the uplifted horsts of Kondelioussa in the northwest and Tilos in the southeast. In both horst areas the Mesozoic formations of the Alpine basement are uplifted. A volcanic edifice (? dome) with a small crater has been found during a submersible survey (Fig. 2.13) east of Kondelioussa.

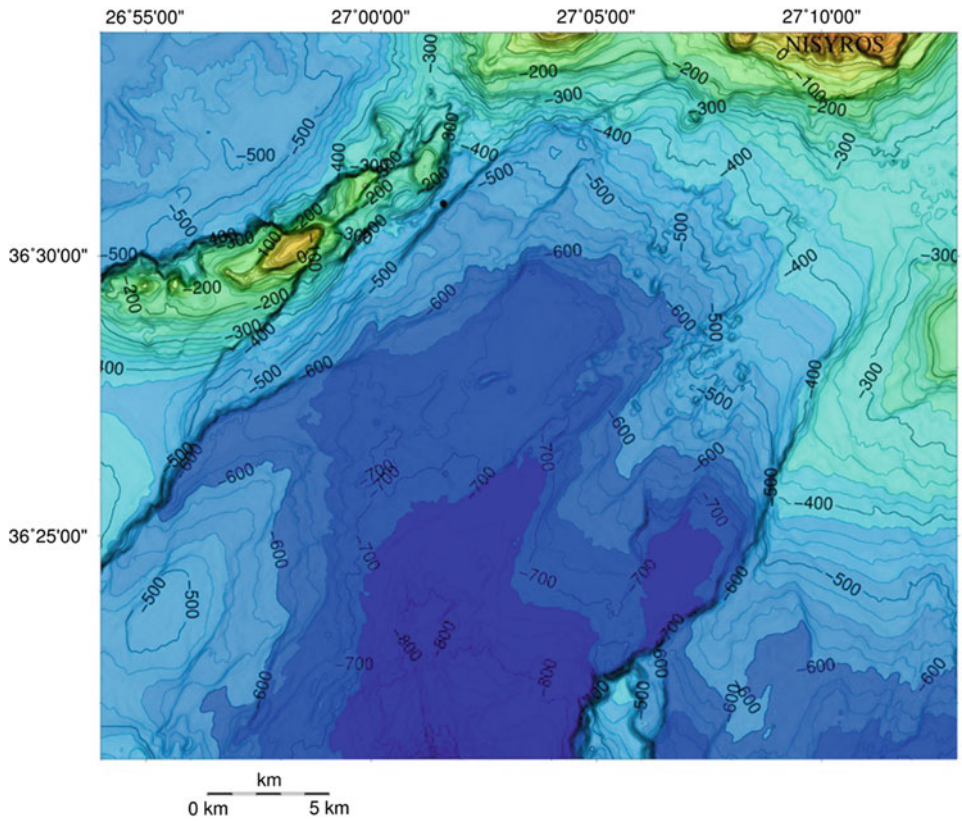

Fig. 2.12 Bathymetric Map of the Southern Nisyros Basin using 5 m isobaths. Note the submarine volcanic landslides south-southwest of Nisyros and the two steep marginal fault zones in the NE-SW direction (Nomikou 2004; Nomikou and Papanikolaou 2010a; Nomikou et al. 2013c)

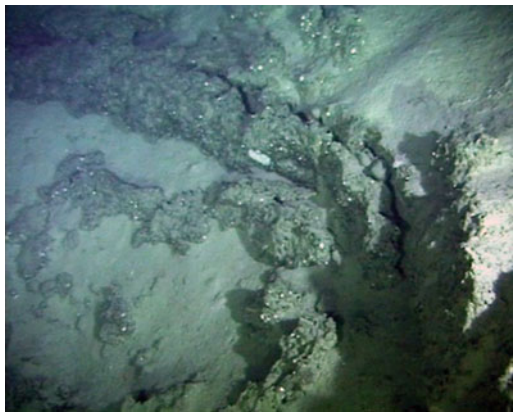

Fig. 2.13 Edge of volcanic crater (4.5 m diameter and 2 m height) from the volcanic dome east of Kondelioussa at 430 m depths (Nomikou and Papanikolaou 2000; Nomikou 2004; Nomikou et al. 2013a)

The basin is closed towards the northeast by the submarine slopes of the Nisyros volcanic edifice. Hammock morphology, due to several submarine landslides can be observed over a large area of the southwestern Nisyros slopes, e.g. a volcanic debris avalanche reaching 420–680 m of depth (Tibaldi et al. 2008a). The blocks reach 80 m in diameter with different shapes and orientations in a chaotic distribution on the sea floor.

2.3.2.5 Pachia-Pergousa Basin

The Pachia-Pergousa Basin is developed within the intra-volcanic area of the Nisyros volcanic field surrounded by the volcanic islets of Pachia to the west, Pergousa to the south and Yali to the north (Fig. 2.14). Nisyros Island borders the

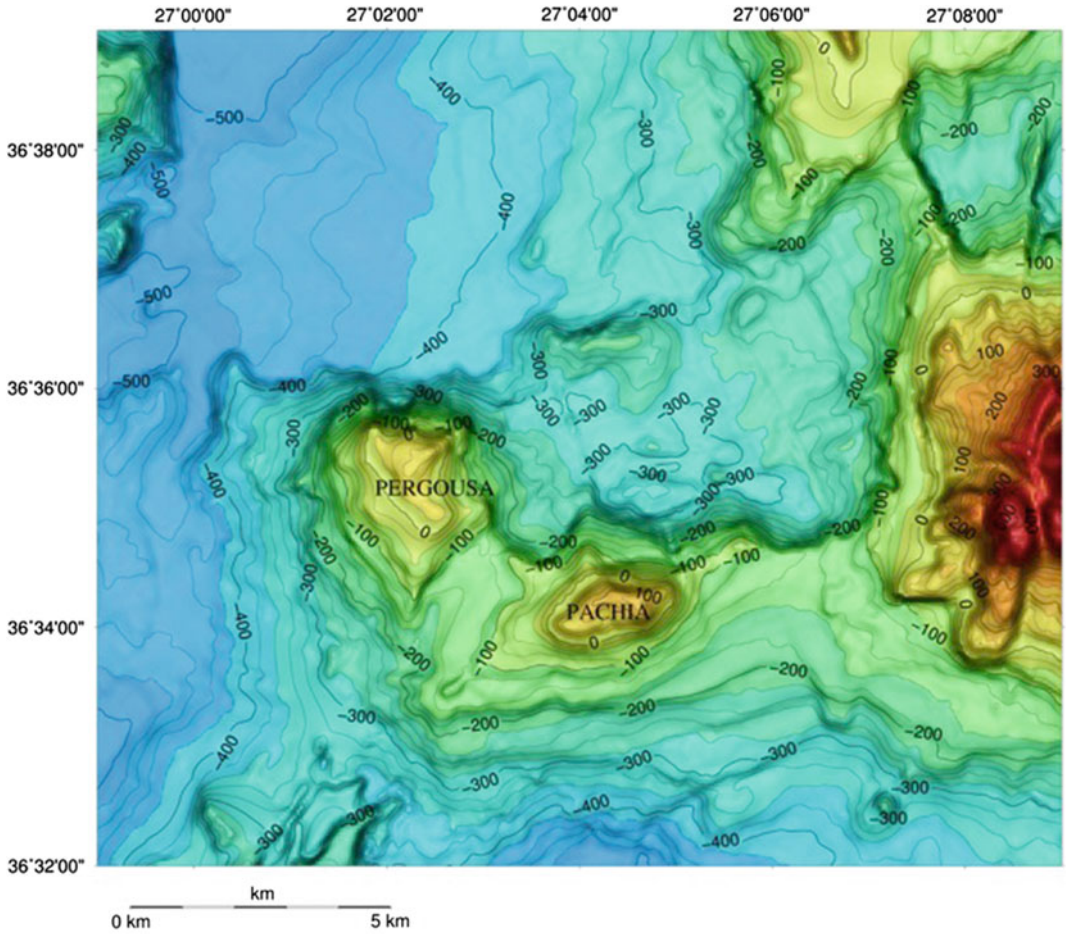

Fig. 2.14 Bathymetric map of the Pachia-Pergousa Basin using 10 m isobaths (Nomikou 2004; Nomikou and Papanikolaou 2010a)

basin to the east. A number of small fluctuations embossed the seabed likely because of volcanic intrusions. The 300 m isobaths to the north of Pachia delimits the flat part of the basin whose maximum depth reaches 345 m. The slopes to the east and to the south present an abrupt increase of depth shown by dense isobaths due to faults in the N-S and E-W direction. The basin is separated from Western Kos Basin towards the northwest by a ridge of 100 m hypsometric difference, roughly from the isobaths of 300 up to the isobaths of 200 m. Toward east and northeast it is separated from the Yali-Nisyros Basin by a small submarine ridge oriented NNW-SSE at 160 m of depth.

The Yali-Nisyros Basin occurs within the intra-volcanic area of the Nisyros volcanic field and is bordered by Nisyros Island in the south and Yali Island in the north (Fig. 2.15). The basin comprises two sub-basins oriented N-S which are separated by an N-S ridge between Nisyros and Yali islands. The western sub-basin is delimited to the west by the seismic fault zone that was activated in July 1996 and produced extensive damage in Mandraki Town, adjacent to the Panaghia Spiliani Monastery (Nomikou and Papanikolaou 2000). The submarine survey showed a topographic difference across the fault of about 100 m, with the uplifted block to the west at 140 m of depth and the sub-sided block to the east at 235 m depth. The eastern sub-basin

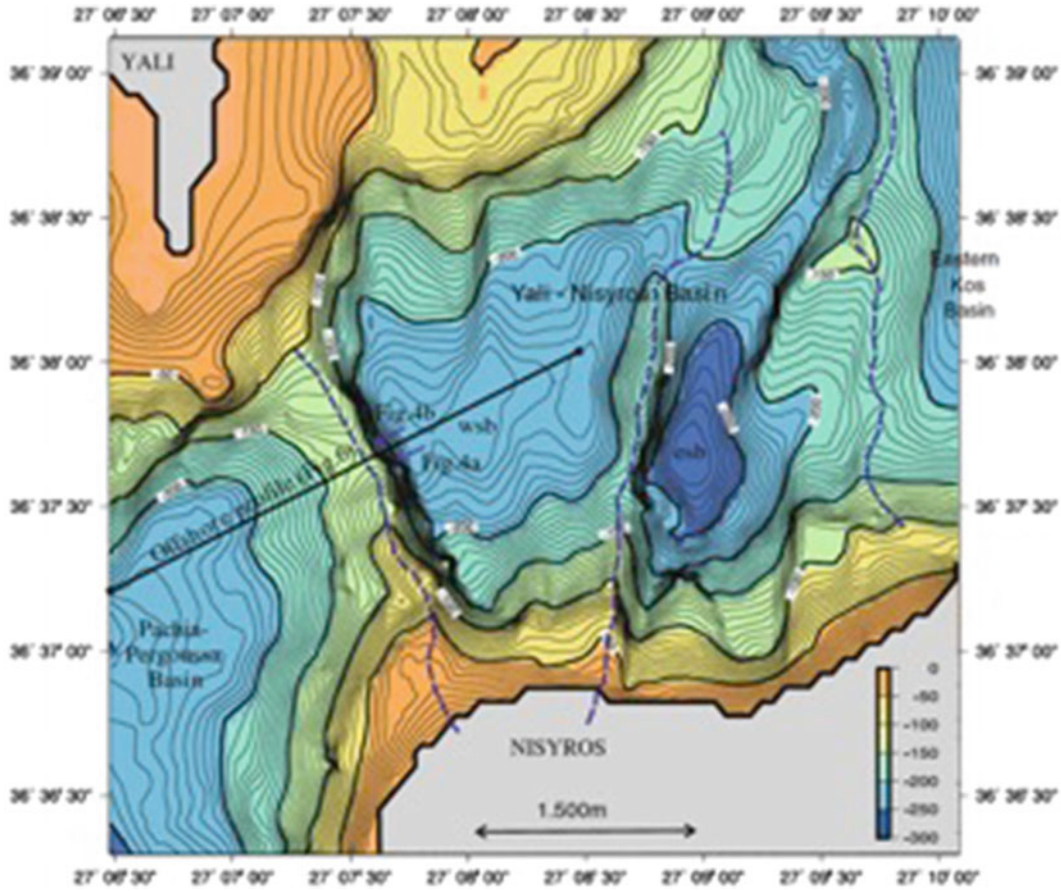

Fig. 2.15 Bathymetric map of the Yali-Nisyros Basin using 10 m isobaths. Nomikou 2004; Nomikou and Papanikolaou (2011)

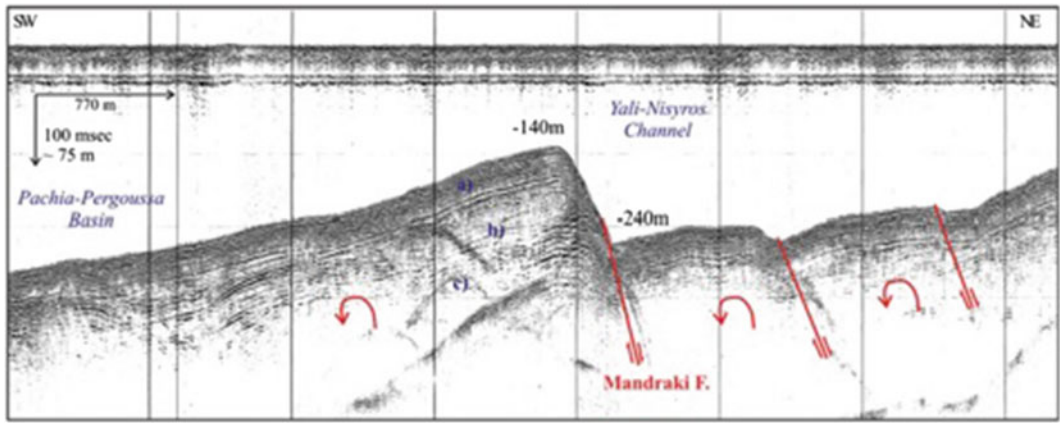

Fig. 2.16 Representative SW-NE air-gun profile of the small basin between Yali and Nisyros (Fig. 2.16), showing a succession of tilted blocks to the west, associated with the system of NNW-SSE normal faults (Papanikolaou and Nomikou 2001; Nomikou 2004; Nomikou and Papanikolaou 2011)

is developed also in the N-S direction with deeper maximum depth at 290 m.

Northward extension of the NNW-SSE trending Panagia Spiliani Fault of western Mandraki in the submarine area between Nisyros and Yali. This fault, reactivated during the 1996 earthquakes, caused the damages in the houses and roads of Mandraki exclusively along its strike, without any influence over the rest of the town. The fault throw is estimated on the basis of submarine profiling of about 100 m with an extension of approximately 5 km (Fig. 2.16); Nomikou and Papanikolaou (2000, 2011).

2.3.2.6 Tilos Basin

The Tilos Basin is developed to the north of Tilos Island and to the southeast of Nisyros Island (Fig. 2.17). Our map comprises only its western part because of its extension into the Turkish waters towards the east, where it is developed south of the Datça Peninsula. Towards the southeast it terminates in the area north of Simi Island. Towards the north it is bordered from the Eastern Kos Basin by the E-W oriented rise of Nisyros–Datça. The northern slopes of the basin towards Nisyros Island are smooth, progressively deepening from 300 m to the bottom of the basin at 570 m of depth. On the contrary the southern slopes of the basin towards Tilos Island are more abrupt with dense isobaths and steep slopes >20%. This steep morphological zone is due to a major E-W trending fault zone, developed along the northern margin of Tilos Island. The western part of the basin towards its link to the Southern Nisyros Basin is occupied by a special morphology with numerous hills and longitudinal ridges between water depths of 250 and 380 m. The overall morphology of this area southeast of Nisyros Island can be viewed as a large deposit of volcanic debris avalanche with a seaward termination displaying an irregular pattern characterized by elongated lobes. These lobes and the elongation of the single elevations might represent a series of aligned ridges emplaced parallel to the flow of the debris avalanches from the Nikia rhyolitic volcanic rocks which predated the Nisyros volcano major caldera explosion (Tibaldi et al. 2008a, b; Nomikou et al. 2009).

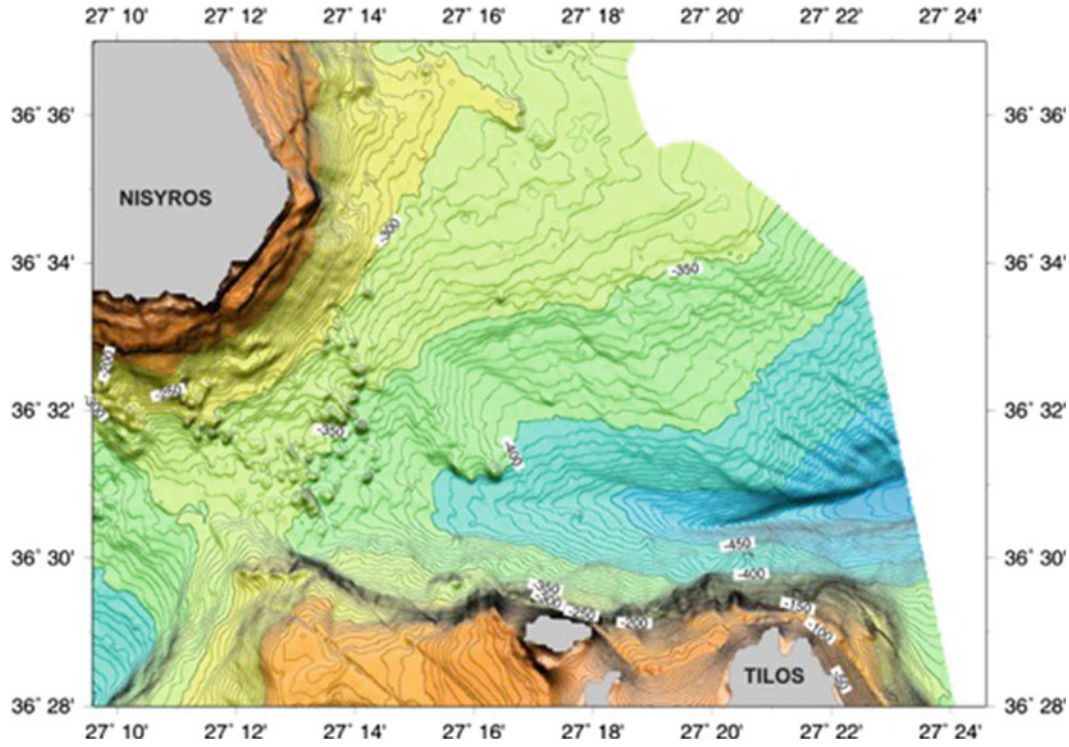

Fig. 2.17 Bathymetric Map of the Tilos Basin using 5 m isobaths. Note the deposition of the volcanic debris avalanche, which give the seafloor a hammock topography south of Nisyros; Nomikou 2004; (Tibaldi et al. 2008a; Nomikou et al. 2013c; Livanos et al. 2013)

2.3.3 Volcanic Eruptive Centers

2.3.3.1 Kos Island

Kos Island is built up by complex "Stockwerk tectonics", including Paleozoic metamorphic basement rocks, allochtonous Alpine Mesozoic thrust sheets, a 12 Ma Miocene monzonite intrusion, upper Miocene to Pleistocene volcanics and superficial present-day thermal manifestations (Böger et al. 1974; Böger 1978; Bellon and Jarigge 1979; Keller 1982; Dalabakis 1986, 1987; Bardintzeff et al. 1989; Papanikolaou and Lekkas 1990; Davis et al. 1993; Triantaphyllis 1994; Triantaphyllis and Mavrides 1998; Lagios et al. 1998) that relate to the extensional tectonics in the eastern sector of the island arc. Two major fault systems, ENE–WSW, WNW–ESE, and NNW-SSE faults, led to the present-day structure of the island (Fig. 2.18).

Volcanic activity has been occurring since Late Miocene time in the southern area of Kos Island (Kefalos Peninsula) and can be divided into two periods (La Ruffa et al. 1999). The oldest volcanics (a trachytic welded ignimbrite) were deposited during the Upper Miocene and are related to a pre-Aegean Volcanic Arc subduction zone (Keller 1982). Pliocene volcanic activity started around 3.4 Ma building dacitic domes (Dalabakis 1987; Keller et al. 1990), and continued between 2.7 and 1.6 Ma with rhyolitic domes, the pyroclastics of the Kefalos tuff ring (Francalanci et al. 2005; Allen et al. 2009) and the Zini perlitic obsidian dome. Later activity may have caused the small caldera collapse of the Kamari Bay (Dalabakis and Vougioukalakis 1993; Francalanci et al. 2005). Plinian type eruptions produced large volumes of rhyolitic ignimbrites over a time span of 10 million years and terminated in the largest event 161,000 years ago with 100 km^3 of magma deposited as ignimbrites and ashes ("Kos Plateau Tuff": Stadlbauer 1988; Allen 2001; Bachmann 2010).

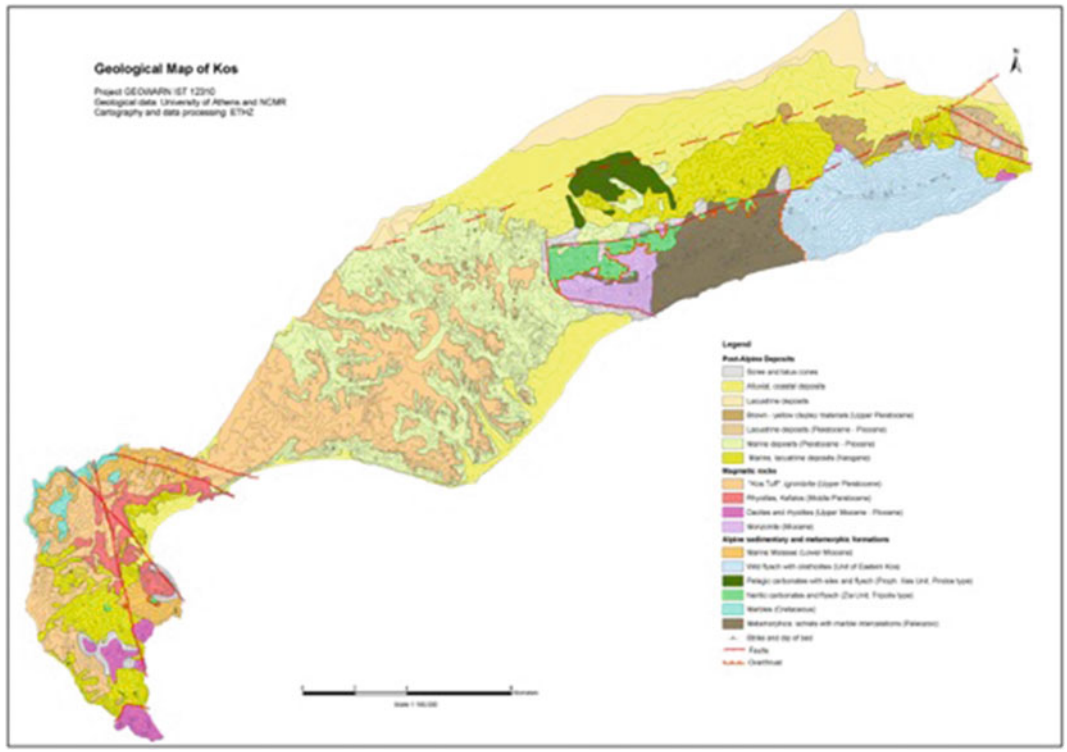

Fig. 2.18 Simplified geological map of Kos island after Nomikou (2004)

2.3.3.2 The Kos Plateau Tuff

The largest volcanic deposit of the Kos-Nisyros area (the Kos Plateau Tuff, hereafter KPT, Figs. 2.18, 2.19, 2.20, 2.21, 2.22, 2.23, 2.24 and 2.25) erupted ~161 k.y. BC (Ar–Ar dating; Smith et al. 1996), generating >60 km^3 of non-welded rhyolitic ash and pumice (Keller 1969; Allen 1998, 2001; Pe-Piper et al. 2005; Bachmann et al. 2010) covering an area ~5000 km^2 (Stadlbauer 1988). The young age of deposits, and their excellent preservation in the dry Mediterranean climate provides an exceptional opportunity to dissect such a unit using the latest analytical techniques in petrology and geochemistry. The KPT is best preserved on Kos, but is also exposed on the neighbouring Greek islands of Tilos, Kalymnos, Pachia and on the Turkish peninsula of Bodrum and Datça (Allen 2001). Isopach (Fig. 2.20), isopleths and transport direction data indicate that the vent areas for the KPT were situated in the bay between southwest Kos and Nisyros volcano. The eruption is inferred to have formed a caldera at least 6–11 km in diameter, and perhaps as much as 20 km (Allen 2001; Pe-Piper et al. 2005).

Ash-layers are found in deep-sea sediments 500 km southeast of Kos, near Cyprus (W-3 deep sea ash layer, Federman and Carey 1980). The source of this eruption and caldera can be inferred on the basis of the distribution of extensive lag deposits as between the present southeast Kefalos/Kos coast and the islets of Pergousa and Pachia in the area of the present day island of Yali in the Pachia-Pergousa Basin.

A presumed large flooded caldera in this area has been probably obliterated by post caldera activity. Younger eruptions, which built up Nisyros and Yali volcanic islands, as well as tectonic uplift and downfaulting in the complex horst-graben system have changed the original morphology of the environment.

The KPT eruptive stratigraphy has been studied in detail by several authors (Allen 1998, 1999, 2001; Allen and Cas 1998a, b; Allen and McPhie 2001).

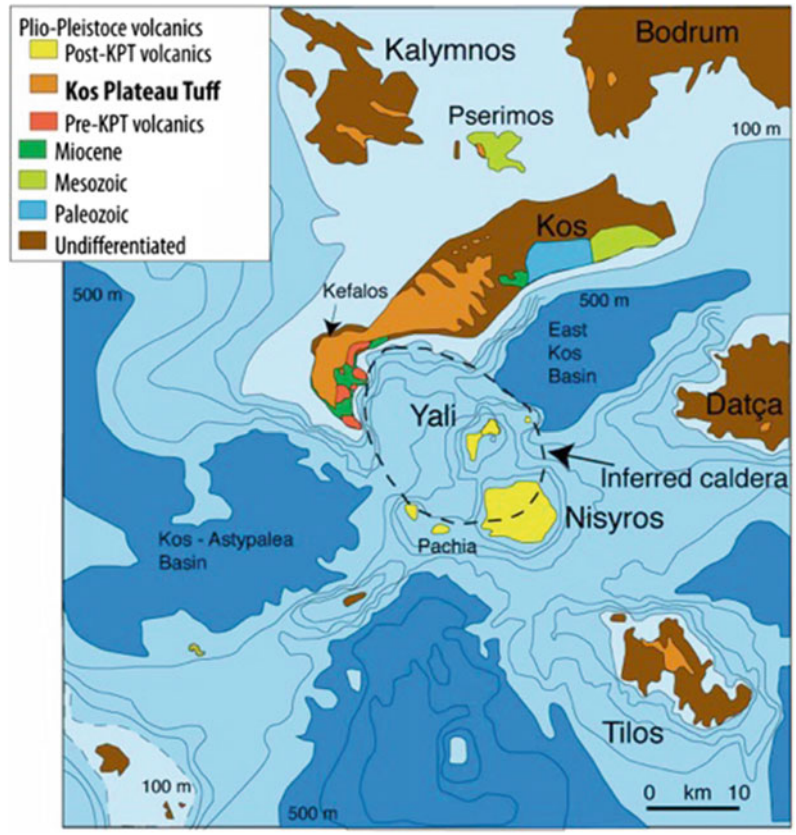

Fig. 2.19 The Pleistocene (Calabrian) Kos Plateau Tuff (KPT) covered an area of $\sim$5000 km^2 with pumice flows; modified after Pe-Piper et al. (2005) and Bachmann (2010)

The eruption began and ended with phreato-plinian activity (Units A, B and F in Figs. 2.21, 2.24 and 2.25: Allen and Cas 1998a; Allen 2001). As the eruption waxed, the style of activity changed to magmatic-volatile-driven, with the generation of relatively widespread, topographically-controlled ignimbrites (Unit D). Most of the volume was erupted during the climactic caldera-forming phase, which produced a widespread, highly energetic pyroclastic flow (Unit E). The change in fragmentation style from phreato-plinian to pre-climactic and climactic is recorded in the morphology of the pumice clasts and ash shards.

The KPT is a non-welded pyroclastic deposit, consisting of juvenile components (pumice clasts, glass shards, crystal fragments) and lithic fragments (some up to 3–4 m in diameter) from different provenance (mainly andesite to dacite clasts, but also rare occurrences of schist, metabasalt, sandstone, limestone and rhyolite; Smith et al. 2000; Allen 2001). During the climactic part of the eruption (unit E, Fig. 2.23), granitic clasts, some containing 10–20 vol.% interstitial melt, were also erupted. These are juvenile, or co-magmatic clasts, as they have the same zircon age range as the pumice samples (Bachmann et al. 2007). Several types of pumices can be distinguished on the basis of macroscopic characteristics (Allen 2001). Three petrologic useful categories can be isolated: (1) crystal-rich pumice (comprising both tube and frothy pumices), (2) crystal-poor pumices, and (3) banded (or grey) pumices. The texture, whole-rock composition, and mineralogy of each type of juvenile clasts are detailed below (see Electronic Supplementary Material Appendix 1 for pictures of thin sections and hand samples of all four pumices in the KPT).

Crystal-rich pumices have crystal contents between $\geq$25 and 35 vol.% crystals (Bouvet de Maissonneuve et al. 2008) and by far dominated the clast assemblage (>99%). Crystal-poor pumices (<5–10 vol.% crystals), while the are

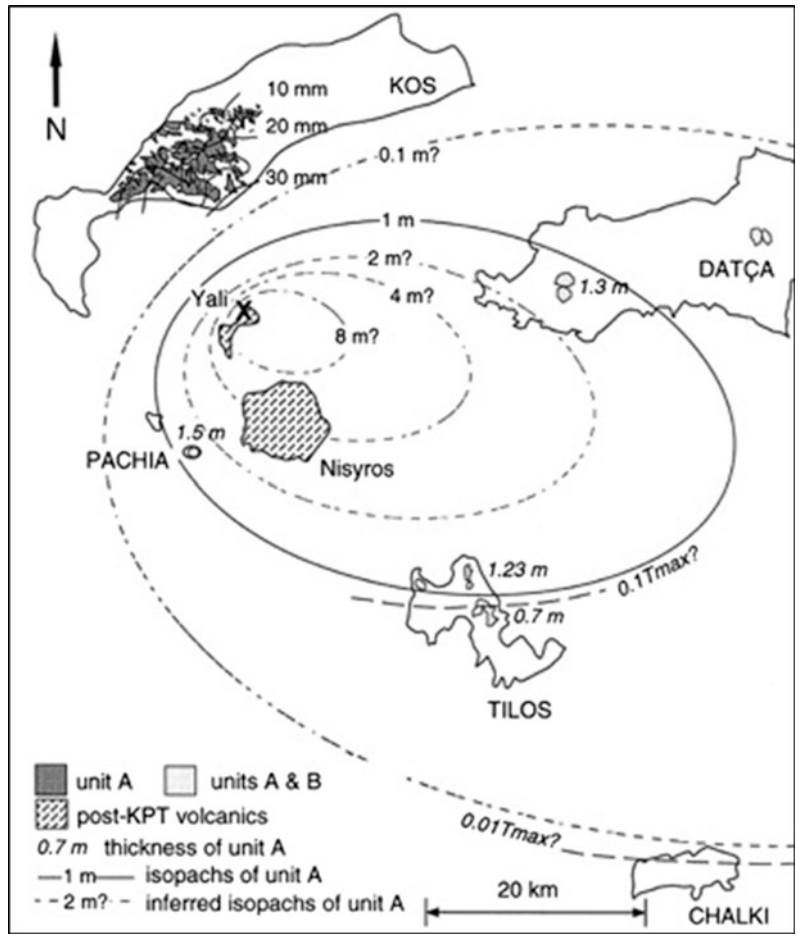

Fig. 2.20 The Kos Plateau Tuff: regional distribution of the pyroclastic deposits *A* and *B*, and extrapolated isopachs of unit *A*. *Units A* and *B* cover the central Kos plateau north of the inferred vent *X* in the area of Yali. *Unit A* occurs also south and east of the vent on Pachia, Tilos and the Datça peninsula. The 1 m and 30, 20 and 10 mm isopachs of *unit A* are shown, along with the inferred 0.1, 2, 4, and 8 m isopachs. Estimated 0.1 and 0.01 Tmax are also shown. *Copyright note* modified after Allen and Cas (1998a)

only found in the early parts of the eruptions (subunits A and B), while grey and banded pumices can be found throughout the eruption sequence, although they are more conspicuous in units D and E (Bachmann 2010). The main mineral phases are, in decreasing order of abundance; plagioclase, quartz, sanidine, and biotite. Some pyroxene and rare olivine can be found in grey and banded pumices (Piper et al. 2010). Accessory phases include Fe–Ti oxides, apatite, zircon and monazite.

Many juvenile, granitic enclaves, can be found in the KPT (mostly in unit E: Keller 1969; Allen 2001; Bachmann 2010). These granitic enclaves are texturally variable (Bachmann 2010); most contain glass at the boundaries between minerals (that has vesiculated, making samples very friable) but others are holocrystalline (no interstitial melt). The enclaves show a textural gradation from coarse-grained (with mm-sized crystals) to fine-grained, through intermediate bimodal textures. Enclaves are typically finer-grained holocrystalline, suggesting more rapid cooling. When interstitial melt is present, it is mainly located at the grain boundaries, forming meandering channels. In some places, crystals faces are found against glass, suggesting late growth from a residual melt rather than partial melting. Melt content varies from 0 to ~40 vol.%, (Keller 1969; Bachmann 2010).

Combined textural, petrologic and geochemical information (Bachmann et al. 2007; Bachmann 2010) suggest that (1) the system evolved dominantly by crystal fractionation, with limited amounts of crustal assimilation, from (mostly non erupted) more mafic parents, (2) the magma

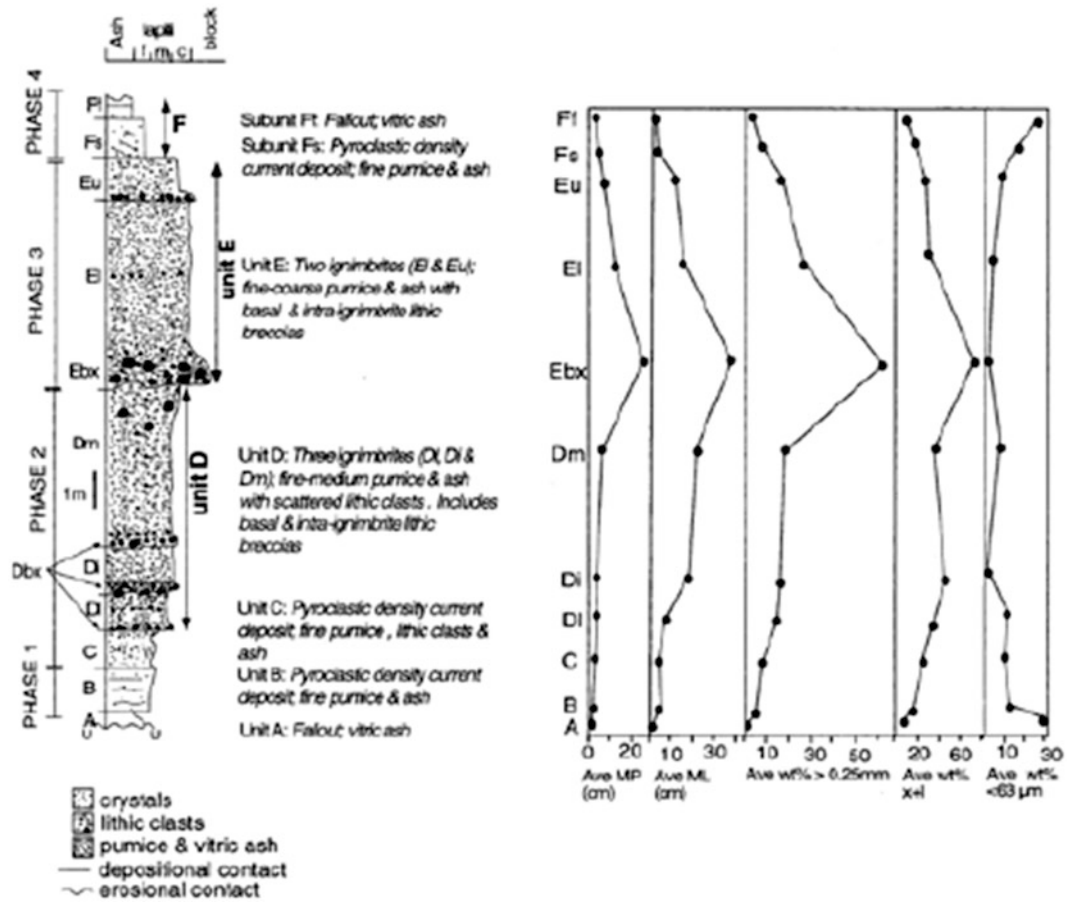

Fig. 2.21 Composite graphic stratigraphic log of the KPT from showing the six units and four eruptive phases of the KPT. '*Dry*' refers to the dry magmatic volatile-driven explosive phases and '*wet*' refers to the phreatomagmatic phases. *Copyright note* Allen et al. (1999)

reservoir grew over $\geq$250,000 years at shallow depth ($\sim$1.5–2.5 kb) and magma was mostly stored as a volatile-rich crystalline mush close to its solidus ($\sim$670–750 °C), (3) the eruption occurred after a reheating event triggered by the intrusion of hydrous mafic magma at the base of the rhyolitic mush. Rare banded pumices indicate that the mafic magma only mingled with a trivial portion of resident crystal-rich rhyolite (Piper et al. 2010); most of the mush was remobilized following partial melting of quartz and feldspars induced by advection of heat and volatiles from the underplated, hotter mafic influx, as is commonly seen for crystal-rich deposits in many volcanic provinces around the world (Pallister et al. 1992; Nakamura 1995; Murphy et al. 2000; Couch et al. 2001; Bachmann et al. 2002; Molloy et al. 2008; Cooper and Kent 2014; Kiss et al. 2014). Figures 2.3, 2.24 and 2.25 represent various outcrops along the southern coast of Kos Island between Kefalos and Kardamena.

Fig. 2.22 The Pleistocene "Kos Plateau Tuff" seen from south (Kefalos). In the foreground Kamari beach and the islet of Kastri (ignimbrite relict). In the background the 161,000 years ignimbrites of the Kos plateau; Mount Dikeos (842 m) in the far background. *Photo* V. Dietrich

Fig. 2.23 The "Kos Plateau Tuff" on *top* of the Pliocene pumice deposits hillside of Kefalos (north of the upper village of Kamari), which constitutes unit E in the upper 10–15 m *top*, however with limited unit D, units A and B missing (Stadlbauer 1988). *Photo* V. Dietrich

Fig. 2.24 The "Kos Plateau Tuff" exposed in an isolated up to 100 m high table mountain west of Kardamena close to the southern coast of Kos island, presumably representing the most proximal facies near the original source. Units A to D representing the 1st and 2nd cycles of the eruption are present: units A and B form the base, covered with vegetation, C and D constitute the monumental *upper part*, C being a 8 m thick wavy-massive non-welded ignimbrite, overlain by 8 m thick fine-grained ignimbrite, which passes into a massive lithic-rich ignimbrite facies at the *top*; characterised by the erosional holes. *Photo* V. Dietrich

Fig. 2.25 Detail of the transitional zone between units A, B and E in the central part of Kos island (roadcut through the Plaka forest approximately 2 km west of the airport). 1–2 m of unit B is represented by fine wavy-stratified facies, discordantly overlain by an ignimbrite containing lithics of varies size at the base. *Photo* V. Dietrich

2.3.3.3 Nisyros Volcanic Field

The submarine region of Nisyros, extending from Kos in the north to Tilos in the south, constitutes a large tectonic graben divided into several basins with 600 m average depth (Fig. 2.26). This basin is penetrated by a complex volcanic group forming the volcanic islands of Nisyros, Pachia, Pergousa, Yali and Strongyli and small intra-volcanic basins with less than 350 m of depth. The volcanic formations are found at 680 m depth (Avyssos in the Eastern Kos Basin) and at the eastern base of the Strongyli volcanic cone up to 700 m of altitude (rhyodacitic domes of Prophitis Ilias on Nisyros) creating a total volcanic relief of more than 1400 m (Nomikou and Papanikolaou 2011). This middle zone with an ENE-WSW general trend from Kondelioussa in the west to Datça Peninsula to the east represents an uplifted tectonic horst above sea-level, the pre-Pleistocene Alpine basement in Kondelioussa Island together with a voluminous cover of volcanic and volcano-sedimentary rocks of the Nisyros volcanic field, separating the large graben zone into two adjacent grabens to the north and to the south. Such a large, recent volcano-morphological situation demonstrates the powerful geodynamic processes of the eastern edge of the active South Aegean Volcanic Arc.

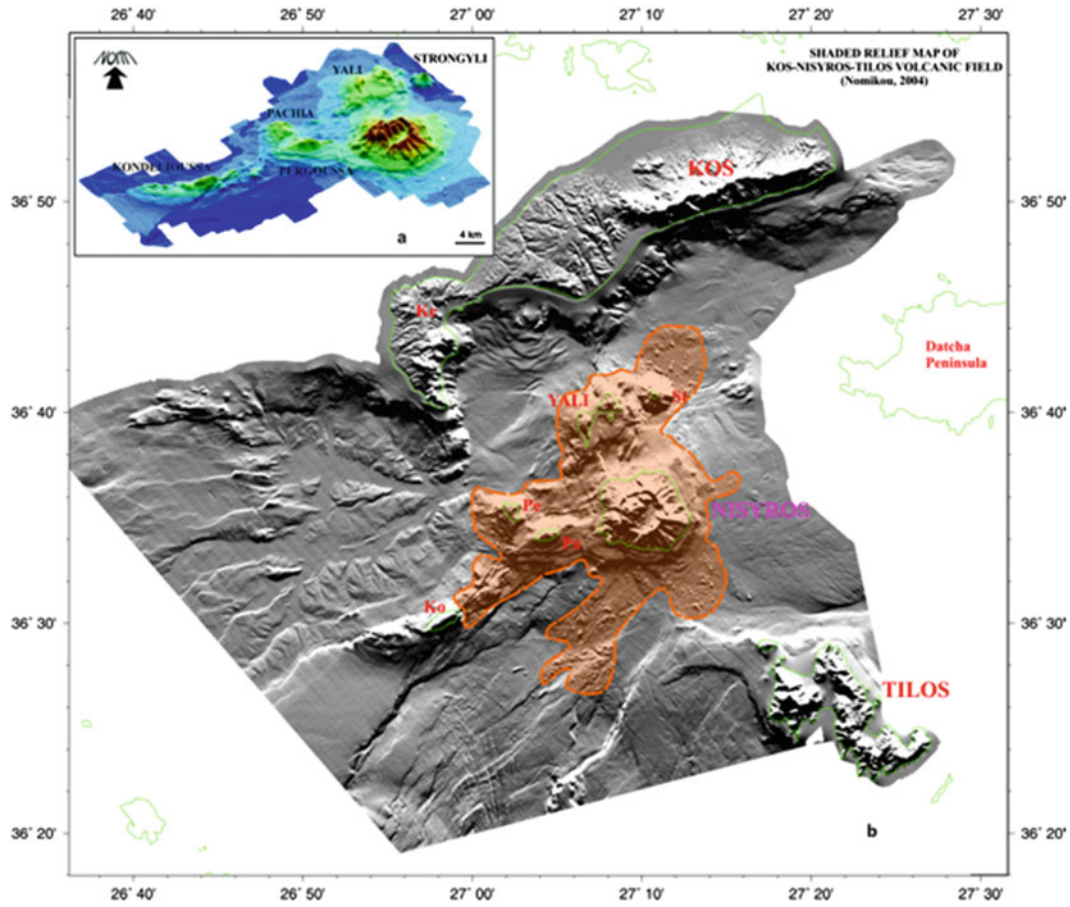

Fig. 2.26 *Shaded onshore* and *offshore* topographic relief map of the Kos-Yali-Nisyros Volcanic Field based on data obtained from multi-beam bathymetric survey during 2000–2002 and combined with onshore hypsometric data. The volcanic outcrops and the resulting volcanic relief around Nisyros volcano are contoured by orange line. *Ko* Kondelioussa, *Pe* Pergousa, *Pa* Pachia, *St* Strongyli, *Ke* Kefalos; (Nomikou 2004; Nomikou and Papanikolaou 2010b; Nomikou et al. 2013a)

A number of volcanic centers exist around Nisyros (Fig. 2.26), which developed within the neotectonic graben, in shallow areas. These are: (1) The Nisyros caldera with a top of the rim at + 580 m and a bottom at +80 m; (2) The Yali volcanic cone which exhibits a partly submerged caldera (bottom ≈ 300 m, top +170 m); (3) The Strongyli volcanic cone, which starts from 650 m depth of the seafloor up to +120 m; (4) The submarine Avyssos Crater northeast of Strongyli in the depth of ≈ 670 m up to ≈ 590 m; (5) The Pergousa volcanic cone (bottom ≈ 400 m, top +100 m); (6) The domes of Prophitis Ilias (bottom ≈ 270 m, top +698 m); (7) The volcanic domes of Pachia islet (bottom ≈ 250 m, top +150 m); (8) The submarine volcanic domes to the east of Kondelioussa islet (bottom ≈ 400 m, top ≈ 80 m).

2.3.3.4 Yali Island

The Yali volcanic island, an Upper Quaternary rhyolitic edifice with a max. altitude of 165 m, is located north of Nisyros Island and exhibits parts of a submerged caldera which are dissected by a post-caldera N-S fault (Figs. 2.27 and 2.29). Yali seems to represent the youngest volcanic centers of the Nisyros volcanic field. The south-western part of the island is made of two pumice

Fig. 2.27 Aerial view from northeast of the *hourglass shaped* island of Yali. In the *background* the stratigraphically older part made up by the voluminous rhyolitic pumice deposits, in the *foreground* the Kamara perlitic obsidian dome and flows covered by pumice breccia and pyroclastic fallout; in the southern part the isolated islet of Ag. Antonios (Fig. 2.33), which consists of an andesitic lava covered by a thin paleosol, reworked lower pumice and Kamara pyroclastics. *Photo* Snipe view Wikipedia

Fig. 2.28 The Yali pumice deposits are exposed as 60–100 m high cliffs, dipping 10° towards SW and comprise a minimum volume 0.3 km^3, with the base and submarine portion unknown. The deposits are dissected by normal faults with max. Displacement of up to 100 m: dominantly trending NW–SE and subordinately E–W and NE-SW (Fig. 2.29). *Photo* V. Dietrich

successions, the "Lower and Upper Pumice" (Figs. 2.28 and 2.36), divided by silty sandstones, whereas the north-eastern part of Yali comprises rhyolitic obsidian-perlitic lava domes and flows at 24 Ka (Wagner et al. 1976), which are locally covered by pumice deposits, equivalent to the upper pumice of western Yali. Marine terrace deposits, rich in clasts of the Lower Pumice and marine fossils in calcite cement separate these two volcanic parts of the island (Fig. 2.29).

The islet south of Yali, Ag. Antonios (Figs. 2.29, 2.36, 2.37 and 2.38) is built up by gray dacitic porphyritic lavas, with phenocrysts

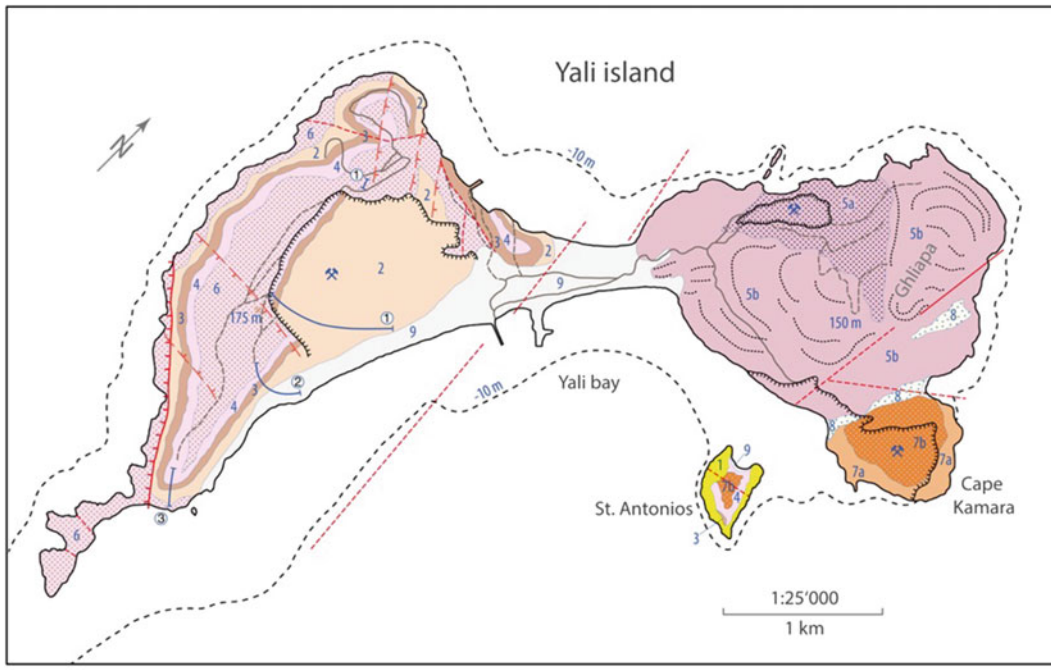

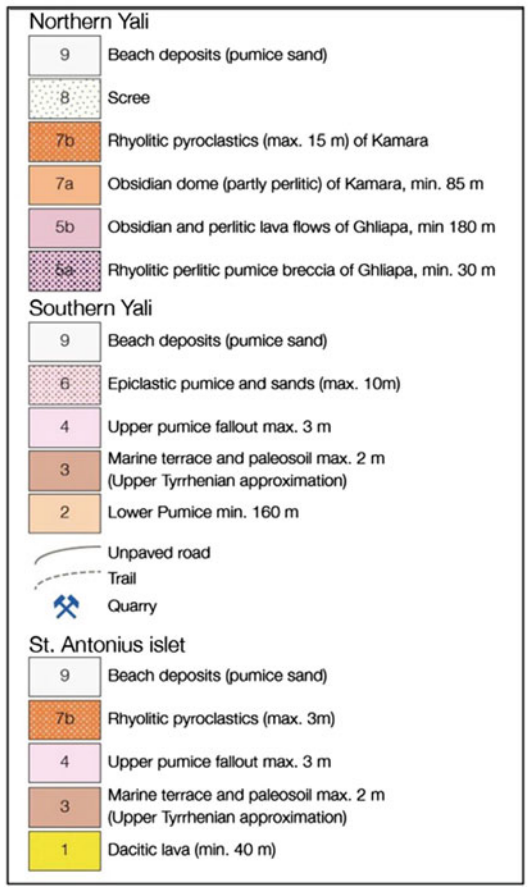

Fig. 2.29 Geological map of Yali Island and Ag. Antonios islet (geology *redrawn* and modified after "Nisyros sheet", geological map of Greece 1:25,000, IGME 2003). *Blue lines* with *encircled numbers 1*, *2* and *3* from north to south refer to lithostratigraphic columns of Fig. 2.36 (Allen and McPhie 2000)

Fig. 2.30 Obsidian flow (7a) overlain by rhyolitic breccias (Fig. 2.40) and topped by a pyroclastic pumice fall and surge succession (7b) in the eastern coastal cliffs of Cape Kamara Yali. *Photo* V. Dietrich

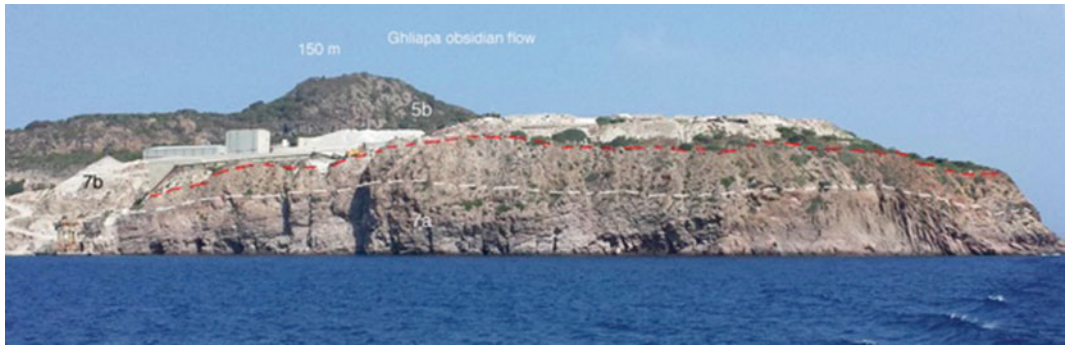

Fig. 2.31 Obsidian flow (7a) overlain by rhyolitic breccias and topped by a pyroclastic pumice fall and surge succession (7b) in the southern coastal cliffs of Cape Kamara Yali; buildings: perlite exploitation and processing company. In the *background* the Ghilapa obsidian flow (5b). *Photo* V. Dietrich

of plagioclase, clinopyroxene, orthopyroxene, and magnetite, rich in andesitic enclaves.

The rhyolitic obsidian-perlite lavas and small endogenous domes of Kamara (Figs. 2.30, 2.31 and 2.32) contain sparse phenocrysts of plagioclase, hornblende, biotite, corroded quartz and magnetite and are covered by up to 8 m of bedded fallout deposits with parallel horizons of angular lapilli and ash of perlitic aphyric pumice. Phenocrysts are plagioclase, hornblende, clinopyroxene, biotite and magnetite (Figs. 2.34 and 2.35).

Allen and McPhie (2000) divided the Yali pumice breccia into a "Lower Pumice" of submarine origin and into an "Upper Pumice" of subaerial origin. The transition between the two major units and the detailed lithostratigraphy of the Upper Pumice is shown in Fig. 2.30, as well as in the outcrop photographs (Figs. 2.36, 2.37 and 2.38).

The white, rhyolitic, aphyric "Lower pumice breccia", varying in size from coarse ash to boulder, moderately-well sorted and diffusely-stratified reaches an outcropping thickness of 150 m. The larger clasts are prismatic with quenched surfaces and internal polyhedral joints. The smaller pumice clasts, although compositionally, texturally, and prismatic, lack the quenched surfaces. Characteristic minerals of the white pumice are rare microphenocrysts of plagioclase and corroded quartz, whereas a rare percentage (3–5%) of gray pumice contains abundant microphenocrysts of plagioclase, clinopyroxene, orthopyroxene, hornblende and

Fig. 2.32 *Upper part* of rhyolitic obsidian lava and breccia at the southern shore of Kamara. *Photo* V. Dietrich

Fig. 2.33 Ag. Anthonios islet, view from North. The base is made up of at least 40 m dacitic lava, covered by 3 m of upper pumice fallout (*above beach*) and thick rhyolitic pyroclastics. *Photo* V. Dietrich

magnetite. These deposits are gradationally overlain by a 0.3 m thick, fossiliferous limestone and by a sandy brownish bioclastic sandstone (Fig. 2.38).

The ≤ 3 m thick well-sorted and cemented angular fallout lapilli of the "Upper Pumice" is comprised of white (70%) and gray pumice and obsidian fragments. Microphenocrysts are plagioclase, hornblende, clinopyroxene and magnetite, as well as rare muscovite and quartz. Federman and Karey (1980) assumed an age of 31 Ka correlating the Upper pumice with a tephra horizon in deep-sea sediment cores. The paleosol is covered by redeposited epiclastic pumice in a shallow marine environment containing rounded clasts, subangular obsidian fragments, and shells. The uppermost part turns into a sandy paleosol, rich in ceramic potshards and obsidian blades, witnesses of a Neolithic settlement on the island.

Allen and McPhie (2000) proposed for the Yali pumice breccia formed via a submarine phreatomagmatic eruption (Fig. 2.39): The lavas extruded with phreatomagmatic explosions and passive disintegration of large quenched pumice clasts. Deposition occurred continuously and involved simultaneous resedimentation from a more proximal site on the seafloor.

Fig. 2.34 Quarried rhyolitic breccia, partly perlitic, at the *top* of the large obsidian flow in the northern part of Kamara. *Photo* V. Dietrich

Fig. 2.35 *White* and *gray* pumice fallout deposits at Kamara containing interbedded fine ash layers and layers of angular perlitic pumice lapilli, which are exploited. *Photo* V. Dietrich

None of the underwater slopes of Yali had been explored prior to the Nautilus cruise NA011 in 2010. The ROV Hercules was used to explore the eastern flank of Yali identified on the multibeam map of the area (Nomikou 2004). The outcrops of volcanic rocks at the sea bottom are covered by heavy encrustations or by biogenic and concreted layers. ROV exploration of the eastern flank revealed spectacular wave type structures in the sediments on the seafloor (ripples) with dark sediments on the ridges of the undulations and light sediments in the troughs (Figs. 2.15 and 2.16). Some linear fractures were explored at various depths (Nomikou et al. 2011).

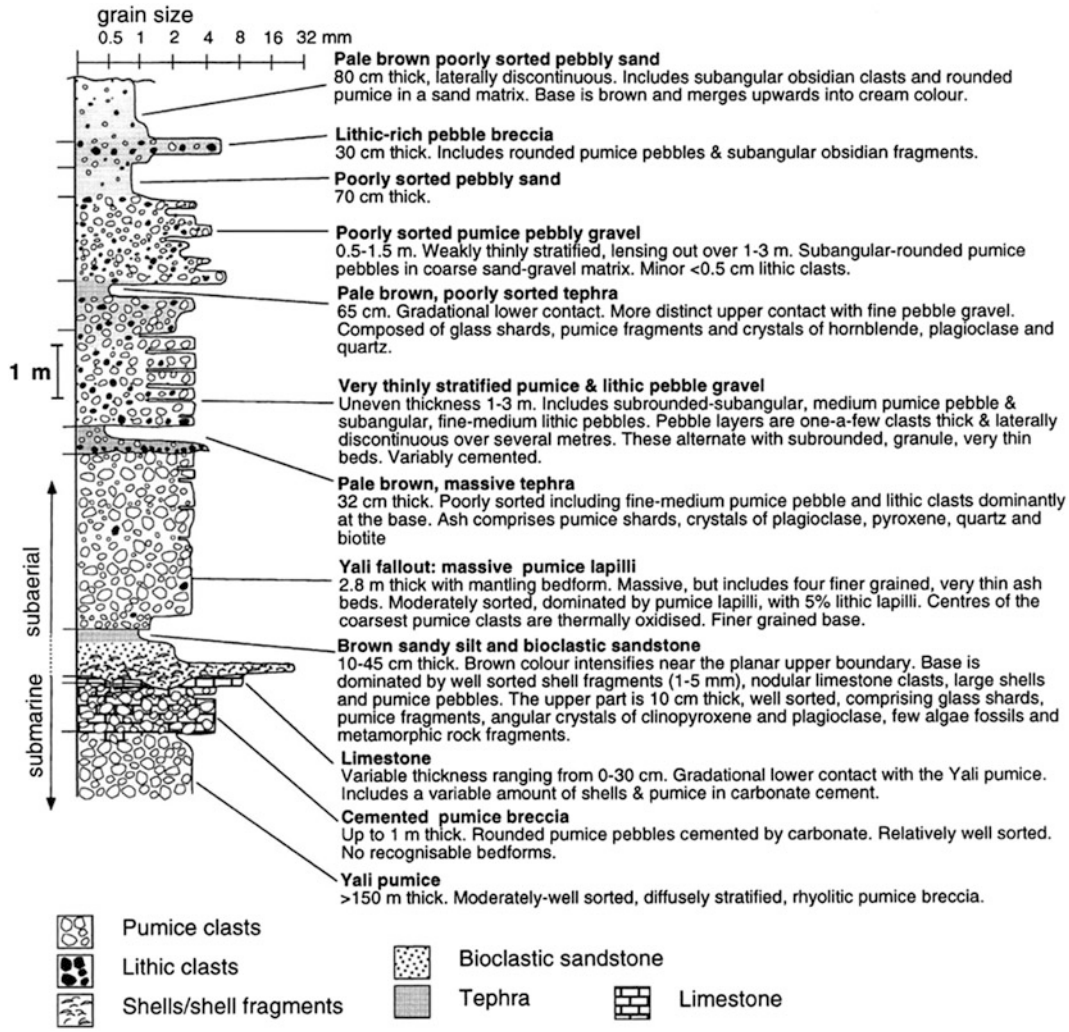

Fig. 2.36 *Copyright note* Lithostratigraphic columns through the upper part of the Yali pumice breccia at cross section 3 (Fig. 2.29) and the overlying sedimentary and volcanic units after Allen and McPhie (2000). The sequence represents an upward progression from submarine to subaerial depositional environments. Locality in the uppermost southwestern parts of the pumice quarries (Figs. 2.29, 2.37 and 2.38)

Fig. 2.37 Transitional zone between the *lower* and *upper* pumice sequences close to the *top* of the southwestern quarry walls (Figs. 2.28 and 2.29). From *bottom* to *top*: approximately 2 m of "lower pumice breccia", 1 m of *white* cemented pumice breccia, up to 0.5 m of *brown* sandy silt and bioclastic sandstone, up to 3 m of *white* "Yali fallout" of pumice lapilli with thin ash beds, and up to several meters of poorly sorted reworked pumice pebble gravel including lithic clasts. The *top* is covered by redeposited epiclastic pumice from a shallow marine environment containing rounded clasts, subangular obsidian fragments, and shells and passes up into a sandy paleosol, rich in ceramic pot shards and obsidian blades, witnesses of a Neolithic settlement on the island. *Photo* V. Dietrich

Fig. 2.38 *Brown* sandy silt and sandy *brownish* bioclastic sandstone dividing the *lower* and *upper pumice* sequences (see Fig. 2.36), unconformely overlain by *white* "Yali fallout" of pumice lapilli; locality close to the *top* of the southwestern quarry walls. *Photo* V. Dietrich

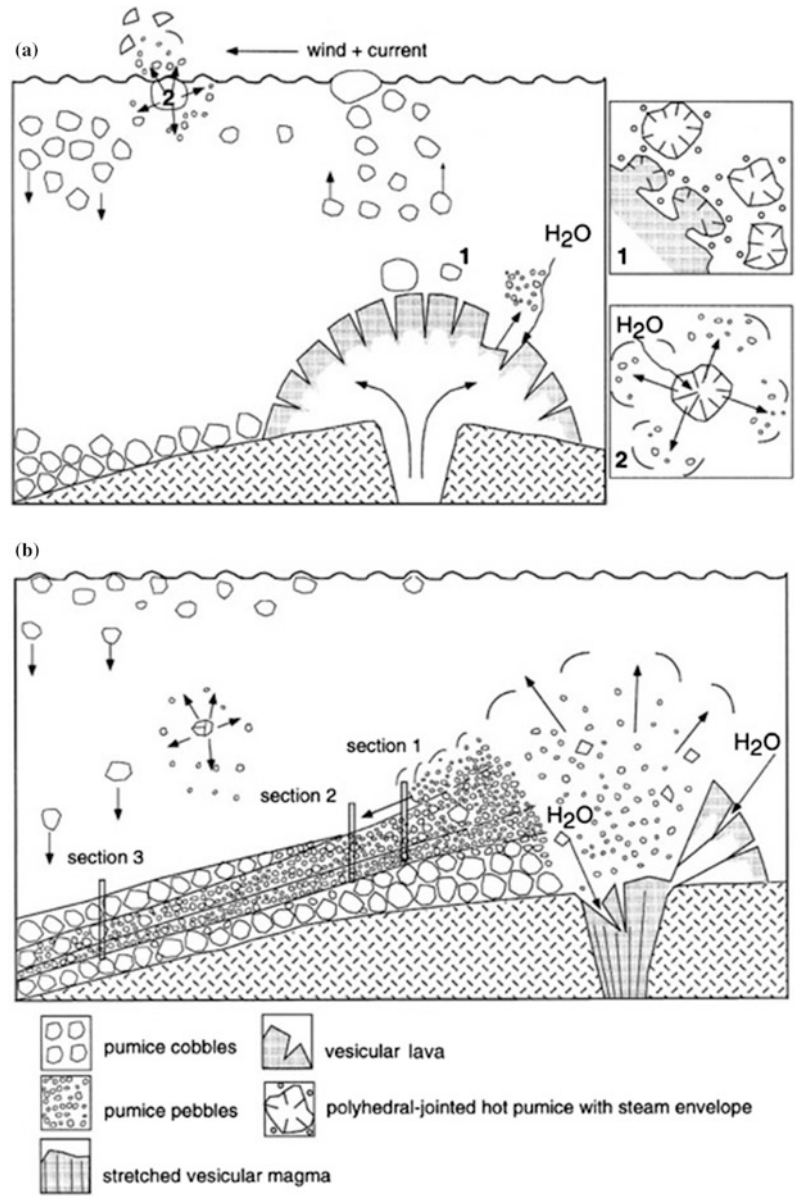

Fig. 2.39 *Copyright note* Submarine eruptive and depositional model for the generation of the Yali pumice breccia (Allen and McPhie (2000). **a** Shallow submarine effusive state with dome formation including simultaneous degassing, vesciculation, expansion and fragmentation of rhyolitic lava; **b** during pulses of stronger magma ascent and degassing explosive phreatomagmatic activity occurred creating an unstable apron of smaller pumice clasts that was continuously subjected to downslope resedimentation by gravity flows

2.3.3.5 Strongyli Volcano

The Strongyli volcanic cone is located north of Nisyros emerging from 650 m depth at the sea-floor with a diameter of 3.5 km and reaching the top of Strongyli islet at 125 m above sea level (Fig. 2.40). Its ideal cone-shaped morphology with up to 50° steep flancs contains a 300 m wide crater at the top. At 50 m altitude conglomerates indicate recent uplift. The entire edifice is made up of gray andesites and minor pyroclastics. The age of formation is unknown, but must be older the Yali edifice, since rhyolitc pumice from Yali with up to 2 m thickness occurs in several morphological depressions and pockets.

Submersible dives with Thetis of Hellenic Center for Marine Research (HCMR) in 2000 in the NW flank of the volcanic cone discovered an underwater crater of several meters of diameter

Fig. 2.40 The Strongyli volcanic cone seen from southeast. The broken flank exhibits highly oxidized reddish lava surfaces at lower levels. Pyroclastic deposits cover the upper slopes. *Photo* V. Dietrich

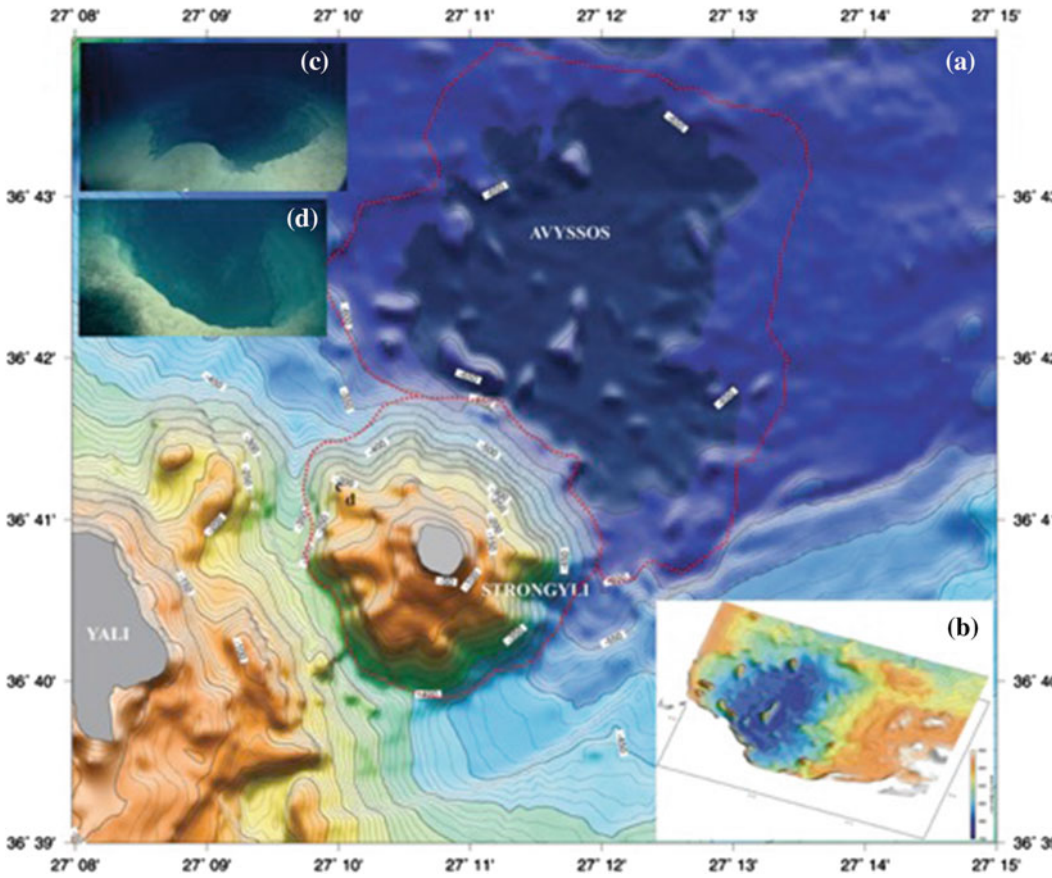

Fig. 2.41 **a** Swath bathymetric map of Strongyli and Avyssos volcanoes using 10 m isobaths. *Red dotted lines* delineate the submarine volcanic outcrops; **b** 3-D map of the submarine caldera of "Avyssos" at depths between 600 and 680 m, using 2 m isobaths; **c** underwater crater observed during the dive of submersible THETIS in 2000 at 192 m depth, on the northwestern slopes of Strongyli (point **c**); **d** underwater crater observed at depths ranging between 193 m (*at the top*) and 199 m (*at the bottom*) during 2010 exploration with ROV. The location (point **d**) is very close to the previous crater. A 6 m profile observed within the craters is made of layers of alternating pumice and ash. Nomikou 2004; Nomikou et al. (2013a, b)

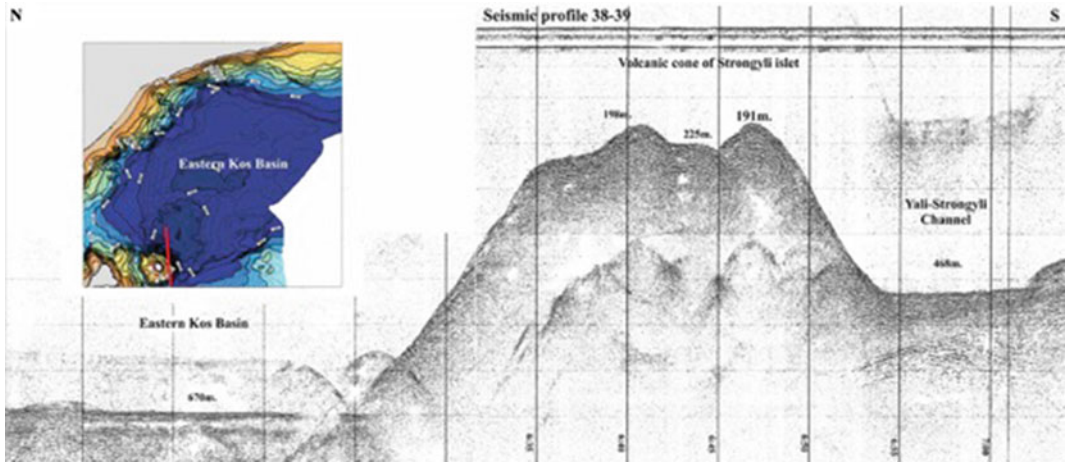

Fig. 2.42 Representative air-gun profile from the area near Strongyli islet, showing characteristic hyperbolic reflectors corresponding to possibly submarine extinct cinder cones (Nomikou 2004; Nomikou and Papanikolaou 2010b; Nomikou et al. 2013a, b)

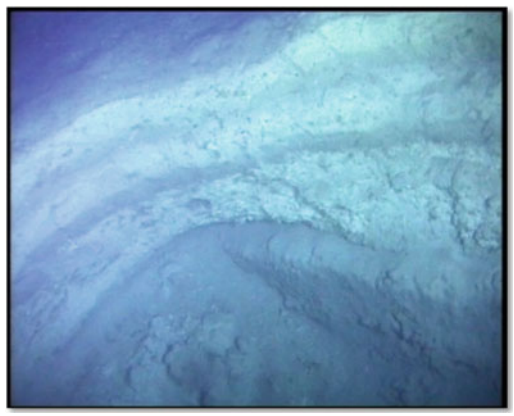

Fig. 2.43 Part of the volcanic crater (8–10 diameter and 3,5–4 m height) at the Strongyli volcano at 240 m depth. *Photos* were taken by THETIS during 2000; (Nomikou 2004)

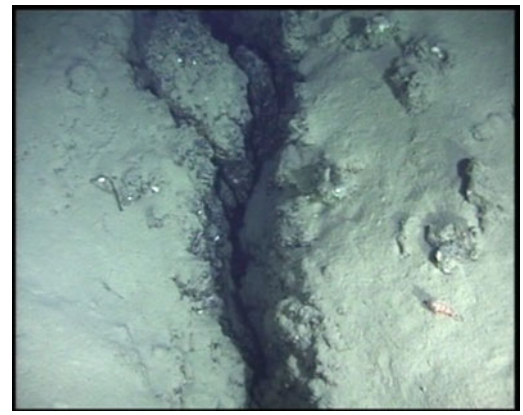

Fig. 2.44 Open fracture across the slopes of the Strongyli volcanic cone at 390 m depth. *Photos* were taken by THETIS during 2000; (Nomikou 2004)

(Fig. 2.41c and 2.43) and several open fractures across the slope (2.44). Three transects of Strongyli's flanks were carried out using the ROV Hercules and Argus during the Nautilus cruise NA011 in 2010. These transects provide important information about the volcanic stratigraphy, underwater morphology, and structural features of the volcanic cone, such as fractures in different directions ranging mainly between NE-SW to E-W. The walls of the fractures are made of heavily cemented bio-encrusted lava. Steep lava walls with evidence of shear are observed at the western part, covered by bio-encrusted sediments. Other outcrops at the northern slopes are covered by sediments with numerous small slide scars and most of the lava walls are heavily cemented and encrusted. New craters without any sign of hydrothermal activity,

aligned in the ENE-WSW direction, were discovered at depths around 190–200 m (Fig. 2.41d). The original morphology of the crater region is partially obliterated by thick pumice layers. An air-gun profile 38–39 (Fig. 2.42) across Strongyli islet shows the different level of the Avyssos abyssal plain (670 m) with respect to the Yali-Strongyli channel (470 m) on both sides of the Strongyli volcanic cone. An acoustically semi-transparent seismic unit with internal chaotic reflectors and diffraction hyperbolae appears either below the lower sequence or emerge above them in some areas between Nisyros and Yali and especially near the Strongyli islet (Nomikou and Papanikolaou 2010b; Nomikou et al. 2013a, b). These reflections reveal volcano-sedimentary deposits and volcanic domes.

2.3.3.6 Avyssos Crater

The largest underwater volcanic crater is located NE of Strongyli islet and was named "Avyssos Crater" because of its depth (600–700 m). This locality may correspond to a vent, from where the large volume of the "Kos Plateau Tuff" erupted. Since its discovery from swath mapping and air-gun seismic profiling, it has not been investigated until the Nautilus cruise NA011 in 2010 (Nomikou 2004a). The ROV Hercules was used to explore the slopes of the crater and the volcanic domes, which were identified on the base of detailed bathymetry obtained from multibeam data (Fig. 2.41a).

The "Avyssos Crater" dimensions are 3 km in the NW-SE direction and 4 km in the NE-SW direction. A hill of about 1 km length occurs at the center of Avyssos with relief of about 60–70 m, representing later intrusions of volcanic rocks within the almost planar base of the caldera (Fig. 2.41b). The stereographic diagram of Avyssos was constructed with 2 m isobaths to demonstrate the geometry of the volcanic structure. The peak of the central volcanic dome lies at 610 m depth, rising 66 m above the planar base of the caldera, which is at 676 m depth. The caldera rim lies at about 630 m depth forming a submarine circular cliff of 40–50 m topographic difference.

Seismic profiles had shown that there are only a few meters of sediment overlying the volcanic formations. The exploration of the Avyssos Crater showed that it is covered with fine-grained sediment, full of bioturbation holes and mounds without any evidence of hydrothermal activity. A few samples were collected from the intra-caldera volcanic hills, where the lavas are primarily cemented together with consolidated sediment bearing a black crust on the surface. Volcanic rocks were also sampled from the southern part of the crater.

2.3.3.7 The Volcanic Islets Pergousa and Pachia

The **Pergousa** volcanic edifice (Figs. 2.45 and 2.46) with altitudes between 65 and 83 m resembles in parts the pre-existence of a strato-volcano comprising weathered thick lava flows and domes of covered by pumice deposits of the Kos Plateau Tuff. The latter contain bivalves and biogenic remains, indicating their submarine deposition. Several monolithic blocks and pyroclastic deposits are interpreted as witnesses of a nearby collapse structure. The predominantly porphyritic lavas are of andesitic to dacitic composition. Characteristic mineralogical features are abundant, partially resorbed amphibole, biotite, large plagioclase phenocrysts (up to 1 cm) and two pyroxenes and magnetite. The interstitial groundmass is made up of sparse glass and microliths of plagioclase, pyroxene and magnetite. No pumices from Nisyros and Yali have been found on both islands, Pergousa and Pachia, which points to a subaqueous position during the time of the young plinian eruptions on Nisyros and Yali and to a very recent uplift to expose the Kos ignimbrite deposits.

At the northwest coast of Pergousa islet, a gray, 1 m thick tuffite, rich in sponge needles, occurs. Marine terraces, similar to those on Yali Island, crop out along the shoreline of Pergousa. They are made up from calcite cement and contain abundant marine shells.

The volcanic edifice of **Pachia** islet (Figs. 2.45 and 2.47) is similar to that of Pergousa.

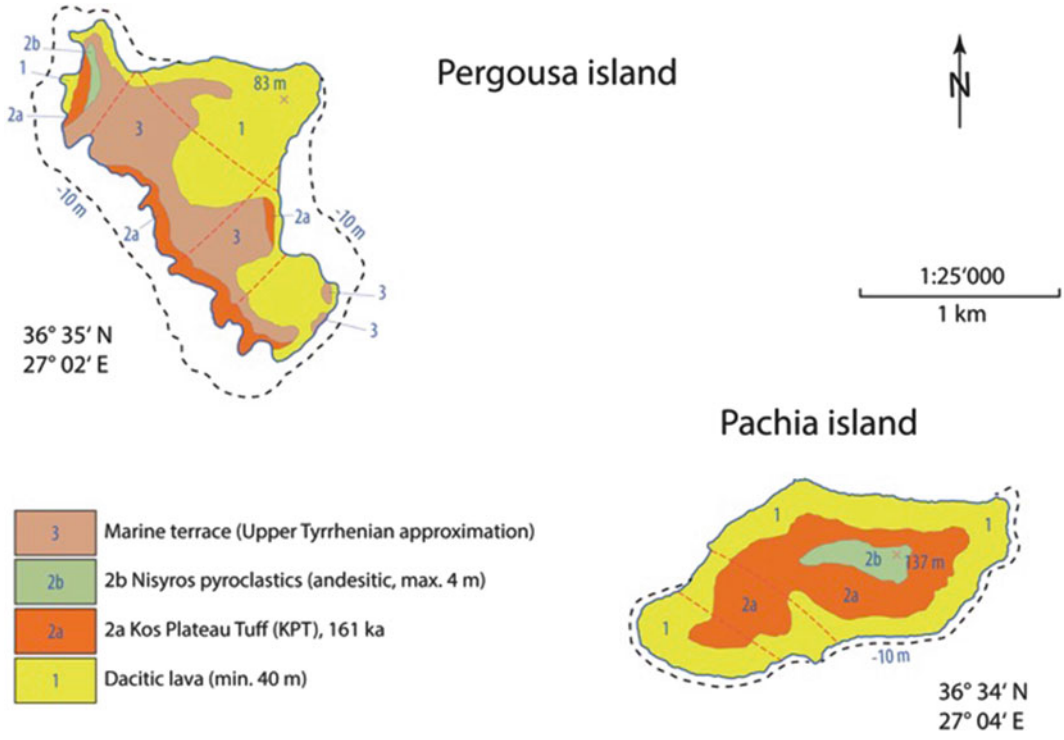

Fig. 2.45 Geological maps of the isletgs of Pergousa and Pachia (geology redrawn and modified after "Nisyros sheet"; geological map of Greece 1:25,000, IGME (2003)

Fig. 2.46 The volcanic islet of Pergousa (Google earth). The relief shows terraces covered with conglomerates. Gastropodes indicate a Pleistocene age. *Image* Google Earth

The basal dacitic lavas are overlain by two significant pumice sequences, (Fig. 2.45), which are correlated with the 161 ka Kos plateau eruption (Stadlbauer 1988; Keller et al. 1990; Vougioukalakis 1998). A lower, up to 3 m thick sequence consisting of fine white ash with sub-parallel or cross-bedding layering, which contain sparse rounded white pumice lapilli and thin matrix-supported layers with reverse grading. These sedimentary structures are interpreted

Fig. 2.47 The volcanic islet of Pachia. *Image* Google Earth

as depositions from surge pyroclastic density currents in sandwave phases.

The upper, ≤ 5 m thick sequence consists of a non-stratified lapilli tuff of white to gray pumice, which contains lithic blocks up to 1 m. One isolated lava block reaches a max. dimension of 6 m. Phenocrysts of sanidine, plagioclase, and biotite are present in the pumice. Equivalent deposits of the upper pumice sequence, up to 10 m thick, also occur in lower elevated parts of Pergousa islet.

The highest elevation part of Pachia islet is covered by a 1.5 m thick layer of gray coloured ash and fallout lapilli of andesitic composition containing a 10–15 cm thick with an interbedded paleosol, which may be correlated with an eruptive cycle during the period of the Nisyros composite stratovolcano (e.g. Nos. 18 and 19, Afionas tuff cone).

2.3.3.8 Kondelioussa Islet

Kondelioussa islet with an altitude of 100 m (Fig. 2.48a) forms a neotectonic horst consisting of Upper Jurassic (Malm) limestones (Fig. 2.45) is bordered by two marginal normal faults trending ENE-WSW, which have produced a subsidence of more than 1.3 km both towards the Western Nisyros Basin to the north and towards the Southern Nisyros Basin to the south (Nomikou and Papanikolaou 2010b). The above fault throw is the minimum displacement, as estimated from the depth of the two basins (about 600 m for Western Nisyros and more than 1000 m for Southern Nisyros) and the thickness of the sediments below the sea bottom overlying the Alpine Mesozoic formations. The Kondelioussa limestones are detected all over the offshore continuation of the horst structure towards the west-southwest, below a post-Alpine sedimentary cover of about 100–150 m. The overall morphology of the horst offshore forms a platform with sediments tilted by 15–20° to the SW.

The analysis of the detailed swath bathymetric map and the seismic profiling has revealed several volcanic domes northeast of the islet and southwest of Nisyros (Nomikou 2004, Nomikou et al. 2013a). Submersible dive with THETIS of HCMR in 2000 at the northern flank of one of the volcanic domes discovered an underwater crater of several meters of diameter at 430 m depth (Fig. 2.48d), and thus confirmed the volcanic origin of the domes (Papanikolaou and Nomikou 2001). In 2010 on the E/V Nautilus, ROV Hercules explored the same area and found large fields of feather corals with elasmobranches shark egg cases on them and patches of biogenic sediments with lots of sponges at 350 m depth. Other domes, northeast of Kondelioussa were explored in detail for the first time and their volcanic origin was confirmed but without any sign of hydrothermal

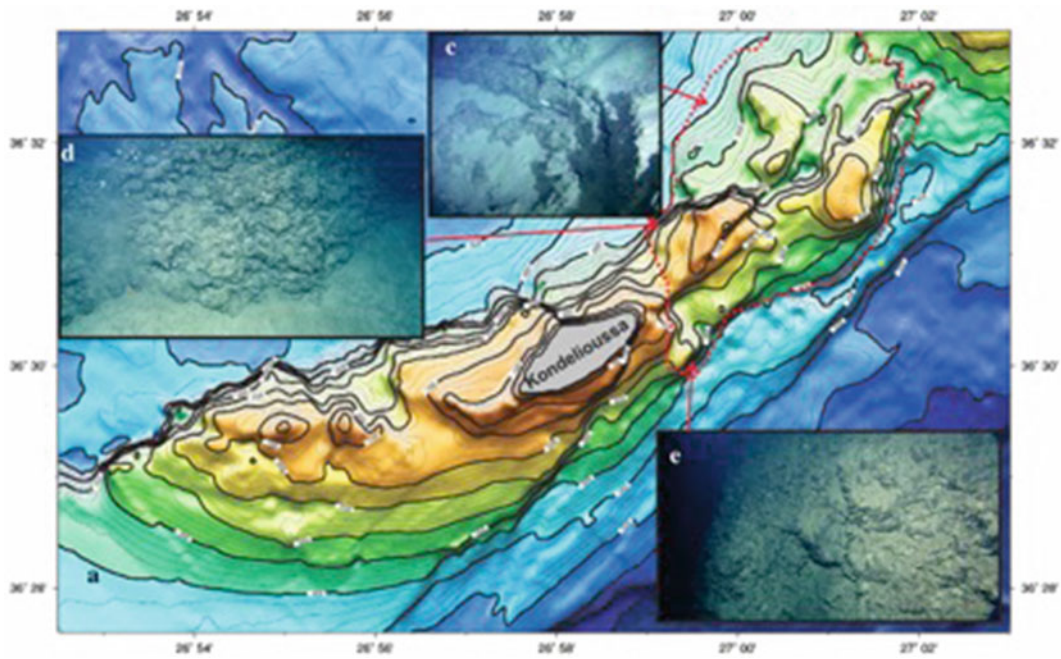

Fig. 2.48 **a** Swath bathymetric map of Kondelioussa. The volcanic outcrops are delineated by *red dotted line*; **b** air gun single channel profile showing the volcanic domes east of Kondelioussa islet. The volcanic rocks form a horst structure separating the Western Nisyros Basin to the north (416 m) from the Southern Nisyros Basin to the south (522 m); **c**–**e** *Photos* were taken by THETIS during 2000 (crater at point **c**: and by ROV "Hercules" during 2010, showing steep vertical northern flank of the volcanic dome, NE of Kondelioussa at 330 m depth (point **d**: and large steep shear wall of lava covered by bio-encrusted sediments south of Kondelioussa (point **e**); Nomikou (2004), Nomikou et al. (2013a)

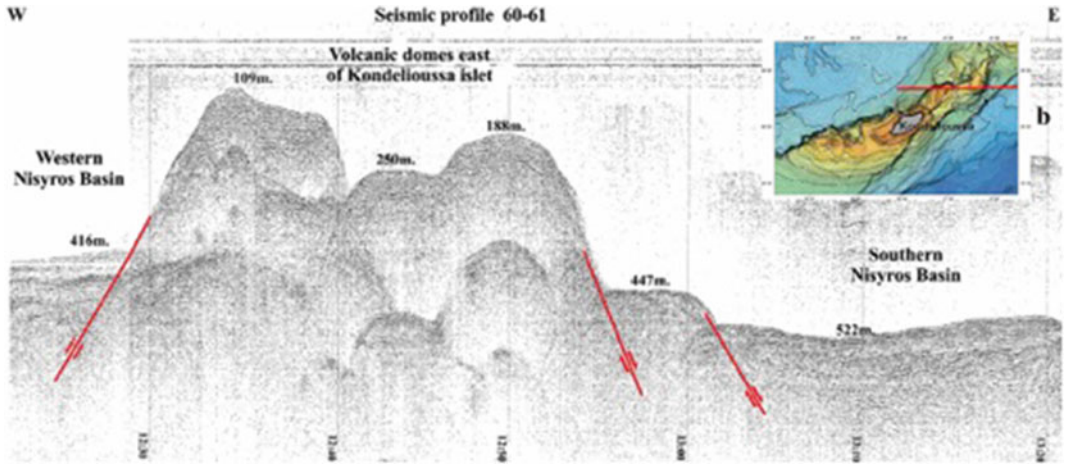

Fig. 2.49 E-W seismic profile north of the island of Kondelioussa. Nomikou (2004), Nomikou et al. (2013a)

activity. The steep cliffs of the volcanic domes were sub vertical with many bio-encrustations (Fig. 2.48d, e). Lava samples were collected at the base of the lava outcrop with great difficulty.

ROV exploration of the northern vertical wall of the nearest volcanic dome NE of the islet indicated the location of the major NE-SW fault zone and revealed bio-encrusted solid lava layers (Fig. 2.48d, e) or fragmented pillow lavas covered by bio-encrustations at 263 m depth, as well as a reverse angle wall. Towards the west, columnar basalts were observed whereas at the SE margin of the islet steep rock surface with sub vertical lineations occurred along the tectonic boundary between the Mesozoic limestones towards the southwest and the recent volcanic rocks towards the northeast.

Several submarine volcanic domes have been found to the east of Kondeliousa islet (Fig. 2.49).

References

Allen SR (1998) Volcanology of the Kos Plateau Tuff, Greece: the product of an explosive eruption in an archipelago. PhD thesis, Monash University Australia

Allen SR (2001) Reconstruction of a major caldera-forming eruption from pyroclastic deposit characteristics: Kos Plateau Tuff eastern Aegean Sea. J Volcanol Geotherm Res 105:141–162

Allen SR, Cas RAF (1998a) Lateral variations within coarse co-ignimbrite lithic breccias of the Kos Plateau Tuff Greece. Bull Volcanol 59:356–377

Allen SR, Cas RAF (1998b) Rhyolitic fallout and pyroclastic density current deposits from a phreatoplinian eruption in the eastern Aegean Sea Greece. J Volcanol Geotherm Res 86:219–251

Allen SR, McPhie J (2000) Water-settling and resedimentation of submarine rhyolitic pumice at Yali eastern Aegean Greece. J Volcanol Geotherm Res 95:285–307

Allen SR, Stadlbauer E, Keller J (1999) Stratigraphy of the Kos Plateau Tuff: product of a major quaternary explosive rhyolitic eruption in the eastern Aegean Greece. Int J Earth Sci 88:132–156

Allen SR, Vougioukalakis GE, Schnyder C, Bachmann Dalabakis P (2009) Comments on: on magma fragmentation by conduit shear stress: evidence from the Kos Plateau Tuff Aegean Volcanic Arc by Palladino Simei and Jyriakopoulos (JVGR 178 807-817). J Volcanol Geotherm Res 18:487–490

Bachmann O (2010) The petrologic evolution and pre-eruptive conditions of the rhyolitic Kos Plateau Tuff (Aegean Arc). Cent Eur J Geosci. 2:270–305

Bachmann O, Dungan MA, Lipman PW (2002) The fish Canyon magma body San Juan volcanic field Colorado: rejuvenation and eruption of an upper crustal batholith. J Petrol 43:1469–1503

Bachmann O, Charlier BLA, Lowenstern JB (2007) Zircon crystallization and recycling in the magma chamber of the rhyolitic Kos Plateau Tuff (Aegean Arc) Geology 35(1):73–76

Bachmann O, Schoene B, Schnyder C, Spikings R (2010) $^{40}Ar/^{39}Ar$ and U/Pb dating of young rhyolites in the Kos-Nisyros volcanic complex, Eastern Aegean Arc (Greece): age discordance due to excess ^{40}Ar in biotite. Geochem Geophys Geosyst 11:1–14

Bardintzeff JM, Dalabakis P, Traineau M, Brousse R (1989) Recent explosive volcanic episodes on the island of Kos Greece: associated hydrothermal paragenesis and geothermal area of Volcania. Terra Nova 1:75–78

Bellon H, Jarrige JJ (1979) Le magmatism néogène et quarternaire de l'île de Kos (Grèce): données géologiques. CR Acad Sci Paris Ser D 228:1359–1362

Böger H (1978) Sedimentary history and tectonic movements during the Late Neogene. In Closs H, Roeder D, Schmidt K (eds) Alps Apennines Hellenides IUGS Rept, vol 38, pp 506–509

Böger H, Gersonde R, Willmann R (1974) Das Neogen im Osten der Insel Kos (Aegäis Dodekanes), Stratigraphie und Tektonik. N Jb Geol Paläontol Abh 145:129–152

Bouvet de Maisonneuve C, Bachmann O, Burgisser A (2008) Characterization of juvenile pyroclasts from the Kos Plateau Tuff (Aegean Arc): insights into the eruptive dynamics of a large rhyolitic eruption. Bull Volcanol. doi:10.1007/s00445-008-0250-x

Burri C, Tatar Y, Weibel M (1967) Zur Kenntnis der jungen Vulkanite der Halbinsel Bodrum (SW-Türkei). Schweiz Miner Petro Mitt 47:833–853

Collins AS, Robertson AHF (1998) Process of late Cretaceous to late Miocene episodic thrust-sheet translation in the Lycian Taurides. J Geol Soc Lond 155:759–772

Cooper KM, Kent AJR (2014) Rapid remobilization of magmatic crystals kept in cold storage. Nature 508:554

Couch S, Sparks RSJ, Carroll MR (2001) Mineral disequilibriumin lavas explainedby convective self-mixing in open magma chambers. Nature 411:1037–1039

Dalabakis P (1986) Une des plus puissantes éruptions phréatomagmatiques dans la Méditerranée orientale: l'ignimbrite des Kos (Grèce). Compt Rend l'Academie Sci Serie 2 Mecanique Physique Chimie Sciences de l'Univers. Sci Terre 303:505–508

Dalabakis P (1987) Le volcanisme recent de lisle de Kos. PhD Thesis, Univ Paris Sud Orsay Paris France 1987, 266 pp

Dalabakis P, Vougioukalakis G (1993) The Kefalos tuff ring (W Kos): depositional mechanisms vent position and model of the evolution of the eruptive activity. Bull Geol Soc Greece 28(2):259–273 (in Greek with English abstract)

Davis E, Gartzos E, Pavlopoulos A, Tsagalidis A (1993) Petrological and geochemical research of perlites and rhyolites from Kefalos peninsula (island of Kos) and their quantitative evaluation (in Greek). In: Special volume in honour of Prof AG Panagos Athens A, pp 284–303

Dietrich VJ, Oberhänsli R, Mercolli I, Gaitanakis P (1991) Geological Map of Greece Aegina Island (Saronic Gulf) 1:25,000 with expl. Stiftung Vulkaninstitut Immanuel Friedlaender Zürich Verlag Birkhäuser Basel und IGME (Athen)

Di Paola GM (1974) Volcanology and petrology of Nisyros Island (Dodecanese Greece). Bull Volcanol 38:944–987

Drakopoulos J, Delibasis N (1982) The focal mechanism of earthquakes in the major area of Greece for the period 1947–1981. Univ of Athens Seismological Laboratory No. 2

Federman AN, Carey SN (1980) Electron microprobe correlation of tephra layers from Eastern Mediterranean abyssal sediments and the Island of Santorini. Quatern Res 13:160–171

Francalanci L, Vougioukalakis GE, Perini G, Manetti P (2005) A west-east traverse along the magmatism of the South Aegean Volcanic Arc in the light of volcanological chemical and isotope data In: M Fytikas, GE Vougioukalakis (eds) The South Aegean active volcanic arc present knowledge and future perspectives developments in volcanology. Elsevier, Amsterdam, pp 65–112

Fytikas M, Guiliani O, Innocenti F, Marinelli G, Mazzuoli R (1976) Geochronological data on recent magmatism of the Aegean Sea. Tectonophysics 31:29–34

Fytikas M, Innocenti F, Manetti P, Mazuoli R, Peccerilo A, Villari L(1984) Tertiary to quaternary evolution of the volcanism in the Aegean region. In: Dixon JE, Robertson AHF (eds) The geological evolution of the Eastern Mediterranean, vol 17, pp 687–699 (Geol Soc London Spec Pub)

Geotermica Italiana (1983) Nisyros 1 geothermal well PPC-EEC report, pp 1–106

Geotermica Italiana (1984) Nisyros 2 geothermal well PPC-EEC report, pp 1–44

GEOWARN (2003) GEOWARN geo-spatial warning system—synthesis report GEOWARN consortium Athens (Greece) and Zurich (Switzerland), 57 pp (http://www.geowarn.org)

Hurni L, Dietrich VJ, Gaitanakis P (1995) Geological map of Greece Methana (Saronic Gulf) 1:25,000 with expl Stiftung Vulkaninstitut Immanuel Friedlaender Zürich Verlag Birkhäuser Basel and IGME (Athen)

IGME (2003) Nisyros sheet, geological map of Greece 1:25,000. Inst Geol Miner Explor, Athens Greece

Innocenti R, Manetti P, Pecerillo A, Poli G (1981) South Aegean volcanic arc: geochemical variations and geotectonic implications. Bull Volcanol 44:377–391

Jackson J (1993) Rates of active deformation in the Eastern Mediterranean. In: Boschi E et al (eds) Recent evolution and seismicity of the Mediterranean region. Kluwer Dordrecht, pp 53–64

Jackson J (1994) Active tectonics of the Aegean region. Ann Rev Earth Planet Sci 22:239–271

Jarigge X (1978) Etudes neotectoniques dans I'arc volcanique egeen. Les lies de Kos, Santorini, Milos. Thesis Univ Paris XI Paris France

Keller J (1969) Origin of rhyolites by anatectic melting of granite and crustal rocks the example of rhyolitic pumice from the island of Kos (Aegean Sea). Bull Volcanol 33:942–959

Keller J (1982) Mediterranean island Arcs. In: RS Thorpe (ed) Andesites. John Wiley, New York, pp 316–325

Keller L, Rehren Th, Stadlbauer E (1990) Explosive volcanism in the Hellenic arc; a summary and review. In: Hardy DA, Keller J, Galanopoulos VP, Flemming NC, Druitt TH (eds) Thera and the Aegean world III proceedings of the third international congress, vol 2. The Thera Foundation, London, pp 13–26

Kiss B, Harangi S, Ntaflos T, Mason PRD, Pál-Molnár E (2014) Amphibole perspective to unravel pre-eruptive processes and conditions in volcanic plumbing systems beneath intermediate arc volcanoes: a case study from Ciomadul volcano (SE Carpathians). Contrib Mineral Petrol 167:1–27

La Ruffa G, Panichi C, Kavouridis T, Liberopoulou V, Leontiadis J, Caprai A (1999) Isotope and chemical assessment of geothermal potential of Kos island Greece. Geothermics 28:205–217

Lagios E, Galanopoulos D, Hobbs BA, Dawes GJK (1998) Two dimensional magnetotelluric modelling of the Kos island geothermal region (Greece). Tectonophysics 287:157–172

Le Pichon X (1982) Land-locked oceanic basins and continental collision: the Eastern Mediterranean as a case example. In: Hsü KJ (ed) Mountain building processes, vol 263, pp 201–211

Le Pichon X, Angelier J (1979) The Hellenic arc and trench system: a key to the evolution of the Eastern Mediterranean. Tectonophysics 60:1–42

Livanos I, Nomikou P, Papanikolaou D, Rousakis G (2013) Volcanic debris Avalanche at the SE submarine slopes of Nisyros Volcano Greece. Geo Mar Lett 33:419–431

Makris J (1977) Geophysical investigations of the Hellenides. Hamburger Geophysikalische Einzelschriften 33:128 pp

Makropoulos KC, Burton PW (1984) Greek tectonics and seismicity. Tectonophysics 106:275–304

Makropoulos K, Drakopoulos J, Latoussakis J (1989) A revised earthquake catalogue for Greece since 1900. Publ No 2. Geophys J Int 98:391–394

McKenzie DP (1972) Active tectonics of the Mediterranean Region. Geophys J R Astron Soc 30:109–185

Molloy C, Shane P, Nairn I (2008) Pre-eruption thermal rejuvenation and stirring of a partly crystalline rhyolite pluton revealed by the Earthquake Flat Pyroclastics deposits, New Zealand. J Geol Soc London 165:435–447

Müeller St, Kahle HG (1993) Crustmantle evolution, structure and dynamics of the Mediterranean-Alpine region. In: Smith, Turcotte (eds) Contributions of Space Geodesy to Geodynamics: crustal Dynamics, American Geophysical Union (AGU), Geodynamics Series, Washington D.C. 23:249–298

Murphy MD, Sparks RSJ, Barclay J, Carroll MR, Brewer TS (2000) Remobilization of andesitic magma by intrusion of mafic magma at the Soufrie're Hills Volcano Montserrat West Indies. J Petrol 41:21–42

Nakamura M (1995) Continuous mixing of crystal mush and replenished magmain the ongoing Unzen eruption. Geology 23:807–810

Nomikou P (2004) Geodynamics of Dodecanese islands: Kos and Nisyros volcanic field. PhD thesis, Department of Geology University of Athens 467 pp

Nomikou P, Papanikolaou D (2000) Active geodynamics at Nisyros the eastern edge of the Aegean volcanic arc: emphasis on submarine surveys proceedings of the 3rd international conference geology East Mediterranean Sept 1998, pp 97–103

Nomikou P, Papanikolaou D (2010a) A comparative morphological study of the Kos-Nisyros-Tilos volcanosedimentary basins. Bull Geol Soc Greece 43:464–474

Nomikou P, Papanikolaou D (2010b) The morphotectonic structure of Kos-Nisyros-Tilos volcanic area based on onshore and offshore data XIX Congress of the Carpathian-Balkan geological association Thessaloniki Greece 23–26 Sept 2010. Proc Spec 99:557–564

Nomikou P, Papanikolaou D (2011) Extension of active fault zones on Nisyros Volcano across the Yali-Nisyros Channel based on onshore and offshore data. Mar Geophys Res 32:181–192

Nomikou P, Papanikolaou D, Alexandri S, Ballas D (2004) New insights on the Kos–Nisyros volcanic field from the morphotectonic analysis of the swath bathymetric map. Rapp Comm Int Mer Medit 37:60

Nomikou P, Tibaldi A, Pasquare F, Papanikolaou D, (2009) Submarine Morphological analysis based on multibeam data of a huge collapse at the SE flank of Nisyros volcano International Conference on Seafloor Mapping for Geohazard Assesment 11–13 May Ischia Italy. Rend Soc Geol It 7:177–179

Nomikou P, Bell KLC, Vougioukalakis G, Livanos I, Martin Fero J (2011) In: Bell KLC, Fuller SA (eds) Exploring the Nisyros volcanic field: p 27. In: New frontiers in ocean exploration: the E/V nautilus 2010 field season. Oceanography, vol 24(1) supplement

Nomikou P, Papanikolaou D, Alexandri M, Sakellariou D, Rousakis G (2013a) Submarine volcanoes along the Aegean volcanic arc. Tectonophysics 507–508:123–146

Nomikou P, Croff Bell K, Papanikolaou D, Livanos I, Fero Martin J (2013b) Exploring the submarine flanks of Yali and Strongyli volcanic islets at the eastern edge of the Aegean Volcanic Arc. Zeitschrift Geomorphologie 57(Suppl 3):125–137

Nomikou P, Papanikolaou D, Tibaldi A, Carey S, Livanos I, Bell KLC, Pasquarè FA, Rousakis G (2013c) The detection of volcanic debris Avalanches along the Hellenic volcanic arc through marine geophysical techniques. In: Submarine mass movements and their consequences, 5th vol, pp 337–349 (Chapter 30)

Pallister JS, Hoblitt RP, Reyes AG (1992) A basalt trigger for the 1991 eruptions of Pinatubo volcano? Nature 356:426–428

Papadopoulos GA (1984) Seismic properties in the eastern part of the South Aegean Volcanic Arc. Bull Volcanol 47:143–152

Papadopoulos GA, Kondopoulou DP, Levendakis GA, Pavlides SD (1986) Seismotectonics of the Aegean region. Tectonophysics 124:67–84

Papanikolaou DJ (1993) Geotectonic evolution of the Aegean. Bull Geol Soc Greece 18:33–48

Papanikolaou DJ, Lekkas E (1990) Miocene tectonism in Kos Dodekanese islands IESCA Izmir 1990 abstracts, pp 179–180

Papanikolaou D, Nomikou P (1998) The Palaeozoic of Kos: "A low grade metamorphic unit of the basement of the External Hellenides Terrane" Spec Publ Geol Soc Greece 3, IGCP Project 276 Newsletter 6:155–166

Papanikolaou D, Nomikou P (2001) Tectonic structure and volcanic centres at the eastern edge of the Aegean volcanic arc around Nisyros island. Bull Geol Soc Greece 34:289–296

Papanikolaou DJ, Lekkas EL, Sakelariou DT (1991) Geological structure and evolution of Nisyros volcano. Bull Geol Soc Greece 25:405–419

Pe G, Piper DJW (1972) Volcanism at subduction zones. The Aegean area. Bull Geol Soc Greece 9:113–144

Pe-Piper G, Piper DJW (2002) The igneous rocks of Greece. The anatomy of an orogen. Gebr Bornträger, Berlin Stuttgart 573 pp

Pe-Piper G, Piper DJW (2005) The South Aegean active volcanic arc: relationships between magmatism and tectonics. In: Fytikas M, Vougioukalakis GE (eds) The South Aegean active volcanic arc present knowledge and future perspectives developments in volcanology. Elsevier, Amsterdam, pp 113–134

Pe-Piper G, Piper DJW, Kotopouli CN, Panagos AG (1994) Neogene volcanoes of Chios Greece: relative importance of subduction and back-arc extension. In: Smellie JL (ed) Volcanism associated with extension at consuming plate margins. Geol Soc Lond Spec Publ 81:213–232

Piper DJW, Pe-Piper G, Lefort D (2010) Precursory activity of the 161 ka Kos Plateau Tuff eruption Aegean Sea (Greece). Bull Volcanol. doi:10.1007/s00445-010-0349-8

Robertson AHF, Dixon JE (1984) Introduction aspects of the geological evolution of the eastern Mediterranean In: Dixon J, Robertson AHF (eds) The geological evolution of the eastern Mediterranean. Geol Soc Lond Spec Publ 17:1–74

Smith AG (1971) Alpine deformation and the oceanic areas of the Tethys Mediterranean and Atlantic. Geol Soc Am Bull 82:2039–2070

Smith PE, Evensen NM, York D (2000) Under the volcano: a new dimension in Ar-Ar dating of volcanic ash. Geophys Res Lett 27:585–588

Smith PE, York D, Chen Y, Evensen NM (1996) Single crystal $^{40}Ar/^{39}Ar$ dating of a late quaternary paroxysm on Kos Greece, concordance of terrestrial and marine ages. Geophys Res Lett 23:3047–3050

Stadlbauer E (1988) Vulkanologisch-geochemische Analyse eines jungen Ignimbrits: der Kos-Plateau-Tuff (Südost-Ägäis). PhD thesis Albert-Ludwigs-Universität Freiburg im Breisgau, 184 pp

Tibaldi A, Pasquarè FA, Papanikolaou D, Nomikou P (2008a) Discovery of a huge sector collapse at the Nisyros volcano Greece by on-land and offshore geological-structural data. J Volcanol Geotherm Res 177:485–499

Tibaldi A, Pasquarè FA, Papanikolaou D, Nomikou P (2008b) Tectonics of Nisyros Island Greece by field and offshore data and analogue modeling. J Struct Geol 30:1489–1506

Triantaphyllis M (1994) Geological map of Greece western Kos, sheet (Kefalos) 1:50,000 inst geology mineral exploration (IGME) Athens Greece

Triantaphyllis M, Mavrides A (1998) Geological map of Greece Eastern Kos, sheet (Kos) 1:50,000 inst geology mineral exploration (IGME) Athens Greece

Volentik A, Vanderkluysen L, Principe C, Hunziker JC (2005) Stratigraphy of Nisyros Volcano (Greece). In: Hunziker JC, Marini L (eds) The petrology and geochemistry of lavas and tephras of Nisyros Volcano (Greece). Mém Géologie (Lausanne) 44:26–66

Vougioukalakis GE (1998) Blue volcanoes: Nisyros Nisyros. Regional Council Mandraki 78pp

Wagner GJ, Storzer D, Keller J (1976) Spaltspurendatierungen quartärer Gesteinsglaser aus dem Mittelmeerraum. N Jb Miner Mh 2:84–94

Geology of Nisyros Volcano

3

Volker Jörg Dietrich

Abstract

The heart of the book is found in this Chapter, the geology of Nisyros Volcano. The compilation of the new "Geological Map of the Island of Nisyros (Dodecanese Archipelago)" with cross sections serves as the basis for the interpretation of the eruptive history of Nisyros volcano. The volcano-tectonic structures of the 698 m high stratovolcano are marked by the central, almost circular caldera with a diameter of 3.6 km and a drop of 300–400m of its steep walls. This dominant structural feature is crosscut by two conjugate major and three minor fault systems. Since accurate geochronological data are still missing due to the rarity of potassium bearing minerals, such as sanidine and biotite as well as to other petrologic and chemical reasons, the eruptive history can only be based on relative ages of a detailed lithostratigraphy of thirty-two mappable eruptive units. A major division into five volcanic cycles has been devised using eruptive successions, contact relationships, epiclastic deposits and intercalated paleosols. Volcanic activity started with shallow submarine basaltic-andesitic lavas during the "Early Shield Volcano Cycles" evolving into a subaerial environment with local lacustrine lakes. Progressively, a composite stratovolcano built up the circular shape of Nisyros Island, with eruptions on the northern and southern part of the island, the latter with effusion of rhyolitic lava. Along the east coast, mainly explosive eruptions

Electronic supplementary material The online version of this chapter (doi:10.1007/978-3-319-55460-0_3) contains supplementary material, which is available to authorized users.

V.J. Dietrich (✉)
Institute of Geochemistry and Petrology, Swiss Federal Institute of Technology, ETH Zurich, ETH-Zentrum, CH 8092 Zürich, Switzerland
e-mail: volker.dietrich@erdw.ethz.ch

V.J. Dietrich and E. Lagios (eds.), *Nisyros Volcano*, Active Volcanoes of the World,
DOI 10.1007/978-3-319-55460-0_3

produced two larger tuff cones of andesitic and dacitic compositions. During an evolved stratovolcanic stage, basaltic-andesites and andesites were emitted as lavas and pyroclastics from several smaller cinder, spatter and scoria cones covering the southern, western and northern slopes of the island. The "Composite Stratovolcanic Cycles" ended with the effusion of a large dacitic dome in the northern part of the island, which generated a major dome collapse of the northern slopes into the sea. With an unknown time gap, voluminous eruptions of rhyolitic pyroclastics started from the northern and southern eruptive centers, "Caldera Eruptive Cycles", followed by a first caldera collapse and successive voluminous rhyolitic lava flows, which extruded towards southeast. The youngest major explosive rhyolitic eruption occurred after an unknown time interval from a northern centre, covering the northern and eastern slopes with major pumice deposits and inducing a second-stage of the caldera collapse. Afterwards, during the "Post Caldera Eruptive Cycle", voluminous effusions of rhyodacitic magma filled the western part of the caldera with large domes and flows that extend towards the sea, in the southwest. Since then, Nisyros Volcano remains in a dormant stage. Magmatic counterparts, such as gabbroic and dioritic intrusives, as well as mafic cumulates have generated a large hydrothermal system at depth, which is still highly active today.

3.1 The Geological Map of the Island of Nisyros (Dodecanese Archipelago) (1:15,000 with Geological Cross Sections)

The first geographic and geological studies on Nisyros Island were undertaken by the Italian geologists Martelli (1917), Chap. 5.2, Fig. 5.4 and Desio (1931). Detailed geological investigations started in the late sixtieth (Davis 1967), followed by Di Paola (1974), and Papanikolaou et al. (1991) with geological sketch maps at various scales. Vougioukalakis (1993) presented the first geological map of Nisyros Island on a topographic base in the scale of 1:12,500, which was updated in the Sheet Nisyros, Geological Map of Greece, 1:25,000 (2003) by IGME (Institute of Geology and Mineral Exploration, Athens, Greece).

During the GEOWARN—IST 12310 project (2003) a Topographic and a Geological Map of Nisyros in the scale 1:10,000 with equidistance 10 m contour lines resulted using a completely new digital technology. As basis served an orthorectified 3D IKONOS-2 satellite image from Nisyros volcanic island (2000) with a 1 m resolution on ground, cartographic field mapping and extraction from the topographical map 1:50,000 (Hellenic Military Geographical Service 1972). This work was done by the Institute of Cartography and Geoinformation, Department of Civil, Environmental and Geomatic Engineering, Swiss Federal Institute of Technology, Zurich, Switzerland. The detailed Geological Map of Nisyros Volcano 1:12,500 by Volentik et al. (2005) was the first result of the accurate topography.

The current updated digital and fully vectorised version of the "Geological Map of the Island of Nisyros (Dodecanese Archipelago) 1:15,000 with Geological Cross Sections" represents a compilation of all available former geological data, as well as unpublished results of field mapping during the periods 2000–2003, 2010–2015. The online version of the "Geological Map of the Island of Nisyros (Dodecanese Archipelago)" 1:15,000 with "Geological Cross Sections" as well as

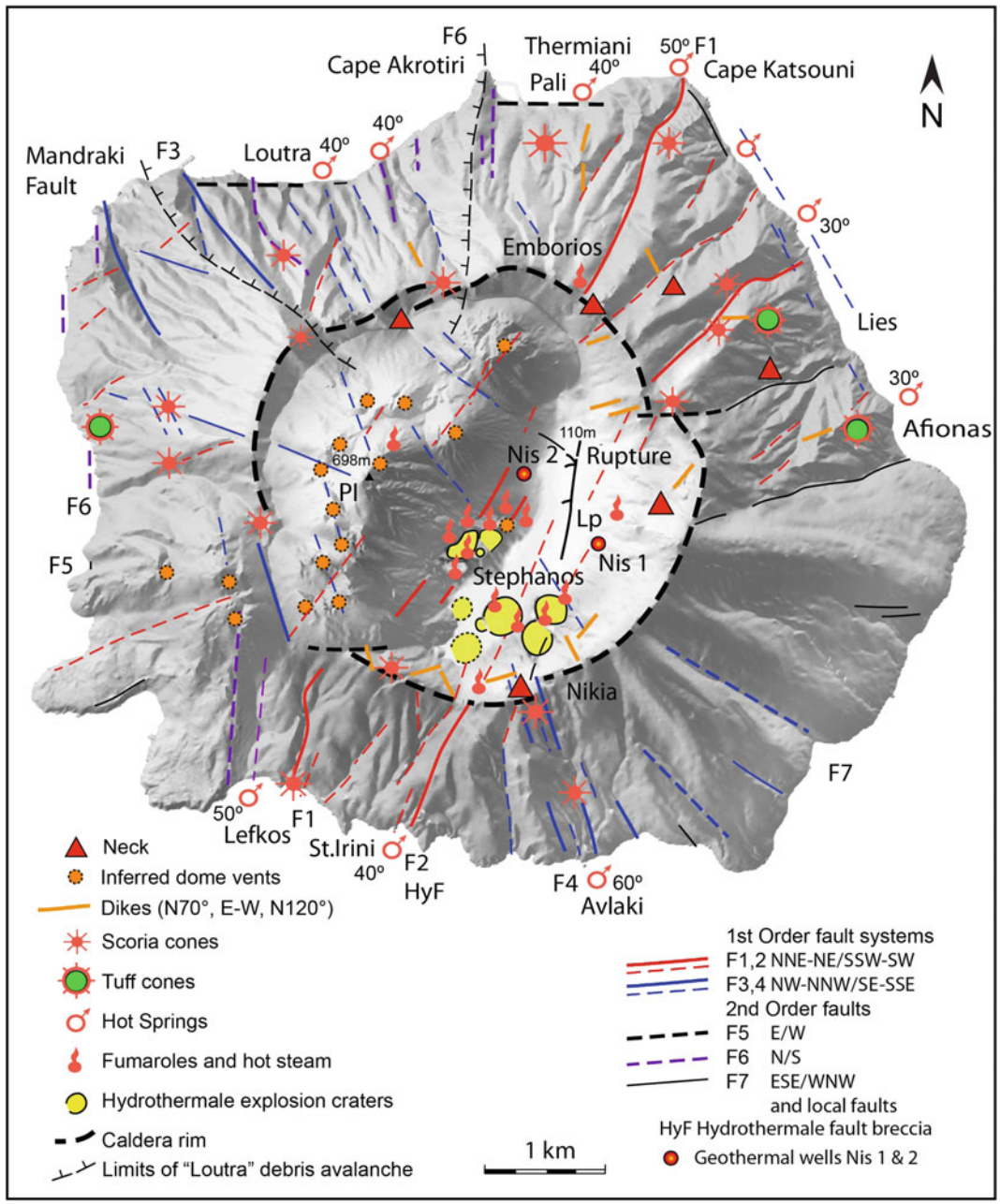

Fig. 3.1 The present-day structural map of Nisyros volcano deduced from the digital elevation model (*DEM*) of Nisyros Island, has been derived by digitizing the 1:5000 scale topographic map sheets of Nisyros Island, 1983, published by the Hellenic Military Geographical Service, Greece

detailed descriptions of the lithostratigrapjic units to Chap. 3 are available to authorized users.

Lithostratigraphic units (LSU) with numbers from 1 (lower most outcropping rocks on the island) to 33 (upper most or bounded with unconformity rocks) were used to designate mappable lavas and pyroclastic sequences. The numbering system of the units bears the advantage to the reader to recognize immediately their stratigraphic position. Local names and

abbreviations were restricted to a minimum to avoid confusion. On Nisyros Island the same or similar names occur for different localities and have changed throughout time. The grouping and division of units into cycles is based on unconformities, erosional surfaces, interbedded soils and epiclastic deposits.

The map is compatible with the *Hellenic Geodetic Reference System GGRS 87*, *Datum WGS 84* and the *Projection UTM Zone 35N (24E–30E)*. All geographic features are updated to 2015.

3.2 Volcanic and Volcano-Tectonic Structures

The present-day structural map of Nisyros volcano (Fig. 3.1) comprises volcanic eruption vents, such as necks, inferred dome vents, scoria cones (spatter and cinder cones included), tuff cones and sub-volcanic dikes, as well as hydrothermal explosion craters and emission spots: fumaroles, hot steam, and hot springs.

3.2.1 The Caldera

The most characteristic and dominant structural feature of Nisyros volcano is the caldera with an approximate diameter of 3.6 km (Fig. 3.2). The assumption of its post eruptive collapse origin led no doubts to all precious workers (see introduction) due to its almost circular structure and steep walls with a drop of 300–400 m between the northern and eastern rim down to the Lakki plain of 110 m a.s.l and to the filling of the western part with voluminous rhyodacitic domes up to 698 m. After the recognition of the two

Fig. 3.2 Aerial view of Nisyros volcano from northeast; the caldera with an approximate diameter of 3.6 km the filling of the western part with voluminous rhyodacitic domes up to 698 m (Profitis Ilias); the almost circular structure and steep walls with a drop of 300–400 m between the northern and eastern rim down to the Lakki plain of 110 m above sea level. *Photo* hellasmounts.com

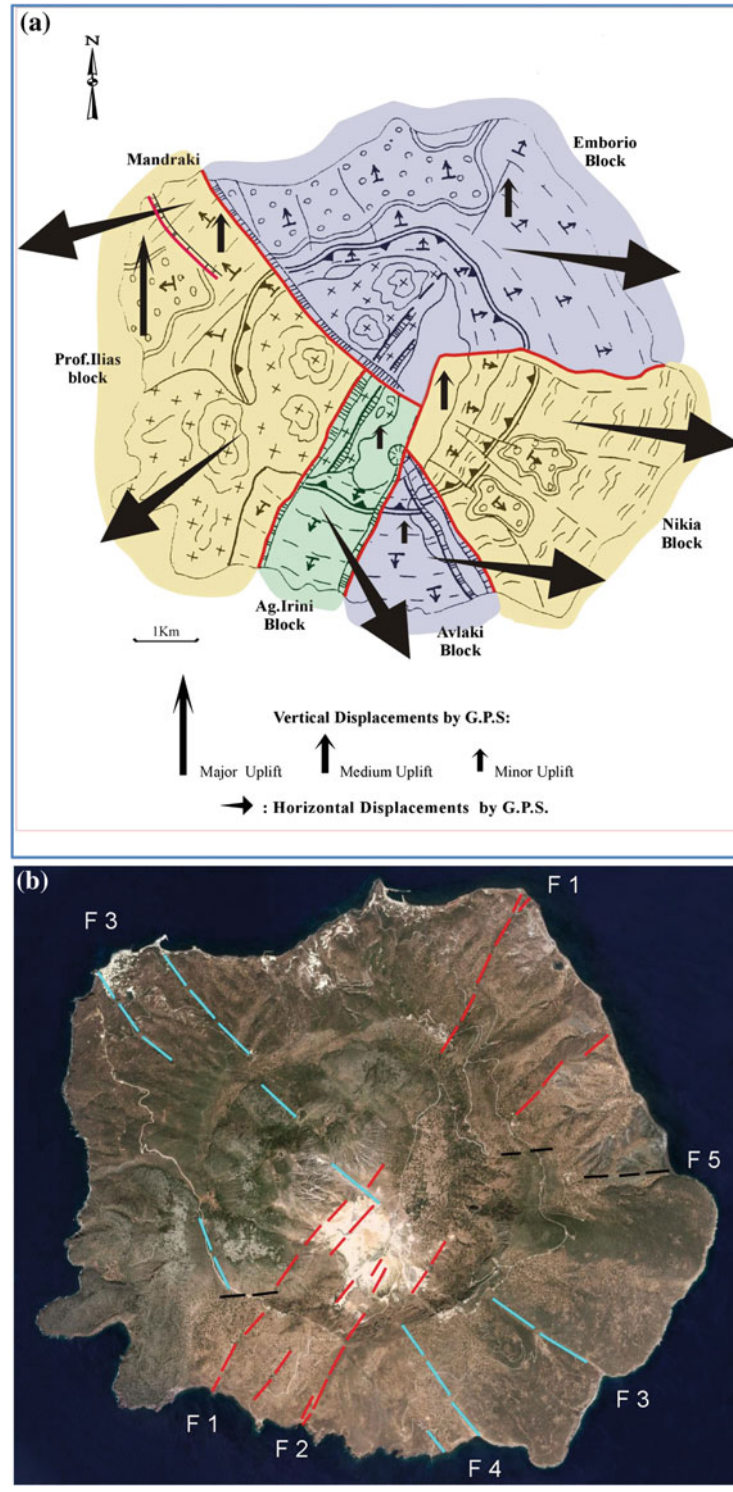

Fig. 3.3 **a** Simplified schematic geological map of Nisyros Island showing the major neotectonic blocks (Profitis Ilias block in *yellow*, Aghia Irini block in *green*, Avlaki block in *orange* and Emborio/Nikia block in *yellow*) resulting from the four major fault zones F1, F2, F3, F4, and F5 (Papanikolaou and Nomikou 2000); **b** F1–F5 fault zones on google earth image

major young plinian eruptive cycles, which produced the lower and upper pumice, as well as the large rhyolitic lava flows in the southeast of the island, the discussion focused on caldera formation during one or two collapse episodes (Papanikolaou et al. 1991; Limburg and Varekamp 1991; Vougioukalakis 1998). However, it is possible that the general shape and structure of the present-day caldera resulted from earlier depression, which is indicated by two large stratovolcano flank collapses, prior or simultaneously to the plinian eruptions. Volentik et al. (2005) could establish three older phreato-magmatic to sub-plinian eruptive phases during the early shield volcano cycles, which also emitted large volumes (lithostratigraphic units Nos. 4, 6, 11, Electronic Supplementary Material Appendix 3.3) of pumice fallout, pyroclastic flows, and surges. The existence of two lacustrine cycles could be interpreted as an early internal lake-stage with limited dimensions of probably few hundred meters only (Volentik et al. 2002) as an expression of a depression in north–eastern center of the island.

Despite alteration effects, no large hydrothermal deposits or strong hydrothermal alteration have been recognized as possible earlier indications of high-crustal level magma reservoirs accompanied with a post-eruptive caldera forming collapse.

3.2.2 The Fault Systems

Two major and three minor fault systems can be distinguished within the volcanic edifice of Nisyros Island (Figs. 3.1 and 3.3). The directions are in accordance with previous structural and geological investigations (Papanikolaou et al. 1991; Vougioukalakis 1993; Nomikou and Papanikolaou 2000, 2011):

- (F1, 2) N30E 1st order faults with local changes to NE directions
- (F3, 4) N30W 1st order faults with changes between N0° and N40°W
- (F5) E–W 2nd order faults
- (F6) N–S 2nd order faults
- (F7) WNW–ESE 2nd order faults (approx. 120°)

The NE–SW (F1, 2) 1st order fault system

F1 Fault Zone. It is located along the central part of the caldera comprising two or three parallel fault surfaces with a N30°E strike and a 70–80° dip to the SE. Its throw is more than 100 m and it separates the Profitis Ilias lavas and domes to the northwest from the caldera deposits to the southeast (Figs. 3.1 and 3.7a, b). Its morphological impact is very strong within the caldera and less outside of it. Towards the northeast it is not very prominent and there is no abrupt break of the caldera rim in the area of Emborios village.

F2 Fault Zone. This fault zone is parallel to F1 and runs along the southern caldera wall roughly 1.5 km southeast of F1 (Figs. 3.1 and 3.4). It strikes N30°E and dips 70–80° to the WNW forming a tectonic graben with the opposite facing F1 (Figs. 3.7a, b and 3.8). This graben structure comprises the remnant of the 160,000 years Kos caldera plain with lacustrine and alluvial deposits, known as Lakki plain. Its throw may be estimated to be about 100–120 m, on the basis of the offset of the lavas and pyroclastics of the lithostratigraphic units 17, 21, and 22 (Figs. 3.6, 3.7 and 3.8).

Horizontal displacements of the F1 fault system with dextral strike-slip motion and extension SE–NW have been interpreted from focal mechanisms of major earthquakes ($M > 5$) at shallow and intermediate crustal depths (Drakopoulos and Delibasis 1982).

The F1 system seems also to have played a major role during the emplacement of the post-caldera dacites (Fig. 3.7a, b). Their eruptive centers are aligned along an N30°–40°E striking fault plane. Since these magmas were derived from reservoirs at deep crustal levels, the F1 fault system must document a zone of weakness reaching the deepest crustal parts. Further evidence of such an interpretation can be taken from the spatial distribution of earthquake epi- and hypocenters.

The NW–SE (F3, 4) 1st order fault system

The major N30 W fault system have steep inclinations of 70°–80° at the surface changing

Fig. 3.4 Eastern part of the caldera rim with central and eastern hydrothermal craters with faults F1 and F2 (*red lines*). *Photo* V.J. Dietrich

Fig. 3.5 Fault breccia (autobrecciated dike) within the major NW–SE fault zone (F2) at the southeast rim of the caldera (road to monastery Ag. Stavros, Fig. 3.1); *Photo* V.J. Dietrich

the direction of dips depending on the geotechnical rock properties between NE and NW. These faults run perpendicular to the large Kos horst-graben system (Figs. 3.1, 3.9, 3.10 and 3.11). Characteristics of this fault system are extensional features and downfaulting up to 70 m. They extend from the northwestern parts of Tilos Island into Nisyros Island in the area of Avlaki, crosscut the entire island, run along the western part of Yali and merge into Kos Island at the "Paradise bubble beach".

The F3 fault zone is located in the northwestern part of Nisyros Island with a general trend to N30°W and dip 70–80° to the NE (Figs. 3.9 and 3.10). It juxtaposes different stratigraphic formations both within and outside the caldera. Inside the caldera it separates the main outcrops of the Profitis Ilias lava domes

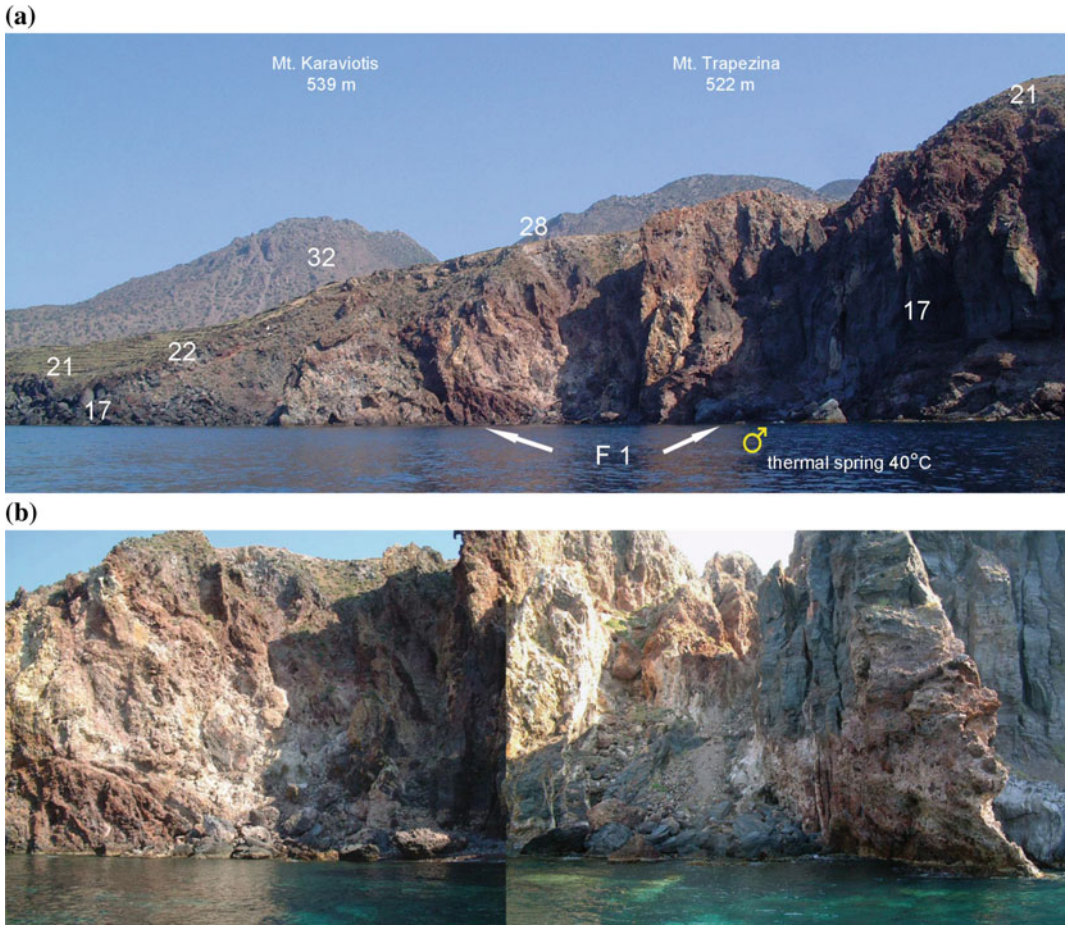

Fig. 3.6 **a** and **b** (close up) the major NE–SW (F2) fault system with chaotic hydrothermally altered fault breccia approx. 500 m east of Aghia Irini (Fig. 3.1). Numbers refer to lithostratigraphic units. *Photo* V.J. Dietrich

from the smaller domes to the northeast whereas outside the caldera it separates the outcrops of white pumice to the down faulted block in the northeast from the uplifted block in the southwest (where the pillow lavas No. 1 occur just above sea level). Its throw is more than 100 m.

The Mandraki fault runs parallel to the F3 fault zone at a distance of about 1 km to the southwest. The kinematic characteristics of the two faults are similar, with a general strike in the NNW–SSE direction and dip towards the ENE. The Mandraki fault is normal with a throw of about 100 m a.s.l indicated by the offset of the characteristic stratigraphic formations (Fig. 3.11a, b). The western block is topographically higher by 100 m and hosts the two important monuments of the island, which are the ancient castle of 4th century B.C. and the Panaghia Spiliani Monastery within the Byzantine/Venetian castle. The eastern block comprises the town of Mandraki with its westernmost buildings reaching the valley running along the Mandraki fault known as "Langhadi".

In continuation, a series of NW–SE parallel faults cut the Nisyros Island in the area of Avlaki and Aghia Irini (Figs. 3.1 and 3.6). Best evidence for downfaulting of the Aghia Irini block can be taken from the offset of the southern caldera rim. The fault system runs through the Stefanos Crater extending into the hydrothermal craters of Mikros Polyvotis and Megalos Polyvotis. One branch cuts through the domes of Profitis Ilias and Nifios into the northwestern crater rim and

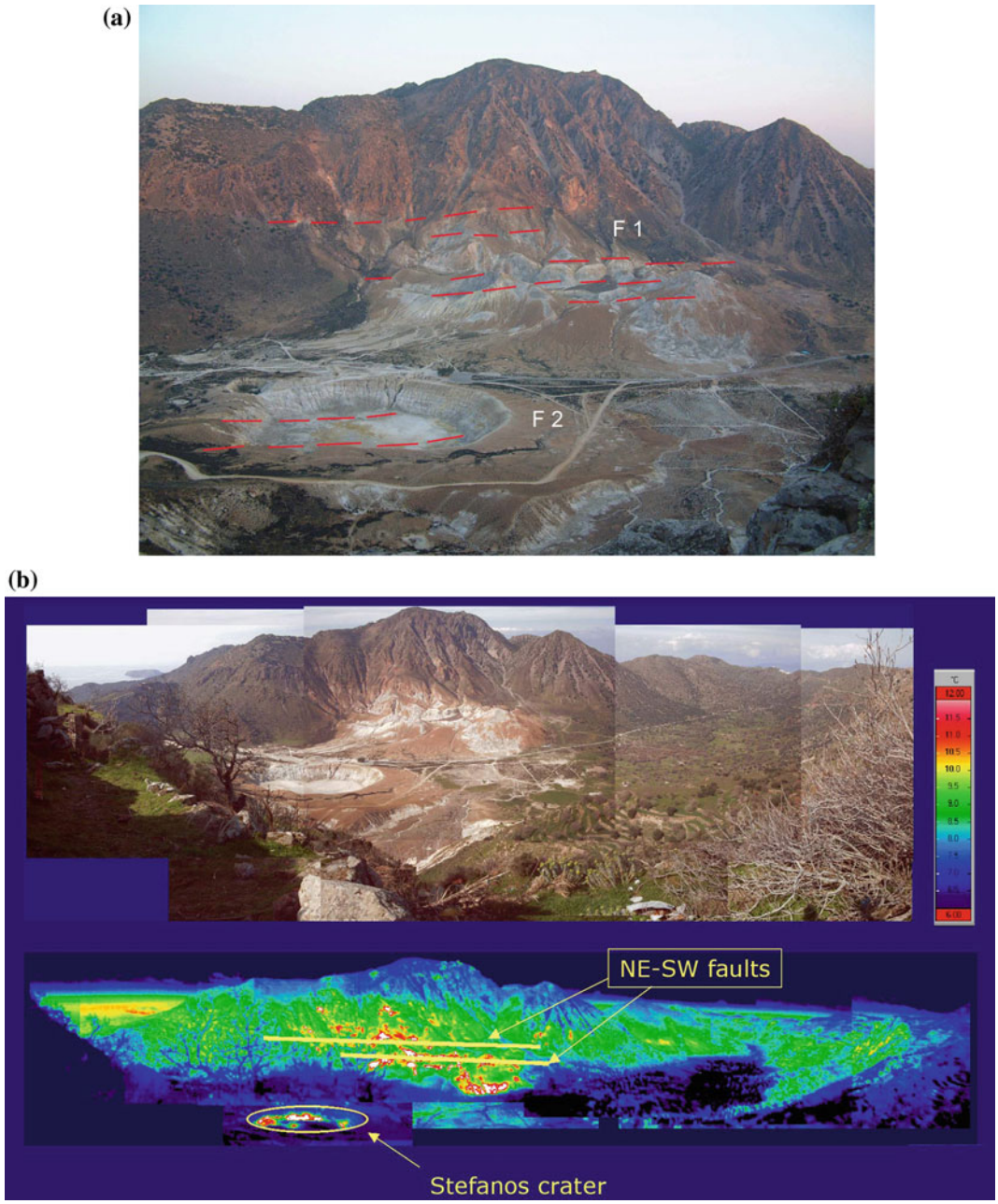

Fig. 3.7 **a** Recent fault systems inside the caldera linked to the hydrothermal explosion craters with faults F1 and F2. View from Nikia. **b** Thermal imaging of the hydrothermal crater field and the spatial distribution of the fractures and inferred faults F1 within the Profitis Ilias rhyodacitic domes. GEOWARN (2003). *Photo* V. J. Dietrich

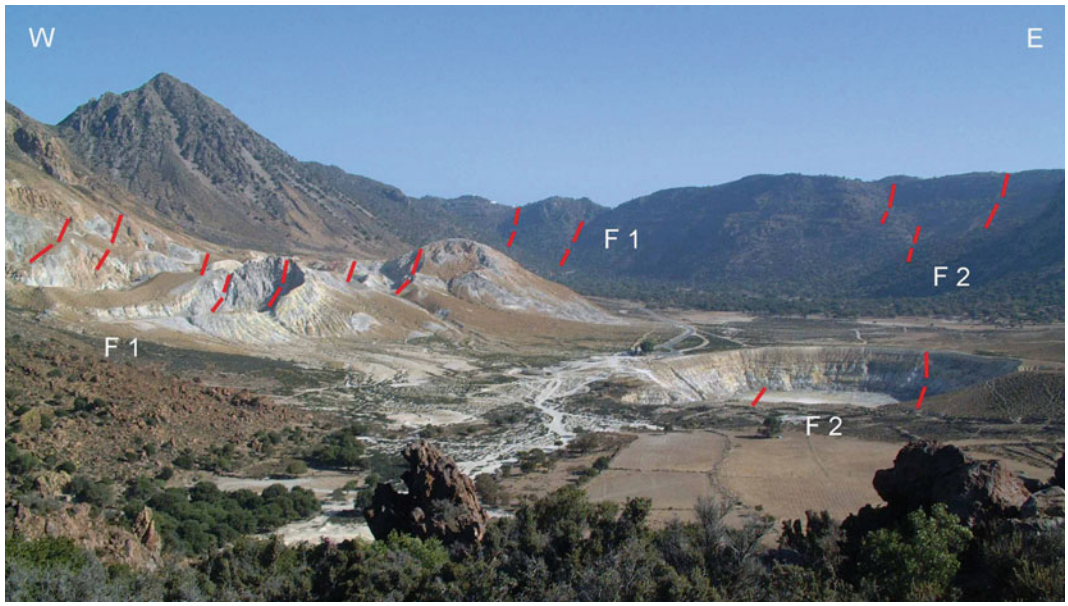

Fig. 3.8 Listric F1 and F2 fractures and faults in the northern part of the caldera rim and in the western and central hydrothermal craters. *Photo* V.J. Dietrich

splits into several minor faults west and east of the Monastery Evangelistra. There, the system forms a series of step-like downfaulted blocks between the Monastery Spiliani, the town of Mandraki and Loutra.

The F4 fault zone on Nisyros defines a tectonic graben, striking N20W, consisting of two conjugate faults with opposing dips. This fault zone is younger than the Nikia rhyolites (No. 30) and its throw is about 40–50 m. These fault zones of Nisyros Island produce a number of neotectonic blocks, each characterized by its relative uplift or subsidence (Fig. 3.3). The maximum uplift is observed in the western block/horst bounded by the F1 and F3 fault zones, which incorporates the maximum elevations of Profitis Ilias and surrounding summits. The maximum subsidence is observed in the southern block/graben of Aghia Irini, bounded by the F1 and F2 parallel fault zones.

All hydrothermal explosion craters are located in the intersections between the conjugate fault system F1, F2 and F4. At the northern and southern extensions of the F1 system, hot springs occur at sea level (Cape Katsuni and Thermiani in the north and Lefkos in the south). It is obvious from the bathymetric digital elevation model (BDEM) that these faults extend northeastward into the eastern Kos basin bordering the down-faulted slopes of Kos and the peninsula of Datça.

The rest of Nisyros Island constitutes the large neotectonic block of Emborio/Nikia, east of the F3 and F4 fault zones, with intermediate kinematic character since it has subsided with respect to the western block but has been uplifted with respect to the southern block. The Emborio area of the block is made of the stratovolcano stratigraphic formations, whereas the Nikia area is made of the Nikia rhyolite flows. A minor neotectonic block bounded by the F2 and F4 fault zones is observed in the southern part of Nisyros at the area of Avlaki with transitional character between the Aghia Irini and the Emborio/Nikia blocks.

The E–W (F5) 2nd order faults

The E–W oriented fault system seems to occur at present only at a local scale (Figs. 3.1 and 3.32a) and might represent a result of the deep reaching conjugate fault system F1 and F3. Surface expressions are visible along the north coast of Nisyros at the town of Mandraki, between the harbors Mandraki and Loutra, between Pali and

Fig. 3.9 F3 fault extension towards N and NW into Yali. *Photo* V.J. Dietrich

Fig. 3.10 Active NNW–SSE fault of Mandraki (*center*) extending into the central part of Yali island (*background*). *Photo* V.J. Dietrich

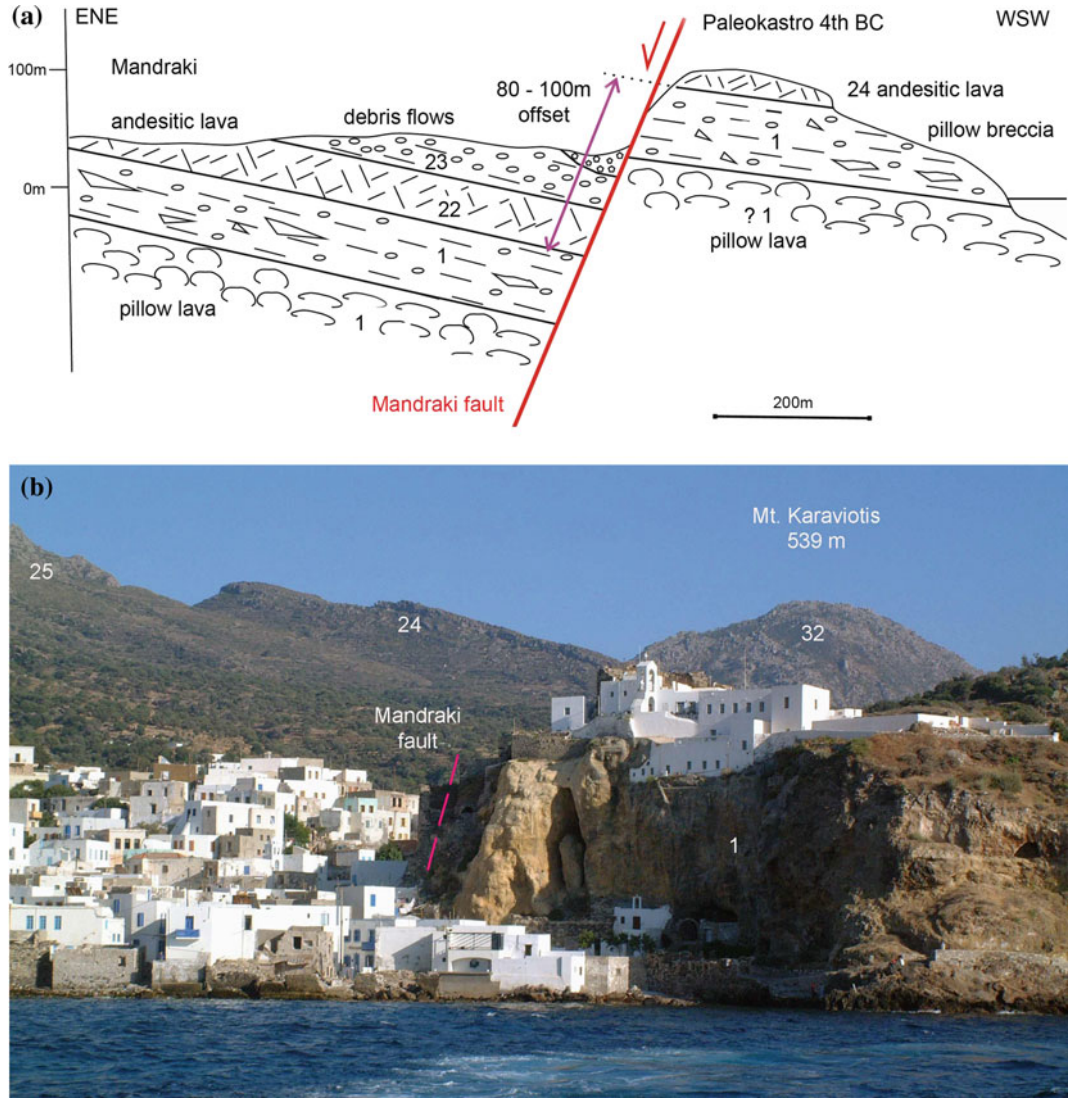

Fig. 3.11 **a** Vertical offset at the northwestern corner of Nisyros Island due to the NNW–SSE trending steep Mandraki fault F3 (Fig. 3.11b). Sketch *redrawn* after Papanikolaou and Nomikou (2011). **b** Monastery Panaghia Spiliani on the uplifted cliffs at the Northwest corner of Nisyros Island with the western end of Mandraki; view of the active Mandraki fault F3 from north between the western boundary of Mandraki. In the background lavas of LSU units Nos. 24 and 25 and Karaviotis dome Unit No. 32. *Photo* V.J. Dietrich

Faros, along the western Karaviotis lava flows bordering the Kateros cove and in the valley between the Monastery Panagia Kyra and the southern border of Pachia Ammos beach. The hot spring of Afionas at sea level might also be a result of this fault system.

The N–S (F6) 2nd order faults

A subordinate N–S fault system can be locally established in the volcanic edifice of Nisyros Island (Fig. 3.12): Along the northwest coast, between the rhyodacitic domes of Karaviotis and Trapezina and at Cape Akrotiri. According to the

Fig. 3.12 Cape Akrotiri with N–S fault. *Photo* V.J. Dietrich

bathymetric map (BDEM) the latter fault seems to extend into a small N–S graben between Yali and Strongyli (Fig. 2.6, Chap. 2). An equivalent system appears to also be present in the peninsula of Kefalos on Kos. Similar to the F4 system, the N–S might also be a result of the dominant conjugate F1 and F3 systems.

3.2.3 The Lakki Rupture 2001, 2002, and 2011

3.2.3.1 Annual Episodes of Rupturing

A large N–S trending fracture ("Lakki rupture") opened in the Lakki plain of the Caldera in early December 2001 (Figs. 3.13 and 3.14). Although this large rupture extended over a distance of 350 m and up to 5 m wide and up to 10 m (in few cases 20 m) deep, neither gas and thermal waters were recognized nor seismic signals were recorded. In December 2002, the fracture continued to extend southward for another 500 m showing smaller perpendicular offsets (Fig. 3.15). During a heavy rainstorm during November 12/13, 2011 another large rupture was formed (Figs. 3.16 and 3.17) intersecting the 2001/2002 rupture in the central part of the Lakki plain. The direction of the new rupture was NNW–SSE with approximately 320°, starting in the south as reactivation of the 2001 rupture and continuing for approximately 450 m towards NNW crossing the road. The northern and the southern parts of the old rupture were not affected.

3.2.3.2 Interpretation and Origin of Ruptures

The rupture is interpreted as surface stress release in the consolidated and cemented epiclastic and hydrothermal sediments of the caldera floor, due to progressive uplift and East–West extension of the central parts of the island since the seismic crisis 1996/1997 and a possible magma input at greater crustal depth (GEOWARN project 2003). No significant earthquake activity has been recorded during the formation of all ruptures.

In addition, subrosion by meteoric waters and their drainage from large cavities and tunnels several tens of meters beneath the Lakki plain

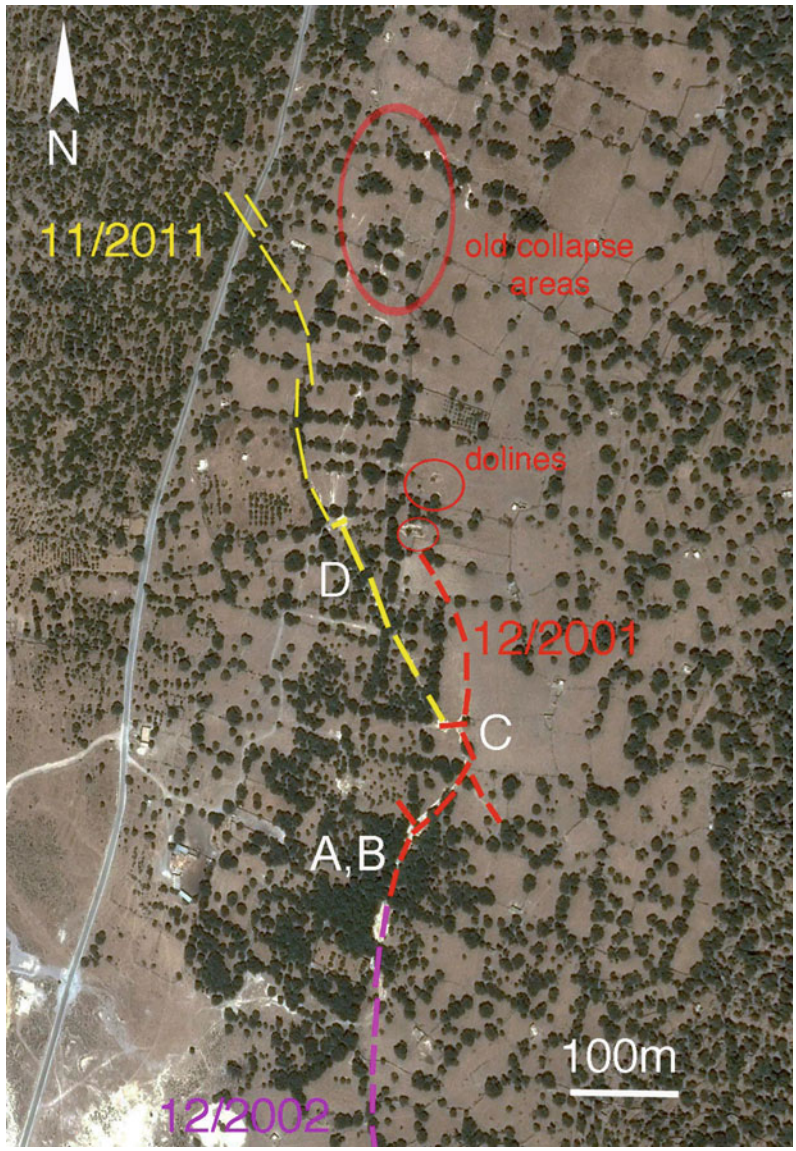

Fig. 3.13 Localization of the surficial, up to 20 m deep ruptures in the central part of the Lakki plain, which formed during three episodes during abnormally high precipitation in winter times: November 2001, December 2002, and November 2011. Image google earth

may have enhanced the stress release, leading to breakdown of ruptures and "doline type" holes (Fig. 3.13, location D). This interpretation is favored by the timing of the rupture formation after a long dry summer and fall during and shortly after the first large rainstorm in the beginning of wintertime (e.g. ruptures: 12/2001, 12/2002 and 11/2011).

The direction of the 11/2011 ruptures coincides with well-known NW–NNW trending fractures and faults cross cutting the island. Therefore, deeper zones of weakness in the island, expressed in form of fractures and faults enhance the weakening of the Lakki plain. However, the new rupture must be regarded as a simple surface phenomenon, since no heat, gases and hot waters have been recognized.

Fig. 3.14 Surficial, up to 10 m deep ruptures in the central part of the Lakki plain, which formed during the first episode in November 2001. Neither vertical nor strike-slip displacements are visible. Locality A in Fig. 3.13 view towards south; picture taken December 9, 2001. *Photo* A. Ganas

Fig. 3.15 Surficial, up to 20 m deep rupture in the central part of the Lakki plain, which was reactivated during the second episode during December 2002; The rupture partially widened and was filled with mud bushes and trees; locality B in Fig. 3.13 view towards south, picture taken March 13, 2003. *Photo* V.J. Dietrich

Fig. 3.16 Intersection of the 2001/2002 ruptures (*right* foreground with the rupture of the third episode, November 2011 (*left*, background). Indication of the intersecting process is demonstrated in the sharp surface edges. The rupture also partially widened and was filled with mud due to torrents caused by the strong rainstorms; The wall expose the upper several meters of argillitic to sandy layered sediments of the Lakki plain. Locality C in Fig. 3.13 view towards southwest; picture taken November 21, 2011. *Photo* V.J. Dietrich

Fig. 3.17 6–8 m deep and 8 m in diameter "doline-type" hole next to the rupture of November 2011. The filling was washed away through a drainage hole leading to a deeper system of subroded tunnels; locality D in Fig. 3.13; picture taken December 3, 2011. *Photo* V.J. Dietrich

According to all observations, the Lakki rupture does not indicate any volcanic phenomena or reactivation of magmatic activity at depth.

3.3 Detailed Lithostratigraphy of Nisyros Volcano

Volcanoes in oceanic and continental arc environments are built up mainly by eruptions of water-bearing ranging from basalts to rhyolites and eruptions of typically volatile-rich magmas. The life-time of a single volcanic edifice can vary from thousands to several millions of years depending on the geotectonic and geodynamic environment, thickness and constitution of the crust, and consequently on the emplacement and differentiation mechanism of the magmas through the crust to the surface (Hildreth 2007). The construction of these volcanoes occurs during eruptive episodes, that typically follow a cyclic pattern: An eruption generally starts with hydro-magmatic explosions, is followed by phreato-magmatic eruptions producing mostly fallout deposits and surges, then grades into magmatic explosive activity, feeding surges and pyroclastic flows, before, final emplacement of degassed lavas forming, domes and necks. These eruptive cycles are then followed by periods of dormancy, during which magma reservoirs get refilled. Hydrothermal activity can be important while the volcano is dormant, and the edifice typically undergoes intense erosion, sometimes catastrophically by flank collapse.

As the Nisyros volcanic history is based on the litho- and tephrostratigraphy of the edifice (mostly defined by the mapped lavas and pyroclastic rocks), it is best to describe it using these cycles of eruptive activity, separated by epiclastic deposits and the paleosols, which mark the periods of dormancy (Table 3.1). Depending on the state of development of these volcanoes, one can find initial, embryonal stages with short cycles of years to hundreds of years, and more evolved stages, composed of numerous equivalent short eruptive cycles merging into a major cycle with long temporal intervals.

The detailed lithostratigraphy of the Geological Map of the Island of Nisyros is given in the Electronic Supplementary Material Appendix of this chapter.

Table 3.1 Comprehensive presentation of the Nisyros lithostratigraphic units (LSU) 1–32, divided into eruptive cycles

LSU	Eruption mode	Thickness	Rocktype
	Post-Caldera eruptive cycle		
32	Lava domes, flows	Max. 600 m	Rhyodacite
	Epiclastic deposits	Max. 2 m	
	Caldera eruptive cycles and Caldera collapse		
31	FI-WS-FI-PbS-succ.	Outcrop 30 m	Rhyolite
30	Lava flows	Max. 150 m	Rhyolite
29	Epiclastic deposits	Max. 20 m	
28	F-FI-WS-FI-succ.	Outcrop 20 m	Rhyolite
27	Lava flow	Max. 10 m	Andesite
	Composite Stratovolcano cycles		
26	Dome collapse breccia	Outcrop 20–30 m	Dacite
25	Flows	Max. 150 m	Dacite
24	Flows	Max. 25 m	Bas. And.- Andesite
23	Epiclastic deposits	Max. 20 m	
22	Flows	Max. 10 m	Bas. And.- Andesite
21	F-PbS-PyFI-succ	Outcrop 15 m	Bas. And.- Andesite
20	Epiclastic deposits	Max. 20 m	

(continued)

Table 3.1 (continued)

LSU	Eruption mode	Thickness	Rocktype
19	F-S-F-3S-F-F-xS-F-succ.	Outcrop 50 m	Bas. And.to Dac.
19	F-PbS-FI-succ.	Outcrop 40 m	Dacite
18	Lava flow	? Max. 10 m	Dacite
17	Lava domes, flows	Max. 60 m	Rhyolite
16	S-FI-succession	Outcrop 30 m	Basaltic Andesite
15	Lava flow	Max. 40 m	Andesite
14	Lava flow	Max. 25 m	Dacite
13	Lava flow	Max. 40 m	Bas. And.- Andesite
12	Epiclastic deposits	Max. 2 m	
	Early shield Volcanic cycles		
11	F-FI-F-S-FI-succ.	Outcrop 35 m	Bas. And.- Andesite
10	Lava flows	Max. 70 m	Basaltic Andesite
9	Lacustrine deposits	Max. 5 m	
8	Lava flow	Max. 5 m	Basaltic Andesite
7	Lacustrine deposits	Max. 5 m	
6	S-F-FI-S-FI-succ.	Outcrop 60 m	Basaltic Andesite
5	Lava flows	Max. 40 m	Andesite
4	F-FI-S-F-succ.	Outcrop 30 m	Andesite
3	Lava flow	Max. 35 m	Basaltic Andesite
	Submarine Volcanic base		
1, 2	Pillow and lava flows	? Max. 50 m	Basaltic Andesite

3.4 The Eruptive History of Nisyros Volcano

3.4.1 Introduction

The island of Nisyros is a Quaternary composite stratovolcano located at the easternmost end of the Aegean volcanic arc, in the Dodecanese archipelago, south of Kos. The island is almost circular, with an average diameter of 8 km, covering an area of about 42 km^2. It lies above a basement of Mesozoic limestone (Geotermica Italiana 1983, 1984) and a thinned crust, with the Moho located at a depth of about 27 km (Makris and Stobbe 1984). The references of previous studies in volcanology, petrology, geochemistry of volcanic rocks, fumarolic gases and hydrothermal waters has been listed chronologically at the end of this chapter; geological maps have been published by Di Paola (1974), Papanikolaou et al. (1991), Vougioukalakis (1993, 1998, 2003), GEOWARN (2003), Volentik et al. (2005).

The volcanic edifice of Nisyros with a summit caldera of a 4 km average diameter is the result a large variety of explosive and effusive eruptions producing calc-alkaline pyroclastic deposits and lavas from basaltic andesitic, dacitic, rhyodacitic, and rhyolitic composition. According to previous studies, the volcanic history has been generally assigned to four major episodes: starting with shallow marine to subaerial basaltic to andesitic volcanism followed by moderate andesitic explosive and effusive activity, building up a first major strato-cone surrounded by several satellite eruption centers (scoria and tuff cones). The present morphology of the island is finally due to two major rhyolitic plinian explosive phases each accompanied with consecutive effusive voluminous lava flows and domes, which may have followed the caldera collapses.

3.4.2 Early Shield Volcano Cycles of Nisyros

3.4.2.1 Submarine Volcanic Base

Nisyros is entirely volcanic: metamorphic or sedimentary rocks have been mapped anywhere on the island. Geothermal drilling from the lowest part of the caldera in the Lakki plain (Well NIS 1 in the southeastern side at 110 m altitude asl and NIS 2 at the eastern foot of the young rhyodacitic Lofos dome at the western side at 145 m a.s.l) reached Mesozoic limestones at a depth of approximate 650 m depth bsl. The 750 m caldera filling consist of unconsolidated talus and alluvial deposits in the upper 150 m and poorly-documented tuffs, pyroclastic flows intercalated with basaltic to andesitic flows and epiclastic breccias in the last 600 m (Geotermica Italiana 1983, 1984). The evolution of the volcanic history of Nisyros Island described in this paper is solely based on the outcropping litho- and tephrostratigraphic successions.

The oldest occurrence of volcanic activity is represented by a shallow submarine to subaerial formation of hyaloclastites (LSU No. 1), pillow breccia, and pillow lava of up to 50 m thickness in the north–western corner of the island in the cliffs of Monastery Panagia Spiliani at Mandraki and in the western coastal part between Hochlaki beach (Fig. 3.18) and Cape Kanoni (Fig. 3.20). The hyaloclastics and loosely packed pillows and pillow breccia appear to be the front of subaerial basaltic andesite lava flows, which covers the brecciated units. A few dikes cut the whole formation; internal tilting and faulting is present. Extrusions from submarine fissures seem to be unlikely, since no typical close-packed pillow lava is present. To produce such high amounts of pillow breccia and hyaloclastic, palagonized material, an explosive origin from shallow submarine a subaerial vents, similar to processes forming peperites (Skilling et al. 2002; de Goer de Herve 2008) are envisaged. Such a process might be supported by intercalated lava lenses of variable thickness (up to 10 m) within the pillow-hyaloclastic sequence, partly mixed with intensively hydrothermally altered tuffs and tuffites (LSU No. 2, Fig. 3.20). The outcrops occur at Cape Kanoni and along its southern coastal strip. Since they are aligned to NE–SW (approx. 30°) tending faults, they could also be interpreted as channel fills.

Similar volcanic and volcanoclastic sequences have not been clearly linked to specific units in

Fig. 3.18 Basaltic andesite "pillow-hyaloclastite" formation (unit No. 1, Figs. 3.11b and 3.19), the lowest outcropping volcanic rocks of Nisyros volcano. The whole unit has an inclination of 20°–30° towards W–NW. The horizontal hatched *lines* represent erosional levels of different stages of uplift. *Photo* V.J. Dietrich

Fig. 3.19 The majority of the basaltic andesite clasts and pillow fragments, with an average diameter of 10–15 cm are embedded in a consolidated *yellow* to *orange* palagonitic cement. Isolated irregular pillows have variable diameters from 0.5 to ca. 8 m and occur mainly at the base of the unit. *Photo* V.J. Dietrich

Fig. 3.20 West coast at Cape Kanoni LSU units Nos. 1, 2, 20–24, and 28. From sea level to top: Talus, No. 1 (hyaloclastite formation; lower part "pillow breccia" overlain by tuffaceous deposits), No. 2 (tuffaceous deposits), 21 (pyroclastic flow), No. 22 (Basaltic andesite lava flow), No. 23 (Paleokastro epiclastic deposits), No. 24 (Basaltic andesite lava flow with thick red scoria sole and top and columnar jointing, unit 28 (lower pumice). *Photo* V.J. Dietrich

the geothermal wells. However, between −480 and −540 m b.s.l depth, breccias and a fine tuff/tuffite occurs on top a several ten meter thick "blocky tuff in a palagonitic matrix" (−540 to −585 m b.s.l). These units are suspiciously similar in two ways, and either they represent equivalents of the KIU-formation, the "Kos acoustically incoherent unit within the sedimentary cover in the west- and east Kos basins (Fig. 2.10) as part of the 161 ka Kos-Plateau-Tuff (KPT) eruption cycle (Stadlbauer 1988; Smith et al. 1996; Allen 2001; Bachmann 2010), or local eruptive equivalents of the early volcanic cycles of Nisyros Island.

A paleogeographic reconstruction of the volcanic environment is difficult to achieve because of the lack precise data from the geothermal drill holes in the caldera. However, the thickness and extension of the "hyaloclastite formation" units Nos. 1 and 2 allows to establish a volcanic edifice similar to a subaerial shield volcanic structure, most probably with vents aligned a NE–SE trending fracture zone from were the lavas were emitted. In addition, a tilting towards NW is obvious due to unconformities in the hyaloclastite formation, e.g. within the uplifted cliffs of the M. Panaghia Spiliani.

The autobrecciation of the atypical pillow lava and pillow breccias without typical glassy rims und textural changes between outer and inner parts of the pseudo-pillow fragments leads to an interpretation either of water intrusion into the vents at very shallow aquatic levels or lava into muddy tuffaceous sediments, and thus instant brecciation. Similar brecciation processes have been described for the formation of peperites within small volcanic maar-lakes (for review see Skilling et al. 2002).

Up to now, no marine fossils have been found within the yellowish palagonitic matrix.

3.4.2.2 Early Nisyros Shield Volcano Cycles

The following volcanic activity comprises three major cycles, producing pyroclastics and lavas with basaltic andesite composition, but slightly different in their eruption characteristics. The exposures of these cycles are limited to the eastern parts of the inner caldera cliffs between Kato Lakki and Chonia and represent mainly proximal facies deposits (Figs. 3.21 and 3.22). Time intervals between these cycles must have been short, as erosional contacts or signs of paleosol are missing.

At the north–eastern lower part of the inner caldera above the Lakki plain, a subaerial lava flow up to 35 m thick and covering a distance of 1.2 km, records a first major subaerial eruption (unit No. 3). The lower part appears in several places strongly tectonised, which likely indicate recent faulting, such as break down and collapse of

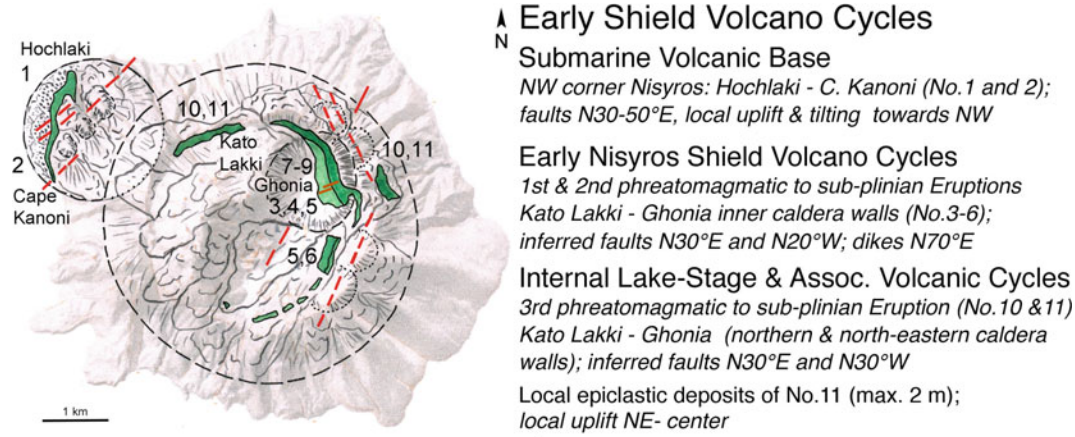

Fig. 3.21 Evolution of Nisyros volcano during the "Early Volcanic Cycles": Submarine volcanic base, early shield volcano cycles, internal lake-stage volcanic cycles

Fig. 3.22 View from S towards northeastern inner caldera walls with the lithostratigraphic units 3–15; *P* Parletia rhyolitic neck. *Photo* V.J. Dietrich

the caldera. It is possible that this cycle started with a major strombolian eruption, producing surges and pyroclastic flows, although such deposits are not preserved due to the coverage with talus and alluvial filling of the caldera. Papanikolaou et al. (1991) have correlated this lava flow with the stratigraphically lowermost basaltic andesite pillow and hyaloclastite sequence at the north–western corner of the island.

A second eruptive cycle (Fig. 3.23), producing ca. 35 m of pyroclastic deposits during a violent explosive phase (unit No. 4) seems to have started within a short time interval after the effusion of the underlying lava. The eruption started with a typical sub-plinian phase followed by a sequence of fine-grained pyroclastic flows and surges and terminated again with sub-plinian eruptions. The subsequent effusion produced an up to 40 m thick lava flow with a basaltic andesite composition (unit No. 5).

The explosive phase of the third cycle (unit No. 6) started with the deposition of coarse-grained planar-bedded surges indicating a high water/magma interaction ratio. After a short period of fallout, two thick pyroclastic flows, disrupted by two coarse-grained surges, planar bedded and with sandy-waves, were deposited.

The geometrical distribution and chemical similarity of the volcanic edifice produced during these three eruptive cycles during one consecutive period of time leads to the assumption of the generation of a subaerial shield volcano with a maximum diameter of several kilometers and a height of a few hundred meters. The large volume of erupted material during the third cycle, producing up to 60 m of pyroclastic deposits, the high lithic content of large fragments with an average size of 25 cm in the upper pyroclastic flow and the dip of the underlying lavas with respect to the present day caldera depression, support a collapse of the early shield volcano, leaving a small caldera behind (Volentik et al. 2002).

The geometric distribution and thickness of the lava and pyroclastics allow to a certain extent a reconstruction of the early volcanic edifice. A subaerial volcanic shield with a center more or less in respect to the present day caldera seems to be the most feasible interpretation. The lavas show slight inclinations and reduction of thickness outward. Indication of the position of the original vents can only be taken from the direction of a few dikes in the north–eastern caldera wall, which trend N 70°E. We assume that at this early volcanic stage the general structural trends

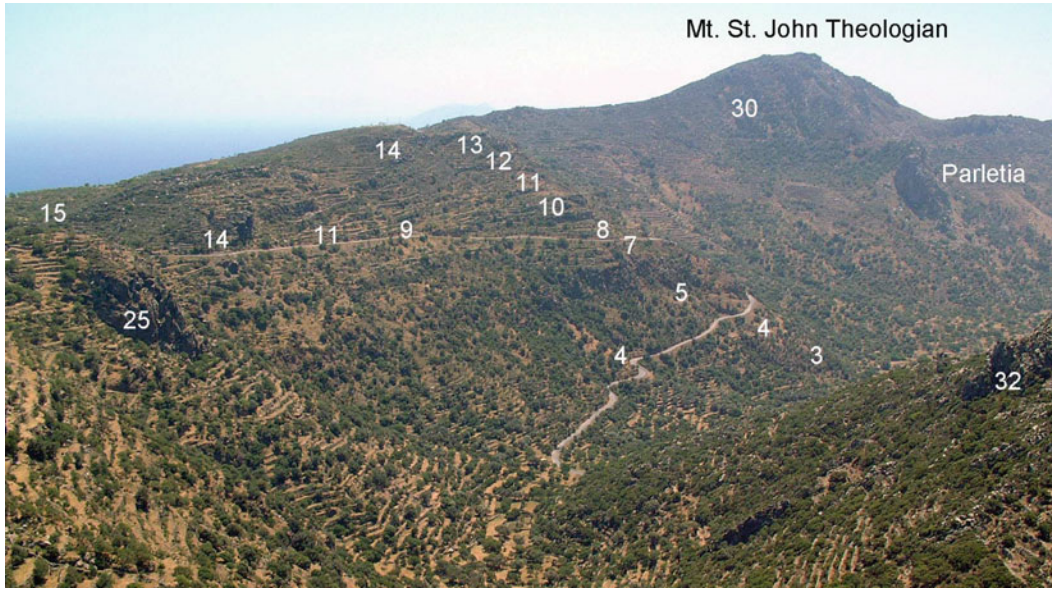

Fig. 3.23 View towards SE of the north–eastern inner caldera walls with the main road to the caldera floor (Lakki plain); in the background Mt. St. John Theologian 589 m and Parletia neck (rhyolite). Successions of the caldera walls from *bottom* to *top*: Lithostratigraphic units Nos. 3–15. The highest mountain of the eastern caldera rim St. John Theologian 589 m. *Photo* V.J. Dietrich

and tectonics of the regional volcanic field controlled the emplacement of magmas from the upper mantle through the crust to the surface. The conjugate faults, N30°E and N20°W seem to have played the most important role.

3.4.2.3 Internal Lake-Stage and Associated Volcanic Cycles

In the north–eastern part of the internal caldera cliffs between Kato Lakkì— Ghonia and on top of the three pyroclastic and lava cycles described above, two volcanoclastic, lacustrine sedimentary successions (LSU Nos. 7, 9) are found (Figs. 3.24 and 3.25). They are continuous over a distance of five hundred meters, divided by a few meters thick subaerial basaltic andesite lava (unit No. 8), indicating the presence of an "internal lake" within a period of minor volcanic activity. The fact that the lower contact of the intermediate lava flow is very sharp and without any sign of scoria or development of pillowed breccia shows that the early lake must have been shallow.

The varved beds of the two intra-caldera lakes and associated volcanic cycles indicate sedimentation of volcanic ashes and fine-grained lapilli mixed with sandy layers within an aqueous system (details in Electronic Supplementary Material Appendix 3.3; Volentik et al. 2002). Characteristic maar-type phreatomagmatic sedimentary structures have not been observed. These sediments seem to be limited in their lateral extension to the north–eastern segment of the caldera, since they are absent in other similar stratigraphic positions inside the caldera wall. Surge deposits are few in the lowest part of the section, but become abundant at the upper part. The lifetime of the two lacustrine cycles could not have exceeded several hundred to a thousand years due to the restricted thickness of the varved successions.

The lake stadium was terminated by an effusive cycle (unit No. 10), which produced several basalt-andesitic flows with scoriaceous base and top, building up 70 m of the northern and north–eastern caldera walls (Fig. 3.26), forming the cliffs below the village of Emborio, and cover the eastern slopes towards Kremastos. Since these units are also exposed in the southern inner caldera cliffs, although with reduced thickness, they

Fig. 3.24 Lapilli tuffs, varved tuffaceous sandstones (unit No. 7) with impact sag. The main part of the varved lacustrine beds consists of fine-grained purple and whitish sandstones, partly with cross-bedding. *Photo* V.J. Dietrich

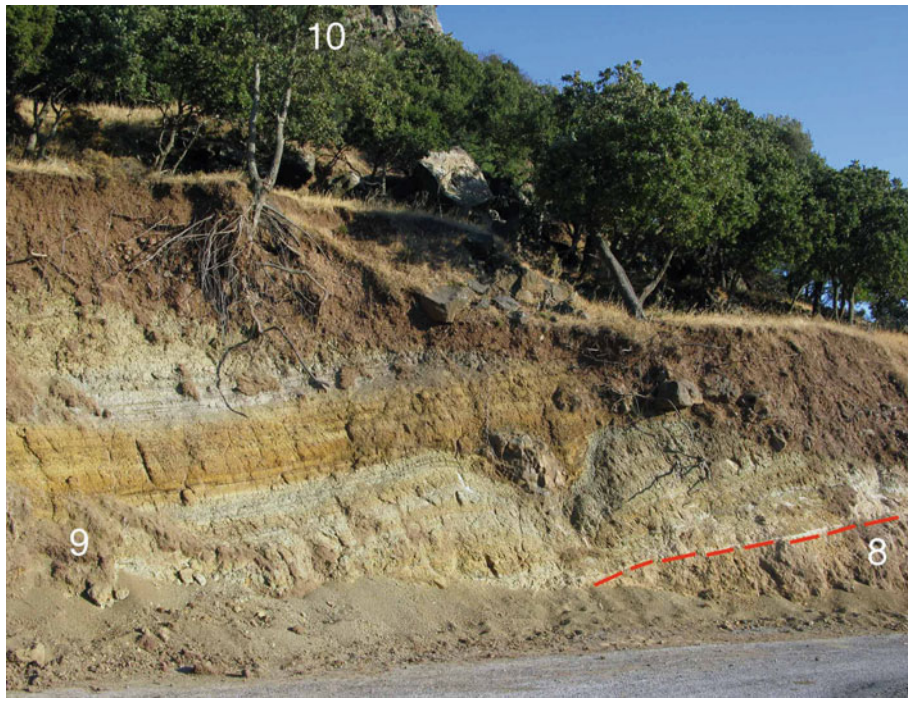

Fig. 3.25 Lower part of the second (*younger*) lacustrine succession of alternating siltstones (*purple*) and epiclastic sandstones (No. 9) with sharp contact to underlying reworked andesitic scoria of No. 8; large andesitic impact sag in the centre of picture; outcrop along the caldera road. *Photo* V.J. Dietrich

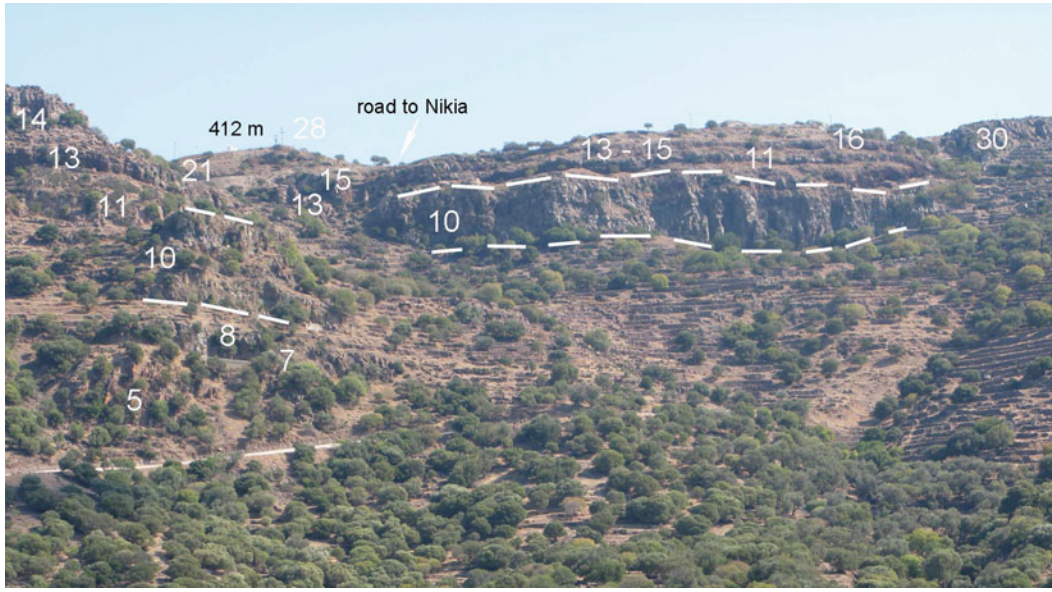

Fig. 3.26 Sequence of lavas and pyroclastic LSU Nos. 5–16 in the north–eastern inner caldera walls. *Photo* V. J. Dietrich

likely represent the filling of the early caldera with a diameter similar but smaller than the present day one. The neck west of the Kato Lakki plain can be seen as one of the eruptive centers.

Soon after the end of this effusive episode, a major explosive cycle started from a vent most probably located within the northern part of the caldera, covering the northern and eastern slopes of the island with 35 m of pyroclastic deposits (unit No. 11). This cycle started with a high explosive sub-plinian activity erupting a characteristic red pumice fall-out and intermittent fine-grained surges followed by strong pyroclastic flows including large blocs of lithics and pumice at their base.

The cycle terminated with a minor surge and fallout. The growth of a stratovolcano on top of the relicts of the early caldera may have been the result of the last strong explosive cycle. Minor epiclastic deposits (unit No. 12), which contain reworked material of the underlying pyroclastic succession, indicate both a time gap of volcanic activity permitting erosion and tectonic movements, e.g. local uplift between the NE corner and central part of the island and could be interpreted as bulging effect of a magma emplacement in the upper crust.

3.4.3 Composite Stratovolcano Cycles

3.4.3.1 Transition from Shield Volcano to Stratovolcano (Northern and Eastern Eruptive Centers)

After an unknown time gap, several short volcanic cycles contributed to the growth of a stratovolcano, erupting more evolved magmas from a central vent and from peripheral volcanic vents more or less aligned along the major regional fault systems (N30–50°E & N30°W; dike N20°W). This volcanic period can be limited between the early epiclastic deposits (unit No. 12) and the wide spread epiclastites and conglomerates of Paleokastro (unit No. 23) and with a sequence of three dominant lava flows (LSU Nos. 13–15) derived from northern and eastern central eruptive centers (Fig. 3.27). These flows form the upper parts of the caldera walls in the northern, northeastern and eastern segments and cover the north–western slopes down from Monastery Evangelistra and the eastern slopes between the areas of Linevrochia and Kremasto.

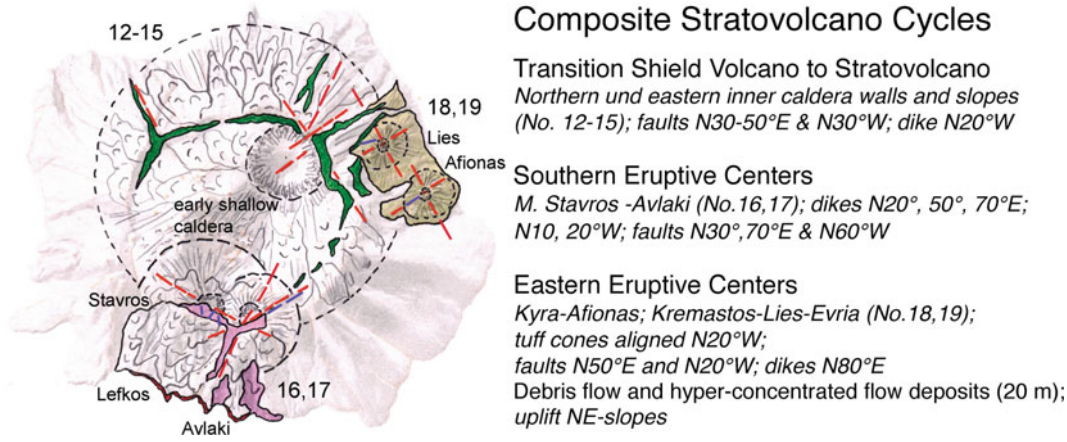

Fig. 3.27 The transition from shield volcano to stratovolcano and the clear distinction between two eruptive areas, the southern and eastern eruptive centers

Fig. 3.28 Neck (up to 40 m) within the andesitic lava flow, unit No. 13, exposed towards north outside the caldera call east of Emborios. *Photo* V.J. Dietrich

During this new cycle, more differentiated (andesite and dacite) magmas reached the surface. The first, 40 m thick andesitic lava flow (unit No. 13, Fig. 3.28) was emitted from a main central vent, since it appeared all around the upper caldera walls with the exception in the southwest, where the young Profitis Ilias rhyodacitic lava flows probably cover it. An andesitic neck and a small scoria cone in the upper eastern slopes close to the present day caldera rim represent two additional satellite eruptive centers.

A 25 m thick dacitic lava flow (unit No. 14), which covered the andesitic lava without any observable time break, erupted most probably from the same central vent. It is present from the village of Emborio throughout the northern and eastern segments of the upper caldera cliffs and extends towards south in the cliffs below the village of Nikia. This unit contains up to 30% of andesitic inclusions with both reddish and grey colors. The grey enclaves appear quenched, and likely indicate the reinjection of andesitic magma into a dacitic reservoir. The red oxidized andesitic inclusion, in contrast, are interpreted as older lithic material incorporated into the dacitic magma during the emplacement.

The final, 40 m thick andesitic lava flow (unit No. 15) forms the top of the "lava trilogy cycle" with a thick base of red scoria. It covers mainly the upper northern segment of the caldera and parts of the northeastern slopes of the island.

3.4.3.2 Southern Eruptive Centers (Monastery Stavros—Avlaki)

The following volcanic sequences can mainly be assigned to remnant eruption centers, which are exposed in the southern segment of the caldera walls below the Monastery of Stavros and cover the southern slopes (between the coves of Lefkos in the southwest and Aghios Nikolakis, Avlaki) with pyroclastic flows and lava (Figs. 3.27 and 3.29). They are assigned to one eruptive cycle slightly younger than the previous "trilogy cycle". The beginning of this cycle starts with a 30 m thick basaltic andesite pyroclastic succession of several small base surges of grey lapilli followed by pyroclastic flows, rich in andesitic lithics (unit No. 16). The strong hydrothermal alteration, within this unit (including the lithics) requires the existence of a larger magma reservoir at higher crustal depth and heat supply to a hydrothermal system.

Fig. 3.29 View towards southwest from Nikia (Monastery Stavros and Pachia island in the background). Note the depression of the western segment controlled by two major fault zones. On the *left* the rhyolitic lava flows and neck of Tsimi hill with the Mylos tower (old mill). *Photo* V.J. Dietrich

Fig. 3.30 Rhyolitic lava, unit No. 17 with internal flow folding and original surface. South coast, west of Avlaki *Photo* V.J. Dietrich

The cycle ends with the effusion of voluminous, up to 40 m black, massive, partly glassy, and perlitic rhyolitic lava flows (unit No. 17, Fig. 3.30). The Tsimi neck west of the Village of Nikia at the southern caldera rim marks one eruptive center of the blocky lava. Other vents are probably covered by the young rhyodacitic domes and lavas in the southwestern segment of the caldera.

The different trends of the dikes N20°, 50°, 70°E; N10, 20°W, as well as the measurable faults N30°, 70°E and N60°W indicate a complex extensional system along which the magmas were emplaced.

3.4.3.3 Eastern Eruptive Centers (Tuffs Cones of Kyra—Afionas; Kremastos—Lies—Evria)

The eastern flanks of the island comprise several similar eruptive cycles represented by successions of surges, pyroclasic flows and fallout which may have been derived from at least two major eruptive centers, the hills of Afionas and Lies, both remnants of large tuff cones (Fig. 3.27). Most of the unconsolidated tuffs have been eroded and washed down into the sea during rainstorms and mudflows, causing small frontal deltas and submarine channels close to the shore. In addition, the entire area of the eastern slopes resembles a large down-faulted block between major regional fault systems (Fig. 3.29 and structural Sect. 3.2). The two cones tuff cones seem to have been aligned along N20°W faults intersecting N50°E faults. A dike strikes N80°E.

Their ages cannot be precisely determined by lithostratigraphy. On the eastern slopes, these successions overlay older andesitic and dacitic lavas derived from the eastern caldera walls (the "trilogy cycle", units Nos. 13–15), while, to the South, everything is covered by the thick younger rhyolitic lavas flowing down from the south–eastern caldera rim. Only one light grey dacitic flow (unit No. 18), occurring at sea level along the shore at the base of Afionas tuff cone over a distance of 300 m between the beaches of Lies and Pachia Ammos, could be correlated with the first dacitic flow of the island (unit No. 14). However, this flow has slightly different

petrographic characteristics (e.g. the lack of abundant andesitic inclusions). Over a distance of 150 m, the surface of this grey dacite contains up to 1.6 m deep pockets filled with a strange brecciated fine-grained whitish rhyolitic flow with irregular enclaves of "andesitic schlieren" and mafic cumulates. In places, the yellowish color indicates the formation of a paleosol.

The andesitic to dacitic pyroclastic successions of the *Afionas tuff cone* (No. 19, Figs. 3.31 and 3.32), with a maximum thickness of 80 m, comprises at least three major explosive cycles from the same vent, separated by erosional contacts and thin paleosols. The deposits consist of light gray surges, proximal strombolian fallout and minor pyroclastic flows. The fallout contains lithics of andesite lava fragments and cumulates, in addition to limestones and contact metamorphic marbles and calc-silicate skarns. The fresh lithic andesitic fragments suggest that a recharge of andesitic magma into a dominantly dacitic reservoir occurred shortly prior to the eruption. A detailed stratigraphic description is given in the Electronic Supplementary Material Appendix 3.3.

Fig. 3.31 Tuff cone of Afionas (LSU Nos. 18, 19). The white-hatched line designates the general division of the Afionas tuff cone (Rehren 1988). *Photo* V.J. Dietrich

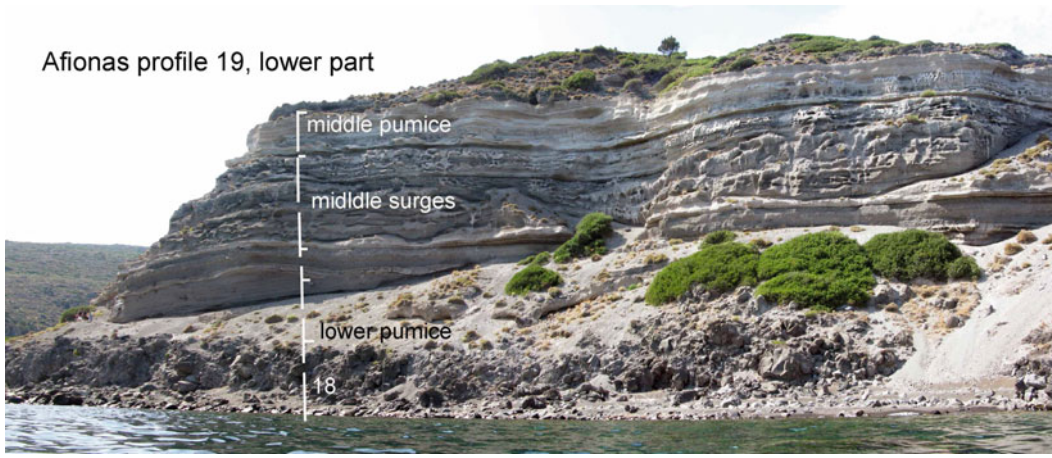

Fig. 3.32 Tuff cone of Afionas. At sea level dacite lava flow (unit No. 18), unconformatly overlain by a fall-surge-fall-surge-fall succession of bimodal composition, andesite and dacite. The *white* characteristic layer is made up surge deposits with planar-bedded and sandwave structures. *Photo* V.J. Dietrich

3.4.3.4 The Composite Stratovolcano (Mandraki—Pali—Kremares)

Lavas and pyroclastic deposits from the growing composite Stratovolcano occur throughout the island, typically in lateral cones, and are associated only in parts with the underlying sequences. They include remnants of cinder, spatter and scoria cones. This random distribution indicates that smaller eruption centers as lateral vents from radial feeder dikes could were formed around a central growing stratovolcano within the limits of the early caldera. The deposits from the peripheral vents contributed to the growth of the entire island.

The locations of the vents seem to be controlled at the by main fault pattern, N30°E, N70°E, as well as N30°W, N60°W, and E–W (Fig. 3.33).

The duration of this volcanic activity period can only be estimated by relative litho-stratigraphy and by the appearance of erosional features and paleosols. Since the latter time markers are missing, a rather short time period of several hundred to a few thousand years is envisaged. This assumption is compatible with the occurrence of the basal debris flows on the eastern flanks and in channels (unit No. 20), which require uplift, leading to massive (up to 20 m thick) debris flow deposits of reworked underlying pyroclastics (unit No. 19), channeled within deep valleys in the eastern flanks.

In addition, remnants of basaltic andesite cinder/scoria cones of strombolian activity have been recognized all over the island (unit No. 21, e.g., East of Ag. Marina and east of Koftaka (western flanks), south and north of M. Evangelistra, west of Akimaronas at the caldera rim, at Linevrochia and Kremastos on the eastern flanks (Fig. 3.34), at M. Stavros and at Tsimi on the southern caldera rim, and north of Avlaki in the southern flank (Fig. 3.35).

These small individual eruptive cycles have been combined into one up to 20 m thick pyroclastic unit of black lapilli, red and black scoria fallout deposits, spatter cone facies with agglutinated fragments of fresh lava and of planar-bedded surges (Fig. 3.36). In few cases, proximal thick and unsorted basal fallout deposits indicate violent strombolian eruptions as early phases. Often the scoria cone deposits contain abundant lithic components, such as fresh andesitic lava, anorthositic and amphibole-pyroxene-rich cumulates, limestones, contact metamorphic marbles and skarns. Several small basaltic andesite lava flows (unit No. 22) with individual thickness up to 10 m are closely associated with pyroclastic deposits described above and have originated as effusive part from the same spatter and scoria cones.

The stratovolcano period probably ended with a major summit collapse since up to 20 m thick debris flows with hyper-concentrated flow

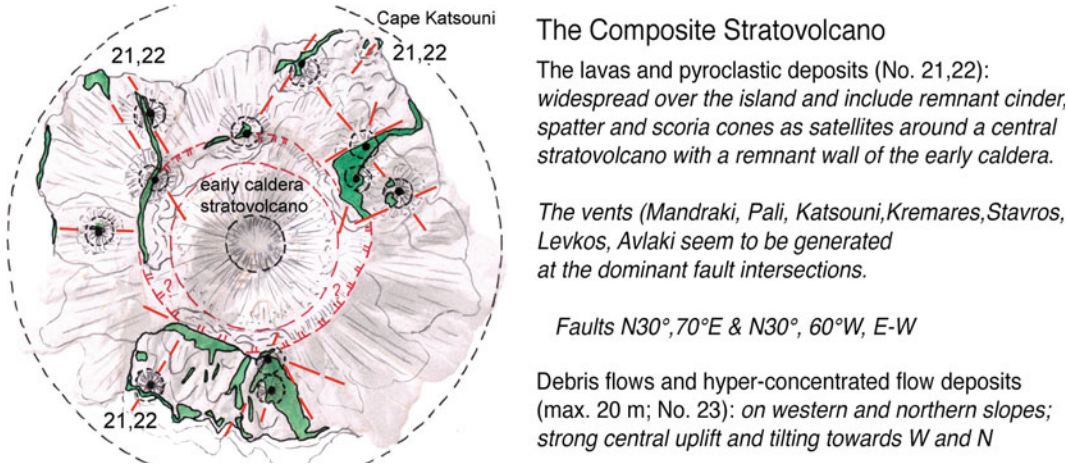

Fig. 3.33 The growth of a "Composite Stratovolcano" and distribution of small peripheral extrusive centers and flows

Fig. 3.34 The Kremares Cave at Cape Katsouni (NE corner of Nisyros). Basaltic andesite lava flow (unit No. 22) with red scoria sole and top above vent breccia (cave center) overlain by epiclastic debris flows (unit No. 23), "lower pumice" (unit No. 28), and "upper pumice" (unit No. 31) deposits. *Photo* V.J. Dietrich

Fig. 3.35 Ruins of Avlaki thermal bath; hot spring at sea level in the fault zone. Typical lava—pyroclastic succession (units Nos. 21 and 22) from a scoria cone in the southern slopes north of Avlaki. *Photo* V.J. Dietrich

deposits occur on western and northern slopes. The latter process also required strong central uplift and tilting towards W, NW and N, which also favored the formation of beach conglomerates (unit No. 23) at the north–western corner of the island.

Fig. 3.36 Planar-bedded surge deposits (unit No. 21, *dark-grey* layers) from an unknown source (e.g. tuff or scoria cone) overlain by epiclastic debris flows (unit No. 23, *top light-grey* blocky layer) and covered by a cap of "lower pumice" (unit No. 28, *orange*) and "upper pumice" (unit No. 31, *whitish*); in the northern slopes above Pali along the main road. *Photo* V.J. Dietrich

3.4.4 Terminal Cycle and Dome Collapse

The following volcanic cycle, subsequent to the stratovolcano cycles and after a significant period of dormant activity, can be bracketed by the appearance of epiclastic debris flows at its base and by the large « Loutra » debris avalanche as a result of a collapse of the northern caldera rim, probable at the end. These cycles differ from all previous volcanic cycles because of the dominance of their effusive eruption styles. Large volumes of differentiated lavas contributed to the filling of the northern sectors of the caldera and coverage of the northwestern and northern slopes of the island (Fig. 3.37). The cause of the dramatic change of the eruptive mode from all previous strombolian to sub-plinian explosive cycles to mainly effusive cycle is not clear, but it might be related to a sudden change in the geotectonic environment or to a major change in the magma reservoir.

Evidently, all lavas cover large portions of the upper slopes of the northern half of the island and may have derived from fissures and eruptive centers along a northern early caldera rim controlled by faults N30°E and N30–50°W generating intersections, thus extensional ways for magma emplacement. In addition, strong uplift of the central and south–eastern parts of the island is required to facilitate the east- and northward flow directions of all lavas. An associated process was the doming of dacitic magmas in the resurging caldera after the stratovolcano collapse.

During the first effusive cycle, a series of thin basaltic andesite-to-andesite lava flows with a total thickness of ca. 25 m (unit No. 24) was emitted from vents aligned along the early western caldera rim and covered the western slopes down to the sea. The second effusive cycle produced large volumes of dacitic lava flows with a thickness up 150 m, the "Emborio" lava dome and a neck (unit No. 25).

The time gap between the terminal caldera cycle and the collapse of the northern caldera rim is difficult to establish. The most plausible hypothesis favors a collapse after the emplacement of the voluminous dacitic lava flows. At the

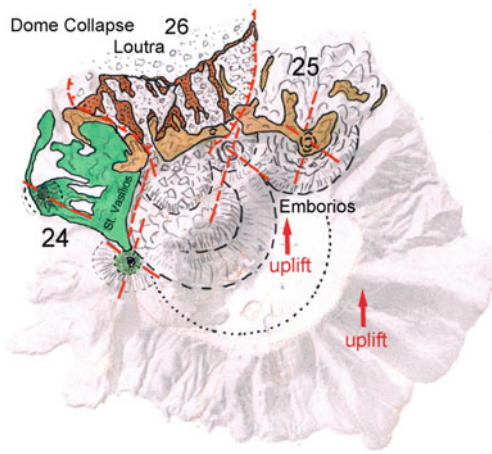

Terminal Cycle and Dome Collapse

Up to 10 basaltic andesite-to-andesite lava flows (No.24) on the western slopes (St. Vasilios) probably derived from vents on the western rim of the early caldera along faults N30°E & N60°W.

The up to 150m thick dacitic lava flows and Emborios lava dome (No.25) cover large portions of the upper slopes of the northern half of the island and may have derived from fissures along the northern early caldera rim at intersections of faults N30°E & N30-50°W.

The debris avalanche (No.26) covers the northern slopes from Mandraki to Pali (type locality "Loutra"), *interpreted as "dome collapse breccia" or break-off along intersections of faults N30°,70°E & N30°W.*

Fig. 3.37 Summary of the "Terminal Cycle and Dome Collapse"

Fig. 3.38 The "Emborio" dacitic lava dome and a neck (unit No. 25) forming the upper northern caldera wall between Mt. Akimaronas (453 m) and the village of Emborio. From *top* to *bottom* unit No. 25, Emborio dacitic lava; unit No. 15, andesitic lava; unit No. 14, dacitic lava rich in andesitic inclusions, unit No. 13, andesitic lava with red scoria sole; unit No. 11, pyroclastic sequence; unit No. 10, *thick* basaltic andesitic lava flow. *Photo* V.J. Dietrich

base of the chaotic collapse breccias, a 0.3–1 m horizon of dacitic ejecta with normal gradiation and fragments of dacitic lava have been observed in certain places. This deposit is interpreted as an indication of the start of a new cycle, emplacement of new magma from depth and bulging of high crustal levels.

The giant debris avalanche deposit (unit No. 26), named after the most diagnostic type locality "Loutra", reached variable thickness depending on the pre-existing morphology of the northern slopes between Mandraki and Pali (Figs. 3.37, 3.38, 3.39 and 3.40). The most characteristic megascopic feature of this large

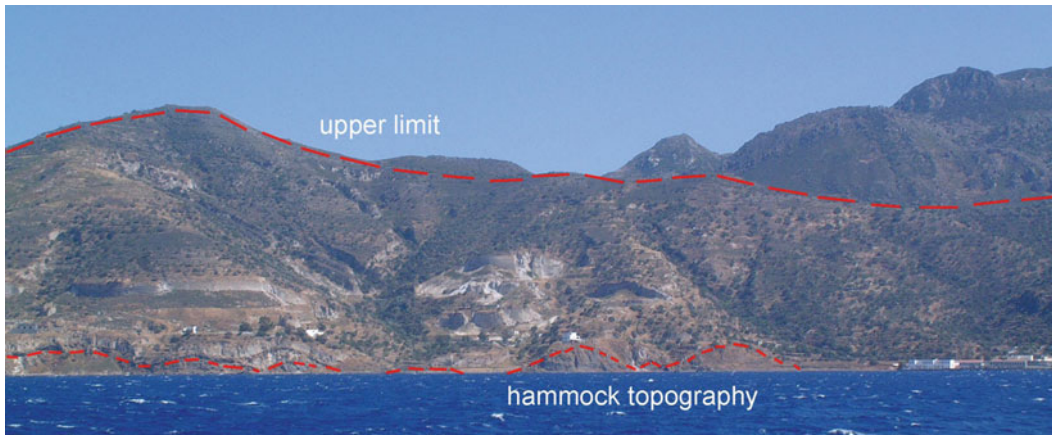

Fig. 3.39 The eastern part of the giant "Loutra debris avalanche": The "Loutra Bath" at the right side. The long hatched *red line* marks the *upper* limit of relict debris outcrops, whereas the short *stippled line* outlines the hammock topography at sea level. The hammocks are made of chaotic debris. *Photo* V.J. Dietrich

Fig. 3.40 "Loutra" debris avalanche east of Loutra. Compact block flow with little matrix support. Note that the smaller lithic components are partially rounded and thus may represent component of older volcanics and pyroclastics, e.g. reworked epiclastic deposits. *Photo* K. Kyriakopoulos

epiclastic unit is the hammocky topography, forming small hills of 20–30 m heights in the lower slopes along the shore. In fresh road cuts and in the cliffs along the shore, the chaotic internal structure of these unconsolidated deposits is evident. Fragments are mostly of dacitic composition, but rare pieces of andesites and red scoria from earlier strombolian eruptive cycles are also found.

An isolated andesitic lava flow, ~7–10 m in thickness (unit No. 27), appeared after the emplacement of the "Loutra" avalanche in the slopes of Loubounia (south of Loutra). It seems that the flow poured out of a fissure inside a scarp, produced by the Loutra avalanche. Apparently this flow marks the last andesitic eruption in the volcanic history of the island.

3.4.5 Caldera Eruptive Cycles and Caldera Collapse

A paleosol covers in many places the debris flows (unit No. 23), the dacitic lavas of Emborio (unit No. 25) and parts of the "Loutra" debris avalanche (unit No. 26). This is the indication that a large time interval and repose period occurred between the last dacitic and andesitic magmatic activity and the beginning of a major cycle of high explosive activity from highly differentiated rhyolitic magmas. During the "Caldera Eruptive Cycles", two vast successions of rhyolitic pumice derived from plinian eruptive cycles, designated as "lower and upper pumice", were deposited and divided by epiclastic deposits, the effusion of voluminous rhyolitic lava flows and the breakdown of a large caldera to the present day dimensions (Fig. 3.41). The lifetime of volcanic activity of each individual cycle, as well as of the total time-span is still not known, despite the occurrence of two widespread paleosols separating these two cycles, well exposed at Cape Katsouni (Fig. 3.42).

3.4.5.1 First Eruptive Cycle

The first voluminous (up 20–30 m thick) rhyolitic pyroclastic sequence, the "First Eruptive Cycle", designated as "lower pumice" (unit No. 28) resulted from a major plinian eruption and were deposited all over the island. Major occurrences are still present on the southern

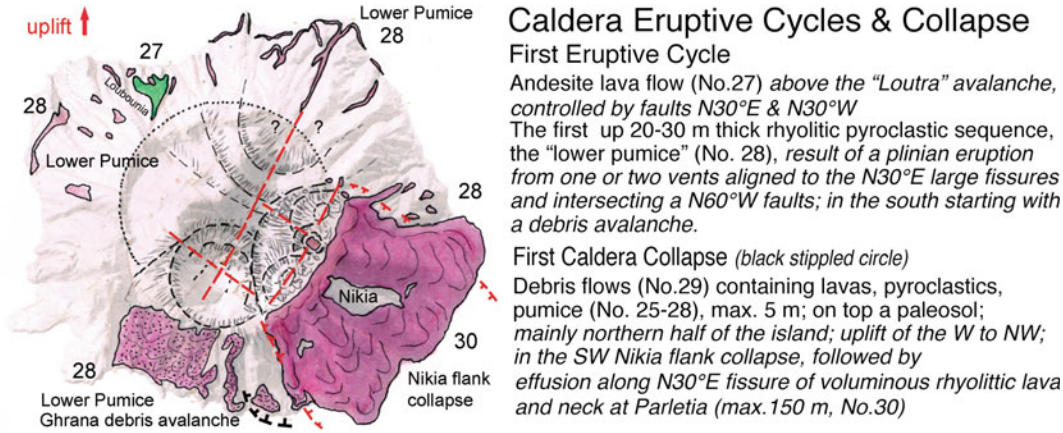

Fig. 3.41 Caldera cycles—Caldera collapse: first eruptive cycle combined with a first caldera collapse and SE flank collapse

Fig. 3.42 Lithostratigraphic pumice successions of the "Caldera Eruptive Cycles", the "Lower and Upper pumice" sequences, units Nos. 28 and 31 respectively at Cape Katsouni overlaying older lava (unit No. 20) and epiclastic (unit No. 23) deposits. *Photo* V.J. Dietrich

slopes, because of lack of coverage with younger pumice deposits (Fig. 3.41). However, no stratigraphic contacts occur to the northern and eastern equivalent of the "lower pumice units". Both are overlain by a paleosol and the large eastern rhyolitic lava flows (unit No. 30) of the second eruptive cycle.

Explosive phase

The explosive phase of the "lower pumice" LP can be divided into (1) in the lower part, plinian fall deposits, which contain lag breccias and up to 50% of lithics (some up to meter size) (unit No. 28a and b) and (2) in the upper part, poorly bedded fall layer with surges and pyroclastic flows (unit No. 28c). Both parts were probably deposited during one eruptive event since no major unconformity has been recognized within the deposits. The lithics include metamorphic limestones, skarns, hydrothermally altered rocks, unaltered volcanics and mafic cumulates, thus witnesses of a larger magma reservoir and an existing hydrothermal system. Yellowish weathering is a widespread feature within the "lower pumice". A chaotic debris-avalanche deposit has been recognized in the south–eastern coastal cliffs and along the beach at Ghrana bay over a distance of at least 500 m overlaying the basal pumice fallout flows indicating a southern slope failure during the initial phase of the first plinian fallout (Fig. 3.43).

Two eruption vents may have occurred in areas between the present southern and northeastern caldera rim aligned to a N30°E trending fissure and intersecting a N60°W faults (Fig. 3.41). The wide distribution of large fallout pumice blocks and lithic fragments, the presence of lag-breccias, poor bedding and sorting, as well as the greatest amount of fine-grained ash indicates proximal deposition in the southern part (Fig. 3.44a, b). In contrast, the plinian fallout of the northern part along the north and east cost exhibit more distal features (large lag breccia but thinner deposits, smaller diameters of pumice blocs and lapilli, sorting, reverse grading, and much lower lithic contents; Fig. 3.45). In addition, small ash- and mudflows occur.

The uneven areal distribution in grain size of the lower pumice pyroclastics on the island and the scarcity of the lower pumice deposits at the western half of the islands suggest an uplift of the western area during or shortly after the eruptive "lower pumice" cycle. Additional evidence of the uplift exists in the appearance of debris flows, mainly on the northern half of the island (unit No. 29), with components of lavas, pyroclastics and pumice (No. 25–28). All deposits are covered by a paleosol.

First Caldera Collapse

The "First Caldera Collapse" can only be estimated in space and time. We tend to place the collapse after the vast explosive phase. The highly differentiated rhyolitic magma may have been derived from rather shallow reservoirs in the upper crust (see later chapter of petrology and magma dynamics). As consequence of eruption the large volume deficiency could have generated a surficial depression and thus, initiated a first collapse that caused a first caldera. In addition, a major break in the steep morphology into two steps of the south–eastern caldera walls indicates

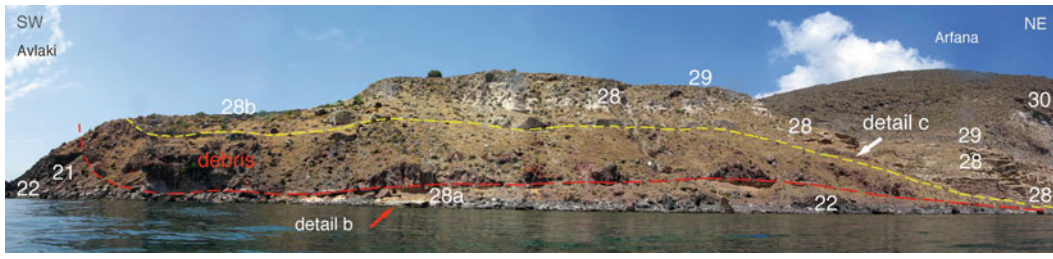

Fig. 3.43 "Lower pumice" (unit No. 28) deposits along the southeastern coast of Ghrana bay forming the base (*red arrow* and Fig. 3.75b in Electronic Supplementary Material Appendix 3) and top (*white arrow* and Fig. 3.75 c in Electronic Supplementary Material Appendix 3) of a coeval debris avalanche. *Photo* V.J. Dietrich

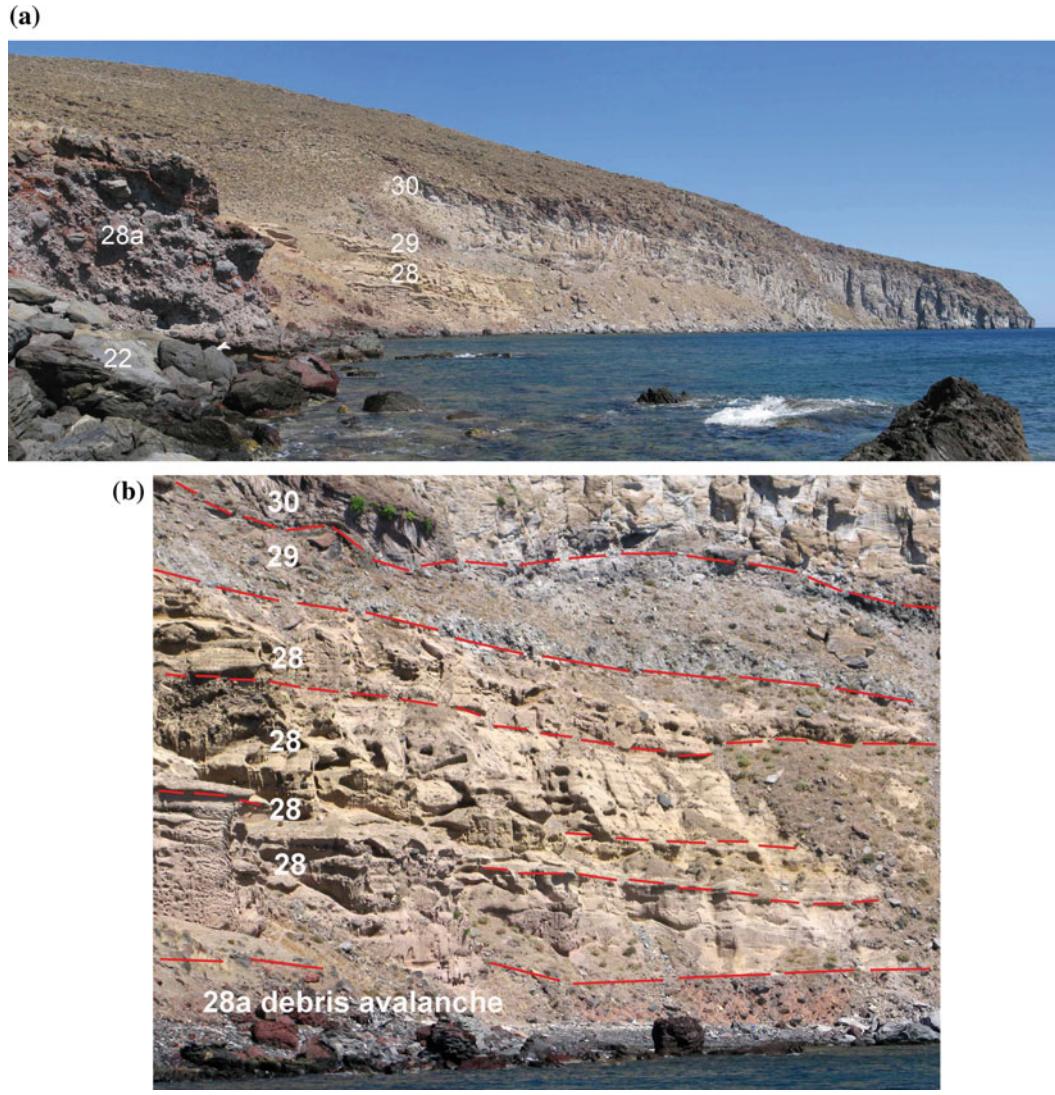

Fig. 3.44 **a** Debris avalanche (unit No. 28a) and "Lower pumice" succession (unit No. 28b, c) at the base of brecciated zone (unit No. 29) and rhyolithic lava (unit No. 30) in the southwestern flanks of Arfana, SW of Cape Avlaki. **b** Detail of (**a**) from *bottom* to *top*: (1) Debris-avalanche (unit No. 28a), (2) Lower pumice sequence (unit No. 28b, c) with intermediate lag breccia. (3) Heterogeneous breccia (unit No. 29) (4) Basal part of rhyolitic flow (unit No. 30) (5) Rhyolitic flow, unit No. 30. *Photo* V.J. Dietrich

a breakdown along slightly concentric normal N30°E striking fault before the extrusion of the rhyolitic flows (Fig. 3.41). The subsequent emplacement and doming of rhyolitic magma in the south–eastern part of the first caldera may have triggered a large flank collapse, ("Nikia Flank Collapse") and causing a major debris avalanche similar as the one on the northern half of the island ("Loutra" debris avalanche"). The voluminous rhyolitic lava flows do not flow into the caldera but into a major pre-existing south-east direction towards the sea.

The SE Nikia Flank Collapse

A major lateral collapse at the SE flank of Nisyros volcano (Fig. 3.46) has been recognized based on sea floor topography covered with

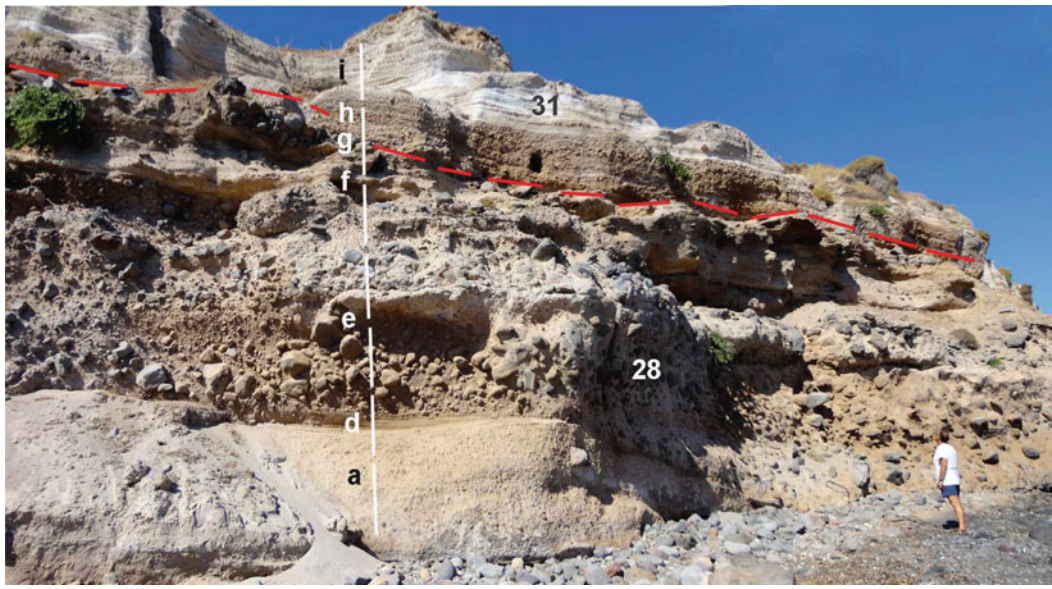

Fig. 3.45 Northern continuation of coastal profile at Louros Karanas (see Fig. 3.79a–c in Electronic Supplementary Material Appendix 3). Coarse blocky lag breccias between pyroclastic flows with matrix-rich pumice layers of the "Lower pumice" sequence (detailed description in Electronic Supplementary Material Appendix 3.3). *Photo* V.J. Dietrich

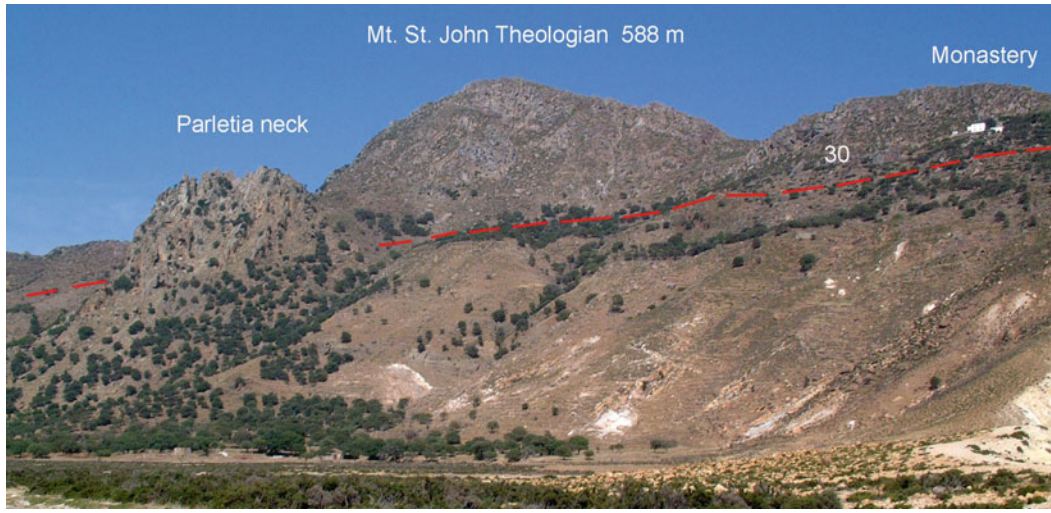

Fig. 3.46 Thick rhyolitic lava flows (unit No. 30) forming the eastern caldera rim with the highest elevation of Mt. St. John Theologian 589 m. In front *left* the rhyolitic Parletia neck (Medieval fort). Note the major break in the steep morphology into two steps of the south–eastern caldera walls, which indicates a breakdown along slightly concentric normal N30°E striking fault before the extrusion of the rhyolitic flows ("Nikia Flank Collapse"), limited to the north by the Parletia neck. *Photo* V. J. Dietrich

hammocks at a water depth of 250 and 380 m offshore the southeastern Nisyros flank. The large debris avalanche deposit covers an area of about 18 km^2 with a volume of about 1 km^3 and an average thickness of 40–50 m. The elongated hummocks show a fan-shaped distribution of

Fig. 3.47 Up bending rhyolitic flow front at Cape Avlaki. *Photo* V.J. Dietrich

their major axes with the apex pointing to the southeastern flank of Nisyros Island (Tibaldi et al. 2008; Nomikou et al. 2009). The evidence is based on multibeam data and lithoseismic profiles from the oceanographic research vessel "AEGAEO" of the H.C.M.R. The large debris avalanche deposit covers an area of about 18 km^2 with a volume of about 1 km^3 and an average thickness of 40–50 m.

Effusive phase

At least three major rhyolitic lava flows with a thickness up to 150 m and a total volume >1 km^3 (unit No. 30) represent a cycle during an extensive period of effusion (Fig. 3.41). A large morphological depression must have existed during that time in the southeastern part of the island since it facilitated the major flow directions towards southeast. The glass-rich, partly perlitic flows plunge down from the area in the present day eastern caldera walls between the Monastery Panaghia Kyra and the village of Nikia and enter the sea between the beach of Pachia Ammos and Avlaki (Fig. 3.47). Domes and a neck at Parletia piled up forming the eastern rim of the caldera. In several cases, the blocky surface of the flows is covered by a paleosol. The rhyolitic lava flows are younger than the plinian "lower pumice" deposits and older than the beginning of the second plinian eruptions of the "upper pumice". However, the time gap between these cycles remain unresolved up to now.

3.4.5.2 Second Eruptive Cycle

The palaeosol on top of the lower pumice forms a characteristic "marker horizon" between "lower and upper pumice" on the northern slopes of the volcano. However, the duration of this time gap is still not known. A debris flow (unit No. 29), containing components of lavas, pyroclastics and pumice of older units (units No. 23–26), with a maximum thickness between 5 and 20 m occurs along the northern coast close to the little harbour of Loutrà.

The first volcanic phase of the "Second Eruptive Cycle" (Fig. 3.48) is not well documented. Only one outcrop (at the base of the Nikia lava), a 1 m thick fallout horizon occurs above the "lower pumice", which consists of lapilli and blocks of slightly vesicular perlitic obsidian, indicating an explosive beginning before the effusion and emplacement of the major rhyolitic lava flow on top.

Explosive phase

The climactic explosive cycle produced an up to 60 m thick rhyolitic pyroclastic sequence, the "upper pumice" UP (unit No. 31) with a

fall-surge-flow-surge sequence, which has been deposited all over the island (Fig. 3.48). Major occurrences lie between Loutrà, Pali and Cape Katsouni in the northern and northeastern slopes of the island (Figs. 3.49 and 3.50). Smaller occurrences exist on the SE slopes, on the Nikia rhyolite. Deposits have not been found in the western and southern part of the island.

The proximal-to-distal transition in these bedforms may result from cooling of hot, dry steam propelled surges with condensation of water in the more distal zones (Limburg and Varekamp 1991). Water condensation caused the formation of accretionary lapilli and accelerated rates of deposition of fines, leading to thicker deposits and climbing ripple sets

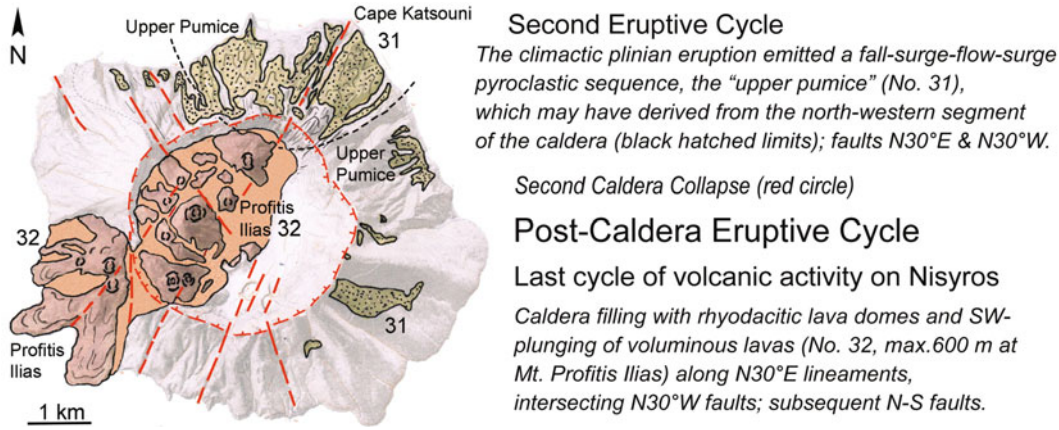

Fig. 3.48 Second eruptive cycle and second caldera collapse; the last cycle of volcanic activity on Nisyros

Fig. 3.49 Upper pumice pyroclastic sequence, unit No. 31 with max. 60 m total *thickness*. North–east coast between Plomos and Cape Katsouni. The numbers refer to the generalised tephrostratigraphic succession; detailed stratigraphic description in Electronic Supplementary Material Appendix 3.3. *Photo* V.J. Dietrich

Fig. 3.50 "Upper pumice" unit No. 31a at Plomos. Beginning with plinian pumice fall and wavy surge, then continuation with pyroclastic block flow (6–20 m *thickness*). *Photo* V. J. Dietrich

(Fig. 3.50). The upper units were deposited as non-turbulent pyroclastic flows with massive bedding, but absence of grading and stratification. They also contain lithic-rich layers and in the northeast coastal deposits several wavy surge layers. The upper part of the eruptive cycle represents a sequence massive surge deposits with extreme fragmentation, may be the result of water-magma interaction (Fig. 3.51).

The eruption centre of the "second eruptive cycle" may have occurred in the north–western segment of the caldera, controlled by intersecting fault zones N30°E and N30°W (Fig. 3.48), since the distribution of the maximum thickness of the fallout as well the pumice bomb and lithic last size clast sizes point towards the north–western and northern half of the island.

Limburg and Varekamp (1991) recognized a progress in the degree of hydrothermal alteration in the lithics from the lower part to the upper part of the entire succession. The temperatures of hydrothermal alteration, according to the mineral assemblages in the lithics start from 70–150 °C (argillite chunks) to >350 °C in epidote and diopside bearing skarns. This is in accordance with temperatures encountered in the geothermal drill holes NIS 1 and 2 below the caldera floor between 1000 and 1880 m depth (Barberi et al. 1988).

Erupted volume and plume shape

A first attempt to estimate the erupted volumes during the "Caldera Eruptive Cycles" was given by Limburg and Varekamp (1991). Isopach and isopleth patterns were derived from of the thickness distribution of the plinian eruptive sequences of both, the first and the second eruptive cycles. For the second plinian eruptive cycle, an 8 m average thickness at the source and a 7 cm thickness at 120 km distance

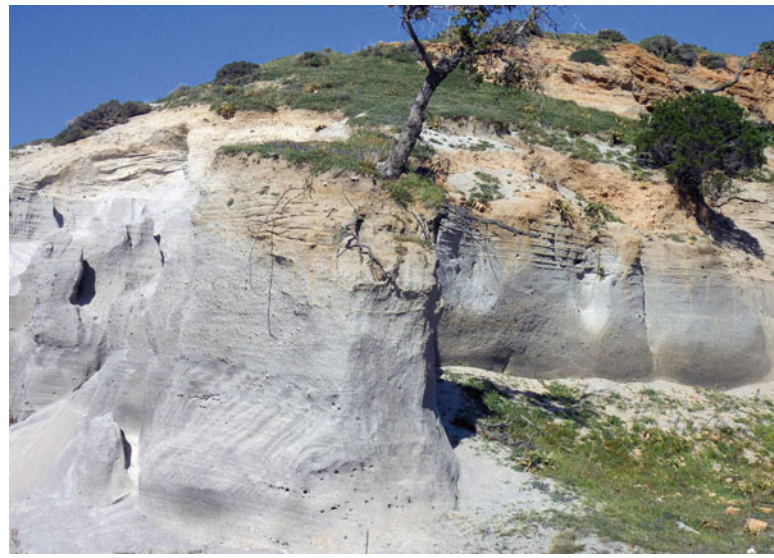

Fig. 3.51 Upper pumice (unit No. 31) south above Cape Katsouni. The succession is composed of ash flow deposits and planar-bedded surges in the *upper part*. The upper most sequence (*orange colors*) consists mainly of planar-bedded surges. *Photo* K. Kyriakopoulos

(Vinci 1983) was assumed. Using a model with circular isopachs and exponential thickness decay, the calculation showed an upper volume of 32 km^3, which is equivalent to a DRE ("Dry Rock Equivalent") of 10 km^3. The more realistic approach, using an elliptical distribution of isopachs reduced roughly the volume by the factor 4, which means a volume of 2–3 km^3. A crude volume calculation of the caldera before infill of ca. 100 m of talus and alluvial deposits yielded a maximum of extracted volume of 5 km^3. The approximate half-width of 1.9 km and a height of 15 km for the column during the plinian phase at minimum cross-wind was calculated using the 7 cm lithic isopleth distribution. A maximum column height of 20 km was estimated from the shape of the isopleth and isopach pattern. Longchamp et al. (2011) derived an "erupted volume for the south vent (considered as the best vent location) ranges between 2 and 27 $x10^8$ m^3 for the LP and between 1 and 5 $x10^8$ m^3 for the UP based on the application of four different methods (integration of exponential fit based on one isopach line, integration of exponential and power-law fit based on two isopach lines, and an inversion technique combined with an advection-diffusion model)".

The second Caldera collapse

During both eruptive cycles, large volumes of similar magnitudes of highly differentiated magmas were discharged. According to the lithics (composition, metamorphic state (Limburg and Varekamp 1991), they originated from magma reservoirs at high crustal levels. The mass deficiency after each eruptive cycle must necessarily have caused an internal collapse of the central part of the island and formation of the caldera structure. The first eruptive cycle was possibly followed by a first caldera collapse. The second caldera collapse must have happened in a very similar way. The possible evidence for such a situation is found in the hydrothermally altered clay chunks as part of the first caldera alluvial beds in the lower fall-flow sequence of the second eruptive cycle. However, the first caldera must have had a smaller diameter than the present day one, which formats the present day state.

3.4.6 Post-caldera Eruptive Cycle

The post-caldera rhyodacitic lava domes comprise six groups of endogenous domes and with light gray perlitic lava flows originating from them

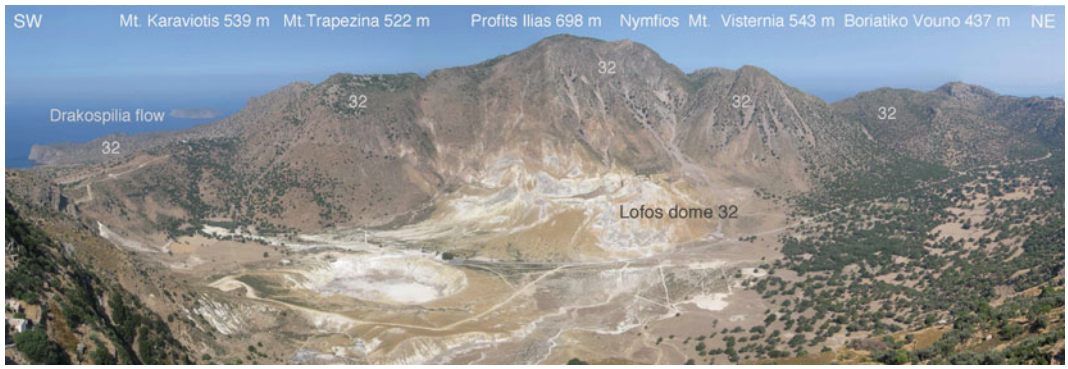

Fig. 3.52 The Nisyros caldera with the hydrothermal explosion crater field surrounded by rhyodacitic domes (from *left* to *right*), Mt. Karaviotis, Mt. Trapezina, Profitis Ilias, Nymfios, Mt. Visternia, Lofos dome, and Mt. Boriatiko Vouno. *Photo* V.J. Dietrich

(unit No. 32). They fill up the western half of the caldera with a max. thickness of 600 m and seem to be aligned along three parallel 30°NE trending fissure zones intersecting several N30°W fault zones (Figs. 3.48 and 3.52). They were emitted during the last eruptive cycle of Nisyros volcano during purely effusive phases and lack any sign of explosive precursors. The domes are: Mt. Profitis Ilias (698 m), Boriatiko Vouno (437 m), Nymfios, Visternia, Dhiavatis, Trapezina, and Karaviotis (539 m). In addition, a small dome (Lofos, 214 m) is found in the southeastern edge, which has been devastated by recent hydrothermal explosions and fumarolic activity. All domes can be subdivided into four older central groups, Dhiavatis—Profitis Ilias, Nymfios, Visternia, Trapezina, and Lofos and two much younger domes, Boriatiko Vouno in the Northeast and Karaviotis with the silicic flow lobes of Kateros, Kilia, and Drakospilia in the Southwest. They exhibit steep spines and scoria at the surface, as well as they lack soil deposits and minor proximal scree deposits.

3.5 Geochronology

Geochronological data of volcanic rocks and soils from Nisyros Island and the Kos-Yali-Nisyros Volcanic Field are relatively few. During the past 40 years numerous attempts have been undertaken, however without consistent and conclusive results in most cases. Earlier data are controversial and accompanied with large errors (Table 3.2). The following methods have been applied:

- ^{14}C fission track analysis on obsidian glass,
- K–Ar on whole rock and volcanic glass,
- $^{40}Ar/^{39}Ar$ on feldspars, and
- U–Th disequilibrium measurements on paleosols sandwiched between volcanic and pyroclastics, the latter discussed in Büttner et al. (2005),
- Th/U measurements on whole rocks and zircon and Pb–U dating on zircon using laser ablation inductively coupled plasma mass spectrometry (LA–ICP–MS, Guillong et al. 2014).

Reliable age determinations with the $^{40}Ar/^{39}Ar$ method have been obtained from the Kos Plateau Tuff (KPT) with 161 ± 1 and 166 ± 2 ka (Smith et al. 1996; Bachmann et al. 2010). The new Pb–U ages of the youngest zircons (Guillong et al. 2014) measured from the Nisyros silicic volcanics provide the first geochronological estimates, which are in accordance with the established lithostratigraphy and interpreted as maximum ages of their eruption: The Lower Pumice with 124 ± 35 ka (unit No. 28), the Nikia rhyolite flows with 111 ± 42 ka (unit No. 30), and the upper Pumice with 70 ± 35 ka (unit No. 31). The K–Ar data of 66 ± 2 and 24 ka on fission track (Table 3.1) are of restricted geological meaning.

Table 3.2 Geochronological data of volcanic rocks and soils from Nisyros Island and Kos Plateau Tuff (KPT); *SHRIMP* sensitive high resolution ion microprobe, *ID–TIMS* isotope-dilution thermal ionization mass spectrometry

Lithostratigraphic unit	Age	Method	Reference
Yali obsidian	24 ka	Fission track on glass	Wagner et al. (1976)
Yali pumice (No. 33)	31 ka	Oxygen isotope stratigr.	Federmann and Carey (1980)
Upper pumice (No. 31)	>44 ka	^{14}C	Limburg & Varekamp (1991)
Upper pumice (? No. 31)	110 ± 40 ka	Fission track on glass	Barberi et al. (1988)
Upper pumice (? No. 31)	24 ka	Sediment, rate, extrapol.	Vinci (1985)
Upper pumice (No. 31)	**70 ± 35 ka**	LA-ICP-MS Pb–U, zircon	Guillong et al. (2014)
Nikia Rhyolite (No. 30)	**111 ± 42 ka**	LA-ICP-MS Pb–U, zircon	Guillong et al. (2014)
Lower pumice (No. 28)	**124 ± 35 ka**	LA-ICP-MS Pb–U on zircon	Guillong et al. (2014)
Lower pumice (No. 28)	35 ka	Sediment, rate, extrapol.	Hardimann (1999)
Paleosol (? No. 21)	24.26 ± 0.56	^{14}C on charcoal	Rehren (1988)
Dacite Afionas (No. 18)	37 ± 24 ka	K–Ar on plagioclase	Rehren (1988)
Dacite Afionas (No. 18)	39 ± 26 ka	K–Ar on groundmass	Rehren (1988)
Rhyolite Argos (No. 17)	66.6 ± 2 ka	K–Ar on plagioclase	Keller et al. (1990)
Rhyolite Argos (? No. 17)	200 ± 50	K–Ar on bulk rock	Di Paola (1974)
Andesite (? No. 24)	100 ± 100	K–Ar on bulk rock	Matsuda et al. (1999)
Andesite (? No. 1)	800 + 700	K–Ar on bulk rock	Matsuda et al. (1999)
Kos Plateau Tuff (KPT)	**161 ± 1 ka**	$^{40}Ar/^{39}Ar$ on sanidine	Smith et al. (1996)
Kos Plateau Tuff (KPT)	**166 ± 2 ka**	$^{40}Ar/^{39}Ar$ on sanidine	Bachmann et al. (2010)
Kos Plateau Tuff (KPT)	**160 ± 2 ka**	SHRIMP, LA-ICP-MS, ID-TIMS	Guillong et al. (2014)

Some of the major reasons for the lack of accurate geochronological data are as follows:

- The rarity of sanidine and biotite in the evolved rocks of Nisyros volcano do not permit high-precision Ar/Ar analyses. Low-K Amphibole and plagioclase crystals do not provide reliable ages for such young systems, and glass (where most of the potassium is) is typically unreliable (hydration, alteration).
- ^{14}C analysis in soils, charcoal and paleosols on Nisyros Island may be contaminated by the strong CO_2 degassing all over the volcano (in the order over 1000 tons/day, see Chap. 5).

Future age determination studies using LA-ICP-MS U/Pb dating on single zircon crystals may help resolving some of these issues.

References

Allen SR (2001) Reconstruction of a major caldera-forming eruption from pyroclastic deposit characteristics: Kos Plateau Tuff eastern Aegean Sea. J Volcanol Geotherm Res 105:141–162

Bachmann O (2010) The petrologic evolution and pre-eruptive conditions of the rhyolitic Kos Plateau Tuff (Aegean Arc). Cent Europ J Geosci. doi:10.2478/v10085-010-0009-4

Barberi F, Navarro JM, Rosi M, Santacroce R, Sbrana A (1988) Explosive interaction of magma with ground water: insights from xenoliths and geothermal drillings. Rend Soc Ital Mineral Petrol 43:901–926

Buettner A, Kleinhanns IC, Rufer D, Hunziker JC, Villa IM (2005) Magma generation at the easternmost section of the Hellenic Arc: Hf, Nd, Pb and Sr isotope geochemistry of Nisyros and Yali volcanoes (Greece). Lithos 83:29–46

Davis EN (1967) Zur Geologie und Petrologie des Inseln Nisyros und Jali (Dodecanese). Praktika Akademy of Athens 42:235–252

De Goer de Herve A (2008) Chapter 5, Peperites from the Limagne Trench (Auvergne, French Massif Central), a distinctive feature of phreatomagmatic pyroclastics. History of semantic drift. In: Leyrit H, Montenat C (eds) Volcaniclastic rocks, from magmas to sediments. Taylor Francis, 270 p

Desio A (1931) Le Isole Italiane dell'Egeo—Studi geologici e geografici-fisici. Mem descrittive della Carta Geologica d'Italia. R. Ufficia Geologica d'Italia

Di Paola GM (1974) Volcanology and petrology of Nisyros Island (Dodecanese Greece). Bull Volcanol 38:944–987

Drakopoulos J, Delibasis N (1982) The focal mechanism of earthquakes in the major area of Greece for the period 1947–1981. Univ of Athens Seismological Laboratory No. 2

Federman AN, Carey SN (1980) Electron microprobe correlation of tephra layers from Eastern Mediterranean abyssal sediments and the Island of Santorini. Quatern Res 13:160–171

Geotermica Italiana (1983) Nisyros 1 geothermal well PPC-EEC report, pp 1–106

Geotermica Italiana (1984) Nisyros 2 geothermal well PPC-EEC report, pp 1–44

GEOWARN (2003) GEOWARN Geo-spatial warning system—synthesis report GEOWARN consortium Athens (Greece) and Zurich (Switzerland), p 57 (http://www.geowarnorg)

Guillong M, von Quadt A, Sakata S, Peytcheva I, Bachmann O (2014) LA–ICP–MS Pb–U dating of young zircons from the Kos-Nisyros volcanic centre SE Aegean arc. J Anal At Spectrum 29:963–970

Hardimann JC (1999) Deep sea tephra from Nisyros Island eastern Aegean Sea Greece. In: Firth CR, McGuire WJ (eds) Volcanoes in the Quaternary, vol 161. Geological Society of Special Publication London, pp 69–88

Hildreth W S (2007) Quaternary magmatism in the cascades- geological perspectives. US Geological Survey Professional Paper 1744, p 125

Keller J, Rehren Th, Stadlbauer E (1990) Explosive volcanism in the Hellenic Arc; a summary and review. In: Hardy DA, Keller J, Galanopoulos VP, Flemming NC, Druitt TH (eds) Thera and the Aegean World III proceedings of the third international congress The Thera Foundation London, vol 2, pp 13–26

Limburg EM, Varekamp JC (1991) Young pumice deposits on Nisyros Greece. Bull Volcanol 54:68–77

Longchamp C, Bonadonna C, Bachmann O, Skopelitis A (2011) Characterization of tephra deposits with limited exposure: the example of the two largest explosive eruptions at Nisyros volcano (Greece). B Volcanol 73:1337-1352

Makris J, Stobbe C (1984) Physical properties and state of the crust and upper mantle of the Eastern Mediterranean Sea deduced from geophysical data. Mar Geol 55:347–363

Martelli A (1917) Il gruppo eruttivo di Nisiro nel mare Egeo. Mem Mat Fis Soc Ital Sc (detta dei XL) Serie 3a Tome 20:79–167

Matsuda J-I, Senoh K, Maruoka T, Sato H, Mitropoulos P (1999) K–Ar ages of the Aegean volcanic rocks and their implications for the arc–trench system. Geochem J 33:369–377

Nomikou P, Papanikolaou D (2000) Active geodynamics at Nisyros the eastern edge of the Aegean Volcanic Arc: emphasis on submarine surveys. In: Proceedings of the 3rd international conference on geology East Mediterranean, Sept 1998, pp 97–103

Nomikou P, Papanikolaou D (2011) Extension of active fault zones on Nisyros Volcano across the Yali-Nisyros Channel based on Onshore and Offshore data. Mar Geophys Res Spec Issue Seafloor Map Geohaz Assess. doi:10.1007/s11001-011-9119-z

Nomikou P, Tibaldi A, Pasquare F, Papanikolaou D (2009) Submarine morphological analysis based on multibeam data of a huge collapse at the SE flank of Nisyros volcano. In: International conference on seafloor mapping for geohazard assesment 11–13 May, Ischia Italy Rend Soc Geol It, vol 7, pp 177–179

Papanikolaou DJ, Lekkas EL, Sakelariou DT (1991) Geological structure and evolution of Nisyros volcano. Bull Geol Soc Greece 25:405–419

Rehren TH (1988) Geochemie und petrologie von Nisyros (Oestliche Agais). PhD Thesis Univ Freiburg

Skilling IP, White JDL, McPhie J (2002) Peperite: a review of magma-sediment mingling. J Volcanol Geotherm Res 114:1–17

Smith PE, York D, Chen Y, Evensen NM (1996) Single crystal $^{40}Ar/^{39}Ar$ dating of a late quaternary paroxysm on Kos Greece; concordance of terrestrial and marine ages. Geophys Res Lett 23:3047–3050

Stadlbauer E (1988) Vulkanologisch-geochemische Analyse eines jungen Ignimbrits: der Kos-Plateau-Tuff (Südost-Ägäis) PhD Thesis. Albert-Ludwigs-Universität Freiburg im Breisgau, 184 p

Tibaldi A, Pasquarè FA, Papanikolaou D, Nomikou P (2008) Discovery of a huge sector collapse at the Nisyros volcano Greece by on-land and offshore geological-structural data. J Volcanol Geotherm Res 177:485–499

Vinci A (1983) A new ash layer "Nisyros layer" in the Aegean sea sediments. Boll Oceanol Teor Appl 1:341–342

Vinci A (1985) Distribution and chemical composition of tephra layers from Eastern Mediterranean abyssal sediments. Mar Geol 64:143–155

Volentik A, Vanderkluysen L, Principe C, Hunziker JC (2005) Stratigraphy of Nisyros vollcano (Greece). In: Hunziker JC, Marini L (eds) The petrology and geochemistry of lavas and tephras of Nisyros Volcano (Greece), vol 44. Mém Géologie (Lausanne), pp 26–66

Volentik A, Vanderkluysen L, Principe C (2002) Stratigraphy of the Caldera walls of Nisyros volcano Greece. Eclogae Geol Helv 95:223–235

Vougioukalakis G (1993) Volcanic stratigraphy and evolution of Nisyros Island. Bull Geol Soc Greece 28:239–258

Vougioukalakis GE (1998) Blue volcanoes: Nisyros Nisyros. Regional Council Mandraki, p 78

Vougioukalakis G (2003) Nisyros sheet, geological map of Greece 1:25,000 IGME Institute of Geology Mineral Exploration, Athens Greece

Wagner GJ, Storzer D, Keller J (1976) Spaltspurendatierungen quartarer Gesteinsglaser aus dem Mittelmeerraum. N Jb Miner Mh 2:84–94

Petrology and Geochemistry of Lavas and Pyroclastics

4

Volker Jörg Dietrich and Răzvan-Gabriel Popa

Abstract

This chapter offers a comprehensive overview of the main petrologic of geochemical characteristics of the Nisyros volcanic products, integrating published data and some new observations. The mineralogy and petrography of the magmatic rocks are described, including a brief presentation of enclaves, xenoliths and xenocrysts. The disequilibrium textures of amphibole are also presented, in light of the thermodynamic changes recorded by their breakdown structures and reaction rims. The chapter contains a holistic overview of the whole-rock major and trace element geochemistry of the rocks, obtained by compiling the available published data. Calc-alkaline and arc tholeiite trends are inferred, and the silica-gap is observable just before amphibole fractionation starts. A brief description of the main petrographic and geochemical features of each lithostratigraphic unit, according to the map, is offered. The chapter concludes with a discussion on the petrogenetic evolution of the island, including crustal assimilation, fractional crystallisation, magma mixing and mingling, crystal-retention-liquid-segregation, the probable depth of the magma chamber and models for generating the highly silicic magmas characteristic for the younger eruptive events, from the parental basaltic andesite melts that were erupted in the earlier stages.

Electronic supplementary material The online version of this chapter (doi:10.1007/978-3-319-55460-0_4) contains supplementary material, which is available to authorized users.

V.J. Dietrich (✉) · R.-G. Popa
Institute of Geochemistry and Petrology, Swiss Federal Institute of Technology, ETH Zurich, ETH-Zentrum, 8092 Zürich, Switzerland
e-mail: volker.dietrich@erdw.ethz.ch

R.-G. Popa
e-mail: razvan.popa@erdw.ethz.ch

4.1 Introduction

The volcanic products of Nisyros Island: lavas, domes and pyroclastic deposits, have compositions ranging from basaltic andesite to rhyolite and belong to the typical calc-alkaline island-arc magmatic series. In the past 50 years the mineralogy, petrography, geochemistry and isotope

V.J. Dietrich and E. Lagios (eds.), *Nisyros Volcano*, Active Volcanoes of the World,
DOI 10.1007/978-3-319-55460-0_4

Table 4.1 Summary of petrography and mineral content according to lithostratigraphic rock units

LSU	Eruption mode	Thickness (m)	Rocktype	special texture	Plagioclase	Clinopyrox.	Orthopyr.	Olivine	Amphibole	Biotite	Oxides	Apatite	Zircon	Sanidin*	Quartz	LSU
	Post-Caldera Eruptive Cycles															
32	Lava domes, flows	600	Rhyodacite	hypocryst. porph.	P15, M	P<5, M	P<5, M	TR (Fayal.)	P<5, RC		P<5			TR,Or70	TR	32
32	Enclaves			quenched, porphy.	P, M	M			P, M, RC							32
	Caldera Eruptive Cycles and Caldera Collapse															
31	Fl-WS-Fl-PbS-succ.	max. 30	Rhyolite	pumice, P.I. 10	P<5	P<5, M	P<5		P<5, RC		P<5	P<5	P<5			31
31	Enclaves			quenched, porphy.					P<M, RC							31
30	Lava flows	150	Rhyolite	hypocryst. porph.	P<5, M	P<5	P<5, M		P<5, M	TR	P<5			TR,Or54		30
30	Enclaves			quenched, porphy.	P, M	M			P, M, RC							30
28	F-Fl-WS-Fl-succ.	max. 20	Rhyolite	pumice, P.I. 5	P<5, M		P<5, M		TR, RC		P<5	P<5	P<5		TR	28
28	Enclaves			quenched, porphy.	P, M	M			P, M, RC							28
27	Lava flow	max. 10	Andesite	porph., P.I. 10-15	P<5, M	P<5, M		P<5			P<5, M					27
	Composite Stratovolcano Cycles															
26	Dome collapse breccia	20-30	Dacite	porph., P.I. 20-30	P5-10, M	P<5, M	P<5, M		P<5, RC	TR	P<5	P<5	P<5			26
26	Enclaves 1-2%		Andesite	quenched	P, M	P, M			P, M, RC							26
25	Flows, dome	150	Dacite	porph., P.I. 20-30	P5-10, M	P<5, M	P<5, M		P<5, PR, RC	TR	P<5, M	P<5	P<5	TR,Or42		25
25	Enclaves 1-2 %		Andesite	quenched	M				P, M, RC							25
24	Flows	max. 25	Bas. Andes.	glomeroporhyr.	P<5-15, M	P<5-10, M	M	P<5			P<5, M					24
22	Flows	max. 10	Bas. Andes.	glomeroporhyr.	P<5-20, M	P<5-10,AC, M	P<1	P<5			P<5, M					22
21	F-PbS-PyFl-succ.	max. 15	Bas. Andes.		P<5-10, M	P<5-10, M	P<1	P<5			P<5, M					21
19	F-S-F-3S-F-F-xS-F-succ.		Bas.And.- Dac.		P<5, M	P<5, M	P<5, M				P<5, M				TR	19
18	Lava flow	10 ?	Dacite	porph., P.I. 20-30	P10, M	P<5, M	P<5, M		P<5		P<5, M	P<5	P<5			18
17	Lava domes, flows	max. 60	Rhyolite	vitrophyr., perlitic	P<5-10,AC, M	P<5, M	P<5, M		P<5	M	P<5, M	P<5	P<5	M,TR	TR	17
16	S-Fl-succession	30	Bas. Andes.	porph., P.I. 20-30	P10	P<5	P<1	PR			P<5					16
15	Lava flow	max. 40	Andesite	glomeroporhyr.	P<5-10, AC, M	P<5, AC, M	P<1	P<5			P<5, M					15
14	Lava flow	max. 25	Dacite	porph., P.I. 20-30	P15, M	P<5, M	P<5, M	P<5	RC	TR	P<5, M	P<5				14
14	Enclaves up to 30%		Andesite	porp., quenched	P, M	P, M	P<1		P, M, RC							14
13	Lava flow	max. 40	Andesite	porph., P.I. 2-15	P<5-15, M	P<5-10, M	P<1	P<5, PR			P<5, M					13
	Early Shield Volcano Cycles of Nisyros															
11	F-Fl-F-S-Fl-succ.	35	Andesite		P5-20, AC, M	P<5, M	M	P<5, PR			P<5, M					11
10	Lava flows	70	Bas. Andes.	scoria-rich	P5->20, AC, M	P5-15, M	TR	P<5, PR			P<5, M					10
8	Lava flow	5	Bas. Andes.	porph., P.I. 40-50	P5-20,AC, M	P<5-15, M	TR	P<5-10			P<5, M					8
6	S-F-Fl-S-Fl-succ.	60	Bas. Andes.		P<5, M	P<5, M	TR	P<5	TR, RC		P<5, M					6
5	Lava flows	40	Andesite	glomeroporhyr.	P<5-15, M	P<5-10, M	P<5	PR			P<5, M					5
4	F-Fl-S-F-succ.	30	Andesite		P<5, M	P<5, M	P<1	P<5	TR, RC		P<5, M					4
3	Lava flow	35	Bas. Andes.	porph., P.I. 20-30	P10-20, AC,M	P10, M	TR	P<5			P<5, M					3
	Submarine volcanic base															
1,2	Pillow & lava flows	max.50 ?	Bas-Andes.	partly hyaloclast.	P10-20, AC,M	P10	TR	P<1	TR, RC		P<5, M					1,2

Phenocryst abundance in vol.% of total rock

P phenocryst, *P < 1* max. 1 vol.%, *P < 5* max. 5 vol.%, *P10* max. 10 vol.%, *P15* max. 15 vol.%, *P10–20* 10–20 vol.%, *P.I.* porphyritic index vol.%, *M* Microphenocryst, *RC* resorbed cryst, *X* Xenocryst, *TR* traces, *F* fall, *Fl* flow, *PyFl* pyroclastic flow, *S* surge, *WS* wavy surge, *PbS* planar bedded surge, *LSU* litho-stratigraphic unit, *Mica* Biotite/phlogopite, *Sanid.** Seymour and Vlassopoulos (1992)

chemistry have been described in numerous contributions (e.g. Davis 1967; Di Paola 1974; Vougioukalakis 1984, 1993; Bohla and Keller 1987; Rehren 1988; Wyers and Barton 1989; Lodise 1987; St. Seymour and Lalonde 1990, St. Seymour and Vlassopoulos 1989, 1992; Ganseki 1991; Limburg and Varekamp 1991; Francalanci et al. 1995; Innocenti et al. 1981; Volentik et al. 2002; Vanderkluysen and Volentik 2002; Buettner et al. 2005; Volentik et al. 2005; Vanderkluysen et al. 2005; Francalanci et al. 2007; Martin 2008; Zellmer and Turner 2007; Longchamp et al. 2011; Bachmann et al. 2011; Spandler et al. 2012; Guillong et al. 2013; Zouzias and Seymour 2014). These papers provide an ever-expanding data set, with which the evolution of the magmas from their generation in the mantle and until their eruption at the surface can be deduced.

The following chapter forms an attempt to compile all available published data (mineralogy, petrography and bulk-chemistry of major and trace elements, and isotope geochemistry) to provide an up-to-date discussion on the magmatic evolution of the volcano in space and time.

A summary of the mineralogy and petrographic characteristics of the units is presented in Table 4.1, based on the studies of Di Paola (1974), Seymour and Vlassopoulos (1989, 1992), Limburg and Varekamp (1991), Francalanci et al. (1995), Wyers and Barton (1989), Vanderkluysen et al. (2005) and own unpublished data and observations. The volcanic products are described according to their litho-stratigraphic succession and regional distribution as it has been done in the previous geological and volcano-tectonic (structural) chapters. Although a large amount of mineralogical observations and bulk-chemical analyses of volcanic and pyroclastic rocks have been published, detailed mineralogical studies are very sparse and partly incomplete.

4.2 Mineralogy and Petrography of the Magmatic Products

This section of the book is meant to give a general overview of the petrographic features recognized in the volcanic products of Nisyros. A detailed petrographic description is given in the Electronic Supplementary Material Appendix of Chap. 4.2 (4.3 ff.).

4.2.1 General Features

A summary of the main mineralogical and petrographic characteristics of the volcanics is given in Table 4.1. A characteristic feature of both mafic and felsic rocks is their highly porphyritic texture, with up to 60 vol.% phenocrysts.

The crystallization sequence, observed in thin section is:

(1) Basaltic andesites to andesites: Plagioclase + clinopyroxene/amphibole + orthopyroxene ± olivine ⟶ plagioclase + clinopyroxene/amphibole + orthopyroxene;
(2) Basaltic andesites to rhyolites: Plagioclase + clinopyroxene/amphibole + orthopyroxene ± olivine ⟶ plagioclase + amphibole + orthopyroxene ± clinopyroxene, apatite, zircon, sanidine, biotite, and quartz.
(3) Dacites and rhyodacites are volcanic rocks derived from differentiated magmas, which underwent magma mixing and mingling processes to various degrees exhibiting antecrysts, xenocrysts, quenched magmatic enclaves and xenoliths. The groundmass consists of rhyolitic residual glasses.

Plagioclase (plg), up to 5 mm in size, shows the highest phenocrysts proportion in all units with up to 70 vol.%, and is mostly zoned (Figs. 4.1 and 4.3), with frequent resorbed cores and often exhibits disequilibrium sieve textures (Fig. 4.2). Its composition ranges from An_{90} in the basaltic andesites to $An_{25–35}$ in the rhyolites. Compositions in basaltic andesites and andesites are: cores $An_{88–55}$, rims: $An_{82–35}$.

Plagioclase crystals in the dacites, rhyodacites, and in some rhyolites have oscillatory zoning (ranging from bytownite to oligoclase) that is sometimes related to disequilibrium textures. Their counterparts from the mafic enclaves are generally reversely zoned. Enclave phenocrysts exhibit rounded cores with distinct rims, normal and superimposed oscillatory zoning;

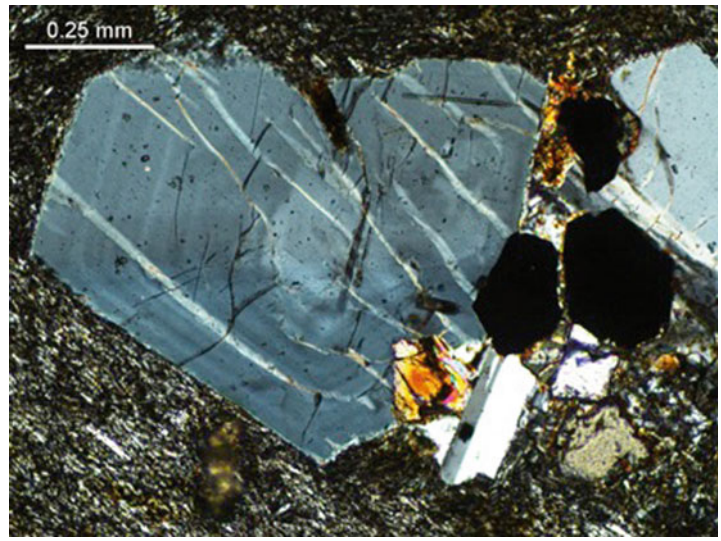

Fig. 4.1 Plagioclase with oscillatory zoning, plagioclase, olivine, and clinopyroxene within a hyalopilitic and fluidal matrix of plagioclase, clinopyroxene and glass. XPL (*crossed polarized light*) image

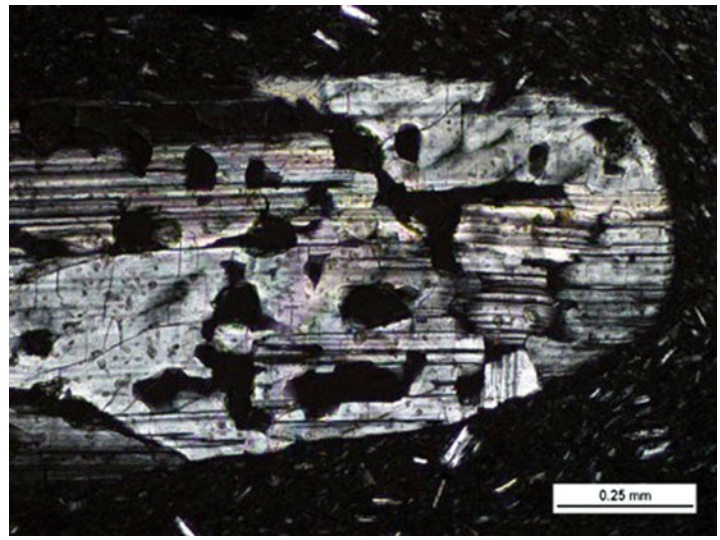

Fig. 4.2 Resorbed twinned plagioclase with sieve textures represented by glass inclusions [PPL, XPL]. Locality: rhyolite (unit No. 17) west of Avlaki Bay

cores $An_{66–33}$ and rims $An_{36–27}$ (Wyers and Barton 1989; Seymour and Vlassopoulos 1992; Braschi et al. 2014; Zouzias and Seymour 2014).

Olivine (ol), slightly zoned, occurs in basaltic andesites and andesites as phenocrysts (Figs. 4.4 and 4.5) and microphenocrysts reaching 0.07 mm in size and ranges from Fo_{82} in basaltic andesites to Fo_{65} in the andesites, partly iddingsitized and rimmed by orthopyroxene. The core composition ranges from $Fo_{82–67}$ whereas the rims are of $Fo_{78–60}$.

Clinopyroxene (cpx) is ubiquitous throughout the series from basaltic andesites to rhyolites, however in various different compositions from augite to ferroaugite, partly reversely zoned. Resorbed pigeonite is also present in some of the rhyolites, but in subordinate amounts. Cpx are frequently rounded and resorbed within the intermediate andesitic, dacitic and rhyodacitic rocks. In the dacites and rhyodacites it is often rimmed by dark, fine-grained opaques reaction assemblages. Reversely zoned pyroxenes are present in enclave-bearing lavas. The following ranges of cpx composition have been reported by Wyers and Barton 1989; St. Seymour and

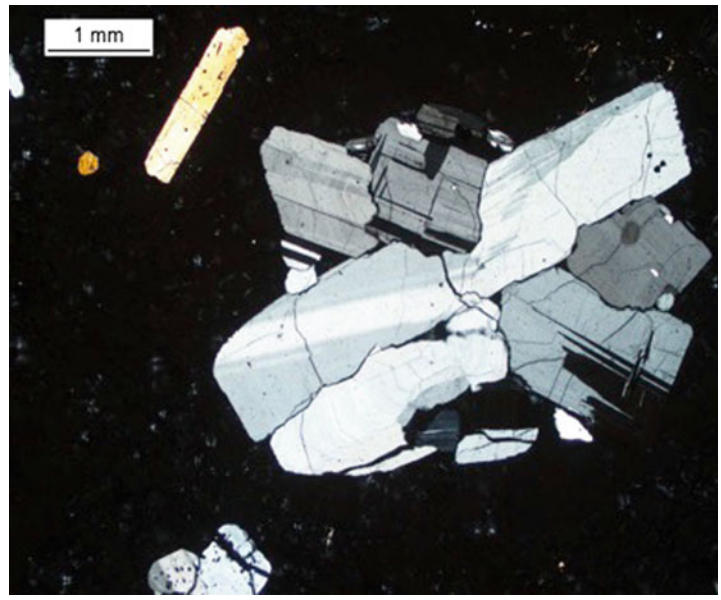

Fig. 4.3 Plagioclase and enstatite in fresh, vesicle-rich glassy matrix from the *upper pumice* (unit No. 32); XPL image

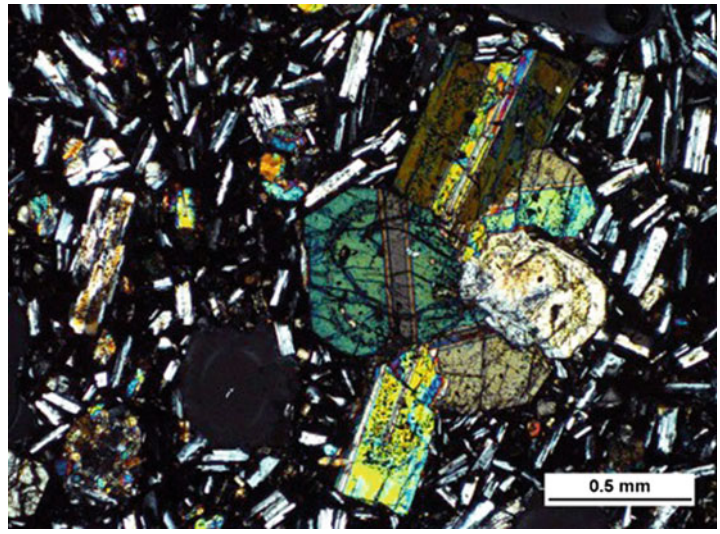

Fig. 4.4 Cross-twins of zoned clinopyroxene and zoned altered plagioclase phenocrysts embedded in a hyalopilitic matrix of pillow lava (unit No. 1); XPL images

Vlassopoulos 1992; Mitropoulos and Tarney 1992; Martin 2008:

- Basaltic andesites cores Mg/(Mg + Fe^{2+}) = 0.814–0.690, rims Mg/(Mg + Fe^{2+}) = 0.836–0.690;
- andesites cores Mg/(Mg + Fe^{2+}) = 0.810–0.702, rims Mg/(Mg + Fe^{2+}) = 0.798–0.694;
- dacites and rhyodacites cores Mg/(Mg + Fe^{2+}) = 0.780–0.691 and rims Mg/(Mg + Fe^{2+}) = 0.734–0.676, and reversely zoned cores Mg/(Mg + Fe^{2+}) = 0.719–0.665.

Magnesium-rich orthopyroxene (opx), enstatite occurs in the andesites and evolves to more *iron-rich compositions* with grain sizes up to 2 mm in the dacites and rhyolites. The compositional ranges of the reversely zoned orthopyroxene in the dacites, rhyodacites and rhyolites are: cores Mg/(Mg + Fe^{2+}) = 0.674–0.580 and rims Mg/

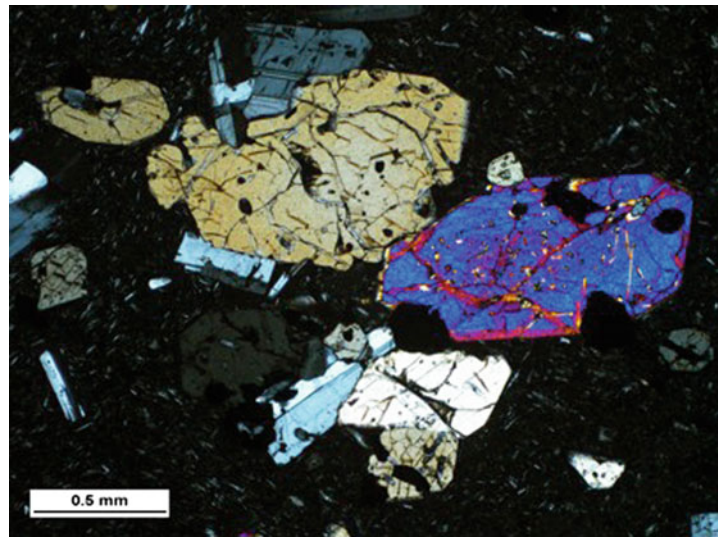

Fig. 4.5 Clinopyroxene clots with interstices filled with glass in dacite (unit No. 25). XPL images

$(Mg + Fe^{2+}) = 0.640–0.590$. Rare occurrences in basaltic andesites and andesites are resorbed antecrysts, partly rimmed by clinopyroxene.

Amphibole (amph) occurs in rhyodacites, rhyolites and dacites as magnesio-hastingsites, sometimes resorbed and often rimmed by opacitic reaction coronas and affected by the oxy-hornblende reaction (thus changing the colors of the crystals and increasing their pleochroism). In addition, kaersutite has been found in dacites (Seymour and Vlassopoulos 1992), pargasite, ferroan-pargasite, magnesium-hornblende and actinolitic-hornblende in gabbro-cumulates and in evolved interstitial melts.

Biotite (bio) phenocrysts have only been found as interstitial phase in some dacites and rhyolites of units 17, 25, 28, 30 (e.g., Electronic Supplementary Material Appendix of Figs. 4.36c and 4.39c).

Sanidine is mostly absent in the evolved dacites to rhyolites. However, Seymour and Vlassopoulos (1989) and Vanderkluysen and Volentik (2002) reported traces as microphenocrysts in dacites, rhyodacites and rhyolites. The rarity of sanidine explains the lack of proper absolute age determinations. Microprobe analyses have shown that potassium is concentrated in the microcrystalline matrix and glass.

Quartz is rare and occurs sporadically as anhedral and partly resorbed crystals in rhyodacites and rhyolites.

Fe–Ti Oxides are rare in basaltic andesites and occur mainly as microphenocrysts. They also occur sporadically in andesites as inclusions in plagioclase, clinopyroxene and olivine. Titanomagnetite (mgt) varies in composition; Al_2O_3 varies from 1.5 to 2.5 wt%, MgO from 0.97 to 1.94 wt%. Ilmenite shows small compositional variations and occurs in dacites, rhyodacites and rhyolites.

Accessory minerals are: Apatite, zircon and various sulfides. Apatite occurs as inclusions in clinopyroxene and in plagioclase. In the evolved lavas it is found as microphenocrysts and within gabbroic clots. Zircon is very rare and occurs in the evolved lavas either within Fe–Ti oxides or as microphenocrysts.

4.2.2 Crystal Clots (Glomerocrysts Syn.)

Crystal-clot minerals (Stewart 1975; Boettcher 1977; Garcia and Jacobson 1979; Girard and Stix 2009; Ellis et al. 2014), synonym to glomerocrysts as polycrystal aggregates occur in many basaltic andesites, andesite, dacite, rhyodacite and rhyolitic lavas of Nisyros and represent primary igneous phase assemblages. According to the theory of (Williams et al. 1954) crystal clots are random accumulations of phenocrysts that may have formed during flowage of a crystal-rich magma. However, they could also originate from

the cumulate layer in a magma reservoir. In the Nisyros lavas, the mineralogy of the crystal clots usually resembles that of the phenocryst phases. For each eruptive unit they display diverse modal proportions. Basaltic andesites and andesites contain clots of ol+plag+mg (Fig. 4.6), cpx+mgt, opx+mgt, cpx+opx+plag+mgt, cpx+plag+mgt, opx+plag+mgt, and plag+mgt (Fig. 4.7), whereas dacites, rhyodacites, and rhyolites show clots of opx+mgt, cpx+opx+plag+mgt, opx+plag+mgt, and amph+plag+mgt+-ilmenite, amp+mgt+-ilm, and plag+mgt. These clots could not have been originated from breakdown reactions of amphibole precursors.

4.2.3 Xenoliths and Enclaves

Properly crystallized and irregular shaped rock inclusions, which were solid prior to the eruption of the magmas, are described as xenoliths, whereas ovoid to irregular shaped inclusions bearing indicators of cooling processes (quench phenomena representing rapid cooling and

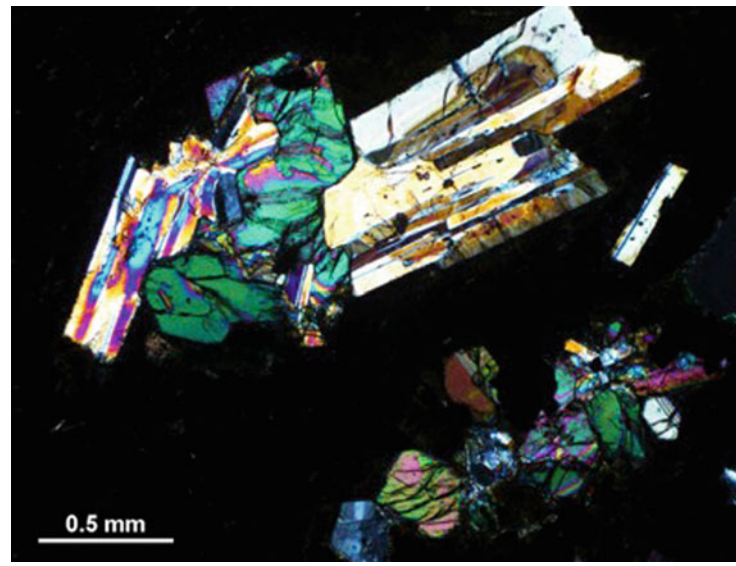

Fig. 4.6 Glassy basaltic andesites lava No. 10 with sparsely porphyritic and vitrophyric texture; plagioclase-olivine-clinopyroxene clots embedded in a hyaline to hyalopilitic glassy matrix. Locality: *middle part* of inner caldera road. XPL image

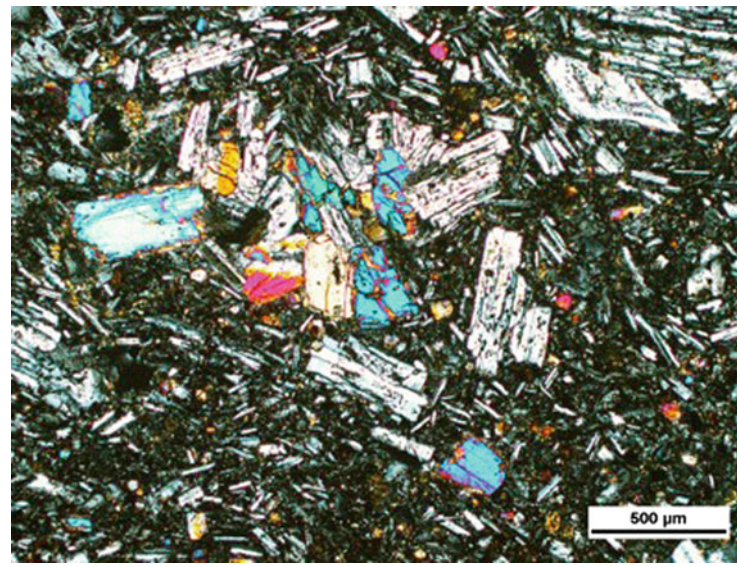

Fig. 4.7 Andesite lava No. 5 with highly porphyritic and glomeroporphyritic textures; plagioclase-clinopyroxene clots embedded in a hyalopilitic matrix of subhedral plagioclase and clinopyroxene micro-phenocrysts and glass. Larger clinopyroxene crystals are rimmed by orthopyroxene. Olivine is rare. Locality: *lower part* of inner caldera road. XPL image

crystallization, quenched rims, vesicular, arborescent, intersertal, hypocrystalline, and hypohyaline textures with interior acicular an skeletal mineral shapes) are designated as enclaves.

Injection of hot basaltic to andesitic melt into a magma reservoir filled with cooler dacitic to rhyolitic melt may cause rapid cooling and quenching leading to rounded and elliptical shapes of enclaves (Eichelberger 1980; Bacon 1986; Dietrich et al. 1988; Dietrich 1989; Feeley and Dungan 1996). Therefore, the enclaves can be regarded as important witnesses with respect to magmatic mixing and mingling processes.

The xenoliths, which occur in the lavas and pyroclastics throughout the entire history of Nisyros Volcano, have been recognized and described already in certain detail by Di Paola (1974), Vougioukalakis (1984), Lodise (1987), Wyers and Barton (1989), Francalanci et al. (1995), Vanderkluysen et al. (2005), Spandler et al. (2012). Di Paola (1974) did not differentiate inclusions into xenoliths and enclaves and grouped them as "hornblende-rich lavas, hornblende-rich cumulates and contact metamorphic rocks". Lodise (1987) distinguished three types of "enclaves" according to their textures in the "Lower and Upper pumice", as well as in the rhyolitic and rhyodacitic lavas: (1) Granular aggregates of crystals in vesicular glass; (2) Hornblende-rich enclaves of variable textures with quenched rims and amphiboles up to several centimetre forming the interior part; (3) Irregular shaped enclaves with quenched rims and interiors less vesicular but variable in texture from hypocrystalline to porphyritic with granular plagioclase and acicular amphibole.

Wyers and Barton (1989) added a genetic distinction for all inclusions designating them only as xenoliths: (1) Cognate xenoliths on the basis of mineral paragenesis in both the host lavas and occurring xenoliths; (2) Amphibole-rich xenoliths; (3) Accidental xenoliths.

4.2.3.1 Rare Mafic Xenoliths (Gabbro-Cumulates and Gabbro-Diorites)

Sub-rounded and rounded mafic xenolithic inclusions with granular and cumulate textures (aggregates) containing plagioclase, clinopyroxene, orthopyroxene, minor olivine, hastingsitic amphibole and titanomagnetite have been observed in the pyroclastic deposits of the "Lower and Upper pumice". These pyroxenitic, anorthositic, gabbroic and dioritic xenoliths and blocks vary in sizes on a millimeter to several decimeter scale. One large example of a gabbro cumulate is shown in Figs. 4.8a, b and 4.9a–f, one example of dioritic xenolith in Figs. 4.10a, b and 4.11a–c.

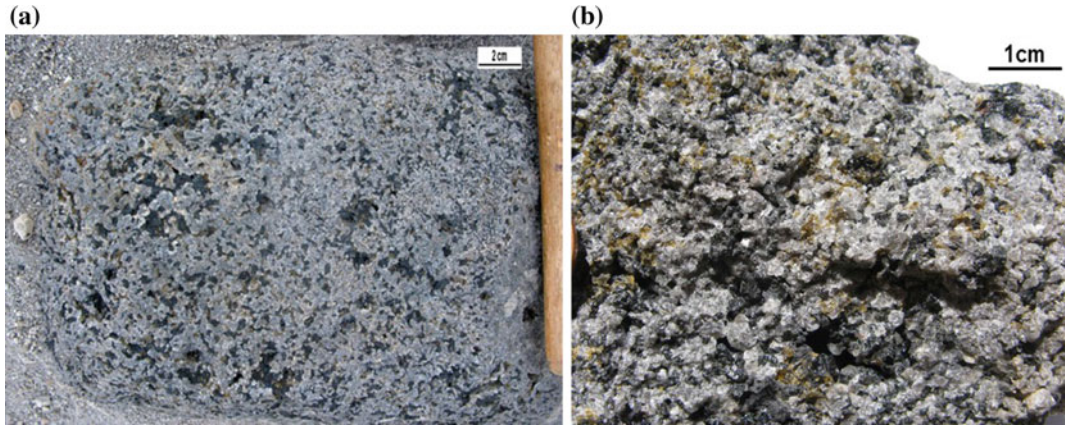

Fig. 4.8 **a** Gabbroic cumulate block (~20 × 30 cm) found in "*lower pumice*" (unit No. 28); grey crystals: plagioclase; *dark-green* and *black* crystals: clinopyroxene and amphibole; *yellowish-green* crystals: olivine. **b** Fresh, broken hand-specimen showing the cumulate and granular texture with crystals up to a few millimetre in size (Fig. 4.9a–f). The interstitial microcrystalline and porous dacitic matrix is partly broken out

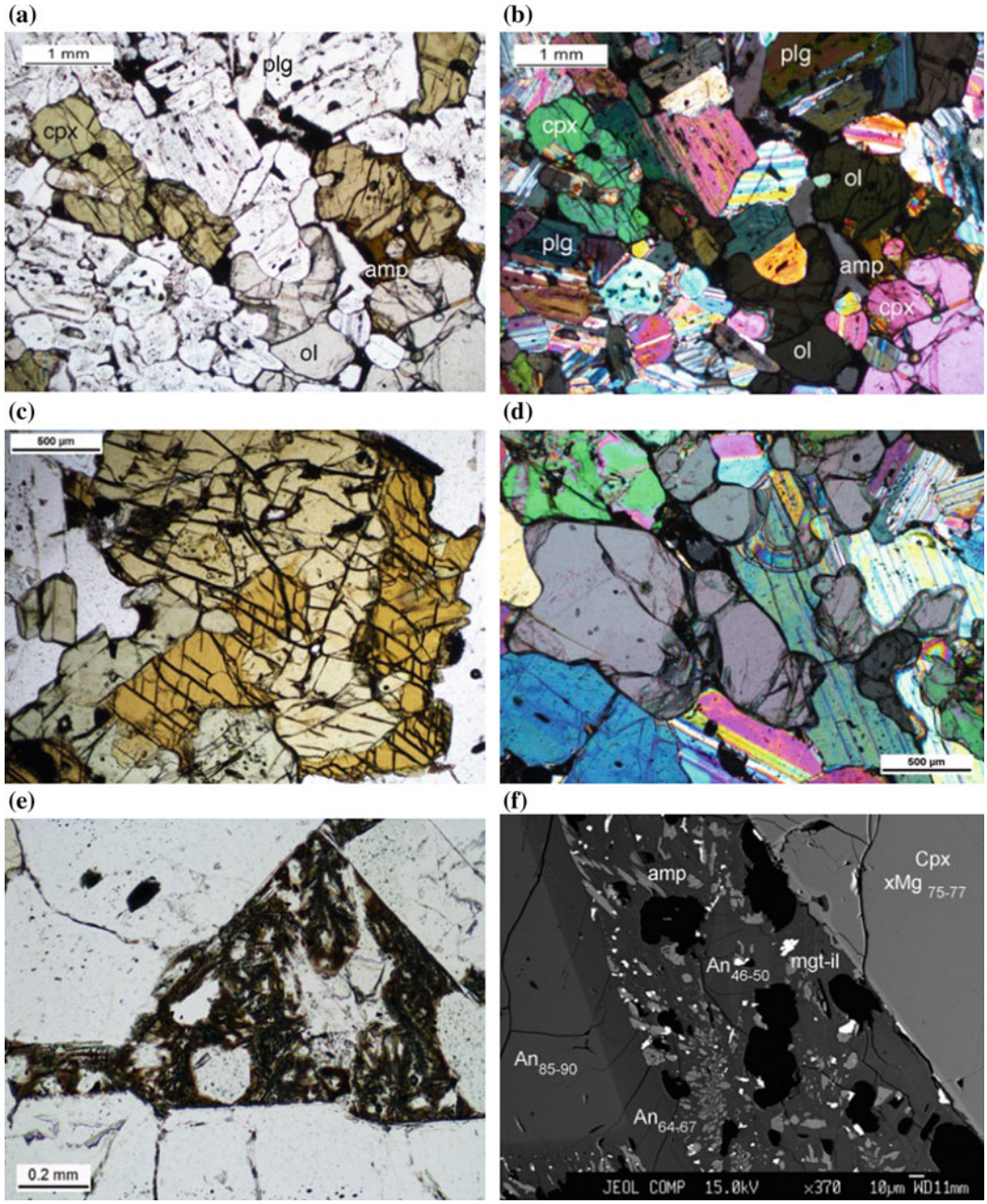

Fig. 4.9 **a** and **b** Gabbroic cumulate with well-equilibrated adcumulate texture of plagioclase (*plg*), clinopyroxene (*cpx*), olivine (*ol*), and amphibole (*amp*) as rims around clinopyroxene and interstitial microcrystalline quenched basaltic matrix. Plagioclase is sieved with fine melt inclusions. (**a** *PPL* plan polarized light and **b** *XPL* cross polarized light). **c** Intergrowth of magnesio-hastingsitic amphibole (*x*Mg = 0.79 and small pargasitic rims with *x*Mg = 0.74); augitic clinopyroxene (*x*Mg = 0.75–0.77) in gabbroic cumulate; (PPL). **d** Intergrowth of olivine (*x*Mg = 0.77) with (**c**) clinopyroxene and twinned plagioclase in gabbroic cumulate (XPL, $An_{85–90}$, rimmed with $An_{64–67}$). **e** Close-up of interstitial microcrystalline quenched basaltic matrix between plagioclase crystals consisting of plagioclase microliths and quenched glass of andesitic to dacitic composition (**e** PPL). **f** Backscatter image of the interstitial matrix with relicts of quenched glass, intermediate plagioclase ($An_{64–67}$ and $An_{45–50}$), ferroan-pargasite, magnesio-hornblende, actinolitic-hornblende and magnetite-ilmenite. *PPL* plane polarized light, *XPL* crossed polarized light

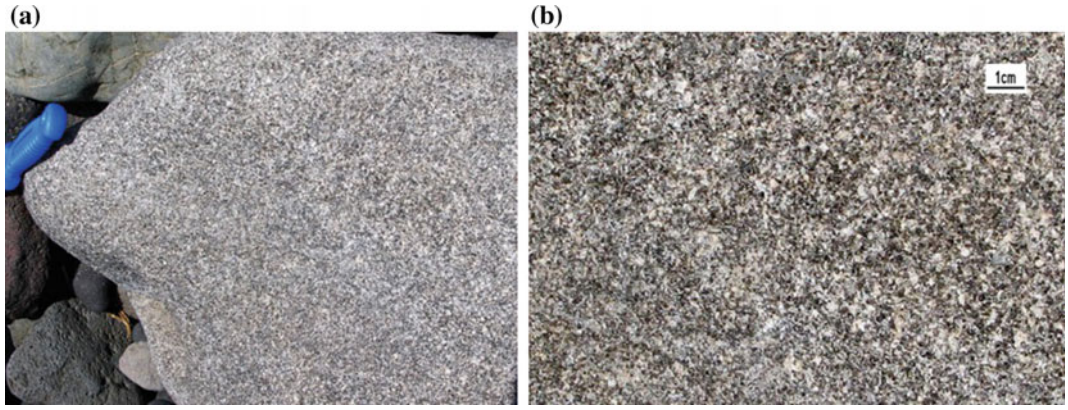

Fig. 4.10 **a** Fine-grained gabbro-dioritic block (~30 × 40 cm) with weathered surface found in rhyolitic pyroclastics (unit No. 28, lower pumice); *grey* crystals: plagioclase; *dark-green* and *black* crystals: clinopyroxene and amphibole. **b** Fresh, broken hand-specimen showing the granular texture with crystals up to a few millimeter size

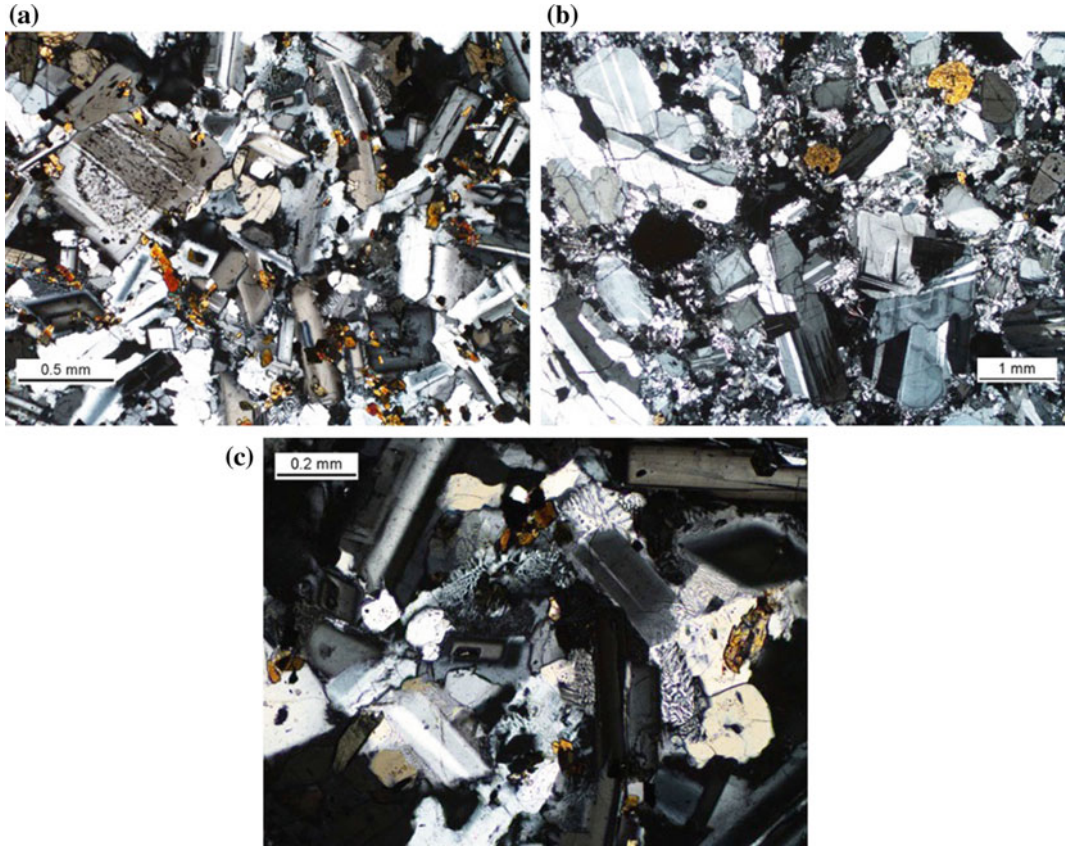

Fig. 4.11 **a–c** Weakly porphyritic micro-diorite (xenolith from lower pumice No. 28) with intergranular texture of plagioclase. Plagioclase phenocrysts are zoned with higher anorthitic cores and sieve texture. The interstices are occupied by small grains of euhedral green amphibole, minor clinopyroxene, and opaques. In addition, many interstices are filled with myrmekite patches (quartz worms penetrating plagioclase **b** and **c**). All images XPL

4.2.3.2 Quenched Mafic Enclaves

The abundance of enclaves increases in time and space: enclaves are very rare in the early volcanic cycles. No dacitic magmas have been formed during this period. During the composite strato-volcano cycles, dacites (Unit No. 14) were extruded within the central part of an early Nisyros volcanic environment and contained up to 30% andesitic enclaves (Figs. 4.12 and 4.13). However, they differ from enclaves in the younger rocks due to the absence of amphibole. Amphibole-bearing enclaves appears in the younger dacites in the lavas and pyroclastics of Afionas and Lies tuff cones (Units No. 18 and 19) and in the rhyolitic lava domes and flows of Stavros and Avlaki (Unit No 17). Up to 2% andesitic enclaves carrying minor amounts of amphibole are included in the voluminous dacitic lavas of Emborios (Unit No. 25). Lodise (1987) and Gansecki (1991) described a steady increase of enclave frequency from the lower pumice (Unit No. 28) throughout the lava flows of Nikia

Fig. 4.13 Dacite from lava (No. 14), rich in *grey* and *reddish* enclaves that make up to 30 vol. %

Fig. 4.12 Polished block of enclave-rich dacitic lava (No. 14), which is dominated by reddish, oxidised enclaves in a black glass-rich matrix, the latter appearing to be less than 10 vol.%. Under the microscope the components seem to be only agglutinated and not welded

Fig. 4.14 Quenched enclaves of andesitic composition from the Drakospilia lava flow (Unit No. 32) in the southwest of Nisyros volcano. *Photo* Barry's Ramblings

(unit No. 30) and the upper pumice deposits (unit No. 31) to the post-caldera rhyodacite domes (unit No. 32) (Fig. 4.14).

The enclaves found in the post-caldera lavas are dominated by intergrowths of acicular amphiboles and plagioclase crystals, have vesicular textures and can vary on a centimetre to decimetre scale (Fig. 4.15). They usually show quenching textures. These lavas also contain numerous millimetre-sized round and oval xenolithic undeformed inclusions with hypocrystalline, intergranular, and intersertal textures, which do not exhibit quench textures but resemble small fragments of pre-existing hypabyssal lavas.

4.2.4 Amphiboles as Phenocrysts and Resorbed Xenocrysts

Amphiboles are common mafic minerals in the volcanic rocks of Nisyros Island. They occur in dacitic, rhyodacitic and rhyolitic lavas and pyroclastics, but are less frequent in andesites and only as relics in basaltic andesites. Depending on the magmatic environment, the amphiboles show a large variation in mineral chemistry from magnesio-hastingsite (close to pargasitic transition) through evolved hastingsite to hornblende (Table 4.2). Tschermakitic hornblende and kaersutite have been found in dacites and rhyodacites with relatively high TiO_2 between 3.2 and 4.2 wt % and K_2O between 0.34 and 0.7 wt% (Wyers and Barton 1989; Seymour and Vlassopoulos 1992). The amphiboles in rhyolites display greenish to light brownish pleochroic colours and euhedral shapes (Fig. 4.16) and are mainly of magnesio-hastingsite composition with lower TiO_2 values between 2.1 and 2.8 wt%. However, in most cases the amphiboles are partly resorbed and also show black, opacitic rims of variable thickness (Figs. 4.17, 4.18 and 4.19). There is clear evidence that the amphiboles decomposed to crystallize clinopyroxene, orthopyroxene, titanomagnetite and ilmenite and to release water (Figs. 4.17, 4.18 and 4.19; Table 4.3).

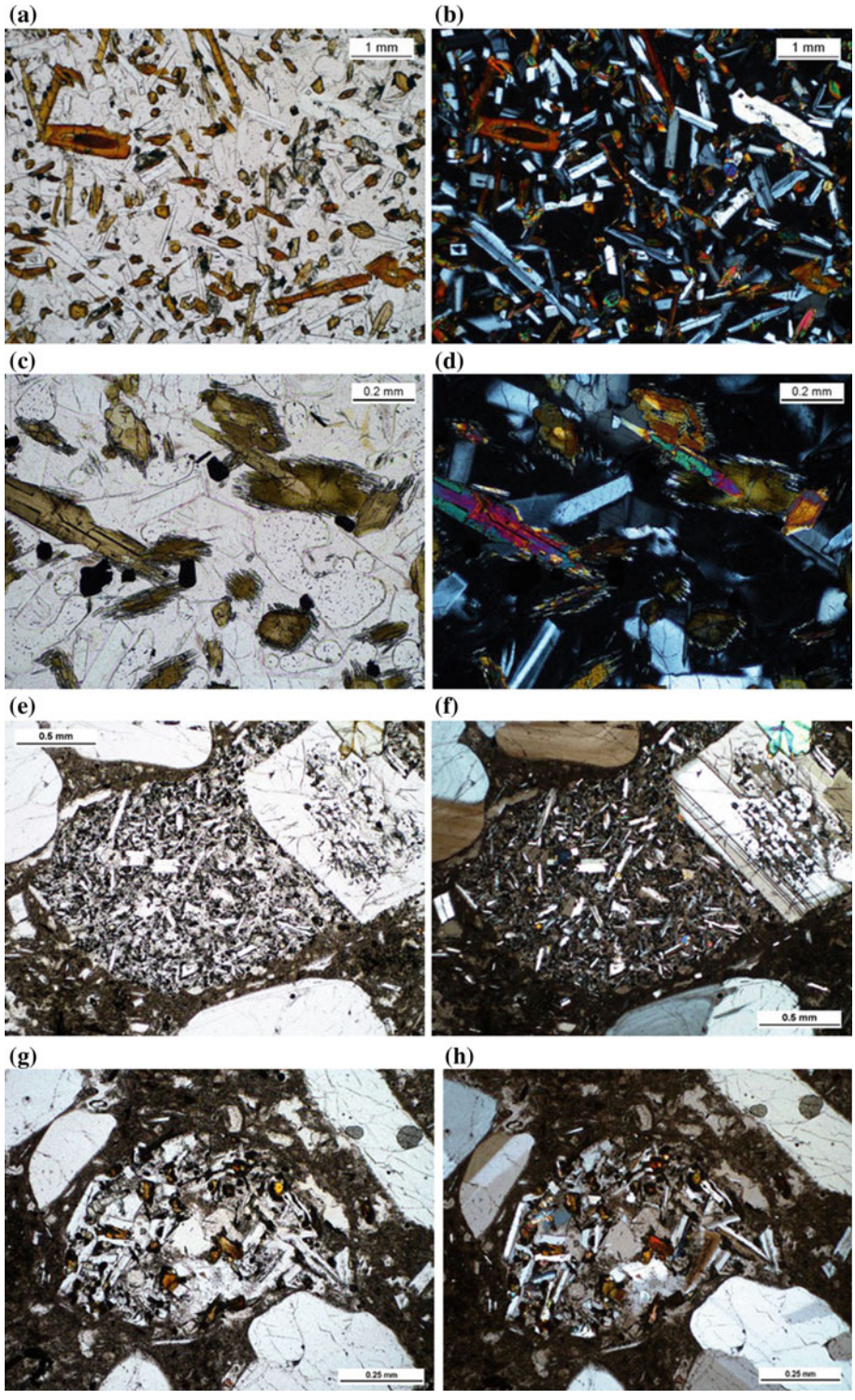
(a)
1 mm
(b)
1 mm
(c)
0.2 mm
(d)
0.2 mm
(e)
0.5 mm
(f)
0.5 mm
(g)
0.25 mm
(h)
0.25 mm

◀ **Fig. 4.15** **a**, **b** Detail of weakly vesicular enclave with intersertal texture, consisting of plagioclase and *red brown* acicular hastingsitic amphibole. Larger euhedral plagioclase is zoned. Clinopyroxene is subordinate. Titanomagnetite is accessory. **c**, **d** Vesicular enclaves are dominated by up to several millimetre size acicular *brownish-green* amphiboles intergrown with plagioclase. The amphiboles show reaction coronas of *light green* orthopyroxene. Clinopyroxene and small euhedral shaped titanomagnetite is accessory. The interstitial groundmass with hypohyaline texture consists of plagioclase, partly devitrified glass and numerous small round vesicles. **e**, **f** Small (<0.5 mm) round xenolithic inclusion mainly consisting of plagioclase and minor amphibole and orthopyroxene. **g**, **h** Very small (<0.25 mm) round xenolithic inclusion, mainly consisting of two generations of plagioclase and minor amounts of orthopyroxene and Fe–Ti oxides

The euhedral amphiboles within the magmatic enclaves are magnesio-hastingsites (Figs. 4.5a, b) with higher Al, Ti, Ni and Na but lower Mn contents than the amphiboles in the rhyodacites. They display strong brownish to red brownish pleochroic colours. They are often normally zoned with Fe-enrichment towards the rims. The magnesio-hastingsites, pargasites, and ferroan pargasites, found in the gabbro cumulate (Fig. 4.5) have compositional ranges, which are shown in Table 4.2.

4.2.5 Amphibole Breakdown Reactions Rims

Amphibole reaction rims are common phenomena in andesites, dacites and rhyolites of arc magmas and display a broad range of textures and mineralogy. A first classification was given by Garcia and Jacobson (1979), later by Rutherford and Hill (1993); a comprehensive review combining experimental studies by De Angelis et al. (2015). In the South Aegean

Table 4.2 Amphibole compositions in the gabbro-cumulate xenolith found in the "lower pumice" (Unit No. 28) of Nisyros Volcano

wt%	Magnesio-hastingsite	Pargasite	Ferroan pargasite	Magnesio hornblende	Actinolitic hornblende
SiO_2	42.0–42.4	41.9–42.2	41.6	45.7–48.5	51.9
TiO_2	3.2–3.5	3.1–3.5	2.35	1.9–2.41	1.51
Al_2O3	12.5–12.7	12.5–12.8	12.3	6.5–7.1	12.53
Cr_2O3	0.05–0.10	0.05–0.12	0.02	<0.01	<0.01
Fe_2O_3	2.7–3.1	0.1–0.4	0.75	n.d.	n.d.
FeO	6.9–7.3	9.2–9.5	13.18	10.4–12.3	9.6
MnO	0.07–0.15	0.09–0.13	0.24	0.27–0.34	0.3
NiO	0.0–0.01	0.01–0.05	0.01	0.0–0.2	0.02
MgO	15.0–15.2	15.1–15.3	13.7	12.7–13.15	8.54
CaO	11.5–11.7	11.6–11.7	9.85	17.5–17.65	10.49
Na_20	2.54–2.70	2.54–2.65	2.62	0.56–1.05	3.56
K_20	0.31–0.33	0.31–0.33	0.38	0.01–0.03	0.53
H_2O	2.06–2.07	2.06–2.07	2.01	2.04–2.09	2.14

Ad-cumulate amphiboles are of magnesio-hastingsite, pargasite and ferroan pargasite composition, whereas magnesio-hornblende and actinolitic-hornblende are found in the interstices. The amphibole compositions, using the nomenclature of Leake (1978) and Leake et al. (1997), were normalised by assuming (i) fixed $Fe^{3+}/(Fe^{3+} + Fe^{2+})$ ratio of 0.2 and 23 oxygens, and (ii) cations—Ca–Na–K = 13, as well as the program of Spear and Kimball (1984) estimating Fe^{3+} based on stoichiometric constraints of the total amphibole crystal chemistry

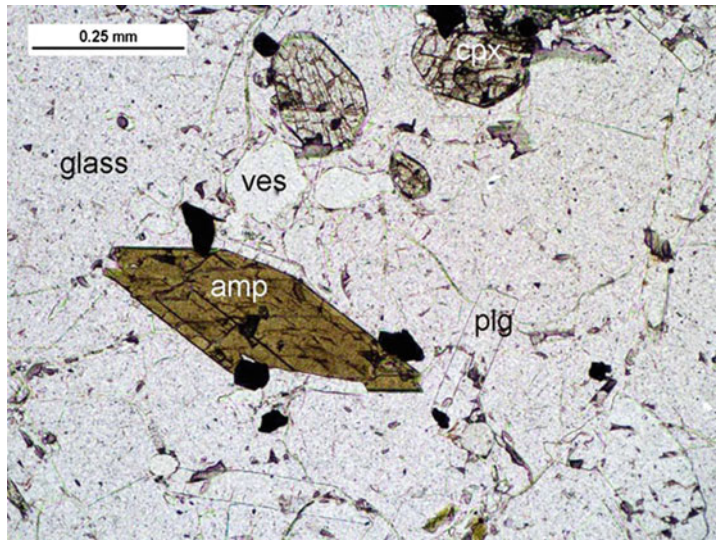

Fig. 4.16 Euhedral shaped hastingsitic amphibole with thin opacitic black rims, sodic plagioclase and clinopyroxene in the glassy part of the Nikia rhyolitic lava (No. 30); opaque crystals are Ti-magnetite and ilmenite; vesicles (*ves*) are partly filled with fluid inclusions; PPL image

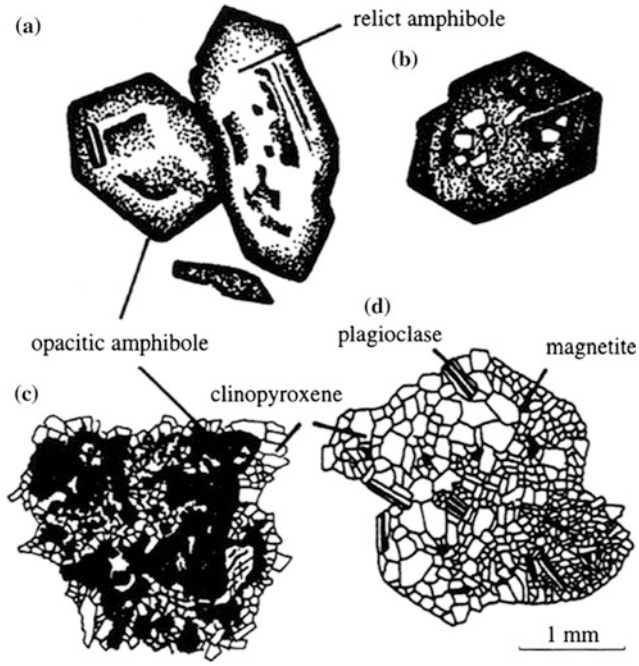

Fig. 4.17 **a** The *black-rimmed* phenocryst type of amphiboles with euhedral to anhedral and rounded shapes and very fine black and dusty aggregate rims of iron oxides (e.g. ilmenite) and small pyroxene crystals. **b** The *black rim* growth proceeds inward from the crystal margin. **c**, **d** show the "gabbroic type" reaction, which is caused by the breakdown reaction of the amphibole and leads to crystal growth of coarser clinopyroxene-plagioclase-magnetite aggregates. The opacite aggregate sometimes contains relicts of amphibole, preserving its original composition. The figure is taken from Dietrich et al. (1988)

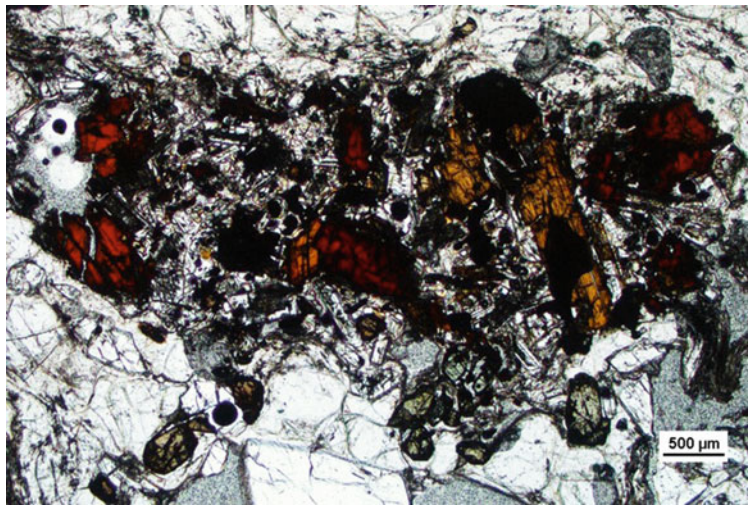

Fig. 4.18 Typical disintegrated amphibole, plagioclase, ortho- and pyroxene, Fe–Ti oxide assemblage in a glassy, vesicle-rich rhyolitic lava (Unit No. 30). The amphibole relics have *reddish pleochroitic colours*, due to oxy-hornblende reactions; image under PPL

Volcanic Arc amphibole breakdown reaction rims have been described in detail by Dietrich et al. (1988) and Gartzos et al. (1999) (Figs. 4.17a–d). In contrast to crystal clots, crystal reaction rims form microliths to equigranular assemblages (syn. corona) of opx +cpx+Fe–Ti oxide ± plagioclase that occur around relict amphibole. The amphiboles in the Nisyros lavas and pyroclastics are in the majority of cases of hastingsitic composition and show all steps of breakdown reactions (Figs. 4.3 and 4.4).

According to Garcia and Jacobson (1979) two distinct types of amphibole reaction products occur in the evolved lavas and formed as a result of dehydration:

(1) The majority of amphiboles occur as the "black-rimmed type". Some of the amphibole is partly or entirely replaced by a very fine black and dusty aggregate of iron oxides (e.g. ilmenite) and small pyroxene crystals (Fig. 4.17a, b as well as in Fig. 4.19a–c, g, h). In several cases, the reaction coronas consist of orthopyroxene, clinopyroxene, plagioclase, and Fe–Ti oxide aggregates (Fig. 4.19d, e). The assemblage in the reaction rims is identical with the phenocryst assemblage of the host lava. Besides the rim reaction, the amphiboles sometimes display evidence of the oxy-hornblende reaction (Graham et al. 1984), due to a rise of temperature: the OH bonds are broken and the crystal turns into reddish-brownish colours with intense pleochroism (Fig. 4.19a–c). As heat grades up, other bonds are also broken, the crystal resorbs and other anhydrous minerals start to crystallize.

Fig. 4.19 **a**, **b** Various steps of amphibole breakdown reactions in the rhyolite lava west of Avlaki (Unit No. 17) and Nikia rhyolite (unit No. 30). **a** Isolated euhedral magnesio-hastingsite, slightly rounded with very thin black rim adjacent to anorthitic plagioclase; **b**, **c** up to 40 µm *thick black* rims, formed out of submicroscopic aggregates of Fe–Ti oxides and orthopyroxene; **c** amphibole partly pseudomorph as a micro-granular aggregate of pyroxene and plagioclase; **d** amphiboles with a well developed corona of orthopyroxene needles; **e**, **f** amphibole disintegrated into a granular aggregate of pyroxene, plagioclase and Fe–Ti oxides within a vesicle-rich glassy matrix (**e** in dacite flow unit No. 25 and f in rhyolite flow unit No. 30); **g**, **h** small amphibole grains totally transformed into *black* aggregates of Fe–Ti oxides and pyroxenes. All images in PPL ▶

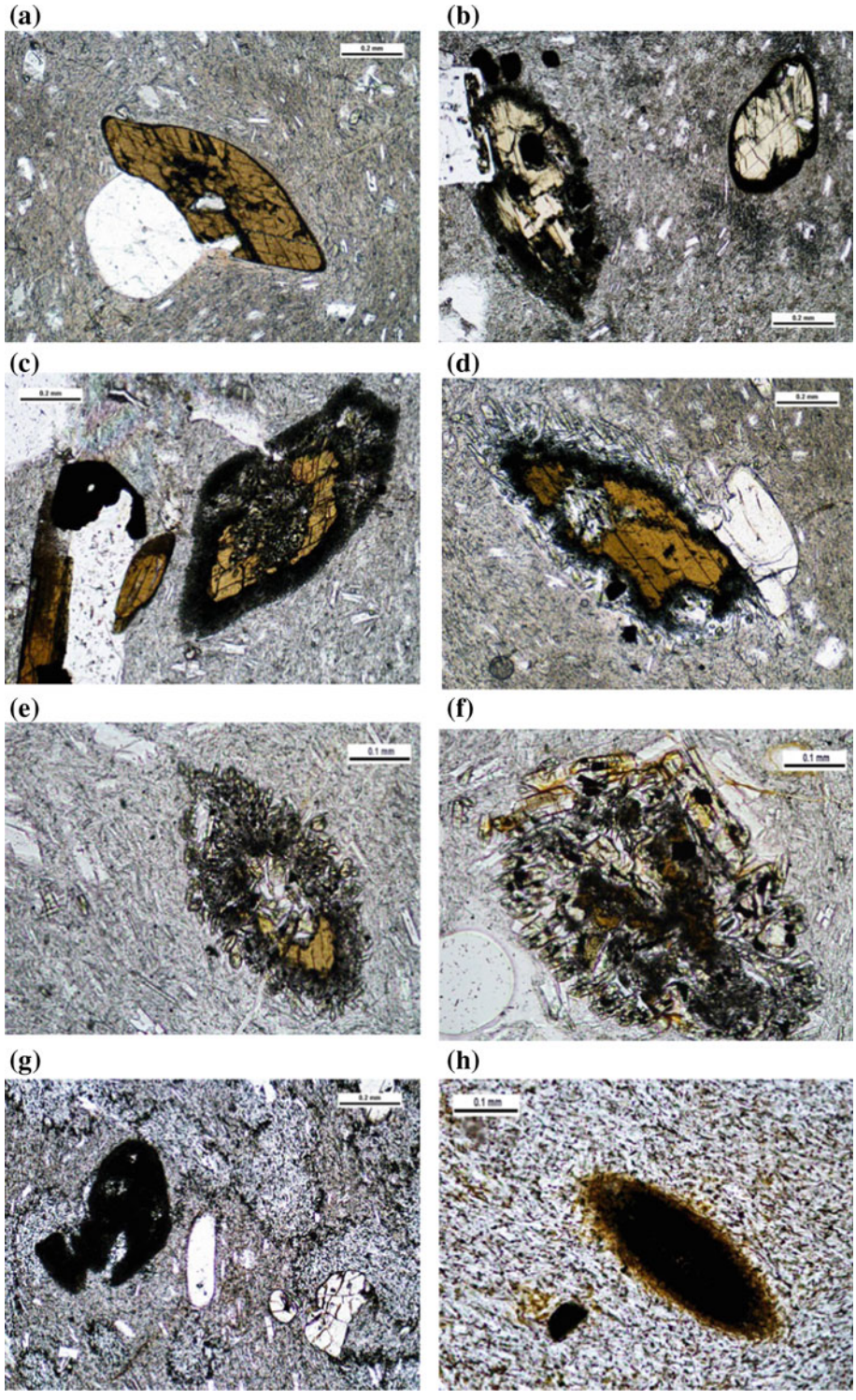
(a)
(b)
(c)
(d)
(e)
(f)
(g)
(h)

Table 4.3 Representative amphibole compositions in the evolved lavas (Units No. 25, 30 and 32) and their mafic enclaves of Nisyros volcano

Mineral	Kaersutite	Mg-hasting	Mg-hasting	Mg-hasting	Mg-hasting	Tscherm.Ho.	Mg-hasting
wt%							
SiO_2	37.8	40.31	41.37	41.51	41.82	43.01	42.75
TiO_2	4.56	2.32	2.12	2.79	2.48	3.2	2.16
AI_2o_3	14.19	12.99	13.32	12.72	13.06	10.88	12.52
FeO(t)	17.8	15.35	11.3	14.45	13.6	13.62	10
MnO	0.28	0.17	0.13	0	0.19	0.17	0.12
MgO	14.75	15.3	15.51	12.48	12.93	12.87	16.21
CaO	0.05	10.84	10.84	11.05	11.7	11.3	11.38
Na_2O	0.56	2.5	2.56	2.47	2.62	2.11	2.33
K_2O	8.14	0.43	0.36	0.34	0.34	0.52	0.38
Total	98.13	100.21	97.51	97.81	98.74	97.68	97.85
Unit	25	30	30	30	30	32	32
Rock	Dacite		Rhyolite		Mat. enclave	Rhyodacite	Maf. enclave

Data from Wyers and Barton (1989) and Seymour and Vlassopoulos (1992)

(2) The rare amphibole type is the so-called "gabbroic type" (Garcia and Jacobson 1979; Rutherford and Hill 1993), which has been observed in the evolved lavas, in the basaltic andesite and andesites. The amphibole is partially replaced by a fine-grained granular aggregate of anhedral ortho- and clinopyroxene, plagioclase and Fe–Ti oxide with mosaic textures (Figs. 4.17c, d and 4.19d–f). In the fine-grained equigranular gabbroic glomerophyres, plagioclase never shows oscillatory zoning.

Both amphibole reaction products, "black-rimmed" and the "gabbroic type" occur in the same lava units. Also minor opacitic relics of amphibole can be recognised in the cores of well-shaped pseudomorph aggregates of clinopyroxene, plagioclase and oxides. These breakdown reaction products may lead to continuous crystal growth of pyroxenes and plagioclase to produce random types of aggregates (Fig. 4.18) and not typical glomeroporphyritic clots.

Often, the euhedral shaped, black-rimmed amphiboles embedded in pumice show no other stages of resorption and dusty effects.

4.3 Whole-Rock Major and Trace Element Geochemistry

A collection of 250 analyses from rock samples with known localities published by Rehren (1988), Seymour and Vlassopoulos (1992), Francalanci et al. (1995), Vanderkluysen et al. (2005), Zellmer and Turner (2007) and Spandler et al. (2012) has been compiled. Whole rocks were analysed for major and trace elements mainly by XRF (i.e. Nb, Zr, Y, Sr, Rb, Pb, Ga, Zn, Cu, Ni, Cr, V, and Ba), whereas Th, Hf and rare earth elements by neutron activation and laser ablation inductively-coupled plasma mass spectrometry (LA-ICP-MS). The values are given in Electronic Supplementary Material Appendix A.

An overview of this data is given in Table 4.4, according to the lithostratigraphic units, rock types and silica contents (SiO_2 wt%).

The chemical trend of all Nisyros volcanics is typical for low to medium potassic calc-alkaline rocks (Fig. 4.20). According to the TAS diagram, the volcanic products of Nisyros fall in the basaltic andesites, andesites, dacites, rhyodacites and rhyolites fields. Since the bulk chemical

Table 4.4 Overview correlation between lithostratigraphic units, lava flows with their enclaves, domes, pyroclastics, rock types and silica contents (SiO_2 wt%)

LSU	Eruption mode	Thickness	Rocktype	Bulk rock	Enclaves	SiO2 wt.%	87Sr/86Sr	LSU
				SiO2 wt.%	SiO2 wt.%	52 54 56 58 60 62 64 66 68 70 72 74		
	Post-Caldera Eruptive Cycle							
33	Lava domes, flows	max. 600 m	Rhyodacite	67.0 - 71.3	54 - 57*		0.70379-0.70462	33
	Caldera Eruptive Cycles and Caldera Collapse							
31	Fl-WS-Fl-PbS-succ.	outcrop 30 m	Rhyolite	67.2 - 72.8	56 - 60*		0.70456	31
30	Lava flows	max. 150 m	Rhyolite	68.5 - 71.8	53 - 56*		0.70419-0.70454	30
28	F-Fl-WS-Fl-succ.	outcrop 20 m	Rhyolite	68.5 - 73.7	57 - 61*		0.70424	28
27	Lava flow	max. 10 m	Andesite	58.9 - 59.5				27
	Composite Stratovolcano Cycles							
26	Dome collapse breccia.	outcrop 20-30m	Dacite	65.0 - 67.0				26
25	Flows	max. 150 m	Dacite	65.0 - 68.7*	58.3 - 60.6		0.70402-0.70462	25
24	Flows	max. 25 m	Bas. And.- And.	53.0 - 59.0			0.70426-0.70465	24
22	Flows	max. 10 m	Bas. And.- And.	54.0 - 59.5			0.70413-0.70459	22
21	F-PbS-PyFl-succ	outcrop 15 m	Bas. And.- And.	54.2 - 58.8			0.70499	21
19	F-S-F-3S-F-F-xS-F-succ.	outcrop 50 m	Bas. And.to Dac.	54.3 - 60.7		?	0.70477-0.70521	
19	F-PbS-Fl-succ.	outcrop 40 m	Dacite	63.4 - 67.6				19
18	Lava flow	? max. 10 m	Dacite	63.5 - 64.8*				18
17	Lava domes, flows	max. 60 m	Rhyolite	69.4 - 73.2*			0.70415-0.70427	17
16	S-Fl-succession	outcrop 30 m	Bas. Andes.	50.8 - 52.0				16
15	Lava flow	max. 40 m	Andesite	58.5 - 59.7			0.70338-0.70466	15
14	Lava flow	max. 25 m	Dacite	65.7 - 67.0	57.8 - 58.5			14
13	Lava flow	max. 40 m	Bas.And.- And.	54.0 - 59.7				13
	Early Shield Volcanic Cycles							
11	F-Fl-F-S-Fl-succ.	outcrop 35 m	Bas.And.- And.	53.7 -56.7				11
10	Lava flows	max. 70 m	Bas. Andes.	54.3 - 55.7				10
8	Lava flow	max. 5 m	Bas. Andes.	53.7 - 56.7				8
6	S-F-Fl-S-Fl-succ.	outcrop 60 m	Bas. Andes.	51.7			0.70354-0.70463	6
5	Lava flows	max. 40 m	Andesite	55.7 - 60.0				5
4	F-Fl-S-F-succ.	outcrop 30 m	Andesite	55.9 - 57.8				4
3	Lava flow	max. 35 m	Bas. Andes.	53.3				3
	Submarine Volcanic Base							
1,2	Pillow & lava flows	? max. 50 m	Bas. Andes.	52.6 - 56.9*			0.70377-0.70452	1,2
						52 54 56 58 60 62 64 66 68 70 72 74		

F fall, *Fl* flow, *S* surge, *PbS* planar bedded surge, *WS* wavy surge, *PyFl* pyroclastic flow, *Encl* enclaves, $^{87}Sr/^{86}Sr$ data from: Francalanci et al. (1995), Gülen (1987, 1990)

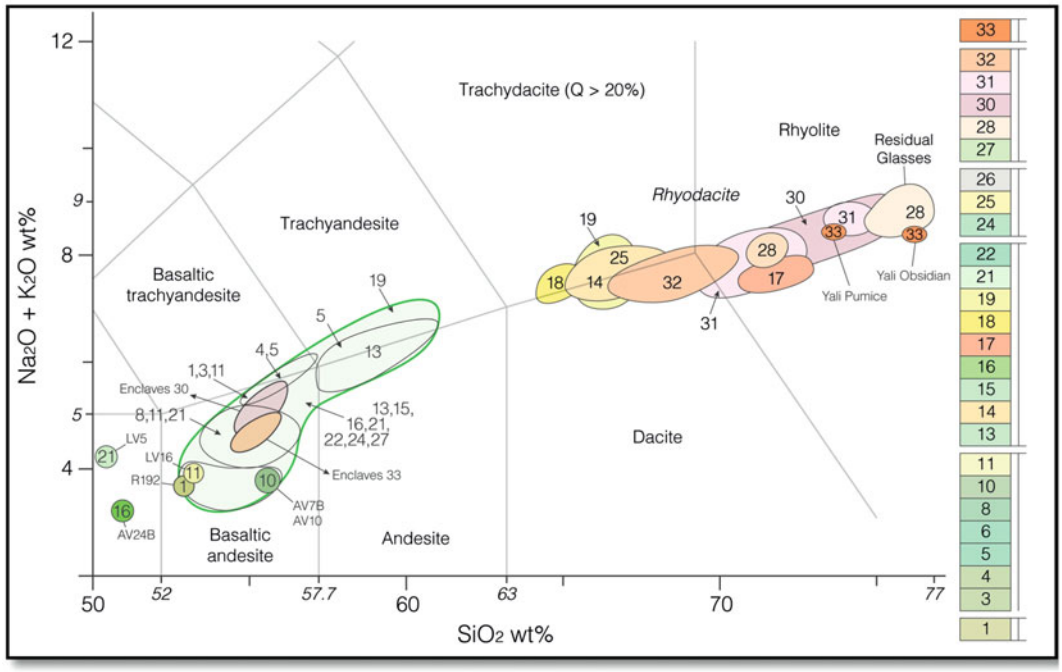

Fig. 4.20 TAS diagram for Nisyros volcanics. The point distribution of the analyzed rocks has been converted into approximate overlapping fields. *Numbers* and *colors* refer to the lithostratigraphic units given in the geological map and lithostratigraphic profiles: from the oldest (*1*) to the youngest (*33*) eruptive unit

composition of these rocks covers a wide range, we describe them in the lithostratigraphic order.

4.3.1 General Geochemical Characteristics

The general differentiation trends of major and selected trace elements of Nisyros volcano are shown in Figs. 4.21, 4.22, 4.23 and 4.24 and overlap with those reported from all volcanic rock series in the Aegean volcanic island arc. They are characterized by an increase of SiO_2, K_2O, Na_2O, Rb, Ba, Ce, La, Zr, Nb and a decrease of MgO, CaO, FeO_{tot}, Al_2O_3, Cr and Ni, which fits the general calc-alkaline trend, marked CA with down-bending arrows in Fig. 4.5. Using the FeO_{tot}/MgO versus SiO_2 diagram of Miyashiro (1974), several basaltic andesites and andesites of the early caldera cycles straddle the arc tholeiitic to calc-alkaline separation line with no apparent compositional gap in the differentiation series (Fig. 4.21). This is also expressed in two compositional trends for basaltic andesites and andesites that allow a division into several differentiated groups, i.e. a normal calc-alkaline trend and a tholeiitic trend towards higher TiO_2 (Tables 4.5 and 4.6; Fig. 4.21). In a few cases, the analyses with high Al_2O_3 contents reveal peraluminous characteristics (Fig. 4.21), which might be an effect of high modal abundances of plagioclase in the samples.

Fig. 4.21 Bulk rock composition of Nisyros volcanics: major oxides plotted against SiO_2 and MgO. **a** The FeO_{tot}/MgO versus SiO_2 diagram (Miyashiro 1974) shows an arc tholeiitic affinity (TH) of several basaltic andesites and andesites of the early caldera cycles, which is also apparent in the TiO_2/MgO and $TiO_2/FeO_{(tot)}$. **c**, **d**: the calc-alkaline trend is marked CA with down-bending arrows in plots (**a**), (**d**), (**e**) and (**h**). In a few cases, the analyses with high Al_2O_3 contents (**e**) reveal peraluminous characteristics. Note the compositional gap in plots (**a**) and (**b**) between andesites and dacites, e.g. already recognized by Wyers and Barton (1989) ►

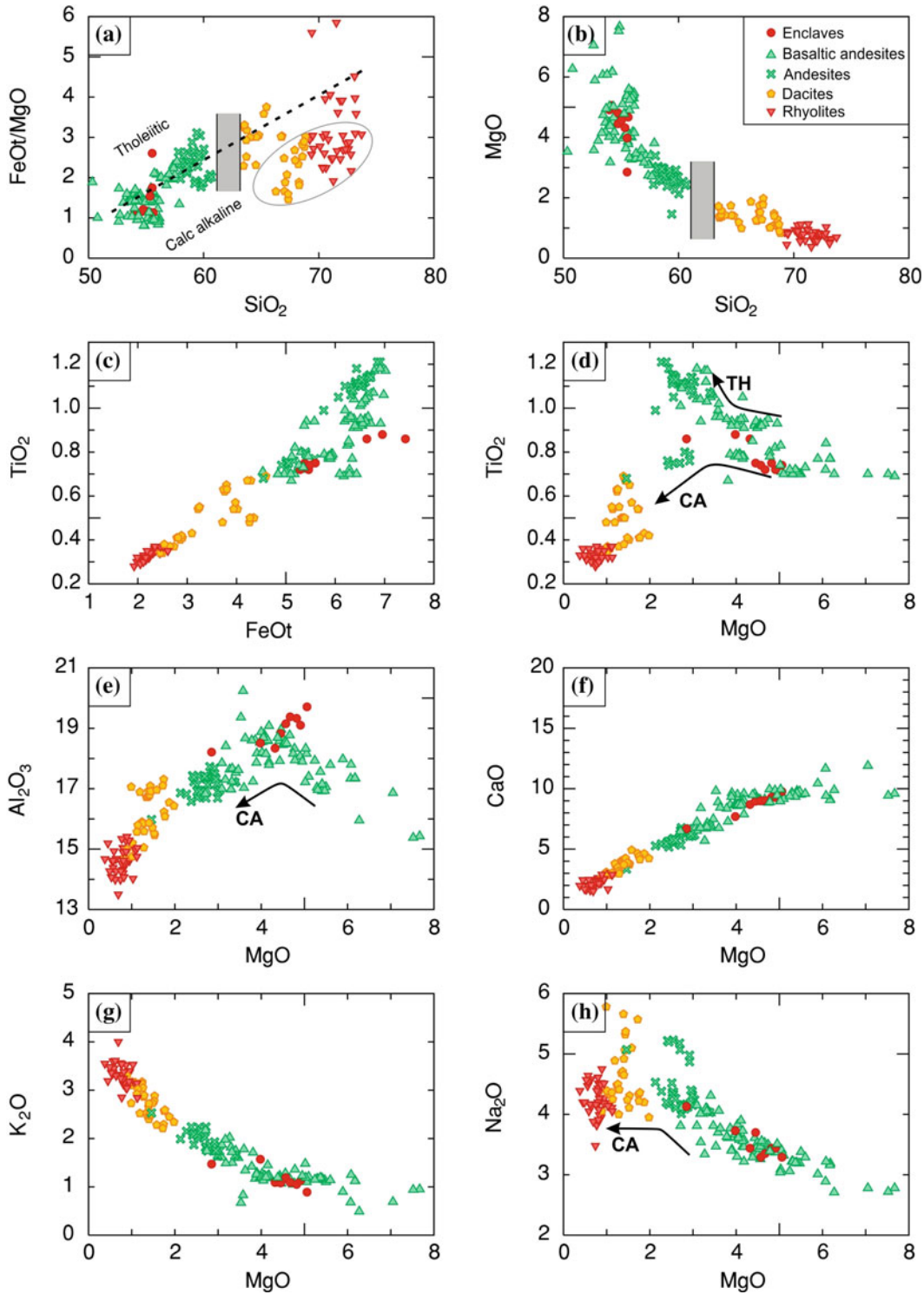
(a)
FeOt/MgO
SiO2
Tholeiitic
Calc alkaline
(b)
MgO
SiO2
Enclaves
Basaltic andesites
Andesites
Dacites
Rhyolites
(c)
TiO2
FeOt
(d)
TiO2
MgO
TH
CA
(e)
Al2O3
MgO
CA
(f)
CaO
MgO
(g)
K2O
MgO
(h)
Na2O
MgO
CA

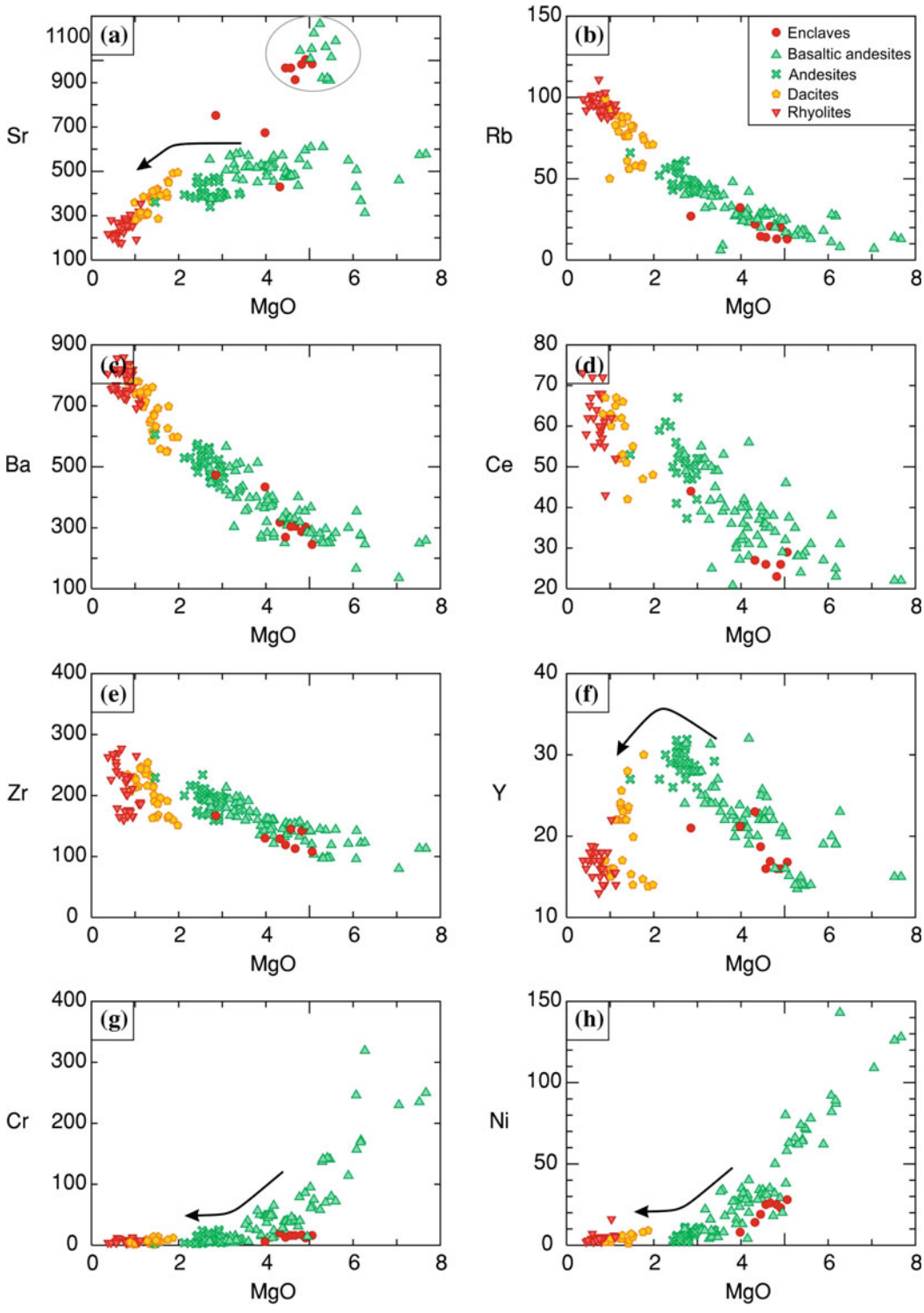

Fig. 4.22 Bulk rock composition of Nisyros volcanics: selected incompatible (Rb, Sr, Ba and Ce) and compatible trace elements (e.g. Ni, Cr, Zr, and Y) plotted against MgO. The calc-alkaline trend is marked with down- and up bending *arrows* in plots (**a**), (**f**), (**g**) and (**h**)

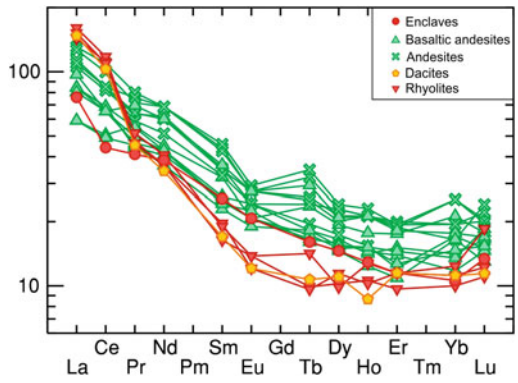

Fig. 4.23 Chondrite normalized rare earth element (REE) patterns (MacDonough and Sun 1995) of selected Nisyros lavas and enclaves (values in Electronic Supplementary Material Appendix)

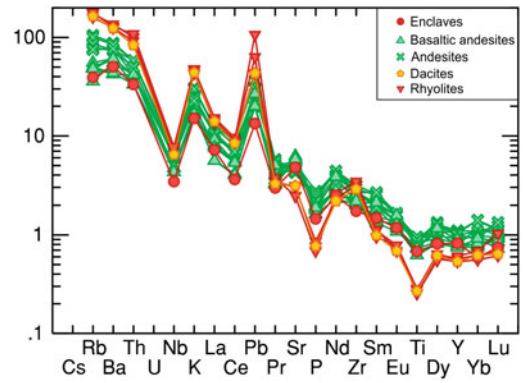

Fig. 4.24 Bulk chemical composition of Nisyros volcanics expressed as "multi-element variation diagram" of selected major and trace elements, normalized to normal N-type mid-ocean ridge (MORB) basalt composition (Sun and MacDonough 1989)

Table 4.5 Division into groups of chemical compositional variations of basaltic andesites and andesites of Nisyros pre-caldera lavas from Units No. 1 and 2

Rock type	Basaltic andesites			
Unit-sample	1 A-R192	1-B1	1-B2	1-C
wt%				
SiO_2	52.2	55.0–56.0	55.0–56.0	54.0–55.4
TiO_2	0.7	0.7–0.8	0.7–0.8	0.93–0.95
AI_2o_3	16.8	17.0–18.6	17.0–18.0	17.9–18.5
Fe_2O_3(t)	7.1	5.0–6.0	5.4–6.4	6.2–7.5
MnO	0.12	0.1	0.09	0.13
MgO	7.1	4.8–5.5	5.0–5.4	3.9–4.4
CaO	11.9	9.5–10.0	9.5–9.8	9.5–9.7
Na_2O	2.78	3.2–3.5	3.2–3.5	3.4–3.8
k_2O	0.69	1.07–1.17	1.1–1.7	1.22–1.29
p_2O_5	0.12	0.18–0.20	0.16–0.18	0.16
ppm				
Nb	n.d.	6	5.7–6.3	8–13
Zr	168	97–130	98–120	120–150
Y	n.d.	14	14	20–23
Rb	7	18–22	15–18	27–28
Sr	460	500–610	910–1050	500–530
Ni	109	32–62	62–72	13–24
Cr	230	50–140	65–140	11–24
V	200	140	140–143	167
Ce	n.d.	28	28	39
Ba	135	250–370	250–290	250–284
La	n.d.	13	13	14–15

Submarine volcanic base

Sources Rehren (1988), Wyers and Barton (1989), Seymour and Vlassopoulos (1992), Francalanci et al. (1995), Vanderkluysen et al. (2005), Zellmer and Turner (2007) and Spandler et al. (2012). *n.d.* not determined

Table 4.6 Bulk chemical composition of basaltic andesites and andesites from the LSU Nos. 3–24 of the early shield volcanic cycle (Nos. 3–11) and the composite stratovolcano cycles (Nos. 13–24)

Rock Type	Bas.And.	Andesite	Andesite	Bas.And.	Bas.And.	Bas.And.	Bas.And.	Bas.And.	Andesite	Bas.And.	Andesite	Bas.And.	Bas.And.	Bas.And.
LSU	3	4	5	6	8	10	11	13	15	16	19	21	22	24
Thickn. m	30	40	40	60	5	70	35	max. 40	max. 40	30	80	max. 15	max. 15	max. 25
wt.%														
SiO_2	53.3	56.0–57.8	55.7–60.0	51.7	53.7–56.7	54.3–55.7	52.7–57.7	54.0–60.0	58.5–59.7	53.3	60.0–61.2	54.2–58.8	54.0–59.0	53.0–59.5
TiO_2	1.05	1.18	1.17–1.0	0.76	0.83–1.23	0.69–0.78	0.77–1.04	0.92–1.2	1.11–1.15	0.7	0.7–0.8	0.72–1.12	0.8–1.2	0.78–1.16
Al_2O_3	18.58	17.4	17.7–16.8	16.9	17.9–17.1	17.9–15.4	18.8–16.8	18.6–16.8	17.4–17.0	16.5	17.5–18.0	17.6–16.7	18.7–16.6	18.8–16.9
Fe_2O_3(t)	7.36	7.4–7.2	7.8–6.4	3.24	6.9–7.9	6.9–5.9	7.0–7.35	6.0–7.7	7.16–7.46	6.3	5.6–6.2	5.9–7.3	5.9–7.7	6.0–7.5
MnO	0.12	0.10	0.13	0.09	0.12	0.0–0.11	0.13	0.11–0.14	0.12–0.14	0.11	0.12	0.09–0.13	0.09–0.14	0.11–0.13
MgO	4.15	3.3–2.4	3.3–2.1	1.56	6.1–2.7	7.7–4.8	5.9–2.7	4.4–2.25	3.0–2.5	6.8	2.5–3.2	6.18–3.0	5.24–2.38	4.9–2.2
CaO	9.08	5.7–5.2	7.2–5.3	10.57	9.5–6.3	9.6–9.0	10.4–6.5	9.05–5.3	6.8–5.9	1014	5.8–6.3	9.3–6.1	9.4–5.44	9.8–5.7
Na_20	3.47	3.3–4.2	4.1–4.5	2.20	3.1–3.9	2.7–3.3	3.0–4.1	3.4–4.4	4.0–4.5	2.84	4.8–5.3	3.2–4.2	3.06–4.20	3.4–4.3
K_2O	1.45	1.9–2.0	1.5–2.2	1.86	1.2–1.7	0.94–1.48	0.9–2.2	1.5–2.2	1.8–2.1	0.5	1.9–2.1	1.12–1.75	1.14–2.24	1.13–2.15
P_2O_5	0.23	0.25	0.25–0.30	0.20	0.2–0.25	0.14–0.19	0.18–0.3	0.21–0.28	0.25–0.27	0.48	0.23–0.25	0.18–0.25	0.18–0.30	0.19–0.26
ppm														
Nb	14	13–16	13–17	13	10–13	6–8	9–14	Dec–17	14–17	8	n.d.	6–14	6–17	10–16
Zr	148	174–200	165–235	156	140–174	113–144	145–194	150–216	180–210	123	159–175	120–200	140–215	125–200
Y	23	25	26–31	21	20–30	14–16	20–24	22–30	31–29	23	n.d.	15–28	14–29	20–36
Rb	31	43–46	33–59	61	24–37	13–20	18–40	27–56	43–55	8	41–47	16–44	15–57	27–59
Sr	559	530–470	470–395	404	610–430	575–1090	550–570	570–340	380–405	312	450–470	1060–400	1165–380	595–400
Ni	4	4	3	6	82–18	128–50	62	34–5	8–2	143	3–10	90–9	66–9	30–<3
Cr	12	4	3	16	157–10	250–40	114	39–3	9–5	319	14–24	170–5	58–3	86–25
V	172	230–150	230–140	117	240–175	140–155	170–100	180–215	220–195	160	100–135	170–210	130–230	160–210
Ce	40	37–50	25–67	46	29–46	22–34	27–53	37–61	48–56	31	n.d.	23–52	35–60	30–45
Ba	385	300–480	400–550	400	286–400	250–320	300–500	320–535	465–535	246	500–565	275–480	280–565	275–505
La	20	21–25	19–31	24	16–23	11–15	18–27	18–30	24–29	15	n.d.	12–26	16–34	14–24

Data sources Rehren (1988), Wyers and Barton (1989), Seymour and Vlassopoulos (1992), Francalanci et al. (1995), Vanderkluysen et al. (2005), Zellmer and Turner (2007) and Spandler et al. (2012).
n.d. not determined

SiO_2 contents range between 52 and 75.7 wt% (Electronic Supplementary Material Appendix Fig. 4.50), from basaltic andesite to rhyolite with dacites from 64 to 68 wt% and rhyodacites from 68 to approximately 70 wt%. Only two lavas of units 16 and 21 showed basaltic composition, with SiO_2 of 50 wt% and MgO of 6.3 wt%, and 3.5 wt%, respectively. The most primitive basaltic andesites have MgO contents of 7.0–7.7 wt% with SiO_2 contents that range from 52 to 55 wt% (Table 4.5). The samples that contain >5 wt% MgO are mafic enclaves. Al_2O_3 spans a range of 15.4 –18.5 wt%; it increases in the plagioclase rich basaltic andesites and decreases progressively from the andesites through dacites and rhyolites. FeO_{tot} and TiO_2 decrease as MgO decreases (e.g., Fig. 4.21c, d), while K_2O and Na_2O show the opposite trend (Fig. 4.21g, h).

The major element data shows a silica gap from 61.5 to 64.0 wt%, between andesites and dacites (Fig. 4.21a, b). The discontinuity in MgO and TiO_2 trends roughly coincides with the occurrence of the silica gap. Taking into account the petrographic observations in dacitic lavas, such as contamination with xenocrysts and millimetre size andesitic enclaves, the gap might actually be larger, as postulated by Wyers and Barton (1989) and Seymour and Vlassopoulos (1992). Mingling and mixing effects are clearly reflected by the lower values of FeO_{tot}/MgO for dacites, rhyodacites and rhyolites (encircled in Fig. 4.21a), which results from the random amount of enclaves and xenocrysts.

K_2O typically ranges between 1 and 3 wt%, but reaches as high as 4 wt% in some rhyolitic samples. It fits and overlaps the potassium array of all other calc-alkaline suites of the South Aegean volcanic arc (Mitropoulos et al. 1987; Pe-Piper and Piper 2002). However, glass microprobe analyses range from 3 to 4 wt% K_2O in the Argos and Nikia rhyolites (Units Nos. 17 and 30) and in the post-caldera rhyodacites (unit No. 32), reaching up to 6 wt% in some samples. The sodium content scatters within the dacitic compositions, whereas it decreases within the high-silica rhyolites.

The variations in selected trace element abundances are shown on the MgO diagrams in Fig. 4.22. The variation of the incompatible, large-ion lithophile elements (LILE) Sr, Rb, Ba is rather large with factors up to 4, whereas the high field strength elements (HFSE) Zr and Y vary only by a factor of 2.7.

Ba and Ce (Fig. 4.22c, d) generally increase with decreasing MgO, Ce displaying significant scatter in the basaltic andesite compositions between 6 and 3 wt% MgO. Sr (Electronic Supplementary Material Appendix Fig. 4.52a) systematically increases with decreasing MgO from about 200 to over 500 ppm, followed by a bend at around 2 wt% MgO that marks a trend of decreasing Sr content in the dacites and rhyolites. Independently, several basaltic andesites and enclaves with MgO between 4.2 and 5.6 wt% contain high Sr values between 900 and 1100 ppm. The highly incompatible element Rb (Fig. 4.22b) varies by up to a factor of 10 for a given MgO content, but most of these variations are confined to the basaltic andesites. Zr varies by a factor of 3 over the entire compositional range, with larger variation for differentiated basaltic andesites (Fig. 4.22e). Y generally decreases in the dacites and rhyolites and thus follows the iron-titanium enrichment and subsequent decrease of the calc-alkaline trend (Fig. 4.21f). It does not show the arc tholeiitic trend expressed in the TiO_2/MgO variation diagram. Ni and Cr are positively correlated with MgO (Fig. 4.22g, h), decreasing from generally 200 ppm for Cr in basaltic andesites to values <3 ppm. Ni contents decrease from 100 to <3 ppm.

The low Nb contents, only shown in Tables 4.5, 4.7, 4.8 and 4.9 are typical for island-arc subduction related magmas.

Chondrite-normalized rare earth element (REE) patterns of selected Nisyros lavas and enclaves (Fig. 4.23) display moderate La/Yb ratios of 3.5 for basaltic andesites to highly fractionated ratios La/Yb > 10 for dacites and rhyolites. Light-rare earth elements (LREE) are enriched relative to the heavy-rare earth elements (HREE). Some of the more evolved samples are also depleted in Dy, Ho, and Er. Generally,

Table 4.7 Division of five groups from basaltic andesites to andesites on the basis of characteristic major and trace element contents, which constitute the flows and pyroclastic deposits of Units No. 21 and 22

	SiO_2	TiO_2	MgO	Cr	K_2O	Rb	Sr	Nb
A	54.4	0.78	6.2	170	1.12	27	500	10
B2	55.8	0.72	5.3	70	1.2	16	1060	6
c	54.8	0.93	4.5	40	1.2	25	480	11
D	58	1.1	3.3	6	1.7	28	400	14
E	58.8	1.2	2.4	5	1.8	29	450	17

Oxide values are listed in %, elemental values in ppm

almost all REE (i.e. Pr, Nd, Sm, Eu, Tb, Dy, Ho, Er, Yb, Lu) show increasing concentrations from the basaltic andesites to the andesites. In contrast, spoon-shaped depletion occurs in the middle REE (MREE) to heavy REE (HREE) patterns in the rhyolites and dacites.

Table 4.8 Compiled bulk chemical compositional variation of dacites in Unit 14* (Zellmer and Turner 2007), Units 18** and 19** (Rehren 1988; Vanderkluysen et al. 2005) from the Afionas tuff cone, and Unit 25*** from Emborios flows and dome (Francalanci et al. 1995; Volentik et al. 2005)

Rock type	Dacite flow	Dacite flow	Dacite pyroclastics	Dacite flow
Unit No.	14*	18** ***	19**	25* ***
wt%				
SiO_2	67	64.0–65.5	65–67	64.5–69.0
TiO_2	0.65	0.6–0.5	0.7–0.5	0.64–0.54
AI_2O_3	15.5	17.3–17.0	17.5–17.0	16.4–15.6
Fe_2O_3(t)	4.2	5.0–4.8	4.5–3.8	4.9–3.6
MgO	1.5	1.5–1.2	1.7–0.7	1.25–1.1
CaO	3.7	4.1–3.8	5.5–2.7	3.5–3.0
Na_2O	4.3	4.8–5.5	4.3–5.5	4.3–5.4
K_2O	2.9	2.5–2.6	1.9–2.8	2.7–3.2
ppm				
Nb	15	16	n.d.	17–19
Zr	168	195–240	190–240	235–255
Y	20	22	n.d.	18–24
Rb	83	76	44–78	80–88
Sr	286	385–396	300–490	300–320
Ni	6	<3	<3	4
Cr	14	2–14	<3	8–9
V	90	50–40	n.d.	48–50
Ce	n.d.	n.d.	n.d.	70
Ba	692	645–690	550–744	670–760
La	n.d.	n.d.	n.d.	36

Major- and trace element data are on water free basis

All four different types of dacites show overlapping compositions with very similar characteristics. However, the spread within the Afionas eruptive cycle seems to be larger than the earlier and later cycles, which is expressed by CaO, K_2O, Rb, Sr and Ba; *n.d.* not determined

Table 4.9 Compiled rhyolitic compositional variation of pyroclastics and lavas, which erupted during the "caldera– and post caldera cycles", compared to the Stavros Avlaki rhyolite of the "composite stratovolcano cycle"

Volcanic edifice	Lower pumice	Nikia flows	Upper pumice	Prof. Ilias domes, flows	Avlaki dome, flows
Unit	28	30	31	32	17
wt%					
SiO_2	74.5–75.5	69.3–74.8	69.2–72.66	66.3–70.35	70.3–73.2
TiO_2	0.34–0.31	0.37–0.32	0.38–0.30	0.43–0.32	0.37–0.28
AI_2O_3	14.6–13.9	15.5–14.5	15.45–14.35	16.5–15.1	14.2–14.9
Fe_2O_3(t)	2.50–2.30	3.1–2.5	3.0–2.55	3.4–2.5	2.7–2.3
MgO	1.05–0.64	0.95–0.45	1.3–0.60	2.0–0.9	0.95–0.64
CaO	1.75–1.57	2.6–2.0	3.2–2.3	4.3–2.9	2.54–2.0
Na_2O	4.7–4.3	4.6–4.25	4.5–4.0	4.8–4.0	4.–4.1
K_2O	3.5–4.1	2.9–3.5	2.9–3.6	2.35–3.15	3.2–3.54
ppm					
Rb	89–97	88–100	84–99	71–103	95–111
Sr	180–210	290–200	315–255	495–305	224–280
Ba	690–750	735–810	815–725	600–815	804–859
La	35–41	32–37	37–39	29–31	34
Ce	62–65	55–58	57–60	48–52	53
Zr	265–280	265–280	200–250	150–190	160–180
Nb	14–20	10–19	15–17	12–14	14–21
Y	18–20	22–17	16–18	14–30	17–13
Ni	<3–16	<3–2	<3–3	5–9	5
Cr	<3–12	2–20	4–17	5–12	10–13
V	19–18	40–18	31–20	57–32	34–27
Sr 87/86	0.70424	0.704539	0.70456	0.70432	n.d.

Major- and trace element data on water free basis from Francalanci et al. (1995) and Vanderkluysen et al. (2005); strontium isotope ratios from Francalanci et al. (1995)

The general bulk chemical island-arc type characteristics of selected lavas and their enclaves can clearly be recognized using a "multi-element diagram" (Fig. 4.24) of selected Nisyros volcanic rocks. A depletion in high field strength elements (HFSE) relative to REE is observed. In the highly differentiates rhyolites, incompatible elements are enriched while compatible elements are depleted.

The typical island arc characteristics are expressed in the enrichment up to ten times in low field strength elements (LFSE) such as K, Rb, Sr, Ba, Th, and the light rare earth elements (e.g. Ce) and to a lesser extent Sr, Hf and Zr. In contrast, the basalts are depleted in high field strength elements (HFSE), such as Zr, Nb, Ti, Y, and the heavy rare earth elements (e.g. Yb). The pattern of the basaltic andesites, andesites and that of the enclaves are very similar, which indicates the close magmatic relationship. Basaltic andesites, andesites and dacites have a pronounced positive Pb anomaly and negative Nb, Ce and P anomalies; dacites, rhyodacites and rhyolites show strong Nb, P and Ti anomalies.

The compositions of the intermediate and evolved lavas, such as the dacites and rhyodacites are enriched in Rb, Ba, Th and LREE up to a hundred times when compared to the MORB.

Positive correlation of K, Rb and Ba with Th is evident. This also holds for Nb, Zr, Hf, and the LREE, whereas the compatible minor and trace elements Cr (incl. Ni), V, and Sc display a negative correlation with Th. In this respect, the Nisyros lavas do not significantly differ from the younger 'Main Volcanic Series' on Santorini (Nicholls 1971, 1978; Mann 1983; Barton and Huijsmanns 1986; Mitropoulos et al. 1987; Huijsmans et al. 1988; Fytikas et al. 1990).

4.3.2 Early Nisyros Shield Volcanic Cycles

4.3.2.1 Submarine Volcanic Base

Lithostratigraphic Units (LSU) No. 1 and 2 that form the pillow lavas and hyaloclastites of the submarine volcanic base are composed of basaltic andesites. Four groups A, B1, B2, and C of varying differentiated chemical compositions can be recognized based on the available analyzed data (Table 4.5). It has to be noted that neither the exact lithostratigraphic position of these samples is known from the thick pillow sequence nor their exact position within each pillow. A smooth differentiation trend in the major (i.e. TiO_2 and K_2O increasing, MgO decreasing) and incompatible trace elements (i.e. Rb and Nb increasing, Cr and Ni decreasing) can be seen from A to C. The only exception is Sr in B2 with higher values. Oxide values are listed in %, elemental values in ppm.

4.3.2.2 Early Shield Volcanic Cycle

Within the "Early Nisyros Shield Volcanic Cycles" (*Units Nos. 3–11*) the lavas vary in composition from basaltic andesite to andesite. This variation is not correlated with the lithostratigraphic sequence (relative age) (Table 4.4). Some lavas can be divided into groups (Tables 4.5A–C and 4.7A–E) according to their bulk chemistry. Oxide values are listed in %, elemental values in ppm (Table 4.6). A comprehensive description of the bulk chemical characteristics of the individual lithostratigraphic units is given in the following paragraphs:

Unit No. 3: Basaltic andesite varies within the range of the pillow lava of the groups B and C of the submarine volcanic base (Units Nos. 1 and 2), slightly more differentiated; *Unit No. 4:* Lava of andesitic composition; *Unit No. 5:* The 40 m thick flows vary slightly in andesitic composition similar to Unit 4; *Unit No. 6:* There is only one analysed sample available for the 60 m thick basaltic andesite pyroclasic succession. It seems to be more differentiated than the older units, despite the lower SiO_2 of 51.7 vol.%.

4.3.2.3 Internal Lake-Stage and Associated Volcanic Cycles

Unit No. 8: The 5 m thick lava flow is of highly porphyritic basaltic andesite composition, similar to group B1, including a more differentiated level (Table 4.6). *Unit No. 10:* The 70 m thick lavas, wide spread within the caldera walls, are of rather primitive basaltic andesite composition, similar to group A (Table 4.5). Some samples seem to be slightly more differentiated and differ significantly in high Sr concentrations up to about 1090 ppm; *Unit No. 11:* The 35 m thick pyroclastic flow succession marks the end of the "Early Volcanic Cycles" and varies from basaltic andesite to andesitic composition. However, some levels are similar to group B1, Table 4.5).

4.3.3 Composite Stratovolcano Cycles

4.3.3.1 Transition from Shield- to Stratovolcano

Unit No. 13: The Lavas of the "Early Caldera Composite Stratovolcano Cycles" are mainly of andesitic composition, some levels seem to be slightly less differentiated basaltic andesites. A significant difference between unit No. 13 and the older andesitic lavas occurs in the strontium values; *Unit No. 14:* For the first time in the eruptive cycles of Nisyros Volcano a

25 m thick lava flow of dacitic composition occurs within the uppermost part of today's northern caldera wall. The outstanding characteristic is the large amount of andesitic enclaves, which generally reaches 30% of the total rock volume and in some cases even up to 70–80%. The composition of a sample, free of macroscopically visible enclaves is shown in Table 4.8. Unusual are the high Ba values; *Unit No. 15:* In the northern eastern parts of the caldera and outer slopes the dacites are followed by a 40 m thick andesitic flow, which is chemically very similar in composition with the andesitic rocks of unit No. 13.

4.3.3.2 Southern Eruptive Centers (M. Stavros—Avlaki)

Unit No. 16: The 30 m thick succession of surge and pyroclastic flows in the southern and southwestern lower caldera wall consists of rather primitive basaltic composition; *Unit No. 17:* 60 m of rhyolithic flows and domes cover the southern segment of the island. They are very homogeneous and they lack enclaves and lithic xenoliths (Table 4.9).

4.3.3.3 Eastern Eruptive Centers (Afionas—Lies)

Unit No. 18: Two large tuff cones are building up the eastern slopes of the composite stratovolcano. The base of the southern Afionas cone consists of a dacite flow, which is rather free of enclaves and less differentiated than the older dacite of unit No. 14. Its chemical composition is listed in Table 4.8); *Unit No. 19:* Within the lifetime of the Afionas tuff cone several eruption cycles occurred, which erupted in alternating sequences andesitic and dacitic pyroclastics. The andesitic composition is quite variable, which seems to be dependent of sample inhomogeneity (Table 4.6).

4.3.3.4 The Composite Stratovolcano

Units Nos. 21 and 22: The bulk chemical compositions of these two units (Table 4.6) have to be grouped together since the small flows and pyroclastic deposits (strombolian activity), listed in Table 4.7, are scattered around several small scoria cones, which are spread all over the island. According to the existing analyzed samples five groups can be distinguished. They differ in the degree of differentiation and in their primary chemical characteristics, i.e. high values of strontium and low values of titanium and niobium.

4.3.3.5 Terminal Cycle and Dome Collapse

Unit No. 24: This unit is represented by thin lava flows of basaltic andesite to andesitic composition, which may have erupted after a time gap, since they are separated from the older lithostratigraphic units in several localities by epiclastic deposits, indicating erosion and tectonic activity. A series of thin basaltic andesite lava flows cover the western slopes of the island. The chemical characteristics of the basaltic andesites are similar to the previous units No. 21 and 22 and listed in Table 4.7.

Unit No. 25: Since the beginning of the volcanic activity of Nisyros, this eruptive cycle produced the largest volume of dacitic lava flows and domes, with a max. thickness of 150 m, containing a few percent of andesitic enclaves and xenolithic material. The variable chemical composition is shown in Table 4.8.

4.3.4 Caldera Eruptive Cycles and Caldera Collapse

4.3.4.1 First Caldera Cycle

Unit No. 28: The Caldera Cycles started with a succession of rhyolitic pumice fallout, surges and pyroclastic flows ("lower pumice") showing a normal trend of differentiation (Table 4.9). *Unit No. 29:* The major components of the blocks and debris of the heterogeneous breccia (Unit No. 29) are rhyolitic fragments from the overlying flows of Unit No. 30.

4.3.4.2 Second Eruptive Cycle

Unit No. 30: This is characterized by the effusion of the Nikia lava flows and Parletia neck, with a wide range of rhyolitic compositions listed in Table 4.8. In the Le Maitre classification (Fig. 4.20) diagram, the composition of the

porphyritic rocks with a high proportion of phenocrysts and small proportion of xenocrysts and quenched andesitic enclaves starts in the dacitic field. The evolved composition relates mainly to glassy rocks with small proportions of phenocrysts. The final glassy matrix composition and the plagioclase-hosted melt inclusions yield SiO_2 average values of 77.5 and 75.8 wt% respectively, at very low values of TiO_2, $FeO_{(tot)}$, CaO, and MgO (Seymour and Vlassopoulos 1989).

The mafic quenched enclaves are listed in Table 4.10. The spread of their compositions indicate that they must have derived from different stages of magmatic differentiation due to variable magmatic processes, such as fractional crystallization, magma mixing and contamination (see Sect. 4.4 and Fig. 4.20). The latter seem to be indicated by the higher calcium and strontium values.

Unit No. 31: This second large eruptive cycle ("upper pumice") started after an unknown time gap and produced a 30 m thick succession of pumice fallout, surges and pyroclastic flows, the "upper pumice". The variation in composition (Table 4.8) overlaps with the composition of the voluminous rhyolitic lavas of unit 30 and might also reflect certain contamination through small xenocrysts and xenolithic material, as well as effects of magma mingling.

Table 4.10 Compiled bulk chemical compositional variation of mafic enclaves in unit No. 30 (Nikia flows) and No. 32 profitis Ilias domes and flows

rock type	Basaltic andesites	Basaltic andesites
Unit	30 Enclaves	32 Enclaves
wt%		
SiO_2	55.3–55.54	54–55.6
TiO_2	0.86	0.75–0.72
AI_2O_3	18.2–18.5	18.8–19.7
Fe_2O_3(t)	7.4–8.2	5.9–6.2
MgO	2.9–4.3	4.4–5.0
CaO	6.7–8.69	9.0–9.8
Na_2O	3.4–4.1	3.3–3.4
k_2O	1.1–1.6	0.9–1.2
ppm		
Nb	8–13	7–8
Zr	129–167	108–145
Y	21–23	16–17
Rb	22–32	13–20
Sr	430–750	910–1000
Ni	8–14	23–28
Cr	6–20	13–16
V	140–190	140
Ce	27–44	23–29
Ba	320–470	269
La	18–27	13–15

Major- and trace element data on water free basis from Francalanci et al. (1995), Vanderkluysen et al. (2005) and Zellmer and Turner (2007)

4.3.5 Post-caldera Eruptive Cycle

Unit No. 32: The surficial emplacement of domes (i.e. Profitis Ilias) in the western part of the caldera and effusion of thick southwestward-directed lava flows with a max. thickness of 600 m represents the last volcanic cycle of Nisyros Volcano. The bulk chemical composition (Table 4.8) varies over a wide range from dacite to rhyolite, which led to the designation of the name rhyodacite (in the map and in all descriptive parts). End-member compositions have been analyzed in plagioclase-hosted melt inclusion and residual interstitial glass with SiO_2 average values of 75 and 73 wt% respectively (Seymour and Vlassopoulos 1989). In general the lavas and domes seem to be less evolved than the glassy rich rhyolitic flows of unit 30 (Table 4.8). However, the reason might be simple due to the large amount of phenocrysts and high proportions of quenched enclaves, which vary in size from millimeter to decimeter (see Sect. 4.2).

The amount of enclaves seems to increase in time from northeast to southwest, the youngest domes and lavas containing the most (Gansecki 1991). All enclaves (Table 4.9) are basaltic andesites with a narrow range of chemical composition, but distinctly different from all other prior basaltic andesites (Table 4.6). Unusual are the higher aluminum and strontium contents at low titanium and yttrium values.

4.4 Isotopic Evidence of Crustal Assimilation and Contamination

A number of bulk-rock and mineral isotope studies have been performed on Nisyros samples in order to assess the effects of crustal assimilation, of subduction-related magmatic and fluid input, as well as of differentiation in magma reservoirs.

Potential contamination and assimilation could be achieved at high crustal levels through the addition of fluids and materials from the altered Quaternary volcano-sedimentary rocks or Neogene marls. At deeper crustal levels the main contaminants are the Mesozoic limestones, the ophiolitic mélange and the metamorphic rocks of the Alpine basement, encountered in the geothermal wells in the Nisyros caldera (Geotermica Italiana 1983, 1984; Marini et al. 1993).

Although a large number of non-radiogenic and radiogenic isotope measurements including $^{87}Sr/^{86}Sr$, $^{143}Nd/^{144}Nd$, $^{176}Hf/^{177}Hf$, lead and uranium isotope series exist (Gülen et al. 1987; Gülen 1990; Wyers and Barton 1989; Francalanci et al. 1995; Buettner et al. 2005; Zellmer and Turner 2007; Braschi et al. 2014), stable isotope data is still missing. On the basis of $^{87}Sr/^{86}Sr$ analysis, Wyers and Barton (1989) assumed crustal contamination and assimilation, which could be implied based on the occurrence of calc-silicate xenoliths and clinopyroxene xenocrysts in the basaltic andesites of the early submarine volcanic cycle (Spandler et al. 2012). It has been suggested that carbonate assimilation of the Neogene and Mesozoic basement rocks may release CO_2, which could form a free vapor phase due to the low CO_2 solubility of basaltic magmas (Spandler et al. 2012).

The variation of $^{87}Sr/^{86}Sr$ ranges from 0.703384 in a basaltic andesite of the composite stratovolcano cycle to 0.705120 in a dacite of the Afionas-Kyra cycle (Units Nos. 18 and 19); Table 4.4. Vanderkluysen et al. (2005) interpreted this as a result of the differentiation from basaltic andesite to rhyolite. However, when taking all available data into consideration, a correlation between differentiation and $^{87}Sr/^{86}Sr$ ratios becomes indistinguishable. The low $^{87}Sr/^{86}Sr$ ratios are interpreted as mantle-like values reflecting abundant hydrous fluids in the source (Buettner et al. 2005), excluding major contamination and assimilation of crustal components (Table 4.4; Fig. 4.25).

Generally, the isotopic variability of the South Aegean Volcanic Arc rocks changes from east to west. The lowest $^{87}Sr/^{86}Sr$ isotope ratios are encountered at Nisyros and Santorini (0.7033 and 0.70328 respectively) and are comparable with those measured at ocean-ocean subduction zones (Briqueu et al. 1986). Crommyonia volcano shows the highest ratio of about 0.713 (Pe 1975). An overview of the isotopic values measured at

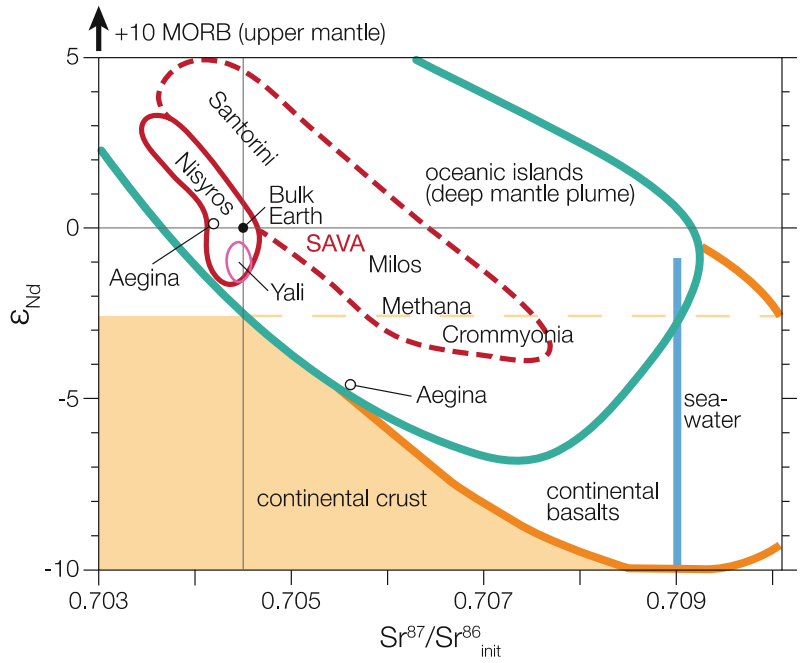

Fig. 4.25 Nd and Sr isotope variation for the South Aegean Volcanic Arc. Data from Pe (1975), Barton et al. (1983), Briqueu et al. (1986), Gülen (1987, 1990) Mitropoulos et al. (1998), Pe-Piper and Piper (2002), Buettner et al. (2005), Francalanci et al. (2007)

each volcanic island is given in Electronic Supplementary Material Appendix Fig. 4.55.

Further indicators of crustal assimilation appear in the range of neodymium isotope ratios (Buettner et al. 2005). $^{143}Nd/^{144}Nd$ ratios of the pre-caldera rhyolites (Unit No. 30) range between 0.512622 and 0.512675 (with values averaging at +0.2 E_{Nd}). Post-caldera (Unit No. 32) rhyodacites and the products of Yali Island (No.32) yield $^{143}Nd/^{144}Nd$ ratios between 0.512553 and 0.512607 (with E_{Nd} values averaging around −1.2). However, the Nisyros Nd isotope data is less radiogenic than the typical E_{Nd} of normal N-type MORB, averaging +10. This is in agreement with $^{176}Hf/^{177}Hf$ ratios. Whilst pre-caldera units range between 0.282914 and 0.282940 (with E_{Hf} values around +5.4), the post-caldera volcanics scatter between 0.282794 and 0.282917 (with less radiogenic E_{Hf} values of +2.4) compared to the typical E_{Hf} of N-MORB of +17. Thus, both Nd- and Hf-isotope systematics clearly indicate assimilation of crustal material, which is more apparent in the Yali and in the post-caldera volcanics. In addition, $^{206}Pb/^{204}Pb$, $^{207}Pb/^{204}Pb$ and $^{208}Pb/^{204}Pb$ ratios of Nisyros and Yali volcanic rocks support mixing of mantle material with a lower crust equivalent (Buettner et al. 2005).

Based on U–Th isotopic data (Zellmer and Turner 2007), the post-caldera rhyodacites (No. 32) have been interpreted as a remobilized magma from a young igneous protolith, activated by an influx of fresh mafic magma. In general, all rocks show small ^{238}U excess of up to ca. 10%. Mafic enclaves show higher U/Th ratios than their evolved host lavas, eliminating the simple fractionation hypothesis.

4.5 Petrogenetic Evolution of the Nisyros Volcanic Rocks

4.5.1 Introduction

The magmatic evolution of the Nisyros volcanics is inferred from mineralogical, petrologic and geochemical observations. Since the 1970s numerous petrogenetic models were proposed,

including various differentiation processes of mantle-derived, hydrous, calc-alkaline and arc tholeiitic basaltic magmas to generate evolved intermediate to silicic magmas. Fractional crystallization involving olivine, clinopyroxene, calcic-plagioclase, amphibole, biotite and Ti-magnetite at deep crustal magma reservoirs is regarded as the major differentiation mechanism (Bowen 1928). In particular, early crystallization of amphibole drives the differentiated magmas to dacitic, rhyodacitic and even to peraluminous tonalitic compositions (e.g. Cawthorn et al. Cawthorn and O'Hara 1976; Hürlimann et al. 2016).

In the case of Nisyros, the presence of xenoliths, reversely-zoned phenocrysts of plagioclase, clinopyroxene, amphibole and bulk rock trace element and isotopic characteristics led to the interpretation of multiple differentiation processes besides fractionational crystallization, such as crustal assimilation (AFC), magma mixing and mingling, and crystal retention-crystal-liquid-segregation. The role of crustal assimilation and contamination throughout the volcanic cycles has been recognized not only in the presence of xenocrysts and lithoclasts of the carbonate-rich basement rocks and their contact metamorphic equivalents, but also in the bulk chemical trace element and isotopic variations (Di Paola 1974; Limburg and Varekamp 1991; Seymour and Vlassopoulos 1992; Francalanci et al. 1995, 2005; Buettner et al. 2005; Vanderkluysen et al. 2005; Zellmer and Turner 2007; Spandler et al. 2012). Magma mingling and mixing between basaltic andesites and rhyolitic end-members generated dacites and rhyodacites, as suggested on the basis of mineral chemistry (plagioclase zonations), micro-textures and incompatible trace element systematics (Seymour and Vlassopoulos 1989, 1992; Zouzias and Seymour 2014). Using U–Th and Sr–Nd isotope systematics, Zellmer and Turner (2007) suggested remobilization of a young igneous protolith by injection of hot basaltic magma in order to produce dacitic melts.

4.5.2 The Depth of Magma Reservoirs, Amphibole Stability Fields and Ascent of Magmas Through the Crust

Several volcanological and petrologic characteristics of Nisyros Island allow an interpretation of the depth and origin of the magmas:

- The formation of a caldera with a diameter of 4 km points to the presence of a magma reservoir at shallow crustal depth between 3 and 7 km from which the highly differentiated rhyodacitic to rhyolitic magmas erupted.
- The existence of an active hydrothermal system indicates that cooling magma bodies at present are responsible for conductive and convective heat transfer.
- The existence of high-temperature brines has been proven by two deep geothermal wells, Nis-1 and Nis-2, reaching a maximum depth of 1816 m and 1547 m, respectively.
- The presence of Magnesium-rich hastingsitic amphiboles as xenocryst phases in the lavas and in the magmatic enclaves in dacites and rhyodacites indicate emplacement of mafic magmas from deeper crustal levels into a shallow crustal reservoir.
- The common presence of breakdown reaction rims on hastingsitic amphiboles testifies either heating by recharge with hot mafic melts or decompression during ascent through the crust.
- Olivine-rich hornblende-gabbro and pyroxenitic cumulates, however rare, point to an existence of deeper crustal reservoirs.

Mg-rich hastingsitic amphibole and anorthitic plagioclase are present in various proportions as the major phenocryst phases in most of the lavas in the volcanic islands of the South Aegean Volcanic Arc and therefore play a key role with respect to fractional crystallisation and mixing processes (Huijsmans et al.

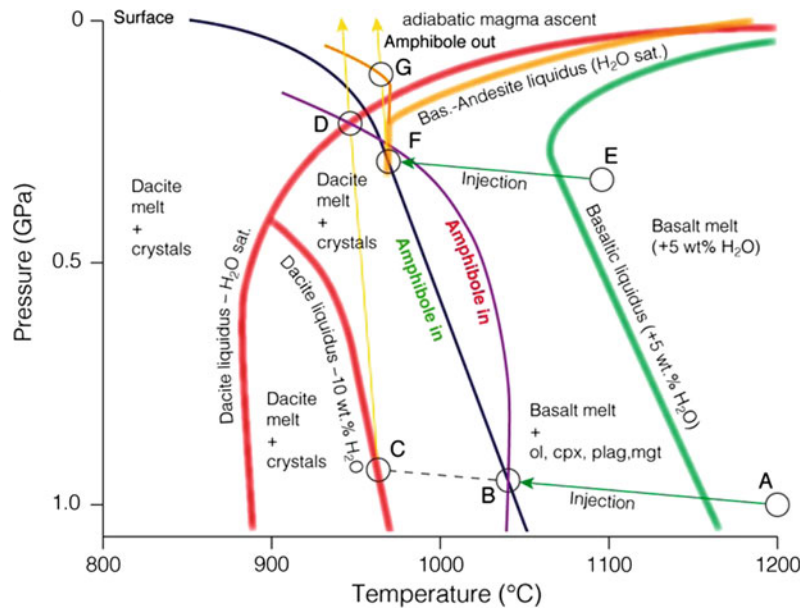

Fig. 4.26 The behaviour of water-bearing calc-alkaline magmas in the crust with regard to the stability fields of amphibole. Basalt liquidus with 5% H_2O (Foden and Green 1992), water-satured basaltic andesite (Moore and Carmichael 1998), dacite water-saturated with 10 wt% H_2O liquidus (Annen et al. 2006)

1988; Dietrich et al. 1988; Wyers and Barton 1989; Mitropoulos et al. 1987; Seymour and Vassolopoulos 1992; Mitropoulos and Tarney 1992; Francalanci et al. 1995; Gartzos et al. 1999).

Magnesio-hastingsites, pargasites, and ferroan pargasites, which have been found in the Nisyros gabbroic cumulates (Table 4.2) crystallised from water-rich melts of basaltic to andesitic composition. The stability fields of calcic-amphiboles vary over a wide pressure range of about 1–20 kbar and over a temperature range of up to 950 °C (Schmidt 1992). According to Ridolfi and Renzulli (2012), magnesio hornblendes and tschermakitic pargasites crystallize in equilibrium with calc-alkaline melts at low P, T conditions of up to 3kbar and within a range of temperatures between 800 and 920 °C, whereas magnesio hastingsites and pargasite are spread over a large field of pressures up to approx. 20 kbar and temperatures of 950–1100 °C. These results were confirmed by Nandedkar et al. (2014). Thus, the magnesio-hastingsites and pargasites of Nisyros may have crystallized in deep seated crustal magma reservoirs while magnesio-hornblendes and actinolitic hornblendes with Al_2O_3 = 6.5–7.1 wt% may have crystallised during the ascent of the rhyodacitic and rhyolitic melts and within shallow magma reservoirs.

The PT-diagram (Fig. 4.26) should illustrate the results of experimental research with regards to the stability field of amphiboles in water-bearing calc-alkaline magmas ascending from the upper mantle through the crust (review articles in Ulmer 2001; Müntener et al. 2001; Annen et al. 2006; Krawczynski et al. 2012; Dessimoz et al. 2012; Ridolfi et al. 2010; Ridolfi and Renzulli 2012; Nandedkar et al. 2014; De Angelis et al. 2015; Hürlimann et al. 2016).

The lower green arrow shows the injection of basaltic magma into lower crust (e.g. 25–30 km depth) from point A to B. Crossing the basaltic liquidus (+5 wt% H_2O), olivine, clinopyroxene, titanomagnetite and plagioclase start to crystallize along the path, forming orthocumulates. At point B amphibole starts crystallizing instead of clinopyroxene with adcumulate texture. At point C dacitic (or rhyolitic) residual melt is extracted by crystal fractionation from the basaltic melt remaining at depth or ascending adiabatically.

Between C and D the dacitic melt ascents through the liquidus field and thus any entrained crystal may be resorbed. At point D the melt

passes the liquidus and starts to crystallize but outside the amphibole stability field.

Path E to F shows a basalt melt injection and fast cooling into the upper crust that crystallizes olivine, clinopyroxene, titanomagnetite and plagioclase until amphibole appears at point F at the expense of clinopyroxene. During an adiabatic ascent the extracted differentiated basaltic andesite melt crystallizes amphibole until it reaches the stability boundary at point G, at high crustal levels. Here it leads to the crystallization of gabbroic and dioritic intrusives or to the extrusion of basaltic andesite and andesitic melts containing partly resorbed amphibole phenocrysts or cumulate relicts.

4.5.3 Magmatic Processes

The magmatic processes responsible for the evolution of Nisyros Volcano have been discussed by Wyers and Barton (1989) and Francalanci et al. (1995) on the basis of major and trace element chemical and isotopic composition of lavas and mineral chemistry.

A multi-stage pragmatic model (Fig. 4.27) has been chosen to demonstrate in a simple way the major magmatic processes, which control the petrogenetic evolution of magmas in crustal reservoirs. This model is coupled with the magma emplacement mechanisms at depth and

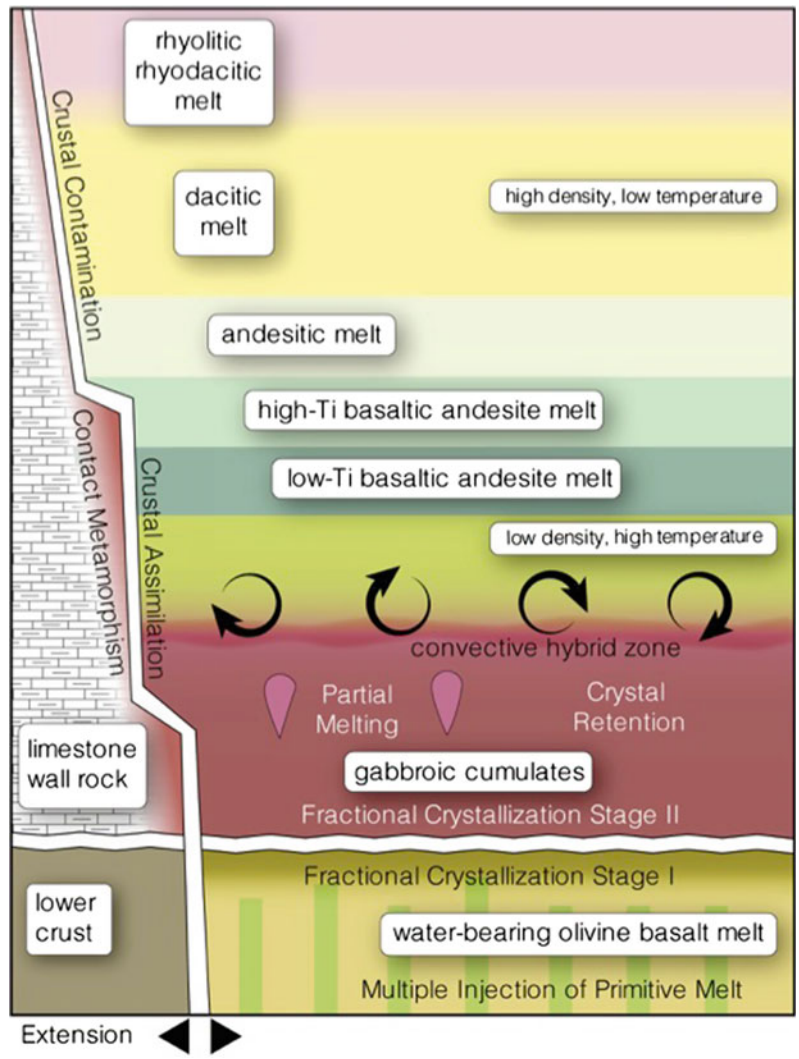

Fig. 4.27 Multi-stage model of a layered magma reservoir in the crust. Two steps of fractional crystallization, crustal assimilation, partial melting of cumulates and crystal retention are discussed as major magma differentiation processes in the text (modified after Dietrich et al. 1988)

its eruption at the surface and consists of two stages of fractional crystallization.

4.5.3.1 Fractional Crystallization

Stage I: Early fractional crystallization from primitive hydrous Mg-rich basaltic melts

Primary calc-alkaline and arc tholeiitic basaltic melts in volcanic island arcs may have originated by partial melting from a rather depleted mantle wedge of harzburgitic composition at approximately 120–130 km depth. Such a mantle is enriched in water and in the hygromagmatophile elements K, Rb, Ba, Sr, Th, U, and LREE, derived from the breakdown of subducted high-pressure phases (antigorite, phlogopite etc.), from altered and metamorphosed oceanic crust (e.g. Davies and Stevenson 1992; Sisson and Grove 1993a, b; Ulmer and Trommsdorff 1995; Tatsumi and Eggins 1995; Ulmer 2001). During ascent through the lithosphere and most probably at the mantle-crust boundary, the primary magmas underwent high-pressure fractional crystallization of olivine, clinopyroxene, amphibole and Cr-spinel under an open system and oxygen buffered conditions (e.g. Osborn 1976; Osborn and Rawson 1980; review in Annen et al. 2006). Experimental studies confirm such an assumption (Grove et al. 2002, 2005 and 2005; Nandedkar et al. 2014; Hürlimann et al. 2016).

Therefore, parental olivine basalts, generated from a primary hydrous basaltic melt, are seen as a first stage of crystal fractionation (Fig. 4.27). So far, no olivine basalts have been found on Nisyros Island. An early stage I fractionation process can only be inferred to some other cases in the South Aegean Volcanic Arc, e.g. lavas in the islands of Santorini, Aegina, and Methana.

Stage II: Fractional crystallization and assimilation

Wyers and Barton (1989) showed that crystal fractionation played a major role in the differentiation of Nisyros magmas, and implied that the compositional gap between basaltic andesites and dacites could not be explained by a simple isobaric fractionation. They concluded that the higher abundance of olivine in the andesites compared to the basaltic andesites could only be achieved by polybaric fractionation processes from variable parental magmas.

Francalanci et al. (1995) tried to explain the "jumps in the degree of evolution present in the stratigraphic series, accompanied by changes in the porphyritic index", in a simplified magma reservoir not through fractional crystallization, but through mechanisms of convection, assimilation, crystallization and crystal retention, combined with resorption and accumulation of major phenocryst phases (plagioclase and clinopyroxene).

Taking these possible complex magmatic differentiation processes under non-equilibrium conditions into consideration, a compositionally layered magma reservoir can be envisaged. Disturbances within an inversely layered system, variable in density, temperature and sensitive to convection and turnover, can easily be generated by injection of subsequent hot and less dense hydrous fresh melt.

Breakdown reactions of amphibole may contribute significantly to the amount of fluids. Assimilation of carbonate rocks bordering magma reservoirs may also release fluids rich in hygromagmatophile elements like strontium and light rare earth elements (LREE) into the melts. Pelitic rocks can release aluminum, potassium and rubidium.

The least differentiated lavas of Nisyros Volcano, which can be used as parental melt for the fractional crystallization model (Fig. 4.27), have been found in the basaltic andesites from units No. 10 and No. 16, inner caldera wall at Kato Lakki and Stavros, respectively (samples AV7B and AV24B, Table 4.5, Vanderkluysen et al. 2005, in wt%).

Important phases that control fractionation processes at stage II are olivine, anorthitic plagioclase, clinopyroxene, orthopyroxene, Fe–Ti oxides and Mg-rich amphiboles, the latter already occurring as early cumulate phases (e.g. adcumulates, Sect. 4.2.5). Basaltic andesites, andesites and evolved dacitic to rhyolitic melts are differentiation products depending on temperature and pressure conditions, the amount of fluids (oxygen fugacity) and the proportions of the fractionating phases.

4.5.3.2 Generation of Evolved Silicic Melts from a Parental Basaltic Andesite Magma

Major oxide modeling should give realistic solutions to derive dacitic and rhyolitic melts by fractional crystallization of plagioclase, olivine, clinopyroxene, Mg-rich amphibole and titanomagnetite. The fractionation of these minerals, in particular amphibole drastically changes the composition of the remaining melt by extracting Mg, Ti, Fe, Al, Ca and other elements, driving the remaining melt to a silicic composition. The most satisfactory model calculation leads to the generation of a rhyolitic magma (Table 4.11). The differences between calculated and natural TiO_2, K_2O, and Na_2O concentrations can be explained by the lack of Fe–Ti oxide data and the variation of alkali compositions in the basaltic andesites and rhyolites, respectively. Of course, such a model assumes fractionation from a single parental magma under equilibrium conditions. The mobilisation of rhyolitic melt can leave large volumes of amphibole-rich cumulates and gabbros behind. The gabbroic and dioritic clots found in the evolved magmas are witnesses of such processes

Least-squares mixing calculations (Bryan et al. 1969) were performed to test the effects of Mg-rich amphiboles included in the stage II fractional crystallization. Fractionation from a parental high-Mg basaltic andesite magma (e.g. Stavros lavas, Unit No. 16, Table 4.6) of the minerals found in the grabbro cumulate xenolith from the Lower pumice deposit (Unit No. 28) should generate either a residual dacitic or a rhyolitic melt.

The model calculation shows that approximately 65 wt% hornblende gabbro cumulate should crystallize from a basaltic andesite melt in order to generate 35 wt% rhyolitic melt, which implies the existence of large plutonic volumes at depth.

Recent fractional crystallization experiments by Nandedkar et al. (2014) with temperatures from a near-liquidus interval at 1117 °C to near-solidus temperature at 700 °C at a pressure of 0.7 GPa confirmed the fractionation model based on petrographic and geochemical evidence. About 40 wt% of ultramafic plutonic rocks have to crystallize to generate basaltic–andesitic liquids, and an additional 40 wt% of amphibole–gabbroic cumulate to produce granitic melts.

Table 4.11 Cumulative mineral and rock proportions (wt%) obtained by least-squares fractionation modelling

Sample	AV24B	Amp 15	0111	Cpx 11	Pig 12	Ti-mgt	Rhyolite	BasAnd.C.
Unit	16	28	28	28	28	0	30	
SiO_2	54.86	43.23	38.09	50.91	45.77	0.49	71.54	54.85
TiO,	0.74	3.33	0.06	0.71	0.05	2.32	0.33	1.02
AI_2O_3	16.96	12.88	0.02	3.80	34.53	2.89	14.70	16.98
FeO(t)	6.50	9.84	20.58	5.76	0.48	89.26	2.45	6.49
MgO	6.91	15.57	40.76	15.66	0.05	4.49	0.78	6.92
CaO	10.52	11.99	0.14	22.73	17.81	0.28	2.45	10.52
Na_2O	2.89	2.76	0.04	0.26	1.21	0.00	4.31	2.43
K_2O	0.51	0.34	0.00	0.00	0.10	0.00	3.43	1.06
Total	99.89	99.93	99.69	99.83	100.00	99.72	100.00	
Modes		32.85	0.44	9.94	21.09	2.17	36.46	
Errors		22.88	6.06	6.66	6.57	0.92	3.24	
R2	0.735							

Basaltic andesite (Stavros lava, Unit No. 16, recalculated to water free composition)—(Olivine Fo_{77}, plagioclase, clinopyroxene, amphibole, Ti-magnetite) = rhyolite (average Nikia lavas, Unit No. 30). *R2* residual squared from the linear regression

4.5.3.3 Magma Mingling and Mixing

Magma mixing is understood as a homogenisation process involving at least two magmas of different chemical compositions and rheology (McBirney 1980). Often it might be the subsequent step following magma mingling.

Magma mingling applies in particular to the Main Caldera and Post Caldera Eruptive Cycles. Examples of mingling are given in previous chapters and shown on Fig. 4.13 for the dacitic lavas No. 14 and on Fig. 4.14 for the rhyodacitic lavas No. 32.

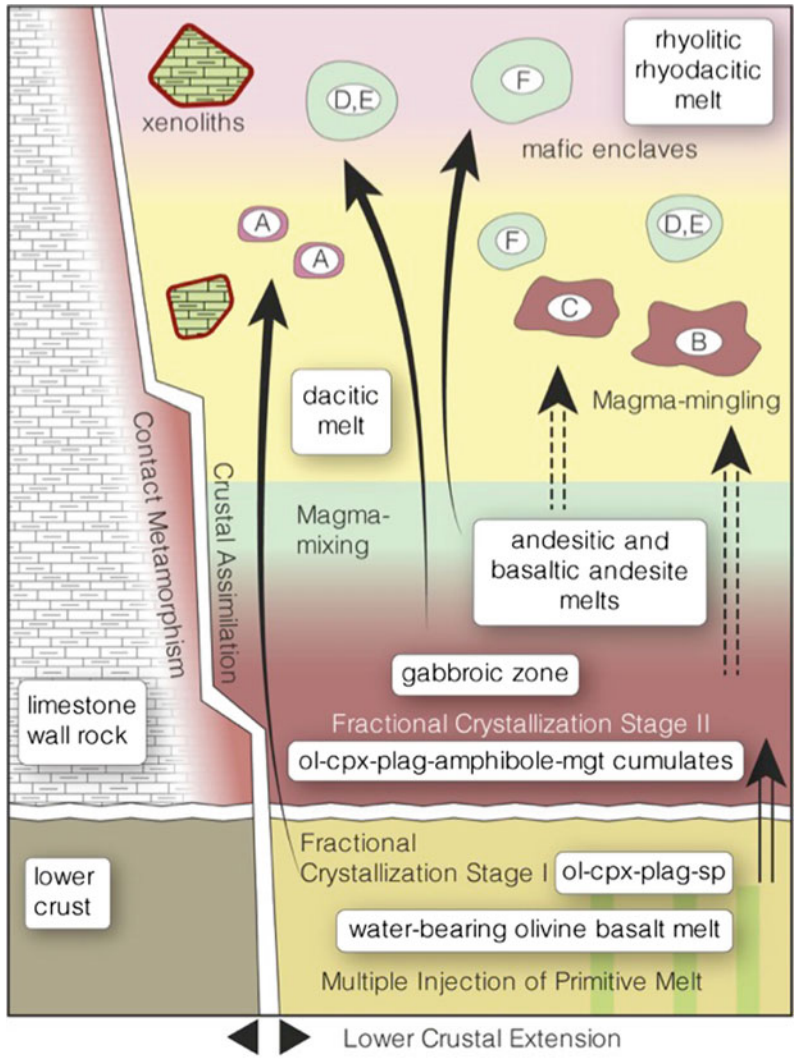

Fig. 4.28 Schematic model of magma mixing and mingling processes within magma reservoirs, independent of depth (figure modified after Dietrich et al. 1988). The capital letters denote the following inclusions in dacitic, rhyodacitic, and rhyolitic melts: *A* small cumulate crystals (e.g. Fo-rich olivine and spinel) from an early fractionation stage I; *B* and *C* clots of large cumulate xenoliths from a later fractional crystallization stage II, partially resorbed and molten; *D* and *E* gabbroic and dioritic xenoliths from the igneous zone of the magma reservoir; *F* mafic enclaves from the layered zone of basic to intermediate melts; *red rims* indicate contact metamorphic xenolith from the border regions (i.e. roof) of the magma reservoir. Sedimentary xenoliths consist of limestone, marbles and skarn (e.g. albite/hedenbergite, pyroxenites, muscovite-bearing, biotite-bearing mafic assemblages). Xenoliths of metamorphic rocks, which are abundant in the pyroclastic unit of the nearby Yali islet, are very rare in the Nisyros rocks. Black arrows denote the pathways of the enclaves

Examples of magma mixing have been recognized in all lavas from basaltic andesites to rhyolites throughout the history of Nisyros Volcano (e.g. Seymour and Vlassopoulos 1989, 1992; Francalanci et al. 1995; Zouzias and Seymour 2014). Evidence of magma mixing involving basic melts consists of mingled enclaves, crystal clots, minuscule quenched mafic enclaves, inverse compositional zonation of plagioclase and disequilibrium textures of plagioclase and amphiboles (Figs. 4.28, 4.2 and 4.10 respectively). The compositions of the xenocrysts found in dacites are similar to those of the phenocrysts from the basaltic andesites and andesites, whereas the dacite phenocrysts are more or less similar to those found in the rhyolites.

The effects of magma mingling and inefficient magma mixing are also evident in the bulk rock chemical variation of the rocks, expressed as a scatter of major and trace elements (Sect. 4.4 and Figs. 4.20, 4.21, 4.22, 4.23 and 4.24), exceeding by far the analytical errors.

A significant melting process that can be regarded as a result of a mixing process may happen during the injection of fresh hot magma into a pre-existing magma reservoir. Oberhänsli et al. (1985, 1989) and Dietrich et al. (1987) have described the role of mixing induced partial melting in cumulates from the volcanic islands of Aegina and Methana, which led to the generation of hybrid high Ti- and Al andesites. Cumulate xenoliths with similar textural characteristics have not yet been found in the Nisyros lavas. However, basaltic andesites in the pre-caldera lavas of Nisyros with higher Ti- and Al-contents may imply such a process (Tables 4.5 and 4.6).

References

Annen C, Blundy JD, Sparks RSJ (2006) The genesis of intermediate and silicic magmas in deep crustal hot zones. J Petrol 47:505–539

Bachmann O, Deering CD, Ruprecht JS, Huber C, Skopelitis A, Schnyder C (2011) Evolution of silicic magmas in the Kos-Nisyros volcanic centre, Greece: a petrological cycle associated with caldera collapse. Contrib Mineral Petrol 163:151–166

Bacon CHR (1986) Magmatic inclusions in silicic and intermediate volcanic rocks. J Geophys Res 91:6091–6112

Barton M, Salters VJM, Huijsmans JPP (1983) S-isotope and trace element evidence for the role of continental crust in calk-alkaline volcanism of Santorini and Milos, Aegean Sea, Greece. Earth Planet Sci Lett 63:273–291

Barton M, Huijsmanns JPP (1986) Post-caldera dacites from the Santorini volcanic complex, Aegean Sea, Greece: an example of the eruption of lavas of near-constant composition over a 2,200 year period. Contrib Mineral Petrol 94:472–495

Boettcher AL (1977) The role of amphiboles and water in circum-Pacific volcanism. In: Manghnani MH, Akimoto S (eds) High pressure research application in geophysics. New York Academic Press, pp 107–125

Bohla M, Keller J (1987) Petrology of plinian eruptians of Nisyros Volcano. Hellenic arc. Terra Cognita 7:171

Bowen N (1928) The evolution of the igneous rocks. Princeton University Press, Princeton

Braschi E, Francalanci L, Tommasini S, Vougioukalakis GE (2014) Unrevaling the hidden origin and migration of plagioclase phenocrysts by in situ Sr isotopes the case of final dome activity at Nisyros Volcano, Greece. Contrib Mineral Petrol 167:988–1013

Briqueu L, Javoy M, Lancelot JR, Tatsumoto M (1986) Isotope geochemistry of recent magmatism in the Aegean arc: Sr, Nd, Hf, and O isotopic ratios in the lavas of Milos and Santorini—geodynamic implications. Earth Planet Sci Lett 80:41–54

Bryan WB, Finger LW, Chayes F (1969) Estimating proportions in petrographic mixing equations by least-squares approximation. Science 163:926–927

Buettner A, Kleinhanns IC, Rufer D, Hunziker JC, Villa IM (2005) Magma generation at the easternmost section of the Hellenic Arc: Hf, Nd, Pb and Sr isotope geochemistry of Nisyros and Yali volcanoes (Greece). Lithos 83:29–46

Cawthorn RG, O'Hara MJ (1976) Amphibole fractionation in calc-alkaline magma genesis. Am J Sci 276:309–329

Davies JH, Stevenson DJ (1992) Physical model of source region of subduction zone volcanics. J Geophys Res 97:2037–2070

Davis E (1967) Zur Geologie und Petrologie der Insel Nisyros und Jali (Dodecanes) Proc Akad Athen 42:235–252

Davis E, Gartzos E, Dietrich VJ (1998) Magmatic evolution of the Pleistocene Akrotiri volcanoes. In: Casale R, Fytikas M, Sigvaldasson G, Vougioukalakis GE (eds) The European laboratory volcanoes, proceedings of the 2nd workshop, 2–4 May 1996, Santorini, Greece, EUR 18161 EN. European Commission, Luxembourg, pp 49–67

De Angelis SH, Larsen J, Coombs M, Dunn A, Hayden L (2015) Amphibole reaction rims as a record of pre-eruptive magmatic heating: an experimental approach. Earth Planetary Sci Lett 426:235–245

Di Paola GM (1974) Volcanology and petrology of Nisyros Island (Dodecanese, Greece). Bull. Volcanol. 38:944–987

Dessimoz M, Muntener O, Ulmer P (2012) A case for hornblende dominated fractionation of arc magmas: the Chelan complex (Washington Cascades). Contrib Mineral Petrol 163:567–589

Dietrich V (1989) Intramagmatic pillowing. Terra 1 (1):278 (abstract)

Dietrich VJ, Mercolli I, Oberhänsli R (1987) The complexity of discontinous fractionation in water-bearing magmas. Program IAVCEI 3:407.

Dietrich VJ, Mercolli I, Oberhänsli R (1988) Dazite, high-alumina Basalte und Andesite als Produkte Amphibol dominierter differentiation (Aegina und Methana, Aegäischer Inselbogen). Schweiz Mineral Petrogr Mitt 68:21–39

Eichelberger JC (1980) Vesiculation of mafic magma during replenishment of silicic magma reservoirs. Nature 288:446–450

Ellis BS, Bachmann O, Wolff JA (2014) Cumulate fragments in silicic ignimbrites: the case of the Snake River Plain. Geology 42:431–434

Feeley TC, Dungan MA (1996) Compositional and dynamic controls on mafic-silicic magma interactions at continental arc volcanoes: evidence from Cordón el Guadal, Tatara-San Pedro complex, Chile. J Petrol 37:1547–1577

Foden JD, Green DH (1992) Possible role of amphibole in the origin of andesite: some experimental and natural evidence. Contrib Mineral Petrol 109:479–493

Francalanci L, Varekamp JC, Vougioukalakis G, Defant MJ, Innocenti R, Manetti P (1995) Crystal retention, fractionation and crustal assimilation in a convecting magma chamber, Nisyros Volcano, Greece. Bull Volcanol 56:601–620

Francalanci L, Vougioukalakis GE, Perini G, Manetti P (2005) A west–east traverse along the magmatism of the south Aegean volcanic arc in the light of volcanological, chemical and isotope data. Dev Volcanol 7:65–111

Francalanci L, Varekamp JC, Vougioukalakis GE, Innocenti F, Manetti P (2007) Is there a compositional gap at Nisyros Volcano? A comment on: magma generation at the easternmost section of the Hellenic arc: Hf, Nd, Pb and Sr isotope geochemistry of Nisyros and Yali volcanoes (Greece). Lithos 95(3–4):458–461

Fytikas M, Kolios N, Vougioukalakis G (1990) Post-Minoan volcanic activity of the Santorini volcano, volcanic hazard and risk forecasting possibilities. In: Thera and the Aegean World III, vol 2. The Thera Foundation, London, pp 183–198

Ganseki C (1991) Petrology of the domes and inclusions of Nisyros Volcano, Dodecanese islands, Greece. BA thesis, Wesleyan University, Middletown, CT, 97 pp

Garcia MO, Jacobson SS (1979) Crystal clots, amphibole fraction and the evolution of calc-alkaline magmas. Contrib Mineral Petrol 69:319–327

Gartzos E, Dietrich VJ, Davis E (1999) Amphibole-plagioclase fractionational crystallisation and magma mixing nas major differentiation processes in the Akrotiri volcanic complex, Santorini, Greece. Schweiz Mineral Petrogr Mitt 79:231–262

Geotermica Italiana (1983) Nisyros 1 geothermal well. PPC-EEC report, pp 1–106

Geotermica Italiana (1984) Nisyros 2 geothermal well. PPC-EEC report, pp 1–44

Girard G, Stix J (2009) Magma recharge and crystal mush rejuvenation associated with early post-collapse upper basin member rhyolites, Yellowstone caldera, Wyoming. J Petrol 50:2095–2125. doi:10.1093/petrology/egp070

Graham CM, Harmon RS, Sheppard SMF (1984) Experimental hydrogen isotope studies: hydrogen isotope exchange between amphibole and water. Am Miner 69:128–138

Grove TL, Parman SW, Bowring S, Price RC, Baker MB (2002) The role of an H_2O-rich fluid component in the generation of primitive basaltic andesites and andesites from the Mt. Shasta region, N California. Contrib Mineral Petrol 148:542–565

Grove TL, Baker MB, Price RC, Parman SW, Elkins-Tanton LT, Chatterjee N, Müntener O (2005) Magnesian andesite and dacite lavas from Mt. Shasta, northern California: products of fractional crystallization of H2O-rich mantle melts. Contrib Mineral Petrol 148:542–565

Grove TL, Elkins-Tanton LT, Parman SW, Chatterjee N, Müntener O, Gaetani GA (2005) Fractional crystallization and mantle-melting controls on calc-alkaline differentiation trends. Contrib Mineral Petrol 145:515–533

Guillong M, von Quadt A, Sakata S, Peytcheva I, Bachmann O (2014) LA–ICP–MS Pb–U dating of young zircons from the Kos-Nisyros volcanic centre SE Aegean arc. J Anal At Spectrum 29:963–970

Gülen L (1990) Isotopic characterization of Aegean magmatism and geodynamic evolution of the Aegean subduction. Proceedings of conference on international earth science colloquium on the Aegean region, Oct 1–6 (1990) Izmir/Turkey, vol 2, pp 143–166

Gülen L, Hart SR, Salters VJM, Wyers GP, Barton M (1987) Sr, Nd, Pb, isotopic constraints on the petrogenesis of the Aegean arc volcanics. Terra Cognita 7:170–171

Huijsmans JPP, Barton M, Salters VJM (1988) Geochemistry and evolution of the calc-alkaline volcanic complex of Santorini, Aegean Sea, Greece. J Volcanol Geotherm Res 34:283–306

Hürlimann N, Müntener O, Ulmer P, Nandedkar R, Chiaradia M, Ovtcharova M (2016) Primary magmas in continental Arcs and their differentiated products: Petrology of a post-plutonic dyke suite in the tertiary Adamello Batholith (Alps). J Petrol 57(3):495–534

Innocenti R, Manetti P, Pecerillo A, Poli G (1981) South Aegean volcanic arc: geo-chemical variations and geotectonic implications. Bull Volcanol 44:377–391

Krawczynski MJ, Grove TL, Behrens H (2012) Amphibole stability in primitive arc magmas: effects of temperature,

H_2O content, and oxygen fugacity. Contrib Mineral Petrol. doi:10.1007/s00410-012-0740-x

Leake BE (1978) Nomenclature of amphiboles. Am Mineral 63:1023–1052

Leake BE, Wooley AR, Arps CES, Birch WD, Gilbert MC, Grice JD, Hawthrone FC, Kato A, Kisch HJ, Krivovichev VG, Linthout K, Laird J, Mandarino JA, Maresch WV, Nickel EH, Rock NMS, Schumacher JC, Smith DC, Stephensen NCN, Ungaretti L, Whittaker EJW, Youzhi G (1997) Nomenclature of amphiboles: report of the subcommitee on amphiboles of the international mineralogical association, commission on new minerals and mineral names. Am Mineral 82:1019

Limburg EM, Varekamp JC (1991) Young pumice deposits on Nisyros. Greece Bull Volcanol 54(1):68–77

Lodise L (1987) Petrology and geochemistry of Nisyros Volcano (Dodecanese, Greece). MA thesis, Wesleyan University, Middletown CT USA: 245 pp

Longchamp C, Bonadonna C, Bachmann O, Skopelitis A (2011) Characterization of tephra deposits with limited exposure: the example of the two largest explosive eruptions at Nisyros Volcano (Greece). Bull Volc 73:1337–1352

Mann AC (1983) Trace element geochemistry of high alumina basalt—andesite—dacite—rhyodacite lavas of the main volcanic series of Santorini volcano, Greece. Contrib Mineral Petrol 84:43–57

Marini L, Principe C, Chiodini G, Cioni R, Fytikas M, Marinelli G (1993) Hydrothermal eruptions of Nisyros (Dodecanese, Greece)—past events and present hazard. J Volcanol Geotherm Res 56:71–94

Martin L (2008) The petrology and geochemistry of mafic volcanic units from Nisyros Volcano, Greece: implications for magma evolution in island arcs. Master thesis University Bewrne, 113 pp

McBirney AR (1980) Mixing and unmixing of magmas. J Volcanol Geoth Res 7:357–371

McDonough WF, Sun SS (1995) The composition of the Earth. Chem Geol 120:223–253

Mitropoulos P, Tarney J (1992) Significance of mineral composition variations in the Aegean Island Arc. J Volcanol Geotherm Res 51:283–303

Mitropoulos P, Tarney J, Saunders AD, Marsh NG (1987) Petrogenesis of Cenozoic volcanic rocks from the Aegean Island Arc. J Volcanol Geotherm Res 32:177–193

Mitropoulos P, Tarney J, Stouraiti C, Notsu K, Arakawa Y (1998) Sr isotopic variation along the Aegean Arc: constraints on magma genesis on the basis of new Sr isotope data. Bull Geol Soc Greece 32:215–224

Miyashiro A (1974) Volcanic rock series in island arcs and active continental margins. Am J Sci 274:321–355

Moore G, Carmichael ISE (1998) The hydrous phase equilibria (to 3 kbar) of an andesite and basaltic andesite from western Mexico: constraints on water content and conditions of phenocryst growth. Contrib Mineral Petrol 130:304–319

Müntener O, Kelemen P, Grove T (2001) The role of H_2O during crystallization of primitive arc magmas under uppermost mantle conditions and genesis of igneous pyroxenites: an experimental study. Contrib Mineral Petrol 141:643–658

Nandedkar RH, Ulmer P, Müntener O (2014) Fractional crystallization of primitive, hydrous arc magmas: an experimental study at 0.7 GPa. Contrib Mineral Petrol 167:1015, doi:10.1007/s00410-014-1015-5

Nicholls IA (1971) Petrology of Santorini Volcano, Cyclades, Greece. J Petrol 12(1):67–119

Nicholls, IA (1978) Primary basaltic magmas for the pre-Caldera volcanic rocks of Santorini. In: Doumas C (ed) Thera and the Aegean World I, pp 109–120

Oberhänsli R, Mercolli I, Dietrich VJ (1985) The amphibole andesite connection. Terra Cognita 5 (2/3):181

Oberhänsli R, Dietrich VJ, Mercolli I (1989) Origin of high-al basalts by hybridization of cumulates. Terra 1 (1):277

Osborn EF (1976) Origin of calc-alkali magma series of Santorini volcano type in the light of recent experiments phase equilibria. Proc Int Cong Therm Waters Geotherm Energy Volcanism Med Area 3:154–167

Osborn EF, Rawson SA (1980) Experimental studies of magnetite in calc-alkaline rocks. Carnegie Inst Wash Yearb 79:281–285

Pe GG (1975) Strontium isotope ratios in volcanic rocks from the northwestern part of the Hellenic Arc. Chem Geol 15:53–60

Pe-Piper G, Piper DJW (2002) The igneous rocks of Greece the anatomy of an orogen. Gebr Bornträger Berlin Stuttgart, 573 pp

Rehren Th (1988) Geochemie und Petrologie von Nisyros (Oestliche Agaeis). PhD thesis Univ Freiburg

Ridolfi F, Renzulli A, Puerini M (2010) Stability and chemical equilibrium of amphibole in calc-alkaline magmas: an overview, new thermobarometric formulations and application to subduction-related volcanoes. Contrib Mineral Petrol 160(1):45–66

Ridolfi F, Renzulli A (2012) Calcic amphiboles in calc-alkaline and alkaline magmas: thermobarometric and chemometric empirical equations valid up to 1130 °C and 22 GPa. Contrib Mineral Petrol 163:877–895

Rutherford MJ, Hill PM (1993) Magma ascent rates from amphibole breakdown: an experimental study applied to the 1980–1986 Mount St Helens eruptions. J Geophys Res B Solid Earth 98:19667–19685

Schmidt MW (1992) Phase compositions and relationships in tonalite: an experimental approach. PhD thesis ETH Zurich, Nr 9897, 113 pp

Sisson TW, Grove TL (1993a) Experimental investigations of the role of H_2O in calc-alkaline differentiation and subduction zone magmatism. Contrib Miner Petrol 113:143–166

Sisson TW, Grove TL (1993b) Temperatures and H_2O contents of low-MgO high-alumina basalts. Contrib Miner Petrol 113:167–184

Spandler C, Martin LHJ, Pettke Th (2012) Carbonate assimilation during magma evolution at Nisyros (Greece), South Aegean Arc: evidence from clinopyroxenite xenoliths. Lithos 146–147:18–33

Spear FS, Kimball KL (1984) RECAMP—A FORTRAN IV program for estimating Fe3+ contents in amphiboles. Comput Geol 10:317–325

St Seymour K, Lalonde AE (1990) Monitoring oxygen fugacity conditions in pre-, syn- and postcaldera magma chamber of Nisyros Volcano, Aegean island arc, Greece. J Volcanol Geotherm Res 46:231–240

St Seymour K, Vlassopoulos D (1989) The potential for future explosive volcanism associated with dome growth at Nisyros, Aegean Volcanic Arc, Greece. J Volcanol Geotherm Res 37:351–364

St Seymour K, Vlassopoulos D (1992) Magma mixing at Nisyros Volcano, as inferred from incompatible trace-element systematics. J Volcanol Geotherm Res 50:273–299

Stewart DC (1975) Crystal clots in calc-alkaline andesites as breakdown products of high-Al amphiboles. Contrib Miner Petrol 53(3):195–204

Sun SS, MacDonough WF (1989) Chemical and isotopic systematics of oceanic basalts: implications for mantle composition and processes. In: Saunders AD, Norry MJ (eds) Magmatism in Oceanic basins. Geol Soc Spec Publ Lond, pp 313–345

Tatsumi Y, Eggins S (1995) Subduction zone magmatism. Blackwell Scientific, Oxford

Ulmer P (2001) Partial melting in the mantle wedge—the role of H_2O in the genesis of mantle-derived 'arc-related' magmas. Phys Earth Planet Inter 127:215–232

Ulmer P, Trommsdorff V (1995) Serpentine stability to mantle depths and subduction-related magmatism. Science 268:858–861

Vanderkluysen L, Volentik A (2002) Etude géophysique et hydrothermalisme du complexe volcanique de Nisyros, Greece. Diploma thesis Univ Lausanne, 200 pp

Vanderkluysen L, Volentik A, Principe C, Hunziker JC, Hernandez J (2005) Nisyros volcanic evolution: the growth of a stratovolcano. In: Hunziker JC, Marini L (eds) The petrology and geochemistry of lavas and tephras of Nisyros Volcano (Greece). Mémoires de Géologie (Lausanne) 44:100–106

Volentik A, Vanderkluysen L, Principe C (2002) Stratigraphy of the Caldera walls of Nisyros Volcano, Greece. Eclogae Geol Helv 95:223–235

Volentik A, Vanderkluysen L, Principe C, Hunziker JC (2005) Stratigraphy of Nisyros vollcano (Greece) In: Hunziker JC, Marini L (eds) The petrology and geochemistry of lavas and tephras of Nisyros Volcano (Greece). Mémoires de Géologie (Lausanne) 44:26–66

Vougioukalakis GE (1984) Studio vulcanologico e chimico-petrografico dell'isola di Nisyros (Dodecanneso, Grecia). Università di Pisa, Tesi di laurea

Vougioukalakis G (1993) Volcanic stratigraphy and evolution of Nisyros island. Bull Geol Soc Greece 28(2):239–258

Williams H, Turner FJ, Gilbert CM (1954) Petrography. Freeman and Co, San Francisco, p 406

Wyers GP, Barton M (1989) Polybaric evolutian of calc-alkalinc magmas from Nisyros, southeastern Hellenic Arc, Greece. J Petrol 30(1):1–37

Zellmer GF, Turner SP (2007) Arc dacite genesis pathways: evidence from mafic enclaves and their hosts in Aegean lavas. Lithos 95(3–4):346–362

Zouzias K, St Seymour K (2014) Magma mixing and magma mingling episodes throughout the volcanic history of Nisyros Volcano, SE extremity of the Aegean volcanic arc, as registered by the plagioclase record. Neues Jahrbuch für Mineralogie Abhlg (J Min Geochem) 191(2):189–214

The Hydrothermal System and Geothermal Activity

5

Volker Jörg Dietrich, Giovanni Chiodini and Florian M. Schwandner

Abstract

Nisyros volcano's activity is characterized by high seismic unrest, hydrothermal explosions, degassing through fumarolic activity and diffuse degassing structures. Hydrothermal explosions in the caldera floor of unknown age until recently created a complex set of intersecting crater structures with evident structural controls. Low-temperature thermal springs and fumaroles occur along known and inferred fracture systems and their crossing points, springs preferentially along the coast and fumaroles within the caldera and its hydrothermal explosion craters. Their chemical and isotopic signatures reflect phase separation and mixing to varying degrees with magmatic, hydrothermal, meteoric, and seawater components. A deep hot hydrothermal brine with seawater and magmatic influence feeds thermal fluid and gases by vapor separation into a set of intermediate thermal aquifers, which have been explored by drilling. A shallow low-temperature aquifer results from steam condensation and the resulting surface manifestations emit hot steam-gas mixtures at up to boiling temperature. Widespread diffuse degassing of CO_2 demonstrates the permeable nature of the Nisyros hydrothermal system, focusing along fault systems, releasing 68 t d^{-1} of CO_2 and 58 MW of thermal energy. The last magmatic activity of Nisyros, even if of unknown age, is considered relatively old, based on morphological considerations and on the absence of historical magmatic eruptions. Nevertheless, there are many

V.J. Dietrich (✉)
Institute of Geochemistry and Petrology, Swiss Federal Institute of Technology, ETH Zurich, ETH-Zentrum, 8092 Zurich, Switzerland
e-mail: volker.dietrich@erdw.ethz.ch

G. Chiodini
Sezione di Bologna, Istituto Nazionale di Geofisica e Vulcanologia, 40128 Bologna, Italy
e-mail: giovanni.chiodini@ingv.it

F.M. Schwandner
Jet Propulsion Laboratory, M/S 233-300, California Institute of Technology, Pasadena, CA 91109, USA
e-mail: florimax@schwandner-web.org

V.J. Dietrich and E. Lagios (eds.), *Nisyros Volcano*, Active Volcanoes of the World,
DOI 10.1007/978-3-319-55460-0_5

geochemical indications supporting the presence of a magmatic source at depth, which feeds the hydrothermal system. This evidence is mainly constituted by the isotopic composition of H_2O, S, and He discharged by the Nisyros fumaroles.

5.1 Introduction

Although the last volcanic activity on Nisyros dates back at least 24,000 years, the geodynamic activity, expressed by high seismic unrest, fumarolic activity and hydrothermal explosions is continuously present.

At present, steam and fumarolic activity occurs in the hydrothermal craters along faults, as well as from several minor fractures in the Profitis Ilias dome (PI, Fig. 5.1). Thermal springs, known since historical times, partly combined with CO_2 and H_2S emissions and temperatures up to 60 °C are bound to faults along the northern, north-eastern and southern

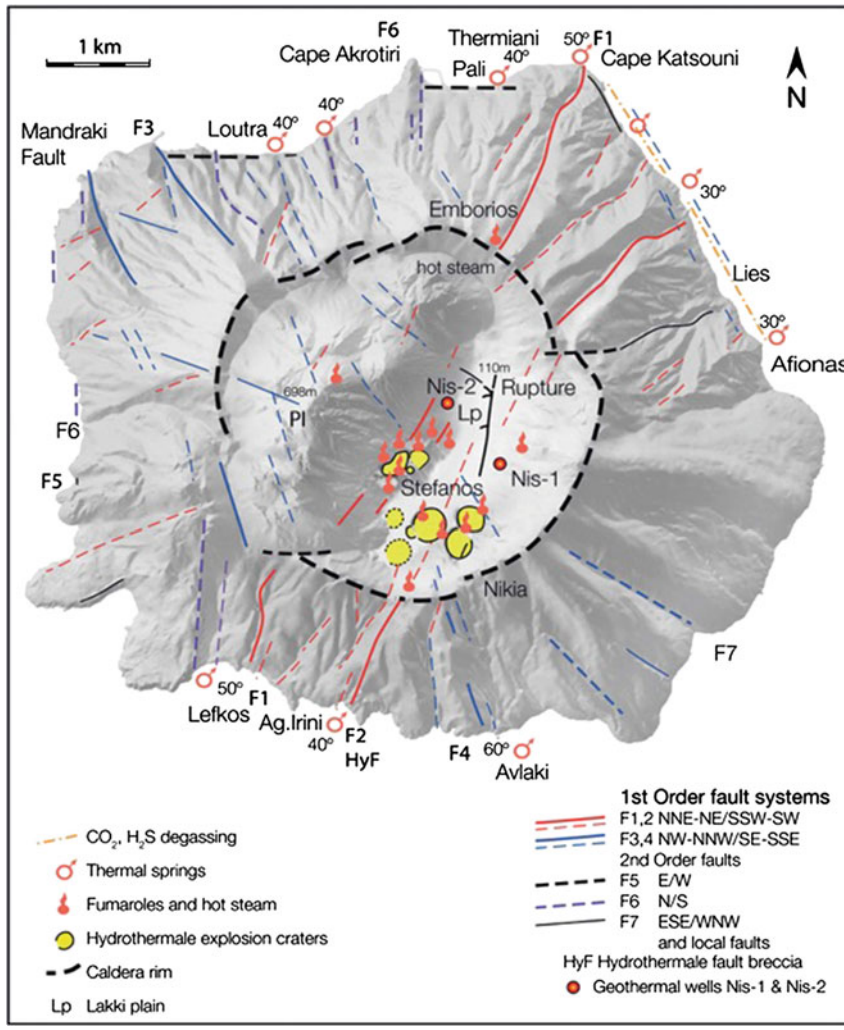

Fig. 5.1 Sites of surface emissions of the Nisyros hydrothermal system: hydrothermal fault breccia, hydrothermal explosion craters, fumarolic and steam emissions, thermal springs and geothermal wells Nis-1 and Nis-2

shores at sea level (Fig. 5.1). The waters are mixtures of magmatic, meteoric and marine origin.

5.2 The History of Gas- and Hydrothermal Explosions in the Nisyros Caldera

5.2.1 Historical Records

A first short note of the hydrothermal activity of Nisyros is given by Strabo in the "Liber Insularum Archipelagi" (Geographia, lib. X, chap V; 1st century B.C.). A first detailed information of the Aegean islands has been published by the Florentine monk Cristoforo Buondelmonti, who visited Nisyros between 1414 and 1420. His description of the Nisyros volcano and hydrothermal activity in comparison to the Italian Aeolian island volcanoes Stromboli and Lipari is unique for its time (Fig. 5.2).

It appears, that Cristoforo Buondelmonti went down and up a footpath from Nikia to the Lakki plain and Stefanos crater (shown in his map as a lake), passing by the fumaroles of the Kaminakia craters. The central mountain as shown in his map, Profitis Ilias, seemed to have emitted strong fumarolic gases. According to some reports, the largest hydrothermal explosion that left the 300 m wide Stefanos crater behind, happened before Buondelmonti's visit.

Four hundred years later, the German archaeologist Ludwig Ross visited Nisyros Island on 9–11 August 1841 and described the Lakki plain in the caldera and Stefanos crater as follows (Ross 1843):

Fig. 5.2 Folio 36r, Nisyros, half-page, 97 mm by 121 mm., with five towns including the harbor at Mandraki described by Buondelmonti (Buondelmonti 1420): *«In the centre of the island is a very high mountain which emits sulphurous flames from the underground during day and night, as it is the case in the island of Stromboli, near Lipari. Only a stone's throw down from the mountain is a hot spring from where waters descend into a deep, dark lake on the plain below. The islanders collect the sulphur in great quantities and sell it to passing traders. From half way up the mountain to the summit the heat is so intense that no one dares ascend without wooden shoes to protect his feet»*

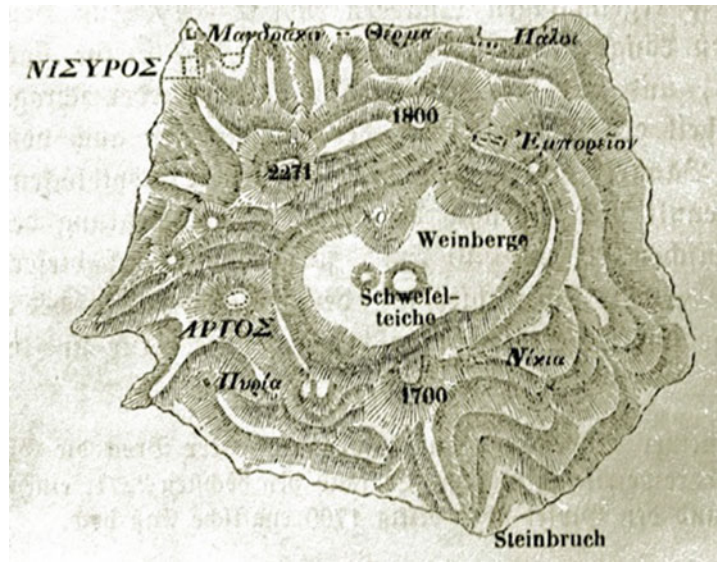

Fig. 5.3 Ludwig Ross's map (Ross 1843)

> «We found the ground quite dry and, with the exception of a few, similar places, firm under our feet; on the southern rim of the crater, however, along a stretch of some 50 paces, the ground was seething and there were muffled explosions to be heard, repeated every 20 to 30 seconds.
> There was also a strong smell of sulphur, which the north wind carried over the village of Nikia, and which we could still perceive early this morning, on the southern coast of the island, some one and a half hours walking distance away. After heavy rainfall and especially when the prevailing wind is westerly, the fire apparently becomes much fiercer: A thick steam arises and the explosions become so loud that one can hear them over an hour's walking distance away».

In his sketch map and description, Ross described in detail the Stefanos crater, two smaller sulfur ponds, probably referring to Megalos Polyvotis and Flegethron, and two sulfur hills in the crater walls (Kaminakia craters), Fig. 5.3; all areas subjected to sulfur mining. In addition, he described a spot of pure hot steam at "Pyria" (Arodaphnes area) coming out of a crack in the southern slopes, which marks the major SW-NE fault zone.

5.2.2 The Hydrothermal Explosions 1871–1873

The French geologist H. Gorceix, who visited Nisyros at the end of November 1871, reported a realistic description of a hydroclastic to hydrothermal eruption. His subsequent reports of hydrothermal explosive eruptions are published in six articles (Gorceix 1873a, b, c, 1874a, b, c). Gorceix (1873a, b, c) stated that the islanders had recognized an increase of fumarolic gases in the area of Polyvotis since the beginning of 1871. Strong explosive eruptions started after a violent earthquake, probably at the end of October or November. South of Lofos dome, two craters, Megalos Polyvotis and Flegethron opened up, covering the island with steam. Mud and rock fragments were ejected only in the vicinity.

> «After series of violent earthquakes the inhabitants of Nisyros heard detonations compared to thunders; red and yellow flames shooting into the air, higher than the steams before; the fields at the base of the caldera were covered in white dust. That same night, two huge fumaroles (syn. craters) opened up and since this time have not ceased to vomit their steams».

During 1873 tremors and hydrothermal activity continued. The French Academy of Sciences decided to send H. Gorceix again to the island. On the 3rd of June 1873 the island was shaken by violent tremors, a large vent appeared, the Flegethron crater, and opened a 50 m N22°E trending long fracture, connecting Flegethron with the existing Polyvotis crater. Then the eruptions started, throwing up black waters, mud

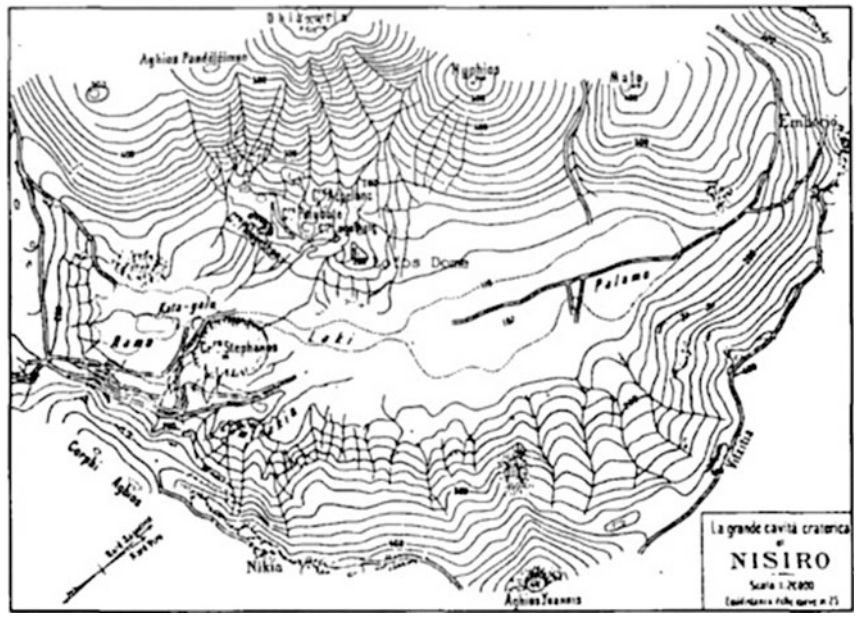

Fig. 5.4 The Nisyros hydrothermal field as sketch map by Martelli (1917) shows the situation of 1914 with the morphologically well-preserved craters and debris outflows

and rocks for 3 h, which left thick patches of sodium- and magnesium chlorides behind. Rivers of hot mud discharged from Flegethron and covered a 150 m wide area to its south over a distance of 500 m. The steam and hot brine drenched the trees and left stalagmites of salt as evaporites on the branches.

From June to September, only small seismic tremors were recorded, while the craters emitted H_2S-rich amounts of steam and ejecta. On September 11, a powerful earthquake caused damages to the houses, the church and to the monastery Spiliani of Mandraki. A great underwater fracture opened up, extending from Mandraki northwards. Gas emissions turned the seawater milky. Another big fissure opened approximately 5 km north of Mandraki and cut across Yali.

On 26th September 1873, new eruptions of hot brine and mud begun, however less important than the 1871 eruptions, from both Flegethron and Polyvotis. Rocks from the Polyvotis explosions covered half the floor of the preexisting Megalos Polyvotis depression. Steam emissions from Flegethron continued for a few months, while Polyvotis from time to time behaved like a geyser, ejecting columns of hot water and steam up to a height of 30 m. The Polyvotis and Flegethron eruptions continued for several days while the tremors lasted until December 1873.

The most recent explosive hydrothermal activity happened in 1887 with the formation of the Mikros Polyvotis crater. A description is given by the Italian geologist Martelli (1917), see Figs. 5.4 and 5.5. According to Nisyrians working in the sulfur mines, it was an eruption of mud and altered rocks with a strong emission of steam and gas.

During April 23, 1933 a major earthquake south of Kos destroyed 80% of the mountain village of Emborios, which led to a total exodus of its inhabitants. No reports about increased hydrothermal activity in the Lakki plain exist after this event. During the next 60 years the hydrothermal system seemed to be dormant at constant level despite several large earthquakes on Nisyros Island and vicinity with magnitudes around 6 on the Richter scale (Aggelidis et al. 1990).

A strong seismic crisis occurred during 1996 to 1998 causing rock falls in the hydrothermal

Fig. 5.5 The situation of Polyvotis crater in the center of the large Megalos Polyvotis crater of unknown age as result of the hydrothermal explosions 1871–1873 (*Photo* Martelli 1917). Most of the ejecta in the explosive halo have been washed away with debris flows and deposited outside the crater area

crater field and damages along the Mandraki fault (Papadopoulos et al. 1998). According to historical reports it seems likely that earthquakes play an important role in triggering hydrothermal eruptions (Marini et al. 1993), opening fractures, and thus, permitting the rise of deep hot fluids. This time, the earthquakes did not cause another hydrothermal eruption, but an increase of fumarolic activity and boiling occurred in the craters Stefanos, Flegethron and Micros Polyvotis. In addition, significant changes in the chemistry of the gases were recognized during sampling campaigns 1997–2001 compared to earlier results (Chiodini et al. 1993a, 2002).

5.3 The Hydrothermal System

The existence of a large hydrothermal system (Figs. 5.1 and 5.6) is documented by the formation of five larger hydrothermal craters within the central caldera with its steam and fumarolic activity. The presence of hydrothermal brines at depth has been proven by the two geothermal wells Nis-1 and Nis-2, which reached a maximum depth of 1816 and 1547 m, respectively (Geotermica Italiana 1983, 1984; Marini et al. 1993).

Two distinct hydrothermal aquifers may be present underneath the Nisyros caldera, according to fluid geochemistry, the physical-chemical characteristics of (i) the fumarolic gases and (ii) the thermal waters at the surface, and the fluids in the deep geothermal wells. The deep hydrothermal aquifer is characterized by temperatures >300 °C and high salinity, whereas the shallow hydrothermal aquifer close to the surface, which is fed by condensates, discharges steam and gases through fumaroles at 96–100 °C at 1 bar pressure, and thermal energy through diffuse soil degassing.

5.3.1 The Shallow Discharge Area of Hydrothermal Fluids

The main evidence of hydrothermal activity at Nisyros is the presence of recent craters in the southern Lakki plain, produced by local 'explosions' of hydrothermal fluids. The same area is characterized by large zones of hot and altered soils, and by fumarolic activity. In order to

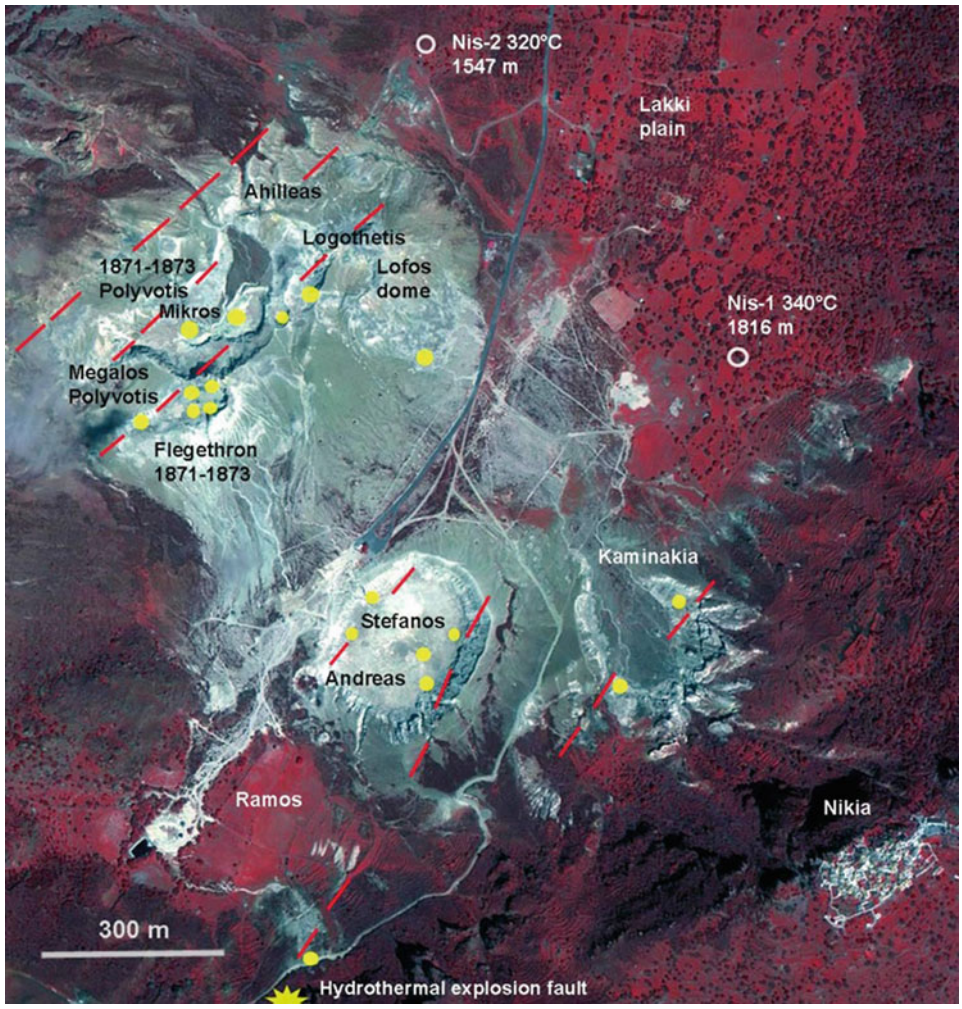

Fig. 5.6 The Nisyros hydrothermal craters taken from the orthorectified IKONOS image (2001): Mikros Polyvotis (1887), Polyvotis (1871–1873), Flegethron (Alexandros syn.) (1871–1873), Ahilleas (unknown), Megalos Polyvotis (unknown), Logothetis (unknown), Andreas (unknown), Stefanos (probably historic), Kaminakia (unknown) and the localities of the geothermal wells Nis-1 and Nis-2. Fumarolic vents (*yellow points*); inferred faults (*red stippled lines*). Hydrothermal explosion fault (NNE-trending main fault system); site: road cut along unpaved south-caldera road to monastery Stavros at 280 m altitude (south caldera rim)

highlight the areas affected by hydrothermal alteration, an IKONOS infrared image has been analysed (Fig. 5.7). After spectral analysis of CIR (Conventional Infrared false colour composite image) (IKONOS bands RGB-421) corrected for topographical and sun illumination effects, the 0–65 RGB colour bands have been extracted. These bands show the surface distribution of hydrothermal alteration, anthropogenic structures and different illumination azimuths. After removing the anthropogenic structures, the 0–65 RGB bands map of the Lakki Plain has

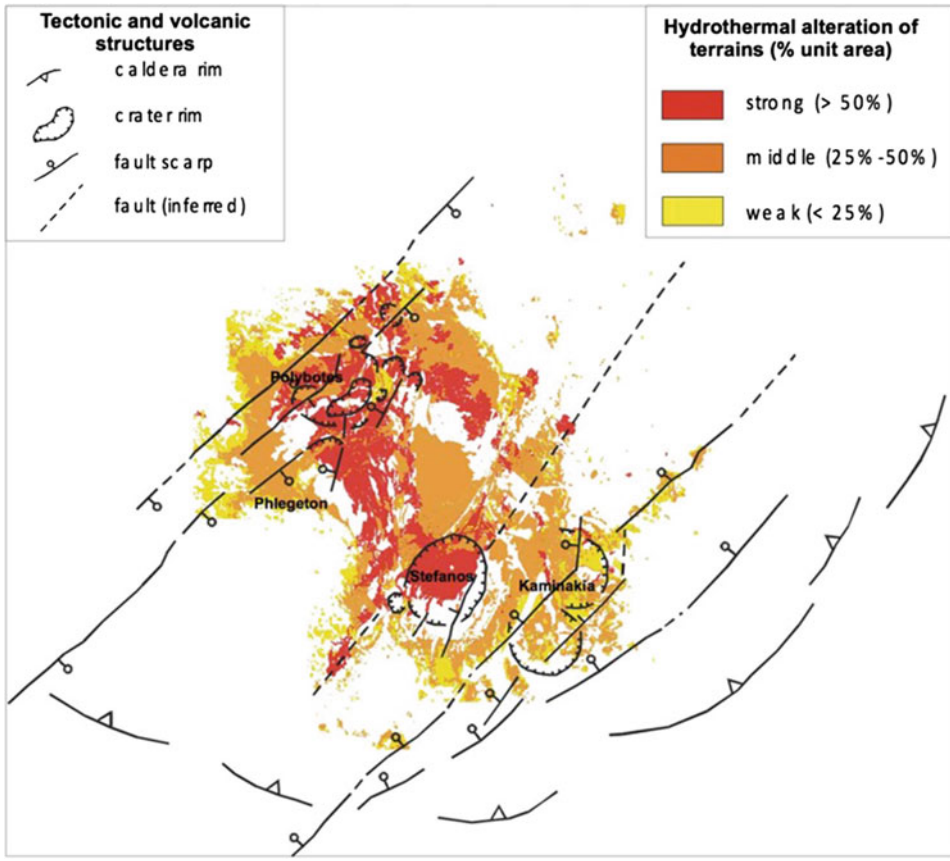

Fig. 5.7 Map of the distribution of hydrothermal alteration in the hydrothermal field of the southern Lakki plain during 2001 (GEOWARN 2003)

been produced from the IKONOS image by using 50 × 50 m domains with a 20 m moving window, and the surface covered by 0–25%, 25–50% and >50% of 0–65 RGB colour. Because the 0–65 RGB band mainly reflects the distribution of hydrothermal alteration within the Lakki plain, the coloured areas in the obtained image (Fig. 5.7) indicate where hydrothermal alteration occurs.

The more severely altered terrains concentrate in the central sector, where the debris- and mudflow deposits of the historical hydrothermal eruptions occur, and at the Stefanos crater. However, 0–65 RGB classified terrains, i.e. hydrothermal alteration, also occur outside the diffuse degassing structures (DDS) along NE-SW tectonic structures. Limiting to this procedure is that the spectral analysis is not able to differentiate areas affected by currently active alteration processes, from areas where the alteration has occurred in the past.

5.3.2 Hydrothermal Explosion Faults

The southern tectonic block of the island is truncated and bordered by the major NNE-SSW trending fault systems F1 and F2 (Chap. 3). The eastern fault seems to have also acted in the past as a hydrothermal explosion fault (Fig. 5.6), since in parts it is filled with a chaotic auto-brecciated mass of lithic blocks cemented by a

Fig. 5.8 Hydrothermal explosion fault with autobreccia-tion (NNE-trending main fault system); locality: road cut along unpaved south-caldera road to monastery Stavros at 280 m altitude (south caldera rim). Andesitic (*black*) and altered rhyolitic (*white*) components in andesitic (*black*) and altered rhyolitic (*white*) components in a lithified matrix within the hydrothermal explosion fault zone within the hydrothermal explosion fault zone. *Photo* V. Dietrich

lithified silicic matrix (Fig. 5.8). Toward the south and in the coastal section, this fault opens up to a 50 m wide funnel-shaped zone (Figs. 5.9 and 5.10), filled with altered blocks, pyroclastics, sulfur and gypsum deposits. At the beach and underwater, a low temperature thermal spring and gas emissions occur.

5.3.3 The Hydrothermal Explosion Craters

Steam and gas explosions of uprising fluids, fed by the shallow hydrothermal system, formed the hydrothermal craters (Figs. 5.11, 5.12, 5.13, 5.14, 5.15, 5.16, 5.17, 5.18, 5.19, 5.20, 5.21,

Fig. 5.9 Funnel-shaped, 50 m wide hydrothermal explosion fault within rhyolite lavas (unit No. 17). This major NNE-trending main fault system, which starts at this cove, extends toward the southern crater rim and into the eastern floor of Stefanos crater. The matrix is highly fractionated and filled with chaotic altered lithic breccia within a sandy and clayey matrix rich in sulfur and gypsum. At the beach and underwater low temperature thermal spring and gas emissions. Site: south coast, 500 m east of Aghia Irini. *Photo* V. Dietrich

Fig. 5.10 Western wall of a funnel-shaped, 50 m wide, hydrothermal explosion fault filled with oxidized, andesitic blocks within a probably reworked older magmatic explosive conduit. *Photo* V. Dietrich

Fig. 5.11 Southern part of the caldera floor (Lakki plain at approximate 110 m a.s.l.) with hydrothermal explosion craters (Stefanos crater in the foreground); Profitis Ilias dacitic domes in background (698 m). *Photo* V. Dietrich

Fig. 5.12 Two crescent shaped hydrothermal Kaminakia craters. *Red circles* indicate the position of the 2000–2002 fumarolic vents. *Photo* V. Dietrich

Fig. 5.13 The southern extension of the Kaminakia-Stefanos hydrothermal zone with an isolated fumarolic spot along the unpaved road from the Lakki plain (Stefanos crater) to the monastery of Stavros and to the circular road around the islands towards west. *Photo* V. Dietrich

Fig. 5.14 Stefanos crater, the largest hydrothermal explosion crater. Fumarolic activity is aligned along a NE trending fault at the base of the eastern wall with surface gas and steam temperatures of approx. 100 °C. The small Andreas crater in the southwest of Stefanos cuts the Stephanos crater rim. Its products unconformably overlie the Stephanos deposits. *Photo* V. Dietrich

Fig. 5.15 The 27 m high Stefanos crater walls exhibit the upper part of the stratigraphic succession of the Lakki plain from bottom to top: grey argillic alluvial talus rich in altered andesitic fragments, which is covered by a red silty argillic stratum. *Photo* V. Dietrich

Fig. 5.16 Flegethron (1873, syn. Alexandros) (*left*); the oldest Logothetis crater on the western flank of Lofos dome (*center*), and Stefanos crater (*right*). *Photo* V. Dietrich

Fig. 5.17 Lofos crater area along the eastern slopes of the Profitis Ilias rhyodacite domes; Flegethron crater (*left*), debris flow delta (*center*), Lofos rhyodacite dome (*right*). Picture taken from eastern caldera rim. *Photo* V. Dietrich

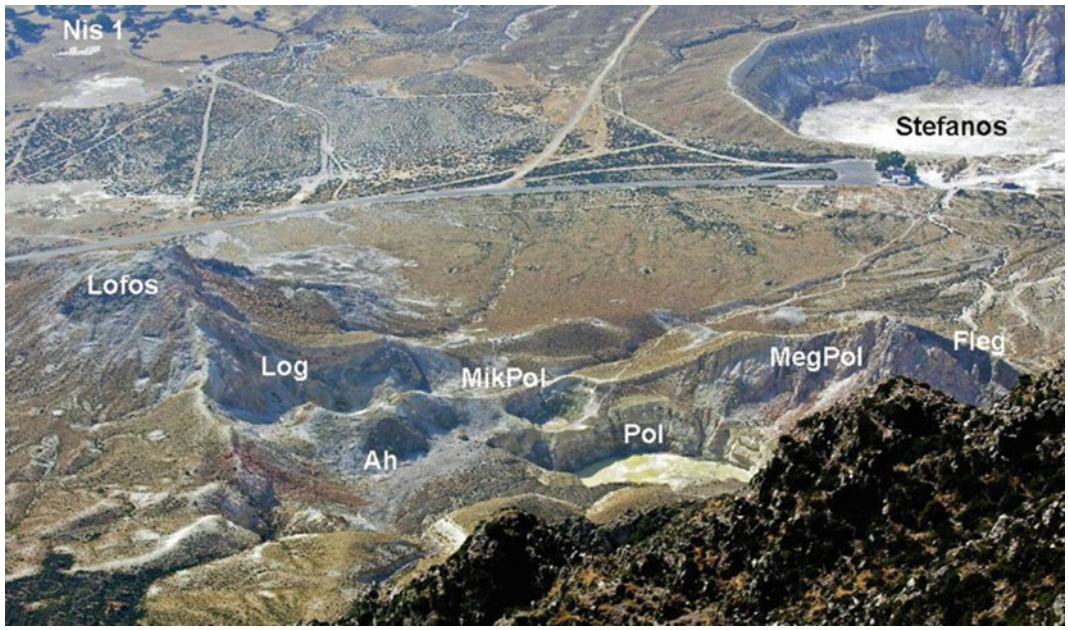

Fig. 5.18 Lofos crater area along the foot of the eastern slopes of the Profitis Ilias rhyodacite domes; from north (*left*) to south (*right*): Lofos rhyodacite dome, Logothetis (Log), Ahilleas (Ah), Mikros Polyvotis (MikPol, 1887), Polyvotis (Pol, 1871–1873), Megalos Polyvotis (MegPol, unknown age), Flegethron crater (Fleg, 1871–1873), Nis-1 (geothermal well 1983). Picture taken from west. *Photo* V. Dietrich

5.22 and 5.23). Hence, they are mainly caused by steam overpressure and not by a magmatic eruption. Such explosions can occur if fresh hot magma is injected from deep crustal magma reservoirs into a shallow magma chamber. There, the magma is able to release gases due to lower lithostatic pressure and transmit heat to the surrounding hydrothermal system.

Fig. 5.19 Lofos rhyodacite dome and Logothetis crater on its eastern shoulder; water-filled floor of Mikros Polyvotis crater (1887) at the *lower left*. *Photo* V. Dietrich

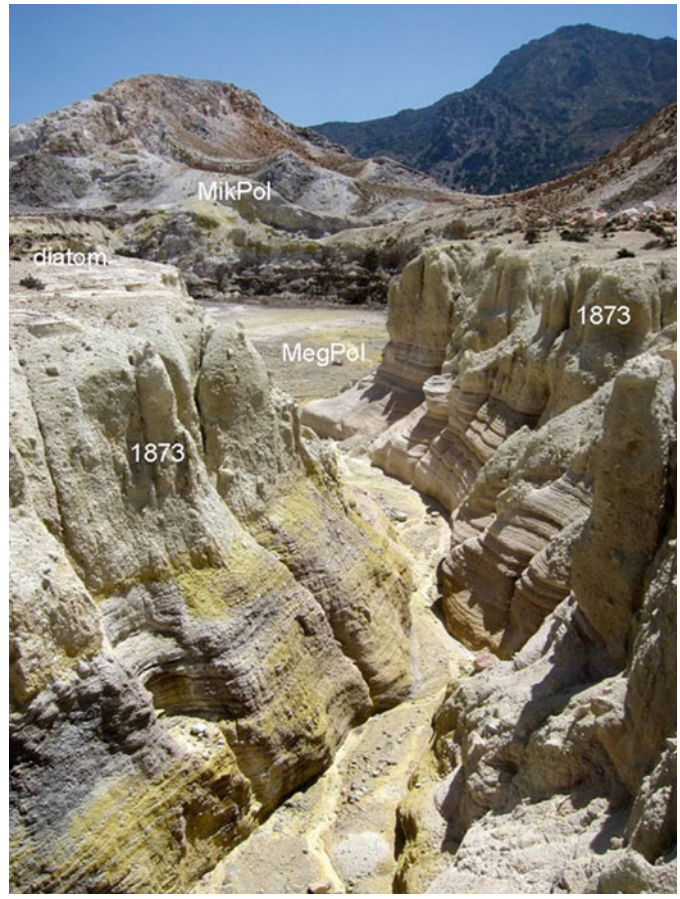

Fig. 5.20 The lower part of the 180 × 350 m Megalos Polyvotis crater (MegPol) seen from south; in the background Mikros Polyvotis (MikPol). Strong erosion during the past 100 years formed the southern outlet through the lower part of older lacustrine sequences (Fig. 5.15), indicating a rather long period of quiet hydrothermal activity. The 1873 eruptive deposit is covered by diatomaceous clays and debris. *Photo* Barry' Ramblings

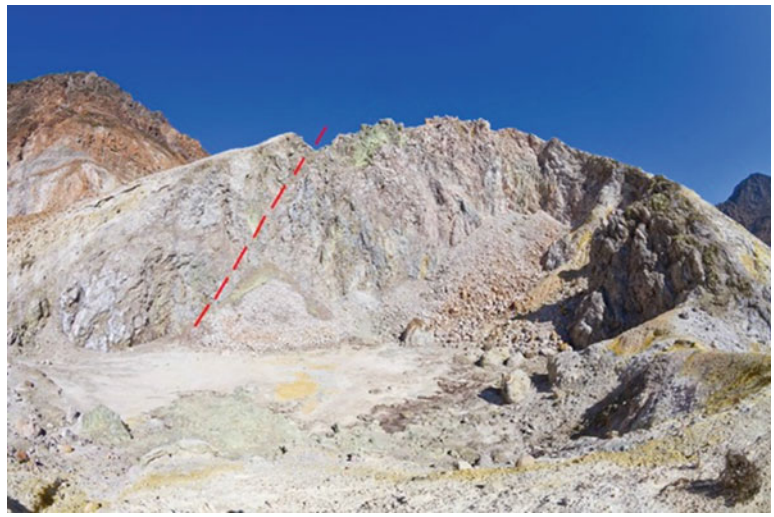

Fig. 5.21 Flegethron (Alexandros, syn.) hydrothermal explosion crater of 1873. The opening towards south of the steep and elongated crater may have been caused by reactivation of the NE-SW fault system (*red hatched line*) as indication of the fault plane with a dip towards SE (Tibaldi et al. 2008) which also caused internal rock falls during the seismic crisis 1996–1997 and beyond. The high crest and the altered and highly fractured rhyodacitic material suggest that its substrate belonged to a former southern part of the Lofos dome; situation early morning on a dry summer day in 2002. *Photo* V. Dietrich

Fig. 5.22 The funnel-shaped and at the floor 30 m wide Mikros Polyvotis, which truncates the eastern rim of the large Megalos Polyvotis. *Photo* V. Dietrich

The present-day hydrothermal field in the southeastern part of the caldera floor, the Lakki plain in the area of Ramos includes ten well-preserved hydrothermal explosion craters (more or less circular and less than 300 m in diameter). They are aligned along active NE-trending faults bordering the Lakki plain and are concentrated at the foot of the caldera walls below Nikia and in the western slopes between Profitis Ilias and Lofos dome. Fumarolic vents and mud pools within the craters testify to continuous hydrothermal activity since historical times. In

Fig. 5.23 Mikros Polyvotis. Its halo is made up of mud and altered rocks and considered to be a product of the explosive cycle of 1887 (Martelli 1917). The inner walls below consist of altered and highly fractured rhyodacite. *Photo* V. Dietrich

addition to the morphologically and historically well-documented craters, traces of older craters occur in the flats at the southern end of the Lakki plain.

The names of the craters were given by A. Rallis who started a commercial exploitation of sulfur in 1879 and built an enrichment plant with a small harbour at Aghia Irini on the south coast (Economakis and de Vries 2001).

The sedimentary deposits of all craters (local debris and lacustrine deposits) indicate that they resulted from hydrothermal explosions of steam and gases, accompanied by mud, solidified older lavas and pyroclastics without fresh magmatic components. A crude distribution of the surface hydrothermal alteration is given in Fig. 5.7.

All deposits exhibit similar mineralogical and chemical characteristics. The clayey to sandy white to yellowish matrix consists of variable amounts of clay minerals, such as illite/kaolinite/montmorillonite mixtures, gypsum, sulphur and iron oxide/hydroxide. The lithic ejecta, mainly lava blocks of variable composition, size, shape, and alteration generally show brown-reddish coatings of hydrous iron oxides, which seem to be a result of leaching (likely Fe, Mn) from the host rock by sulphuric acid, derived from the photo-oxidation of hydrogen sulphide with ambient air. Larger blocks are often fractured and healed with gypsum crystals.

In most cases, the block/matrix ratio is very low, whereas the amount of blocks does not exceed 20–30%. The situation of the youngest ejecta, from Polyvotis and Flegethron craters (1871–1873) shows that the most of the blocks have been transported laterally and secondarily deposited by later debris flows during heavy rainstorms.

A certain sequential chronology of the explosive craters has been given on the basis of their morphological preservation and relative stratigraphy of the lacustrine deposits (Principe 1989).

5.3.3.1 The Kaminakia Craters

The two crescent shaped hydrothermal craters, the **Kaminakia Craters** (Figs. 5.12 and 5.13), are carved into the base of the southeastern caldera walls with a diameter of about 150 m each and partly filled with debris from the caldera cliffs and with explosive ejecta from Stefanos crater. The craters are breached, partly eroded and open towards the Lakki plain. The fumarolic activity in the crater walls is still present and linked to a NE-trending fracture, which seems to be offset from the most dominant NE-SW fault zone passing through the Stefanos crater.

The age of the Kaminakia craters is unknown, most probably they represent an earlier stage of the entire hydrothermal explosive system.

5.3.3.2 The Stefanos Crater

The elliptical (260 × 350 m) **Stefanos Crater**, having a maximum depth of 27 m, is the largest crater of the hydrothermal field (Figs. 5.14, 5.15 and 5.16) of unknown age, but probably prehistoric according to its morphologically well preserved shape. Its shape seems to be a result of two major NE trending active faults marked by an alignment of fumarolic vents (Fig. 5.24). This crater marks the northeast extension of an older completely filled crater close to the foot of the southern caldera cliffs.

The 27 m high stratigraphic succession of the Stefanos crater is best exposed in the eastern cliffs and consists of several diagnostic units from bottom to top (Fig. 5.15):

1. up to 5 m of dark gray, black and green highly altered andesitic lava;
2. 1–3 m mafic argillic epiclastics, which plunge down towards the northwest; It terminates with a sharp reddish erosional contact;
3. 0.5–1 m fine laminated light pink argillitic layers pinching out towards the north;
4. 5–8 m whitish layered, fine grained lacustrine unit, consisting of varved layers alternating with argillic epiclastics;
5. 1–2 m compact white unit, which turns reddish toward the south with an increased thickness up to 4 m. This unit has probably been produced during the explosion of the Kaminakia craters; this unit is rich in sulfur deposits and leaks sulfuric waters through irregular fissures and cracks, in particular from its lower contacts;
6. up to 5 m light greenish-layered unit, spotted with large blocks of several m size. This unit consists of the deposits from the eruption of Stefanos itself. The sandy matrix is rich in

Fig. 5.24 Fumarolic vents along NE-SW fractures on the Stefanos crater floor along the foot of the eastern walls with temperatures close to 100 °C; situation spring 2002. *Photo* V. Dietrich

gypsum, while anhydrite veins occur in the lava blocks;

7. a 1–3 m greenish, white and orange triple unit of fine-grained argillic to sandy layers which may have been produced during the explosions of the Polyvotis craters.

5.3.3.3 The Lofos Hydrothermal Area

The Lofos hydrothermal area comprises a complex field of several explosive hydrothermal craters within the lower southeastern flanks of the Profitis Ilias rhyodacitic domes, and the crest of the small Lofos dome, and seems to be aligned along a series of NE trending faults.

The oldest crater of this area is **Logothetis** at the western flank of Lofos dome, since it is partly filled with ejecta from the 1871–1873 and 1887 explosions from the **Flegethron** and **Polyvotis** craters (Figs. 5.16, 5.17, 5.18 and 5.19). Towards the south, the Logothetis crater wall is breached and destroyed.

The small, elliptically shaped **Ahilleas crater** (Fig. 5.18) crater marks the northern border of the Lofos hydrothermal area and is located north of Megalos Polyvotis. Two other unnamed small craters just south of Ahilleas also penetrate the rhyodacitic talus of Profitis Ilias dome and the altered lava of Lofos dome. Several meters of Megalos Polyvotis ejecta cover the slopes of the rhyodacite domes next to Ahilleas crater. However, no eruptive hydrothermal material was found inside the Ahilleas crater. Therefore, the Ahilleas explosive event occurred prior to the Megalos Polyvotis eruption but probably after the Polyvotis-Flegethron 1871–1873 eruptions.

The early and strongest hydrothermal explosive cycle of the Lofos area produced the elliptical (180 × 350 m) **Megalos Polyvotis** crater (Fig. 5.20). Its 3–5 m thick ejecta are partly covered by Flegethron products, which originated from a later event. The Megalos Polyvotis material consists of altered lava fragments and rhyodacitic blocks in a clayey to sandy matrix. The lava blocks are rimmed by brown-reddish oxide coatings and crosscut by anhydrite veins.

The crater walls reveal a 15–20 m layered succession of diagenetic whitish to yellowish lacustrine sediments at the base, which are overlain by few meters of unconsolidated dark clayey material. The upper part consists of 8–10 m chaotic ejecta, made up of altered lava fragments and rhyodacitic detritus within a clayey to sandy matrix mixed with sulfur and gypsum. The western part of the crater floor often turns into a lake after a rainstorm and consists of 1.5 m thick yellow and purple colored varved diatomaceous clayey layers (background in the picture). The eastern part of the crater floor (foreground in Fig. 5.20) is filled with local sandy conglomerates and talus.

The large elliptical **Flegethron** crater (Figs. 5.21 and 5.28) occupies the southeastern flank of Lofos dome and morphologically intersects the southern crest of Megalos Polyvotis at a wall, which consists of altered rhyodacite of the Lofos dome. Towards the southwest, following the direction of the major NE-SW fault system, the crater is collapsed and partly filled with its own debris. The ejecta are similar to those of Megalos Polyvotis and consist mainly of rhyodacitic lava fragments from Lofos dome. The floor of the southern part is covered with lacustrine sediments.

The **Mikros Polyvotis** crater with a floor diameter of 30 m is the youngest hydrothermal crater of the Lofos area, intersects the eastern rim of Megalos Polyvotis, and is the result of the 1887 explosion (Figs. 5.22 and 5.23).

5.3.4 Fumarolic Activity 1997–2014

Fumarolic vents are often aligned along NE-SW fractures (e.g., on the Stefanos crater floor along the eastern and western foot of the crater walls, and in the Kaminakia and Flegethron craters, Fig. 5.6) discharging steam and gases at outlet temperatures from 96 to 100 °C. Degassing and steaming mud pools are present in the central parts of Stefanos and Polyvotis craters. They vary in size, from a few centimeters to a meter in diameter and are the result of boiling and steam from the uppermost level of the upper hydrothermal cell. Their activity is dependent on seasonal rainfall and humidity (Figs. 5.24, 5.25, 5.26, 5.27 and 5.28). Main components of the fumarolic discharges are H_2O

Fig. 5.25 Diffuse fumaroles with sulfur deposits at the southeastern floor of Stefanos crater; situation spring 2002. *Photo* © Tobias Schorr, Nature Discovery Tours

Fig. 5.26 Typical opening of a fumarole covered by fresh sulfur (*yellow*) and gypsum (*white*) crystals (Stefanos crater); width of picture is 10 cm. *Photo* V. Dietrich

Fig. 5.27 Sulfur cascades from fumaroles at the southeastern floor of Kaminakia crater; situation spring 2002. *Photo* Barry' Ramblings

Fig. 5.28 Flegethron (Alexandros syn.) hydrothermal explosion crater of 1873. Situation early morning after a rainstorm on a summer day in 2002. The fumarolic activity is well visible by the steam escaping from its upper rim. *Photo* V. Dietrich

Fig. 5.29 The floor of Stefanos crater with its mud pools during springtime after a rainstorm. *Photo* © Tobias Schorr, Nature Discovery Tours

followed by CO_2 and H_2S; N_2, H_2, CH_4, CO, Ar, and He are minor components (Chiodini et al. 1993a; Dietrich et al. 1998; Brombach et al. 2003). The lack of acid gases such as SO_2, HCl, and HF, and the relatively high CH_4/CO ratios indicate that fumarolic gases are generated from a boiling hydrothermal liquid rather than directly from magma degassing. The boiling muddy waters are close to the $H_2SO_4^- – SO_4^{2-}$ buffer with a pH between 1.5 and 3 (Fig. 5.30).

Another type of fumaroles is bound to disseminated channels and fissures within the walls and rims of the craters (Figs. 5.25 and 5.28), as well as along major fracture zones. The gases with temperatures of a few degrees below or close to 100 °C are also rich in H_2O, CO_2, H_2,

Fig. 5.30 Mud pool at the floor of Stefanos crater. The boiling mud has a temperature close to 100 °C at a pH between 1.5 and 3. Diameter of the pool approx. 1 m; October 2002. *Photo* V. Dietrich

Fig. 5.31 Mud pools encrusted with deposits of sulfur, iron oxides, gypsum and salt. Stefanos crater floor eastern side; during active period 2000–2002. *Photo* V. Dietrich

H_2S, and CH_4. They seem to originate from the deeper parts of the hydrothermal system.

5.3.5 Mud Pools

During the winter and spring seasons, the floors of the hydrothermal craters are covered with water from seasonal rainstorms, often forming internal lakes. In areas of floor weakness and along hidden fractures, bubbling acidic mud pools with water temperatures close to 100 °C and a pH between 1.5 and 3 develop (Figs. 5.29, 5.30, 5.31 and 5.32). During the summer season, the floors get very dry and hard, whereas during winter, early spring and late fall the conditions of the floor can vary from mud to a lake. At these stages the instability of the ground and possible breakdowns of mud pools will become very hazardous and the entrance to the floors should be closed to the public.

Fig. 5.32 Dry mud pools in Stefanos crater floor partly covered with sulfur, gypsum, and other salts; late fall 2000. *Photo* V. Dietrich

During the few years following the seismic crisis of 1996–1998 the fumarolic and boiling activity seemed to have increased, marked by large encrustations in the mud pool fields with sulfur, iron oxides, gypsum and salt (Figs. 5.31 and 5.32).

5.3.6 Geothermal Wells Nis-1 and Nis-2

Geothermal exploration by Geotermica Italiana started in 1983 and continued in 1984. Two wells Nis-1 and Nis-2 were drilled in the southern part of the Lakki plain north of the hydrothermal explosion craters. All activities had to be stopped due to overheating and overpressure on drilling equipment and high steam production in well Nis-1, as well as to boiling effects and pipe sealing with salt deposits.

The Nis-1 well crossed carbonate sedimentary rocks from a depth of 691 m down to 1350 m, whereas the Nis-2 well did not encounter this carbonate sequence, which indicates that the caldera underwent a deeper collapse than the peripheral area (Fig. 5.33). Both drillings stopped in quartz-dioritic subintrusives and contact thermometamorphic rocks, the latter being completely transformed by conductive heat transfer of cooling magmatic bodies from composite magma reservoirs at different depth, as well as from convective fluids from deep reservoirs.

Both wells passed through a shallow and a deeper permeable zone (Fig. 5.33). The shallow permeable sequence is thicker in well Nis-1 (400–700 m depth) than in the Nis-2 well (250–350 m depth). A detailed division into metamorphic mineral zones has been suggested by Ambrosio et al. (2010).

Nis-1 well

0–300 m depth—Argillic Zone: Clay minerals with transitional appearance of chlorite in the deeper parts (temperature range of 120–150 °C);
300–800 m—Phyllitic–Chlorite Zone: Chlorite associated with chalcedony, quartz, sericite and zeolites, as well as with pyrite, anhydrite and carbonates (temperature range of 150–200 °C). The abundance of chlorite in the Nis-1 well may be explained by rock-sea water interaction, indicating that the peripheral zone of the caldera has been affected by seawater inflow;
801–1485 m depth—Hydrothermal Zone: Hydrothermal minerals only as vein paragenesis in carbonates, mainly pyrite and anhydrite (inferred temperature range of 150–200 °C);
1486–1790 m depth—Propylitic Zone: Characterised by abundance of epidote, adularia, albite,

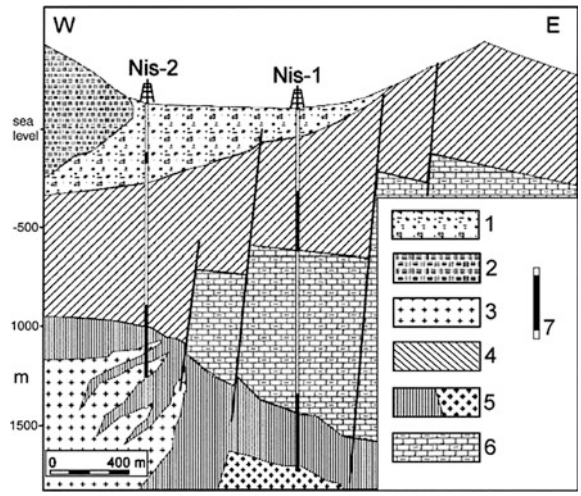

Fig. 5.33 NW-SE cross-section through Nis-1 and Nis-2 geothermal wells 1983/84 in the Lakki plain, from Geothermica Italiana (1984) and Marinelli et al. (1983), modified after Marini et al. (1993) and Caliro et al. (2005). *Symbols 1* Talus, alluvial debris and lacustrine filling of the Lakki plain; *2* Post-caldera dacitic-rhyodacitic domes; *3* Subintrusive quartzdiorite; *4* Andesitic to dacitic tephra and lavas; *5* Diorite and contact metamorphic rocks related to composite magma reservoirs; *6* Carbonate rocks and contact metamorphic marbles; *7* Permeable intervals in geothermal wells

tremolite, arsenopyrite and pyrrhotite with minor amounts of scapolite, brucite, stilpnomelane, quartz, arsenopyrite, pyrite, zeolites (wairakite?) and garnet. The appearance of augite at 1680 m marks the transition from the propylitic zone to a contact metamorphic zone. It seems that the pyroxene composition changes with increasing depth from augite to Fe-hedenbergite (temperature range 230–300 °C);

1791–1816 m depth (well bottom)—High K_2O Propylitic Zone: Stable biotite and absence of epidote and tremolite as the typical assemblage >300 °C.

Nis-2 well

0–90 m depth—Argillic Zone: Characterized by kaolinite and montmorillonite;

90–200 m—Argillic–Phyllitic Zone: Appearance of sericite and chlorite and progressive disappearance of clay minerals (temperatures <120 °C);

200–730 m depth—Phyllitic–Zeolitic Zone: Presence of sericite and less abundant chlorite. Zeolites are widespread in the upper part of the zone (above 480 m), while quartz, pyrite, anhydrite and carbonates are common throughout the zone (temperature range of 120–180 °C);

730–950 m depth—Phyllitic–Propylitic Zone: Appearance of microcrystalline epidote marks the transition from the phyllitic to the propylitic zone. Albite-sericite and more abundant chlorite-epidote are typical assemblages (temperature range 180–230 °C);

950–1547 m depth (well bottom)—Propylitic Zone: Well-crystallised epidote, adularia, albite, quartz, pyrite, chlorite, sericite–muscovite and minor amounts of anhydrite, stilpnomelane, wairakite, garnet, tremolite and pyroxene with temperature range 230–300 °C.

From 1360 to 1530 m the drilled section did not provide a significant hydrothermal mineral paragenesis, probably due to low permeability.

5.3.7 Thermal Springs

In addition to the hydrothermal crater field in the Lakki plain, other important discharge areas are present in the hot springs along the coast of the island with temperatures up to 60 °C (at Avlaki, Fig. 5.34). In historical times, nine hot springs are known along the coast of Nisyros (Fig. 5.1).

Fig. 5.34 Avlaki's old thermal bath, destroyed by southern winter storms and earthquakes. The thermal spring marks the steep westward dipping N-S fault. *Photo* V. Dietrich

Fig. 5.35 Preparation of sampling of Avlaki spring water in front of the old bath house, at sea level. *Photo* V. Dietrich

The thermal waters can be grouped into two types (Chiodini et al. 1993a; Sect. 5.4.7, Table 5.2):

(A) Waters characterized by a very high chloride content between 18,000 and 22,000 mg/L, representing a binary mixture of deep geothermal water and sea water with a minor component of meteoric water (Figs. 5.35, 5.36, 5.37, 5.38, 5.39 and 5.40) and (B) waters with a chloride concentration up to 14,000 mg/L,

Fig. 5.36 The Avlaki thermal spring at sea level. The high saline thermal waters have a recognizable outflow only at low tide and have the highest temperature of surface thermal water on Nisyros Island, up to 60 °C (1997–2003); salinity 25.2 g/kg. *Photo* V. Dietrich

Fig. 5.37 Avlaki thermal spring at sea level. Note the evaporation of salt. *Photo* V. Dietrich

Fig. 5.38 Thermal spring at Lefkos beach half a meter above high-tide sea level. High salinity and pH at 6.5 with rather constant temperatures at 46–52 °C. Green algae coating; salinity 30.7 g/kg. *Photo* V. Dietrich

Fig. 5.39 Thermal spring at sea level 50 m west of Cape Katsouni (or Faros). The hydrothermal water has a high salinity close to seawater with a pH of 6.8–7.1 and temperatures between 40 and 45 °C, subject to seasonal variation. Surrounding andesitic lavas are coated with iron oxides, *whitish* suspension of salt. *Photo* V. Dietrich

Fig. 5.40 Historical spring in the cave of Panaghia Thermiani east of Pali at the northeastern coast. The input of thermal waters with temperatures of approx. 26 °C has been cut off when the modern bath house projects were constructed (1885–1912). The bath activities have been documented back to Roman times. An ancient inscription found nearby records the existence of an earlier Greek "Hippocratic" bath in the area. *Photo* V. Dietrich

produced by mixing of deep geothermal and meteoric water.

The chemical composition (major, trace elements, isotopes, ions) and physical characteristics of the thermal waters are listed in the official GEOWARN reports and in articles by Chiodini et al. (1993a), Kavouridis et al. (1999), Chiodini et al. (2002), Brombach 2000, Brombach et al. (2003) and in Table 5.2. A review of the water composition and its origin is given in Sect. 5.4.7.

5.3.8 Submarine Gas Emissions

Besides local hot springs, which appear at intersections of radial faults from the volcano with regional tectonic faults, bordering the coasts, disperse emission of gases occur along the coasts (Fig. 5.1) mainly consisting CO_2, H_2S, H_2 and CH_4. Examples are at Cape Katsouni and along the northeast coast from Cape Katsouni to Lies, as seen in Figs. 5.41, 5.42, 5.43 and 5.44.

Diffuse gas emissions also occur along the northern coast between Mandraki port and Pali, between Lies and the bay of Pachia Ammos, as well as between Lefkos cove and Avlaki along the southern coast. All localities are easily recognizable due to milky and cloudy waters with higher ambient temperature, bare yellowish bottoms covered with sulfur-rich bacteria colonies, and randomly distributed gas emissions. The typical marine flora and fauna of the euphotic zone is absent.

Fig. 5.41 Fracture N160° parallel to the coast between Plomos and Louros Karanas (south of Cape Katsouni). In many places the bottom is covered with sulfur and sulfur-rich bacteria colonies. *Photo* V. Dietrich

Fig. 5.42 Gas emissions of CO_2, H_2S, H_2 and CH_4 on the seafloor at Louros Karanas (east coast); the rocks are covered with iron oxides, algae and sulfur-rich bacteria; July 29, 2011. *Photo* V. Dietrich

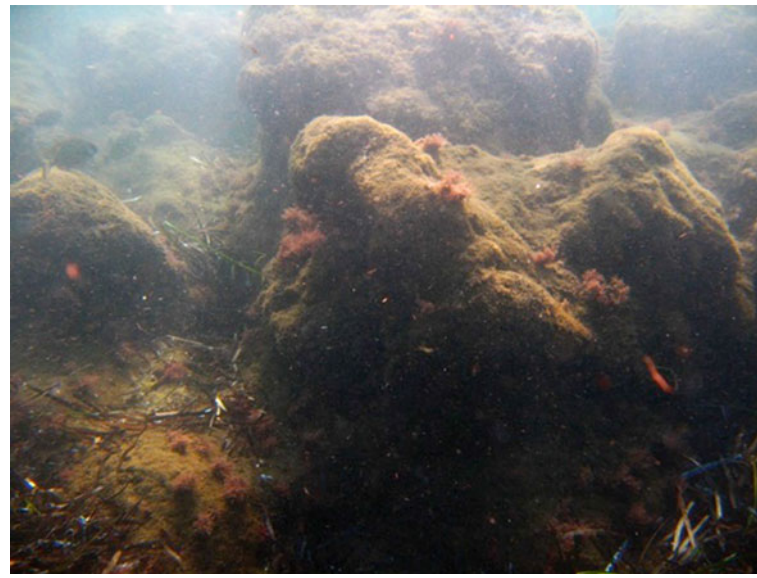

Fig. 5.43 Diffuse gas emission at shallow sea floor close to Faros spring (Cape Katsouni); milky waters with high salinity and low oxygen content causing special bottom seaweed, red algae and sulfur-rich bacteria; July 3, 2011. *Photo* V. Dietrich

Fig. 5.44 Gas emissions of CO_2, H_2S, H_2 and CH_4 on the seafloor at Lies (east coast); anaerobic environment, the bottom is covered with sulfur-rich bacteria; July 29, 2011. *Photo* V. Dietrich

5.4 Fluid Geochemistry of the Hydrothermal System

5.4.1 Introduction

Geochemical investigations of the hydrothermal system of Nisyros volcano started at the beginning of the seventies (Bencini et al. 1981). In 1973, the Greek Energy Authority (PPC) and the Greek Institute of Mining and Exploration (IGME) started a geothermal project to generate electrical power. For the purpose of exploration, two deep wells, Nis-1 and Nis-2 (Fig. 5.45), were drilled inside the caldera and proved to be productive, confirming the existence of a high-enthalpy geothermal reservoir with fluid temperatures above 300 °C (Geotermica Italiana 1983, 1984).

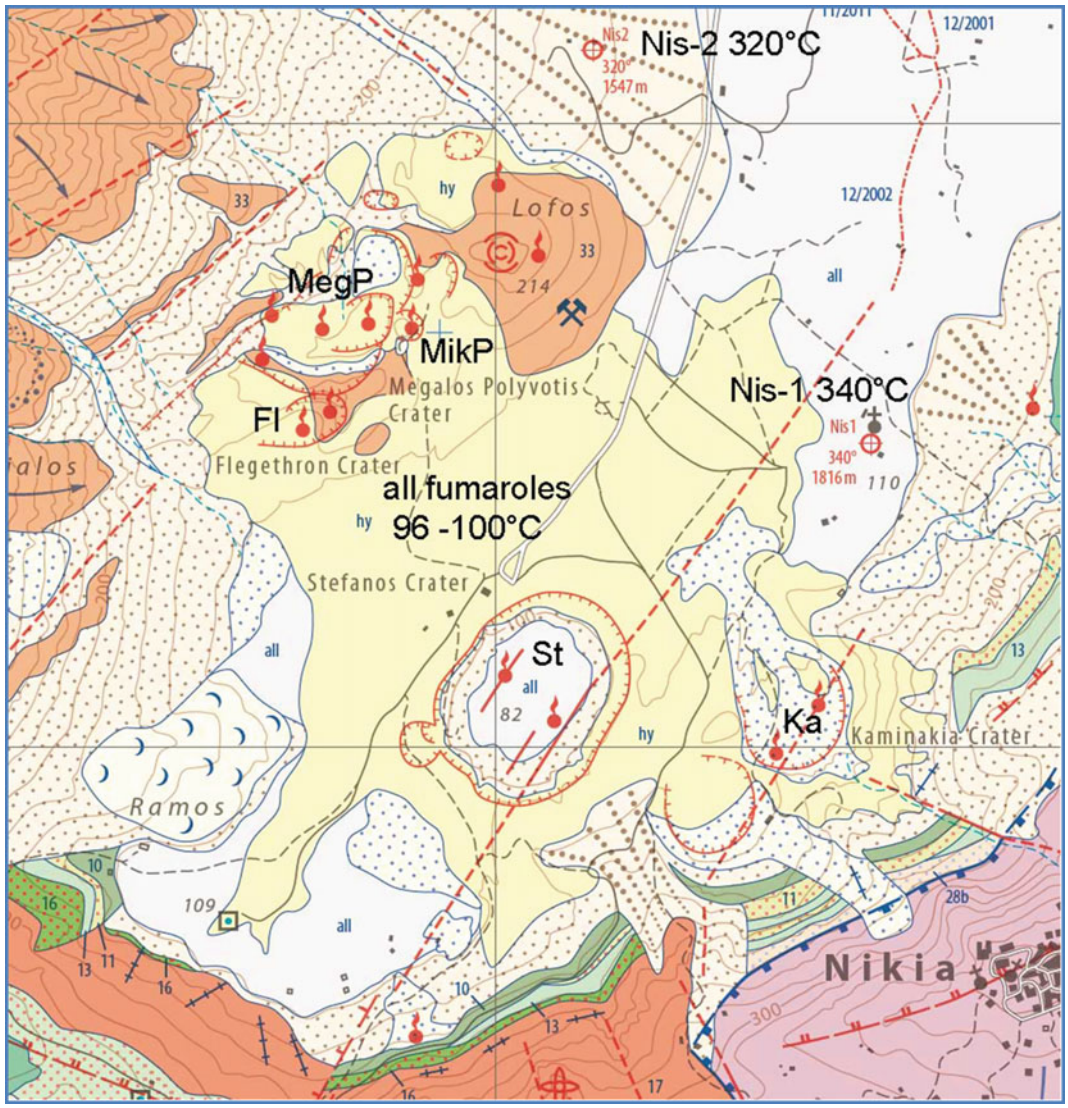

Fig. 5.45 Fumarole location map in the hydrothermal field of Nisyros caldera with hydrothermal explosion craters and geothermal wells; excerpt from the Geological Map of Nisyros Island (Dodecanese Archipelago); Dietrich (2017), this volume as electronic supplementary material of Chap. 3

Detailed geochemical investigations of the entire hydrothermal system followed, with the aim of evaluating the risk of new explosions as a consequence of drilling failure due to overheating and steam production (Chiodini et al. 1993a; Marini et al. 1993). A first hydrochemical model of Nisyros using chemical analyses of fumarolic gases and thermal waters was developed by Chiodini et al. 1993a. During the following years, numerous geochemical investigations related to the fluids of the magmatic-hydrothermal system were undertaken: Minissale et al. 1997; Dietrich et al. 1998; Kavouridis et al. 1999; Brombach 2000; Brombach et al. 2001; Panichi et al. 2000; Panichi and La Ruffa 2001; Chiodini et al. 2002; Marini et al. 2002; Cardellini et al. 2003; Brombach et al. 2003; Fiebig et al. 2004; Shimizu et al. 2005; Caliro et al. 2005; Marini and Fiebig 2005; Dotsika et al. 2006, 2009; Ambrosio et al. 2010; Fiebig et al. 2007, 2009, 2013.

5.4.2 Geochemical Monitoring of Nisyros Volcano

Active volcanoes pose an ongoing threat to populations and infrastructure. The assessment and prediction of their next period of unrest requires an understanding of subsurface processes and of their changes. Unfortunately, the subsurface characteristics of actively degassing volcanoes that have strong hydrothermal systems are hidden from direct observation. Hydrothermal activity complicates and often masks the identification and interpretation of "deep" magmatic signals that may indicate a reactivation of a dormant volcano, possibly followed by an eruption (e.g., Fischer et al. 1996). Fortunately, surface emissions of gas (fumaroles, diffuse degassing, and vent degassing) and thermal water (hot springs, seeps and pools) can be assessed and monitored to permit a better understanding of subsurface processes, and to gauge the significance and criticality of evolving geochemical signals. Short term monitoring and research studies have been conducted over the past three decades on Nisyros (e.g. GEOWARN 2003; Kinvig et al. 2010), however it has not been consistently monitored by a continuous real-time autonomous monitoring network and detailed surveillance. Following the Nisyros seismic crisis in 1996 and 1997, significant changes in the chemical and isotopic composition from Nisyros fumarolic gases and waters were recognized in the years 1997–2001.

The interpretation of evolving geochemical monitoring data must be based on a detailed, meaningful geochemical model of the subsurface hydrothermal-magmatic system. To this aim, the measurement of both intensive variables (chemical and isotopic composition of the fluids circulating in the volcanic system) and extensive parameters (flux of fluids and energy) is required, in as best a geometric context as is possible from spatial measurements, geophysical data, reasoning, and geothermometry/geobarometry.

Typical questions regarding the geochemistry of fluids in active volcanic systems are:

- What is the origin of the fluids discharged by fumaroles, thermal springs and diffuse degassing structures?
- What are the temperature-pressure conditions of the hydrothermal system?
- What is the amount of fluid and thermal energy discharged by volcanoes through hydrothermal activity?

These questions not only help to understand the nature of the hydrothermal system and the contribution from magmatic degassing, but also aid in assessing the potential for future eruption precursors. For example, hydrothermal system drying-out events often precede magmatic reactivation of an active volcano, and a detailed geochemical model enables to discern and detect renewed magmatic gas signatures from benign signals of hydrothermal cycles.

In the previous sections, the physical features of the Nisyros hydrothermal system visible at the surface were described. In the following sections, the surface measurements of fumaroles, diffuse gas emissions and thermal springs will be described. This enables an understanding of the processes and reservoirs acting at depth, resulting in a geochemical model with its principal components.

5.4.3 Gas Emission Point Sources: Fumaroles and Their Gas Geochemistry

Nisyros fumaroles are commonly subdivided into three sets based on their locations on the caldera floor's *Lakki* plain, indicated by acronyms (Fig. 5.45): (a) the fumaroles of the *Stefanos* Stefanos crater (St), (b) the fumaroles of the *Lofos* dome area, including the vents discharging in the craters of *Megalos Polyvotis* (MegP), *Mikros Polyvotis* (MikP) and *Flegethron* (Fl), and (c) the fumaroles of the *Kaminakia* craters (Ka). All fumaroles discharge at temperatures close to the boiling point of pure water at 1 bar pressure (96–100 °C). Fumarolic activity and the

location of the hydrothermal craters are spatially related to a prominent system of parallel SW-NE striking active faults (Marini et al. 1993; Papadopoulos et al. 1998). The faults act as pathways for gases and vapor, those at the westernmost NE-SW faults discharging at the Lofos dome area, and the easternmost NE-SW faults feeding the Kaminakia fumaroles. Less obvious in the field is a buried NE-SW fault, which aligns with the Stefanos fumaroles and has recently been revealed by a detailed diffuse carbon dioxide (CO_2) flux survey (GEOWARN 2003). Figure 5.45 shows the location of the fumaroles and associated structural features.

5.4.4 Origin of Major Gas Constituents and Inert Gases

Fumarolic gas emissions on Nisyros are dominated by water vapor (H_2O) followed by CO_2 and hydrogen sulfide (H_2S). Minor components are nitrogen (N_2), hydrogen (H_2), methane (CH_4), carbon monoxide (CO), argon (Ar), and helium (He). Strongly acidic magmatic components like sulfur dioxide (SO_2), hydrogen chloride (HCl), and hydrogen fluoride (HF) are absent, and the relative contents of CH_4, CO and H_2 ratios are typical for gaseous emissions from hydrothermal-geothermal environments (Chiodini et al. 1993b). The presence of H_2S indicates that the magmatic gas component has undergone slow cooling, since the transformation of SO_2 to H_2S is kinetically slow (Symonds et al. 1994).

Gas geochemical studies of Nisyros fumaroles before 1993 mainly concentrated on establishing the geochemical model of the hydrothermal-magmatic system. These studies largely used subsurface data acquired from two deep geothermal wells drilled in the early 1980s (Fig. 5.33). The presence of hydrothermal reservoirs at depth was confirmed throughout two geothermal drilling campaigns. Both wells discharged aqueous solutions of high salinities, with Cl concentrations up 81,500 mg/kg for the Nis-1 well. Maximum temperatures of 340 and 320 °C were measured at the bottom of Nis-1 and Nis-2 wells, respectively.

Generally, there are multiple sources that can contribute to overall gas production in subduction related volcanic environments. These are the mantel, the overlying crust, the subducted crust and hydrothermal fluids occurring superimposed to the magma. Gas concentration and stable isotope data on the fumarolic discharges can help to identify to what extent these distinct sources are involved in gas generation.

5.4.4.1 The Origin of Fumarolic Water Vapor

The stable isotope compositions of the fumaroles, thermal springs and geothermal brines (Nis-2 well, Dotsika 1992) are shown in the δD versus $\delta^{18}O$ diagram (Fig. 5.46) together with reference compositions of local seawater, the local meteoric water field, and the global meteoric water line.

Isotopic signatures of the fumarolic gases revealed the significant involvement of a magmatic component in the Nisyros hydrothermal system. According to Chiodini et al. (2002) and Brombach et al. (2003), the parent geothermal liquid (MEGPL), which manifests itself through boiling effects in the fumaroles of Nisyros, is a mixture of sea water and an 'andesitic' magmatic water typical of volcanic systems in convergent plate regimes. The estimated δD and $\delta^{18}O$ values of the MEGPL feeding the Stefanos and Mikros Polyvotis crater fumaroles are $-11 \pm 5‰$ and $+4.9 \pm 0.5‰$ versus V-SMOW, respectively, indicating a high fraction of magmatic water (70%). The vents of the Flegethron, Megalos Polyvotis, and Kaminakia area receive a smaller contribution of magmatic gases. Their parent geothermal liquid has a composition similar to that of the Nis-2 well. Consistent with this geochemical evidence is the conclusion that they are situated on the margins of the main upflow zone. Some of the fumarolic vents of Flegethron and Kaminakia are heavily affected by mixing with shallow ground waters and/or condensation, which is likely due to the relatively small input of deep fluids.

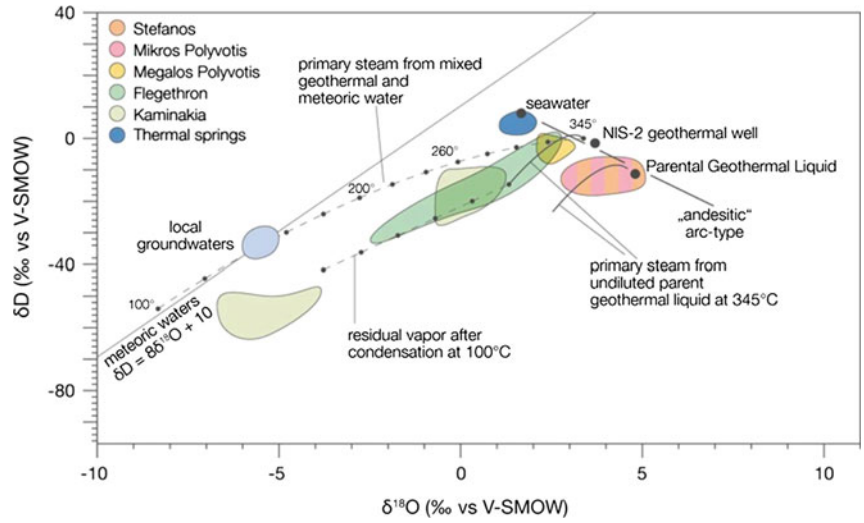

Fig. 5.46 Variation of the δD and $\delta^{18}O$ values of water vapor in fumarolic gases, thermal waters, and seawater from Nisyros. The composition of local groundwater and arc-type magmatic waters is taken from Kavouridis et al. (1999) and Giggenbach (1992), respectively. The isotopic composition of vapors formed through boiling of the undiluted and groundwater-diluted Nis-2 geothermal liquid (T_o = 345 °C), with separation temperatures marked by *small circles*, is also shown (Giggenbach and Stewart 1982). Composition of the vapor that separated a fraction of condensed steam at 100 °C is given for a vapor separated at 100 °C from the Nis-2 geothermal liquid (Brombach et al. 2001). *V-SMOW* standard Vienna Mean Ocean Water

5.4.4.2 The Origin of H_2S

The $\delta^{34}S$ values of H_2S in fumarolic gases vary between +2.5 and +5.1‰ versus CDT (Cañon Diablo troilite standard), while the $\delta^{34}S$ values of total S in thermal waters range from +16.8 to +19.7‰ versus CDT and are close to the local seawater value, +19.8‰ versus CDT (Fig. 5.47).

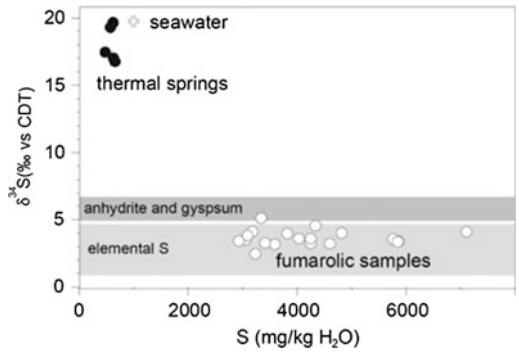

Fig. 5.47 Variation of $\delta^{34}S$ and elemental sulfur content for the thermal waters, fumaroles and seawater of Nisyros Island. The $\delta^{34}S$ composition of elemental sulfur and sulfate minerals is also shown; figure from GEOWARN (2003)

$\delta^{34}S$ values similar to the fumaroles were measured for the sulfate minerals (+4.8 to +6.7‰ vs. CDT) and elemental sulfur sampled in the Lakki plane (+1 to +4.3‰ vs. CDT).

According to Marini et al. (2002), the relatively low values of elemental sulfur, sulfate minerals and fumaroles is consistent with a degassing rhyodacitic magma with a $\delta^{34}S$ value of +6.3 ± 1.5‰ versus CDT. In contrast, the $\delta^{34}S$ values of total sulfur in thermal waters indicate a large involvement of a seawater component in these thermal waters. The slightly lower $\delta^{34}S$ values of the springs with respect to seawater agree with the input of $\delta^{34}S$-poor vapour condensates from the hydrothermal crater area.

5.4.4.3 The Origin of Heliuma

The $^3He/^4He$ values, expressed as R/Ra (ratio of $^3He/^4He$ in the sample and of average air), ranges from atmospheric values (~1) to a more magmatic or mantle value of ~6. The data in Fig. 5.48, compared to the $^4He/^{20}Ne$ ratios, indicate that the samples are mixtures between an

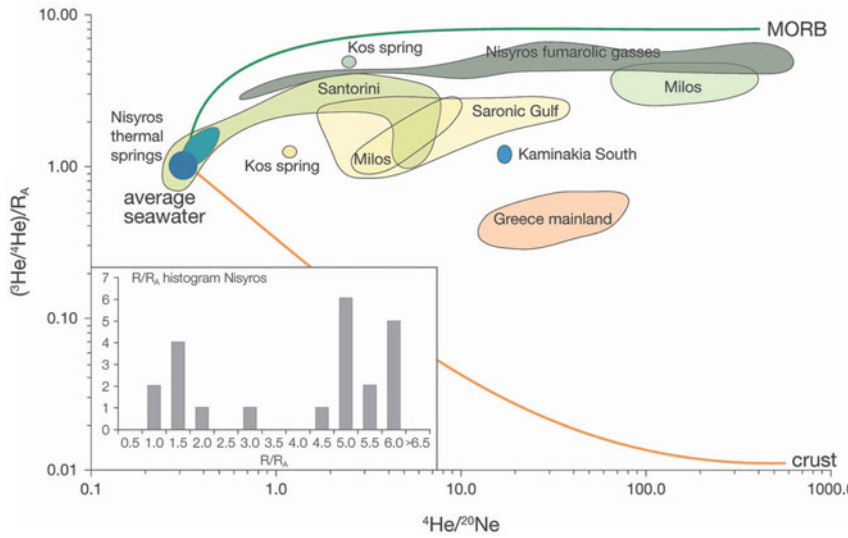

Fig. 5.48 R/Ra versus $^4He/^{20}Ne$ diagram for Nisyros and Kos manifestations. The field occupied by the samples from other sites of Greece are reported as reference. *ASW* air saturated groundwater and seawater; figure from GEOWARN (2003)

air component (e.g. air saturated groundwater) and a mantle derived (magmatic) component, characterised by an R/Ra value of −6. This value is the highest R/Ra measured in gas samples from the Aegean arc volcanism (Dietrich et al. 1998; GEOWARN 2003; Shimizu et al. 2005). The figure inset shows a histogram of all Nisyros R/Ra values, which indicates a bimodal distribution. The lower R/Ra group is dominated by the thermal springs and emissions from Kaminakia, while the higher group indicates the Lofos and Stefanos fumarolic gases, which have a higher mantle component. However, in the timespan 2008–2015 the fumarolic R/Ra values from Kaminakia did not differ significantly from the higher values of Stefanos, Mikros Polyvotis and Flegethron (INGV-database, W. d'Alessandro 2016, personal communication). Therefore, the lower values of Kaminakia must have been contaminated with ambient air during sampling.

Figure 5.49 shows a compilation of Nisyros fumarolic gases in a ternary N_2-Ar–He plot, available from Marini and Fiebig (2005), with an extensive discussion on the origin of noble gases Ar and He. The gases show unusually low N_2/He ratios for arc-related volcanic scenarios and more closely resemble crustal and upper oceanic mantle decompression derived volatiles (N-MORB). On the one hand, Nisyros is considered to be the most geodynamic part of the *Active Aegean Volcanic Arc* and therefore slab-derived fluids are expected to dominate the gas chemistry. The unusual N-MORB-like patterns of gases stand in interesting context with the high heat flow extensional regime of the Aegean flooded and thinned continental crust, which likely is underlain by an upwelling mantle (Kassaras et al. 2005; Komut et al. 2012). The low N_2/He ratios of the gases are consistent with the hypothesis that organic matter may not be involved in overall gas production. In this respect, both the subducted slab and the hydrothermal system could be largely devoid of sedimentary organic matter (Brombach et al. 2003). Alternatively, sufficient extensional decompression causing formation of partial melts by tectonic decompression could lead to volatiles significantly enriched in He without much slab-derived recycled N_2 (e.g. Gomez-Tuena et al. 2007; Mattioli et al. 2016).

5.4.4.4 The Origin of CO_2

Measurements of $\delta^{13}C$ on fumarolic gases of the hydrothermal explosion craters Stefanos,

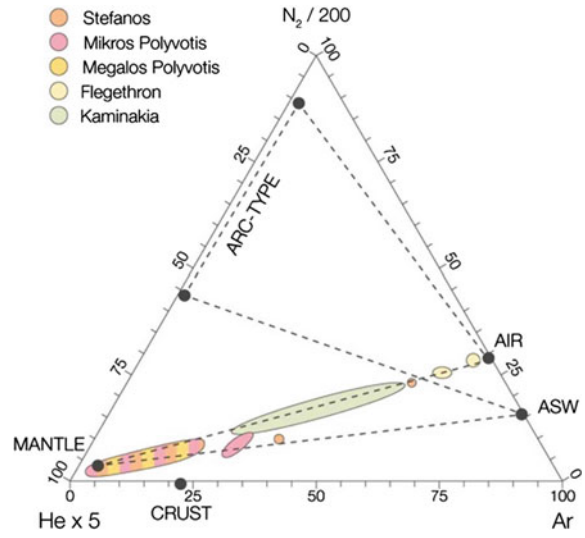

Fig. 5.49 Ternary plot of He, N_2, and Ar compositions of Nisyros fumarolic gases and end member compositions; figure modified after Marini and Fiebig (2005). *ASW* air saturated water

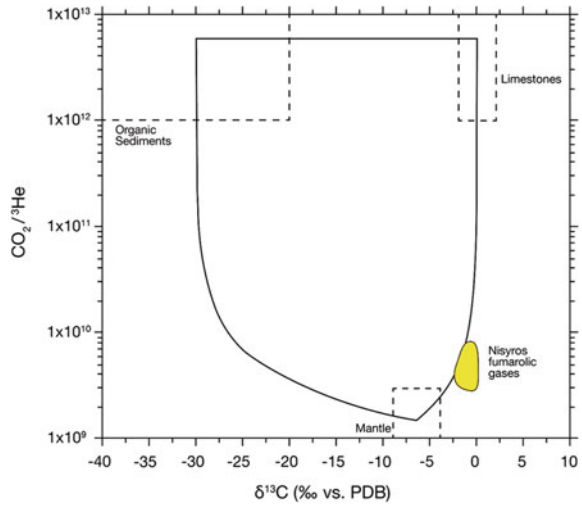

Fig. 5.50 Correlation diagram between $CO_2/^3He$ ratios and $\delta^{13}C$ values of the fumaroles of the Nisyros hydrothermal system. According to Sano and Marty (1995), this plot shows the characteristics of the three main CO_2 sources present in subduction zones (mantle, organic sediments, and marine limestones). Mixing curves characteristic for binary mixtures are shown for comparison. *DPB* Pee Dee Belemnite Vienna standard; figure modified after Marini and Fiebig (2005)

Megalos Polyvotis, Mikros Polyvotis, Flegethron and Kaminakia have been carried out since 1991 (Kavouridis et al. 1999; Panichi et al. 2000) with the goal to evaluate the origin of the discharged CO_2. Several sampling campaigns followed, especially after the seismic crisis 1995–1998 and continued up to 2014. The spread of the data varies from average values of -2.3 ± 0.4 (1 σ) ‰ versus V-PDB before the crisis, to -0.6 ± 0.5 (1 σ) ‰ versus V-PDB in September 2000 (not shown in a diagram). The reason for this variation, which might be due to analytical procedures, has been discussed extensively by Marini and Fiebig (2005). The correlation diagram (Fig. 5.50) therefore shows only the gases collected and analysed by Fiebig et al. (2004), since

the He isotope ratio and the $\delta^{13}C_{CO_2}$ values were both measured on the same samples.

$CO_2/^3He$ ratios and $\delta^{13}C_{CO_2}$ values imply that the evolved CO_2 either derives from a metasomatised mantle or is a mixture between two components; one outgassing from an unaltered mantle and the other released by thermal breakdown of Mesozoic limestones and Neogene marls of the deeper underground. In both cases, ca. 25% of the total CO_2 may derive from the mantle, whereas ca. 75% would derive from marine carbonates.

5.4.5 Hydrothermal Reservoirs

5.4.5.1 Direct Temperature Measurements

Subsurface information (Nis-1 and Nis-2 wells) on the distribution of the permeability and the temperature with depth (Fig. 5.51a, b), and on the hydrothermal mineral paragenesis indicate that at least two distinct hydrothermal reservoirs are present underneath the Lakki plain. The shallower zone (400–700 m depth in Nis-1 well, and 300–500 m depth in Nis-2 well) is a phyllitic-zeolitic hydrothermal mineral paragenesis revealing temperatures of 120–180 °C, while at 1400–1816 m depth in Nis-1 and at 1000–1500 m depth in Nis-2 well, a high temperature propylitic hydrothermal mineral assemblage occurs. Temperatures higher than 290 °C were measured in the deeper permeable zone of the Nis-2 well while temperatures of 330–340 °C were measured in the deeper productive level of the Nis-1 well, where brines having 81.5 g/L of Cl were sampled (Chiodini et al. 1993a).

The deep aquifer, located more than 900 m below sea level, contains Na–Cl saline brines (Cl > 50 g/l, Table 5.2). Direct measurements showed temperatures higher than 320 and 340 °C at the Nis-2 and Nis-1 wells, respectively (Fig. 5.51a, b).

5.4.5.2 Geothermometry Based on Gas-Gas Equilibria

Chiodini and Marini (1998) analyzed emissions from wells around the globe and concluded that hydrothermal temperatures at depth are reasonably well reflected by the H_2O–H_2–CO_2–CH_4–CO geoindicator. Application of this geothermometer presumes that H_2O, H_2, CO_2, CH and CO have attained overall equilibrium at depth, and that it is highly sensitive to CO concentrations. In addition, it can be used to identify the fraction of steam that has been separated from the liquid through boiling. To better understand the boiling conditions of the deep hydrothermal aquifer, a CO based geothermometric evaluation within the H_2O–H_2–CO_2–CH_4–CO gas system (Chiodini and Marini 1998), was investigated by Chiodini et al. (2002)(Fig. 5.52a, b). The results in Fig. 5.52a indicate an apparent overall equilibrium temperature between 180 and 320 °C, focused around 200–260 °C, below those measured during geothermal well testing (Sigurdsson

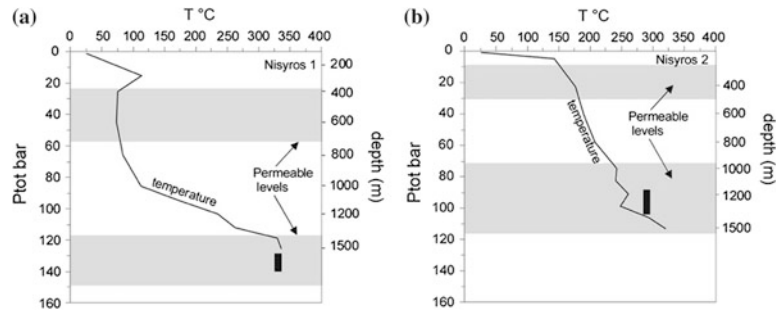

Fig. 5.51 Static P, T profiles of the deep geothermal wells Nis-1 (**a**) and Nis-2 (**b**). The figures show the location of the two permeable zones encountered during drilling operation. The *black rectangles* refer to the P-T equilibrium condition of the C–O–H gas system of the steam discharged by the two wells (Geotermica Italiana 1983, 1984); figure from GEOWARN (2003).

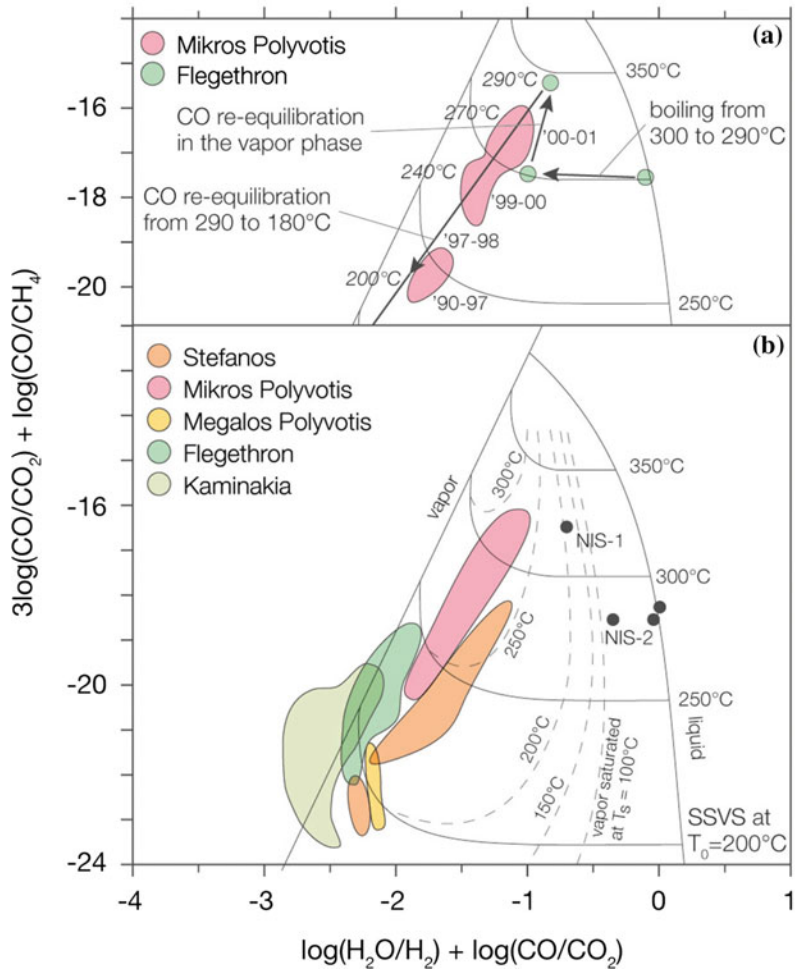

Fig. 5.52 CO geothermometry (Chiodini and Marini 1998) for Nisyros fumarolic gases; figure modified after Chiodini et al. (2002). **a** The equilibrium values in a single saturated vapor phase and in a single saturated liquid phase are given by the vapor line and liquid line, respectively. The SSVS curves refer to isenthalpic *single-step vapor separation* at different separation temperatures, from a single liquid phase of initial (equilibrium) temperature T_o. Filled circles show well samples (Nis-1 and Nis-2). **b** The same plot, for gas samples from Mikros Polyvotis crater only. The CO re-equilibration line was computed by assuming re-equilibration of CO in a single vapor phase at decreasing temperatures, from 290 to 150 °C, and constant concentrations of H_2O, H_2, CO_2, and CH_4 (Chiodini et al. 2002). The initial temperature of the liquid phase was taken equal to 300 °C

1985, 1986). This could imply that CO equilibrates at higher levels within intermediate reservoirs, either in the vapor phase or after being dissolved in a shallower aquifer. Carbon monoxide is known to re-equilibrate readily in high temperature fumarolic gases (Giggenbach 1987; Chiodini et al. 1993b). In Fig. 5.52a, the Stefanos and Lofos dome fumaroles follow somewhat differing trends. Chiodini et al. (2002) expected that here CO has re-equilibrated in the vapor phase upon cooling at nearly constant concentrations of the other gas species.

Fiebig et al. (2004, 2007, 2013) analyzed the carbon isotopic composition of CH_4 contained in the fumaroles (Fig. 5.53). They observed that the apparent carbon isotopic temperature of 340 ± 20 °C derived from carbon isotope partitioning between CO_2 and CH_4 agrees very well

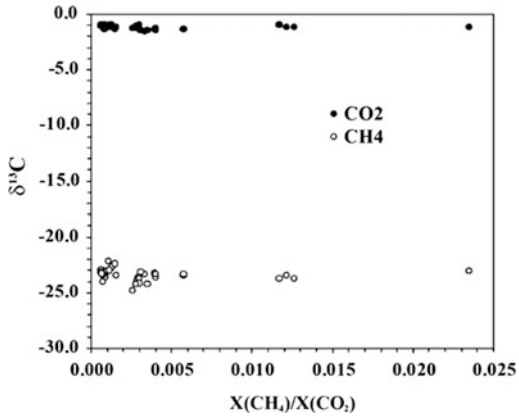

Fig. 5.53 ^{13}C isotopic composition of CO_2 and CH_4 of Nisyros fumaroles The analytical data show an almost constant composition with $\delta^{13}C_{CH4}$ and $\delta^{13}C_{CO2}$ of almost −23‰ and of −1‰, respectively, for all the fumaroles independently of their location (Fig. 5.61). These values give C isotopic equilibration temperatures from 320 to 360 °C, close to the highest temperatures measured in the Nis-1 and Nis-2 geothermal wells; figure from GEOWARN (2003)

with the highest temperatures measured at the bottom of the Nis-1 well. In addition, this temperature coincides with the highest temperatures that were indicated by the H_2O–H_2–CO_2–CH_4–CO geothermometer and is in agreement with propene/propane concentration ratios detected in Nisyros fumaroles. Vesuvius and Ischia represent other examples where the apparent carbon isotopic CH_4–CO_2 temperatures were confirmed by the H_2O–H_2–CO_2–CH_4–CO geoindicator, although the carbon isotopic composition of methane varies by up to 15‰ between these locations. These findings could imply that the CH_4–CO_2 carbon isotope geothermometer can provide reliable information about hydrothermal reservoir temperatures at depths.

5.4.5.3 A Dynamically Changing System in Time

The fumarolic gas composition on Nisyros underwent large changes in the period 1990–2001, especially after the 1996–1997 seismic crisis. In Fig. 5.52b (Chiodini et al. 2002) only data of Mikros Polyvotis fumaroles are shown. Here, the authors calculated a single step vapor phase separation at 290 °C at an initial temperature of 300 °C, allowing the CO content to subsequently re-equilibrate between 290 and 180 °C. The most plausible explanation according to Chiodini et al. (2002) is an increase in the re-equilibration temperature from 210 °C, in 1990–1997, to temperatures as high as 270 °C, after the 1996–1997 seismic crisis (1997–2001). On a mechanistic level, Chiodini et al. (2002) invoked two alternative processes that may explain such temporal trends: (1) A decreasing transit time of gases from the deep hydrothermal reservoir to their surface discharge and/or (2) heating up of the upflow channels or the intermediate reservoirs.

These significant variations of H_2O, CO_2, H_2S, and CH_4 are shown in both the H_2O–CO_2–H_2S ternary plot (Fig. 5.54) and in the H_2S/CO_2 versus CH_4/CO_2 scatter plot (Fig. 5.55), where two well-defined convergent trends are depicted: one trend for the *Stephanos* (St) fumaroles, and the other for the three vent areas *Megalos Polyvotis*, *Mikros Polyvotis* and *Flegethron* (MegP-MikP-Fl). In September 2001, these two trends intersect (Fig. 5.55), indicating a common chemical composition of all the fumaroles. A trend toward this chemical homogenization was recognizable from 1997 onwards. In particular, in 1990–1991 fumaroles in both crater groups (St and MegP-MikP-Fl) had H_2S/CO_2 ratios of 0.2 and 0.13, respectively. Since 1997, a progressive increase in the H_2S/CO_2 ratios was observed and values of 0.33 and 0.38 (for St and MegP-MikP-Fl, respectively) were measured in September 2001. A simultaneous opposite trend was traced by the CH_4/CO_2 ratio, decreasing from 0.006 and 0.004, in 1990 (for St and MegP-MikP-Fl, respectively), to 0.001 in 2001 (Fig. 5.55).

The simultaneous increase of the H_2S/CO_2 ratio with a concurrent decrease in the CH_4/CO_2 ratio of gases from fumaroles at St and MegP-MikP-Fl has two possible explanations. A first hypothesis implies that the observed variations were caused by an increasing steam fraction separated from a deep boiling hydrothermal aquifer, producing diverging ratios due to the solubility differences of H_2S, CO_2, and CH_4. The increasing steam fraction was related to either an increasing temperature of the

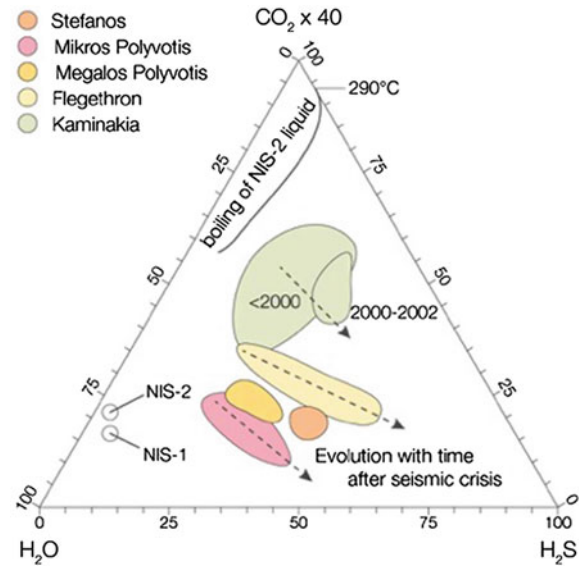

Fig. 5.54 Changes of fumarolic gas compositions in the Nisyros hydrothermal explosion craters during the period 1990–2001, using the ternary plot H_2O–CO_2–H_2S; figure modified after Marini and Fiebig (2005)

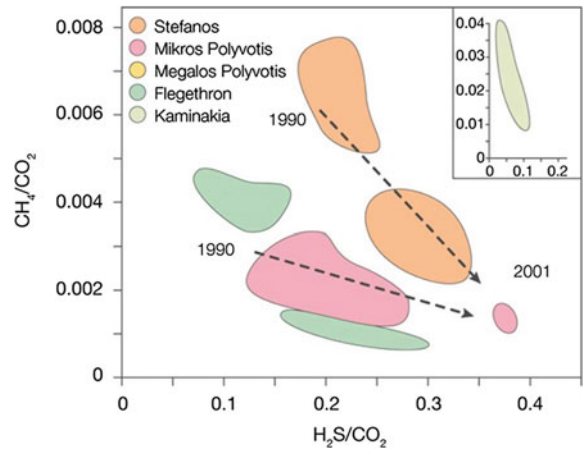

Fig. 5.55 Time variation scatterplot for ratios of CH_4/CO_2, versus H_2S/CO_2; figure modified after Chiodini et al. (2002)

hydrothermal aquifer (heating only), or by depressurization of the system (opening of additional conduits above the aquifer), or both. This interpretation is supported by the principles of progressive boiling in a confined aquifer: Gas species with low solubility preferentially partition into the early separated vapor phase, while gas species of lower solubility partition into late vapors (Giggenbach 1997). The analytical data do not fully confirm this first interpretation: less soluble gases should co-evolve with time, but this is only seen for CH_4, whereas the behavior of the inert species N_2 and He, which were relatively invariant during the study period, was not consistent with this mechanism. The second explanation relates the gas ratios to magma degassing. The Showa-Shinzan dome, Usu volcano, Japan is a good example in comparison, which is a system fairly well constrained by long-term monitoring, where fumaroles are directly fed by a shallow degassing magma batch (Symonds et al. 1996). Here, a relative decrease in soluble SO_2 has been observed over time, while halogens remained constant. C/S and S/Cl ratios decreased from 1954 to 1985, indicating progressive outgassing of the less soluble

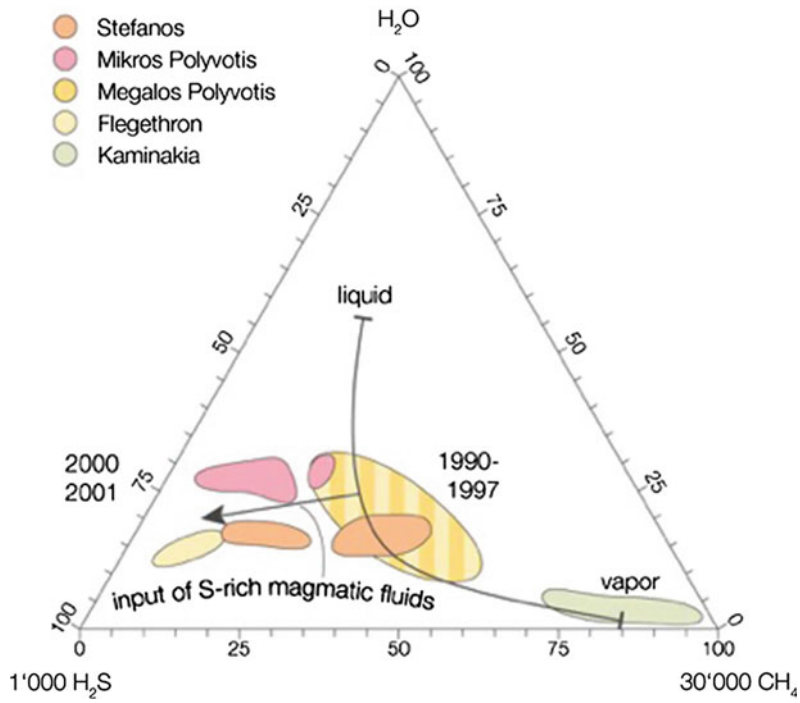

Fig. 5.56 Change of fumarolic gas compositions in the ternary plot of H_2O-H_2S-CH_4. See text for the explanation of the boiling curve; figure modified after Chiodini et al. (2002)

components from magma. While CO_2 and He are the earliest gases released from a cooling or decompressing magma, their gas fraction remains fairly constant in ascending gas as it cools, while the acid gases decrease with progressive cooling (Symonds et al. 1994, 1996). Soluble acid gases are also preferentially removed by subsurface scrubbing, consisting of precipitation, reaction and dissolution processes (Symonds et al. 2001). Consequently, an increasing C/S ratio often heralds the arrival of a fresh batch of a less degassed basaltic component, i.e. a newly arrived batch of basaltic magma from greater depths (Symonds et al. 2001; Cannata et al. 2010; Werner et al. 2012), and increases in SO_2 closely prior to eruptions (Sparks 2003).

At Nisyros, this interpretation is unlike because of its strong hydrothermal system situated between the degassing magma and the surface, during quiescent periods. A period of magmatic reactivation might have occurred from 1990 to 2001, indicated by seismic activity and ground deformation coupled with changes in gas chemistry toward more sulfur gases and more oxidizing conditions (e.g., Zolotov and Shock 2000). It is conceivable that the Nisyros hydrothermal system experienced a progressively increasing input of a magmatic component. In the ternary diagram H_2O–H_2S–CH_4 (Fig. 5.56), the fumarolic gas compositions are put in context of a theoretical boiling curve, computed assuming that the liquid phase is at 300 °C in equilibrium with a pure vapor phase of the composition of the Kaminakia fumaroles. Among the Nisyros gas samples, the Kaminakia samples are the most enriched in less soluble gases (i.e., the most residual in composition).

Chiodini et al. (2001) used vapor-liquid distribution coefficients for a 2 molar NaCl solution to represent saline brines in the Nisyros hydrothermal system. A single-step vapor separation process was computationally simulated, resulting in stepwise separated vapor compositions. This computational model result does not provide a unique answer, since many possible-boiling paths can be postulated for the Nisyros hydrothermal system. However, we deem it sufficiently probable and use it as reference in this discussion. Figure 5.52a indicates that the 1997 fumarolic gas compositions can be

explained by a simple boiling process of a singular liquid composition. In contrast, the 2000–2001 samples deviate significantly from the theoretical boiling curve and are enriched in H_2S, which is consistent with the hypothesis of a progressively increasing input of a sulfur-rich magmatic component. An increasing magmatic component, somewhat masked by hydrothermal processing, would also bring with it more oxidized magmatic carbon and lead to a lesser abundance of processed carbon in the form of CH_4, as is indeed observed at Nisyros. A very well studied example of such patterns is the Solfatara volcano fumaroles (Italy), which has a strong hydrothermal system, similar to Nisyros. In that case, the input of magmatic gases into the hydrothermal system best explains the decrease in the C/S ratio observed before and during the bradyseismic crisis of 1982–84 (e.g., Cioni et al. 1984, 1989; Martini 1986; Chiodini et al. 1996a), which stands in contrast to volcanic systems with less hydrothermal masking, where the C/S ratio increases prior to intense activity (e.g., Werner et al. 2012). CH_4 is the only reduced gas species at Nisyros that decreases with time. Other reduced species remained constant or increased: H_2 at all Lofos dome gases, and CO temporarily spiked after the 1996–1998 seismic crises and then increased gradually for the Stefanos and Mikros Polyvotis gases (Figs. 5.52, 5.53, 5.54, 5.55 and 5.56). Two interpretations might explain the different behavior of CH_4 relative to H_2 and CO: (i) CO and H_2 are less affected by changes in redox conditions than CH_4 and (ii) CO and H_2 fugacities are mainly controlled by temperature (Chiodini and Marini 1998). The increase in H_2 and CO with time could be explained by increasing temperatures at depth, consistent with an increasing influence of magmatic fluids on the hydrothermal system. H_2 and especially CO can also be subject to re-equilibration processes during the ascent of hydrothermal gases towards the surface.

An increase in $^3He/^4He$ ratio was also observed in 1997 (Dietrich et al. 1998) after the intense seismic crisis (Fig. 5.57). During the period from 1995 to 1998, shallow seismic activity was intense around Nisyros Island with a maximum in 1996 (Stavrakakis and Papoulia 1998). Until 1997 the He-isotope ratio was rather constant between 5.5 and 5.75 and increased by 0.5 Ra and more to a maximum of 6.25 in 1999 (Shimizu et al. 2005). Such an increase of mantle helium could be attributed to an increased contribution of magmatic fluids to the hydrothermal system. Similarly, an increase in $^3He/^4He$ ratios was also observed after the eruptions at Izu–Oshima volcano (Japan) by Sano et al. (1991) and at Unzen volcano (Japan) by Notsu et al. (2001) and repeatedly before the eruptions at Mt. Etna (Italy) by Paonita et al. (2016).

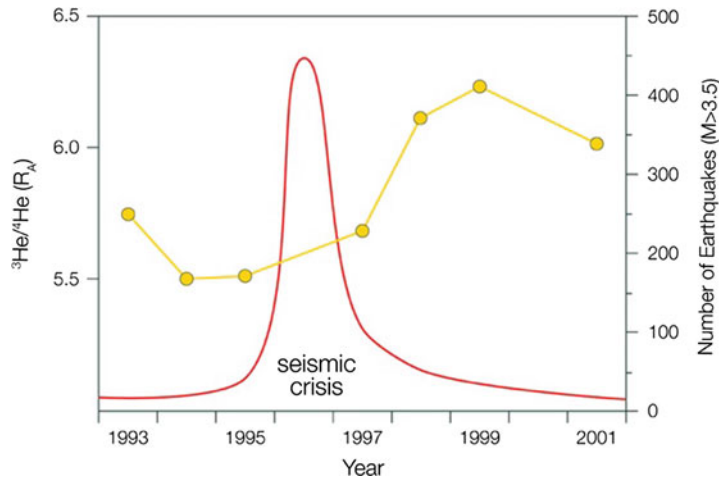

Fig. 5.57 Temporal variation in $^3He/^4He$ ratio of gas samples (*yellow points*) from Nisyros volcano (Dietrich et al. 1998; Shimizu et al. 2005). The number of micro earthquakes (*red curve*) occurring in the proximity of the volcano each year is from Stavrakakis and Papoulia (1998)

5.4.5.4 Conclusion

- All the chemical changes recorded in Nisyros fumarolic gases during the ten-year period 1990–2000 are likely controlled by increasing magmatic fluid and heat contributions to the hydrothermal system. This magmatic component was characterized by relatively high contents of sulfur gases (SO_2 and H_2S) and relatively highly oxidizing conditions. The expected increasing temperatures of the hydrothermal reservoir were confirmed by a concurrent increase of the H_2S/CO_2 ratios and H_2 contents, and decrease of the CH_4/CO_2 ratios.
- CO-based geothermometry indicates lower equilibrium temperatures than CH_4-based geo-indicators, which is attributed to re-equilibration of ascending cooling CO, and possibly by the residence of these gases in secondary, intermediate level reservoir(s). At the Mikros Polyvotis fumaroles, a decreasing trend of CO concentrations was observed, likely related to a decreasing transfer rate of the gases from the hydrothermal reservoir to the surface (fumaroles) and/or to the influence of intermediate reservoirs.
- The increasing magmatic contribution to the recharge of the hydrothermal system shown by the fumarolic gas chemistry has important implications for volcanic surveillance and eruption forecasting. At Nisyros, the last volcanic activity probably took place more than 20,000 years ago (see Geochronology, Sect. 3.5 this volume), most probably leaving behind a residual magma batch at intermediate to shallow crustal depth, subsequently affected by cooling and degassing, giving rise to the hydrothermal system beneath the island.

Frequent hydrothermal eruptions have historically occurred, suggesting that rejuvenating activity is likely. The last hydrothermal events took place in 1871–1873 from the craters of Stefanos, Megalos Polyvotis, and Flegethron and in 1887 from the crater of Mikros Polyvotis (Marini et al. 1993 and references therein). Based on historical chronicles, it seems likely that seismic shocks played a fundamental role in triggering these hydrothermal eruptions (Marini et al. 1993). Earthquakes would have been responsible for fracture opening, favoring the uprising of deep hot fluids to the surface, and/or allowing magma ascent from deeper crustal levels. Similarly, the seismic crisis of 1996–1997 could have caused opening of fractures below the hydrothermal reservoir that received inputs of magmatic fluids. The increased temperature and pressure conditions at depth suggest that the hazard of hydrothermal eruptions is higher at present than in the 1990s. In addition, hydrothermal eruptions have affected this system, possibly acting as precursors of magmatic eruptions, as occurred on the island of Montserrat, Lesser Antilles (Chiodini et al. 1996b) and Guagua Pichincha, Ecuador (Marini et al. 1991).

5.4.6 Gas Emission Area Sources: Diffuse Degassing Structures (DDS)

Upwelling of CO_2 gas and vapour to the soil-air interface result in steam condensation, which is an exothermic process causing the soil to heat up. As a result, large zones of altered terrains have been developed in the areas surrounding the historical hydrothermal explosion craters, within these craters, and along faults (see Sect. 5.3.1; Fig. 5.7).

5.4.6.1 CO_2 Flux

A quantification of the vapour involved in the shallow condensation process, and the mapping of the areas currently affected by the emission of the deep fluid, was approached by performing dedicated campaigns of soil CO_2 fluxes, i.e. by measuring the flux of CO_2 emitted in the Lakki plain through diffuse degassing structures (DDS, Figs. 5.58, 5.59, 5.60). Measurements of soil CO_2 degassing were carried out using the accumulation chamber method (Chiodini et al. 1996a; Chiodini and Marini 1998; Farrar et al. 1995) during the summers of 1999, 2000 and 2001

(Fig. 5.58). Each campaign measured CO_2 flux, heat flux and soil temperature in 80–100 measuring points, regularly spaced at 20 m intervals. Detailed results of each campaign, performed during the GEOWARN project are documented in the final report (GEOWARN 2003). These results have subsequently been reevaluated and refined by Caliro et al. (2005), in order to investigate the structural features controlling the degassing process. A detailed map of the soil CO_2 flux at the Lakki plain (Figs. 5.58, 5.59) has been obtained using 2884 measurements, by applying a sequential Gaussian simulation algorithm (Cardellini et al. 2003).

In general, at hydrothermal sites such as the Lakki plain, the distribution of soil CO_2 fluxes results from two carbon sources: biological activity in the shallow soil, and a deeper, geogenic hydrothermal source. At the Lakki plain, the local biological background CO_2 flux has been established to be 8 g m^{-2} day^{-1} by Cardellini et al. (2003).

In Fig. 5.59, the areas where the simulated values are higher than 3 times the background are highlighted by the colors green, yellow, and red. These areas represent the actual pattern of hydrothermal degassing at the Lakki Plain. Comparison of the CO_2 flux map with the tectonic and volcanic features of the area suggest that geogenic CO_2 is released by:

(a) The hydrothermal craters of the Lofos dome (Flegethron, Megalos Polyvotis), Stefanos and Kaminakia craters;

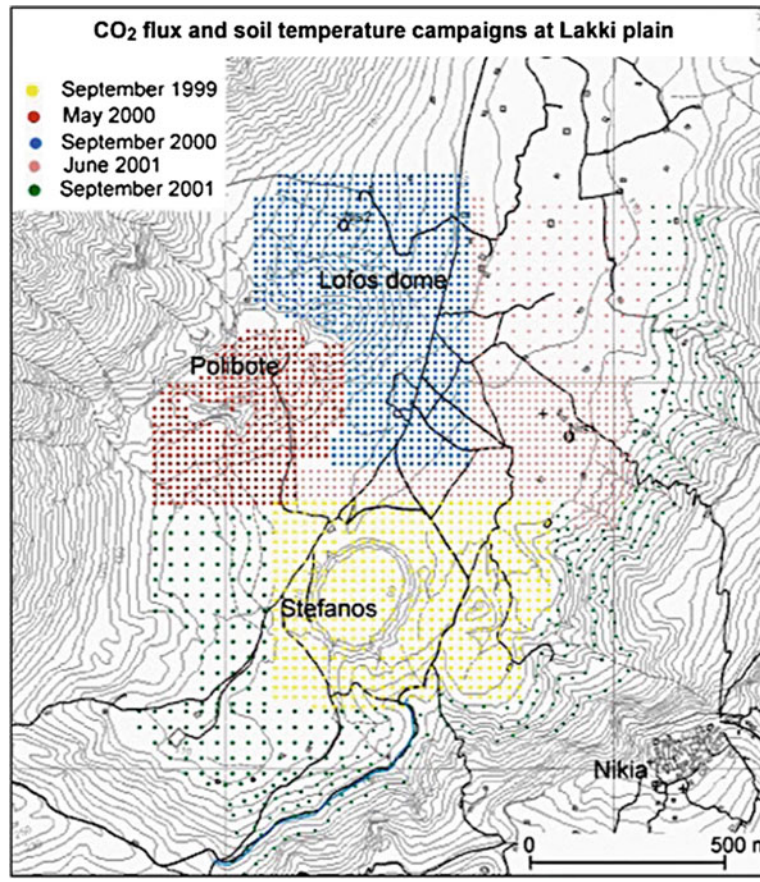

Fig. 5.58 Location of the CO_2 flux and soil temperature measurement points. The different *colors* refer to the different campaigns performed during the GEOWARN project 1999–2001 (GEOWARN 2003)

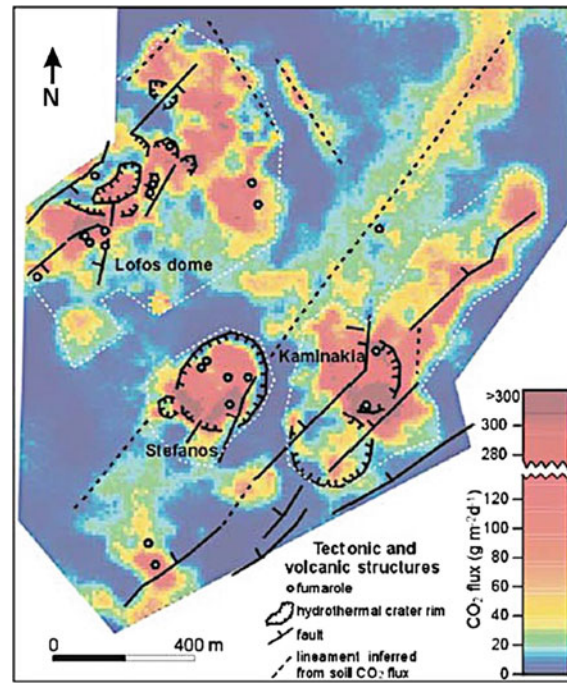

Fig. 5.59 Map of CO_2 flux at Lakki Plain. The map is the result of 300 stochastic simulations performed over a simulation grid formed by 21,000, 100 × 100 m square cells. The colors *green*, *yellow* and *red* characterize the areas where the simulated values are larger than 3 times the background fluxes, thus highlighting the actual pattern of hydrothermal degassing at the Lakki Plain (GEOWARN 2003)

(b) The NE-SW faults affecting the Lakki Plain, in particular the NE-SW fault extending from the Kaminakia craters toward the NE;
(c) Buried tectonic structures generating elongated CO_2 anomalies in zones where field evidence of faults or fractures is lacking. One prominent 'invisible' structure is present in the central sector of the Lakki Plain, where a ~1 km long CO_2 anomaly evidently extends from the northern rim of Stefanos crater toward the NE. This anomaly departs from the Stefanos crater and propagates up to the Nis-1 well. This anomaly is the surface expression of a concentrated flux feature which coincides with a fracture or fault covered by caldera sediments. The southern tip of this structural discontinuity is probably the NE-SW striking fracture affecting the inner, eastern wall of the Stefanos crater;
(d) A NW-SE elongated CO_2 anomaly is also discernable. This anomaly propagates from the Nis-2 well into the central sector of the Lakki Plain. This anomaly likely also derives from faults buried by caldera sediments and otherwise invisible at the surface, and might coincide with the southern tip of the NW-SE striking fault that cross-cuts the Profitis Ilias domes (Fig. 5.1).

Further results of the stochastic simulation method include the total released CO_2 and its uncertainty (i.e. mean and standard deviation of the 300 simulations). The resulting total release is 84.6 ± 4.5 t/days of CO_2. Of this total CO_2 output, 67.9 t/days are released by the deep hydrothermal source, while 16.7 t/days are due to other background sources. The CO_2 anomaly is associated with the raising of a vapor phase, which condenses just beneath the surface (Fig. 5.60).

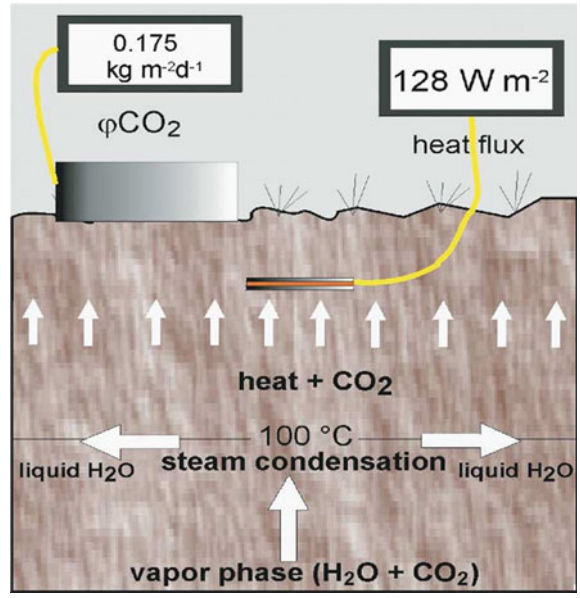

Fig. 5.60 Model of CO_2 diffuse degassing, heat flux and condensation of H_2O (GEOWARN 2003)

5.4.6.2 Loss of Thermal Energy

The fracture-bound release of CO_2 and near-surface condensation of the associated vapor phase released large amounts of thermal energy, which for the Lakki plain was estimated by Caliro et al. (2005). The surveyed area was divided into 4 domains (the Lofos dome, Stefanos crater, Kaminakia crater, and a combination of the other zones), where it was possible to compute the thermal release. The authors calculated a total of 1420 t/day of steam being condensed causing a total thermal energy flux of 42.6 MW (Table 5.1).

Approximately 75% of this thermal energy was released by the degassing structures of the Lofos dome (20.4 MW) and Stefanos crater (12.1 MW). The condensed steam produced in the process (~16 L/s) was most probably partially lost by surface evaporation in the craters, and feeds some forms of a shallow condensate aquifer which discharges at the numerous thermal springs located along the coastline of the island at temperatures between 36 and 62 °C. The chemical and isotopic composition of the thermal springs support this interpretation, which has been established to be the result of mixing of

Table 5.1 Total release of CO_2 and of thermal energy from the degassing structures of the Lakki plain

Area	Lofos dome	Stefanos	Kaminakia	Other areas	Total area
Area (km^2)	0.4	0.08	0.28	1.34	2.1
Total CO_2 (t/d)	26.4	11.8	28.2	18.2	84.6
Hydrothermal CO_2 (t/d)	23.2	11.2	25.9	7.5	67.8
CO_2/H_2O (fumaroles)	29.4	36	6.1	23.8[a]	23.8
Condensed steam (t/d)	681	403	158	178	1420
Thermal release MW	20.4	12.1	4.7	5.3	42.5

[a]Mean value of all the fumaroles of Lakki plain

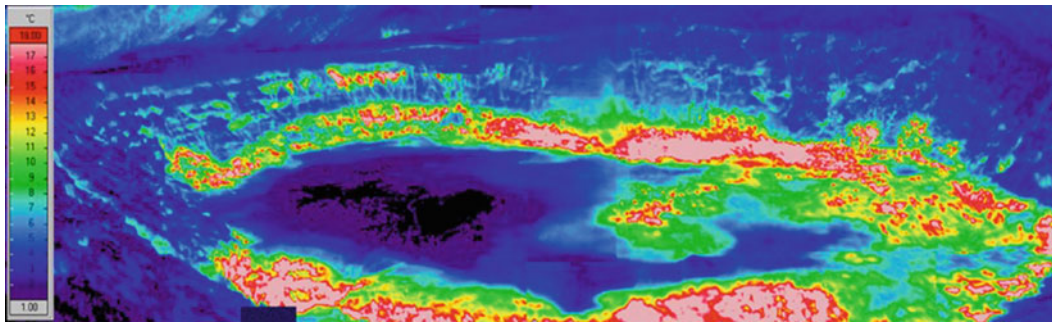

Fig. 5.61 Infrared image taken in the evening of May 2002 of the hot soils, mud pools, and fumaroles at the floor and in the walls of the Stefanos hydrothermal explosion crater; low temperature diffuse degassing and condensation in *green colors*; vertical temperature scale with a maximum temperature of 18 °C (GEOWARN 2003)

heated infiltrated seawater with minor amounts of steam condensates (Brombach et al. 2001, 2003; Brombach 2001).

Spectacular images of the heat released by the Diffuse Degassing Structures (DDS) in the Lakki plain were provided by Infrared images of the hot soils generated during the process of diffuse degassing and condensation. Figure 5.61 shows an example of the temperature anomalies at the DDS in Stefanos crater.

An imaging correlation between CO_2 flux and temperature from the hydrothermal craters in Nisyros is demonstrated in Fig. 5.62.

5.4.7 Chemistry of Thermal Waters

Since historical times hot springs have been known along the northern and southern coasts of the island (Fig. 5.1). A first comprehensive compilation of all Greek mineral and thermal waters has been given by Georgalas (1922 and 1962) followed by numerous compilations (e.g. Barnes et al. 1986; Minissale et al. 1997; Kavouridis et al. 1999; Fytikas et al. 2005; Dotsika et al. 2009; Lambrakis et al. 2014).

Thermal water outflow occurs along the northern, eastern and southern coasts of Nisyros Island, whereas it is absent along the uplifted

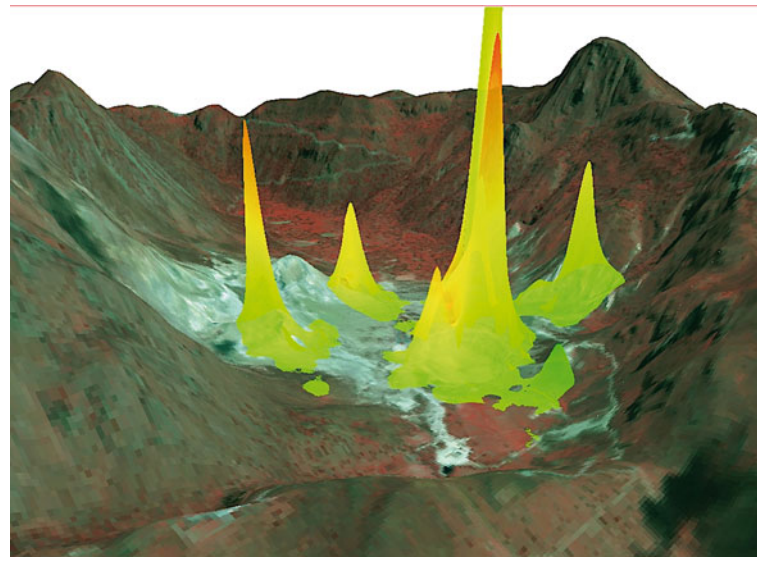

Fig. 5.62 The CO_2 flux (heights) and temperature (*colors*) correlation from the hydrothermal craters in Nisyros during a measuring campaign, combined with the orthorectified 3D IKONOS satellite image (GEOWARN 2003)

western coast. All thermal springs appear at sea level and are placed within fault zones and fractures. In contrast, there are several zones in front of the small alluvial deltas (e.g. along the east coast between Cape Katsouni and Lies) where cold meteoric waters from the island enter the sea.

The physical parameters of the major thermal springs (Loutra public bath, Pali spa/Panagia Thermiani, Faros (Cape Katsouni), Avlaki, Aghia Irini and Lefkos) are given in Table 5.2. It has to be noted that the physical parameters and the chemical composition of all spring waters do not reflect their proper values due to adverse sampling conditions. In general, for many of the water samples seawater infiltration could not be fully impeded. In addition, Table 5.2 contains the available sampling data of the major thermal springs over a time span of 28 years with time intervals up to 10 years. It shows that the chemical parameters for each spring vary little, while the temperatures and the pH show major variations. Apparent are the variations in Mg^{2+} and SO_4^{2-}, which can be attributed to mixing with stagnant seawater of high salinity close to the spring.

The chemistry of the thermal spring waters with outlet temperatures >30 °C, and those of the Nis-1 and Nis-2 wells, can be usefully represented by the SO_4–Cl–HCO_3 (Fig. 5.63) and (Na^++K^+)–Ca^{2+}–Mg^{2+} (Fig. 5.64) triangular Piper plots.

All waters have a sodium-chloride composition with temperatures ranging from 30 to 60 °C, pH values from 6.1 to 7.2, and high TDS (total dissolved solids) values ranging between 20,000 and 35,000 mg/L. They have Cl^- and Na^+ concentrations very close to seawater and are enriched in Ca^{2+} and HCO_3^- and slightly depleted in SO_4^{2+} and Mg^{2+} with respect to seawater, indicating high temperature seawater-rock interaction.

According to the main chemical-physical parameters, the Nisyros waters can be divided into three major types:

1. Thermal waters, which are characterized by a chloride content in the 18,000–22,000 mg/L range. These are essentially binary mixtures of geothermal water and seawater, with a possible minor percentage of meteoric water. This type includes the thermal springs of Avlaki, Lefkos, Faros (Cape Katsouni) and Pali spa, except for Pali Bath, at 37 °C. Significant contributions of a NH_4 and B-rich steam condensate were also recognized (Chiodini et al. 1993a).
2. Thermal waters with a chloride concentration between 9000 and 14,000 mg/L. These are essentially binary mixtures of geothermal water and groundwater, with a subordinate contribution of seawater that occurs in significant amounts in sample 10 only. This group comprises two IGME shallow boreholes and a spring near Pali. Temperatures range between 35 and 40 °C.
3. Cold waters characterized by a chloride content ranging from 200 to 5000 mg/L and temperatures between 17 and 23 °C. These are mixtures between groundwater and seawater, although a minor contribution of geothermal water cannot be ruled out.

The geothermal brine from the geothermal borehole of IGME shows similar concentration to those of seawater, but it shows relatively low concentrations of SO_4^{2-}, HCO_3^-, and Mg^{2+} and high concentration of Ca^{2+} with respect to local seawater. The decrease in Mg^{2+}, Ca^{2+}, SO_4^{2-} and HCO_3^- (e.g. in Nis-2 well) is probably due to precipitation of sulfate and carbonate minerals, epsomite, gypsum and hydro-magnesite, respectively, or reduction to sulfide within the hydrothermal system.

Table 5.2 Physical and chemical data of water samples from thermal springs, wells, and Geothermal wells Nis-1 and Nis-2 (Fig. 5.33)

Locality	Date	pH	T (°C)	TDS	Na	K	Mg	Ca	HCO_3	Cl	Br	SO_4	NO_3	SiO_2
Mandraki well*	10.1992	7.15	24.5	2239	483	86	43	140	171	798		221	198	100
Mandraki well*	07.1980	7.1	19		214	23.5	38.2	121	164	386		259		52.4
NW coast spring*	07.1980	7.05	19	5990	1380	70	47	18	62	2112		296		50
Mira Mare spring*	07.1980	6.8	19	9050	1770	196	107	401	122	3770		179		105
Loutra publ. bath**	07.2008	7.26	39	36,853	10,393	746	698	1653		21,493	61.8	1427	10.5	182
Loutra publ. bath	09.1998	6.9	48.5		10,700	830	550	1020	186	20,500	60.7	1440		107
Loutra publ. bath*	10.1992	6.5	44	36,991	11,040	841	700	1587	259	20,921		1441	12.4	175
Pali spa	09.1998	6.9	30.5											
Pali spa*	10.1992	6.35	39.2	22,895	6440	414	589	1042	281	12,837		1114	43.4	130
Pali spa*	10.1990	6.49	37		4600	258	450	882	195	9210		865		120
Pali spa*	07.1980	6.9	49	42,000	9775	899	613	1472	188	19,170		1368		136
Pali shall. borhole*	07.1980	7.1	35	29,000	6716	626	321	1088	142	13,064		876		111
Panagia Thermiani**	07.2008	7.83	20	29,962	8259	482	730	1362		17,409	61.6	1330	57.7	127
Panagia Thermiani	09.1998	8.2	26.4											
Panagia Thermiani*	10.1992	7.95	25	24,651	7130	500	593	1118	165	13,936		1028	46.5	126
Faros/C.Katsoun**	07.2008	6.56	32	43,064	12,453	583	1274	1278		24,517	77.7	2333	18.6	149
Faros/C.Katsouni	10.2002	6.8	45.4	20,600										
Faros/C.Katsouni	09.1998	5.77	44.2	20,800	11,600	690	900	847	384	21,700		1870		154
NE coast Kethros	07.1980	7.2	23	10,400	2208	117	194	268	255	4118		409		81
Lies well*	10.1992	8.03	23.3	151	21	5	1	18	76	28		10	3.1	
East coast spring*	07.1980	6.9	23	9400	1760	117	212	317	391	3490		356		89.3
Kyra sterna	10.2000	7.8	22	633										
Kyra sterna*	10.1992	8.05	20.8	639	9	4	1	18	567	11		14	3.1	17
Kyra spring	10.1992	7.9	18	834	115	28	38	48	169	266		53	27.9	95
Afionas spring	05.2002	6.24	36.3	24,100										
Avlaki spring	10.2002	6.3	58.9	20,080										

(continued)

Table 5.2 (continued)

Locality	Date	pH	T (°C)	TDS	Na	K	Mg	Ca	HCO_3	Cl	Br	SO_4	NO_3	SiO_2
Avlaki spring	12.2001	6.55	60.7											
Aviaki spring	09.1998	6.4	53.6		11,400	742	705	812	144	21,500	63.7	1720		86.5
Aviaki spring*	10.1996	7.4	56	49,500	12,075	696	1103	992	157	23,075		2265		
Avlaki spring*	10.1992	6.3	58	38,745	11,960	716	795	1291	139	21,985		1585	37.2	
Aviaki spring*	10.1990	6.4	55	49,500	10,540	850	778	1320	137	21,130		1670		
Avlaki spring*	07.1980	6.7	60	45,000	11,385	821	773	1176		21,407		1610		177
Aghia Irini spring**	07.2008	6.7	32	51,200	11,281	472	1215	736		21,575	63.9	2446		22
Aghia Irini spring	09.1998	6.39	39		11,000	622	689	842	258	20,100	60.9	1980		103
Lefkos spring**	07.2008	7	35	31,433	9149	440	814	908		17,934	56.2	1739	12.8	125
Lefkos spring	10.2002	6.08	46.7	29,900										
Lefkos spring	04.2000	6.3	46.9	30,000										
Lefkos spring	09.1998	6	48		10,100	555	666	636	381	17,500	55	1890		110
Lefkos spring*	10.1992	6.75	47	32,643	9890	528	817	906	419	18,085		1796	15.5	180
Lefkos spring	07.1980	6.6	46	42,000	10,523	625	894	800	398	19,028		2133		133
Emborios sauna	10.2000	7	36.5											
Seawater*	10.1992	7.98	24	40,979	12,560	547	1459	486	177	22,694		2959		
Seawater*	07.1980	8.1		47,000	11,960	587	1429	432	157	22,081		2377		
Nis-1 (well)*	12.1982	5.16	340		14,967	2545	1154	10,439	79	48,230		88.2		7.81
Nis-2 (well)*	10.1984	4.87	290	82,994	21,610	2870	78	7340	20	50,390		24.7		6.39

TDS total dissolved solids; HCO_3, Cl, SO_4, and NO_3 in mg/l
Data marked with * are IGME data (Kavouridis et al. 1999); ** d'Allessandro INGV; all other data from Dietrich and Schwandner (unpublished)

5.4.7.1 The Main Anions SO_4–Cl–HCO_3

The relative concentrations of SO_4^{2-}, Cl^- and HCO_3^- demonstrate the variable composition of the waters having a temperature <28 °C, mainly discharged from shallow wells (e.g. Kira Sterna, stagnant pool of Thermiani), which show a significant fraction of seawater (Fig. 5.63). Waters from the Kira sterna that contain Cl^- as the major anion have also relative high HCO_3^- concentrations. The highest HCO_3^-/Cl^- ratio of groundwater was found in a well located on the eastern coast side of the island, which may be due to external addition of CO_2. All along the east coast between Cape Katsouni and Pachia Ammos, diffuse CO_2 and H_2S is discharged in many places at the shallow seafloor (Fig. 5.44).

The thermal springs, such as the Public Bath Loutra, Pali Bath/Thermiani, Avlaki, and Lefkos plot close to the Cl^- corner and yield compositions intermediate between local seawater and geothermal brines. The high-salinity of these thermal waters may originate from underground circulation within pyroclastic formations, as well as along major fractures and fault zones, strongly influenced by seawater and successively modified by admixture with meteoric components and water/rock interaction. The water samples from the Nis-1 and Nis-2 wells plot at the Cl^- corner. Nis-1 was discharged at 1 atm pressure and Nis-2 was a bottomhole sample. The original concentrations of these well waters may be partly modified by precipitation of salts and a strong phase separation (steam fraction of ca. 0.74), which may have occurred in the deep brine reservoir (Chiodini et al. 1993a).

5.4.7.2 The Main Cations ($Na^+ + K^+$)–Ca^{2+}–Mg^{2+}

The relative concentrations of ($Na^+ + K^+$), Ca^{2+} and Mg^{2+} show also that the cold groundwater samples have variable compositions, indicating mixing with seawater and to a little extend with the thermal waters, whereas the thermal waters plot between the deep geothermal water and seawater (Fig. 5.64).

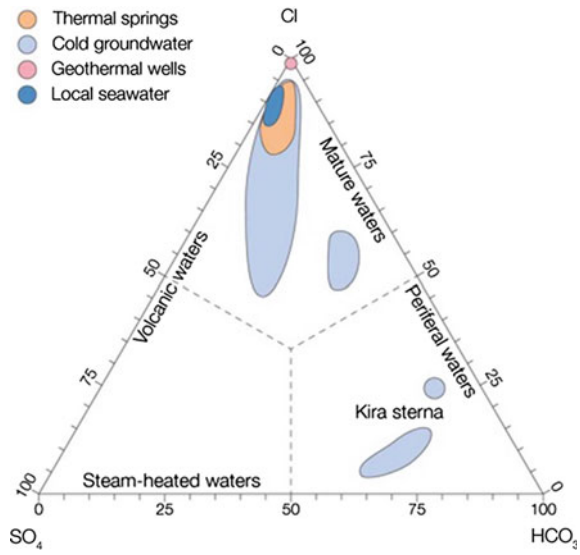

Fig. 5.63 SO_4–Cl–HCO_3 ternary plot (mg/kg) of thermal waters from springs close to sea level, cold groundwater from wells, and the two geothermal liquids of the two Nis-1 and Nis-2 wells. Local seawater composition is reported for comparison; figure modified after Marini and Fiebig (2005)

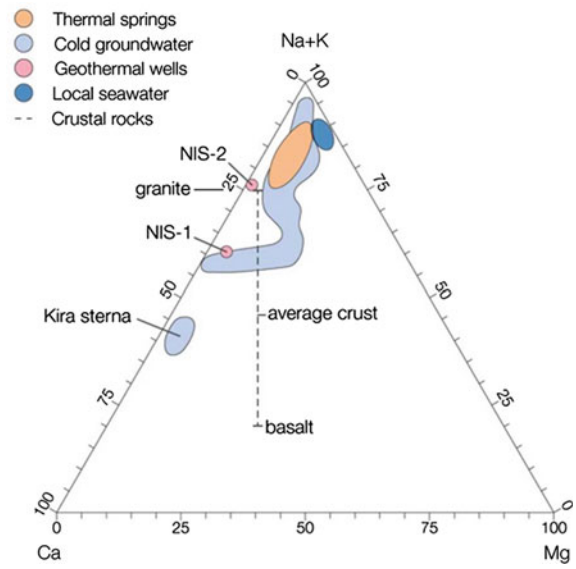

Fig. 5.64 Relative $(Na^+ + K^+)$-Ca^{2+}–Mg^{2+} contents (mg/kg) of thermal waters from springs close to sea level, cold groundwater from wells, and the two geothermal liquids of the Nis-1 and Nis-2 well. Local seawater composition is shown for comparison; figure modified after Marini and Fiebig (2005)

5.4.7.3 Relative Ca, SO_4 and HCO_3 Contents Combined with TDS

The water samples in the triangular plot of Ca^{2+}, SO_4^{2-} and HCO_3^- (Fig. 5.65) depict trends that are likely controlled by dissolution and deposition reactions of calcite and anhydrite (gypsum) and the mixing of cold underground water with seawater (Giggenbach 1988; Kavouridis et al. 1999).

The trend marked A to B shows the dissolution of $CaSO_4$ in low salinity cold groundwater from wells in the pyroclastic deposits in the eastern slopes of the island with TDS (Total Dissolved

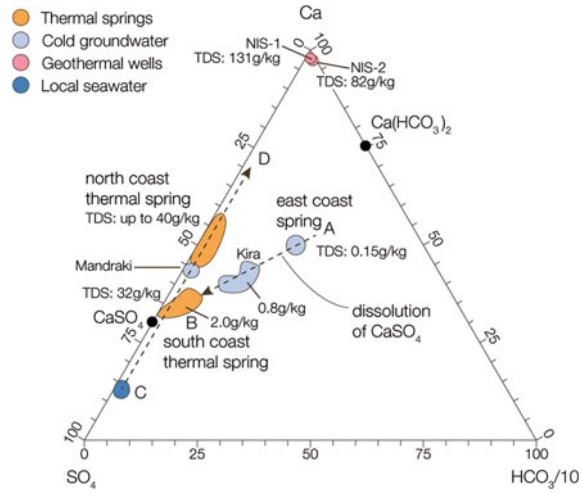

Fig. 5.65 Relative Ca^{2+}, SO_4^{2-} and HCO_3^- contents combined with TDS. $CaSO_4$ are shown relative to seawater, $Ca(HCO_3)_2$ relative to calcite minerals. The AB trend shows the dissolution of $CaSO_4$ in low salinity cold groundwater from wells in the pyroclastic deposits in the eastern slopes of the island. The CD trend points to a high-temperature water/rock interaction of hot underground waters after mixing with seawater; modified after Kavouridis et al. (1999)

Solids) from 0.15 to 2 g/kg, consistent with the SO_4/Ca ratio of anhydrite or gypsum. The C to D trend points to a high-temperature water/rock interaction of hot underground waters after mixing with seawater, indicated by the contents of thermal spring waters from 32 g/kg (Lefkos spring) to 40 g/kg (Avlaki, Pali bath and Loutra bath). The chemistry of the Nis-1 and Nis-2 wells may represent advanced water/rock interaction. This process is proven by the alteration of andesitic pyroclastics and lavas, which produced propylitic hydrothermal minerals observed in cuttings from the Nis-1 well at 1500 m depth (Chiodini et al. 1993a). The high TDS values of Nis-1 and Nis-2 (131 and 82 g/kg, respectively) are likely related to the removal of SO_4^{2-} with the relative increase of Ca^{2+} in the brine (Nis-2 had a low saturation index of −0.8 relative to gypsum at 290 °C sampling temperature) due to seawater infiltration into the hot volcanic underground (Bischoff and Dickson 1975).

All the hydrochemical results prove that thermal spring waters cannot be used for discrimination of a "magmatic" origin since multiple mixing with seawater and meteoric water as well as leaching and precipitation within the porous volcanic underground at variable temperatures obliterates possible chemical tracers.

5.4.8 Isotope Chemistry of Thermal Waters

Additional information about the origin of thermal waters of Nisyros Island is provided by δD and $\delta^{18}O$ values of H_2O (Dotsika and Michelot 1993; Kavouridis et al. 1999; Marini and Fiebig 2005; Dotsika et al. 2009), plotted against chloride concentration and shown in Fig. 5.66a, b. The diagrams include as mixing end members and mixing lines cold meteoric groundwater, seawater and chloride free fumarolic steam from the hydrothermal craters Stefanos, Polyvotis, Flegethron and Kaminakia, the latter expressed by the variation spread of δD (‰ vs. V-SMOW) and $\delta^{18}O$ values (‰ vs. V-SMOW).

The water of a Mandraki well and the stagnant waters of Therminani (Roman thermal bath, Figs. 5.40 and 7.11), which are strongly affected by kinetic effects during variable annual evaporation, are mixtures of mainly groundwater, seawater and small proportions of fumarolic steam in the permeable and fractured underground.

The analytical results of thermal springs during extensive sampling campaigns of the GEOWARN project 2000–2003 show a large field of isotope composition with a major contribution of seawater followed by fumarolic steam (or steam condensates, e.g. Figs. 5.37, 5.38 and 5.39). The mixing of these components occurs along major fault zones penetrating the island (Sect. 3.2.2). The influence of local groundwater, however, seems to be negligible.

A discussion of the geothermometry of the thermal waters is given by Marini and Fiebig (2005). "*Although the use of SiO_2 geo-thermometer is prevented because thermal waters attain saturation with either amorphous silica or opal-CT and the Na-K geo-thermometer gives unrealistic results, average equilibrium temperatures of 100 or 120°C have been estimated based on anhydrite saturation or the K-Mg geothermometer, respectively*".

Fumarolic steam has to be involved when heating seawater at temperatures below 100 °C. This is demonstrated in the steam and steam condensates, occurring in the outlets of fumaroles and mud pools of the hydrothermal craters, as well as in the outlets of thermal springs.

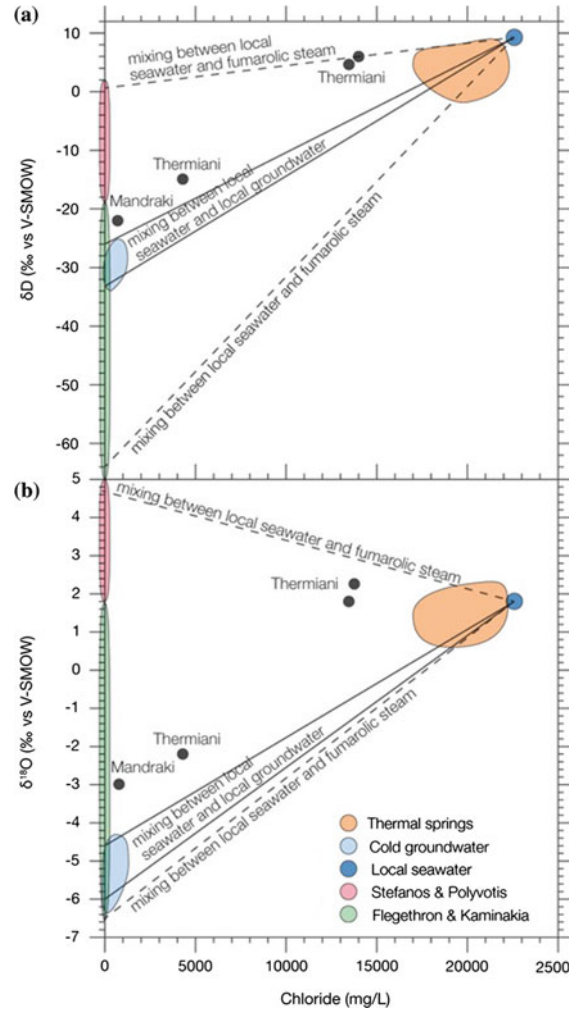

Fig. 5.66 Plots of δD (**a**) and $\delta^{18}O$ (**b**) values of H_2O versus chloride contents of waters on Nisyros Island. In addition, fumarolic steam values from Stefanos and Polyvotis craters are also included; figure modified after Marini and Fiebig (2005). *V-SMOW* standard Vienna Mean Ocean Water

5.5 Conceptual Geochemical Model of the Nisyros Magmatic-Hydrothermal System

The geochemical model of Nisyros discussed here (Fig. 5.67) is based on the surface chemical and isotopic composition of the fumarolic gases and condensates, and thermal spring waters, which have been measured accurately since 1990 (Chiodini et al. 1993a; Dietrich et al. 1998; Kavouridis et al. 1999; Brombach et al. 2003; Marini et al. 2002; Fiebig et al. 2004; Marini and Fiebig 2005). In addition, data from within the hydrothermal system are available from two deep geothermal exploration wells drilled in 1982 and 1983 (Sigurdsson 1985, 1986). The geochemical and well logging data of Nis-1 and Nis-2 wells suggest that the hydrothermal-volcanic system of Nisyros consists of 4 main zones (Chiodini et al. 1993a, b): (a) A magmatic reservoir, (b) a deep saline hydrothermal aquifer, (c) intermediate depth aquifers, and (d) surface manifestations including a shallow condensate aquifer (Fig. 5.67).

(a) The magmatic reservoir supplies heat and magmatic fluids to the hydrothermal system. The presence of a degassing magma body is supported by the isotopic compositions of

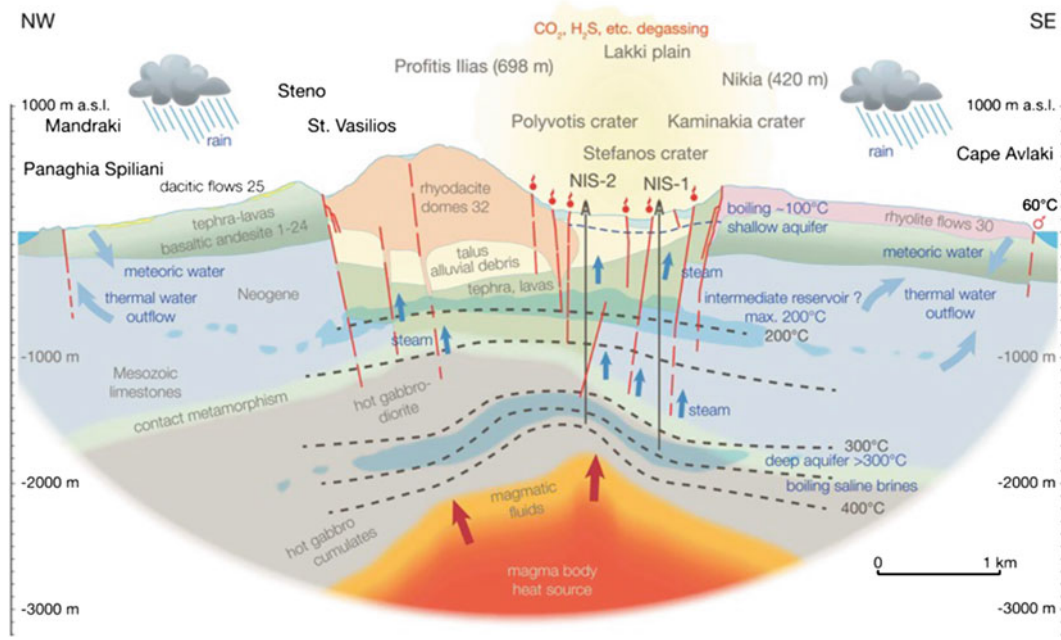

Fig. 5.67 The conceptual geochemical model of the Nisyros hydrothermal system. Cross-section to scale through the Nisyros Caldera and the underlying hydrothermal system. A schematic model is used to show the crustal and lithospheric structure of Nisyros volcanic island. Today the maximum height of the volcano is approximately 1000 m, 698 m (Profitis Illias) above sea level. The volcanic base in 300 m depth lies on top of Mesozoic limestone (Malm formation), which has been proven during drilling of the two geothermal wells in 1983 and 1984 from the caldera floor at approximate 110 m (Lakki plain)

fumarolic H_2O, S and He, possibly with some He deriving from even deeper sources.

(b) The deep hydrothermal saline aquifer has temperatures of 300–350 °C and likely experiences some vapor phase separation. The data of the geothermal wells indicate the presence of Na–Cl brines. The aquifer is fed by a mixture of volcanic and marine fluids. The carbon isotopes of CO_2 and CH_4 in the fumarolic gases are most likely fixed by isotopic exchange at the temperature conditions of this reservoir.

(c) The intermediate depth aquifers at variable temperatures are fed by the vapor produced by the deeper boiling aquifer. The CO content of the vapor is controlled by the lowest temperatures (generally in the range 180–260 °C) of these intermediate reservoirs. A proof for the presence of these intermediate reservoirs is given by the deep drilling data of both Nis1 and Nis2, which found permeable levels at depths from 200 to 600 m;

(d) The discharge area hosts different kinds of manifestations, i.e. soil diffuse degassing structures and fumaroles (located in the Lakki plain), and thermal springs (located along the coast line). A shallow hot aquifer is present in the area, fed by large quantities of condensates. The discharge area releases 68 t/day of hydrothermal-volcanic derived CO_2 and 58 MW of thermal energy, through diffuse soil degassing.

The last magmatic activity of Nisyros, even if of unknown age, is considered relatively old, based on morphological considerations and on the absence of historical magmatic eruptions. Nevertheless, there are many geochemical indications supporting the presence of a magmatic source at depth, which feeds the hydrothermal

system. This evidence is mainly constituted by the isotopic composition of H_2O, S, and He discharged by the Nisyros fumaroles.

References

Aggelidis Z, Pavlidis S, Dikianidou D, Mbalaktsi M (1990) Nisyros an active volcano (in Greek). University Studio Press, Thessaloniki, 36 p

Ambrosio M, Doveri M, Fagioli MT, Marini L, Principe C, Raco B (2010) Water–rock interaction in the magmatic-hydrothermal system of Nisyros Island (Greece). J Volcanol Geotherm Res. doi:10.1016/jjvolgeores201002005

Barnes I, Leonis C, Papastamataki A (1986) Stable isotope tracing of the origin of CO_2 discharges in Greece. In: Morfis A, Paraskevopoulou (eds) Proceedings of the 5th international symposium on underground water tracing, Athens, pp 25–42

Bencini A, Duchi V, Martini M (1981) Thermal waters from the islands of the Aegean arc (Greece). Rend Soc Ital Mineral Petrol 37:921–928

Bischoff JL, Dickson FW (1975) Seawater-basalt interaction at 200 C and 500 bars: implications for origin of sea-floor heavy-metal deposits and regulation of seawater chemistry. Earth Planet Sci Lett 14:274–286

Brombach T (2000) Fluid geochemistry of hydrothermal systems in volcanic island arcs: Guadeloupe (Lesser Antilles) and Nisyros (Greece). PhD thesis, Lausanne University

Brombach T, Cardellini C, Chiodini G, Hunziker JC, Marini L (2001) Soil diffuse degassing and thermal energy fluxes from the southern Lakki plain, Nisyros (Greece). Geophys Res Lett 28:69–72

Brombach T, Caliro S, Chiodini G, Fiebig J, Hunziker JC, Raco B (2003) Geochemical evidence for mixing of magmatic fluids with seawater. Nisyros hydrothermal system, Greece Bull Volcanol 65:505–516

Buondelmonti C (1420) Liber Insularum archipelagi (orig in Latin, illuminated manuscript on vellum; published Sotheby's; Western Manuscripts and Miniatures, London, 22 June 2004)

Caliro S, Chiodini G, Galluzzo D, Granieri D, La Rocca M, Saccorotti G, Ventura G (2005) Recent activity of Nisyros volcano (Greece) inferred from structural, geochemical and seismological data. Bull Volcanol 67:358–369

Cannata A, Giudice G, Gurrieri S, Montalto P, Alparone S, Di Grazia G, Favara R, Gresta S, Liuzzo M (2010) Relationship between soil CO_2 flux and volcanic tremor at Mt Etna: implications for magma dynamics. Environ Earth Sci 61: 477–489

Cardellini C, Chiodini G, Frondini F (2003) Application of stochastic simulation to CO_2 flux from soil: mapping and quantification of gas release. J Geophys Res 108(B9). doi:10.1029/2002JB002165

Chiodini G, Marini L (1998) Hydrothermal gas equilibria: I The H_2O-H_2-CO_2-CO-CH_4 system. Geochim Cosmochim Acta 62:2673–2687

Chiodini G, Cioni R, Leonis C, Marini L, Raco B (1993a) Fluid geochemistry of Nisyros Island, Dodecanese, Greece. J Volcanol Geotherm Res 56:95–112

Chiodini G, Cioni R, Marini L (1993b) Reactions governing the chemistry of crater fumaroles from Vulcano Island, Italy, and implications for volcanic surveillance. Appl Geochem 8:357–371

Chiodini G, Cioni R, Magro G, Marini L, Panichi C, Raco B, Russo M (1996a) Chemical and isotopic variations of Bocca Grande fumarole (Solfatara volcano, Phlegrean Fields). Acta Vulcanol 8:228

Chiodini G, Cioni R, Frullani A, Guidi M, Marini L, Prati F, Raco B (1996b) Fluid geochemistry of Montserrat Island, West Indies. Bull Volcanol 58:380–392

Chiodini G, Brombach T, Caliro S, Cardellini C, Marini L, Dietrich V (2002) Geochemical indicators of possible ongoing volcanic unrest at Nisyros Island (Greece). Geophys Res Lett 29:6-1–6-4

Cioni R, Corazza E, Marini L (1984) The gas/steam ratio as indicator of heat transfer at the Solfatara fumaroles, Phlegraean fields (Italy). Bull Volcanol 47:295–302

Cioni R, Corazza E, Fratta M, Guidi M, Magro G, Marini L (1989) Geochemical precursors at Solfatara Volcano, Pozzuoli (Italy). In: Latter JH (ed) IAVCEI proceedings in volcanology 1, Volcanic Hazards. Springer, New York, pp 384–398

Dietrich VJ, Kipfer R, Schwandner F (1998) Mantle-derived noble gases in the South Aegean volcanic arc: Indicators for incipient magmatic activity and deep crustal movements. Newsletter of the European Centre on Prevention and Forecasting of Earthquakes (Council of Europe) (Sept 1998), pp 28–32

Dotsika E (1992) Utilisation du geothermometre isotopique sulfate-eau en milieu de haute temperature sous influence marine potentielle: les systemes geothermaux de Grece. These en Sciences, Université Paris Sud, No 1781

Dotsika E, Michelot JL (1993) Hydrochemistry, isotope contents and origin of geothermal fluids at Nisyros (Dodecanese). Bull Geol Soc Greece 28:293–304

Dotsika E, Leontiadis I, Poutoukis D, Cioni R, Raco B (2006) Fluid geochemistry of Chios geothermal area, Chios Island, Greece. J Volcanol Geotherm Res 154:237–250

Dotsika E, Poutoukis D, Michelot JL, Raco B (2009) Natural tracers for identifying the origin of the thermal fluids emerging along the Aegean Volcanic arc (Greece): evidence of Arc-Type Magmatic Water (ATMW) participation. J Volcanol Geotherm Res 179:19–32

Economakis R, de Vries C (2001) Nisyros, history and architecture of an Aegean Island. Publishing House Melissa, Athens, Greece, 199 p

Farrar CD, Sorey ML, Evans WC, Howle JF, Kerr BD, Kennedy BM, King CY, Southon JR (1995)

Forest-killing diffuse CO_2 emission at Mammoth Mountain as a sign of magmatic unrest. Nature 376:675–678

Fiebig J, Chiodini G, Caliro S, Rizzo A, Spangenberg J, Hunziker JC (2004) Chemical and isotopic equilibrium between CO_2 and CH_4 in fumarolic gas discharges: generation of CH_4 in arc magmatic-hydrothermal systems. Geochim Cosmochim Acta 68:2321–2334

Fiebig J, Woodland AB, Spangenberg J, Oschmann W (2007) Natural evidence for rapid abiogenic hydrothermal generation of CH_4. Geochim Cosmochim Acta 71:3028–3039

Fiebig J, Woodland AB, D'Alessandro W, Püttmann W (2009) Excess methane in continental hydrothermal emissions is abiogenic. Geology 37:495–498

Fiebig J, Tassi F, D'Alessandro W, Vaselli O, Woodland AB (2013) Carbon-bearing gas geothermometers for volcanic-hydrothermal systems. Chem Geol 351:66–75

Fischer TP, Arehart GB, Sturchio NC, Williams SN (1996) The relationship between fumarole gas composition and eruptive activity at Galeras Volcano, Colombia. Geology 24:531–534

Fytikas M, Andritsos N, Dalabakis P, Kolios N (2005) Greek geothermal update 2000-2004. In: Proceedings of world geothermal congress 2005 Antalya, Turkey, paper 0172

Georgalas GC (1922) Carte des Eaux Minerals de la Grèce. Publications du Bureau Géologique 5, Athènes, Imprimérie Nationale

Georgalas GC (1962) Catalogue of the active volcanoes and solfatara fields of Greece. Catalogue of the active volcanoes of the world Part XII, International Volcanological Association, pp 1–40

Geotermica Italiana (1983) Nisyros 1 geothermal well PPC-EEC report, p 106

Geotermica Italiana (1984) Nisyros 2 geothermal well PPC-EEC report, p 44

Geowarn (2003) Final report project IST-1999-12310 (www.geowarn.ethz.ch)

Giggenbach WF (1987) Redox processes governing the chemistry of fumarolic gas discharges from White Island, New Zealand. Appl Geochem 2:143–161

Giggenbach WF (1988) Geothermal solute equilibria: derivation of Na-K-Mg-Ca geoindicators. Geochim Cosmochim Acta 41:1638–1654

Giggenbach WF (1992) Isotopic shifts in waters from geothermal and volcanic systems along convergent plate boundaries and their origin. Earth Planet Sci Lett 113:495–510

Giggenbach WF (1997) The origin and evolution of fluids in magmatic-hydrothermal systems. In: Barnes HL (ed) Geochemistry of hydrothermal ore deposits, 3rd edn. Wiley, New York

Giggenbach WF, Stewart MK (1982) Processes controlling the isotopic composition of steam and water discharges from steam vents and steam-heated pools in geothermal areas. Geothermics 11:71–80

Gomez-Tuena A, Langmuir CH, Goldstein SI, Straub SM, Ortega-Gutierrez F (2007) Geochemical evidence for slab melting in the trans-Mexican volcanic belt. J Petrol 48:537–562

Gorceix MH (1873a) Sur d'état du volcan de Nisyros au mois de mars 1873. C R Acad Sci (Paris) 77:597–601

Gorceix MH (1873b) Sur la récente éruption de Nisyros. CR Acad Sci Paris 77:1039

Gorceix MH (1873c) Sur l'éruption boueuse de Nisyros. CR Acad Sci Paris 77:1474–1477

Gorceix MH (1874a) Phénomènes volcaniques de Nisyros. CR Acad Sci Paris 77:444–446

Gorceix MH (1874b) Sur l'étude des fumerolles de Nisyros et de quelquesuns des produits l'éruption de 1873. CR Acad Sci Paris 77:1309–1311

Gorceix MH (1874c) Étude des fumerolles de Nisyros et de quelques-uns des produits des éruptions dont cette ile a été le siége en 1872 et 1873. Ann Chim Phys, Paris, 5^{me} sér II: 333–354

Kassaras I, Makropoulos K, Bourova E, Pedersen H, Hatzfeld D (2005) Upper mantle structure of the Aegean derived from two-station phase velocities of fundamental mode Rayleigh waves In: Fytikas M, Vougioukalakis GE (eds) The South Aegean Active Volcanic Arc: present knowledge and future perspectives. Developments in volcanology, vol 7. Elsevier, Amsterdam, pp 19–45

Kavouridis T, Kuris D, Leonis C, Liberopoulou V, Leontiadis J, Panichi C, La Ruffa G, Caprai A (1999) Isotope and chemical studies for a geothermal assessment of the island of Nisyros (Greece). Geothermics 28:219–239

Kinvig HS, Winson A, Gottsmann J (2010) Analysis of volcanic threat from Nisyros Island, Greece, with implications for aviation and population exposure. Nat Hazards Earth Syst Sci 10:1101–1113

Komut T, Gray R, Pysklywec R, Göğüş OH (2012) Mantle flow uplift of western Anatolia and the Aegean: interpretations from geophysical analyses and geodynamic modeling. J Geophys Res 117: B11412

Lambrakis N, Katsanou K, Siavalas G (2014) Geothermal fields and thermal waters of Greecxe: an overview. In: Baba A, Bundschuh J, Chandrasekaram D (eds) Geothermal systems and energy resources, Turkey and Greece. CRC Press/Balkema, Taylor & Francis Group, London, pp 28–46

Marinelli G, Marini L, Merla A, Sini R, Ungemach P (1983) Geothermal exploration in the island of Nisyros, Dodecanese, Greece. In: Strub AS, Ungemach P (eds) Proceedings of the third international seminar on the results of EC geothermal energy research Reidel, Dordrecht, pp 203–205

Marini L, Fiebig J (2005) Fluid geochemistry of the magmatic-hydrothermal system of Nisyros (Aegean arc, Greece). In: Hunziker JC, Marini L (eds) The geology, geochemistry and evolution of Nisyros Volcano (Greece); implications for the volcanic hazards: Memoires de Geologie (Lausanne), vol 44, pp 121–163

Marini L, Agostini A, Cioni R, Guidi M, Leon O (1991) Guagua Pichincha volcano, Ecuador: fluid

geochemistry in volcanic surveillance. J Volcanol Geotherm Res 46:21–35
Marini L, Principe C, Chiodini G, Cioni R, Frytikas M, Marinelli G (1993) Hydrothermal eruptions of Nisyros (Dodecanese, Greece) Past events and present hazard. J Volcanol Geotherm Res 56:71–95
Marini L, Gambardella B, Principe C, Arias A, Brombach T, Hunziker JC (2002) Characterization of magmatic sulfur in the Aegean island arc by means of the d34S values of fumarolic H2S, elemental S, and hydrothermal gypsum from Nisyros and Milos islands. Earth Planet Sci Lett 200:15–31
Martelli A (1917) Il gruppo eruttivo di Nisiro nel mare Egeo. Mem Mat Fis di Soc Ital Soc dei XL ser 3a, 20:79–165
Martini M (1986) Thermal activity and ground deformation at Phlegraean Fields, Italy; precursor of eruptions or fluctuations of quiescent volcanism? A contribution of geochemical studies. J Geophys Res 91(12):255–260
Mattioli M, Renzulli A, Agostini A, Lucidi R (2016) Magmas with slab fluid and decompression melting signatures coexisting in the Gulf of Fonseca: evidence from Isla El Tigre volcano (Honduras, Central America). Lithos 240–243:1–15
Minissale A, Duchi V, Kolios N, Nocenti M, Verrucchi C (1997) Chemical patterns of thermal aquifers in the volcanic islands of the Aegean arc, Greece. Geothermics 26:501–518
Notsu K, Nakai S, Igarashi G, Ishibashi J, Mori T, Suzuki M, Wakita H (2001) Spatial distribution and temporal variation of 3He/4He in hot spring gas released from Unzen volcanic area, Japan. J Volcanol Geotherm Res 111:89–98
Panichi C, La Ruffa G (2001) Stable isotope geochemistry of fumaroles: an insight into volcanic surveillance. J Geodyn 32:519–542
Panichi C, La Ruffa G, Kavouridis T, Leontiadis J, Leonis C, Liberopoulou V, Dotsika E (2000) Geochemical assessment of the thermal fluids emerging, along the Aegean volcanic arc (Greece). In: Proceedings of World geothermal congress, Kyushu –Tohoku, pp 1565–1570
Paonita A, Caracausi A, Martelli M, Rizzo AL (2016) Temporal variations of helium isotopes in volcanic gases quantify pre-eruptive refill and pressurization in magma reservoirs: The Mount Etna case. Geology 44–47. doi:10.1130/G378071
Papadopoulos GA, Sachpazi M, Panopoulou G, Stavrakakis G (1998) The volcanoseismic crisis of 1996-97 in Nisyros, SE Aegean Sea, Greece. Terra Nova 10:151–154
Principe C (1989) Le eruzioni freatiche di Nisyros (Dodecaneso, Grecia): studio geologico preliminare. Boll GNV 931–949
Ross L (1843) Reisen auf den griechischen Inseln II. 70–72 Stuttgart-Tübingen
Sano Y, Marty B (1995) Origin of carbon in fumarolic gas from island arcs. Chem Geol 119:265–274
Sano Y, Notsu K, Ishibashi J, Igarashi G, Wakita H (1991) Secular variations in helium isotope ratios in an active volcano: eruption and plug hypothesis. Earth Planet Sci Lett 107:95–100
Shimizu A, Sumino H, Nagao K, Notsu K, Mitropoulos P (2005) Variation in noble gas isotopic composition of gas samples from the Aegean arc, Greece. J Volcanol Geotherm Res 140:321–339
Sigurdsson O (1985) Nisyros Geothermal Development, Nisyros NIS-1 Injection Tests July 1985. Consultant's Report Public Power Corporation (PCC) Report No: OS-58084, Athens, Greece, 40 p. http://wwwosis/gogn/Skyrslur/OS-1985/OS-85084.pdf. Accessed 20 Sept 2015
Sigurdsson O (1986) Nisyros Geothermal Development, Nisyros NIS-2, Production Characteristics and Fluid Composition Consultant's Report. Public Power Corporation (PCC) Report No: OS-86038, Athens, Greece, 97 p. http://wwwosis/gogn/Skyrslur/OS-1986/OS-86038.pdf. Accessed 20 Sept 2015
Sparks RSJ (2003) Forecasting volcanic eruptions. Earth Planet Sci Lett 210:1–15
Stavrakakis G, Papoulia I (1998) Seismicity of Nisyros Newsl Eur Cent Prev Forecast Earthquakes 2:14–16
Symonds RB, Rose WI, Bluth GJS, Gerlach Terence M (1994) Volcanic-gas studies: methods, results, and applications. Rev Mineral Geochem 30:1–66
Symonds RB, Mizutani Y, Briggs PH (1996) Long-term geochemical surveillance of fumaroles at Showa-Shinzan dome, Usu volcano, Japan. J Volc Geoth Res 73:177–211
Symonds RB, Gerlach TM, Reed MH (2001) Magmatic gas scrubbing: implications for volcano monitoring. J Volcanol Geoth Res 108(1):303–341
Tibaldi A, Pasquarè FA, Papanikolaou D, Nomikou P (2008) Discovery of a huge sector collapse at the Nisyros volcano Greece by on-land and offshore geological-structural data. J Volcanol Geotherm Res 177:485–499
Werner C, Evans WC, Kelly PJ, McGimsey R, Pfeffer M, Doukas M, Neal C (2012) Deep magmatic degassing versus scrubbing: Elevated CO_2 emissions and C/S in the lead-up to the 2009 eruption of Redoubt Volcano, Alaska. Geochem Geophys Geosyst 13(3)
Zolotov MY, Shock EL (2000) A thermodynamic assessment of the potential synthesis of condensed hydrocarbons during cooling and dilution of volcanic gases. J Geophys Res: Solid Earth (1978–2012) 105 (B1):539–559

Magnetotelluric Reconnaissance of the Nisyros Caldera and Geothermal Resource (Greece)

6

Andreas Tzanis, Vassilis Sakkas and Evangelos Lagios

Abstract

A Magnetotelluric reconnaissance survey of 39 soundings was carried out in the caldera of Nisyros, a small island volcano at the eastern end of the Hellenic Volcanic Arc (HVA), Greece, in an attempt to explore the high temperature geothermal resource of the area. Iteratively reweighted least squares was implemented to compute stable and smooth Earth response functions exhibiting 2-D to weakly 3-D attributes, as a result of induction in low-contrast local geoelectric inhomogeneities, superimposed on a dominantly 2-D background structure; coastal and island induction effects are absent due to the low offshore/onshore resistivity contrast at, and below sea level. Application of advanced hypothetical event analysis techniques to study the spatial properties of the telluric field demonstrated that convection and hydrothermal circulation is controlled by a system of antithetic NE-SW oriented active normal faults which form a graben-like structure and define the 2-D background, as well as a conjugate system of NNW-SSE normal faults which is particularly active at the SW quadrant of the island and define the main convection path. It was determined that under these conditions the data could be interpreted with 2-D inversion, which has successfully reconstructed detailed images of the structural and functional elements of the hydrothermal system. The structural elements include a number of shallow hot water reservoirs in the argillic and phyllic alteration zones and a laterally extended deep (approx. 1 km) circulation zone, all embedded in a low-resistivity with very low lateral contrasts. The functional elements include images of the most important convection conduits created by the intersection of major fault planes. The results are corroborated by the logs of two deep exploration wells. Overall, on the basis of a carefully reworked data set, our analysis has provided detailed

A. Tzanis (✉) · V. Sakkas · E. Lagios
Section of Geophysics and Geothermy, National and Kapodistrian University of Athens, Panepistimiopolis, 157 84 Athens, Greece
e-mail: atzanis@geol.uoa.gr

V.J. Dietrich and E. Lagios (eds.), *Nisyros Volcano*, Active Volcanoes of the World,
DOI 10.1007/978-3-319-55460-0_6

images of the volcano's interior and valuable insight into its structure, function and geothermal potential.

6.1 Introduction

Nisyros is a small Quaternary island volcano, located at the eastern terminus of the Hellenic Volcanic Arc (36°35.25′ N, 27°10.0′ E, also see inset in Fig. 6.1). It is an active spot with a history of explosive eruptions, the largest of which formed a caldera dominating the landscape of the island. Immediately afterwards, extrusive activity covered the largest part of the caldera with rhyolitic domes, leaving in its eastern half a small elongate basin of NNE-SSW orientation (Lakki depression, see Fig. 6.1).

The Lakki is defined by a system of NNE-SSW oriented antithetic normal faults forming a graben-like structure that contains a hydrothermal field and high temperature geothermal resource. For this reason, it has been subject to systematic exploration (Ungemach 1983; Geotermica Italiana 1983). Geophysical studies of the geothermal resource have been were conducted between 1989 and 1992 by carrying out Magnetotelluric (MT) surveys both in Lakki and at the southern extension the Lakki graben, with funding from the Public Power Corporation (PPC) of Greece, Department of

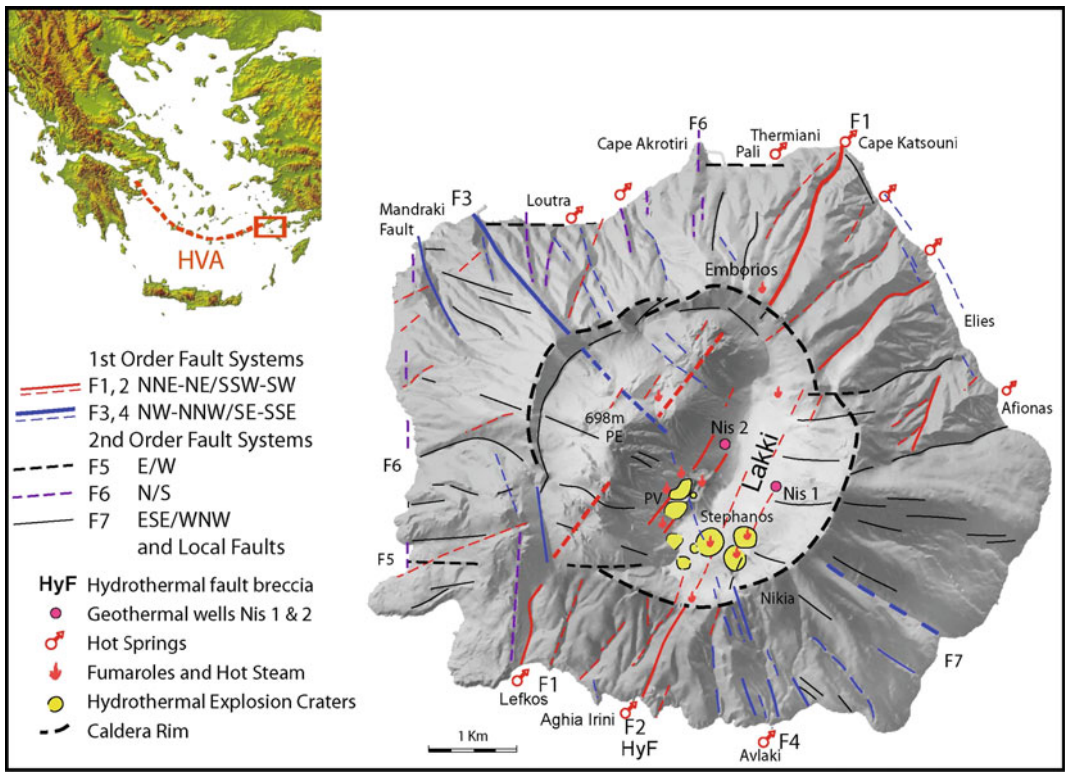

Fig. 6.1 Shaded relief image of Nisyros Island, (36° 35.25′ N, 27°10.0′ E), including the major fault zones, hydrothermal activity sites and important toponyms; the image was modified from Lagios et al. (2005). The *inset* map at the *top-left* indicates the location of Nisyros (*red rectangle*) in the Hellenic (South Aegean) Volcanic Arc (*red dashed line*). PE stands for Prophitis Ilias; PV for the Polyvotis phreatic explosion crater. The figure was modified from Lagios et al. (2005)

Alternative Energy Resources. Some results of these investigations have already been reported by Lagios (1991), Dawes and Lagios (1991) and Lagios et al. (1991). The MT surveys were followed by a multi-parametric study of the southern extension of the Lakki graben comprising self-potential, gravity and VLF measurements (Lagios and Apostolopoulos 1995). The geophysical surveys were conducted under an outstanding requirement of highly accurate results within the first 2 km, including the detection and delineation of reservoir structures with a high degree of confidence and, if possible, the successful detection of geothermal fluid convection and circulation conduits for subsequent evaluation of energy resources.

The previous geophysical work has basically been successful, but the analysis and interpretation of the data was based on methods and techniques of that time (1989–1995). The present paper is devoted to a qualitative and quantitative re-examination of the Magnetotelluric data using improved data processing methods, new hypothetical event analysis techniques to study the spatial configuration of the telluric field and two-dimensional inversion tools. It will be shown that the results vastly expand previous knowledge of the interior structure of the geothermal resource. The results also demonstrate the capability of the Magnetotelluric method to image and delineate fine structural details when accurate data is available; high-resolution images of a small albeit complex geothermal system including convection paths, reservoirs and reservoir related structures are adequately reconstructed and discussed.

6.2 The Nisyros Volcanic Complex and Geothermal Resource

The South Kos and Nisyros volcanic field has been active for at least 3 Ma and continues to show signs of contemporary unrest (e.g. Papadopoulos et al. 1998; Sachpazi et al. 2002; Lagios et al. 2005). Accordingly, it has been the focus of significant research effort which has produced a general model of the petrologic, volcanological and tectonic evolution of the area (Davis 1967; Di Paola 1974; Keller 1982; Ungemach 1983; Geotermica Italiana 1983; Bohla and Keller 1987; Vougioukalakis 1989, 1993; Seymour and Vlassopoulos 1989, 1992; Wyers and Barton 1989; Papanikolaou et al. 1991; Limburg and Varekamp 1991; Varekamp, 1992; Francalanci et al. 2005; Papanikolaou and Nomikou 2001; Volentik et al. 2006; Vanderkluysen et al. 2006a, b; Bachman et al. 2011; Nomikou and Papanikolaou 2011).

Focusing on Nisyros, it is generally accepted that its geological evolution comprises four stages (see Chap. 3, i.e. 3.5 Geochronology). The pre-caldera stage builds the volcanic edifice with extrusive activity through a basement consisting of Mesozoic limestone and Neogene sediments, in several successive phases developing from underwater andesitic to subaerial dacitic and rhyodacitic. K–Ar and δC^{14} dating, as well as tephro-stratigraphy and the absence of the Kos Plateau Tuff deposits (of about 161 Ka BCE) suggest that the subaerial part of Nisyros formed during the last 161 Ka; during this stage significant tectonic activity creates the fault zones F1, F2 and F3. The caldera formation stage follows and comprises two or three phases, each commencing with low-intensity phreatomagmatic explosions fed by rhyolitic magmas; these destroy the volcanic edifice by ejecting a few km^3 of debris and triggering a central caldera collapse. The post-caldera stage begins with extrusion of the rhyolitic—dacitic Prophitis Ilias domes and lava flows, which cover the western part of the caldera only. The major fault zones continue being active. During the contemporary stage volcanic activity died out. The major fault zones reactivate and the (youngest) F4 zone is incited. Secondary faulting episodes take place as well. Intense and often violent hydrothermal activity also occurs, with several episodes of phreatic explosions in historic times (1422–1888 CE). The signatures of at least 11 phreatic explosions are apparent; the greatest of them has formed the Stephanos Crater, an impressive

depression of 20–30 m with a longest dimension of 300 m.

The major fault zones shown in Fig. 6.1 are important in the historic geotectonic and morphological evolution of the volcano and, simultaneously, control contemporary convection and hydrothermal activity. Every single phreatic explosion took place at, or near the intersections of the major fault zones. Accordingly, it is helpful to provide a brief description

- The normal fault zone F1 is striking at N30°, dipping at 70°–80° to the NE with a throw of approx. 100 m. It can clearly be seen within the caldera, comprising a series of large parallel faults producing obvious morphological discontinuities on the eastern flank of the Prophitis Ilias domes. Appreciable hydrothermal activity, with fumaroles and intense alterations can be seen along its strike. The F1 system appears to have been important for the placement of the post-caldera dacites, whose eruptive centers are aligned in a N30°–40° direction; inasmuch as the magmas feeding these extrusions originated in deep crustal chambers, it seems that F1 comprises a deep reaching zone of crustal weakness.
- The normal fault zone F2 is also striking at N30° and dipping at 70°–80° to the WNW, with a throw of 100–120 m. It forms a tectonic graben with the oppositely dipping F1 and while it produces impressive escarpments outside the caldera, its presence within is obscure although it is thought to cross the Stephanos phreatic explosion crater. At the coast of Aghia Irini, southwest of Lakki, F2 is associated with underwater thermal springs with temperatures 40–50°C.
- The normal fault zone F3 appears at the NW part of the island with a strike of N320°–330°, dip 70°–80° to the NE and throw of more than 100 m. It has been verified outside the caldera near the town of Mandraki. Its trace is uncertain in the area of the Prophitis Elias domes, except for a large elongate morphological feature along its projected continuation, where it is thought to separate the main outcrops of the Prophitis Ilias lava domes from the smaller domes to the northeast. F3 appears again as a morphological discontinuity on the NW flank of Lakki, while branches of the system are thought to extend through the Polyvotis and Micros Polyvotis phreatic explosion craters into Stephanos and further SE to the Avlaki and Aghia Irini areas.
- The fault zone F4 appears to play an important role in the formation and functioning of the geothermal field. It forms a graben like depression with two principal and a series of secondary faults, striking N340° and dipping at 70°–80°. Its presence is obvious, inasmuch as it produces dislocation of the caldera rim. Contemporary fumarolic activity and at least 11 phreatic explosion features are located at the intersections of F4 with the system F1/F2. In addition, the debris flow and lacustrine deposits related to the 1873 CE hydrothermal explosion events exhibit a clear N340° distribution, collocated with the trace of the F4 system (shaded area in Fig. 6.5). At the Avlaki area, at the SE end of the island, F4 is associated with underwater thermal springs with temperatures of 60 °C.

Additional to the major faults, three secondary faulting structures can be identified; these are labelled F5, F6 and F7 in Fig. 6.1; albeit minor, they can still influence the circulation and diffusion of hydrothermal fluids with particular reference to F5 and F7. The F5 and F7 systems are oriented E-W and ESE-WNW respectively. They both may result from the interaction between the F1 and F3. Members of this system, which will be shown to have a notable effect on the resistivity structure, are expressed in the area between Lakki, Elies and Afionas. The thermal spring of Afionas at sea level might also be a result of these faults.

The fault zones produce a number of neotectonic blocks, each characterized by its relative uplift, as determined by differential InSAR and GPS observations (Lagios et al. 2005). Maximum uplift and westward to SW-ward horizontal displacement is observed at the western

(Prophitis Ilias) block, which incorporates the Mount of Prophitis Ilias and surrounding summits and is bounded by the F1 and F3 fault zones. Minimum uplift and SE-ward displacement is observed at the Lakki—Aghia Irini graben, bounded by F1, F2 and F4. Intermediate uplift and eastward displacement is observed at the eastern (Nikia) block, bounded by F4, F2 and F5/F7, and at the northern (Emporios) block, bounded by F5/F7, F2 and F3. It is therefore clear that the major and secondary normal fault zones impart divergent differential motion between the west, south and east sectors of the island, thus facilitating the convection and circulation of hydrothermal fluids.

6.3 The Magnetotelluric Survey

6.3.1 Data Acquisition and Processing

The Magnetotelluric data was collected with funding from the Public Power Corporation of Greece, Department of Alternative Energy Resources and in cooperation with the Department of Geology and Geophysics of the University of Edinburgh (Mr. G. J. K. Dawes). The survey was conducted in two phases and comprised a total of 39 soundings, the locations of which are shown in Fig. 6.2. Phase I was carried out in June 1989 and comprised 20 soundings at the southern and central part of Lakki, indicated by code numbers '9xx' in Fig. 6.2; Phase II was carried out in May 1991 and comprised 19 soundings indicated by the code numbers '1xx'. A 1-D interpretation of the Phase I data has already been reported by Dawes and Lagios (1991).

The measurements were carried out with the Short Period Automatic Magnetotelluric system (SPAM) MkIIb, developed by Dawes (1984), in the nominal frequency bandwidth 128 Hz–40 s, using $Pb/PbCl_2$ electrodes and CM11 induction coils. The Magnetotelluric—Telluric measurement mode was implemented, using a 5-component Magnetotelluric configuration at the *Base* site and a 2-component Telluric configuration at a single *Remote* (satellite) site. The Telluric—Magnetotelluric method requires uniformity of the source field over the base and satellite stations, an assumption valid if they are separated by relatively short distances. At the base station (indicated by *'B'*) one measures the horizontal transverse components of the MT field $\mathbf{E}_B = [E_{xB}\ E_{yB}]^{\mathrm{T}}$ and $\mathbf{H}_B = [H_{xB}\ H_{yB}]^{\mathrm{T}}$, whence the impedance tensor $\mathbf{Z}_B$ can be computed. At the satellite stations (indicated by *'R'*), only the telluric field components are measured, i.e. $\mathbf{E}_R = [E_{xR}\ E_{yR}]^{\mathrm{T}}$. Then,

$$\mathbf{E}_R = \mathbf{T}\cdot\mathbf{E_B} \Leftrightarrow \mathbf{E}_R = \mathbf{T}\cdot\mathbf{Z}_B\cdot\mathbf{H}_B \Leftrightarrow \mathbf{E}_R = \mathbf{Z}_M\cdot\mathbf{H}_B$$

where $\mathbf{T}$ is the *telluric transfer tensor* defined as

$$\begin{pmatrix} E_{xR} \\ E_{yR} \end{pmatrix} = \begin{pmatrix} T_{xx} & T_{xy} \\ T_{yx} & T_{yy} \end{pmatrix} \cdot \begin{pmatrix} E_{xB} \\ E_{yB} \end{pmatrix}$$

and $\mathbf{Z_M}$ is the *impedance transfer tensor* by which the base magnetic field $\mathbf{H_B}$ is referred to the remote telluric field $\mathbf{E_R}$.

Given that remote referencing was unavailable at the time of data collection, the Earth responses were estimated in two stages. The first stage comprised standard single-site processing techniques: on the assumption of stochastic (Gaussian) time processes, the impedance tensor elements were computed with the least squares solution of the two-input one-output linear system

$$E_i = Z_{ix}H_x + Z_{iy}H_y + \varepsilon_i, \quad i = x, y,$$

by minimising the noise ε_i (Sims et al. 1971). The quality of the solution can be monitored by means of the predicted coherence function

$$\gamma^2_{1.23} = \hat{E}_i/E_i = \hat{Z}_{ix}H_x + \hat{Z}_{iy}H_y, \quad i = x, y,$$

where $\hat{E}_i$ represents the output electric field component predicted from the estimated elements $\hat{Z}_{ij}$. The estimation of Earth response functions was improved using a robust procedure quite similar to that of Egbert and Booker (1986). The spectral components E_x, E_y, H_x and H_y that

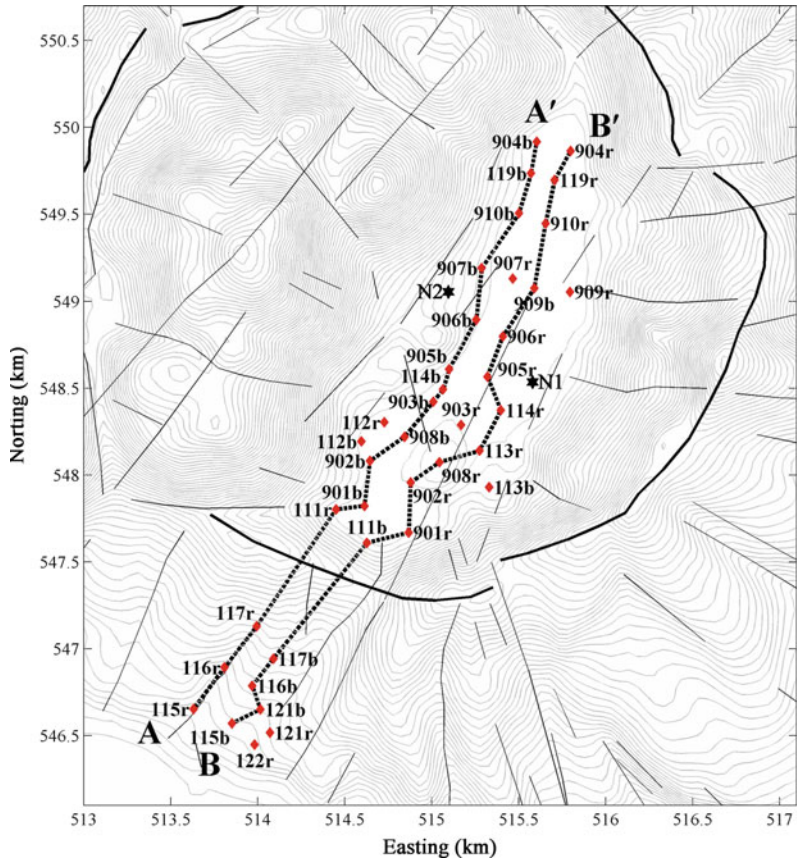

Fig. 6.2 Location of the 39 magnetotelluric sounding sites. N1 and N2 are the positions of the two deep exploration wells. The *dashed lines* AA′ and BB′ indicate the transects along which 2-D inversion has been carried out

yielded impedance tensor realizations with predicted coherence above 0.8 were cast into a system of the form

$$\begin{pmatrix} \Re(E_{i_1}) \\ \Im(E_{i_1}) \\ \Re(E_{i2}) \\ \Im(E_{i_2}) \\ \cdots \\ \Re(E_{i_N}) \\ \Im(E_{i_N}) \end{pmatrix} = \begin{pmatrix} \Re(H_{x_1}) & -\Im(H_{x_1}) & \Re(H_{y_1}) & -\Im(H_{y_1}) \\ \Im(H_{x_1}) & \Re(H_{x_1}) & \Im(H_{y_1}) & \Re(H_{y_1}) \\ \Re(H_{x_2}) & -\Im(H_{x_2}) & \Re(H_{y2}) & -\Im(H_{y_2}) \\ \Im(H_{x_2}) & \Re(H_{x_2}) & \Im(H_{y_2}) & \Re(H_{y_2}) \\ \cdots & \cdots & \cdots & \cdots \\ \Re(H_{x_N}) & -\Im(H_{x_N}) & \Re(H_{y_N}) & -\Im(H_{y_N}) \\ \Im(H_{x_N}) & \Re(H_{x_N}) & \Im(H_{y_N}) & \Re(H_{y_N}) \end{pmatrix} \cdot \begin{pmatrix} \Re(Z_{ix}) \\ \Im(Z_{ix}) \\ \Re(Z_{iy}) \\ \Im(Z_{iy}) \end{pmatrix}, \qquad i = x, y$$

which was subsequently solved with iteratively reweighted least squares using MATLAB's™ robust multi-linear regression tool (for a formal description of the method see Huber 1981). This algorithm may effectively down-weight the influence of non-Gaussian noise, provided that the population of noise-free data dominates the population of noisy data. Its performance is a function of noise and data statistics, progressively deteriorating as the probability of receiving noise waveforms increases, until breakdown

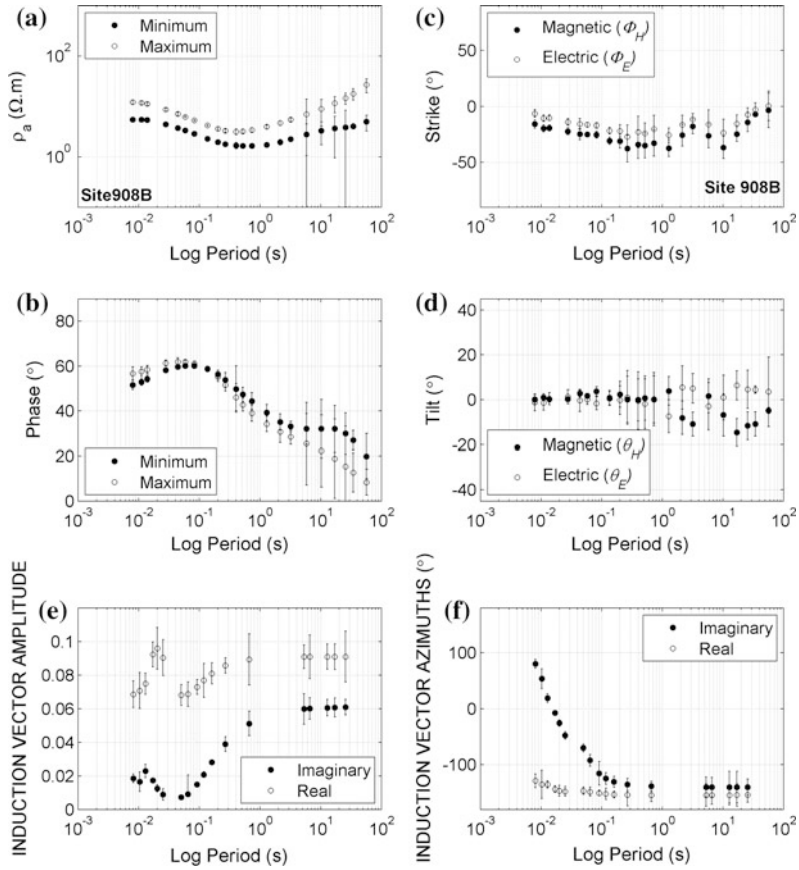

Fig. 6.3 The maximum and minimum states of the impedance tensor at site 908B: **a** maximum and minimum apparent resistivity; **b** maximum and minimum phase; **c** strike of the electric (Φ_E) and magnetic (Φ_H) fields; **d** Tilt of the electric (θ_E) and magnetic (θ_H) fields

when the noise is as likely as the data and can cloak the distribution of the noise-free population beyond recognition and recovery. In this event, the treatment must be case-specific. Moreover, single-site robust methods cannot cope with continuous harmonic multiple-coherent noise, for obvious reasons. In such cases, noisy estimators of the impedance tensor elements were removed with a "low-tech" method, namely "expert judgment" and manual deletion. A similar processing procedure was used to estimate magnetic transfer functions, hence induction vectors. Typical examples of estimated (observed) Earth responses are shown in Figs. 6.3 and 6.4 (see below for details).

6.3.2 Spatial Analysis and Determination of Geoelectric Strike

The *spatial analysis* of the magnetotelluric Earth response endeavours to extract information about the configuration of the induced natural EM fields, which, in turn, depend on the geometry and configuration of lateral inhomogeneities in the geoelectric structure. Herein we implement an anti-symmetric reformulation of the *equivalent* Canonical and Singular Value Decompositions of Yee and Paulson (1987) and LaToracca et al. (1986) respectively. These decompositions are *symmetric* and apply when the electric and

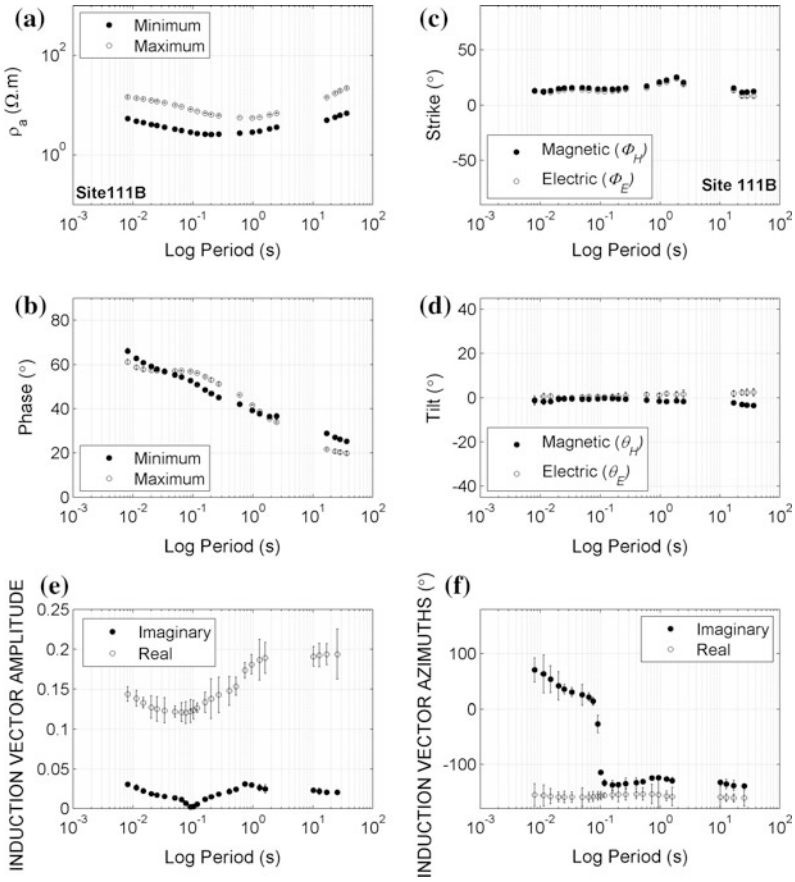

Fig. 6.4 The maximum and minimum states of the impedance tensor at site 111B: **a** maximum and minimum apparent resistivity; **b** maximum and minimum phase; **c** strike of the electric (Φ_E) and magnetic (Φ_H) fields; **d** Tilt of the electric (θ_E) and magnetic (θ_H) fields

magnetic fields are measured in different orthogonal coordinate frames associated by a rotation of 90°. Tzanis (2014) has shown that they constitute proper rotations in 3-D space based on the topology of the SU(2) rotation group and result in a characteristic state—characteristic value (generalized eigenstate—eigenvalue) formulation of the Magnetotelluric induction problem; he has also shown that they can be reformulated into an anti-symmetric decomposition, which is suitable for the analysis of *practical* Magnetotelluric measurements in which the electric and magnetic fields are referred to the *same* coordinate frame and is consistent with the conventional rotation applied in typical Magnetotelluric analysis. The anti-symmetric decomposition reduces the impedance tensor to the form

$$\mathbf{Z} = \boldsymbol{E}(\theta_E, \Phi_E) \cdot \begin{bmatrix} 0 & \zeta_1 \\ -\zeta_2 & 0 \end{bmatrix} \cdot \boldsymbol{H}^{\dagger}(\theta_H, \Phi_H)$$

where (†) denotes Hermitian transposition and $\boldsymbol{\varepsilon}$ and $\boldsymbol{H}$ are SU(2) rotation matrices, of the form

$$U(\theta, \phi) = \begin{bmatrix} \cos\theta\,\cos\phi - i\,\sin\theta\,\sin\phi & -\cos\theta\,\sin\phi + i\,\sin\theta\,\cos\phi \\ \cos\theta\,\sin\phi + i\,\sin\theta\,\cos\phi & \cos\theta\,\cos\phi + i\,\sin\theta\,\sin\phi \end{bmatrix}$$

At any location on the surface of the Earth, the impedance tensor can be re-written as

$$\boldsymbol{\varepsilon}^{\dagger}\mathbf{Z} = \boldsymbol{\zeta}\cdot\boldsymbol{H}^{\dagger} \Rightarrow \begin{bmatrix} \boldsymbol{E_1}(\boldsymbol{\theta_E}, \boldsymbol{\Phi_E}) \\ \boldsymbol{E_2}(\boldsymbol{\theta_E}, \boldsymbol{\Phi_E} + \frac{\pi}{2}) \end{bmatrix} = \begin{bmatrix} \boldsymbol{0} & \boldsymbol{\zeta_1} \\ -\boldsymbol{\zeta_2} & \boldsymbol{0} \end{bmatrix} \cdot \begin{bmatrix} \boldsymbol{H_1}(\boldsymbol{\theta_H}, \boldsymbol{\Phi_H}) \\ \boldsymbol{H_2}(\boldsymbol{\theta_H}, \boldsymbol{\Phi_H} + \frac{\pi}{2}) \end{bmatrix}$$

with $\{E_1(\theta_E, \Phi_E), H_1(\theta_H, \Phi_H)\}$ comprising the *maximum* and $\{E_2(\theta_E, \Phi_E + \pi/2), H_2(\theta_H, \Phi_H + /2)\}$ the *minimum characteristic states* (*eigen-states)* of the electromagnetic field.

The angles (θ_E, φ_E) define a *characteristic* coordinate frame or *eigen-frame* $\{x_E, y_{E,}, z_E\}$ of the electric field, such that x_E is rotated by φ_E clockwise with respect to the x-axis of the experimental coordinate frame and the plane $\{x_E, y_E\}$ is tilted by an angle θ_E clockwise with respect to the horizontal plane $\{x, y\}$. Likewise, the angles (θ_H, φ_H) define the characteristic eigen-frame $\{x_H, y_{H,}, z_H\}$ of the magnetic field such that x_H is rotated by φ_H clockwise with respect to the x-axis of the experimental coordinate frame and the plane $\{x_H, y_H\}$ is tilted by an angle θ_H clockwise with respect to the horizontal plane $\{x, y\}$. Each eigen-frame contains orthogonal, *linearly polarized* components. In the case of 2-D geoelectric structures, $\Phi_E = \Phi_H$ and $\theta_E = \theta_H = 0$. In 3-D structures however, it is possible that $\Phi_E \neq \Phi_H$ and/or θ_E $\theta_H \neq 0$. It follows that in each characteristic state, the associated electric and magnetic eigen-fields are not mutually perpendicular. It is equally important that the electric and magnetic eigen-frames are not horizontal. This should be of no surprise because in 3-D Earth structures the total magnetic and induced electric fields are three dimensional and may be associated with significant gradients, especially in the vicinity of interfaces. Accordingly, they are locally orthogonal and anti-symmetric in complex 3-space and the tilt angles θ_E and θ_H of the electric and magnetic eigen-frames are a measure of the local landscape of the electric and magnetic field respectively.

As a final point, it is important to note that the *projection* of the eigenstates on the *horizontal plane* comprise elliptically polarized components: the normalized projected field vector will have a major axis equal to $\cos\theta$ and a minor axis equal to $\sin\theta$. The ratio of the minor to the major axis is the *ellipticity*, given by $b = \tan\theta$ while $\theta > 0$ implies a counter-clockwise sense of rotation and $\theta < 0$ a clockwise sense. Thus, ellipticity on the horizontal plane is defined in terms of a rotation in higher dimensional space. It is not straightforward to see in this thrifty presentation, but the essence of this analysis is that it approaches the geoelectric structure as the equivalent of a birefringent material at low frequencies and large scales.

Figure 6.3 illustrates the response of sounding 908B in the form of rotated impedance tensors. The data exhibit weak 3-dimensionality at short periods, evident in the variation of the maximum and minimum apparent resistivities and phases (Fig. 6.3a, b), as well as in the non-orthogonal configuration of the electric and magnetic eigen-frames for $T < 1$ s (Fig. 6.3c). Moderate 3-dimensionality appears to develop at longer periods, as manifested by the variability of the strike angles Φ_E and Φ_H at $T > 0.3$ s (Fig. 6.3c) and the non-trivial tilt of the electric and magnetic eigen-frames at periods longer than approx. 1 s (Fig. 6.3d). Figure 6.4 illustrates the Earth responses for sounding 111B as per Fig. 6.3. In this case, 2-D characteristics are evident in all the parameters of the maximum and minimum eigenstates, with the electric and magnetic field strikes being almost identical and the respective tilts generally trivial up to $T \approx 1$ s, with weak 3-D structural attributes appearing at periods longer than 10 s.

The study of individual Earth responses indicates that the geoelectric structure is overall very conductive and generally 2-D or weakly 3-D at short periods, developing to weakly or moderately 3-D at long periods; it also appears to be complex, exhibiting significant lateral variation of the geoelectric strike and that the higher-dimensional inductive effects are generated by low-contrast local inhomogeneities. These general observations are confirmed by mapping the polarization ellipse of the maximum electric field and the real induction vector (RIV). Figure 6.5 illustrates the configuration of these quantities, averaged over the period interval 2–100 s (0.5–0.01 Hz), which contains

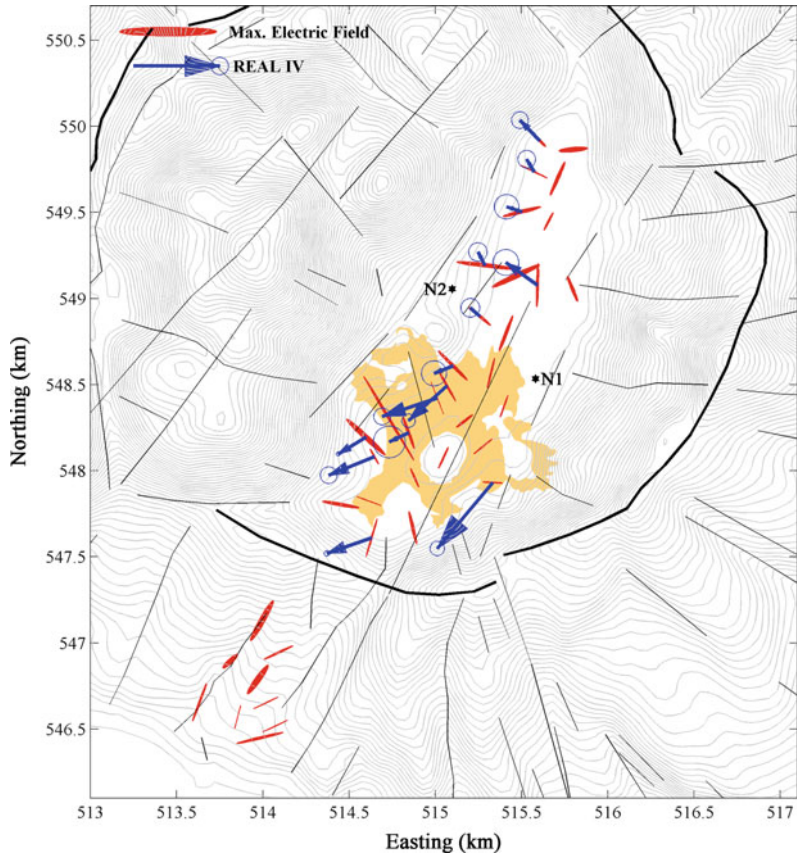

Fig. 6.5 Configuration of the polarization state of the maximum electric field (*red ellipses*) and the real induction vectors (*blue arrows*); both are shown as averages over the bandwidth 2–100 s. The *shaded area* indicates the extent of debris flow and lacustrine deposits related to the 1873 CE phreatic explosion events

responses from the deeper and broader elements of the geoelectric structure.

Focusing on the spatial properties of the maximum electric field, we observe significant lateral variations in the principal direction of the geoelectric structure and may identify three domains with different apparent geoelectric strikes:

(a) Outside of the caldera, at the SW of the Lakki graben, as well as inside the caldera and along the east side of Lakki, between sites 908R (Stephanos Crater) and 119R, the orientation of the polarization ellipse is generally NNE-SSW and is consistent with the strike of the major F1, F2 fault zones and the trend of the Lakki graben.
(b) Inside of the caldera, along the west flank of Lakki and between sites 902B and 905B, the orientation is generally NNW-SSE. This domain includes sites 902R and 901R and generally coincides with the trace of F4 fault zone.
(c) Inside of the caldera, at the SW corner of the Lakki graben, as well as along its west flank between sites 906B and 119B, the orientation of the polarization ellipse is on average E-W and generally associated with the local strike of the depression.

Turning our attention to the real induction vectors, which are drawn in the Parkinson convention, we observe that inside the caldera, the RIV defines two domains with different apparent geoelectric strikes:

(a) At the northern half of the Lakki depression, (north of site 906B), a NNE-SSW geoelectric trend is evident, consistent with the strike of F1 and F2 faults and the trend of the depression.

(b) At the southern half of Lakki (south of site 905B), a NNW-SSE geoelectric trend is clearly seen, consistent with the strike of the F4 fault zone.

The joint consideration of the maximum electric field and real IV configurations points toward the existence of a broader system of elongate background structures consistent with the 2-D approximation and associated with the F1/F2 faulting system, and a superimposed system of local elongate structures also fitting the 2-D approximation and collocated with the F4 faulting system. It also appears that the latter (F4) is associated with higher electrical conductivity and controls local induction and the flow of electric current. This would not only imply that the surface hydrothermal activity developing at the southern part of Lakki is associated with the intersections of F1, F2 and F4, but would also indicate that F4 is the main conduit for the ascent of geothermal fluids to the surface. Finally, local three-dimensionality is plainly evident in the spatial variability of the polarization ellipses and their non-orthogonal configuration with reference to the induction vectors.

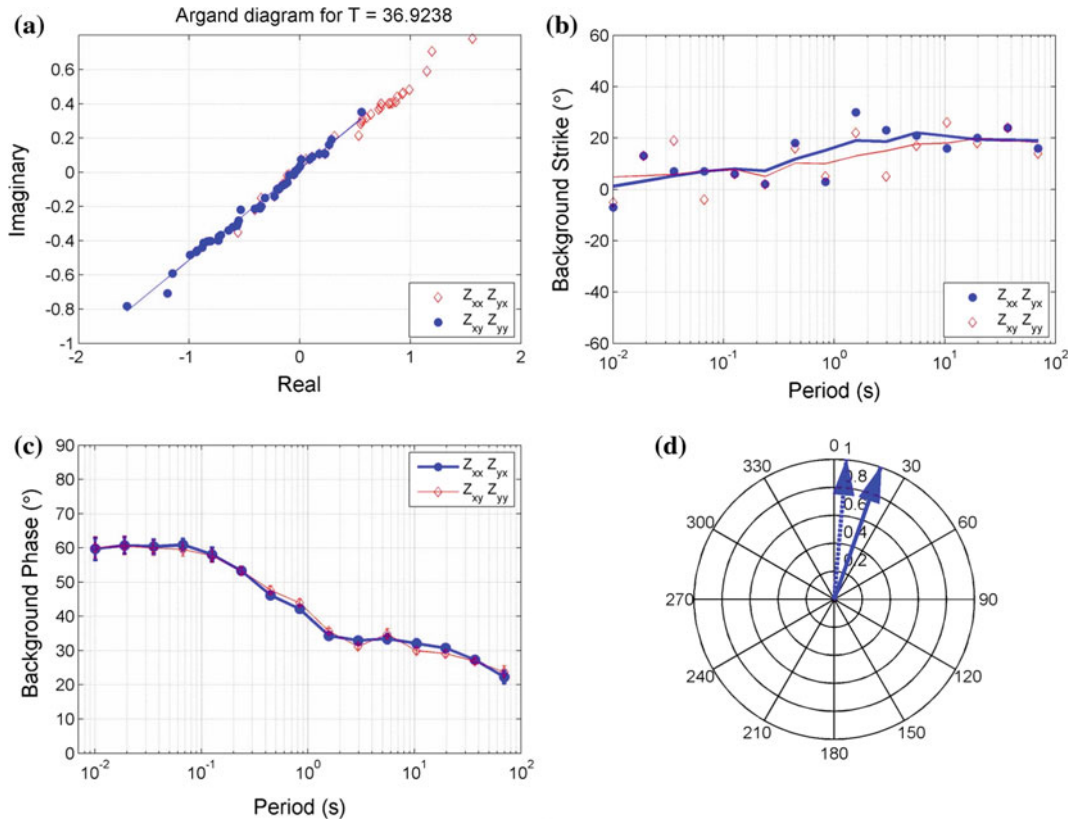

Fig. 6.6 Determination of the background geoelectric strike from the MT tensor impedance data after Banks and Wright (1998). **a** Best fitting of all *straight lines* fitted to the Argand diagram of the rotated telluric (*column*) vector $[Z_{xx}(\phi)\ Z_{yx}(\phi)]^T$, for the interval 20–50 s it is found at the azimuth of ~N20° (*solid blue circles*). The open *red diamonds* are the corresponding elements of the telluric vector $[Z_{xy}(\phi)\ Z_{yy}(\phi)]^T$, the azimuth also being ~N20°. **b** The frequency dependent background strike extracted from all MT data. *Solid blue circles* indicate the strike estimated from $[Z_{xx}(\phi)\ Z_{yx}(\phi)]^T$; open *red diamonds* correspond to $[Z_{xy}(\phi)\ Z_{yy}(\phi)]^T$; the continuous *solid lines* are smoothed versions of the corresponding discrete curves. **c** The corresponding regional phases. **d** Range of variation of the background strike: the *dashed arrow* indicates the mean background strike at short periods; the *solid arrow* is the same for long periods

The existence and strike of a broader, two-dimensional background geoelectric structure can also be investigated on the basis of the collective phase response of the measured impedance tensors. Banks and Wright (1998) proposed a "holistic" approach in determining *regional* geoelectric trends by expanding on the fact that the presence of a regional 2D structure will manifest itself in the common phase of impedance tensor elements belonging to the same column vector. These elements can be regarded to be electric fields produced by a magnetic field parallel or perpendicular to the regional strike. Accordingly, if a group of MT soundings share the same regional response, regardless of the amount of local effects experienced by individual soundings, the real and imaginary parts of the electric fields rotated to the direction of the regional response will plot on a line of constant phase in the complex plane. Conversely, the direction parallel to which we find the best fitting straight line between the real and imaginary parts may be used as a criterion for determining the regional strike. It should be noted that this is a form of hypothetical event analysis, whose basic idea is described by Ritter and Banks (1998).

This concept is implemented by rotating the impedance tensor incrementally by an angle $\phi_i = \phi_{i\text{-}1} + \Delta\phi$, $\phi \in [-90°, 90°]$, and fitting a straight line to the real vs imaginary parts of each column vector $[Z_{xy}(\phi)\ Z_{yy}(\phi)]^T$ and $[Z_{xx}(\phi)\ Z_{yx}(\phi)]^T$ of the impedance tensor. The angle ϕ_0 at which we find the minimum of all misfits should be the direction at which the elements of each column vector have the same phase. For instance, in the frequency interval 20–50 s, this best fitting line is found at the strike direction N20° (Fig. 6.6a). The regional phase is the arctangent of the slope. Repetition of the procedure over several consecutive narrow frequency intervals in the measured band of 130 Hz–100 s, yields the frequency dependent curves of the background strike direction ϕ_0 (Fig. 6.6b), and the corresponding regional phases (Fig. 6.6c).

The background strike is rather unstable if not erratic at short periods, where it exhibits an N-S average orientation, and rather stable at long periods ($T > 1$ s), where it indicates a well-defined N20° orientation consistent with the strike of F1 and F2 systems and the Lakki plain (Fig. 6.6b). By comparison to Fig. 6.5, it is now clear that at the southern part of Lakki the (younger) F4 system is locally dominating EM induction and comprises a major component of hydrothermal activity. It is also interesting to note that the regional phase indicates the existence of two background conductors: one shallow, evident at periods shorter than 0.2 s and presumably associated with the hydrothermal field, and one evident at the interval 2–30 s and presumably associated with a deeper structure of the volcano's interior.

6.3.3 Two-Dimensional Inversion

Based on the above discussion, it is possible to conclude that the weak to moderate 3-dimensionality of the observed responses is a consequence of local 3-D induction due to low-contrast geoelectric inhomogeneities, superimposed on a dominantly 2-D background. In such case, the data can still be interpreted with 2-D inversion tools; the local 3-D effects will not be fully resolved, but the more significant part of the conductivity structure, i.e. reservoirs and main fluid circulation zones will still be detectable. However, in order to implement 2-D inversion techniques we need to define the TE/TM modes of induction over the study area.

Although the impedance and magnetic transfer function responses measured at a given period interval do not normally originate at the same depth range, the configuration of the induced electric and magnetic fields is tell-tale of the principal mode of induction in the vicinity of a sounding. Accordingly, the mode of induction can be inferred by studying the configuration of the maximum polarization ellipses and real induction vectors:

(a) Inside of the caldera, along the west flank of Lakki between sites 902B and 905B, as well as 902R and 901R, the approximate orthogonality of the polarization ellipses and real

induction vectors is consistent with TE mode induction over a NNW-SSE conductive dyke —the dyke presumably being the F4 fault zone.

b) Inside of the caldera, at the SW flank of Lakki, as well as along the west flank between sites 906B and 119B, the polarization ellipses and induction vectors are similarly oriented and consistent with TM induction above the resistive part of a NNE-SSW oriented lateral conductivity interface.

(c) Inside of the caldera and along the east side of Lakki, between sites 908R (Stephanos Crater) and 119R, the orientation of the polarization ellipse is, by inference, consistent with TE induction over a NNE-SSW conductive dyke, which in this case is presumed to be the F2 fault zone.

(d) Outside of the caldera, SW of Lakki, the orientation of the polarization ellipse is consistent with TE induction over a NNE-SSW conductive dyke, which again is presumed to be the F2 system. This interpretation is strongly corroborated by a multi-parametric geophysical survey conducted by Lagios and Apostolopoulos (1995) in that area, which has detected circulation along planes of orientation consistent with that of F2.

The two-dimensional inversion has been carried out with the algorithm of Rodi and Mackie (2001), along transects AA′ and BB′ of Fig. 6.2. The TE and TM modes were simultaneously inverted, using the spatial configuration described above. A finely discretized homogenous half-space with topography, bathymetry and seawater taken into consideration was used as a starting model; the discretization scheme is apparent in Figs. 6.10 and 6.11. Several inversions with different starting models and regularization factors were carried out before the final models were declared. The quality of the final models can be summarized as follows:

West Transect (AA′): The observed and residual TM and TE apparent resistivity and phase responses can be studied in Fig. 6.7. It is apparent that the observed responses are rather successfully reproduced and the final χ^2 misfit is 1357 with an

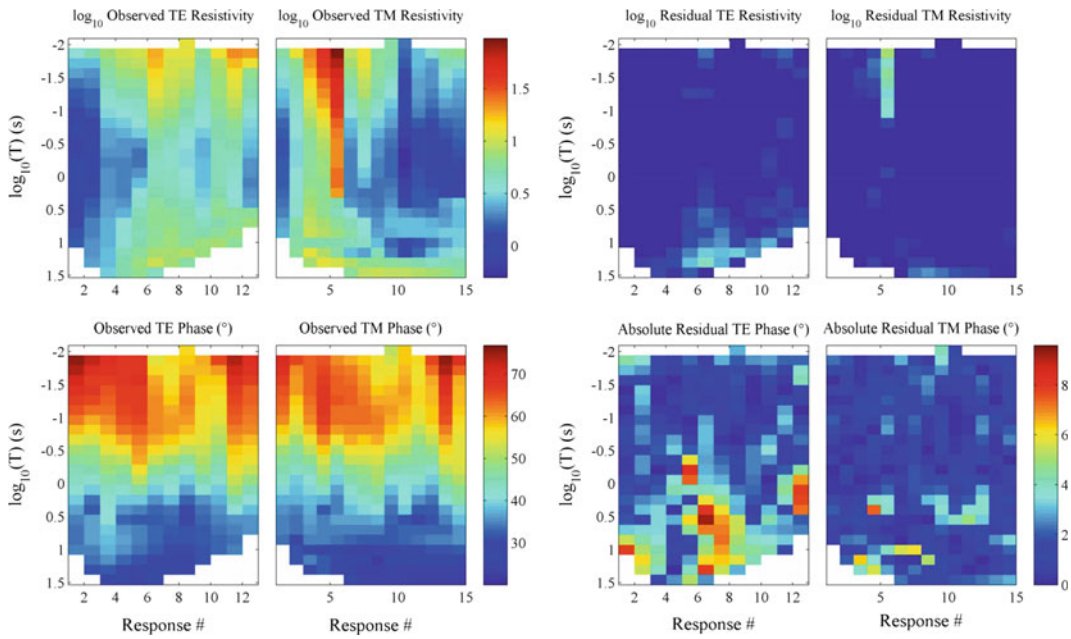

Fig. 6.7 Observed (*left panels*) and residual (*right panels*) apparent resistivities and phases along the West Transect (AA′ in Fig. 6.2). Each column corresponds to one sounding *curve*; the order of columns corresponds to the order of soundings along the Transect

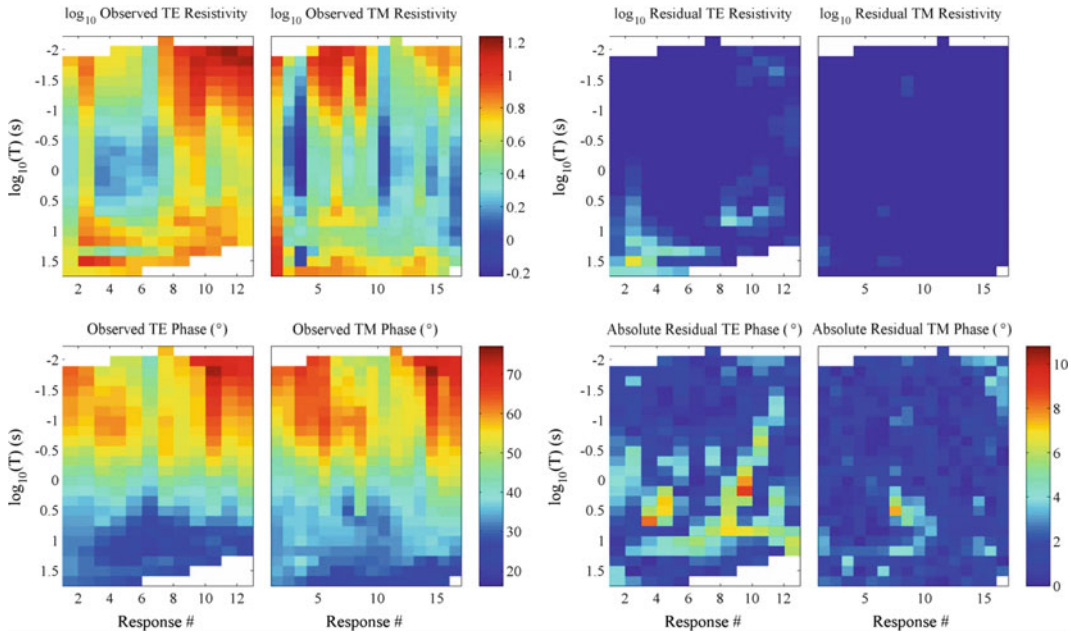

Fig. 6.8 Observed (*left panels*) and residual (*right panels*) apparent resistivities and phases along the East Transect (BB′ in Fig. 6.2). Each column corresponds to one sounding *curve*; the order of columns corresponds to the order of soundings along the Transect

expectation value of 952. The higher than expected χ^2 can be attributed to the moderate local 3-D effects observed at some sounding locations, which cannot be adequately modelled with 2-D interpretation tools, as well as to the low uncertainty (observational error) associated with the measurements (e.g. Figs. 6.3 and 6.4).

East Transect (BB′): The observed and residual TM and TE apparent resistivity and phase responses can be studied in Fig. 6.8. It is apparent that the observed responses are approximated well and the final χ^2 misfit is 1781 with an expectation value of 976. It is rather easy to see that as to the quality of the inversion and the higher than expected χ^2 the same comments as per the West Transect apply.

6.4 The Geoelectric Structure

6.4.1 Constraints from Borehole Data

Figure 6.9 combines data from the two test wells N1 and N2 (Ungemach 1983; Geotermica Italiana 1983), and vertical resistivity profiles extracted from nearest to the boreholes locations of the East and West transects respectively. Available borehole data include: **(a)** The lithological columns. **(b)** Open microfracture domains which, in general correspond to fault zones and exhibit high hydraulic (fracture) permeability, associated with considerable or total loss of drilling fluid. **(c)** Temperature data determined inside the boreholes. Geophysical well logging was not performed, mainly due to the high temperature and pressure conditions. Hydraulic permeability was determined from the rates of loss of drilling fluid and macroscopically, from fractures observed in recovered rock cuttings. Porosity had to be determined from cuttings. According to the well logs, the caldera infill has undergone extensive argillisation, the degree of which reduces with depth. Lava formations experience, in general, less severe alteration than tuff strata. However, some (e.g. brecciated) lava are more altered and exhibit a high degree of secondary porosity and porous permeability. The tuffs are almost completely devitrified; this process is

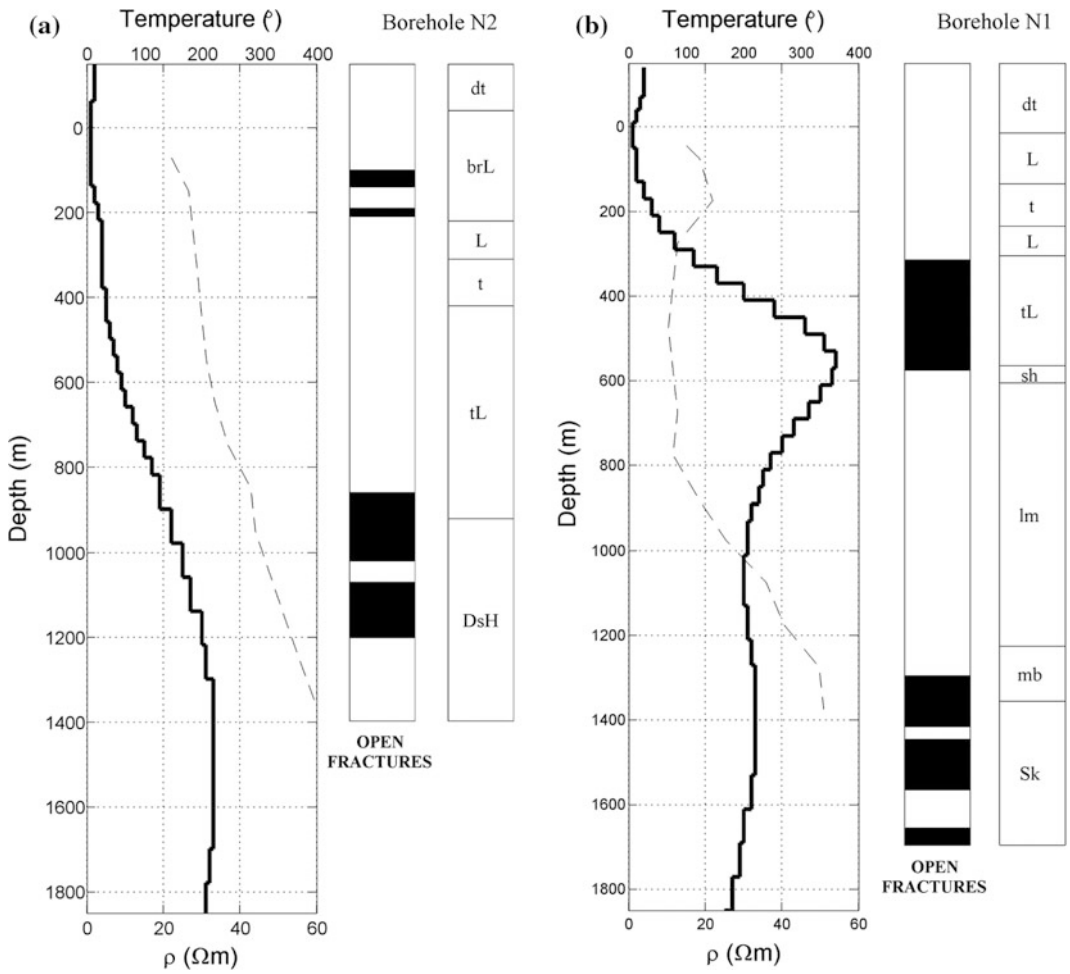

Fig. 6.9 Correlation of borehole N2 (*left*) and borehole N1 (*right*) with the vertical resistivity profiles extracted from nearest to the boreholes locations of the West (*left*) and East (*right*) transects respectively. Borehole information was taken from the technical reports of Ungemach (1983) and Geotermica Italiana (1983). *Black shading* indicates the domains characterized by open fractures and high hydraulic permeability. Lithological abbreviations are as follows: *dt* detritus; *brL* brecciated lava; *L* lava; *t* tuff; *tL* tuff and lava; *DsH* dioritic subintrusives and hornhels; *sh* shales; *lm* limestone; *mb* marble; *Sk* skarn

much more extensive in thick(er) and homogeneous, than in thin(er) and inhomogeneous formations and has generated significant secondary porosity, (or caused manifold increase if some pre-existed). In the upper 300 m (argillic zone), the main product of alteration is the very hydrofile smectite (of the group of montmorillonites).

At depths greater than 300 m, phyllic alteration takes place, which generates less hydrofile minerals. Wet clay formations are known to give very high electrical conductivity signatures. Unfortunately we do not have detailed quantitative data about the fractional distribution of clay minerals with depth and cannot assess their relative contribution to the observed electrical conductivity. Only qualitative interpretations can be made, although it is certain that at shallow depths, both factors will cooperate to produce

very low resistivities. The reduction of the degree of argillization and the transition to the phyllic zone at depths greater than 300 m should produce a detectable overall increase of electrical resistivity within the caldera. The borehole data indicate the existence of a hot water reservoir at depths of 150–300 m below mean sea level. Stephanos phreatic explosion crater also attests to the presence of an aquifer at these depths, inasmuch as analysis of the crater's geometry places the focus of the explosion (and the feeder aquifer) at depths 160–200 m below sea level. N2 indicates a second concentration of geothermal fluids at depths of 900–1300 m and N1 finds a similar formation at 1300–1700 m.

Correlation of N1 and East Transect: The shallow structure is very conductive, with a 1 Ωm conductor appearing at, and just under sea level. In the lithological column, this corresponds to highly altered, low permeability detritus, lava and tuff formations. Given that such depths lie in the argillic alteration zone, it is reasonable to assume that this conductor represents the combination of high fractional volumes of hydrous clay minerals and electrolyte concentration. The temperature exhibits a local peak of approx. 150 °C at depths of 160–200 m, which coincides with the floor of the argillic-phyllic alteration zone. The temperature increase corresponds to a shallow hot water reservoir and is associated with an increase in resistivity to approx. 6–8 Ωm, which may be explained in terms of a significant reduction in the fractional volume of hydrous clay minerals in the phyllic alteration zone.

The temperature drops significantly to 70–90 °C at depths 300–800 m, in coincidence with a fractured, highly permeable domain at depths of 310–600 m which is associated with total loss of drilling fluid and can be attributed to faulting, as it is consistent with the expected positions of fault planes belonging to the F2 system and the gravity fault zone produced by the collapse of the volcano walls during the formation of the caldera. This may imply infiltration of cold seawater spreading to N1 through the F4 and F2 systems. Between 600 and 900 m N1 penetrates the low-permeability pre-volcanic basement (limestones), which has been thermally metamorphosed to marble below 1250 m. At depths greater than 1360 m the drill enters the halo of an old, fractured dioritic intrusion (skarn). According to Vougioukalakis (1993) this should not be much younger than 24 Ka (see Chap. 3.5 Geochronology). The temperature exceeds 300 °C. There is only partial loss of drilling fluid in the fractured domain, indicating medium to high permeability. The origin of the fracturation zone may be partially blocked fault zones, or the emplacement of the dioritic intrusion, or a combination of both factors. At any rate, a deep fluid circulation zone and reservoir appears to develop at 1350–1700 m, within the fracturation zone

At depths greater than 300–400 m, the resistivity profile does not correspond to the lithological column at N1 because the former correspond to formations located within the caldera and at the hanging wall(s) of the F2 system, while the latter is outside of the caldera and at the footwall(s). The resistivity increases locally to approx. 54 Ωm at the depth of 600 m; this can be explained in terms of a dioritic intrusion, possibly the same as that detected in N1 and very likely the same as the one detected in N2 (see below for details). The resistivity drops to approx. 30 Ωm at depths greater than 900 m, remaining at this level to at least 1800 m and further decreasing at greater depths. Such values and variation are comparable to those observed near N2 and, together with the data of that borehole, indicate the possibility of a deep circulation zone and reservoir at 1300–1800 m depth.

Correlation of N2 and West Transect: The detritus observed in the lithological column is associated with very high permeability up to 50 m below sea level and is imaged as a good (approx. 2 Ωm) conductor. The resistivity profile exhibits a very conducting zone of approx. 1 Ωm at depths 50–150 m below sea level, which in the lithological column is associated with a highly altered chaotic formation comprising fractured tuff breccia and subordinate lavas and scoria in blocks—brecciated lavas or brL in Fig. 6.9. Given that these depths are in the argillic alteration zone, as well as the intense hydrothermal activity of the area, it is reasonable to assume the

conductor represents a combination of electrolyte concentration (shallow reservoir) and clay mineralization.

The depths 100–210 m are characterized by the presence of two fracturation zones associated with total loss of drilling fluid, which are situated at the lower parts of the brecciated lavas. The disturbed lithology is likely to be due to the emplacement of the nearby post-caldera rhyodacite domes. This is a plausible cause of fracturing, but the fact that fractures are open (total loss) should probably be attributed to concurrent faulting, which we are inclined to associate with the F1 and F3 systems. The well logs do not elucidate this problem but they contain indication that the fractured domains are part of a fluid circulation zone. Notably, a water bearing formation at 150–300 m depth has been confirmed by N2; this corresponds to a good 2–4 Ωm conductive domain extending between 150–400 m and overlapping with the depth extent of the fracturation zone. According to the well logs, such depths correspond to the phyllic alteration zone. Thus it appears plausible that residual fracturation from the emplacement of the rhyodacites and contemporary faulting combine to develop a circulation zone which is likely to feed a "shallow reservoir" in the argillic alteration zone imaged as a very good 1 Ωm conductor, as well as a circulation zone and deeper reservoir in the phyllic alteration zone imaged as a good 2–4 Ωm conductor.

The circulation zone is followed by a gradual increase in resistivity to approx. 35 Ωm at 1300 m below sea level and a corresponding increase in temperature. It is noteworthy that regardless of the increase, the resistivity still remains at rather low levels! Moreover, the steadily increasing temperature indicates the absence of direct contamination by cold seawater infiltration, as is the case with N1. In the lithological column this range of depths corresponds to a low permeability zone comprising almost completely altered and devitrified tuffs and lavas, (L and t in Fig. 6.9), followed by an intercalation of breccia and andesitic or dacitic lavas, sometimes in blocks (tL in Fig. 6.9). All these formations belong to the phyllic alteration zone; fractures are totally absent, but the material has secondary porosity. In consequence, we interpret the gradual resistivity increase in terms of a corresponding gradual decrease of the concentration of hydrophile clay minerals in the complex background of hydrothermally altered material produced by the formation of the caldera and subsequent emplacement of volcanic intrusives.

The depths 900–1200 m are characterized by intense fracturing and very high permeability. Between 1200 and 1400 m, where N2 was terminated, fracturing cannot be observed albeit permeability is still appreciable. The fractured zone can be interpreted in terms of faulting although it is difficult to pinpoint the responsible fault(s). The lithology of the fractured domain consists of a sequence of quartz dioritic intrusives and intercalated calc silicate and quartz feldspathic hornfels comprising the halo of a dioritic intrusion, which may be related to the one observed at N1. The MT data do not detect an impressive conductor at 900–1200 m, but it is noteworthy that the rate of resistivity increase slows significantly after approx. 1100 m and becomes negative after approx. 1700 m. This behaviour is consistent with the existence of a deep circulation zone and reservoir, as suggested by previous interpretations of the borehole data (e.g. Ungemach 1983; Geotermica Italiana 1983).

6.4.2 West Transect (AA′)

Figure 6.10 illustrates the (logarithm) of the resistivity structure as reconstructed by 2-D inversion. At the SW extension of the Lakki graben, outside of the caldera, the structure exhibits a shallow (less than 0.25 km) and a deep (0.75–2.5 km) conductive zone. It also appears that the latter is connected with the caldera through a relative conductor seen at depths 0.5–0.8 km and distances 1–1.5 km along the profile. These geoelectric features are interpreted as epiphenomenal to fluid circulation in the F1/F2 system.

The gravity fault comprising the southern boundary of the caldera is rather clearly resolved.

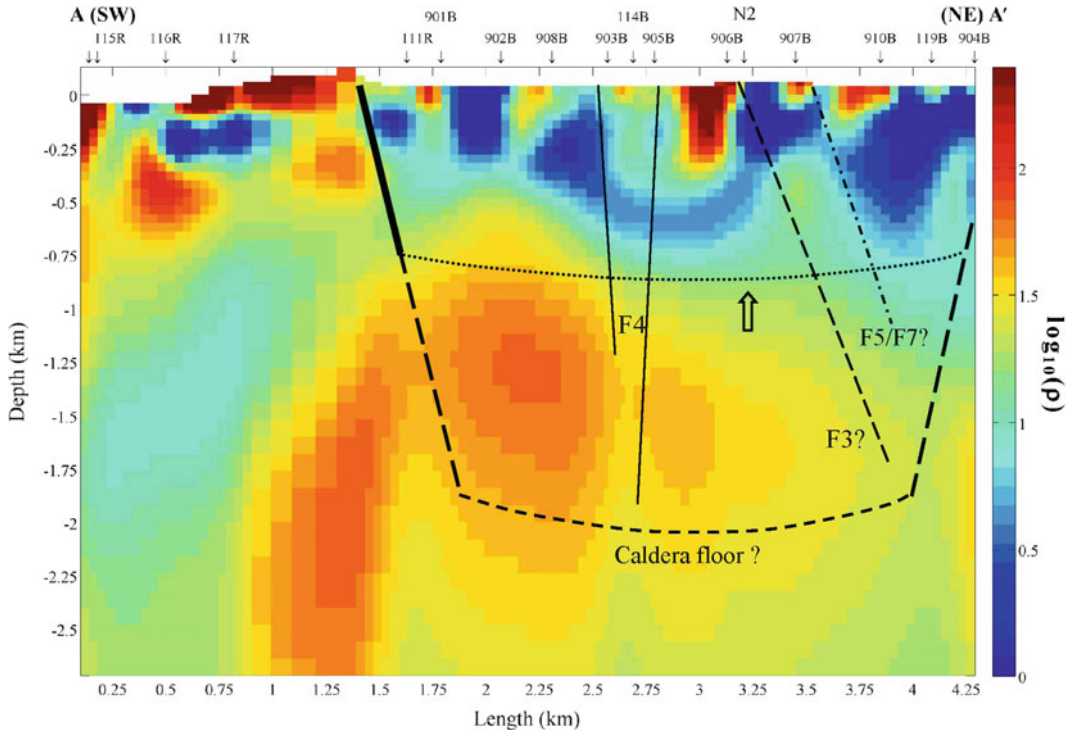

Fig. 6.10 Two-dimensional best-fitting model of the resistivity structure along the West Transect A–A′. N2 marks the nearest to N2 location of the Transect. The *arrow points* to the ceiling of the dioritic intrusion at N2

At depths shallower than 1 km it is outlined by an interface between a relative resistor to the south (foot wall) and a relative conductor to the north (hanging wall), located between 1.4 and 1.6 km along the transect as indicated in Fig. 6.10. At depths greater than 1 km, it can be seen as a lateral discontinuity (notch) in a relatively resistive formation, located between 1.5 and 2 km along the Transect. The northern boundary is not directly observable; its position is postulated by a long-dash line extrapolated from the surface.

The resistive formation observed at depths between 0.8 and 2.5 km beneath the Caldera is almost ideally situated, so as to be identified with the dioritic intrusives found by drilling at N2 (the ceiling of the intrusion is pointed to with an arrow). The floor of the caldera cannot be clearly identified; its location depends on the age of the intrusion, which, as mentioned above, is probably older than 24Ka. Thus, if it is pre-calderic, the floor should be sought near the ceiling of the intrusion, approximately as indicated by the dotted line. If it is syn- or post-calderic, then it is apparently deeper, perhaps as deep as 2 km (dashed line).

The horizontal dotted line indicates the approximate depth extent of the geothermal system, which, evidently, comprises an interconnected network of reservoirs and circulation zones. According to the discussion above, good conductors up to 0.25 km deep represent the combined effect of clay mineralization and fluid concentration in the argillic hydrothermal zone. Deeper (0.25–0.8 km) conductors more likely represent fluid concentration and circulation in the phyllic hydrothermal zone. The deep circulation zone detected in relation to the deep permeable zone at N2 belongs to this part of the system.

As noted above, the deep circulation zones are associated with contemporary faulting. The solid

lines marked F4 connect the projected intersections of F4 with the Transect at the surface, through a deep lateral resistivity discontinuity (notch) in the dioritic intrusion, to a rather good conductor at depths greater than 2 km. The plunge of the lines is consistent with the apparent dip of the F4 faults at their intersection with the Transect. Given the significance of F4 in the function of the hydrothermal system, we interpret the low resistivity notch to be an epiphenomenal signature of the permeable fault zone through which hydrothermal fluids convect.

The bell shaped dome located between sites 906B and 910B and peaking at approx. 0.28 km beneath site 907B is interpreted to be part of the dioritic intrusion. It is noteworthy that the resistivity of the dome decreases from approx. 20 Ωm at the depth of 0.45 km to approx. 12 Ωm at depths 0.6–0.75 ckm. The long-dash line marked F3 starts at the approximate position of the intersection of F3 with the Transect at the surface and plunges at an angle of 70° to the NE; it can easily be seen to pass through the zone of decreased resistivity, which can thus be interpreted as an epiphenomenon of faulting (fluid circulation). The downward extrapolation of same line connects with yet another low-contrast lateral discontinuity in the deeper resistivity structure, located at depths 1.5–2.5 km at a distance of approx. 4 km along the Transect. This is also interpreted to result from the combined effect of several converging faults.

Northward of site 907B, the shallow and deep circulation zones appear to be controlled by the fault network. In addition to F1, F2 and F3, possible "culprits" are the faults of the F5 secondary system. Just to give an example, the dash-dot line marked F5/F7 starts at the projected intersection of a significant F5 and F7 fault with the Transect and plunges at 70° to the NE; this may adequately explain a significant part of the resistivity structure observed in the vicinity of the West Transect.

6.4.3 East Transect (BB′)

Figure 6.11 illustrates the logarithm of the resistivity structure, as reconstructed by the 2-D inversion. At the SW extension of the Lakki depression (outside of the caldera), the structure is generally more conductive in comparison to the corresponding stretch of the West Transect, although the two profiles are separated by only a few hundreds of meters: the shallow and deep conductive zones detected in the West Transect appear to have merged and their connection to interior of the caldera has become, both at sea level and at depth. The significant change (decrease) in resistivity is attributed to fluid circulation and diffusion associated with the F2 system of faults.

The gravity fault defining the southern boundary of the caldera is observable at depths shallower than 0.8 km as an interface between a relative resistor to the south (foot wall) and a good conductor to the north (hanging wall), located between 1.5 and 1.7 km along the Transect. Fumaroles exist on the south wall of Lakki and in the vicinity of F2 (see Fig. 6.1); therefore, the good conductor associated with the hanging wall defines the extent of the circulation zone feeding the fumaroles. At depths greater than 1 km an interface cannot be seen and the boundary is drawn by extrapolation. The northern boundary is not observable and is indicated by a long-dash line extrapolated from the surface. The steeply dipping conductor between sites 119R and 904R may be related to circulation along the associated gravity fault.

The relatively resistive formation observed at depths between 0.4 and 2.3 km is attributed to the same dioritic intrusion as that observed in the West Transect and found by drilling at N2. In consequence and as per the West Transect, the location of the floor depends on the age of the intrusion: it is either located in the vicinity of the horizontal dotted line or at depths of the order of 2 km (dashed line).

The horizontal dotted line again indicates the approximate depth extent of the hydrothermal system. We reiterate that according to the analysis of the borehole data, the shallow, very good conductors located at depths up to 0.25 km represent the combined effect of clay mineralization and fluid concentration in the argillic hydrothermal zone, while the deeper (0.25–0.5 km) good

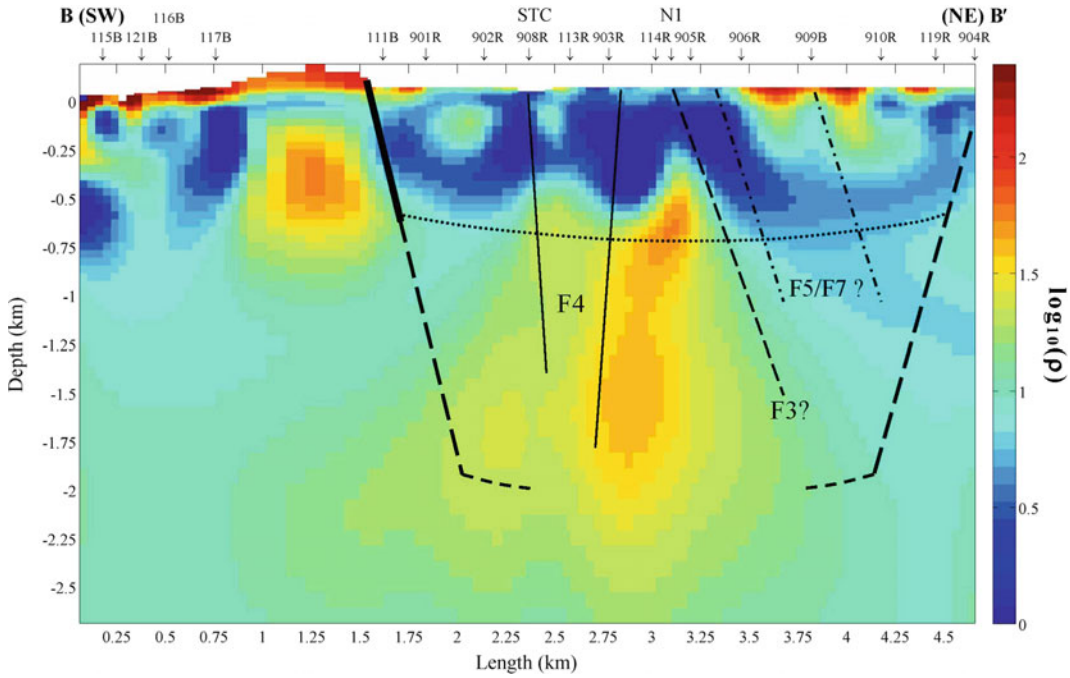

Fig. 6.11 Two-dimensional best-fitting model of the resistivity structure along the East Transect B–B′. STC marks the position of Stephanos phreatic explosion crater; N1 marks the nearest to N1 location of the transect

conductors more likely represent fluid concentration in the phyllic hydrothermal zone.

As also repeatedly noted above, the deep circulation zones are associated with contemporary faulting. Inside as well as outside of the caldera, the geoelectric structure is more conductive in comparison to the corresponding stretch of the West Transect, although the two profiles are separated by a few hundreds of meters. Noting, however, that inside the caldera, the East Transect runs literally on top of the main F2 fault, it is reasonable to propose that the overall lower resistivity is a consequence of increased fluid circulation and diffusion in the immediate vicinity of F2, particularly at the southern part of Lakki.

The lines marked F4 connect the intersections of F4 with the East Transect at the surface, through a very good sub-vertical conductor extending between 0.05 and 0.4 km directly beneath site 908R, to a low resistivity notch in the postulated dioritic intrusion and to a rather good conductor at depths greater than 2 km. The shallow conductor lies directly beneath Stephanos and is thought to represent the combined effect of clay mineralization and fluid circulation through F4. The plunge of the lines is consistent with the apparent dip of the faults at their intersection with the Transect so that the low resistivity notch is again interpreted as the signature of the fault zone through which hydrothermal fluids convect.

The line marked F3 starts at the projected intersection of the Transect with trace of F3 at the surface, and plunging at approx. 70° to the NE through a similarly dipping very good conductor, defines the boundary of the inferred dioritic intrusion. The geoelectric structure of the hanging wall of F3 appears to be very conductive. As in the West Transect, the shallow and deep circulation zones northward of site 905R may be augmented by faults additional to F2 and F3, specifically those of the F5 and F7 secondary system. As an example, the dash-dot lines marked F5/F7 start at the projected intersections of F5 and F7 faults with the Transect and plunge at 70° to the NE: it is apparent that they may explain several details related to the distribution

of near-surface conductors in the vicinity of the Transect.

6.5 Discussion

In general, 2-D inversion yielded satisfactory fitting between observed and calculated responses and rather well-constrained reconstructions of the resistivity structure, including detailed electrical images of fluid reservoirs, circulation and diffusion zones and hydrothermal convection paths.

The geoelectric structure is shown to comprise a quasi-two-dimensional, low-contrast background defined by the regional (first order) faulting systems and decorated by local, low-contrast three-dimensional resistivity inhomogeneities. Low resistivity contrasts are the reasons why in spite of local three-dimensionality, 2-D inversion could successfully reconstruct the principal elements of the geoelectric structure. The low contrasts may be the outcome of continuous intense tectonic and hydrothermal activity resulting in extensive lateral fluid diffusion and pervasive alteration that smears any original high resistivity contrasts, even in a domain as structurally inhomogeneous, as a volcanic caldera. The effects of such processes are much more prominent at shallow depths (up to 1 km), where it is easier for fluids to diffuse (also facilitated by higher effective porosities and lower lithostatic pressures). This is also the reason why the reconstruction (fitting) was more successful at the short-period half of the measured bandwidth.

The resistivity structure at depths 100–300 m is characterized by a number of interconnected, very low resistivity enclosures (<2 Ωm), which are thought to correspond to fluid concentrations (reservoirs) within the argillic alteration zone. At depths between 300 m and 1 km, these merge into laterally extended low resistivity (<12 Ωm) zones which are thought to represent fluid concentrations and circulation in the phyllic and phyllic-propylitic alteration zones (hence the increased resistivity). Unfortunately, the absence of precise data on the fractional volume of clay minerals does not allow a reasonable estimation of the liquid fraction and storage capacity. The development of reservoirs and the lateral circulation and diffusion of fluids at all depths may have been facilitated by both major and minor fault zones, often resulting in the formation of fault-aligned epiphenomenal conductors. At the southern half of Lakki where the hydrothermal field is located, the caldera boundary faults and systems F1, F2 and F4 appear to be major contributors. At the northern half of Lakki, F2, F3, F5 and F7 appear to have more prominent effect.

The deep (>1 km) and more important convection and circulation zones are generally associated with major faults and their intersection. Compelling evidence is presented, indicating that the most significant of those are a system of NE-SW oriented active normal faults (identified as F1 and F2 in Fig. 6.1), intersecting with a conjugate system of NNW-SSE normal faults identified as F4, which is particularly active at the SW sector of the island and defines the main convection path. One line of such evidence relates to the configuration of telluric current flow in the area of most intense thermal activity, at the southern part of Lakki, which has a definite NNW-SSE orientation and correlates with the orientation of F4, as well as with the alignment of thermal phenomena (fumarolic activity, phreatic explosion craters and debris flow and lacustrine deposits related to phreatic explosion events). It is almost straightforward to define a causal connection between active normal faulting and telluric current flow because the conductivity of near surface rock formations is principally electrolytic and depends on the salinity of the liquid fraction, the temperature and the presence (or absence) of clay minerals which may increase the salinity by orders of magnitude through ion exchange interactions and/or hydrolysis. Whereas convection/circulation conduits identify with active normal fault zones, it becomes apparent that electric current should flow easier parallel to the fluid-filled conduits than across them.

At depths between 1 and 2 km, the fault-aligned fluid convection paths associated with F4 have been imaged as sub-vertical

low-resistivity zones etched on relatively more resistive background (presumed dioritic intrusion), which connect the shallow conductive structure with deep conductors presumably related to the heat source. Analogous images have been obtained for the caldera boundaries, which are more or less clearly outlined.

Due to the overall low resistivity of the structure, the long periods of the measured Magnetotelluric field could not penetrate to depths greater than approx. 3 km. In consequence, the heat source in the form of a magma chamber, such as the one inferred to exist at depths of the order of 7 km (Lagios et al. 2005), was not detected: only the conductive halo of the heat source could be probed.

Overall, the analysis has provided detailed images of the volcano's interior, useful information on its geothermal potential and valuable insight into its structure and function. It should be emphasized, however, that the results and conclusions are still approximate: local 3-D induction effects, albeit weak, could not be fully resolved and their effect on the details of the resistivity structure cannot be assessed. It is also difficult to assess the true variation of resistivity between the parallel 2-D transects, which is very important in understanding the geothermal system from both the academic and practical points of view. Such problems can be addressed with 3-D inversion, which is expected to provide definitive images of the geoelectric structure and convection paths. This is a challenge to be taken up and reported in the future.

References

Bachmann O, Deering CD, Ruprecht JS, Huber C, Skopelitis A, Schnyder C (2011) Evolution of silicic magmas in the Kos-Nisyros volcanic center, Greece: a petrological cycle associated with caldera collapse. Contrib Mineral Petrol. doi:10.1007/s00410-011-0663-y

Banks RJ, Wright D (1998) Telluric analysis of distributed magnetotelluric impedance measurements. Annales Geophys Suppl (1–16), C275. In: XXIII EGS Gen Assembly Nice France, 20–24 Apr 1998

Bohla M, Keller J (1987) Petrology of plinian eruptions of Nisyros volcano. Hellenic arc Terra Cognita 7:171

Davis EN (1967) Zur geologie und petrologie des Inseln Nisyros und Jali (Dodecanese). Praktika Akademy of Athens 42:235–252

Dawes GJK (1984) Short period automatic magnetotelluric (S.P.A.M.) system. In: A broadband tensorial magnetotelluric study in the Travale-Radicondoli Geothermal Field. In: EC Final Report, Contract No. EG-A2-031-UK

Dawes GJK, Lagios E (1991) A magnetotelluric survey of the nissyros geothermal field (Greece). Geothermics 20(4):225–235

Di Paola GM (1974) Volcanology and petrology of Nisyros Island (Dodecanese, Greece). Bull Volcanol 38:944–987

Egbert GD, Booker JR (1986) Robust estimation of geomagnetic transfer function data. Geophys J R Astr Soc 87:173–194

Francalanci L, Vougioukalakis GE, Perini G, Manetti P (2005) A west-east traverse along the magmatism of the south aegean volcanic arc in the light of volcanological, chemical and isotope data. In: Fytikas M and Vougioukalakis G (eds) The South Aegean Volcanic Arc, Present Knowledge and Future Perspectives, Elsevier, pp 65–111

Geotermica Italiana (1983) Nisyros 1 geothermal well. PPC-EEC Report, p 106

Huber PJ (1981) Robust statistics. Hoboken NJ, John Wiley & Sons, Inc

Keller J (1982) Mediterranean island arcs. In: RS Thrope (ed) Andesites. Wiley, New York, pp 307–325

Lagios E (1991) Magnetotelluric study of the structure of the Nisyros Geothermal Field. Bull Geol Soc Greece 25(3):393–407

Lagios E, Apostolopoulos G (1995) Integrated geophysical study of the geothermal system in the southern part of Nisyros Island, Greece. J Appl Geophys 34:55–61

Lagios E, Tzanis A, Dawes GJK (1991) Audio-magnetotelluric survey of Nisyros geothermal field, phase II. In: Report submitted to PPC, Department of Alternative Energy Resources, Athens, Greece

Lagios E, Sakkas V, Parcharidis I, Dietrich V (2005) Ground deformation of Nisyros volcano (Greece) for the period 1995–2002: results from DInSAR and DGPS observations. Bull Volc 68(2):201–214. doi:10.1007/s00445-005-0004-y

LaTorraca G, Madden T, Korringa J (1986) An analysis of the magnetotelluric impedance tensor for three-dimensional structures, Geophys 51:1819–1829

Limburg EM, Varekamp JC (1991) Young pumice deposits on Nisyros. Greece. Bull Volcanol 54 (1):68–77

Nomikou P, Papanikolaou D (2011) Extension of active fault zones on Nisyros Volcano across the Yali-Nisyros Channel based on onshore and offshore data. Mar Geophys Res 32:181–192. doi:10.1007/s11001-011-9119-z

Papadopoulos GA, Sachpazi M, Panopoulou G, Stavrakakis G (1998) The volcano-seismic crisis of 1996–97 in Nisyros, SE Aegean Sea, Greece. Terra Nova 10:151–154

Papanikolaou D, Nomikou P (2001) Tectonic structure and volcanic centres at the eastern edge of the Aegean volcanic arc around Nisyros Island. Bull Geol Soc Greece 34(1):289–296

Papanikolaou D, Lekkas E, Sakellariou DT (1991) Geological structure and evolution of Nisyros Volcano. Bull Geol Soc Greece 25(1):405–419

Ritter P, Banks RJ (1998) Separation of local and regional information in distorted GDS response functions by hypothetical event analysis. Geophys J Int 135:923–942

Rodi W, Mackie RL (2001) Nonlinear conjugate gradients algorithm for 2-D magnetotelluric inversion. Geophysics 66(1):174–187

Sachpazi M, Kontoes Ch, Voulgaris N, Laigle M, Vougioukalakis G, Olga Sikioti G, Stavrakakis G, Baskoutas J, Kalogeras J, Lepine JCl (2002) Seismological and SAR signature of unrest at Nisyros caldera, Greece. J Volcanol Geoth Res 116:19–33

Seymour KST, Vlassopoulos D (1989) The potential for future explosive volcanism associated with dome growth at Nisyros, Aegean volcanic arc, Greece. J Volcanol Geotherm Res 37:351–364

Seymour KST, Vlassopoulos D (1992) Magma mixing at Nisyros volcano, as inferred from incompatible trace-element systematics. J Volcanol Geotherm Res 50:273–299

Sims WS, Bostick FX Jr, Smith HW (1971) The estimation of magnetotelluric impedance tensor elements from measured data. Geophysics 36:938–942

Tzanis A (2014) The characteristic states of the magnetotelluric impedance tensor: construction, analytic properties and utility in the analysis of general Earth conductivity distributions. http://arxiv.org/abs/1404.1478 [physics.geo-ph]. Accessed, 1 May 2017

Ungemach P (1983) Nisyros geothermal wildcut drilling, testing, sampling, 6 June, 3 Dec 1982. In: Exec. summary, preliminary report, EEC Contract No EG-A-1-046-G and EG-A-Y-113-I

Vanderkluysen L, Volentik A, Hernandez J, Hunziker JC, Bussy F, Principe C (2006a) The petrology and geochemistry of lavas and tephras of Nisyros volcano, Greece. Implications for the volcanic hazards (44) Mémoires de Géologie Lausanne, pp 79–99

Vanderkluysen L, Volentik A, Principe C, Hunziker JC, Hernandez J (2006b) Nisyros' volcanic evolution: the growth of a stratovolcano. In: Hunziker JC, Marini L (eds) The geology, geochemistry and evolution of Nisyros Volcano (Greece). Implications for the volcanic hazards (44) Mémoires de Géologie, Lausanne, pp 100–106

Varekamp JC (1992) Some remarks on volcanic vent evolution during plinian eruptions. J Volcanol Geotherm Res 54:309–318

Volentik A, Vanderkluysen L, Principe C, Hunziker JC (2006) Stratigraphy of Nisyros volcano (Greece). In: Hunziker JC, Marini L (eds) The geology, geochemistry and evolution of Nisyros Volcano (Greece). Implications for the volcanic hazards (44) Mémoires de Géologie, Lausanne, pp 26–66

Vougioukalakis G (1989) Geological map of Nisyros Island, 1:25.000. In: IGME, Athens, Greece

Vougioukalakis G (1993) Volcanic stratigraphy and evolution of Nisyros Island. Bull Geol Soc Greece 28(2):239–258

Wyers PG, Barton M (1989) Polybaric evolution of calc-alkaline magmas from Nisyros, Southeastern Hellenic Arc, Greece. J Petrol 30:1–37

Yee E, Paulson KV (1987) The canonical decomposition and its relationship to other forms of magnetotelluric impedance tensor analysis. J Geophys 61:173–189

Geophysical Monitoring: Seismicity and Ground Deformation in the Kos-Nisyros-Yali Volcanic Field

7

Jannis Makris, Joanna Papoulia, Myrto Groumpa and Chrysoula Fasoulaka

Abstract

A Vp velocity model of the sediments, crust and upper mantle of the Kos-Rhodos area, southeastern Aegean Sea, was obtained by evaluating wide aperture reflection refraction seismic data, collected by using 4C Ocean Bottom Seismographs (OBS) and stand-alone land stations along 8 seismic lines of 1000 km total length. Seismic energy was generated by air gun shots spaced at 120 m intervals fired by a tuned air gun array of 49 l volume. Velocity modelling by seismic tomography and ray tracing revealed the structure of the crust and sediments. Good Ps, Pg and PmP reflections were recorded at nearly all observed sections, allowing delineating the sediments and crust structure and defining crustal thickness. The sediments are 3–5 km thick. Four sedimentary layers were mapped with velocities ranging from 1.7 to 5.4 km/s. The lateral velocity variations in the sediments and the existence of several faults indicate intense fragmentation and the development of several individual basins, like the western and eastern Kos basins, the Kondelioussa basin, the north Karpathos basin, the south Nisyros basin, the Tilos basin and a number of

Electronic supplementary material The online version of this chapter (doi:10.1007/978-3-319-55460-0_7) contains supplementary material, which is available to authorized users.

J. Makris
University of Hamburg, Hamburg, Germany

J. Papoulia (✉) · C. Fasoulaka
Hellenic Centre for Marine Research, Athens, Greece
e-mail: jpapoulia@gmail.com

M. Groumpa
National Technical University of Athens, Athens, Greece

V.J. Dietrich and E. Lagios (eds.), *Nisyros Volcano*, Active Volcanoes of the World,
DOI 10.1007/978-3-319-55460-0_7

basins west of Rhodos. The upper crust is approx. 6.5 km thick with Vp velocities ranging from 5.8 to 6.5 km/s. The lower crust is 10–12 km thick with Vp velocities 6.8–7.2 km/s. The crust is stretched continental, with the Moho discontinuity located at 17 km towards the Cretan Sea, 20 km below Kos—Nisyros area, thickening to 22 km under Rhodos and western Turkey. Pn velocities have a value of approx. 7.8 km/s, indicating that below the Dodecanese area a low velocity zone exists in the uppermost part of the mantle, limited in depth by a high velocity layer of approx. 8.1 km/s. A deep sub-Moho reflector at 31 km depth was identified, implying the solid nature of rocks in the upper mantle. Magmatic intrusions were identified in the broader Caldera region.

Fig. 7.1 The Aegean volcanic arc and the study area of Dodecanese

7.1 Crustal Thickness and Physical Properties of the Dodecanese Area, Southeastern Aegean Volcanic Arc

7.1.1 Introduction

The deformation of the Aegean Sea is dominated by wrench faulting of NE–SW orientation, inducing trans tension and subsidence of the continental crust and developing sedimentary basins like the North Aegean Trough and the Cretan Sea (e.g. Makris et al. 1977; Ginzburg et al. 1987). High seismicity indicates the on-going deformation (e.g. Makropoulos and Burton 1981; Papazachos and Papazachou 1997).

A well-developed volcanic arc extends from Lichades, Methana, Milos and Santorini islands, terminating to the east Aegean Sea, at the island of Nisyros (Fig. 7.1).

The evolution of the volcanic arc is triggered and controlled by the northeastward subduction of the Ionian oceanic lithosphere beneath the passive Hellenic margin of the European plate (e.g. McKenzie 1972; LePichon and Angelier 1979; Papanikolaou 1993; Jackson 1994). As a result of this on-going subduction, significant magmatic and volcanic activity occurs in the Dodecanese area since late Pleistocene—Holocene. Nisyros and the surrounding islands of Yali, Strongyli, Kondelioussa and Pergousa (Fig. 7.2) represent late Pleistocene—Holocene volcanoes. The island of Nisyros is mainly composed by lava flows, pyroclastic layers and lava domes dated from 160 ka (e.g. Davis 1967; Keller et al. 1990; Allen 2001), forming a cone of 8 km diameter at its base and 4 km caldera at its top. It lies on alpine Mesozoic basement and a thinned continental crust. On the island of Kos, to the north of Nisyros, major magmatic activity has also occurred since late Miocene—Pliocene, and one of the largest volcanic eruptions in the eastern Mediterranean, dated at 0.16 Ma bp, is represented by the Kos ignimbrite (Keller et al. 1990). The products of this eruption covered an area of more than 3000 km^2 (Allen 2001).

Although the east Aegean volcanic activity has been extensively studied (e.g. Keller 1969; Nomikou and Papanikolaou 2000), geophysical studies were limited to geothermal field

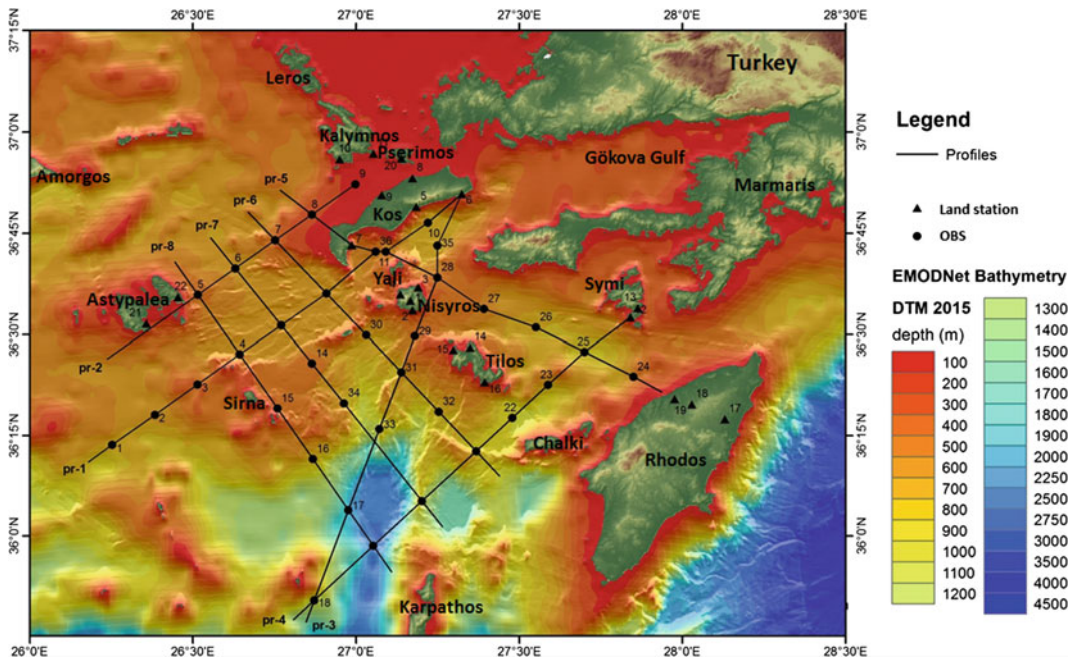

Fig. 7.2 Location of the seismic profiles in the Dodecanese area plotted on the bathymetric map

investigations of the Nisyros area (Marini et al. 1993). Within the EC "GEOWARN" project (Geowarn 2003), a wide aperture reflection refraction seismic survey was carried out, aiming to define crustal thickness and major tectonic elements of the Dodecanese area and revealing the on-going geodynamic evolution associated with the magmatic and volcanic processes. In the following we present the results of this active seismic experiment and discuss them in relation to the geology and tectonics of the east Aegean volcanic regime.

7.1.2 The Seismic Experiment

The locations of the seismic lines, of the 36 OBS (Ocean Bottom Seismographs) and 22 land stations are shown in Fig. 7.2. The land stations were deployed on the islands of Kos, Nisyros, Tilos, Pserimos, Symi, Rhodos and Astypalea. Line lengths varied between 80 and 140 km. Total length of the observed profiles exceeds 1000 km. Shooting inline was generated by a 49 l air gun source. Shots were fired every 120 m and the gun array, operating at 2000 psi, was tuned at low frequencies in order to obtain maximum seismic penetration by recording long offset data. The R/V AEGAEO of the Hellenic Centre for Marine Research was used to perform the seismic acquisition.

All OBS positions were recovered and were available for seismic modelling together with the seismic data from the land stations. Seismic data were subjected to standard processing involving data extraction, demultiplexing and correction of time drift, resampling, determination of OBS positions and reformatting to SEG-Y data files. Band pass filtering was also applied and the data were deconvolved.

The velocity-depth structure was evaluated by first break and layer tomography combined with two point ray tracing forward modelling. In the following we present the velocity results obtained for the 8 seismic profiles.

7.1.2.1 The SW–NE Profile: P1

This profile has a length of 140 km and was evaluated using 8 OBS positions and one land station on the island of Kos. Modelling was further constrained from results obtained at lines P4, P5, P6, P7 and P8 that intersect this SW–NE oriented profile (Fig. 7.2). A Common Receiver Gather (CRG) of OBS position 1 is presented in Fig. 7.3. This CRG, vertical geophone, is plotted with a linear move out using 6 km/s as reduction velocity. All CRGs in this paper are treated in the same way. Seismic energy propagated efficiently for more than 100 km offsets. Ps arrivals from the sedimentary layers are clearly seen. PmP reflections from the crust/mantle boundary (Moho discontinuity) were observed between Km 20 and 40, implying a thinned continental crust. At Km 82 uplifted arrivals indicate the position of high velocity intrusions in the uppermost crust and sediments within the volcanic domain of Kos-Nisyros. Also between Km 45 and 100 deeper arrivals are generated at reflecting interfaces of sub-Moho depths.

In Fig. 7.4 the result of the first break tomography using first arrivals from all OBS positions and the land station on Kos Island is shown. First break velocity-modelling produces a velocity gradient model limited at depth by the offsets of the diving waves. In this way a first approximation of the crustal geometry is developed and used to constrain modelling of later arrivals by tomographic inversion and ray tracing. The initial velocity model for the first break tomography is based on the apparent velocities observed at the CRGs and is limited at depth by wide-angle reflections from the Moho discontinuity. For reasons of brevity in the present paper we discuss the first break tomographic result only for the first line.

Soft sediments thickness varies from 2 to 5 km, with maximum values at the western edge of the profile, and south of Kos (Km 100). Below OBS position 3, at the western part of the profile, sediments of 4.7 km/s velocity are exposed very close below surface, on either side of the OBS, indicating the position of an anticline.

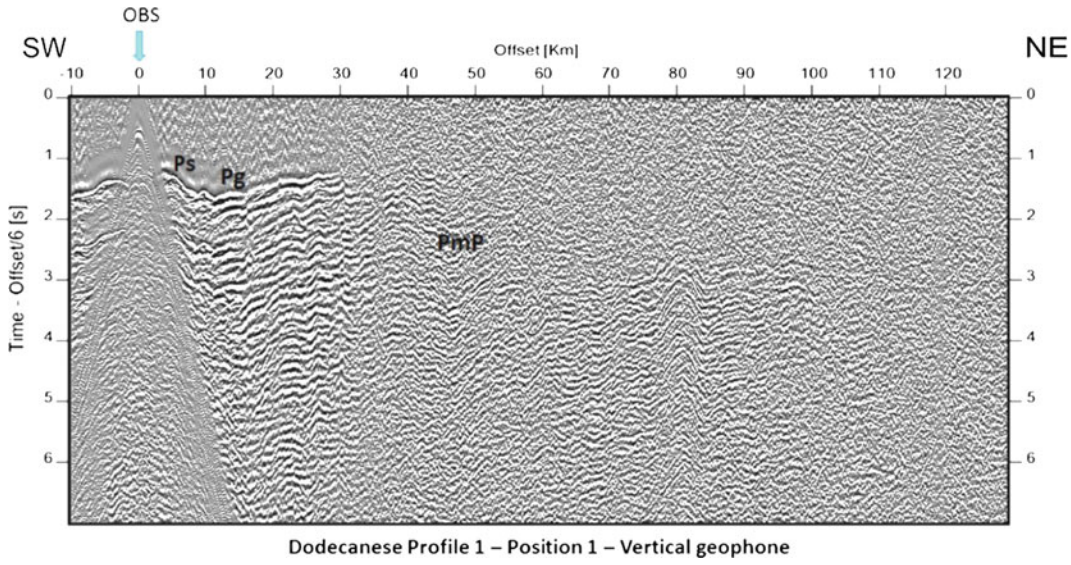

Fig. 7.3 Common Receiver Gather (CRG) for OBS position 1

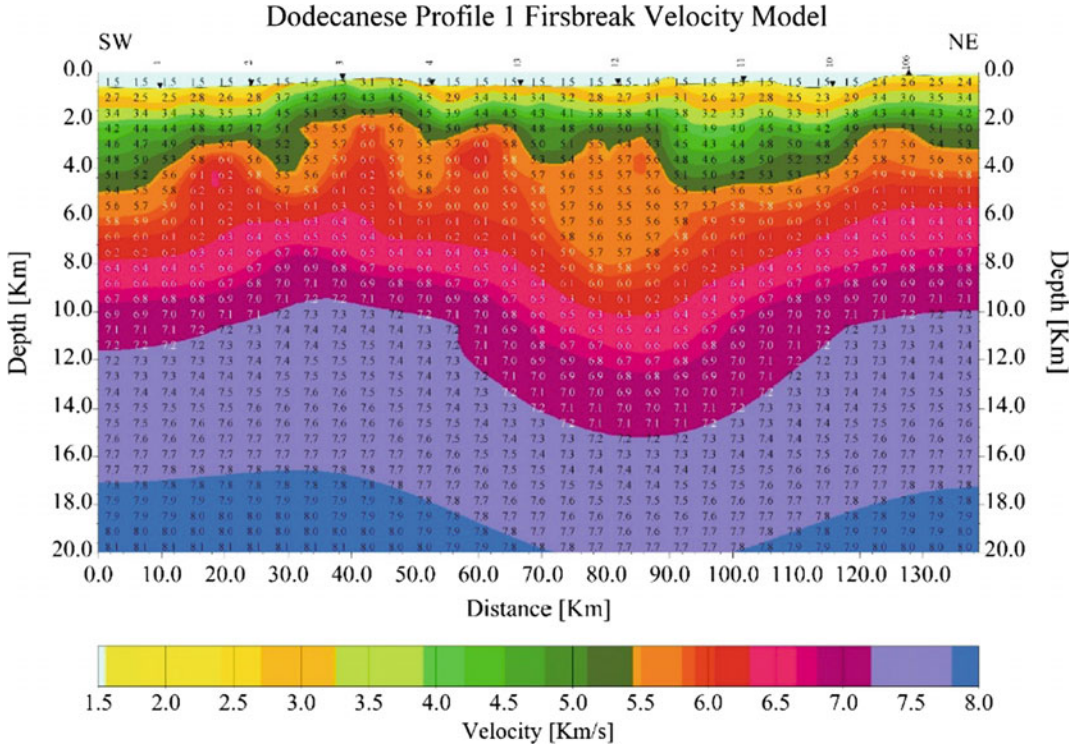

Fig. 7.4 First break tomography of Profile 1. 8 OBS positions and 1 Land station are indicated by triangles along the profile

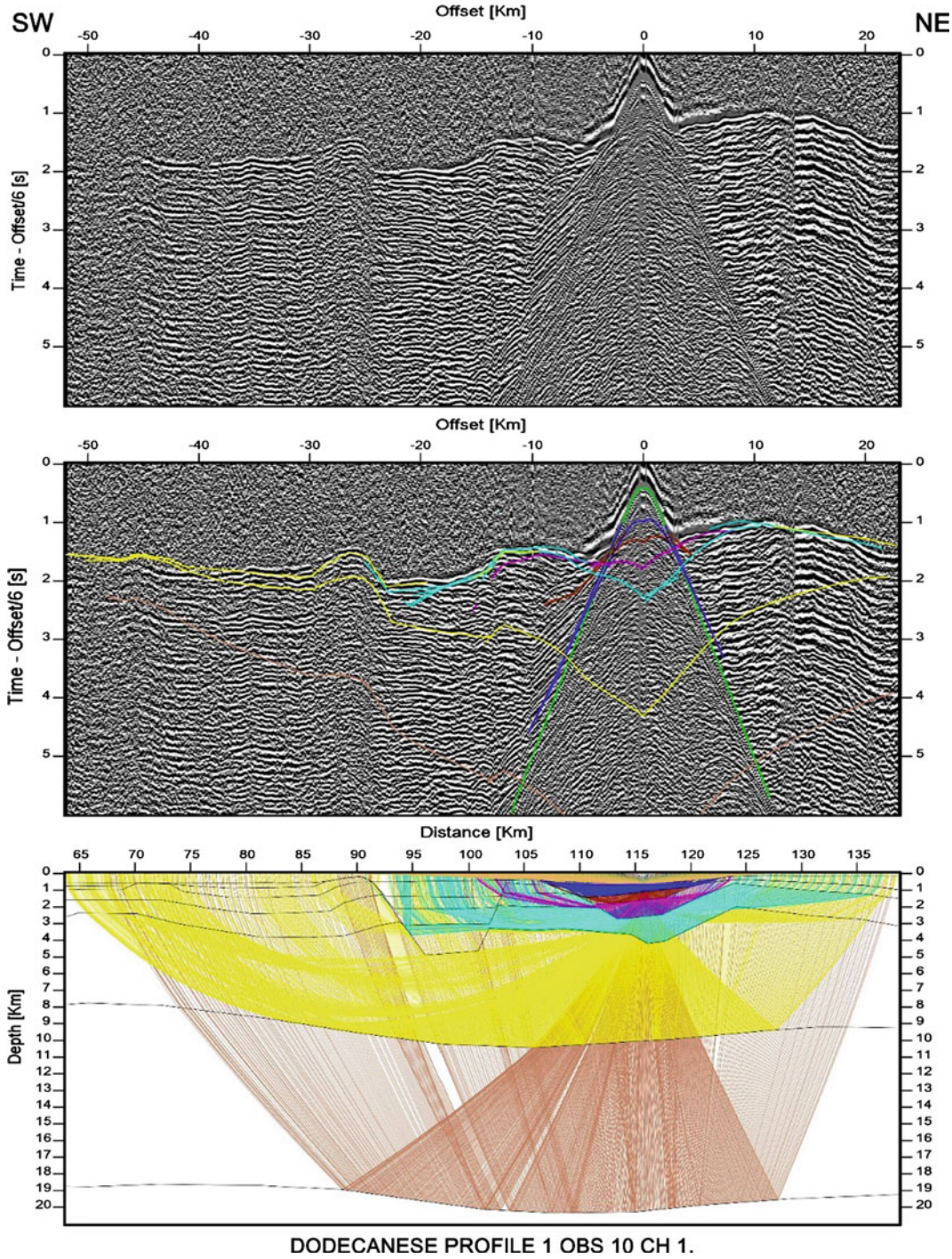

Fig. 7.5 Dodecanese profile 1: Common Receiver Gather of OBS position 10, vertical component (*upper part*) with colour-coded travel times (*middle part*), and corresponding travel paths (*lower part*)

The first break velocity model clearly defines the limits of the west and east Kos basins, between OBS position 12 and land station 106. The west Kos basin is limited to the south by a NE dipping major fault at Km 90, while the east Kos basin is truncated to the north by a SW dipping fault at Km 120.

In order to exploit later arrivals of reflected energy we applied a layer tomography procedure constrained by the first break velocity results. Computations are performed top down, introducing first order discontinuities from shallow to deeper layers. Layer tomography delineates the lateral geometry of an assumed interface and also varies the velocity within a given layer laterally until the best fit between observed and computed travel times of the reflected energy is achieved (Ditmar and Makris 1996). By exploiting forward modelling, using the SEIS84 algorithm (Cerveny and Psencik 1981), the obtained result from the layer tomography, optimizing the fit between the observed and the computed travel times, is controlled. This procedure is continued until the final velocity permits synthetic calculations of travel times and amplitudes that satisfy all observed phases. An example of a ray traced CRG is presented in Fig. 7.5.

The final Vp velocity model of Profile 1 is presented in Fig. 7.6. Four sedimentary layers with Vp velocities of 1.7, 2.7–2.8, 4.4 km/s and 5.2–5.4 km/s were identified. The basis of the consolidated sediments (5.2–5.4 km/s layer), indicated as basement, varies in depth from 2 to 5 km. The west Kos basin is well defined, limited to the south by a major NE dipping normal fault at Km 90. This fault is also seismically active as shown by passive seismic observations (Papoulia et al. 2016). The east Kos basin is truncated by a SW dipping normal fault at Km 120. The down thrown basement and thickening of the low velocity sediments on either side of OBS position 11 outlines the SE–NW extension of the Kos-Nisyros caldera. The igneous crust is approx. 16 km thick, and Moho is encountered at a depth of 19 km, and is slightly depressed to the northeast to 21 km below the caldera region.

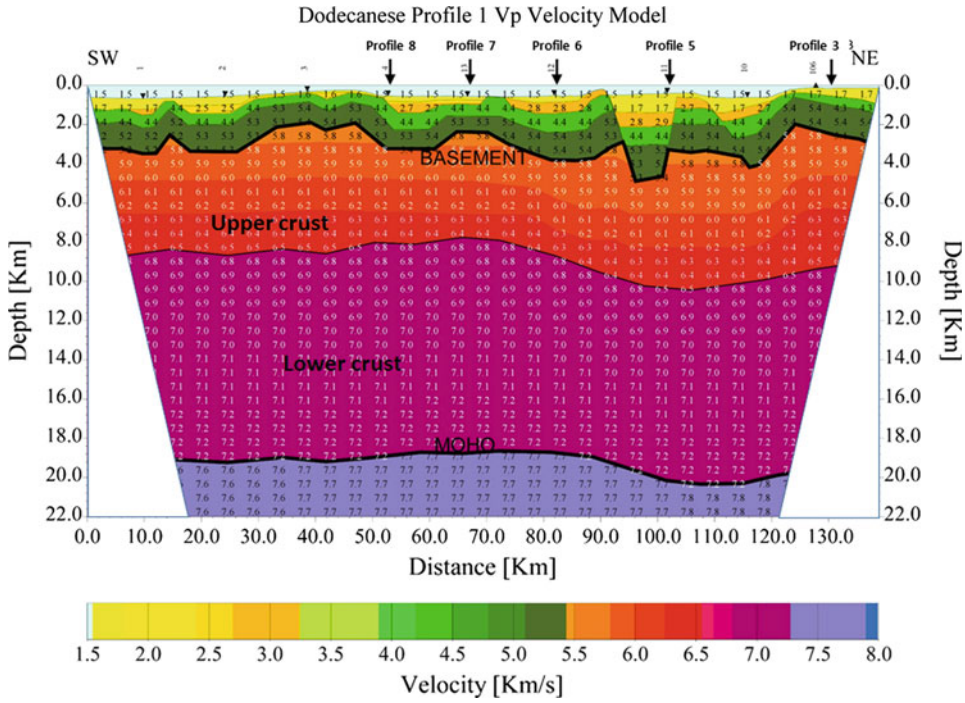

Fig. 7.6 Vp-velocity model along profile P1

7.1.2.2 The SW–NE Profile: P2

This profile, between Astypalea and Pserimos, has a length of 95 km and was observed using four OBS positions, two land stations on the island of Astypalea and one on Pserimos. Modelling was further constrained from results obtained at lines P5, P6, P7 and P8 that intersect this SW–NE oriented profile (Fig. 7.2). Seismic energy propagated efficiently throughout the whole length of the profile. Thickness of the continental crust was mapped by PmP reflections observed at a distance of 20–50 km, northeast of the OBS position (Electronic Supplementary Material Appendix 7.1.2).

The Vp velocity model is shown in Fig. 7.7. Four sedimentary layers were identified with velocities of 1.7, 2.6–2.7, 4.3–4.4 km/s and 5.3–5.4 km/s. Basement depth ranges from 2 to 3.5 km. A major northeast dipping normal fault is mapped at OBS position 9 (Km 80), which is probably connected to a NW–SE trending fault mapped on Kalymnos Island (IGME 1989), whereas several minor faults are mapped along the profile. Between OBS position 5 and 7 the basement is downthrown forming a small basin that is also expressed by the bathymetry. Moho is encountered at 17 km southeast of Astypalea thickening to more than 19 km towards Pserimos Island.

7.1.2.3 The SSW–NNE Profile: P3

This SSW–NNE oriented profile extends from north Karpathos basin to eastern Kos. Seven OBS positions, two land stations on Nisyros and one land station on Kos were deployed along this 140 km long line. Modelling was further constrained from results obtained at lines P4, P5, P6, P7 and P8 that intersect this profile (Fig. 7.2).

A CRG of OBS position 29, south of Nisyros Island, is presented in Fig. 7.8. The complexity of the travel time plot implies that the crust is

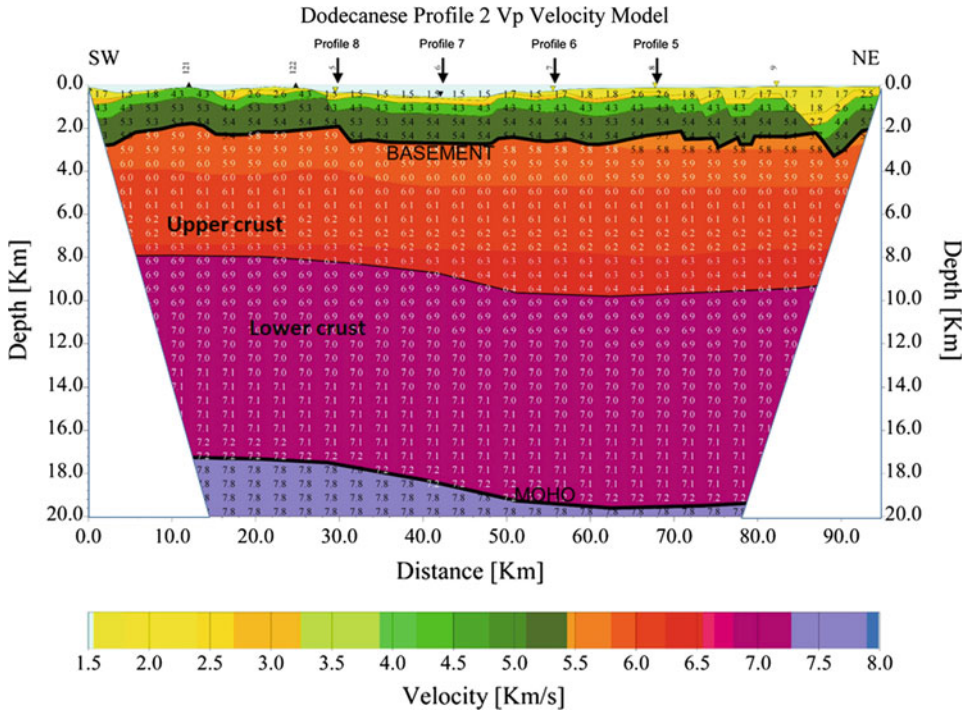

Fig. 7.7 Vp-velocity model along profile P2

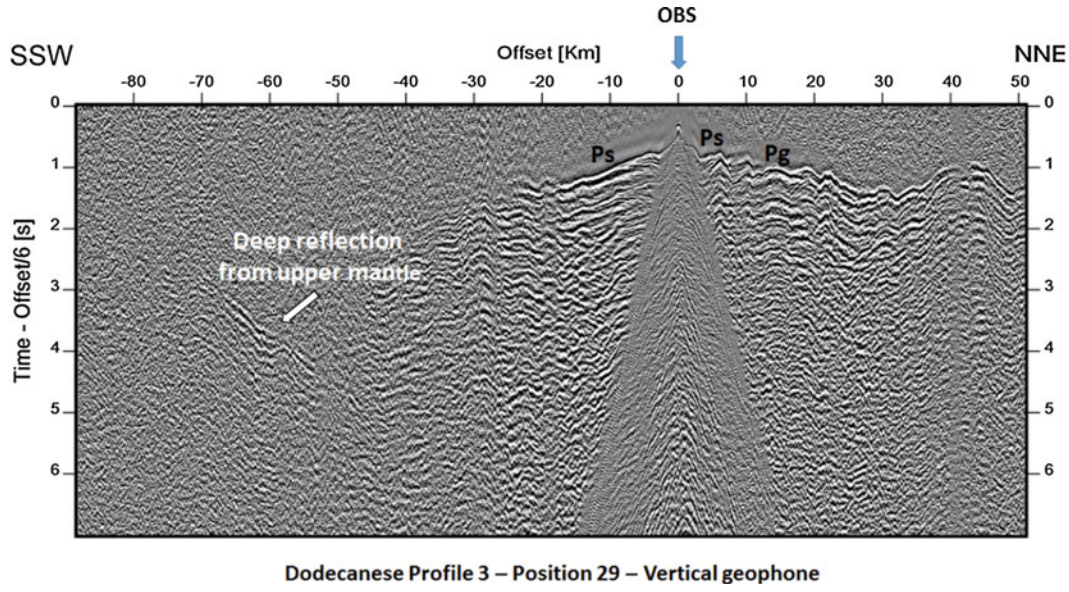

Fig. 7.8 Common Receiver Gather of OBS position 29

significantly fractured. Between 50 and 70 km, west of the OBS position, a deep reflection is recognized. This originates from a sub-Moho discontinuity, in the upper mantle.

An example of a ray-traced model, where arrivals from the sub-Moho discontinuity are also modeled, is given in Fig. 7.9. The Vp velocity model of profile P3 is presented in Fig. 7.10. The four sedimentary sequences observed along the previous lines are also mapped here. The strong morphological depression of the north Karpathos basin, between Km 20 and 60, with water depth exceeding 2000 m, is not followed by increase of the sediment thickness. This implies a very rapid recent subsidence during Holocene—Late Pleistocene times that did not allow recent sediments to accumulate. To the northeast of OBS 28 the east Kos basin is clearly mapped. Between OBS position 33 and 31, the south Tilos basin is mapped. The intense fragmentation of the basement and overlaying sediments by several faults indicate the complexity and strong tectonisation of the crust.

Moho is encountered at 20 km depth, slightly deepening to 22 km below the north Karpathos basin. Wide-angle reflections revealed the existence of a low velocity zone below the Moho, in the upper mantle, extending to 31 km depth at the central part of the profile. This sub-Moho discontinuity could be clearly identified along Profile 3 since this profile is perpendicular to the NNE–SSW orientation of the subduction of the oceanic lithosphere below the Dodecanese area and has also enough offset to the southwest. The low velocity upper mantle layer is probably high temperature asthenosphere that was uplifted below the southern Aegean Sea due to the subduction of the Ionian oceanic lithosphere.

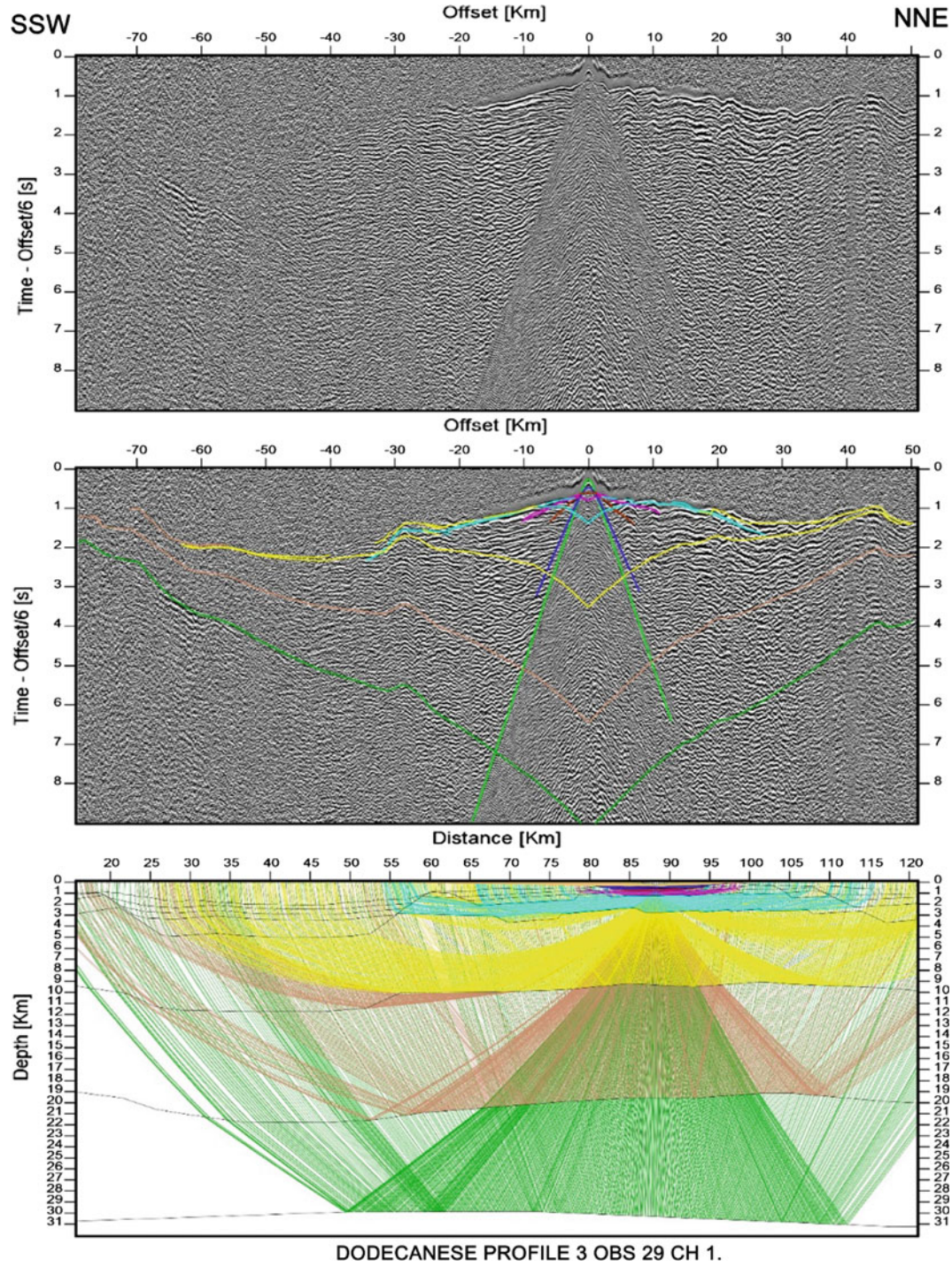

Fig. 7.9 Common Receiver Gather of OBS position 29, vertical geophone (*upper part*) with color-coded travel times (*middle part*), and corresponding travel paths (*lower part*). Arrivals from a deep reflector within the mantle are presented in *green*

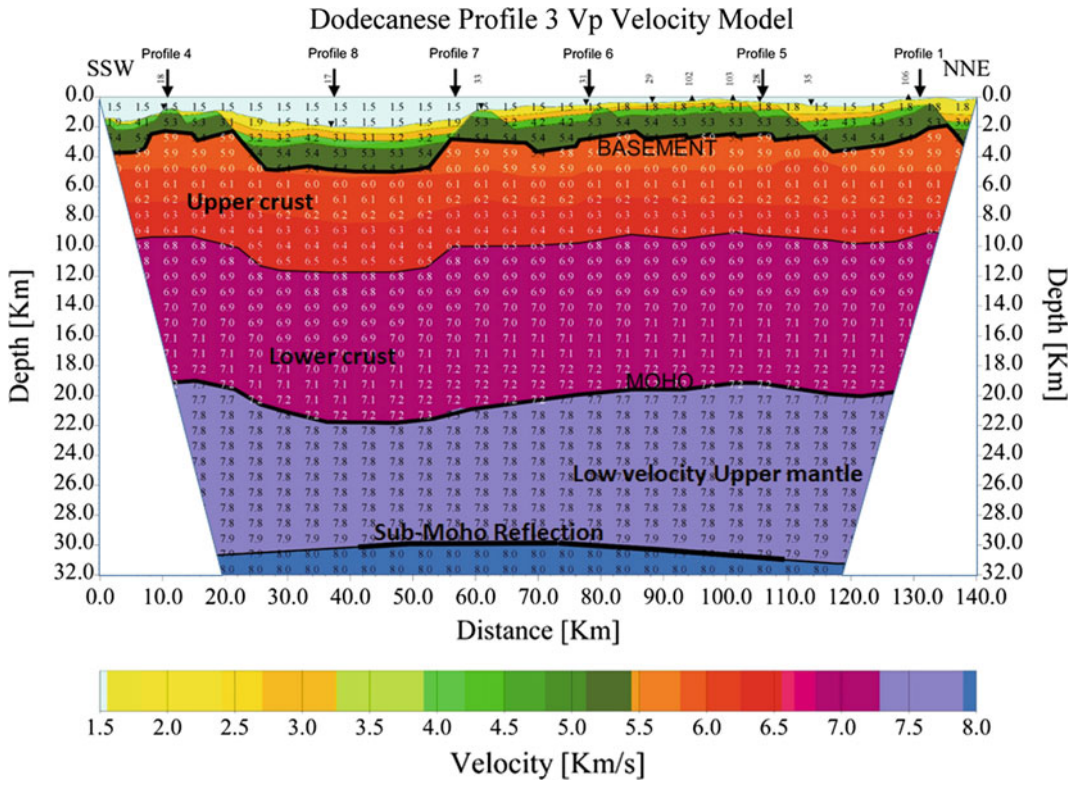

Fig. 7.10 Vp-velocity model along profile P3. The sub-crustal discontinuity at 31 km depth is well constrained from seismic rays between Km 40 and Km 110, as indicated by the *thicker line*

7.1.2.4 The SW–NE Profile: P4

This profile extends from west of Karpathos to the island of Symi, and is parallel to profiles P1 and P2 (Fig. 7.2). Seven OBS positions and two land stations on Symi, were deployed along this 130 km line. Seismic energy propagated for more than 70 km, permitting the identification of PmP reflections from Moho and definition of crustal thickness. The complexity of the travel time curve implies intense tectonisation of the crust and sediments.

The Vp velocity model along this profile is shown in Fig. 7.11. Sediment thickness varies from 2 to 4 km. The north Karpathos basin and its marginal faults are mapped between OBS position 18 and 20. An uplift of sediments and basement occurs around OBS position 23, southeast of Tilos forming an anticline. West and east of this anticline, two sedimentary basins are formed. Moho depth varies from 20 km south of the north Karpathos basin to 21 km below the central part of the profile.

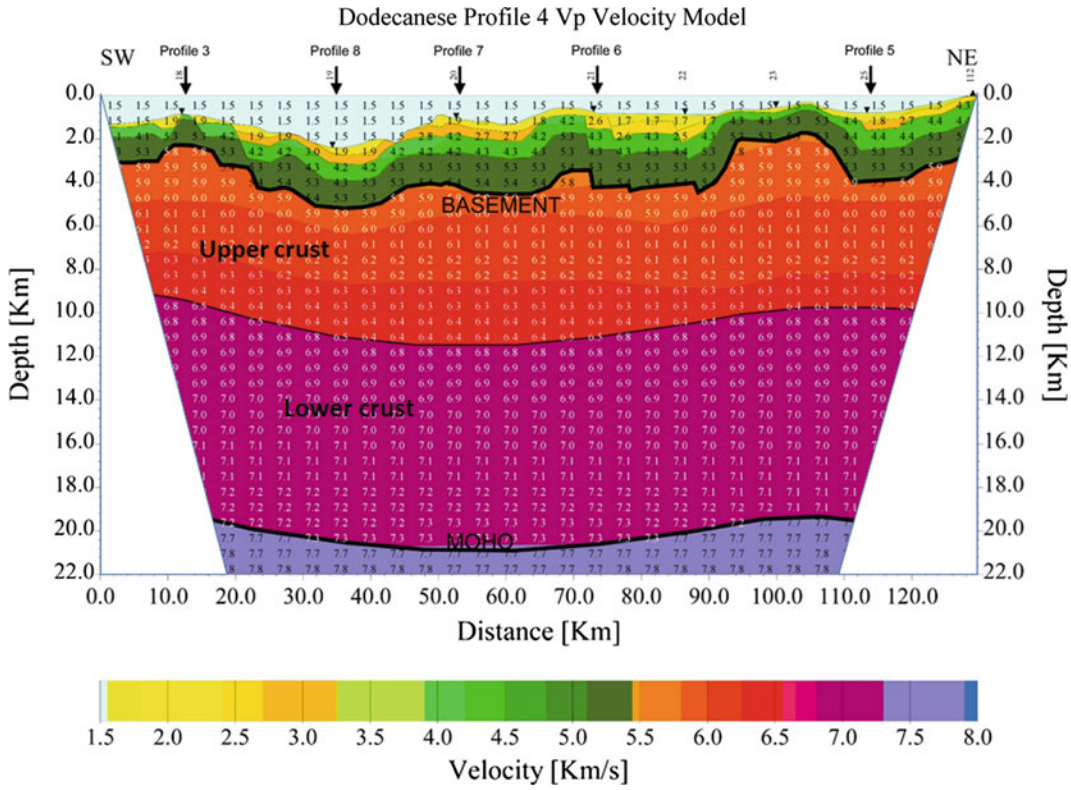

Fig. 7.11 Vp-velocity model along profile P4

7.1.2.5 The NE–SW Profile: P5

This profile has a length of 140 km, extending from southwest of Kalymnos to the northeastern part of Rhodos (Fig. 7.2). Eight OBS positions and four land stations, three on Rhodos and one on Kos Island were deployed. Example of a CRG is presented in Fig. 7.12. Energy propagates efficiently along the entire length of the profile, and good Ps, Pg and PmP seismic arrivals can be observed. The Vp velocity model developed by two point ray tracing (Fig. 7.13) is given in Fig. 7.14. Sediments vary in thickness from 2.5 km at the northwestern part of the line to 5 km below Rhodos Island. The Kos-Nisyros caldera is well defined between Km 20 and Km 45, at the northern part of the profile, where the basement is downthrown and recent sediments with Vp velocities 1.7–1.8 km/s exceed 1 km. This layer is absent on Rhodos island, where the crust is 22 km thick (Moho depth), while below the caldera of Kos-Nisyros area the crust is approx. 20 km thick. Uplift of first break arrivals between Km 10 and Km 20 along the profile is probably connected to magmatic intrusions.

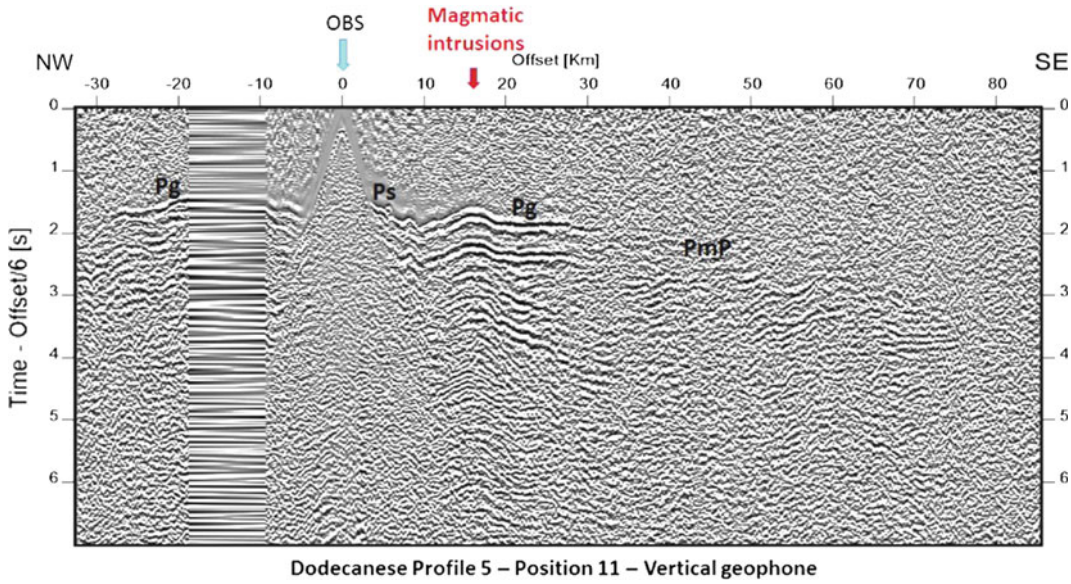

Fig. 7.12 Common Receiver Gather of OBS position 11

7.1.2.6 The Three NW–SE Profiles: P6, P7 and P8

These NW-SE oriented profiles of 100 km length each, extending from northeast of Astypalea towards north Karpathos basin, intersect profiles P2, P1, P4 and P3, and map the crust between the Dodecanese block and the eastern Cretan Sea (Figs. 7.1 and 7.2). As seen in the CRGs (Electronic Supplementary Material Appendix 7.1.2), good Ps, Pg and PmP reflections were observed, allowing to delineate the sediments and crustal structure. The Vp velocity models of these profiles are presented in Fig. 7.15. Ray traced examples for these profiles are given in the Electronic Supplementary Material Appendix 7.1.2. Basement is encountered at 3.5–3.8 km depth in the northeastern edge of the profiles, dipping to more than 5 km towards the southeast. The Kondelioussa basin is crossed by all three profiles between Km 10 and Km 40, of lines P6, P7 and P8. The south Nisyros basin is mapped between Km 60 and Km 90 of line P6, while the abrupt basement depression at Km 70, in both lines P7 and P8, coincides with the north western marginal fault of the north Karpathos basin. The southeastern marginal fault of this basin is mapped at Km 88 of line P7. Thickness of the igneous crust varies from 14 to 16 km at the northwestern end of the profiles, thickening towards the southeast. Moho depth is located at 20 km at the northwest, deepening to the southeast to nearly 22 km if to the crust we add the water depth and sediment thickness.

The Vp velocities of the sediments and crust are very similar with those of the four previous lines. The Pn value of 7.7 km/s at the crust/mantle boundary is lower than the normal Pn values of 8.0 km/s. This is also in agreement with most seismic values obtained in the Aegean Sea (e.g. Makris 1977; Makris and Vees 1977).

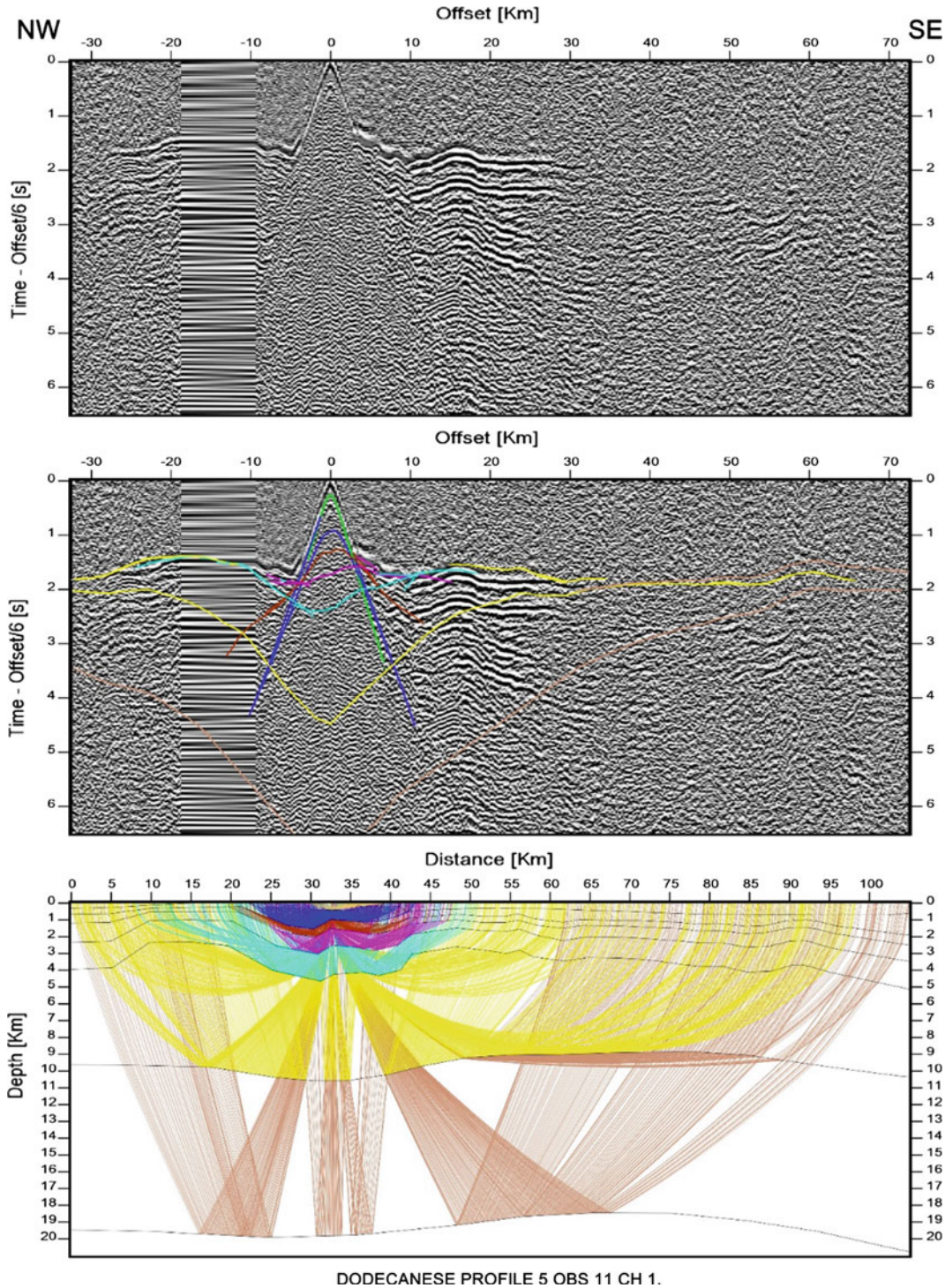

Fig. 7.13 Common Receiver Gather of OBS position 11, vertical geophone (*upper part*) with colour-coded travel times (*middle part*), and corresponding travel paths (*lower part*)

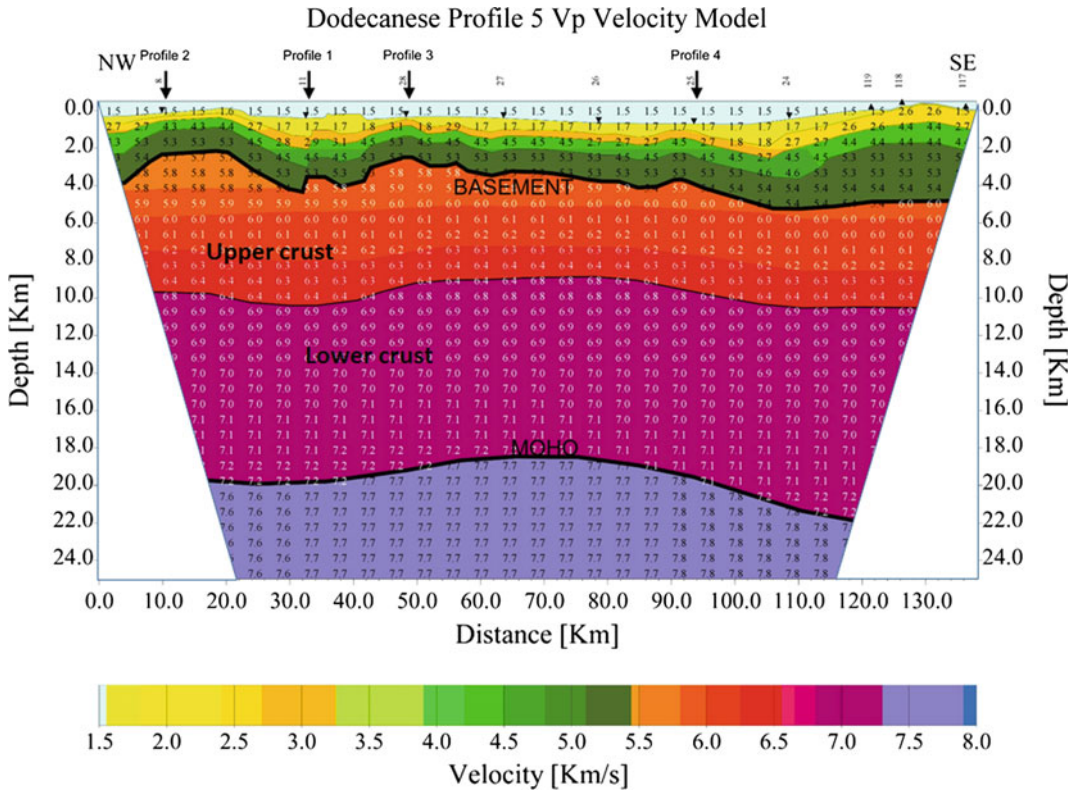

Fig. 7.14 Vp-velocity model along profile P5

7.1.3 Discussion

The velocity structure of the sediments and crust of the Kos-Nisyros volcanic area has been obtained by observing 8 wide aperture reflection refraction profiles of 1000 km total length, using 36 ocean bottom seismographs and 22 stand-alone land stations. The seismic array recorded continuously observing 7500 shots fired along the profiles. The main effort was focused around the Kos-Nisyros volcanic area since the active volcanism presents a significant hazard for the entire region.

Velocity modelling involved first break tomography and layer tomography combined with two-point ray tracing forward modelling. The sediments, crust and locally the upper most mantle below the Dodecanese islands were mapped. Four sedimentary layers have been identified with Vp velocities 1.7, 2.4, 4.2 and 5.2 km/s, quite homogeneously distributed over the Dodecanese block. Variations in thickness are mainly observed for the Vp 1.7 km/s layer, representing the most recent sediments. The crust is fractured by a series of normal faults limiting extensional basins of very recent development. A tectonic map of the Dodecanese area (Fig. 7.16) resulted, considering the results of velocity modelling of all 8 profiles. In compiling this map, part of the faults mapped by Kurt et al. (1999) and Tür et al. (2014) in the gulf of Gökova, were adopted. The system of basins and faults indicate that the Gökova-Kos-Karpathos continuity delineates a major detachment system that separates the Dodecanese block from the southeastern part of the Aegean microplate. Fault plane solutions published by Friedrich et al. (2014) show for the Gökova-Kos-Karpathos system that crustal seismicity is mainly controlled by tensional stresses. They delineate a

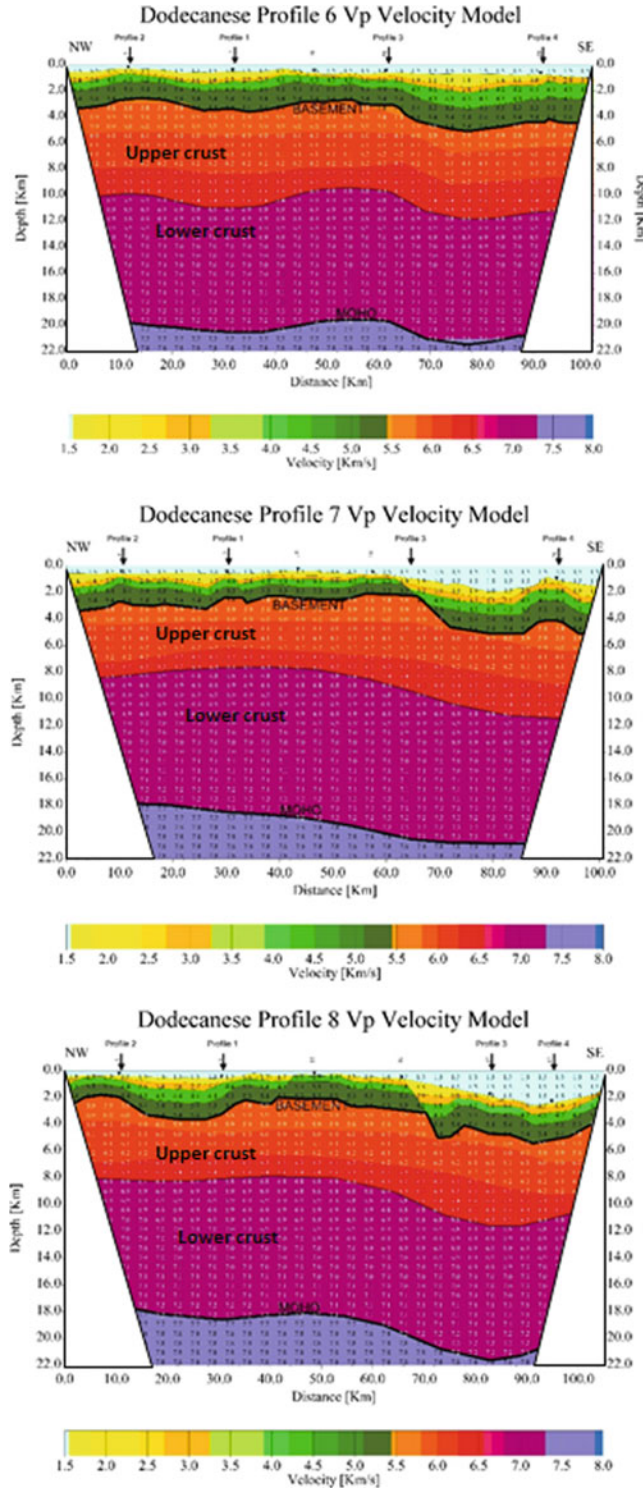

Fig. 7.15 Vp-velocity model along profiles P6, P7 and P8

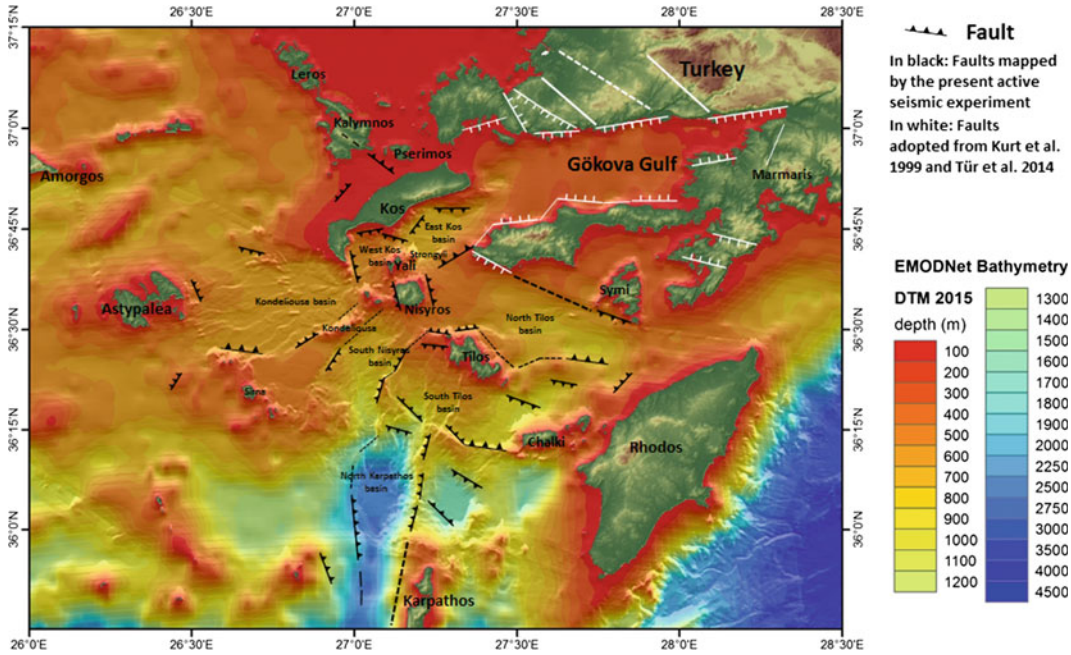

Fig. 7.16 Simplified tectonic map of the Dodecanese area

major detachment fault system of extension that marks the northern and western limits of the Dodecanese block. Also the crustal thickness, ranging from 17 to 22 km, shows a continuity and homogeneity of the Dodecanese block with slight increase towards east west Turkey to 22–23 km, decreasing towards Cretan Sea to 16–17 km (Bohnhoff et al. 2001). This east-west trend of crustal thinning is also confirmed by 3D density modelling (Makris et al. 2013). The driving force of this crustal behaviour of the active separation of the Dodecanese block from the eastern Aegean Sea is to be seeked in the upper mantle and the subduction of the oceanic lithosphere below Crete and the Cretan Sea and Dodecanese. Also Bohnhoff et al. (2001), Makris et al. (2013) and Friedrich et al. (2014) have shown that the subduction direction is of NNE–SSW orientation and obliquely deformed and teared due to lateral differences in thickness of the crust above (Papoulia et al. 2014) and inhomogeneity of the hanging plate at the collision front. The roll-back mechanism of the subducted slab is another reason for fragmentation. Friedrich et al. (op. cited) studied the regional stress field and deformation of the crust and lithosphere below the Aegean Sea by a temporary seismic array. For the Dodecanese area they refer that the down going slab is under down-dip tension and that probably west of Karpathos the slab is vertically teared along an N–S line. This could explain the geometry of the west Karpathos basin that follows the same trend and is morphologically depressed to nearly 2500 m.

The seismicity is tectonically induced and driven by the subduction process and the crustal reaction by fragmentation we have identified. It is only beyond the Kos-Nisyros volcanic area that the seismicity is associated with the volcanic process, intrusives and hydrothermal phenomena they are linked with (Papoulia et al. 2016).

References

Allen SR (2001) Reconstruction of a major caldera-forming eruption from pyroclastic deposit characteristics: Kos Plateau Tuff eastern Aegean Sea. J Volcanol Geotherm Res 105:141–162

Bohnhoff M, Makris J, Papanikolaou D, Stavrakakis G (2001) Crustal investigations of the Hellenic subduction zone using wide aperture seismic data. Tectonophysics 343:239–262

Cerveny V, Psencik I (1981) Two-dimensional two point ray tracing package. Charles University, Prague

Davis EN (1967) Zur Geologie und Petrologie des Inseln Nisyros und Jali (Dodecanese). Praktika Akademy Athens 42:235–252

Ditmar P, Makris J (1996) Tomographic inversion of 2-D WARRP data based on Tikhonov regularization. In: 66th Annual international. Mtg. SHE, Denver CO U.S. A, Extended Abstracts

Friedrich W, Brüstle A, Küperkoch L, Lamara S, Egelados Working Group (2014) Focal mechanisms in the southern Aegean from temporary seismic networks—implications for the regional stress field and ongoing deformation processes. Solid Earth 5:275–297

Geowarn (2003) Final Report of EU Geowarn Project—IST 1999-12310: Geo-spatial warning system, Nisyros volcano (Greece): An emergency case study (www.geowarn.ethz.ch)

Ginzburg A, Makris J, Hirscleber H-B (1987) Geophysical investigations in the North Aegean Trough. Ann Geophys 5B92:167–174

IGME (1989) Seismotectonic map of Greece with seismological data, scale 1:500.000, Athens

Jackson J (1994) Active tectonics of the Aegean region. Ann Rev Earth Planet Sci 22:239–271

Keller J (1969) Origin of rhyolites by analectic melting of granite and crustal rocks. The example of rhyolitic pumice from the island of Kos (Aegean Sea). Bull Volcanol 33:942–959

Keller J, Rehren TH, Stadlbauer E (1990) Explosive volcanism in the Hellenic arc. A summary and review. In: Proceedings of the third scientific congress Thera and the Aegean World III, Earth Sci 2:13–26

Kurt H, Demirbag E, Kuscu I (1999) Investigation of the submarine tectonism in the gulf of Gökova, southwest Anatolia-southeast Aegean Sea, by multi-channel seismic reflection data. Tectonophysics 305:477–496

LePichon X, Angelier J (1979) The Hellenic arc and trench system: a key to the neotectonic evolution of the eastern Mediterranean area. Tectonophysics 60:1–42

Makris J (1977) Geophysical investigations of the Hellenides. Hamburg Geophysical Monographs, vol 34. University of Hamburg, Hamburg

Makris J, Vees R (1977) Crustal structure of the Aegean Sea and the islands Evia, Crete, Greece, obtained by refractional seismic experiments. J Geophys 42:329–341

Makris J, Weigel W, Koschyk K (1977) Seismic studies in the Cretan Sea: The southern Aegean Sea: an extensional marginal basin without sea-floor spreading. In Meteor Forschungsergebnisse Reihe C:27

Makris J, Papoulia J, Yegorova T (2013) A 3D density model of Greece constrained by gravity and seismic data. Geophys J Int 194:1–17

Makropoulos C, Burton P-W (1981) A catalogue of the seismicity in Greece and adjacent areas. Geophys J R Astr Soc 65:741–762

Marini L, Principe C, Chiodini G, Cioni R, Fytikas M, Marinelli G (1993) Hydrothermal eruptions of Nisyros (Dodecanese, Greece). Past events and present hazard. J Volcanol Geotherm Res 56:71–95

McKenzie D (1972) Active tectonics in the Mediterranean region. Geophys J Roy Astron Soc 30:109–185

Nomikou P, Papanikolaou D (2000) Active geodynamics at Nisyros, the eastern edge of the Aegean volcanic arc: emphasis on the submarine survey. In: Proceedings of the 3rd international conference on the geology of the Eastern Mediterranean, pp 97–103

Papanikolaou D (1993) Geotectonic evolution of the Aegean. Bull Geol Soc Greece 27:33–48

Papazachos B, Papazachou C (1997) Earthquakes in Greece. Editions Ziti, Thessaloniki

Papoulia J, Makris J, Tsambas A (2014) Microseismicity and crustal deformation of the Kyparissiakos gulf, south-western Hellenic Arc, using an "amphibious" seismic array and a 3D velocity model obtained from active seismic observations. Bolletino di Geofisica Teor ed Appl 55(2):281–302

Papoulia J, Makris J, Koulakov I, Drakopoulou P, Fasoulaka Ch (2016) Microseismicity and crustal deformation of the Dodecanese volcanic area, southeastern Aegean Sea using an onshore/offshore seismic array (this volume)

Tür H, Yaltirak C, Elitez I, Sarikavak K-T (2014) Pliocene-quaternary tectonic evolution of the Gulf of Gökova, southwest Turkey. Tectonophysics 638:158–176

Seismicity and Tomographic Imaging of the Broader Nisyros Region (Greece)

8

Panayotis Papadimitriou, Andreas Karakonstantis, Vasilis Kapetanidis, George Bozionelos, George Kaviris and Nicholas Voulgaris

Abstract

Nisyros Island is a Quaternary composite volcano located close to the eastern termination of the South Aegean Volcanic Arc. Large destructive earthquakes have been reported in the study area. Nevertheless, seismic activity during the last decades is moderate to low, consisting of both shallow and intermediate depth earthquakes. The main regions of the broader area with observed spatiotemporally clustered seismicity are between Nisyros and Karpathos, east of Kos and in the gulf of Symi. Major events of intermediate depth have occurred near Karpathos and Rhodes Islands while the most significant zone of deep earthquakes is identified in the western Nisyros basin. Evidence for a non-systematic temporal co-incidence of deep events at different regions as well as increase in shallow seismicity after the occurrence of a strong deep event have been observed. Moment tensor inversion, using recordings in local and regional distances, was applied to determine the focal mechanisms of recent moderate events. The solutions, obtained by minimizing the difference between observed and synthetic waveforms, revealed that shallow events are mainly related to normal faulting, whereas intermediate depth events to reverse faulting with important strike-slip component. A tomography study was performed, using manually located events, and identified two areas of high V_p/V_s ratio and low velocity perturbations. The first is located SW of Nisyros and can be attributed to magma intrusion of deeper composition containing fluids and melts. The second, reaching 15 km depth, is possibly related to the magmatic chambers that feed the Yali and Strongyli volcanic centers.

P. Papadimitriou (✉) · A. Karakonstantis · V. Kapetanidis · G. Bozionelos · G. Kaviris · N. Voulgaris
Department of Geophysics and Geothermics, National and Kapodistrian University of Athens, 15784 Panepistimiopolis—Zografou, Greece
e-mail: ppapadim@geol.uoa.gr

A. Karakonstantis
e-mail: akarakon@geol.uoa.gr

V. Kapetanidis
e-mail: vkapetan@geol.uoa.gr

G. Bozionelos
e-mail: gbozionelos@geol.uoa.gr

G. Kaviris
e-mail: gkaviris@geol.uoa.gr

N. Voulgaris
e-mail: voulgaris@geol.uoa.gr

V.J. Dietrich and E. Lagios (eds.), *Nisyros Volcano*, Active Volcanoes of the World,
DOI 10.1007/978-3-319-55460-0_8

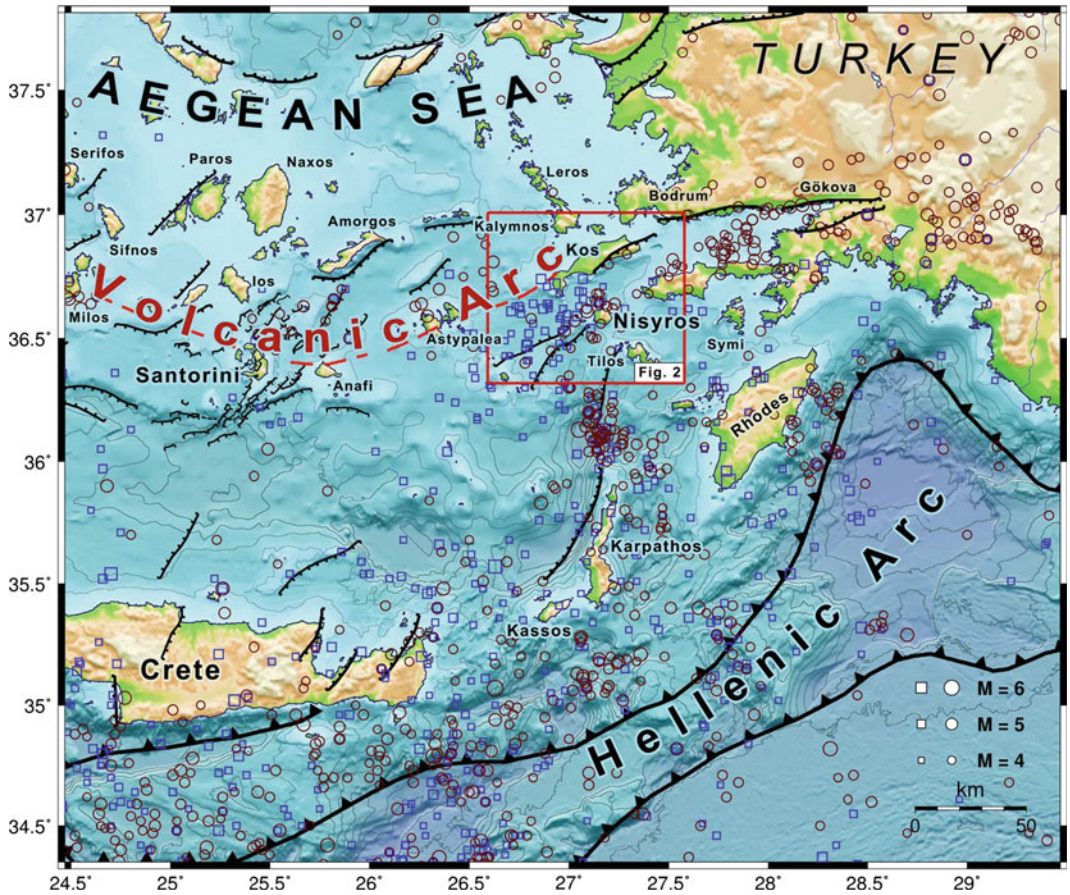

Fig. 8.1 Seismotectonic map of SE Aegean Sea. Epicenters are after Makropoulos et al. (2012) and the magnitude scale is M_s. Shallow events ($H < 40$ km) are represented with *circles*, whereas deeper events ($H \geq 40$ km) with *squares*. Fault lines are after Armijo et al. (1992), Nomikou and Papanikolaou (2011) and modified after Papadimitriou et al. (2015)

8.1 Introduction

South Aegean is characterized by the convergence of the African and Eurasian lithospheric tectonic plates at a rate of approximately 30 mm/yr, resulting in a complex and intense deformation of the Aegean. The region, which is dominated by the presence of the Hellenic Arc, also hosts the Hellenic Volcanic Arc that mainly includes Methana and the islands of Aegina, Milos, Santorini, Kos and Nisyros. Focusing on the broader Nisyros Island region, in the SE Aegean (Fig. 8.1), local deformation is a response to rapid sinking of the subducting plate. The eastern boundary of the Hellenic arc is defined by the sinistral Rhodes Transform Fault (RTF), implying a dominant extension regime in the Aegean during Lower Miocene (Müller and Kahle 1993; Müller et al. 1997). These tectonic movements caused the exposure of geological units of significant importance in the area of Dodecanese Islands in the Mesozoic-Cenozoic geological period (Harbury and Hall 1988; Garfunkel 2004; Kokkalas and Doutsos 2004; Franz et al. 2005). A wide variety of different environments such as the Menderes metamorphic massif, the overthrusted Alpine basement of limestones, in some cases with ophiolite fragments, and the volcanic centers of Nisyros, Yali

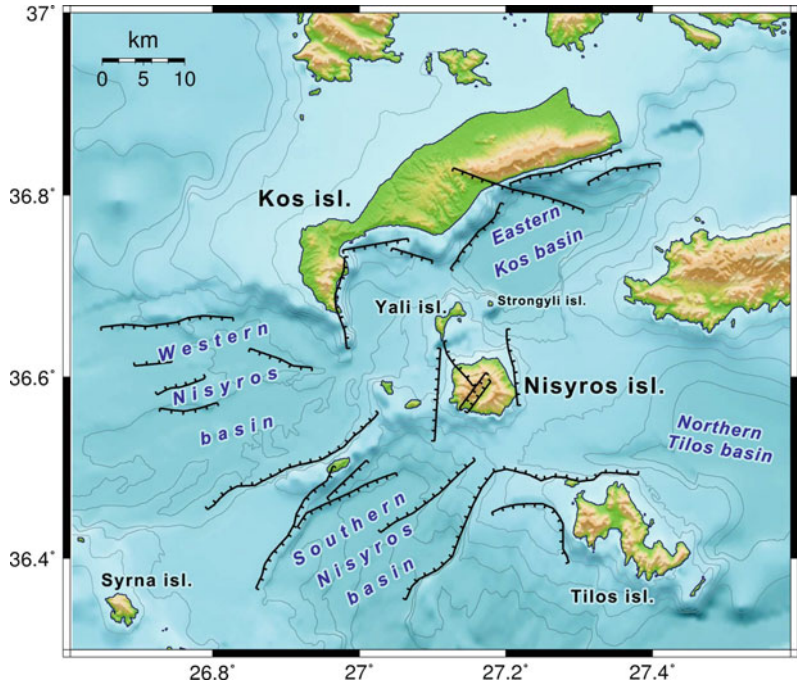

Fig. 8.2 Active faults, after Nomikou and Papanikolaou (2011), and toponyms of the broader Nisyros area (*within the rectangle* shown in Fig. 8.1)

with the surrounding islets of Strongyli, Pachia and Pergousa, form a quite complex geological environment.

The region between Nisyros and Kos Islands (Fig. 8.2) is characterized by Late Miocene-Pliocene magmatic activity, with a major event taking place, 160 ka. The mapped ignimbrite layer of Kos Island provides evidence of this explosive activity (Keller et al. 1990; Allen et al. 1999). Nisyros and the surrounding islets have been formed during the Late Pleistocene-Holocene within an ENE-WSW trending neotectonic graben (Nomikou and Papanikolaou 2010). The island of Nisyros is mainly composed of Quaternary calc-alkaline volcanic rocks which are represented by alternating lava flows, pyroclastic layers and viscous lava domes, formed in five main stages from 160 to 25 ka. The dominant feature on the island is a truncated cone with a base diameter of 8 km and a central caldera of 4 km in diameter (Papanikolaou et al. 1991, 1998; Nomikou 2004; Vanderkluysen et al. 2005; Volentik et al. 2005; Nomikou et al. 2013). The Yali and Strongyli volcanic islands, located north of Nisyros, along with the submarine volcano of Avyssos, are prominent features in the area, bounded by NE-SW normal faults (Wagner et al. 1976; Allen and Cas 2001; Nomikou 2004; Nomikou and Papanikolaou 2010, 2011). The Nisyros late settlement resulted from few to no macroseismic documentation of the activity connected to well stratigraphically-documented eruptions of the volcanic center until around 1400 AD (Higgins and Higgins 1996; Sachpazi et al. 2002). The hydrothermal eruptions of 1871 and 1873 were accompanied by intense seismic activity (Gorceix 1873, 1874; Georgalas 1962) and severe damage to Mandraki village (Galanopoulos 1953).

The seismic activity of the broader Nisyros area is related to both tectonic and volcanic origin. The largest event of the historical era in the broader study area is the M_w = 7.5 intermediate depth event (Stucchi et al. 2013) that occurred on 13 February 1756, whose epicenter lies between Rhodes and Tilos Islands. During the same period, only few large events are reported in the vicinity of Nisyros, mainly to the north, close to Kos Island (Papazachos and Papazachou 2003). The events of 18 October 1493 and of 2 June

1873, of magnitudes $M_w = 6.9$ and $M_w = 5.8$ (Stucchi et al. 2013), respectively, are the ones located close to Nisyros. Since 1900, both shallow and intermediate depth seismicity, reaching 180 km, has been recorded in the study area (Galanopoulos 1981; Tsapanos et al. 1994; Makropoulos et al. 2012). The latter is related to the subduction of the oceanic lithosphere beneath the Aegean microplate, as evidenced by the occurrence of the destructive 26 June 1926 earthquake ($M_w = 7.0$), with a focal depth of the order of 110 km (Galanopoulos 1981; Papazachos and Papazachou 2003; Makropoulos et al. 2012). This event was widely felt in the Eastern Mediterranean region, causing sporadic damage and, in places, destruction over a large area in Rhodes, SW Anatolia, E. Crete and the Nile Delta (Ambraseys and Adams 1998). The largest shallow earthquakes recorded in the vicinity of Nisyros during the instrumental period occurred on 23 April 1933 and 5 December 1968 with $M_w = 6.5$ and $M_w = 5.5$, respectively (Galanopoulos 1981; Makropoulos et al. 2012). The first was located north of Nisyros, close to the south coast of Kos, while the second west of Nisyros. Earthquake swarms felt in Nisyros in 1953 (Bornovas 1953) and in 1970 (Stiros and Vougioukalakis 1996), were not associated with any eruption.

It should be noted that the seismicity of the study area was not well recorded, due to the sparse distribution of permanent stations until 2007, when the seismic networks of the Seismological Laboratories of the Universities of Athens and Patras, of the Department of Geophysics of the Aristotle University of Thessaloniki and of the Geodynamic Institute of the National Observatory of Athens were joined, forming the Hellenic Unified Seismological Network (HUSN). The first seismic crisis that was analysed in detail, using recordings of a local temporary network, occurred in 1995 (Papadopoulos et al. 1998; Sachpazi et al. 2002). More specifically, in November 1995 an intense, shallow seismic activity was initiated in the study area, with the two largest earthquakes of moderate magnitude, $M_w = 4.4$ and $M_w = 4.0$ respectively, occurring on 27 August 1997. Ground deformation measurements based on local GPS observations and interferometric study for the period 1995–2002 showed extended uplift and opening of Nisyros along the major faulting zones that crosscut the island, during the 1995–1997 unrest period (Lagios et al. 2005). Since 1998, the amount of deformation decreased systematically to the pre-crisis values, in agreement with the fact that the aftershock sequence of Nisyros apparently reached its end by October 1997. After 2002 and up to 2012, it appears that subsidence generally takes place at the northern part of the island, which seems to extend offshore, reaching Yali islet to the north (Lagios et al. 2015; Sakkas et al. 2015). Many of the events were strongly felt in Nisyros Island producing cracks in local infrastructures. Since 1998, the activity on Nisyros and the surrounding area has been moderate to low, with some earthquakes occurring offshore close to the island. Nevertheless, during 2015, several moderate events occurred in the vicinity of Nisyros, the largest of which took place on 24 July 2015 ($M_w = 4.9$). The source parameters determination of these events is among the scopes of the present study.

In this manuscript the seismic activity of the broader Nisyros area is investigated and the hypocenters are determined using a 1D velocity model that was calculated for that purpose. Focal mechanisms of moderate magnitude events located in the study area were calculated by moment tensor inversion, using recordings in regional distances. The current research is concluded with seismic tomography, aiming to detect both the location of magmatic features, in a large scale, as well as the presence of discontinuities, along which seismicity occurs.

8.2 Seismicity

During the last decades, Nisyros Island has been characterized by generally low earthquake activity. In the more recent years the data quality and quantity have improved, especially since the implementation of HUSN. In this study, a

preliminary hypocenter location has been performed for the seismicity of the broader area in the period 2006–2015, using the HYPOINVERSE code (Klein 1989) and an initial regional 1D velocity model (Kaviris 2003). Upon selection, the resulting data set was composed of 719 earthquakes. By employing a subset of events located with accuracy better than 4 km and having $RMS < 0.6$ s, the average V_p/V_s ratio and the 1D velocity structure of the area were investigated, using the mean travel-time residuals and location uncertainties (*RMS*, *ERH*, *ERZ*) minimization method (Kissling et al. 1994; Chiarabba and Frepoli 1997; Lopes and Assumpção 2011). A 1D velocity model was obtained (Table 8.1), yielding improved hypocenter solutions for the whole dataset. The calculated median hypocentral location uncertainties, obtained by HYPOINVERSE using the optimum local velocity structure, are $ERH = 1.34$ km, $ERZ = 4.77$ km and $RMS = 0.35$ s, while the corresponding median error values using the regional model are $ERH = 1.41$ km, $ERZ = 6.04$ km and $RMS = 0.38$ s, respectively.

The resolved seismicity in the broader area for the period 2000–2015, with merged data of the National Network in period 2000–2005 (squares) and the locations determined by the custom model of this study for 2006–2015 (circles) is presented in Fig. 8.3. Seismicity has been recorded SW of Nisyros, with the epicentral distribution implying a roughly NNE-SSW direction, whereas some activity can also be identified ~7 km north of Nisyros, near Yali Island. However, dense seismicity is observed in parts of the broader study area, such as the vicinity of Karpathos Island, both onshore and offshore, close to Rhodes and east of Kos Island, towards the coast of W. Turkey.

The magnitude of completeness, M_c, was measured during several time intervals to compare rates in a homogeneous way. The M_c value is determined as the lowest magnitude for which the Gutenberg-Richter (G-R) power law is satisfied. This can be estimated either graphically, by visual inspection of the linear part in the log-log G-R diagram, or by the application of the Maximum Likelihood Estimation method. In the framework of the current study the first method was applied, according to which the largest M_c for the period 2006–2015 was equal to 2.8. The latter was set as a magnitude threshold for the completeness of the catalogue and the histograms of Fig. 8.4. The monthly occurrence of shallow and intermediate depth events in the broader study area is presented in Fig. 8.4a, b, respectively. The corresponding histogram for the vicinity of Nisyros Island is shown in Fig. 8.4c. More specifically, the monthly event occurrence is presented for a selected local region, centered at 36.3661°N, 26.8215°E, with a radius of ~62 km that includes the western Nisyros basin and part of the seismicity between Karpathos and Nisyros. It is evident that the majority of the events are shallow. The almost constant rates in observed seismicity are interrupted by small bursts when earthquake sequences occur. Even in the more recent years, the number of recorded earthquakes is generally low for shallow events and even smaller for deeper ones. In addition, a

Table 8.1 The local 1D velocity model developed for the broader area of Nisyros-Kos Islands

V_p/V_s ratio	1.76	
Layer	P-wave velocity (km/s)	Ceiling depth (km)
1	4.70	0.0
2	5.20	3.5
3	5.70	9.0
4	6.20	11.0
5	6.50	23.0
6	7.10	29.0
7	7.40	32.0
8	8.00	80.0

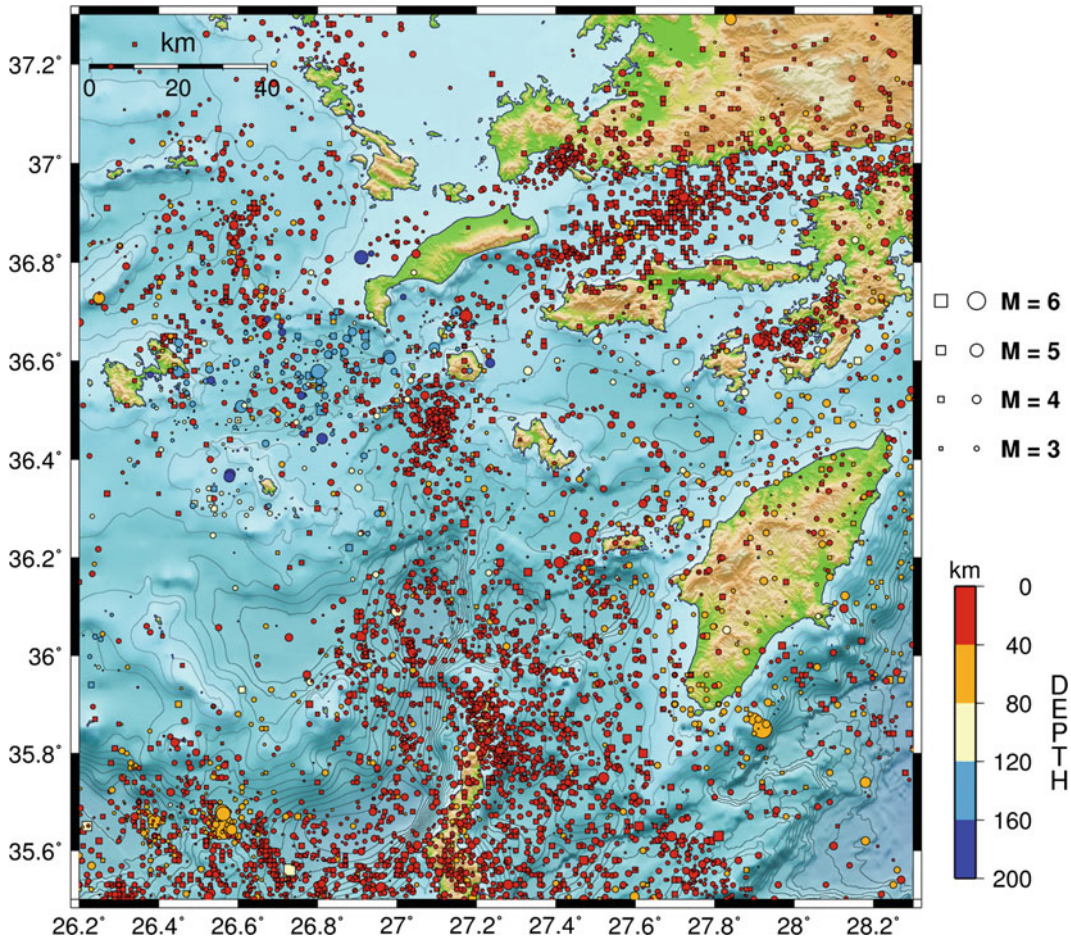

Fig. 8.3 Hypocenter distribution for the time interval January 2000–July 2015 in the broader area of SE Dodecanese islands. *Colours* indicate focal depth. *Squares* represent earthquakes that occurred during the period 2000–2005, while *circles* those during 2006–2015

temporal correlation of shallow and intermediate depth seismic sequences may be observed, whereas continuous low seismicity has been recorded in the local region since 2000 (Fig. 8.4c). Nevertheless, increased activity is observed in 2011 and 2014, as described in more detail below.

For the period prior to 2000, additional data from the seismological catalogues of the Geodynamic Institute of the National Observatory of Athens (GI-NOA) and the International Seismological Center (ISC) were incorporated for the study of monthly seismicity rates in the past years. The magnitude of completeness was estimated at $M_c = 4.0$ for years 1970–1990 and $M_c = 3.7$ for the period 1990–1999. For homogeneity and to allow for unbiased rate comparisons, the cumulative number diagrams of Fig. 8.5a, b have been drawn for events with magnitude greater than or equal to 4.0. Following the $M_w = 5.5$ earthquake which occurred near Nisyros on 5 December 1968, the background seismicity in the study region presents an almost constant rate of ~1.1 event/month during the period 1970–1990 (Fig. 8.5a). In the beginning of 1990, a series of events with $M_w > 4.5$ that led to clustered seismicity, delineated in a N-S direction, was observed in the region ~40 km south of Nisyros and north of Karpathos Islands (Fig. 8.6a, cluster #1), culminating in an $M_w =$

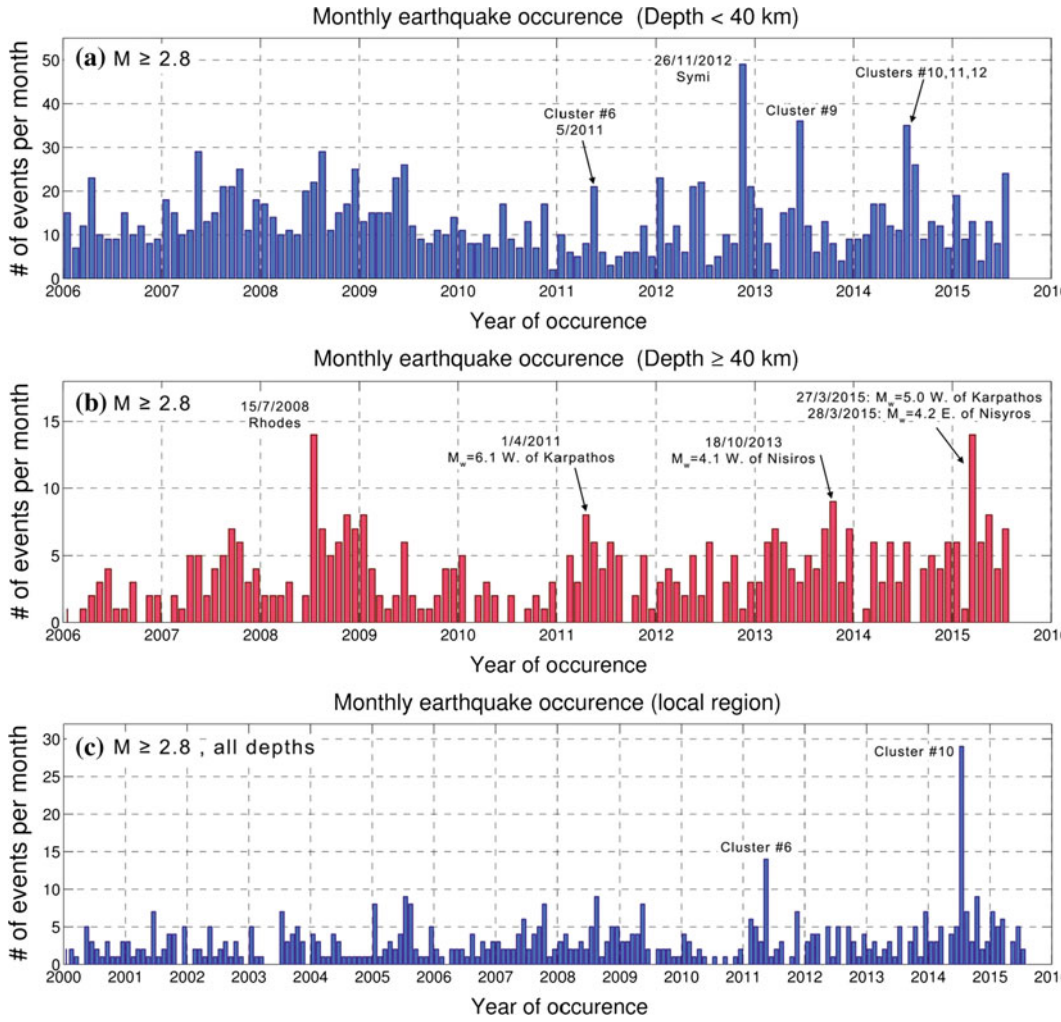

Fig. 8.4 Histograms of the monthly rate of earthquake occurrence in the broader area of study for **a** shallow ($H < 40$ km), **b** intermediate depth ($H \geq 40$ km) earthquakes during the period January 2006–July 2015 and **c** local region cantered at 36.3661°N, 26.8215°E, with a radius of ~62 km for years 2000–2015, independently of focal depth. All rates are calculated for events with $M \geq M_c = 2.8$

4.6 event on 28 August 1990. The same area was re-activated during the period 1996–1997 (Fig. 8.6a, cluster #2), peaking in July 1996, after a major $M_w = 6.2$ earthquake on 20 July 1996 ~10 km W of Rhodes Island, while seismicity in the local area of Nisyros was also observed in 1997, with a peak of activity in August 1997 (Papadopoulos et al. 1998; Sachpazi et al. 2002). The seismicity rate declined to a background level at the beginning of 1999 (Sachpazi et al. 2002), comparable to the rates of the periods 1970–1990 (Fig. 8.5a) and 2000–2003 (Fig. 8.5b). In 2004 seismicity rates increased (Cluster #3), whereas since 2011 the activity appears lower (Fig. 8.5b). The cumulative number of events for the vicinity of Nisyros Island is presented in Fig. 8.5c. An almost constant rate is observed, with two notable sequences occurring in 2011 (cluster #6) and 2014 (cluster #10), while since mid-2015 a period of increased seismic activity seems to have been initiated.

Sachpazi et al. (2002) using data recorded by a temporarily deployed local network,

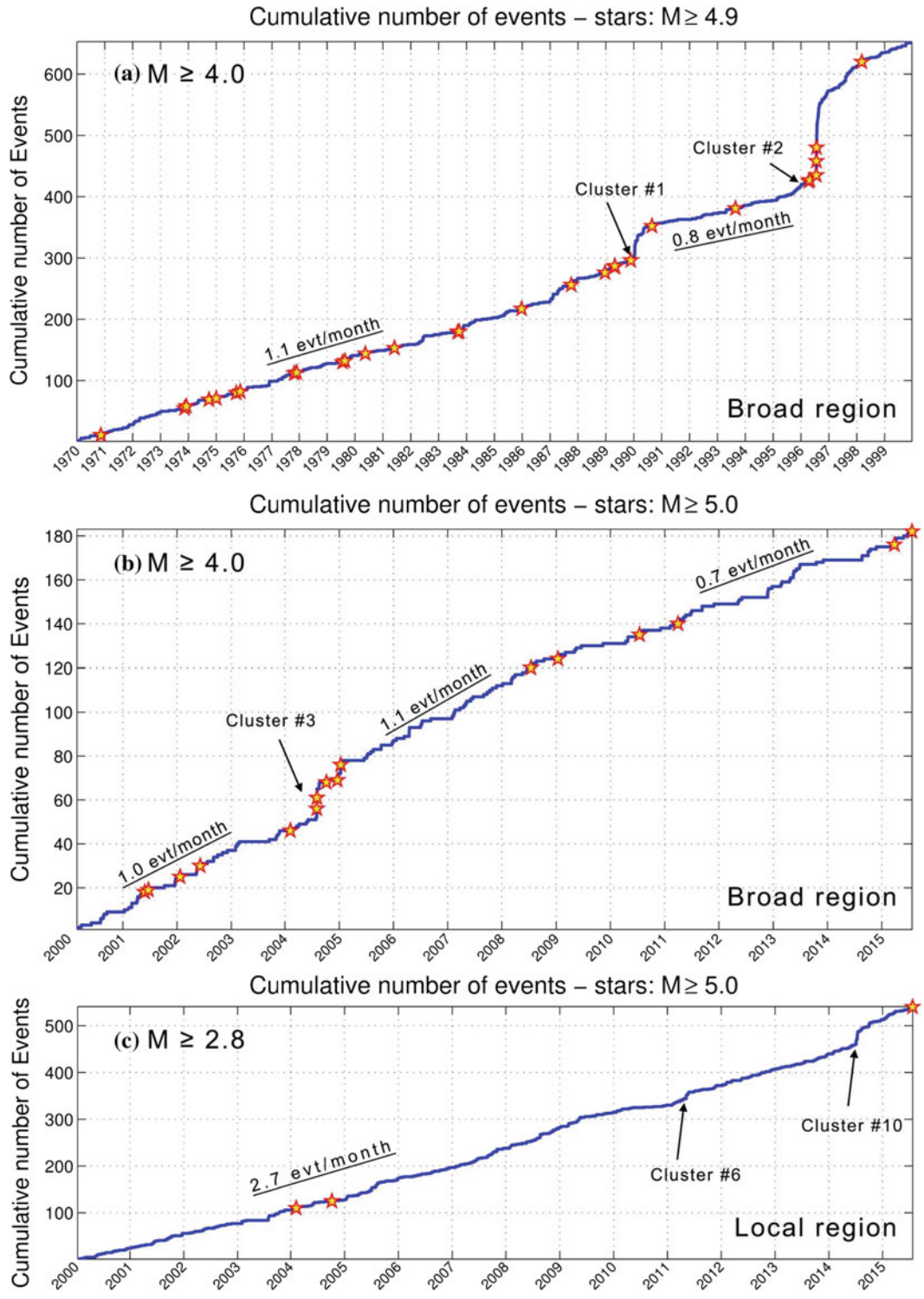

Fig. 8.5 Cumulative number of events in the broader area of study for the periods of **a** 1970–2000, **b** 2000–2015 and **c** for the local region cantered at 36.3661°N, 26.8215°E, with a radius of ∼62 km for years 2000–2015. Magnitude threshold at $M \geq 4.0$ has been used for panels (**a**) and (**b**) while $M \geq 2.8$ for panel (**c**). *Stars* indicate the occurrence of significant events

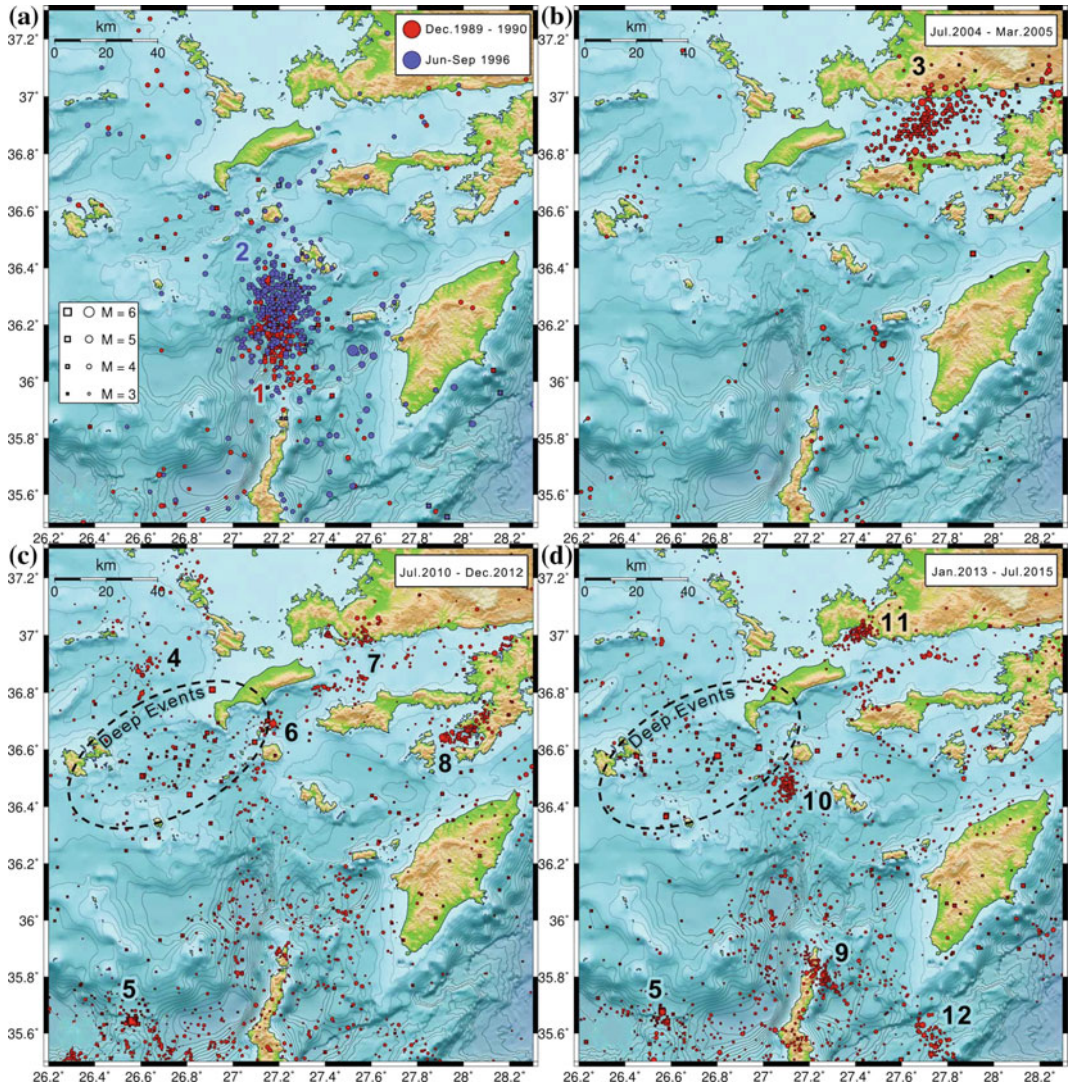

Fig. 8.6 Spatiotemporal distribution of shallow (*circles*) and deep or intermediate focus earthquakes (*squares*) in the broader area of SE Dodecanese islands during the periods **a** December 1989–1990 and June 1996–September 1996, **b** July 2004–March 2005, **c** July 2010–December 2012 and **d** January 2013–July 2015

distinguished the earthquake crisis into two main temporal periods. The first one, between 25 March and 3 April 1997, was concentrated in the area between the northern coast of Nisyros and the island of Yali, in contrast to the second one which was initiated on 6 July 1997 and lasted for one week, when the spatially clustered activity was located north of Nisyros. Both the central and southern parts of the island remained active during July 1997, providing a more disperse seismic distribution, while the depths were mainly superficial, not exceeding 10 km. The absence of reliable focal mechanisms for the recorded events of the 1996–1997 crisis led to the determination of a five-event composite mechanism, which suggested a more oblique direction for the maximum compressive axis that could be explained by a dextral strike slip mechanism which controls the local active tectonics.

During 2001, in the framework of the GEO-WARN Project, a local temporary seismological

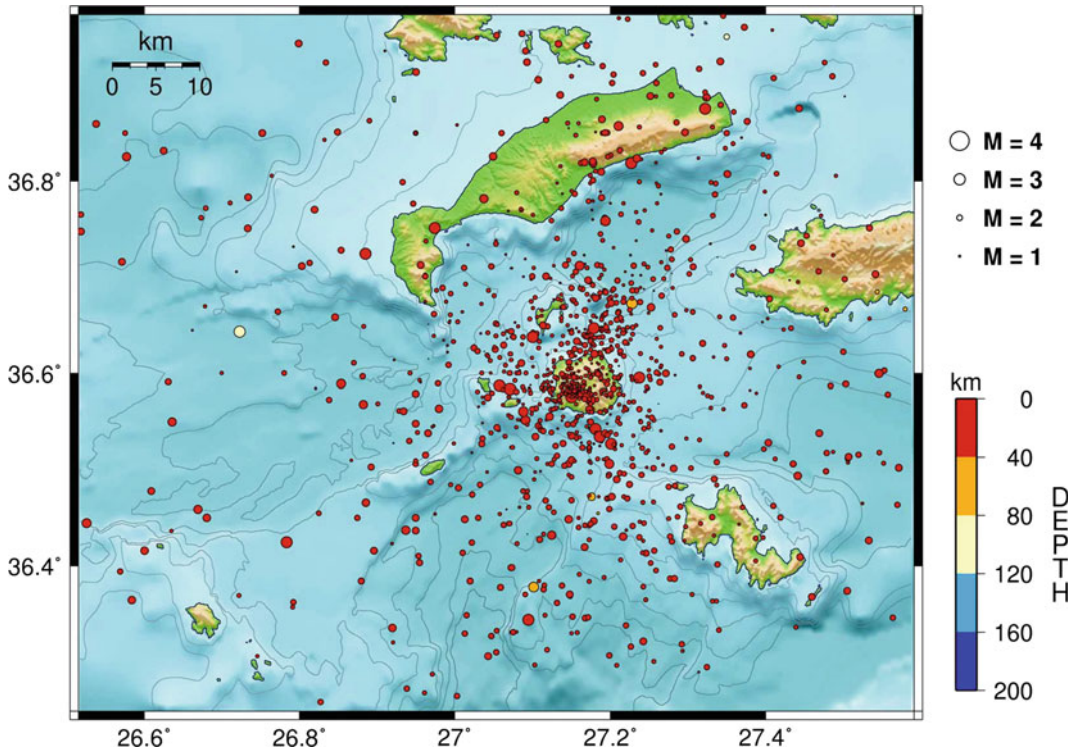

Fig. 8.7 Hypocenter distribution of the seismicity recorded by the local temporary seismological network of the GEOWARN project for the time interval January–October 2001 in the vicinity of Nisyros Island (GEOWARN 2003)

network, consisting of 13 stations, was installed in the study area (GEOWARN, 2003). Four seismographs were installed on Nisyros, three on Kos and one on Tilos Islands, while the remaining five on islets surrounding Nisyros. In the period of January–October 2001 more than 1000 epicenters were located (Fig. 8.7).

This network revealed local seismicity that could not be detected or resolved by the regional National Network, as is clearly evident by comparing the seismicity on Nisyros between Figs. 8.3 and 8.7. The recorded seismicity is mostly concentrated within a radius of $\sim$10 km around the island, with its density being higher at the SW rim of the caldera, but also close to its southern and northern coasts. While no spatiotemporal clusters were observed, as no significant earthquake sequence occurred during the operational period of this temporary network, the detectability threshold of the background shallow seismicity on the island increased from practically nothing (M_c = 2.8 for the broader region during this period) to a magnitude of completeness near M_c = 1.7 between July and October 2001 for the resolved seismicity with the local network. This signifies the great importance of the availability of a local seismological network in regions of particular interest, such as volcanic settings, like the Santorini Volcanic Complex (Kaviris et al. 2015; Papadimitriou et al. 2015), or tectonic environments with high deformation rates, continuous background seismicity and a plethora of swarms and other sequences, such as the western Corinth Rift (Kapetanidis and Papadimitriou 2011; Kapetanidis et al. 2015), to enable the identification of seismic patterns or possible precursors and the delineation of rupture zones, which are crucial for the assessment of seismic risk and hazard.

While the detectability of lower magnitude earthquakes has improved since 2000, the background seismicity rates for $M \geq 4.0$ in the

broader region have remained relatively stable at about 1 event per month (Fig. 8.5b). Clustered activity was recorded E of Kos Island, near the coasts of Turkey in the Gulf of Gökova (Fig. 8.6b, cluster #3) mainly in early August 2004, with an M_w = 5.5 event on 4 August 2004, and in 2005 following an M_w = 5.0 event on 11 January 2005. In the more recent years, after the implementation of HUSN, the completeness magnitude in the broader study area has dropped to $M_c \cong 2.8$, in agreement with the results of D'Alessandro et al. (2011). The observed seismicity has been sparse but for a few spatiotemporal clusters presented in Fig. 8.6c, d, where the groups are numbered according to the order of their activation. Some notable events are related with each group: cluster #4 WNW offshore Kos Island is related to a couple of events on 10 September 2011 (M_w = 4.2) and 24 December 2012 (M_w = 4.1), cluster #5 W of Karpathos Island involves a major M_w = 6.1 event of intermediate depth (70 km) on 1 April 2011. A few km N of Nisyros Island, cluster #6 (also marked in Figs. 8.4c and 8.5c) was activated by an M_w = 5.1 event on 8 May 2011, but could also possibly be related to a deep (135 km) M_w = 4.1 event that occurred on 22 May 2011, confined in the same epicentral region. It is worth noting that during the same period intense seismic activity occurred approximately 160 km to the west, in the Santorini Volcanic Complex area (Papadimitriou et al. 2015), as well, which also comprises an active part of the Hellenic Volcanic Arc. The small clusters in region #7 are related to small earthquakes that occurred in June 2011 and between February and May 2012. A shallow M_w = 4.6 event that occurred on 26 November 2012 activated cluster #8, in the Gulf of Symi, approximately 70 km east of Nisyros. The seismicity in region #5 persisted during 2013 (Fig. 8.6d). In Karpathos Island, an M_w = 4.0 event is related to the activity in cluster #9. Significant activity is related to the spatiotemporal cluster #10 (with notable peaks in Figs. 8.4c and 8.5c), located 5–10 km SW of Nisyros, along the NE-SW trending Fault System bounding the Southern Nisyros Basin (Fig. 8.6 d). This activity, consisting mainly of low magnitude events (M_w < 4), could be linked to a magmatic intrusion, which moves constantly through time, producing volcano-tectonic events. A similar process has also been observed in Etna (Patanè et al. 2002) and Campi Flegrei (Zollo et al. 2003) and should be monitored in a more detailed way. NE of Kos Island, cluster #11 was activated in May and August 2014, with the latter being related to a shallow M_w = 4.0 event on 15 August 2014. Finally, S of Rhodes Island, an M_w = 4.3 event triggered the activity in region #12.

Some other significant events in the broader area during the period of study include the major (M_w = 6.2) deep (90 km) event of 22 January 2002 west of Karpathos Island, the deep event (140 km depth) of 16 July 2010 with M_w = 5.1 (near the W coast of Kos Island, the top of the ellipse of Fig. 8.6c), the M_w = 5.0 event of 27 March 2015 (focal depth = 55 km, located ~50 km W of Karpathos Island) and the 24 July 2015 deep event (M_w = 4.9, focal depth = 140 km, located 30 km W of Nisyros Island, near the middle of the ellipse of Fig. 8.6d). The major M_w = 6.3 event of 15 July 2008 (focal depth = 50 km) at the southern tip of Rhodes Island did not trigger significant or clustered activity N of Karpathos or near Nisyros, according to the regional data.

Intermediate-depth seismicity is a prominent feature of the study area. A specific region has been identified in western Nisyros basin where events down to depths of over 100 km have been located (Fig. 8.6c, d, area marked with an ellipse). The other notable region in the broader area of study with events of intermediate-depth is in the vicinity of cluster #5, W of Karpathos. In a region where events with a wide depth range occur, it is of great interest to examine a possible spatiotemporal correlation between shallow and deeper activity. Concerning the temporal distribution, no systematic correlation between intermediate/deep events and shallower ones can be concluded by direct comparison of their monthly rates. Nevertheless, there are a few cases in which earthquakes with focal depths larger than 40 km have coincided with increased activity at shallower depths in the broader region

near the same time. A series of deep events ($H > 100$ km) on 18 March, 26 April and 12 June 2004 was followed by the $M_w = 5.5$ shallow event of 4 August 2004 (cluster #3) while some months later, on 7 October 2004 a deep ($H = 105$ km) $M_w = 5.2$ event occurred and was followed by the shallow $M_w = 5.0$ event of 11 January 2005 in the same cluster.

At intermediate depths, ~60 km, the most noteworthy cases of major earthquakes are the $M_w = 6.1$ event of 1 April 2011 near Karpathos which was followed by increased shallow activity in cluster #6 a month later (Fig. 8.4) and the $M_w = 6.3$ event of 15 July 2008 in Rhodes which is related to shallower aftershock activity. An increase in deep seismicity was also observed in October 2013 (Fig. 8.4b) including an $M_w = 4.1$ event on 18 October 2013, ~15 km E of Nisyros at a focal depth of 120 km following several other deep events with magnitudes between 2.8 and 3.4. More recently, a large outbreak in deep/intermediate-depth activity was observed after the $M_w = 5.0$ event of 27 March 2015 (Fig. 8.4b) in cluster #5 (Fig. 8.6d), W of Karpathos, which was preceded 10 days earlier by an $M_w = 4.5$ deep event ($H = 165$ km) located at the lower part of the ellipse in Fig. 8.6d, and followed 1 day later (28 March 2015) by an $M_w = 4.2$ event near Nisyros. Finally, near the end of the study period, a major deep event ($H = 140$ km) struck ~15 km SW of Kos on 24 July 2015 ($M_w = 4.9$) within the ellipse of Fig. 8.6d. Approximately the same region was also activated on 16 July 2010 with an $M_w = 5.1$ event at $H = 140$ km. No evidence has been observed for increased shallow activity or major shallow events preceding major deep events or an increase in the rate of occurrence of deep/intermediate-depth events.

8.3 Regional Moment Tensor Inversion

The broader Nisyros region constitutes a complex geotectonic environment, as evidenced by the occurrence of both seismic and volcanic activity. In addition, the focal depths of the earthquake sources vary from shallow to intermediate, leading to a variety of focal mechanisms. The latter is related to both the tectonic setting and to magma–fluid intrusion, depending on the characteristics of the local stress regime. Thus, it is evident that the determination of reliable focal mechanisms is of crucial importance to understand the seismotectonic characteristics, by studying the moderate events in the study area, since no large events have occurred in the vicinity of Nisyros during the last decades. The operation of the HUSN, since 2007, and the increase of the number of broadband seismic stations in Greece, allowed for the calculation of the moment tensor of moderate events using recordings in local and regional distances.

The focal mechanism determination requires the generation of Green functions in the selected epicentral distances. For that purpose several methods have been developed worldwide (e.g. Dreger and Helmberger 1993; Fan et al. 1994; Zeng and Anderson 1995; Fukuyama and Dreger 2000; Ichinose et al. 2003). In the present study, the frequency wavenumber integration method, proposed by Bouchon (1979, 2003), is used for the generation of synthetic waves to be directly compared with the observed ones for a given velocity structure, as described by Papadimitriou et al. (2012). The developed methodology was successfully applied in the recently activated Santorini region, during the 2011–2012 seismic crisis (Papadimitriou et al. 2015).

On 24 July 2015 a moderate event of $M_w = 4.9$ occurred approximately 30 km west of Nisyros Island. This event of intermediate depth is among the largest in the study area during the last decades. The source parameters were calculated using recordings of 12 seismological stations in epicentral distances smaller than 350 km. The selected records were instrumentally corrected and then integrated to produce displacement waveforms. Three component seismograms were used and the data were band-pass filtered between 0.02 and 0.125 Hz. The best fit was obtained for a hypocenter at the depth of 140 km and the calculated seismic moment is $M_0 = 2.8 \cdot 10^{23}$ dynes·cm. The moment tensor inversion indicates strike-slip type faulting with

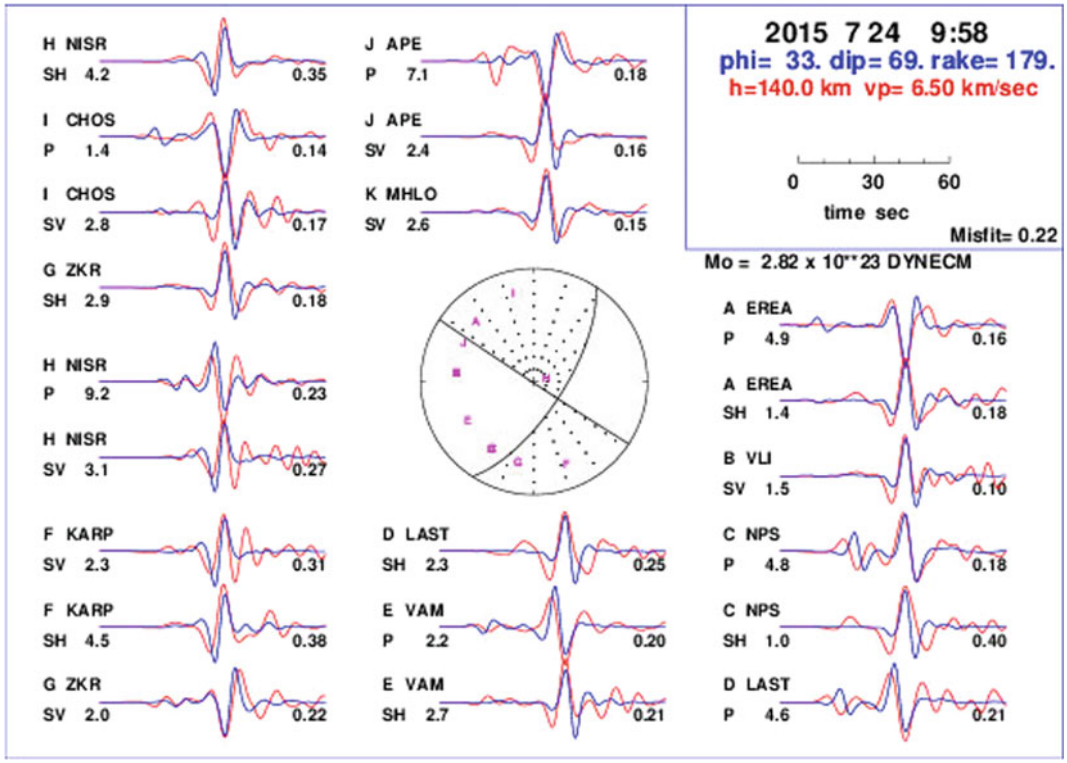

Fig. 8.8 Source parameters determination for the event of 24 July 2015, using moment tensor inversion and recordings in local and regional distances. *Red colour* represents observed waveforms and *blue* synthetics

the focal planes oriented in NNE-SSW (ϕ = 33°, δ = 69°, λ = 179°) and NNW-SSE (ϕ = 123°, δ = 89°, λ = 21°) directions, respectively (Fig. 8.8), while the obtained results for the P- and T-axes are ϕ = 256°, δ = 14° and ϕ = 350°, δ = 15°, respectively.

The second focal mechanism, presented in Fig. 8.9, corresponds to an M_w = 4.1 shallow event that occurred on 24 December 2012, approximately 50 km NW of Nisyros Island. Twelve stations were taken into account, in epicentral distances varying between 50 and 300 km. The obtained fault plane solution of this event revealed normal faulting in a NE-SW direction. More precisely, the details of the two focal planes are ϕ = 219°, δ = 46°, λ = −132° and ϕ = 91°, δ = 58°, λ = −55°. The corresponding results for the P- and T- axes are ϕ = 56°, δ = 60° and ϕ = 157°, δ = 6°, respectively. The depth of the foci was determined at 11 km and the seismic moment was found equal to $2.1 \cdot 10^{22}$ dynes·cm.

Moment tensor inversion was performed for events with $M_w \geq 3.8$ in the broader study area, depending on the quality of the available data. The obtained fault plane solutions are presented in the map of Fig. 8.10, where it is observed that shallow events correspond to normal faulting. Two main groups can be distinguished: the first close to Karpathos Island, with the fault planes striking in an approximate NNE-SSW direction, while the second close to the coasts of W. Turkey in a ∼E-W direction. The latter are related to N-S extension in the region, a regime which also dominates in other active tectonic regions in Greece, such as the Gulf of Corinth (e.g. Papadimitriou et al. 1999; Kapetanidis et al. 2015). On the other hand, earthquakes of intermediate focal depth are related to reverse focal mechanisms, with an important strike-slip

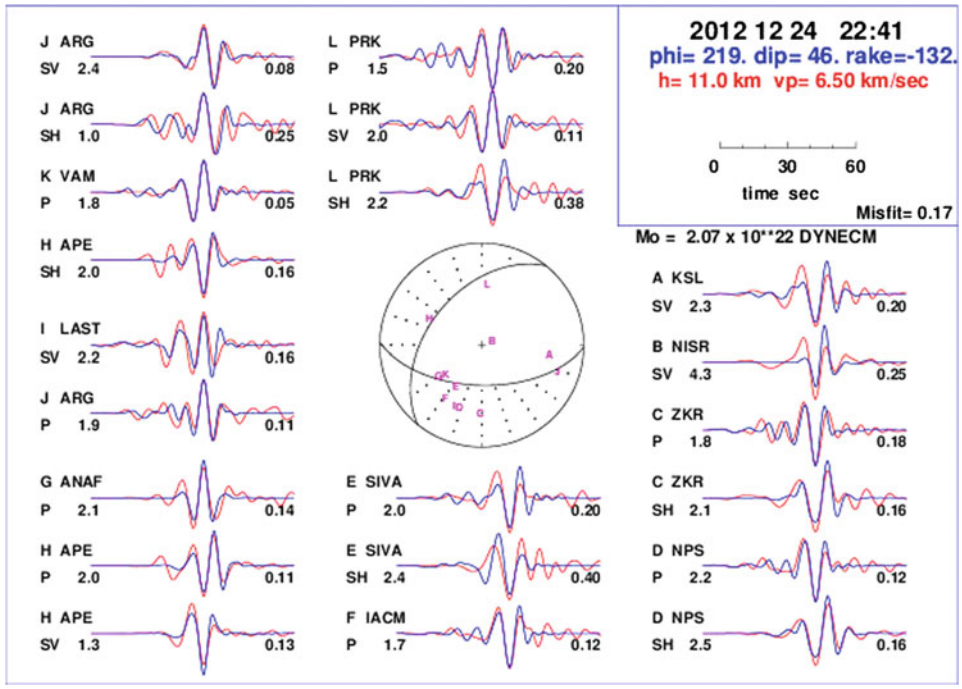

Fig. 8.9 Source parameters determination for the event of 24 December 2012, using moment tensor inversion and recordings in local and regional distances. *Red colour* represents observed waveforms and *blue* synthetics

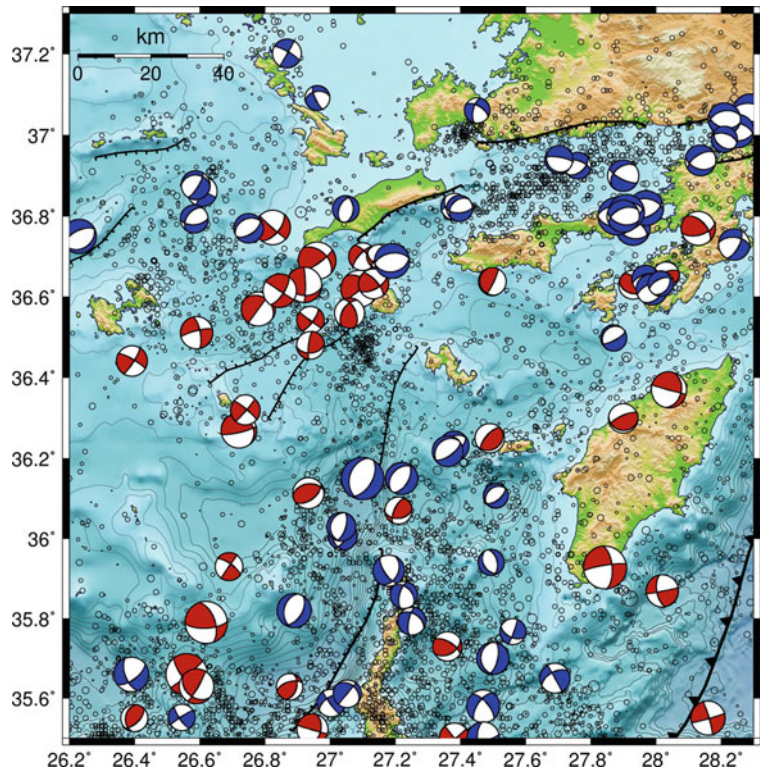

Fig. 8.10 Seismotectonic map of the broader study area. Focal mechanisms are from the Seismological Laboratory of the University of Athens (NKUA) (www.geophysics.geol.uoa.gr). *Colours* indicate shallow (*blue*, $H < 40$ km) and intermediate depth (*red*, $H \geq 40$ km) events

component in most cases. This type of faulting dominates at depth in the vicinity of Nisyros, mainly north and west of the island.

8.4 Local Earthquake Tomography

Seismic tomography is proven an effective tool for the detailed investigation of the Earth's interior. The scope of the present tomography study is to determine the crustal structure in the northern part of Dodecanese Islands, in order to identify the presence of magmatic chambers using manually located events. Local earthquake tomography techniques have been successfully applied to reveal the velocity structure of volcanic regions (Drakatos et al. 1997; Zollo et al. 2003; Vanorio et al. 2005; Lees 2007; Zandomeneghi et al. 2008; Dimitriadis et al. 2010; Koulakov et al. 2013; Papadimitriou et al. 2015). In the present study, the analysis was based on the local tomographic inversion code (LOTOS) by Koulakov (2009). For the tomographic inversion, more than 1000 manually located events were taken into account as a primary catalogue. Synthetic testing (checkerboard) was performed to set the parameter's values that produce better resolution and increase the area of fidelity. For the 3-D tomography inversion, a dataset comprising of 7132 P and 2886 S arrival-times, was selected, with at least 14 phases and ratio of S to P residual smaller than 1.7. Inversion was performed for V_p, V_s and $V_p - V_p/V_s$ to obtain additional constraints concerning the V_p and V_s anomalies. The LOTOS code requires input data of the station coordinates and the arrival times from locally recorded seismicity. The coordinates of the hypocenter and the origin time are not essential, as they are determined during the execution of calculations. However, if preliminary hypocentral locations are available, as in the present case, they are used to decrease the processing time of the operations. Additionally, the obtained 1-D starting velocity model and a set of input parameters for performing the convergence iteration steps, including parameterization, grid dimensions and damping parameter, were considered (Koulakov 2009). Model parameterization of the velocity field delineates, according to the local characteristics, the shape and position of heterogeneities. A nodal representation was employed, since the velocity field that is reconstructed by a three-dimensional grid does not assume a specific geometry of heterogeneities (Toomey and Foulger 1989). The spacing between the nodes of the grid was kept considerably smaller than the expected size of the anomalies (<8 km) to reduce the bias of the resulting models due to the grid configuration. The optimal grid mesh has been determined taking into account the stations/events geometry. In addition, to further decrease the influence of the model parameterization on the solutions, the inversion was repeated using several grid orientations (0°, 22°, 45° and 67°). The obtained results were combined over a 3-D model of absolute P- and S-wave velocities by simple averaging.

8.4.1 Resolution Tests

In the present study, the checkerboard method (Humphreys and Clayton 1988) was applied as indicator of the resolution and errors associated with the inversion to define the fidelity area. This method uses alternating anomalies of high and low velocity, evenly spaced throughout the model in a checkerboard pattern. Data resolution is mainly controlled by ray-path distribution, model parameterization and smoothing (Lees and Crosson 1989).

Checkerboard tests are performed to reproduce the procedure of real data processing. In the initial synthetic model, the size of cells corresponds to the expected anomalies. The applied procedure involves defining many spiked regions with 20% variability in the velocity structure compared to the one-dimensional reference model (Fig. 8.11).

Random noise of 0.1 s for P-wave arrival-time picks and 0.15 s for S-wave picks was added to

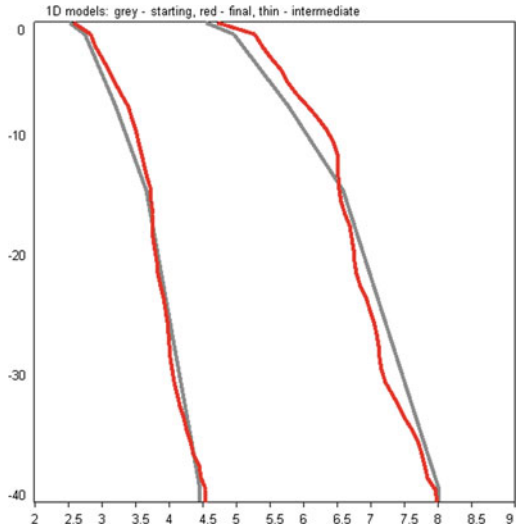

Fig. 8.11 Initial (*grey line*) and resulting (*red line*) 1D model by the first stage of tomographic inversion

the residuals, following a normal distribution, to approximate the uncertainties of the 3D model, using the same parameterization as for the real data (Koulakov 2009). Subsequently, the travel-times for the paths between source and receiver are computed. This procedure corresponds to the real observation system, which uses a 3-D ray tracing that follows the bending algorithm principles. The reconstruction of the synthetic model is performed in the same way as in the real data processing, including the optimization of the 1-D model and the absolute source location. The same values of free parameters, as in the real case, are used to examine the area of fidelity for the obtained results. After several synthetic tests, the set of parameters that provides a greater area of trust and can successfully reconstruct the model of checkerboard anomalies is used for the real data 3-D

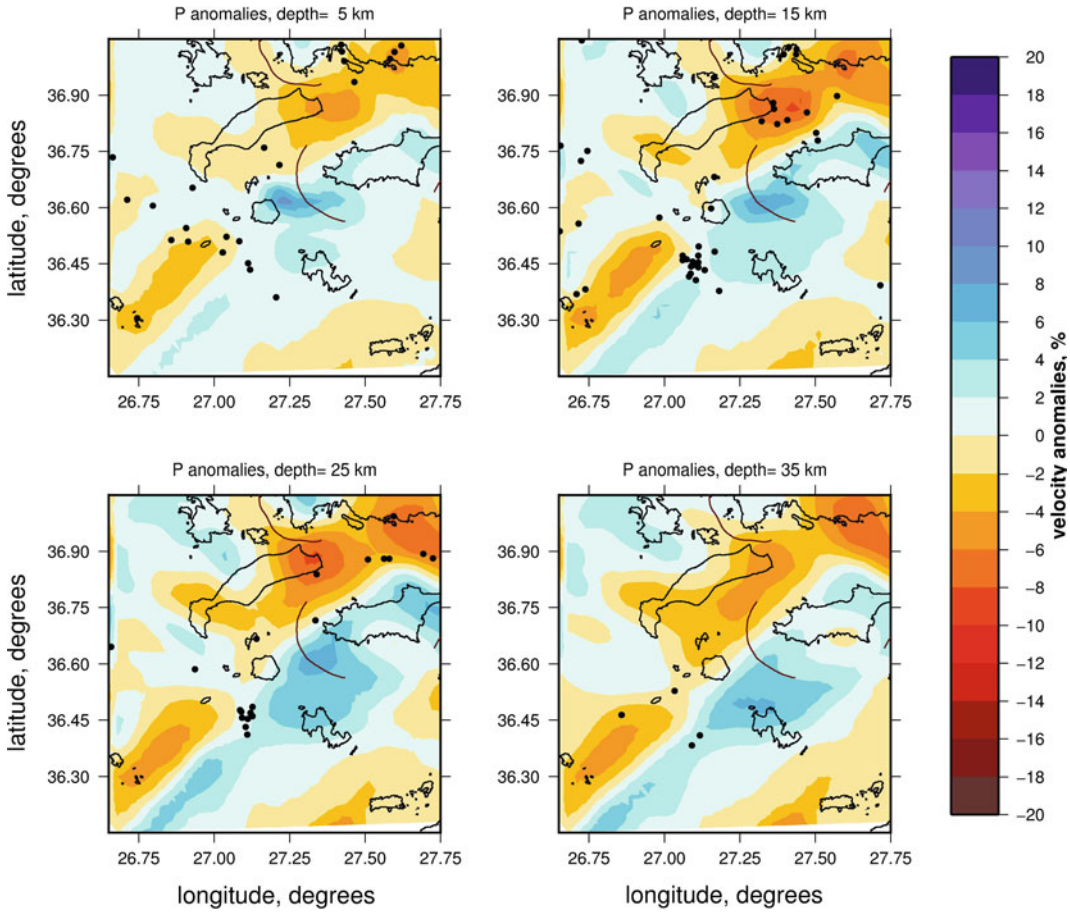

Fig. 8.12 Reconstructed 3D P-wave velocity anomalies (per cent)

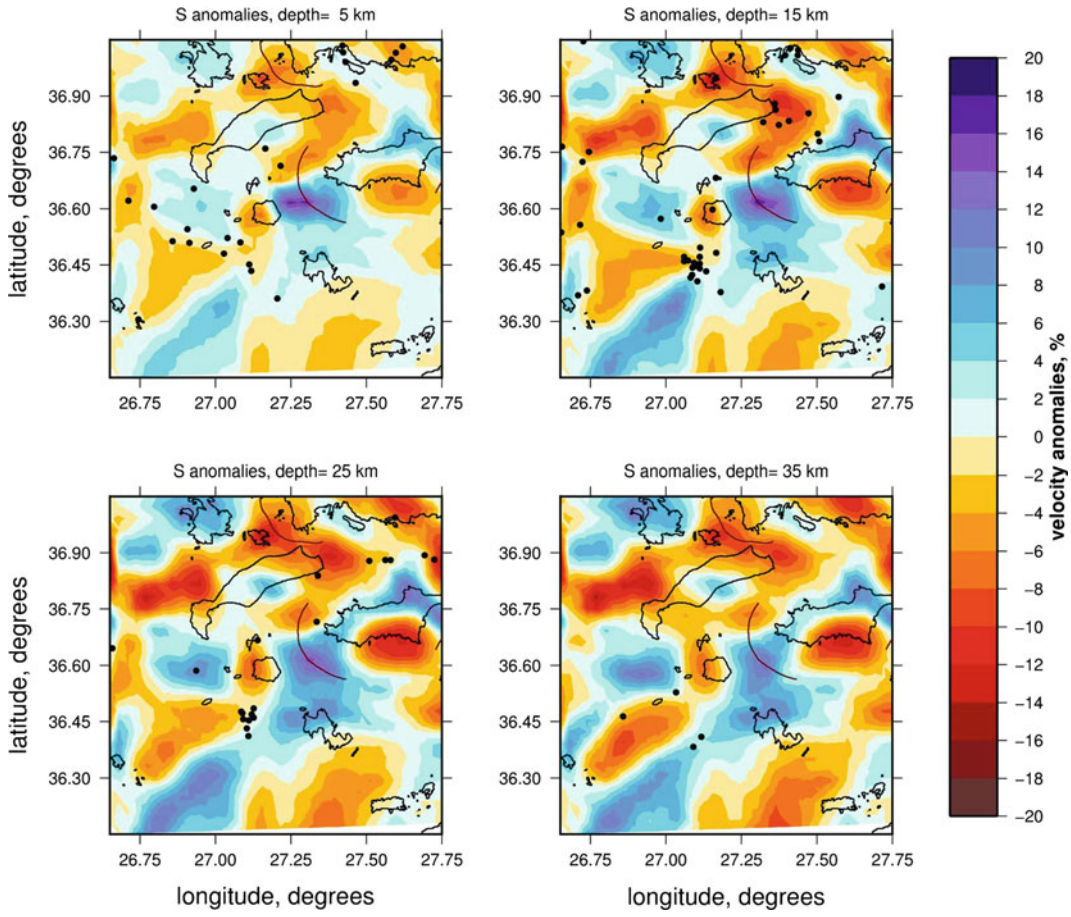

Fig. 8.13 Reconstructed 3D S-wave velocity anomalies (per cent)

tomographic inversion. The inversion variance is controlled by errors in the data, including mis-picks, mis-locations and incorrectly determined ray-paths.

Synthetic tests were performed to investigate the horizontal resolution of the modeling. The variations of V_p and V_s are presented in Figs. 8.12 and 8.13, respectively, at depths of 5, 15, 25 and 35 km. The horizontal resolution of the lateral velocity variations' reconstruction is quite satisfactory in those depth slices, especially within the region between Nisyros and Kos, which is the main area of interest. Concerning the vertical resolution, additional tests were performed, applying a change on the anomaly sign at 5 km depth. It is worth noting that the transition is reconstructed correctly for the largest part of the study area, with only minor horizontal smearing along the ray paths, mainly towards its NW edge. In most cases of passive tomography, vertical resolution is poorer than the respective horizontal one, due to source and velocity parameters trade off (Kasatkina et al. 2014). The size and shape of P- and S-anomalies are reasonably preserved in the central part of the area of interest down to ~35 km. The size and form of the resolved area for the horizontal slices provides reliability to the interpretation of the final results for velocity perturbations, as well as for V_p/V_s tomograms which will be presented in the following section.

8.4.2 Real-Data Inversion

The inversion procedure was initiated with preliminary source location and optimization of the 1D velocity model and, after three iterations, yielded an average RMS travel-time residual of 0.35 s. Moreover, the average P- and S-residuals were reduced from 0.52 and 0.72 s to 0.45 and 0.63 s, respectively. The resulting P- and S-velocity anomalies with respect to the 1-D starting model are shown in Figs. 8.14 and 8.15 in four horizontal slices, at depths of 5, 15, 25 and 35 km. The corresponding results for the V_p/V_s ratio are depicted in Fig. 8.16. The interpretation of the obtained results is limited to regions of the model with adequate reconstruction of the checkerboard model, which is shown in Figs. 8.12 and 8.13. Velocity variations for the superficial layers generally range between +14 and −16% for P- and S-waves, while the respective V_p/V_s ratio varies between 1.55 and 2.00. The velocity structure is resolvable for the depth range 5–35 km according to the synthetic modeling tests.

This fact, combined with the presence of dense ray coverage down to the depth of ~15 km, provides a greater credibility to the outputs of the 3-D inversion and the interpretation becomes more feasible. Strong lateral velocity perturbations were mainly recognized at shallower depth sections (5–15 km). More specifically, at the horizontal sections of 5 and 15 km, a

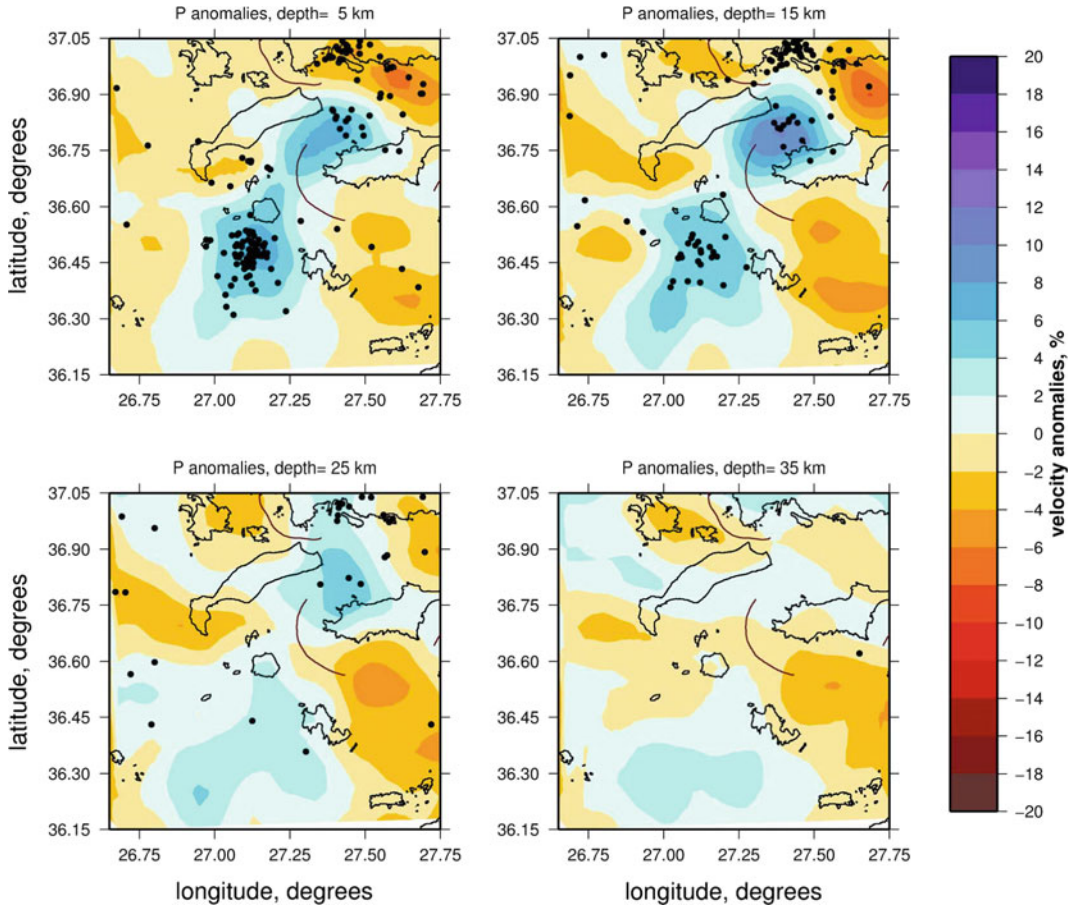

Fig. 8.14 Tomograms of lateral V_p (per cent) variations, with respect to the optimized 1-D V_p model, at 5, 15, 25 and 35 km depths

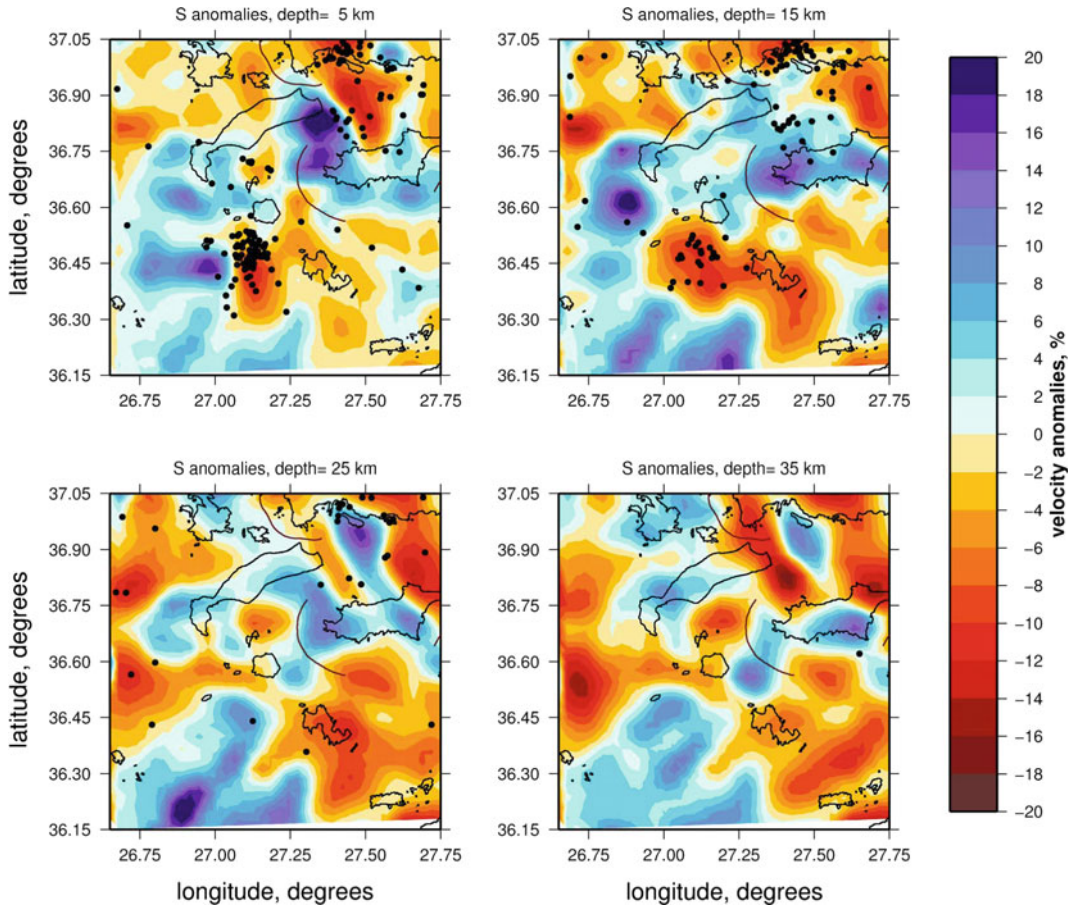

Fig. 8.15 Tomograms of lateral V_s (per cent) variations, with respect to the optimized 1-D V_p model, at 5, 15, 25 and 35 km depths

NE-SW zone of positive P-wave velocity perturbations is observed, which coincides with the Southern Nisyros and Eastern Kos basins. This is anti-correlated with the corresponding low velocity perturbation of the S-waves SW of Nisyros Island. This important feature results in a high V_p/V_s ratio anomaly that can be observed in Fig. 8.16. Moreover, a similar reverse sign between P- and S-wave anomalies can be observed at the northern part of the Nisyros-Kos Caldera that could be attributed to the surface expression of the Yali and Strongyli volcanic centers (Nomikou and Papanikolaou 2011). The resulting low-velocity pattern can be associated with the location of weak zones (local faults) indicated in Fig. 8.2. The fault system represents a weakened part of the crust where penetration of deep fluids and melts is most feasible. The collapsed regions are characterized by a shallow and broad low V_p anomaly down to 15 km depth that is mainly observed offshore, South of Kos Island. In the same area, at the deeper slices, the S-wave velocity perturbation is even more negative than the corresponding V_p, while it becomes positive at the NE part of the study area. This pattern is reflected in the V_p/V_s ratio (Fig. 8.16) value, which is about 1.90.

In order to examine the velocity anomalies in depth, two vertical cross-sections, performed at N140°E and N50°E directions (Fig. 8.17a–c), are shown presenting V_p (Fig. 8.18a–c) and V_s (Fig. 8.19a–c) absolute velocities, as well as the

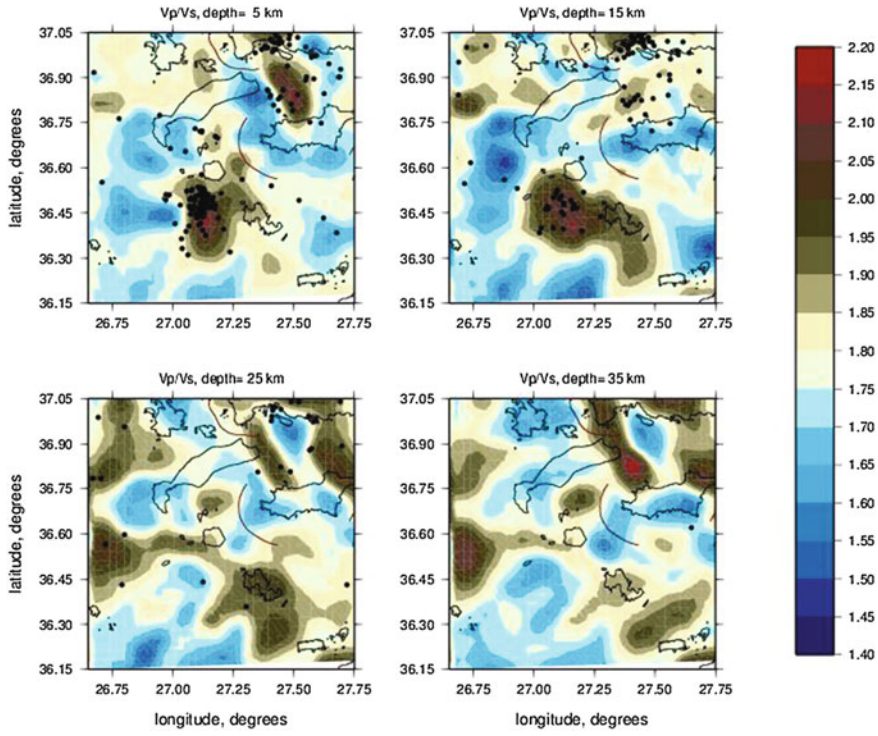

Fig. 8.16 Tomograms of absolute V_p/V_s ratio values at 5, 15, 25 and 35 km depths

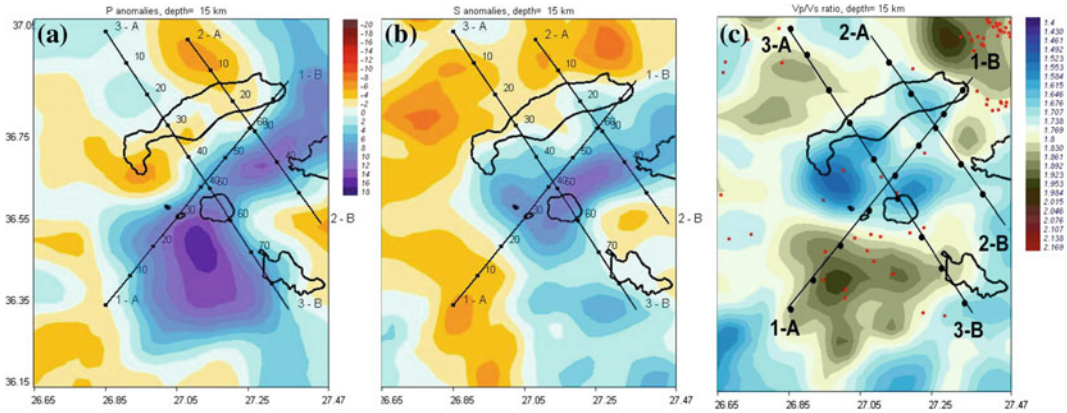

Fig. 8.17 Horizontal projection of the tomographic profiles of absolute values of **a** P-wave velocities **b** S-wave velocities and **c** V_p/V_s ratio

distribution of the V_p/V_s ratio values (Fig. 8.20). Profiles 1A–1B and 3A–3B indicate a low P-velocity layer at 8–17 km depth, in the central part of the study area which may be related to the activation of local ruptures that bound the Yali–Nisyros Basin. This can be justified by the penetration of water fluids through local faults and flat cracks, saturating the hosting rock formation. An anomaly of high V_p/V_s ratio and low V_s perturbations can be observed in an area located 5–10 km SW of Nisyros, between the NE-SW trending Fault System bounding the

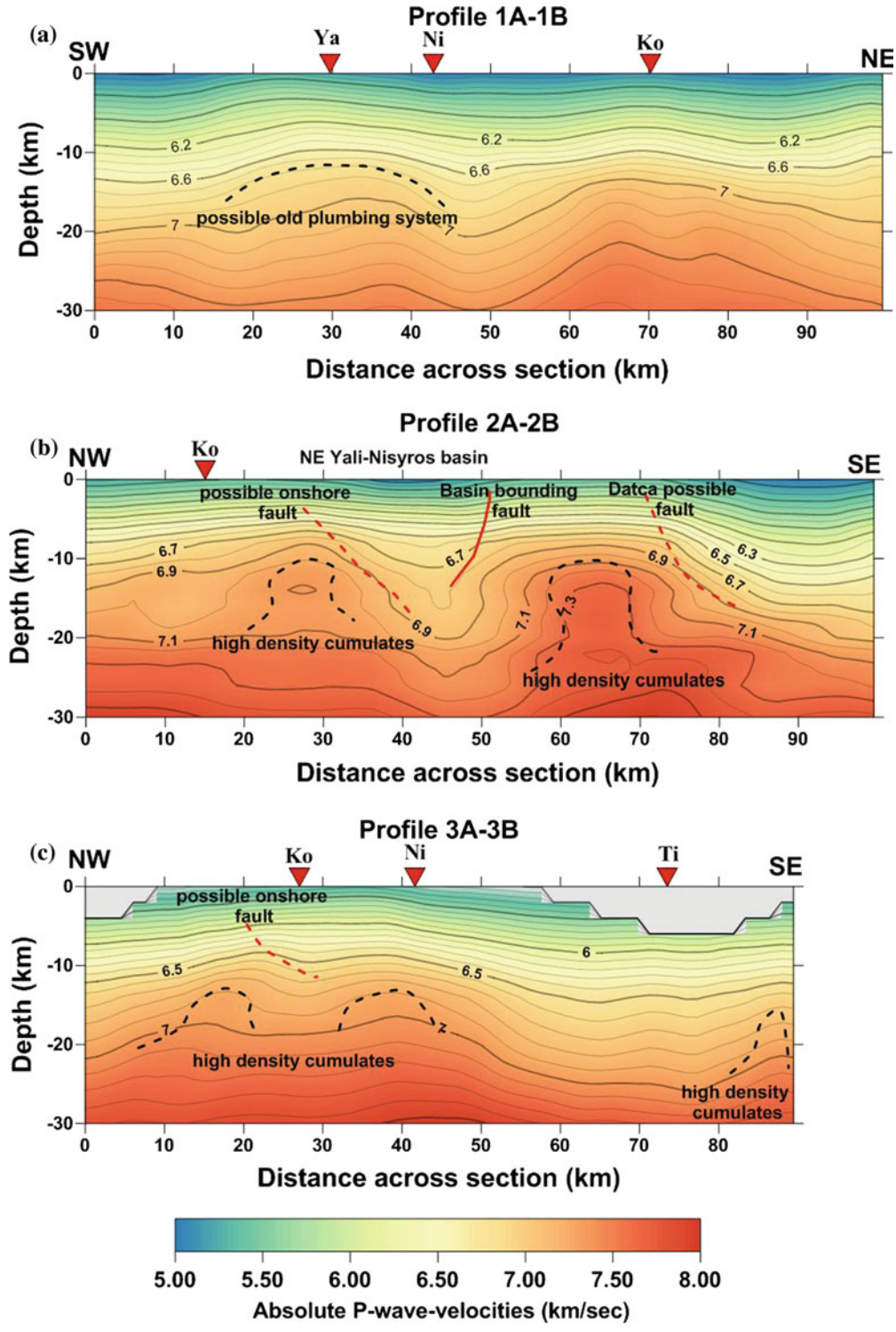

Fig. 8.18 Sections of absolute P-wave velocities for **a** N50°E **b** N140°E (ENE of Nisyros) and **c** N140°E (passing through Nisyros Island)

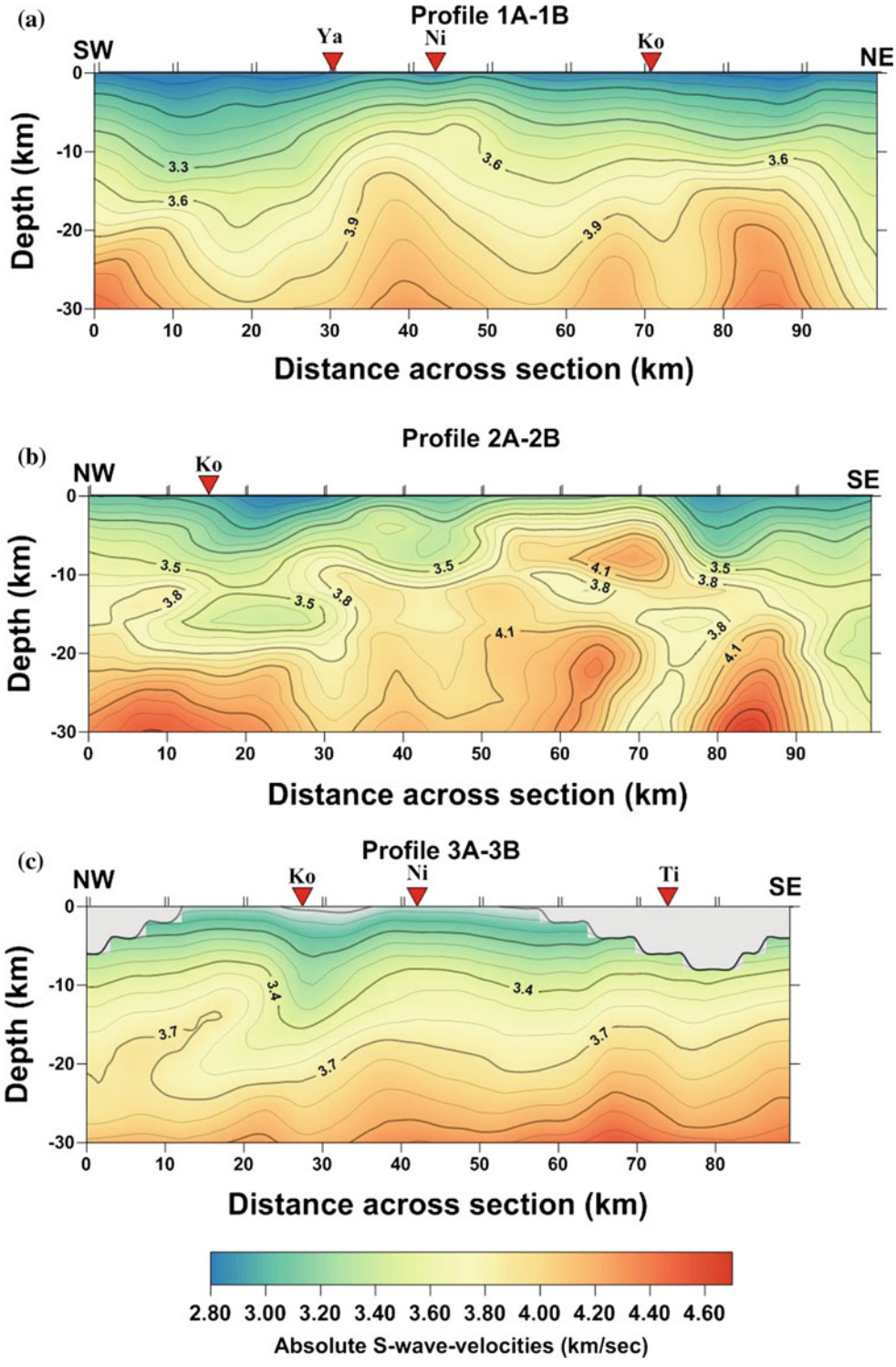

Fig. 8.19 Sections of absolute S-wave velocities for **a** N50°E **b** N140°E (ENE of Nisyros) and **c** N140°E (passing through Nisyros Island)

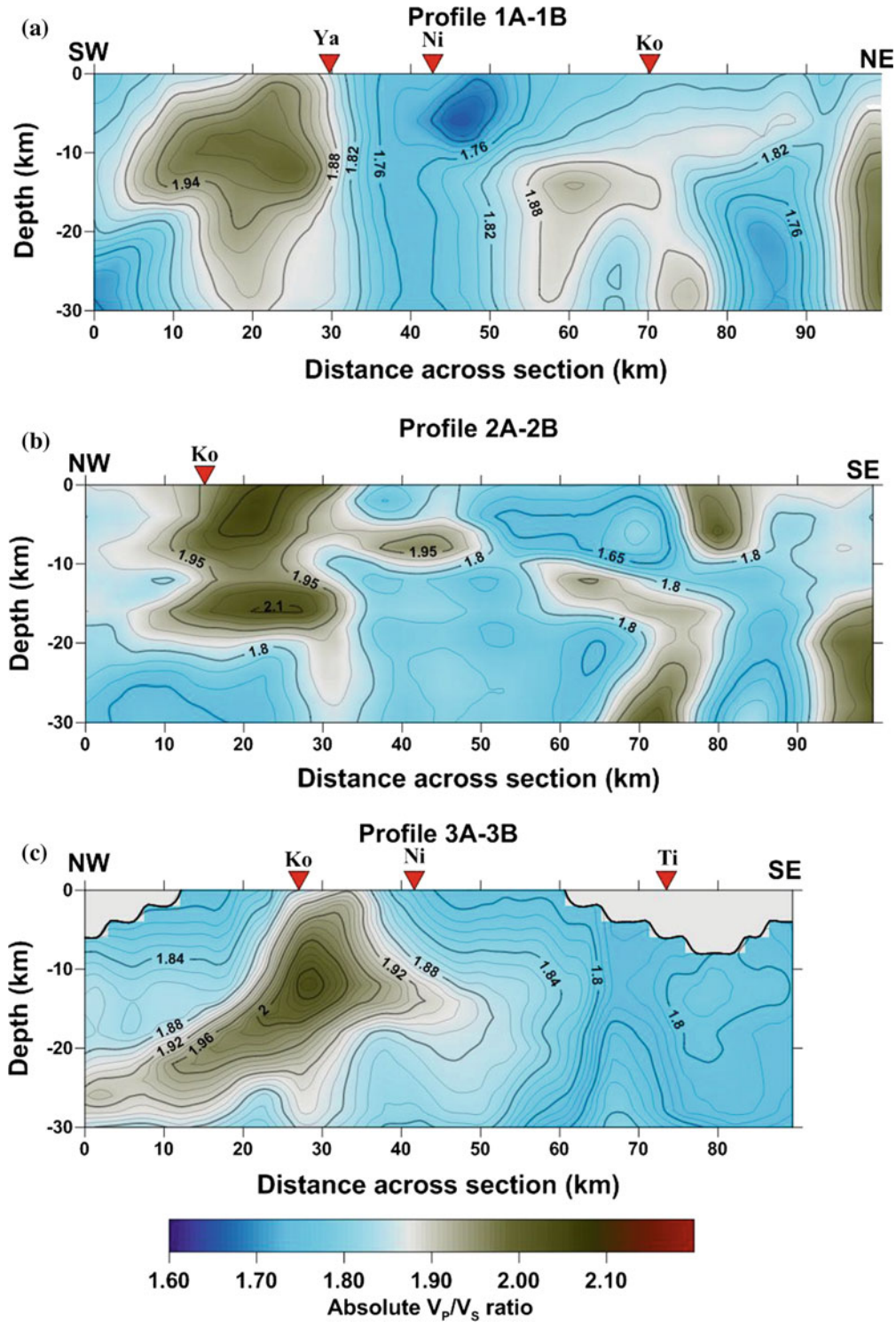

Fig. 8.20 Sections of absolute V_p/V_s ratio values for **a** N50°E **b** N140°E (ENE of Nisyros) and **c** N140°E (passing through Nisyros Island)

Southern Nisyros Basin. This anomaly is anti-correlated with a positive V_p perturbation, which is typical for active volcanoes and may represent magma intrusion of deeper composition containing fluids and melts (Zollo et al. 2003; Sherburn et al. 2003; Koulakov et al. 2013). Furthermore, the obtained results (Fig. 8.16) reveal an area of high V_p/V_s ($\sim$1.95) that can be associated to the possible presence of magmatic chambers which feed the Yali and Strongyli volcanic centers, extending down to about $\sim$15 km. In the respective cross-sections (Fig. 8.18), it appears that these circular-shaped anomalies are connected to a region of low velocity perturbation and high V_p/V_s ratio at larger depths. These observations could be related to the primary magmatic chamber that feeds the superficial ones with melt material through the local fault system. A clear high $V_p - V_p/V_s$ ratio body (6.4–6.8 km/s and V_p/V_s $\sim$1.90), NE-SW oriented and located 5 km E of Nisyros Island, between 5 and 15 km b.s.l. (Fig. 8.18) is possibly connected to high density cumulates, fractionated by the magma during its ascent, stocked and congealed at depth (Patanè et al. 2002). The absolute values of P-wave velocity show a low-velocity zone in the SE edge of the study area, near Tilos Island, at about 35 km depth (Figs. 8.14 and 8.15), which could possibly indicate the presence of a hydrated mantle wedge (Guillot et al. 2001; Dinc et al. 2010). The P-wave velocity is much lower to the eastern part of the study area (Figs. 8.14 and 8.15) than the respective western one, which could be an indirect characteristic of fluid penetration from the lower crust to the mantle diapir, near Northern Tilos Basin.

8.5 Conclusions

The seismic activity of the broader Nisyros region during the last decades is moderate to low, whereas several large earthquakes have been reported in the past. Microseismic activity is not well known, due to the absence of a local permanent seismological network. This fact is proven by the important number of shallow microearthquakes that were located during the operation periods of temporary networks on Nisyros Island and its vicinity. On the other hand, seismicity recorded by HUSN can be divided in earthquakes of shallow and intermediate depths. Very low activity is observed on Nisyros Island, whereas concentration of shallow events is presented SW of Nisyros, along the NE-SW trending Fault System bounding the Southern Nisyros Basin. Important crustal seismicity is also recorded east of Kos Island, within the Gulf of Gökova, mainly related to the N-S extension in the region, as also revealed by the normal-type focal mechanisms. Among the most important characteristics of the study area is the intermediate depth seismicity West of Nisyros Island. Focal depths, determined by moment tensor inversion, mainly vary between 100 and 150 km, while the rupture is consistent with reverse faulting with a significant strike-slip component. Histograms of seismicity monthly rates revealed continuous background activity with both shallow and deeper events occurring frequently through time. Nevertheless, there appears to be no evidence of correlation between crustal and deeper seismicity, as far as the rates are concerned. However, some deeper events in the northern part of the study area have coincided, in a timeframe of several days, with two seismic sequences east of Kos, indicating that this sort of relation may be worth looking into in the future, when more data are available. The study of the spatiotemporal distribution has revealed some zones of particular interest in the broader area, where seismic sequences have occurred, such as the N-S oriented zone between Nisyros and Karpathos, the E-W oriented zone between Kos and the coasts of Turkey, near Bodrum, in the gulf of Gökova and further south in the gulf of Symi. The southernmost part of the area of study, near Karpathos and Rhodes, where two $M_w > 6$ events of intermediate depth have occurred within the last decade, is the zone with the greatest seismic potential, related to the subduction process.

Taking into account the recorded local seismicity, a tomographic inversion was performed. This led to the identification of the location of

possible magmatic chambers, as well as of other processes related to the Hellenic Volcanic Arc. More specifically, low V_p anomalies accompanied by high values of V_p/V_s ratio were obtained for the depth intervals of 5–15 km and 25–35 km, at the northern part of the Nisyros-Kos Caldera. These areas are related to the collapsed Late-Pliocene caldera of Nisyros-Kos, filled with low-density volcanoclastic sediments, and the gas products of Yali and Strongyli volcanic centers. The correlation between absolute V_p and V_p/V_s ratio assisted to the recognition of high density cumulates 5 km to the E of Nisyros Island, that may be connected to volcano-tectonic activity of the last unrest period (1996–1997). Also, a prominent feature was recognized to the SW of Nisyros Island with high absolute values of V_p and V_p/V_s ratio, as a result of the upward migration of deeper composition magmatic intrusions. Moreover, in the SE edge of the study area, near Tilos Island, a low-velocity zone was identified at about 35 km depth, which could be an indirect characteristic of fluid penetration from the lower crust to a mantle diapir.

References

Allen SR, Cas RAF (2001) Transport of pyroclastic flows across the sea during the explosive, rhyolitic eruption of the Kos Plateau Tuff, Greece. Bull Volcanol 62:441–456

Allen SR, Stadlbauer, E, Keller J (1999) Stratigraphy of the Kos Plateau Tuff: product of a major Quaternary explosive rhyolitic eruption in the eastern Aegean Sea. Int J Earth Sci 88:132–156

Ambraseys NN, Adams RD (1998) The Rhodes earthquake of 26 June 1926. J Seismol 2(3):267–292

Armijo R, Lyon-Caen H, Papanastassiou D (1992) East-West extension and Holocene normal-fault scarps in the Hellenic Arc. Geology 20:491–494

Bornovas J (1953) On the earthquakes of Nisyros in January 1953 unpublished report. Institute of Geology and Mineral Exploration, Athens (in Greek)

Bouchon M (1979) Discrete wave number representation of elastic wave fields in three-space dimension. J Geophys Res 84:3609–3614

Bouchon M (2003) A review of the discrete wavenumber method. Pure Appl Geophys 160:445–465

Chiarabba C, Frepoli A (1997) Minimum 1D velocity models in Central and Southern Italy: a contribution to better constrain hypocentral determinations. Ann Geophys 40(4):937–954

D'Alessandro A, Papanastassiou D, Baskoutas I (2011) Hellenic unified seismological network: an evaluation of its performance through SNES method. Geophys J Int 185:1417–1430

Dimitriadis I, Papazachos C, Panagiotopoulos D, Hatzidimitriou P, Bohnhoff M, Rische M, Meier T (2010) P and S velocity structures of the Santorini-Colombo volcanic system (Aegean Sea, Greece) obtained by non-linear inversion of travel times and its tectonic implications. J Volcanol Geotherm Res 195:13–30

Dinc AN, Koulakov I, Thorwart M, Rabbel W, Flueh ER, Arroyo I, Taylor W, Alvarado G (2010) Local earthquake tomography of central Costa Rica: transition from seamount to ridge subduction. Geophys J Int 183:286–302. doi:10.1111/j.1365-246X.2010.04717

Drakatos G, Karantonis G, Stavrakakis G (1997) P-wave crustal tomography of Greece with use of an accurate 2-point ray tracer. Annali di Geofisica XL 1:25–36

Dreger DS, Helmberger DV (1993) Determination of source parameters at regional distances with three component sparse network data. J Geophys Res 98:8107–8125

Dreger DS, Tkalcic H, Johnston M (2000) Dilational processes accompanying earthquakes in the Long Valley Caldera. Science 288:122–125

Fan G, Ni JF, Wallace TC (1994) Active tectonics of the Pamirs and Karakorum. J Geophys Res 99:7131–7160

Franz L, Okrusch M, Seidel E, Kreuzer H (2005) Polymetamorphic evolution of pre-Alpidic basement relics in the external Hellenides, Greece. Neues Jahrbuch für Mineralogie-Abhandlungen 181:147–172

Fukuyama E, Dreger DS (2000) Performance test of an automated moment tensor determination system for the future "Tokai" earthquake. Earth Planets Space 52:383–392

Galanopoulos AG (1953) Katalog der Erdbeben in Griechenland für die Zeit von 1879 bis 1892. Annales Géologiques des pays Helléniques. Première série, Tôme cinquième. Athènes, Laboratoire de Géologie de l' Université, pp 143–163

Galanopoulos A (1981) The damaging earthquakes and the earthquake potential of Greece. Ann Geol Pays Helleniques 30:647–724 (in Greek)

Garfunkel Z (2004) Origin of the Eastern Mediterranean basin: a reevaluation. Tectonophysics 391:11–34

Georgalas GC (1962) Catalogue of the active volcanoes of the world including solfatara fields; Part XII Greece. International Association of Volcanology, Rome, Italy, 40 p

GEOWARN (2003) Final report of EU geowarn project—IST 1999–12310: Geo-spatial warning system, Nisyros volcano (Greece): an emergency case study. www.geowarn.ethz.ch

Gorceix MH (1873) Sur la recente eruption de Nisyros. C R Acad Sci Paris 77:1039

Gorceix MH (1874) Phenomenes volcaniques de Nisyros. C R Acad Sci Paris 78:444–446

Guillot S, Kéiko HH, De Sigoyer J, Nägler T, Auzende AL (2001) Evidence of hydration of the mantle wedge and its role in the exhumation of eclogites. Earth Planet Sci Lett 193:115–127

Harbury N, Hall R (1988) Mesozoic extensional history of the southern Tethyan continental margin in the SE Aegean. Geol Soc London 145:283–301

Higgins MD, Higgins R (1996) A Geological companion to Greece and the Aegean. Duckworth Publishers, London

Humphreys E, Clayton RW (1988) Adaptation of back projection tomography to seismic travel time problems. J Geophys Res 93:1073–1085

Ichinose G, Anderson J, Smith K, Zeng Y (2003) Source parameters of Eastern California and Western Nevada earthquakes from regional moment tensor inversion. Bull Seism Soc Am 93:61–84

Kapetanidis V, Papadimitriou P (2011) Estimation of arrival-times in intense seismic sequences using a master-events methodology based on waveform similarity Geophys J Int 187:889–917

Kapetanidis V, Deschamps A, Papadimitriou P, Matrullo E, Karakonstantis A, Bozionelos G, Kaviris G, Serpetsidaki A, Lyon-Caen H, Voulgaris N, Bernard P, Sokos E, Makropoulos K (2015) The 2013 earthquake swarm in Helike, Greece: seismic activity at the root of old normal faults. Geophys J Int 202 (3):2044–2073. doi:10.1093/gji/ggv249

Kasatkina E, Koulakov I, West M, Izbekov P (2014) Seismic structure changes beneath Redoubt Volcano during the 2009 eruption inferred from local earthquake tomography. J Geophys Res Solid Earth 119:4938–4954. doi:10.1002/2013JB010935

Kaviris G (2003) Study of seismic source properties of the eastern Gulf of Corinth. Ph D thesis, Geophysics-Geothermics Department, Faculty of Geology, University of Athens, Greece (in Greek)

Kaviris G, Papadimitriou P, Kravvariti Ph, Kapetanidis V, Karakonstantis A, Voulgaris N, Makropoulos K (2015) A detailed seismic anisotropy study during the 2011–2012 unrest period in the Santorini volcanic complex. Phys Earth Planet Inter 238:51–88

Keller J, Rehnen TH, Stadlbauer E (1990) Explosive volcanism in the Hellenic arc. A summary and review. In: Proceedings of the third scientific congress "Thera and the Aegean World III". Earth Sci 2:13–26

Kissling E, WL Ellsworth WL, Eberhart-Phillips D, Kradolfer U (1994) Initial reference models in local earthquake tomography. J Geophys Res 99:19635–19646

Klein FW (1989) User's guide to HYPOINVERSE, a program for VAX computers to solve for earthquake locations and magnitudes, US Geol Surv Open-File Rep 89–314

Kokkalas S, Doutsos T (2004) Kinematics and strain partitioning in the southeast Hellenides (Greece). Geol J 39:121–140

Koulakov I (2009) LOTOS code for local earthquake tomographic inversion. Benchmarks for testing tomographic algorithms. Bull Seismol Soc Am 99(1):194–214

Koulakov I, Gordeev EI, Dobretsov NL, Vernikovsky VA, Senyukov S, Jakovlev A, Jaxybulatov K (2013) Rapid changes in magma storage beneath the Klyuchevskoy group of volcanoes inferred from time-dependent seismic tomography. J Volcanol Geoth Res 263:75–91. ISSN:0377-0273

Lagios E, Sakkas V, Parcharidis I, Dietrich V (2005) Ground deformation of Nisyros volcano (Greece) for the period 1995–2002: results from DInSAR and DGPS observations. Bull Volc 68(2):201–214

Lagios E, Sakkas V, Novali F, Ferreti A, Damiata BN, Dietrich V (2015) Reviewing and updating (1996–2012) ground deformation in Nisyros Volcano (Greece) from SqueeSAR™ analysis & GPS measurements, this issue

Lees JM (2007) Seismic tomography of magmatic systems. J Volc Geoth Res 167:37–56

Lees JM, Crosson RS (1989) Tomographic inversion for three-dimensional velocity structure at Mount St. Helens using earthquake data. J Geophys Res 94:5716–5728

Lopes AEV, Assumpção M (2011) Genetic Algorithm Inversion of the Average 1D Crustal Structure using Local and Regional Earthquakes. Comput Geosci 37 (9):1372–1380

Makropoulos K, Kaviris G, Kouskouna V (2012) An updated and extended earthquake catalogue for Greece and adjacent areas since 1900. Nat Hazards Earth Syst Sci 12:1425–1430

Montalbetti JF, Kanasewich ER (1970) Enhancement of teleseismic body phases with a polarization filter. Geophys J R Astron Soc 21:119–129

Müller St, Kahle HG (1993) Crust-mantle evolution, structure and dynamics of the Alpine Mediterranean region. In Contributions of Space Geodesy to Geodynamics: Crustal dynamics 23:249–298

Müller B, Wehrle V, Zeyen H, Fuchs K (1997) Shortscale variations of tectonic regimes in the western European stress province north of the Alps and Pyrenees. Tectonophysics 275:199–219

Nomikou P (2004) Geodynamic of Dodecanise islands: Kos and Nisyros volcanic field. PhD Thesis Department of Geology, University of Athens

Nomikou P, Papanikolaou D (2010) A comparative morphological study of the Kos-NisyrosTilos volcanosedimentary basins. Bull Geol Soc of Greece XLIII/1:464–474

Nomikou P, Papanikolaou D (2011) Extension of Active Fault Zones on Nisyros Volcano across the Yali-Nisyros Channel based on Onshore and Offshore data. Marine Geophysical Research. Special issue on «Seafloor Mapping for Geohazard Assessment»

Nomikou P, Croff-Bell K, Papanikolaou D, Livanos I, Fero-Martin J (2013) Exploring the submarine flanks of Yali and Strongyli volcanic islets at the eastern edge of the Aegean Volcanic Arc. Zeitschrift fór Geomorphologie 57(Suppl 3):125–137

Papanikolaou D, Lekkas E, Sakelariou D (1991) Volcanic stratigraphy and evolution of the Nisyros volcano. Bull Geol Soc Greece 25:405–419

Papanikolaou D Lekkas E, Sakellariou D, Nomikou P (1998) 2. The Nisyros Volcano (Progress report of research project). Newsletter of the European Centre on Prevention and Forecasting of Earthquakes 2:13–14

Papadimitriou P, Kaviris G, Makropoulos K (1999) Evidence of shear-wave splitting in the eastern Corinthian Gulf (Greece). Phys Earth Planet Interiors 114:3–13

Papadimitriou P, Chousianitis K, Agalos A, Moshou A, Lagios E, Makropoulos K (2012) The spatially extended 2006 April Zakynthos (Ionian Islands, Greece) seismic sequence and evidence for stress transfer. Geophys J Int 190(2):1025–1040

Papadimitriou P, Kapetanidis V, Karakonstantis A, Kaviris G, Voulgaris N, Makropoulos K (2015) The Santorini volcanic complex: a detailed multi-parameter seismological approach with emphasis on the 2011–2012 unrest period. J Geodyn 85:32–57. doi:10.1016/j.jog.2014.12.004

Papadopoulos GA, Sachpazi M, Panopoulou G, Stavrakakis G (1998) The volcanoseismic crisis of 1996–97 in Nisyros, SE Aegean Sea, Greece. Terra Nova 10:151–154

Papazachos BC, Papazachou C (2003) The earthquakes of Greece. Ziti Publ Co 286 pp (in Greek)

Patanè D, Chiarabba C, Cocina O De, Gori P, Moretti M, Boschi E (2002) Tomographic images and 3D earthquake locations of the seismic swarm preceding the 2001 Mt. Etna eruption: evidence for a dyke intrusion. Geophys Res Lett 29(10):1497. doi:10.1029/2001GL014391

Sachpazi M, Kontoes Ch, Voulgaris N, Laigle M, Vougioukalakis G, Olga Sikioti G, Stavrakakis G, Baskoutas J, Kalogeras J, Lepine JCl (2002) Seismological and SAR signature of unrest at Nisyros caldera, Greece. J Volcanol Geoth Res 116:19–33

Sakkas V, Novali F, Lagios E, Ferretti A, Vassilopoulou S, Bellotti F, Allievi J (2015) Combined Squee-SARTM and GPS ground deformation study of Nisyros-Yali volcanic field (Greece) for period 2002–2012. Geosciences and remote sensing symposium (IGARSS) 2015 IEEE international Milan Italy, pp 4672–4675

Sherburn S, Bannister S, Bibby HM (2003) Seismic velocity structure of the central Volcanic Zone, New Zealand, from local earthquake tomography. J Volcanol Geoth Res 122(1–2):69–88

Stiros SC, Vougioukalakis G (1996) The 1970 Yali (SE edge of the Aegean volcanic arc) earthquake swarm: surface faulting associated with a small earthquake. Ann Tecton X:20–30

Stucchi M, Rovida A, Gomez Capera AA, Alexandre P, Camelbeeck T, Demircioglu MB, Gasperini P, Kouskouna V, Musson RMW, Radulian M, Sesetyan K, Vilanova S, Baumont D, Bungum H, Fäh D, Lenhardt W, Makropoulos K, Martinez Solares JM, Scotti O, Zivcic M, Albini P, Batllo J, Papaioannou C, Tatevossian R, Locati M, Meletti C, Viganò D, Giardini D (2013) The SHARE European earthquake catalog (SHEEC) 1000–1899. J Seismolog 17(2):523–544

Toomey DR, Foulger GR (1989) Tomographic inversion of local earthquake data from the Hengill-Grensdalur central volcano complex, Iceland. J Geophys Res 94 (B12):17497–17510

Tsapanos TM, Galanopoulos D, Burton PW (1994) Seismicity in the South Aegean Volcanic Arc: relations between seismic parameters and the geophysical fields in the region. Geophys J Intern 117:677–694

Vanderkluysen L, Volentik ACM, Principe C, Hunziker JC, Hernandez J (2005) Nisyros' volcanic evolution: the growth of a strato-volcano. In: Hunziker JC, Marini L (eds) The Geology Geochemistry and Evolution of Nisyros Volcano (Greece) Implications for the Volcanic Hazards, Memoires de Geologie (Lausanne), vol 44, pp 100–106

Vanorio T, Virieux J, Capuano P, Russo G (2005) Three-dimensional seismic tomography from P wave and S wave microearthquake travel times and rock physics characterization of the Campi Flegrei Caldera. J Geophys Res 110(B3):B03201

Volentik A, Vanderkluysen L, Principe C, Hunziker JC (2005) Stratigraphy of Nisyros volcano (Greece). In: Hunziker JC, Marini L (eds) The Geology, Geochemistry and Evolution of Nisyros Volcano (Greece), Implications for the Volcanic Hazards. Memoires de Geologie (Lausanne), vol 44, pp 26–67

Wagner GJ, Storzer D, Keller J (1976) Spaltspurendatierungen quartarer Gesteinsglaser aus dem Mittelmeerraum. Neues Jahrb Miner Monatsh 2:84–94

Wessel P, Smith WHF (1995) New version of the generic mapping tools released. EOS Trans Am Geophys Union 76:329

Zandomeneghi D, Almendros J, Ibàñez JM, Saccorotti G (2008) Seismic tomography of Central São Miguel, Azores. Phys Earth Planet Inter 167(1–2):8–18

Zeng Y, Anderson JG (1995) A method for direct computation of the differential seismogram with respect to the velocity change in a layered elastic solid. Bull Seism Soc Am 85:300–307

Zollo A, Judenherc S, Auger E, D'Auria L, Virieux J, Capuano P, Chiarabba C, de Franco R Makris, J Michelini A, Musacchio G (2003) Evidence for the buried rim of Campi Flegrei caldera from 3-d active seismic imaging. Geophys Res Lett 30(19). doi:10.1029/2003GL018173

9 Microseismicity and Crustal Deformation of the Dodecanese Volcanic Area, Southeastern Aegean Sea Using an Onshore/Offshore Seismic Array

Joanna Papoulia, Jannis Makris, Ivan Koulakov, Chrysoula Fasoulaka and Paraskevi Drakopoulou

Abstract

The seismic activity of the volcanic field of Kos-Yali-Nisyros, south-eastern part of the South Aegean Volcanic Arc, was observed by an "amphibious" seismic network consisting of nine 3C stand-alone land stations and four 4C ocean bottom seismographs. The array operated for a period of four months, from June 28 to October 13, 2001. Accuracy location of the seismic foci was optimized by using a 1D local velocity model obtained by active seismic observations. 1190 micro-earthquakes over a threshold magnitude of 0.7 ML were identified, using arrivals recorded by a minimum of four stations per event. The average RMS of the travel time residuals was better than 0.1 s for events located within the array and 0.2 s for those lying outside. Regional seismicity and focal mechanisms of larger events in the fault system Gökova, Kos-Nisyros and that of Karpathos basins delineate the extensional boundary to the north and west of the Dodecanese islands block. This block unit, although internally strongly fractured, is decoupled from the Aegean microplate. It is anticlockwise rotated with the west Karpathos basin that limits its western flank—having the largest width and maximum subsidence. These processes are very young having their maximum intensity at the bend of the fault system from E-ENE direction to nearly N-S striking. The magmatic intrusions are concentrated in this area of bending. They are driven by the subduction of the Ionian oceanic lithosphere below the Aegean microplate with deep seismic foci of 150 to 180 km depth

J. Papoulia (✉) · C. Fasoulaka · P. Drakopoulou
Hellenic Centre for Marine Research, Institute of Oceanography, Anavyssos, Greece
e-mail: jpapoulia@gmail.com

J. Makris
University of Hamburg, Hamburg, Germany

I. Koulakov
Institute of Petroleum Geology and Geophysics, Tyumen, Russia

V.J. Dietrich and E. Lagios (eds.), *Nisyros Volcano*, Active Volcanoes of the World,
DOI 10.1007/978-3-319-55460-0_9

building a cluster below the Nisyros and Kos islands. The mapped seismicity is mainly induced by the volcanic processes of magma intrusion within 4 km below Nisyros and apophytic branches of magma below Yali and Strongyli islands. The main magma chamber is below 6 km depth and the induced pressure in the upper crust, due to magma injection, generates fractures and hydrothermal circulation followed by high local seismicity of small magnitude events.

9.1 Introduction

The Aegean Volcanic Arc, extending from Lichades, Methana, Milos, Santorini to Nisyros volcano evolved within a back-arc extensional tectonic regime. It was triggered by the north-eastward subduction of the Ionian oceanic lithosphere beneath the passive Hellenic margin of the European plate (e.g. McKenzie 1972; LePichon and Angelier 1979; Papanikolaou 1993; Jackson 1994). As a result of this ongoing subduction, significant magmatic and volcanic activity occurs in the Dodecanese area since late Pleistocene—Holocene times. Nisyros and the surrounding islands of Yali, Strongyli, Kondelioussa and Pergousa represent late Pleistocene—Holocene volcanoes.

The island of Nisyros is mainly composed by lava flows, pyro-clastic layers and lava domes dated from 161 ka to date (e.g. Davis 1967; Keller et al. 1990), forming a cone of 8 km diameter at its base and a caldera of 4 km at the top. It lies on alpine Mesozoic basement and a thinned continental crust, with Moho depth of 20–23 km (Makris et al. 2016). On the island of Kos, to the north of Nisyros, major magmatic activity has also occurred since late Miocene—Pliocene, and one of the largest volcanic eruptions in the eastern Mediterranean dated at 161 ka bp, is represented by the Kos ignimbrite (Keller et al. 1990). Products of this eruption covered an area of more than 3000 sq. km (Allen et al. 1999).

The Dodecanese however is not only exposed to volcanic hazard but is also one of the most seismically active areas in Greece and the Mediterranean region (e.g. Galanopoulos 1960; Makropoulos and Burton 1981; Jackson and McKenzie 1988; Papazachos and Papazachou 1997). Large magnitude earthquakes have repeatedly affected it in recent and historical times that caused severe destruction and human loss. Among the most severe earthquakes are that of Rhodes at 226 BC that destroyed the Colossus of Rhodes, the 1481 Rhodes 7.1 Ms event with 30.000 fatalities, the Chalki 1840 6.5 Mw event with 600 fatalities, and the 1993 6.6 Ms Kos event with 178 fatalities. During the period 1995–1998 increased seismic activity occurred at Nisyros with extended damage at the northwestern part of the Island (Mandraki town). Several studies followed up this seismic activity, incl. a detailed multibeam bathymetric, and a single channel high-resolution air gun survey around the volcano. The R/V AEGAEO of the Hellenic Centre for Marine Research was used for these operations. Several faults were located on- and offshore Nisyros and the shallow sedimentary structure was delineated (e.g. Nomikou and Papanikolaou 2000; Papanikolaou and Nomikou 2001a, b). Further studies of the sediments and crust followed up in 2001, during the "GEO-WARN" project supported by the EC. An on/offshore seismic network was established in the broader area of Nisyros caldera and between the islands of Kos to the north and Tilos to the south (Fig. 9.1), and observed the microseismicity associated with the volcanic activity and the tectonic deformation. The 13 stations seismic array operated for approx. four months, from June 28 to October 13, 2001. In the following we present the results obtained by these observations.

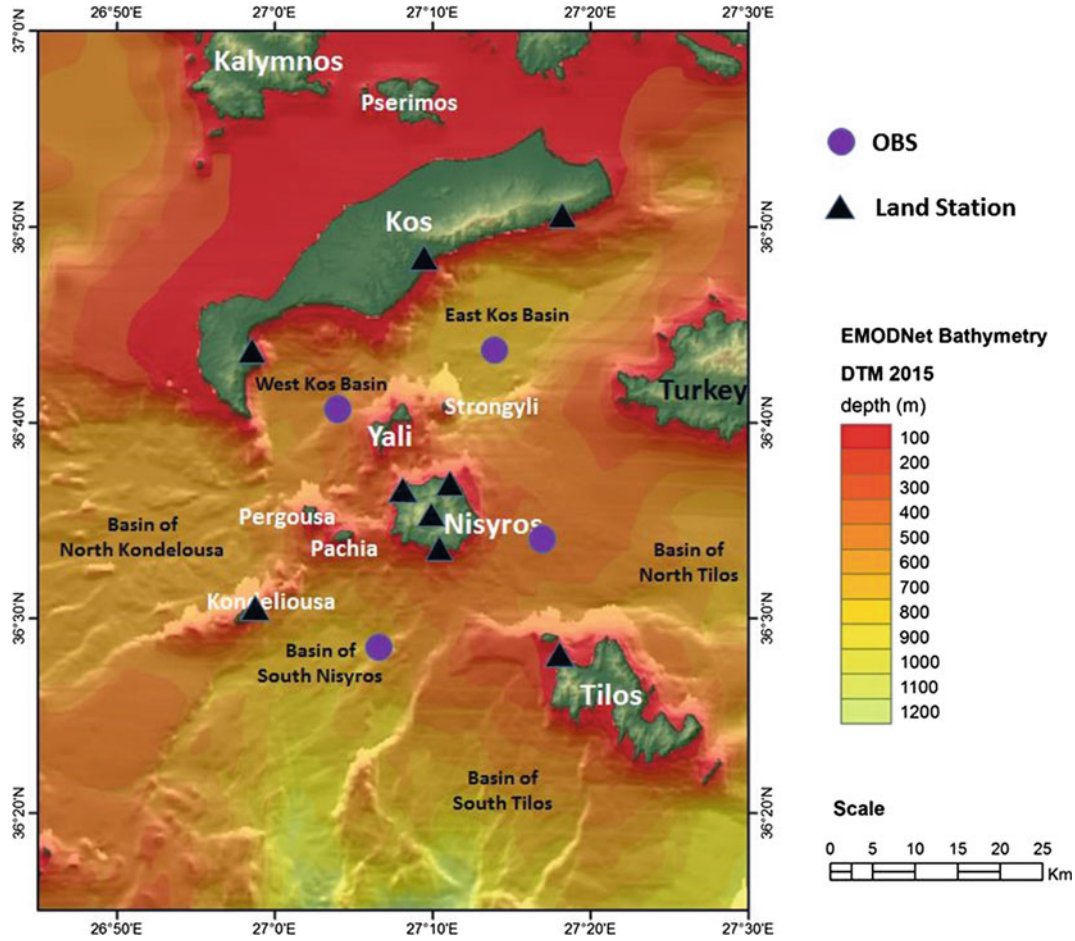

Fig. 9.1 The Geowarn "amphibious" seismic network. Operation period: 28 June–13 October 2001

9.2 The GEOWARN "Amphibious" Seismic Array and Recorded Seismicity

The Geowarn "amphibious" seismic array consisted of 4 Ocean Bottom Seismographs (OBS) and 9 stand-alone land stations (Fig. 9.2). Both marine and land stations were equipped with the SEDIS III seismic recorder developed at the University of Hamburg (Makris and Moeller 1990). This instrument was used offshore integrated in an OBS or as a stand-alone seismic unit onshore. The OBS is a 4-Channel recording station (3 channels for geophones plus one hydrophone) with a 4.3 GB storage capacity. One way alkaline D-size batteries allowed continuous monitoring for approximately 21 days. Timing was obtained by GPS receivers onshore and inbuilt thermo-stabilized quartz clocks of 10^{-6} accuracy and strictly linear drift offshore. Electronic components and sensors are housed in a 17 in. glass sphere that withstands pressure corresponding to more than 6000 m water depth. Onshore stations were equipped with solar panels and batteries that permit continuous operation (Fig. 9.2).

Fig. 9.2 An ocean bottom seismograph on R/V AEGEAO-HCMR before deployment (*left*) and a stand-alone land station equipped with solar panel (*right*)

9.3 Evaluation of the Microseismicity

Data evaluation and location of seismic events was accomplished by applying the hypoinverse code (Klein 1989). We optimized the location procedure by adopting a local velocity model (Table 9.1), averaged from active seismic observations per-formed during an active seismic experiment (Makris et al. 2016).

Magnitudes were defined by the coda lengths of the recorded seismograms, calibrated by local earthquakes also observed by the Seismograph Network of the National Observatory of Athens, applying the Crosson (1972) method.

Table 9.1 Local velocity model for hypocentral location (after Makris et al. 2016)

Velocity Vp (km/s)	Depth (km)
4.40	0.00
5.50	4.00
6.50	10.00
8.00	25.00

In four months, from June 28 to 13 October 2001, 1191 events were located above a threshold magnitude of ML 0.7 that were observed by minimum four stations. On the average 11 events per day were located (Fig. 9.3). The magnitude of completeness is ML 1.8 (Fig. 9.4 left).

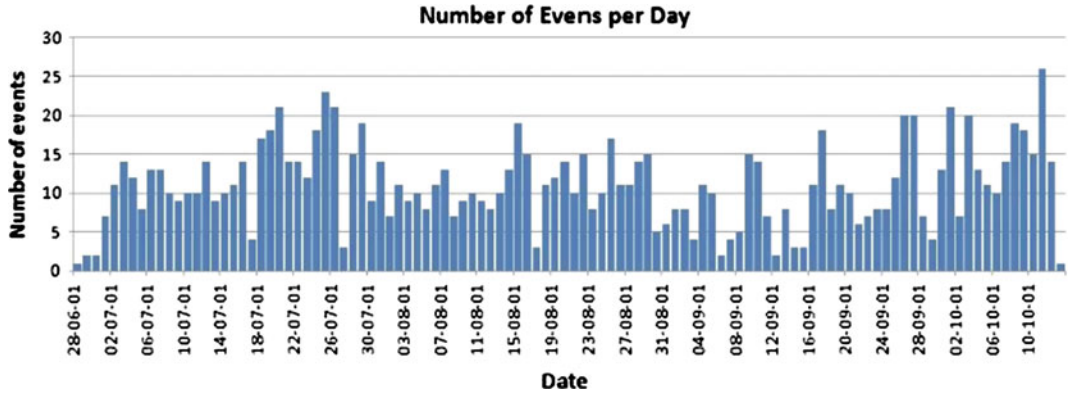

Fig. 9.3 Daily distribution of recorded seismicity

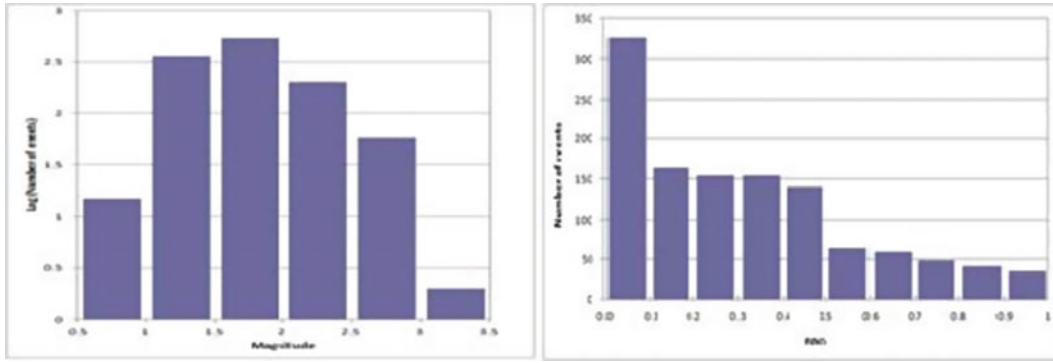

Fig. 9.4 Cumulative distribution of earthquake magnitudes (*left*) and RMS distribution of located events (*right*)

Distribution of the RMS travel time residuals of the recorded seismicity is presented in Fig. 9.4 right, showing that one third of the events has a RMS less than 0.1 s, and only 30% had RMS values greater than 0.2 s for events located outside the seismic array.

Figure 9.5 shows the recorded seismicity on the topography-bathymetry map. Seismic events are mostly of shallow focal depth, located in the upper and lower crust, with very few of intermediate depth, of 90–100 km, associated with the subduction below the volcanoes. As seen, the

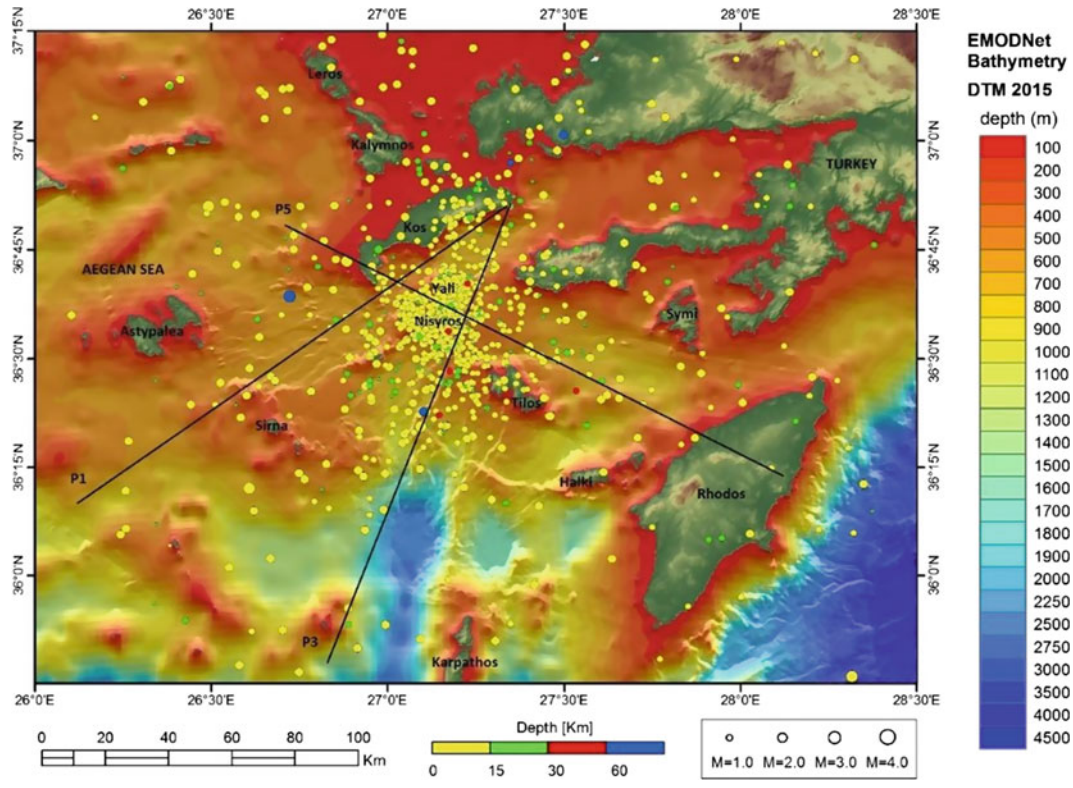

Fig. 9.5 Seismicity recorded by the GEOWARN "amphibious" seismic array. Location of three profiles mapped by active seismic observations is indicated

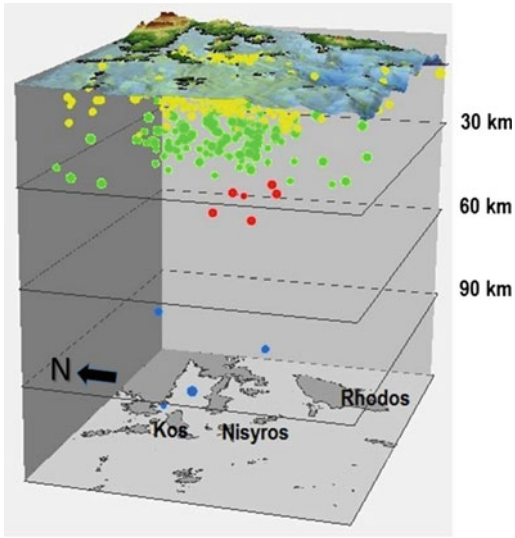

Fig. 9.6 3D distribution of seismicity. View from west

major part of the seismic activity coincides with the caldera of Nisyros and the volcanic formations of Yali and Strongyli islands.

In Fig. 9.6 the seismicity is plotted in a 3D cube. The number of events decreases with increasing hypocentral depth. Of course threshold magnitude is also increasing with depth, and one cannot exclude the existence of small magnitude seismicity at depth that our seismic array could not resolve.

The fact that the northwestern part of the Kos caldera is not very active at present could be interpreted as a consequence of the relaxation that followed the 161 ka bp eruption. This large eruption that produced the extensive volcanic tuffs and ignimbrites of western Kos (Smith et al. 1996) may have emptied this part of the caldera producing the large morphologic depression of the west Kos basin. The caldera exceeds 20 km in diameter, from the coast of western Kos to south Nisyros (Allen 2001; Allen and Cas 2001). The highly active volcanic edifices of Nisyros, Yali and Strongyli were activated after the major volcanic event that affected the areas around western Kos (Allen 2001).

A 3D velocity model (Fig. 9.7) demonstrates the volcanic area developed from active seismic observations accomplished around the island of Nisyros and Yali, and recorded by 6 OBS and 12 land stations. By comparing the 3D magma geometry with the seismicity we see that the

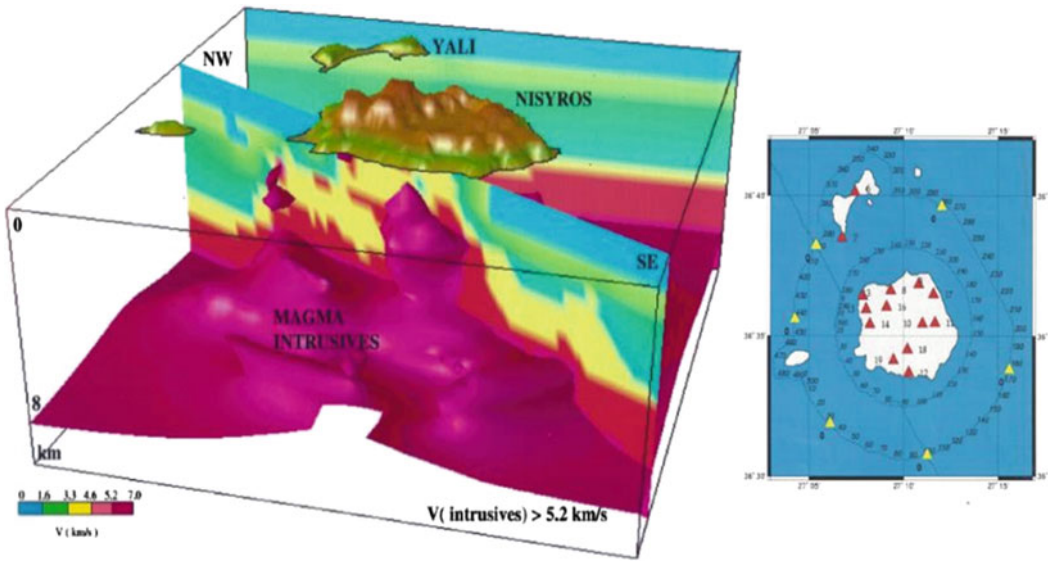

Fig. 9.7 3D velocity tomography of magmatic intrusives below the Nisyros-Yali volcanoes (*left*), locations of shots (*numbers*) and stations (*triangles*) (*right*)

seismicity is directly linked to the magmatic intrusions and the faults above and around the magma chambers. Also the geometry of the large Kos caldera was delineated and the apophytic intrusions below the volcanoes have penetrated the crust 3–4 km below surface. Although the presently active magmatic intrusions and the seismicity are concentrated below Nisyros, Strongyli and Yali, the caldera geometry clearly extends to the southwestern part of Kos, where also intense hydrothermal activity is associated with the bordering faults of the bay of Kefalos, southeastern Kos (e.g. Varnavas and Cronan 1991; Varnavas et al. 1998).

The faults around Nisyros as delineated by the active seismic experiments (Makris et al. 2016) are presented in Fig. 9.8 together with the located seismicity. We can see that the maximum concentration of seismic events is located below Nisyros, where magma intrusions occur at shallow depths. The observed seismicity along three 2D velocity models, mapped by Makris et al. (2016), is plotted to demonstrate the relation between tectonic structures and intrusives. All events located within a 10 km wide stripe on either side of each 2D line were projected into each cross section.

Profile P1 (location Fig. 9.5), is SW–NE oriented, from the eastern Cretan Sea basin towards Kos Island (Fig. 9.9). The major part of the seismicity falls within the caldera region, where the maximum deformation of the sediments and crust were observed and the intrusives penetrated the crust at the highest level.

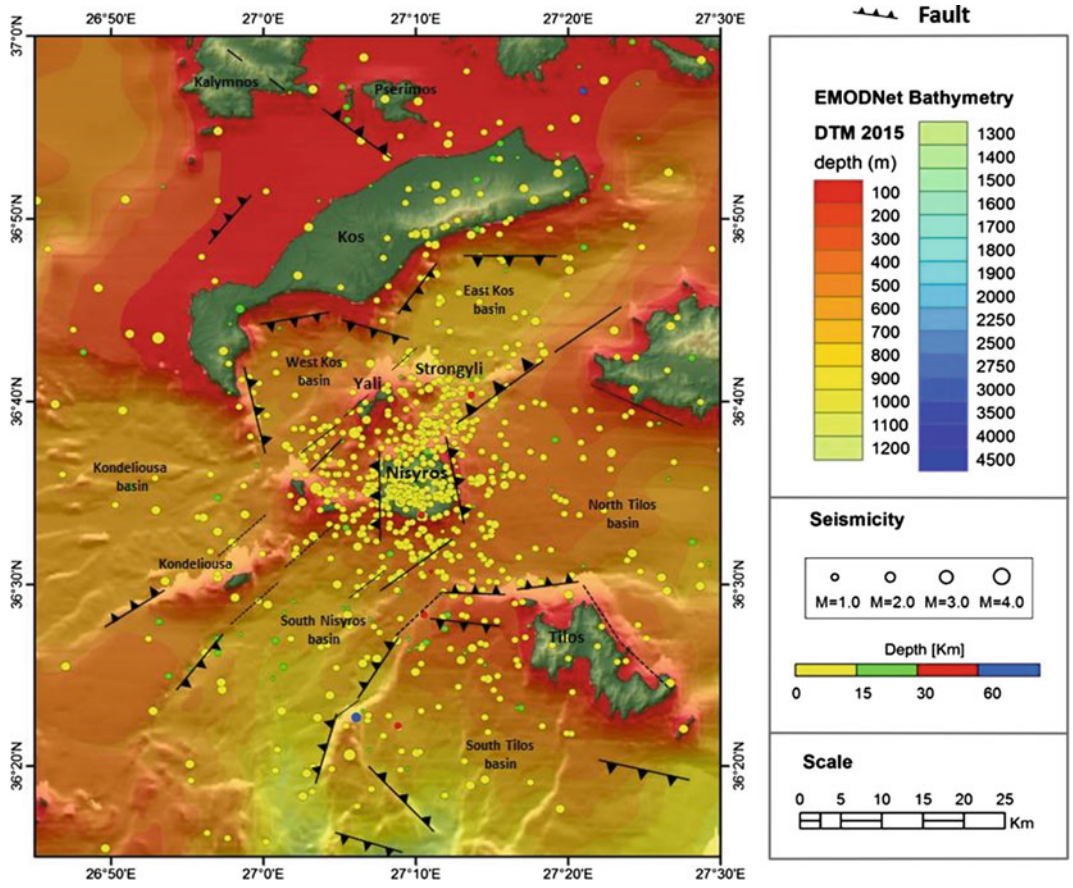

Fig. 9.8 Correlation of recorded seismicity with faults mapped by active seismic observations

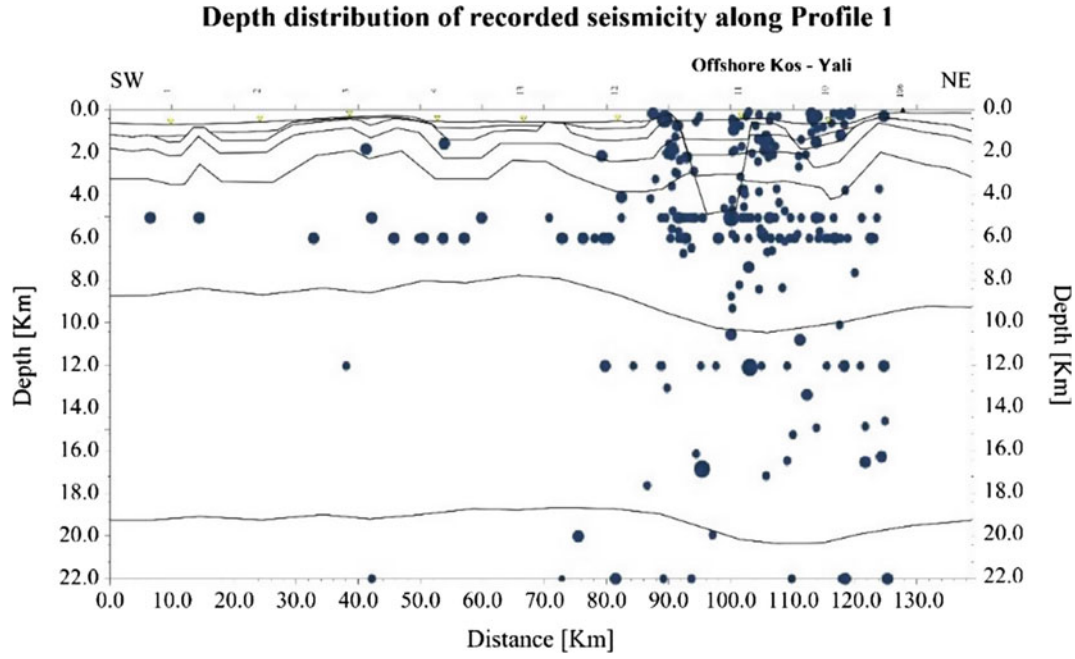

Fig. 9.9 Depth distribution of recorded seismicity along profile 1 (for location Fig. 9.5)

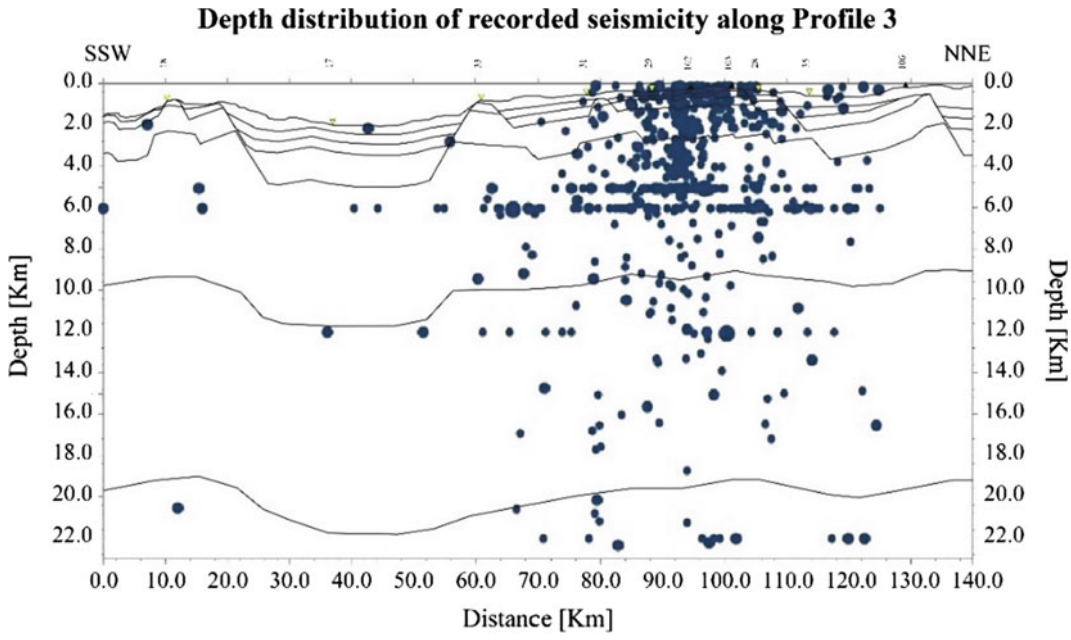

Fig. 9.10 Depth distribution of recorded seismicity along profile 3 (for location Fig. 9.5)

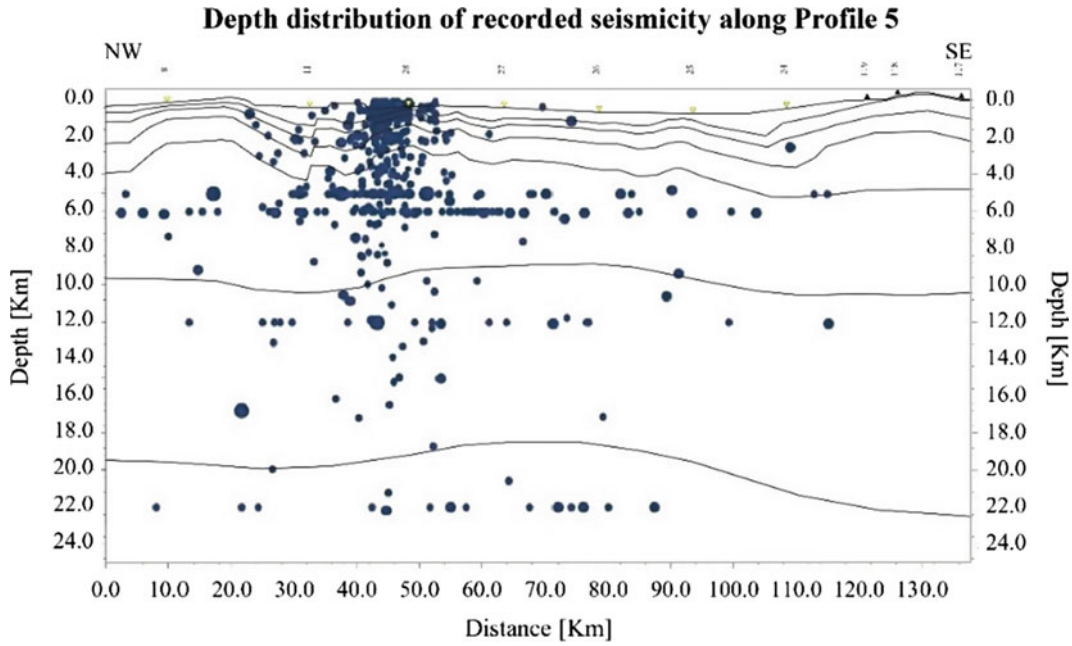

Fig. 9.11 Depth distribution of recorded seismicity along profile 5 (location Fig. 9.5)

Both the western and eastern marginal faults of the western Kos basin—that coincides with the Kos caldera—are seismically active. The seismicity at crustal levels is confined probably by the limits of the magmatic intrusions that feed the magma chambers and the faults that tectonically limit the caldera.

Profile P3 (location Fig. 9.5), is SSW-NNE oriented, from Karpathos basin to eastern Kos. Alpine sediments are more than 3.8 km thick, below the Karpathos basin that has maximum water depth of 2.5 km. Seismicity is mainly associated with the uplifted crustal block of Nisyros and the faults between Nisyros and Tilos. The Kos-Nisyros caldera lies to the north of this cross section (Fig. 9.10).

Finally, profile P5 (location in Fig. 9.5) of NW-SE orientation extends from north-west of Kos to the island of Rhodos crossing the caldera. Alpine sediments are thickening from northwest to southeast, exceeding 5 km below Rhodos. Seismic activity along the profile is mainly concentrated in the area of Yali and Nisyros islands, as previously described (Fig. 9.7). Also the west Kos basin is seismically active (Fig. 9.11).

9.4 Discussion

The local seismic array regionally restricted to the volcanic area of Nisyros mapped high seismic activity directly linked to volcanic and hydrothermal processes. The wider region and the associated tectonic processes cannot be explained from these observations alone. For this reason, we also considered the data recorded by two regional arrays, the CYCNET and EGELADOS networks in the years 2002–2007 (Bohnhoff et al. 2004, 2006, Brüstle 2012; Friedrich et al. 2014).

The graben system Gökova-Kos-Karpathos is impressively marked by crustal seismicity, showing that the Dodecanese crustal block is separated by extension from the Aegean microplate. Bohnhoff et al. (2005) based on stress inversion from focal mechanisms, describe slab pull to be the driving mechanism for the extensional processes in the south Aegean. This is also valid for the Dodecanese volcanic area. Also the focal mechanisms published by Friedrich et al. (2014) from precisely located seismic events

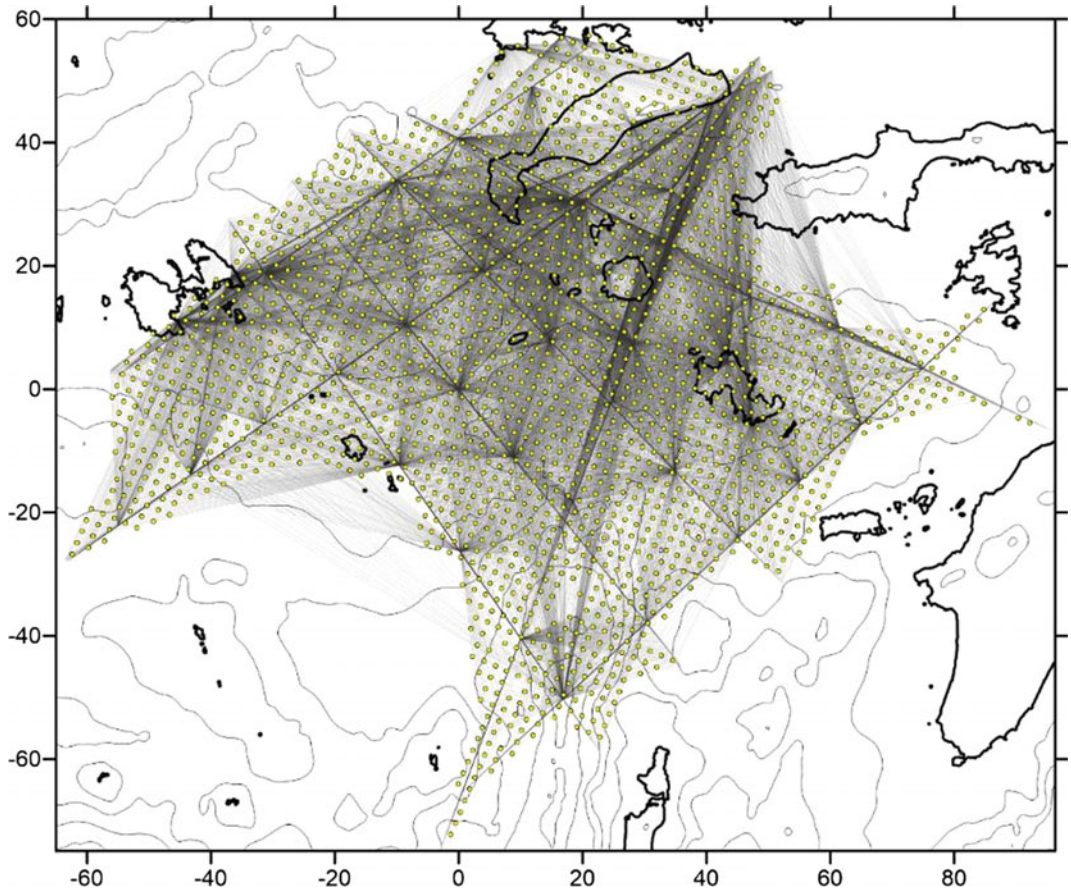

Fig. 9.12 Ray coverage of 3D tomography of the active seismic array

recorded by two regional seismic arrays show extension for the crustal seismicity recorded. They delineate the Dodecanese block that behaves like one crustal unit rotating in anti-clockwise motion out of its present position (Tür et al. 2014).

The basin systems from Gökova to Kos—east to west—and Karpathos—north to south—are the bordering extensional basins that limit the Dodecanese block to the north and west. This trend is also identified by a 3D active tomography we performed in the Dodecanese region (Figs. 9.12 and 9.13). The presented velocity of P-waves and the velocity anomalies for layers at 6, 10 and 14 km show the extensional crustal process mentioned above. The high velocities mapped below Nisyros, trending NE–SW, are due to magmatic intrusives below the volcanic area. High velocity anomalies recorded at the northern part of Kos, and also the island of Tilos, are due to basement highs (see also Makris et al. 2016).

Deep seismicity is focused only below Nisyros and the focal mechanisms of the Nisyros cluster as interpreted by Friedrich et al. (2014) are strongly influenced by magmatic processes connected to the subducted slab below Nisyros. Related focal depths are between 100 and 150 km.

Finally, if we consider the geological situation of Nisyros and the islands around it, the seismicity and magnitude of events recorded so far (e.g. Papazachos and Papazachou 1997;

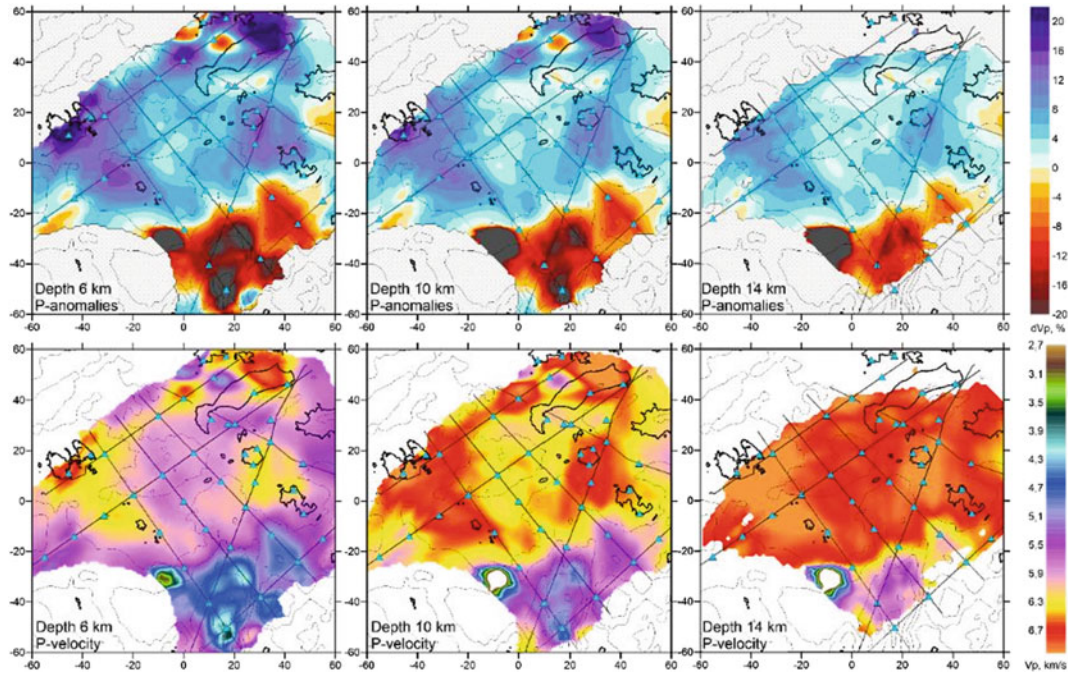

Fig. 9.13 P-wave distribution and anomalies at different depth layers obtained from 3D active seismic tomography

Brüstle 2012; Friedrich et al. 2014) and the volcanic eruptions (e.g. Marini et al. 1993; Nomikou 2004), it is the volcanism that poses the main source of hazard.

References

Allen SR (2001) Reconstruction of a major caldera-forming eruption from pyroclastic deposit characteristics: Kos Plateau Tuff eastern Aegean sea. J Volcanol Geotherm Res 105:141–162

Allen SR, Cas RAF (2001) Transport of pyroclastic flows across the sea during the explosive, rhyolitic eruption of the Kos Plateau Tuff, Greece. Bull Volcanol 62:441–456

Allen SR, Stadlbauer E, Keller J (1999) Stratigraphy of the kos plateau tuff: product of a major quaternary explosive rhyolitic eruption in the eastern Aegean sea. Int J Earth Sci 88:132–156

Bohnhoff M, Rische M, Meier T, Endrun B, Becker D, Stavrakakis G, Harjes H-P (2004) CYC-NET: a temporary seismic network on the Cyclades (Aegean Sea, Greece). Seism Res Lett 75(3):352–359

Bohnhoff M, Harjes HP, Meier T (2005) Deformation and stress regimes at the Hellenic subduction zone from focal mechanisms. J Seismolog 9(3):341–366

Bohnhoff M, Rische M, Meier T, Becker D, Stavrakakis G, Harjes H-P (2006) Microseismic activity in the Hellenic Volcanic Arc, Greece, with emphasis on the seismotectonic setting of the Santorini-Amorgos zone. Tectonophysics 423:17–33

Brüstle A (2012) Seismicity of the eastern Hellenic Subduction Zone. Ph.D. thesis. Ruhr University, Bochum, p 151

Crosson R (1972) Small earthquakes, structure and tectonics of the Puget sound region. Bull Seismol Soc Am 62:1133–1171

Davis EN (1967) Zur Geologie und Petrologie des Inseln Nisyros und Jali (Dodecanese). Prakt Akad Athens 42:235–252

Friedrich W, Brüstle A, Küperkoch L, Lamara S, Egelados Working Group (2014) Focal mechanisms in the southern Aegean from temporary seismic networks—implications for the regional stress field and ongoing deformation processes. Solid Earth 5:275–297

Galanopoulos A (1960) A catalogue of shocks with Io > VI for the years 1801–1958. Publ Nat Obs Athens Seismol Inst 119

Jackson J (1994) Active tectonics of the Aegean region. Ann Rev Earth Planet Sci 22:239–271

Jackson J, McKenzie D (1988) Rates of active deformation in Aegean sea and surrounding regions. Basin Res 1:121–128

Keller J, Rehren TH, Stadlbauer E (1990) Explosive volcanism in the Hellenic arc. A summary and review.

In: Proceedings of the third scientific congress Thera and the Aegean World III, Earth Sci 2:13–26

Klein F (1989) User's Guide to HYPOINVERSE, a program for VAX computers to solve for earthquake locations and magnitudes, U.S. Geol. Surv. Open-File Rep, 89–314

LePichon X, Angelier J (1979) The Hellenic arc and trench system: a key to the neotectonic evoloution of the eastern Mediterranean area. Tectonophysics 60:1–42

Makris J, Moeller A (1990) An ocean bottom seismograph for general use. Technical requirements and applications. In: Hoefeld, J, Mitzlaff A, Polomsky S (eds) Proceedings of symposium "Europe and the sea". Hamburg

Makris J, Papoulia J, Groumpa M, Fasoulaka C (2016) Crustal thickness and physical properties of the Dodecanese area, south eastern Aegean volcanic arc (this volume)

Makropoulos C, Burton P-W (1981) A catalogue of the seismicity in Greece and adjacent areas. Geophys J R Astr Soc 65:741–762

Marini L, Principe C, Chiodini G, Cioni R, Fytikas M, Marinelli G (1993) Hydrothermal eruptions of Nisyros (Dodecanese, Greece). Past events and present hazard. J Volcanol Geotherm Res 56:71–95

McKenzie D (1972) Active tectonics in the Mediterranean region. Geophys J Roy Astron Soc 30:109–185

Nomikou P (2004) Geodynamic of Dodecanese islands: Kos and Nisyros volcanic field. Ph.D. thesis. Department of Geology, University of Athens, p 469

Nomikou P, Papanikolaou D (2000) Active geodynamics at Nisyros, the eastern edge of the Aegean volcanic arc: emphasis on the submarine survey. In: Proceedings of the 3rd international conference on the geology of the eastern mediterranean, pp 97–103

Papanikolaou D (1993) Geotectonic evolution of the Aegean. Bull Geol Soc Greece 27:33–48

Papanikolaou D, Nomikou P (2001a) Tectonic structure and volcanic centres at the eastern edge of the Aegean volcanic arc around Nisyros Island. Bull Geol Soc Greece 34(1):289–296

Papanikolaou D, Nomikou P (2001b) Tectonic structure and volcanic centres at the eastern edge of the Aegean volcanic arc around Nisyros Island. In: Proceedings of the 9th international congress, Athens, Sept 2001, Bull Geol Soc Greece XXXIV:1289–1296

Papazachos B, Papazachou C (1997) Earthquakes in Greece. Editions Ziti, Thessaloniki

Smith PE, York D, Chen Y, Evensen N-M (1996) Single crystal ^{40}Ar–^{39}Ar dating of a late quaternary paroxysm on Kos, Greece: concordance of terrestrial and marine ages. Geophys Res Lett 23:3047–3050

Tür H, Yaltirak C, Elitez I, Sarikavak K-T (2014) Pliocene-quaternary tectonic evolution of the Gulf of Gökova, southwest Turkey. Tectonophysics 638:158–176

Varnavas SP, Cronan D-S (1991) Hydrothermal metallogenic processes off the islands of Nisyros and Kos in the Hellenic Volcanic Arc. Mar Geol 99:109–133

Varnavas SP, Panagiotaras D, Megalovasilis P-S (1998) Chemical characteristics of a submarine hydrothermal system offshore Kos Island, on the Hellenic Volcanic Arc. Rapp Comm Int Mer Medit 35:104–105

10 Reviewing and Updating (1996–2012) Ground Deformation in Nisyros Volcano (Greece) Determined by GPS and SAR Interferometric Techniques (1996–2012)

Evangelos Lagios, Vassilis Sakkas, Fabrizio Novali, Alessandro Ferreti, B.N. Damiata and Volker Jörg Dietrich

Abstract

The southeastern part of the South Aegean Volcanic Arc (SAVA), including Kos, Yali and Nisyros islands, is geodynamically very active. Intense seismic activity occurred on Nisyros Island during 1996–1998, accompanied with strong ground deformation and temperature increase of the fumaroles. Ground-deformation studies based on GPS and differential Interferometry for the period 1996–2000 revealed an "opening" of the island along the main faulting zones together with intense uplift of up to 90 mm that gradually reduced the following two years (2000–2002). Two Mogi point sources related to magmatic chambers fitted the observed ground deformation that was deduced from differential GPS and conventional Interferometry. One source is located onshore at about the centre of Nisyros, and the other is offshore at about 5 km to the north of Nisyros and 2 km to the southeast of Yali. Additional geophysical and geotectonic data support the existence and the location of these two magma chambers. Remeasurement of the Nisyros-Yali GPS network in 2012, combined with the analysis of SqueeSAR™ Interferometric data from ENVISAT ascending and descending imageries (2003–2010), provided the spatial and temporal ground-deformation pattern *after* the period of the seismic crisis. The GPS results indicated intense subsidence (5–10 mm/year) in the northern and central parts of Nisyros that caused the western and eastern flanks of the island to "collapse" towards its centre, as is evident from the horizontal component of the GPS vectors.

E. Lagios (✉) · V. Sakkas
Department of Geophysics & Geothermics, National and Kapodistrian University of Athens, Panepistimiopolis, 157 84 Athens, Greece
e-mail: lagios@geol.uoa.gr

F. Novali · A. Ferreti
TRE ALTAMIRA S.L., Ripa di Porta Ticinese, 79, 20143 Milan, Italy

B.N. Damiata
Cotsen Institute of Archaeology, University of California, Los Angeles, CA 90095-1510, USA

V.J. Dietrich
Institute of Geochemistry and Petrology, Swiss Federal Institute of Technology, ETH Zurich, ETH-Zentrum, CH 8092 Zürich, Switzerland

V.J. Dietrich and E. Lagios (eds.), *Nisyros Volcano*, Active Volcanoes of the World,
DOI 10.1007/978-3-319-55460-0_10

The observed line of sight (LOS) velocity field of the SqueeSAR™ analysis revealed a nearly linear type of ground deformation for that period, exhibiting values ranging between −3 and +3 mm/year with small standard deviations (<0.8 mm/year). The SqueeSAR™ results have generally shown a similar deformational pattern as the GPS one; subsidence is observed along the northern and central parts of Nisyros, while when comparing ascending and descending LOS components of ground velocities, an eastward horizontal component is inferred for the southeastern part of Nisyros. Motions along the main faulting zones that crosscut the island are also clearly identified. Both analyses have shown that the ground deformation on Yali may be associated with a more regional subsidence that takes place to the south and offshore of the islet, as is clearly indicated from the horizontal component of the GPS vectors. The overall pattern of subsidence in the broader area of Nisyros and Yali after 2000 is consistent with the two modelled Mogi sources, and indicates that the pressure inside the two associated magma chambers and the hydrothermal system has likely decreased.

10.1 Introduction

The eastern part of the South Aegean Volcanic Arc, including the islands of Kos, Yali and Nisyros (Fig. 10.1), comprises the largest volumes of volcanic materials. Approximately 160,000 years ago, ignimbrites were emplaced in the region of the NE-striking "Kos Horst-Graben System" in the largest eruption in the Eastern Mediterranean, emitting more than 100 km^3 of pyroclastic material. As a result, a present-day submarine caldera with a diameter of 15–20 km was formed, which is now covered up to several kilometres with volcano-sedimentary materials from younger eruptions. Since 140,000 years ago the volcanic edifices of Nisyros, Yali and Strongyli have grown on the central part and rim of this caldera (Papanikolaou et al. 1991; Vougioukalakis 1993; Longchamp et al. 2011).

Nisyros Island lies above a basement of Mesozoic limestone (Geotermica Italiana 1983, 1984). The exposed rocks are Quaternary volcanics. The evolution of Nisyros Volcano during the past 160,000 years, together with the succession of calc-alkaline lavas and pyroclastic rocks, has been studied in detail by various authors (Di Paola 1974; Keller et al. 1990; Papanikolaou et al. 1991; Limburg and Varekamp 1991; Vougioukalakis 1993; Hardimann 1999; Tibaldi et al. 2008).

Major fault systems have been identified within the volcanic edifices of the Kos-Yali-Nisyros Volcanic Field (Fig. 10.2) on the basis of recent structural and geological investigations (Papanikolaou et al. 1991; Vougioukalakis 1993; Stiros 2000; Papanikolaou and Nomikou 2001a, b; Nomikou and Papanikolaou 2011). The caldera's rim and its accompanying cone-shaped local faults are entirely volcanic structures, which are a result of the collapsing of the caldera after the last Plinian eruptions.

Although the last magmatic activity on Nisyros dates back to at least 15,000 years, volcanic unrest as expressed by seismic activity continuous at present. Such activity has been reported since historical times and is partially a result of the hydrothermal activity at crustal levels less than 1500 m (Lagios 1991; Dawes and Lagios 1991; Lagios and Apostolopoulos 1995; Mendrinos et al. 2010). Its surface expressions are fumaroles and hydrothermal explosion craters within the caldera, as well as several thermal springs that occur around the island. During the latest hydrothermal explosion in 1873, fire and

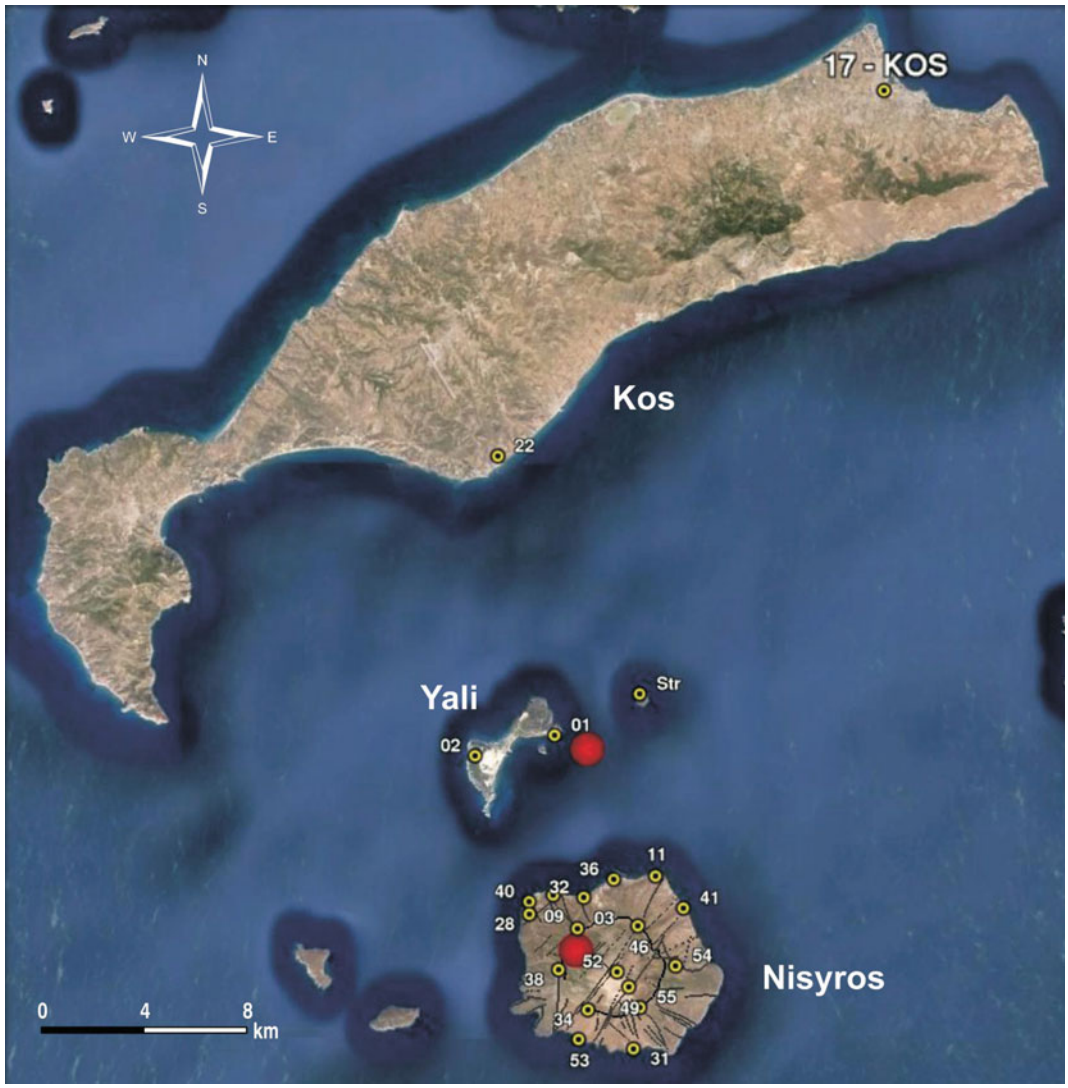

Fig. 10.1 Distribution of stations of the GPS network of the Kos-Yali-Nisyros Volcanic Field. *Solid red circles* represent the two modelled Mogi point sources. *Str* stands for the station established on Strongyli Islet

gas emanations were reported along the coast near Mandraki (Gorceix 1873a, b, c). Two distinct hydrothermal aquifers may be present underneath the caldera based on: (i) geophysical data (Dawes and Lagios 1991); (ii) temperature distribution, fluid geochemistry, and physical chemical characteristics of the fumarolic gases and the thermal waters at the surface; and (iii) results from the deep geothermal drill holes (Geotermica Italiana 1983, 1984). The deeper hydrothermal aquifer is characterized by high temperatures above 300 °C and fluids of high salinity, whereas the shallow aquifer has temperatures around 100 °C and boiling fluids with high concentrations of CH_4, CO_2, H_2 and H_2S gases (Chiodini et al. 1993; Marini et al. 1993; Kavouridis et al. 1999; Chiodini et al. 2002; Nomikou et al. 2013a, b).

Earthquakes have been described throughout historical times as has been reported in detail since 1830 (Gorceix 1873a, b, c; Papazachos and Papazachou 1989; Stiros and Vougioukalakis

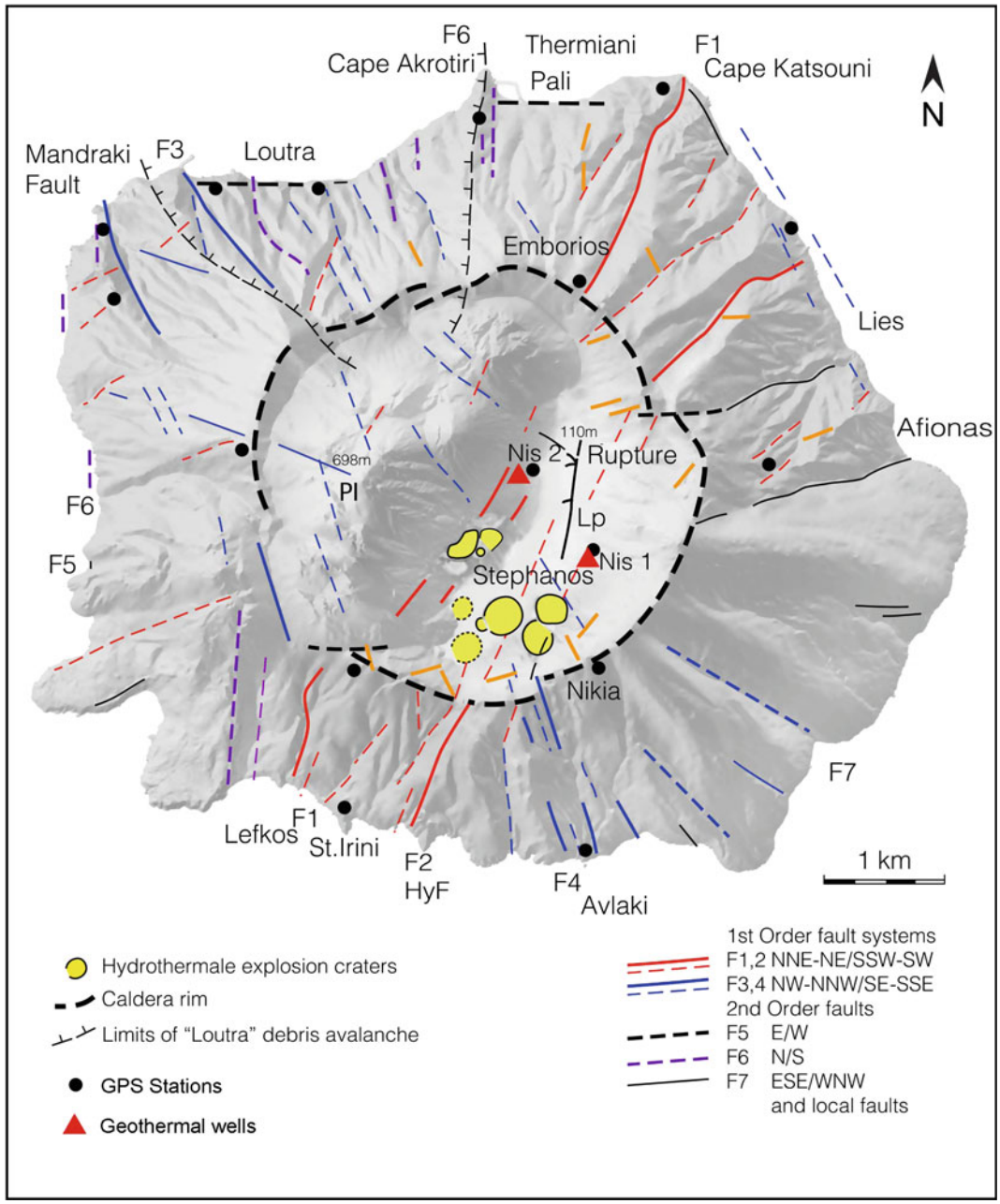

Fig. 10.2 Fault pattern of major faulting systems (F1–F7), location of hydrothermal explosion craters and other significant features superimposed on a digital elevation model of Nisyros Island. Abbreviations of locations; *PI* Prophitis Ilias, *Lp* Lakki plain

1996). Their origin may be a result of regional tectonic processes, magma ascent, degassing phenomena of deep crustal magma and steam explosions within the hydrothermal system. Detailed accounts of the most recent seismic crisis—which started in the beginning of 1996, culminated in 1997, continued through 1998, and returned to the background level at the beginning

of 1999 are given by Papadopoulos et al. (1998), Makris and Chonia (1999) and Sachpazi et al. (2002). The Mandraki Fault (Fig. 10.2) that comprises a branch of the F3 fault system was reactivated in 1996 (Lagios et al. 2005) and caused damage to buildings and other structures within Mandraki (Ioannidis 1998). Tectonic processes expressed by the latest seismicity indicate tensional fracturing (Makris and Chonia 1999) which could reduce the lithostatic pressure and trigger explosive volcanic phenomena, such as those reported in 1871 and 1873 by Gorceix (1873a, 1874).

Efforts for studying the ground deformation on Nisyros started after the outbreak of the seismic activity in 1996 and have involved GPS observations and SAR interferometric analysis (e.g. Lagios et al. 2005; Sachpazi et al. 2002; Sykioti et al. 2003). The present study reviews the ground deformation on Nisyros up to 2002, and subsequently addresses its evolution during the next decade (≈2002–2012) on the basis of combined GPS and advanced SAR interferometric techniques.

10.2 The GPS Measurements

10.2.1 Period 1997–2002

A geodetic GPS network (Fig. 10.1) was established in the broader area of Nisyros in June 1997 in order to study ground deformation. It initially consisted of 21 stations and included a local reference station (17-Kos) at the north-eastern part of Kos Island (Lagios et al. 1998). Another station (benchmark) was installed on Strongyli Islet in 2013. Measurements for all campaigns were made in the static mode using tripods centered above the permanently installed benchmark at a given station.

Geodetic, dual frequency WILD receivers (SR299, SR399, SR9500, AX1202) were employed for all measurements. A local base station (No. 09) that was established in Mandraki was continuously operated for the entirety of a given campaign. Other receivers were used as rovers and recorded for 24–48 h at a given station with a sampling interval of 15 s. Most of the stations were occupied more than once during a campaign. Post-processing was performed using the Bernese GPS Software, versions 4.2 and 5.2 for earlier and later campaigns, respectively (Dach et al. 2007), together with post-computed satellite orbits (available through the International GPS Service) to improve the error estimation. Accuracies of 2–5 and 4–8 mm were achieved for the horizontal and vertical components, respectively.

The GPS network was reoccupied in: September 1997, May and October 1998, June 1999, July 2000, June 2001, July 2002 and August 2012. The results up to 2002, relative to Station 17-Kos, are presented in detail by Lagios et al. (2005). It was found that the amplitude of the horizontal deformation ranged from 20 to 60 mm. The maximum horizontal displacement occurred between 1997 and 1998 during the peaking (1997) and subsequent high level (1998) of seismic activity. For the periods 1998–1999 and 1999–2000, the amplitude decreased to 10–20 mm, and to approximately 10 mm, respectively. However, the deformation increased again to approximately 15 mm at some stations for the subsequent period (2000–2001). Then, Nisyros entered a different mode of deformation with a clear westward increase of the horizontal component in almost all of its western part for the period 2001–2002.

Vertical deformation in the sense of a general uplift of the whole island occurred over almost the entire active period of observation up to 2002, and in particular the majority of stations exhibited uplifts of 40–60 mm between 1997 and 1998. Greater values of uplift were measured at stations installed on the western uplifted side of the activated Mandraki Fault (Fig. 10.2). In subsequent periods, general uplift continued by only 8 mm (1998–1999), followed by a deflation of 15 mm (1999–2000) and further uplift of about 10 mm (2000–2001). For the period 2001–2002, an uplift of about 10 mm occurred in the western, central and northern parts of the island, while the eastern area subsided by about 10 mm.

10.2.2 Period 2002–2012

The GPS network on Nisyros was remeasured in August 2012, which was more than a decade after its establishment. Through this decade (2002–2012), there was no significant seismic activity in the broader area, nor was there any other type of volcanic activity as would be detected via temperature increase in the fumaroles. It may thus be assumed that the ground deformation that occurred in the island was of an almost linear character without any strong fluctuations. The lack of fluctuations is also supported by the Squee-SAR™ analysis that will be presented in the next section. The results for this last remeasured period (2002–2012) are also relative to Station 17-Kos in order to have a common reference point with the previous remeasured periods.

As can be seen on the velocity map (Fig. 10.3), the most prominent aspect of ground deformation is the subsidence that took place in Nisyros and Yali during this ten-year period. The

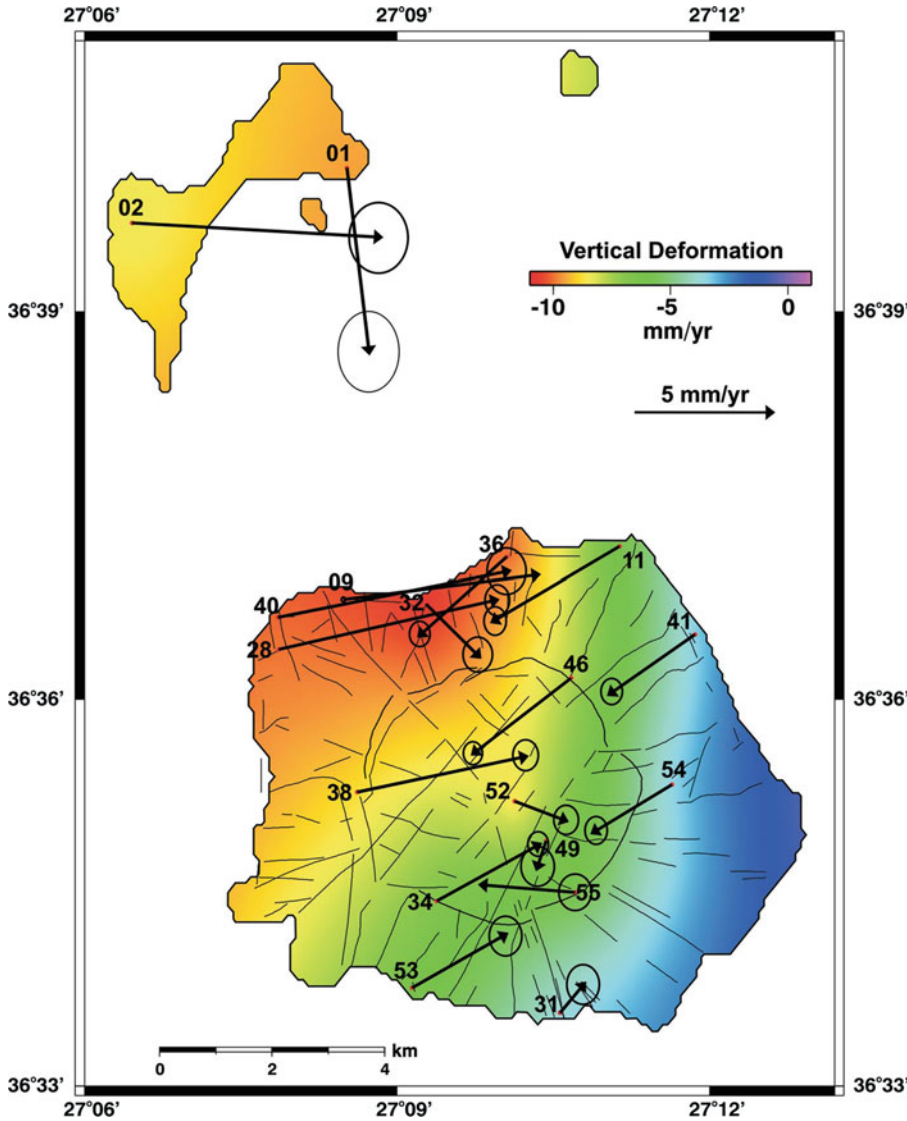

Fig. 10.3 Horizontal and vertical deformation on Yali-Nisyros relative to northeastern Kos for the period 2002–2012

subsidence reached values of up to 10 mm/year in the northern part of Nisyros, but with smaller values (~3–5 mm/year) in the southern and eastern parts. The horizontal velocity vectors of the stations located on the NE had motion to the SW, while the stations on the NW exhibited motion to the ENE. The amplitudes of the horizontal velocity vectors are slightly higher for the stations at the northwestern part (~8.5 mm/year) as compared to the northeastern part (~5 mm/year). The two GPS stations located in Lakki Plain also subsided. Generally, it should be noticed that the stations located outside the caldera's rim had exhibited stronger deformation as compared to those located inside the rim for both horizontal and vertical components. An exception is Station 31 at the southern part of Nisyros (Avlaki), where both its horizontal and vertical components had low values (~2 mm/year). The nearly opposite direction of horizontal motion that is observed for the stations located at the eastern and western parts of Nisyros may be due to the strong subsidence which had taken place at its northern and central parts during this ten-year period, thus forcing the facing eastern and western flanks of the island to 'collapse' towards its centre which produced the observed westward and eastward horizontal motions, respectively.

Significant subsidence (~8 mm/year) had also occurred in Yali islet. The horizontal velocity components of the two stations, located on the extreme eastern and western parts, have similar amplitudes (~8 mm/year) and clearly point off-shore to the west and south respectively. It is concluded that strong subsidence likely occurred in the region between Yali and Nisyros which caused the two edges of the islet to converge toward this area, consistent with the deformational pattern observed at those two stations.

10.3 The SAR Interferometry

Conventional Synthetic Aperture Radar (SAR) Interferometry (InSAR) and GPS measurements are the most widely used techniques to measure the ground deformation in volcanoes. However, techniques like tiltmeters and GPS provide only point coverage, since they are detecting changes at single locations (stations) on the ground surface. Space-borne-radar interferometry has already demonstrated the ability to map ground deformation of volcanoes on a large spatial scale by using short-term data sampling rates (e.g. Amelung et al. 2000; Lagios et al. 2005) and the phase difference between two SAR acquisitions to obtain the interferograms (Hanssen 2001). However, this processing technique has drawbacks relating to atmospheric noise that cannot be efficiently eliminated which can result in unreliable representation of the ground deformation. This deficiency has been overcomed by considering phase changes in a series of SAR images that are obtained at different times over the same region. A series of interferograms with respect to a "master" image can then be produced in which small parts of the study area (pixels) that exhibit coherent phase behaviour may be identified, the so-called permanent scatterers (PS), thus introducing the PSInSAR™ technique (Ferretti et al. 1999, 2000, 2001). This technique has been effectively applied to areas of active tectonism and volcanism (e.g. Peltier et al. 2010; Bonforte et al. 2011; Lagios et al. 2012). Subsequently, PSInSAR™ has been advanced and replaced by the SqueeSAR™ algorithm (Ferretti et al. 2011).

The SqueeSAR™ is a second generation of the PSInSAR™ technique, in which targets from a SAR image include not only identified consistent permanent scatterers (PS), but also homogeneous spatially distributed scatterers (DS). It is noted that the PS usually correspond to man-made objects (e.g. buildings, linear structures, and open outcrops), whereas the DS are typically identified by homogeneous ground surfaces and scattered outcrops, or by uncultivated, desert or debris-covered regions. All identified PS and DS are then jointly processed applying the PSInSAR^{TM} algorithm by taking into account their different statistical behaviour. Because of the high density of identified measurement points (scatterers), and their wider spatial coverage, millimetre accuracy on ground displacement can be achieved, together with

reduced standard deviations, as compared to the previous PSInSAR™ algorithm (Ferretti et al. 2001). Therefore, an increased number of scatterers on the ground results at an increased confidence of the ground motion by identifying and "squeezing" all possible ground-target information relating to acceptable coherent levels for estimated optimum phase values for the SAR interferometric analysis (Ferretti et al. 2011). This technique was successfully applied to a recent study of the Santorini Volcano (Lagios et al. 2013).

10.3.1 Application of SqueeSAR™ Technique

A total of 26 ascending and 22 descending ASAR scenes that were acquired by ENVISAT satellites were processed covering the period

Table 10.1 ENVISAT orbit scenes

ENVISAT ascending orbit scenes				ENVISAT descending orbit scenes			
Track 286				Track 107			
Id	Date	Bn (km)[a]	Bt (days)	Id	Date	Bn (km)[a]	Bt (days)
1	09/03/2003	−0.41	−1715	1	25/02/2003	−0.91	−910
2	22/06/2003	−0.83	−1610	2	02/12/2003	−0.39	−630
3	27/07/2003	−0.58	−1575	3	06/01/2004	0.09	−595
4	31/08/2003	−0.46	−1540	4	10/02/2004	−0.43	−560
5	14/12/2003	0.48	−1435	5	16/03/2004	0.28	−525
6	28/03/2004	−0.52	−1330	6	25/05/2004	0.01	−455
7	02/05/2004	−0.12	−1295	7	03/08/2004	−0.26	−385
8	11/07/2004	−0.17	−1225	8	12/10/2004	−0.04	−315
9	02/01/2005	0.42	−1050	9	21/12/2004	−0.46	−245
10	22/05/2005	−0.28	−910	10	25/01/2005	−0.49	−210
11	31/07/2005	−0.01	−840	11	10/05/2005	0.2	−105
12	02/04/2006	−0.22	−595	12	19/07/2005	0.26	−35
13	29/10/2006	−0.1	−385	(M) 13	23/08/2005	0	0
14	11/02/2007	−0.42	−280	14	01/11/2005	0.1	70
15	09/09/2007	0.14	−70	15	14/02/2006	−0.7	175
(M) 16	18/11/2007	0	0	16	26/12/2006	0.04	490
17	06/04/2008	0.08	140	17	30/01/2007	−0.82	525
18	15/06/2008	−0.31	210	18	06/03/2007	−0.03	560
19	20/07/2008	−0.26	245	19	21/10/2008	−0.18	1155
20	02/11/2008	0.11	350	20	01/09/2009	−0.15	1470
21	11/01/2009	−0.06	420	21	06/10/2009	−0.55	1505
22	31/05/2009	−0.36	560	22	23/02/2010	−0.7	1645
23	09/08/2009	−0.02	630				
24	13/09/2009	0.06	665				
25	11/04/2010	0.11	875				
26	20/06/2010	−0.03	945				

[a]Critical normal baseline fraction (M) master image

February 2003–June 2010 (Table 10.1). More than 3400 and 2200 PS/DS in ascending (Line of Sight—LOS angle 24.62°) and descending (LOS angle 24.24°) geometries, respectively, were identified within an area of about 50 km^2. The reference point for the interferometric analysis is located at the southern part of the island, near a station of the local GPS network that has been remeasured since 2001. The small LOS angles on both acquisitions imply that the velocity vector has a strong vertical component (up to 90%) compared to the horizontal one.

The same ASAR scenes were used to produce the LOS velocity map for Yali. Significantly fewer number of PS/DS points were determined (∼500) that were referred to a point located at the southwestern part of the islet.

10.3.2 The Velocity Field

Figure 10.4 shows the SqueeSAR™ products of the LOS velocity field (in mm/yr.) for both acquisition geometries. It is obvious that the velocity field for the ascending image (Fig. 10.4a) has a significantly higher number of identified points as compared to the descending one (Fig. 10.4b), because of the greater number of scenes, as well as the type of topography which refers to the orientation of the slopes with respect to the geometry of acquisition (Hanssen 2001). Small LOS velocities ranging from −3 to +3 mm/year are observed on both images.

The greater negative LOS velocities (∼2.5 mm/year) are observed along the F3 faulting system, together with the area between F1

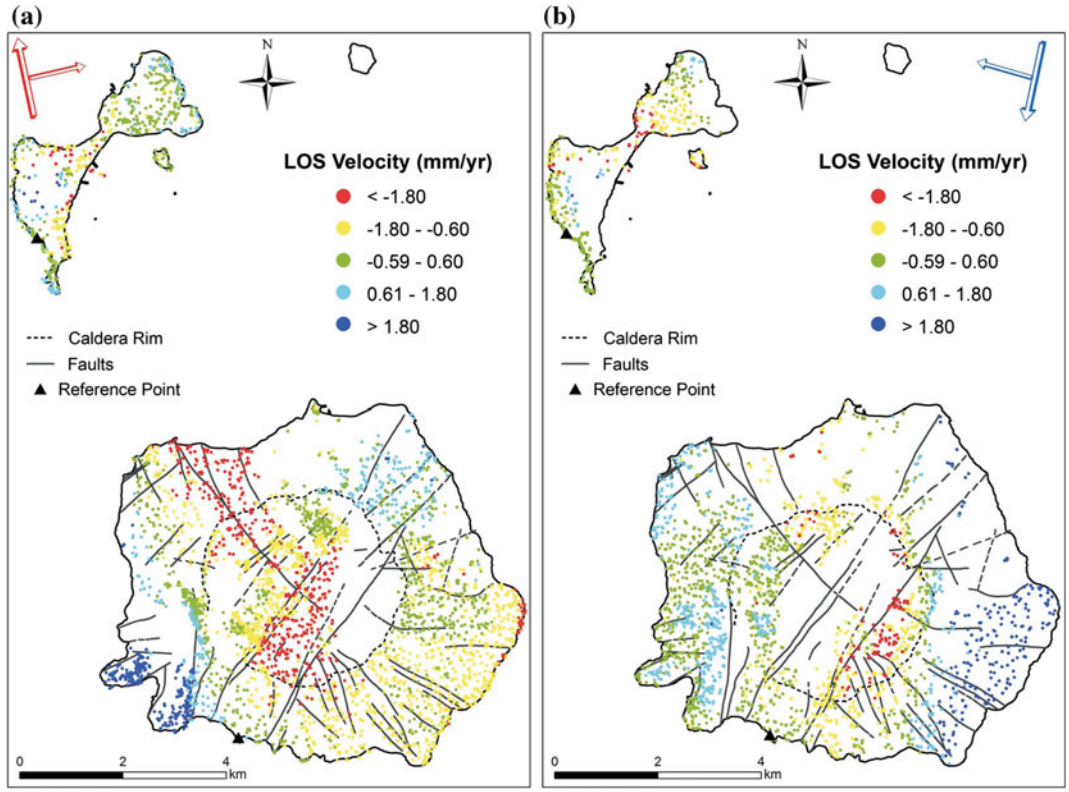

Fig. 10.4 LOS velocity field deduced from the SqueeSAR™ for **a** ascending, and **b** descending orbital geometries, for the period 2003–2010. *Red* and *blue arrows* indicate the orbit and acquisition directions for the ascending and the descending data sets, respectively

and F2 faulting zones inside the caldera, as can been in the ascending image. However, such values are not observed in the descending image for the same area, as there are not many identified PS/DS, except along the westerly facing flanks of the caldera. The area along the western part of Nisyros and to the west of the caldera's rim yielded similar velocities for both images, ranging between relatively stable to slightly positive values ($\sim$1.5 mm/year). The greatest LOS velocities (1.8–3.0 mm/year) in this area are observed on the ascending image in the vicinity of the two small peninsulas at the extreme southwestern part. This region is bounded by the segments of the F1 and F6 faulting systems (Fig. 10.2).

Considering the southeastern part of Nisyros and east of the caldera's rim small negative LOS velocities (about −1.5 mm/year) are observed in the ascending image, while positive values (up to 2 mm/year) are observed in the descending one. This difference indicates that an eastward component of ground deformation took place in this area during the observational period 2003–2010, without being able to verify this issue due to the lack of GPS stations in this particular part of the island. Another interesting observation concerns the area at the northeastern part of Nisyros, which is flanked by segments of the F1 and F2 fault systems. This part had positive LOS velocities on both images (0.6–1.8 mm/year). The limited number of identified PS/DS points at the northern part of the island, which is covered by dense vegetation, yielded an inconsistent pattern of ground deformation.

The deformation of the Yali islet does not exhibit a consistent pattern when comparing both acquisition geometries, except in the northeastern part, which is characterized by relatively stable to small negative LOS velocities. An overall differential motion had occurred between the northeastern and the southwestern parts of the island (in both geometries), but it is still not clearly depicted and may be attributed to differing geological characteristics of the two parts: obsidian is present in the northeast while pumices occur in the southwest.

10.3.3 The Standard Deviation

Two parameters generally affect the calculation of the standard deviation. Firstly, the distance of each PS/DS point from the reference point is considered. In fact, the displacement model is estimated based on the phase difference between the point under analysis and the reference point, in order to mitigate the effect of the atmospheric noise, which is strongly spatially correlated. However, moving away from the reference point, the difference between its atmospheric contribution and the atmospheric contribution of the PS/DS point under analysis tends to increase producing a larger residual after the estimation of the linear model. The latter is represented by the standard deviation of the corresponding estimated average velocity. Therefore, the standard deviation of velocity increases moving away from the reference point. Secondly, the standard deviation of motion from the linear model is considered. Since the standard deviation is associated with the average rate of deformation, a high value will result if a PS/DS point exhibits a strong non-linear motion because of the associated high residual with respect to the linear model. This, therefore, allows identifying areas being affected by motion-dynamics that are more complex than the linear-model assumption, and in any case it shows a clear deviation from a linear ground deformation.

The standard deviation of the velocity field was computed for both the ascending and the descending images (Fig. 10.5). They present generally small values ($\sim$0.5 mm/year); however, the standard deviation of velocity for the descending data (Fig. 10.5b) has slightly higher values than the ascending data (Fig. 10.5a). The smallest values occur near the reference point as expected, and at the northeastern part (Fig. 10.5a). Low moderate values of standard deviation ($\sim$0.4 mm/year) are observed for the rest of both islands (Nisyros and Yali). These overall low values suggest an almost linear type of ground deformation throughout the observational period.

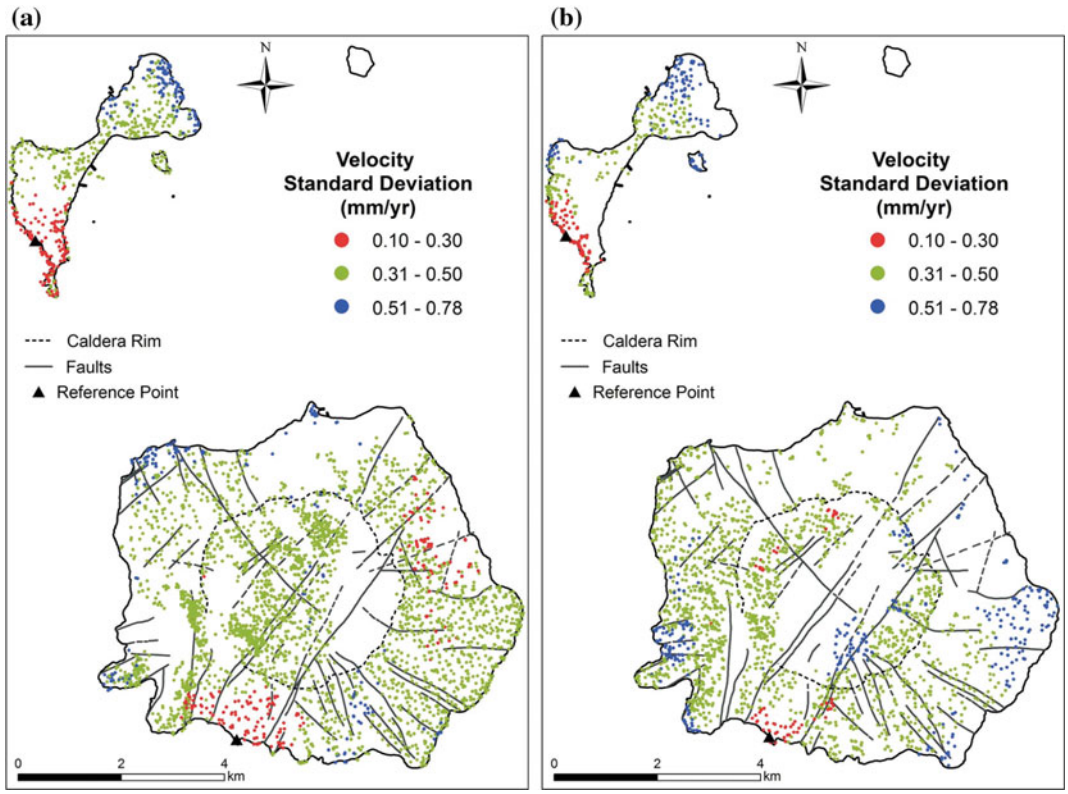

Fig. 10.5 Standard deviation of the LOS velocity field deduced from the SqueeSAR™ for **a** ascending, and **b** descending orbital geometries

10.4 Discussion

The seismicity outbreak in Nisyros in early 1996 mobilized the scientific community to conduct studies of the island and the broader area. The multi-disciplinary EU project GEOWARN (IST 1999—12310; www.geowarn.ethz.ch) constituted the bulk of the research activities. A very detailed digital elevation model (2 m × 2 m) was produced, and a high-resolution IKONOS image was ortho-rectified (Ganas et al. 2002; Vassilopoulou and Lagios 2002; Vassilopoulou et al. 2002) and was used as a background for map projection of all thematic layers (e.g. geology, tectonics, building environment). Thermal satellite images were also used to study the thermal state of the volcano (Lagios et al. 2007; Ganas and Lagios 2003; Ganas et al. 2002, 2010; Zouzias et al. 2011). The monitoring of the ground deformation was one of the major tasks for the study and evolution of the volcanic crisis. It was measured by using repeated GPS observations on the installed network in the Kos-Yali-Nisyros Volcanic Field, and by applying conventional and advanced SAR interferometric techniques.

The ground deformation during the unrest period and up to 2002 was marked by intense non-linear uplift (up to 140 mm along the activated Mandraki Fault) in 1998, which was subsequently reversed to a gradual subsidence after 1999–2000. The former was determined on the basis of both GPS and SAR Interferometry (Lagios 2000; Parcharidis and Lagios 2001; Lagios et al. 2001, 2005; Sachpazi et al. 2002; Sykioti et al. 2003). Interferometric processing of ERS data covering the period 1995–1997 by Derdelakos et al. (2013) showed a total ground deformation ranging from −50 to +50 mm, with

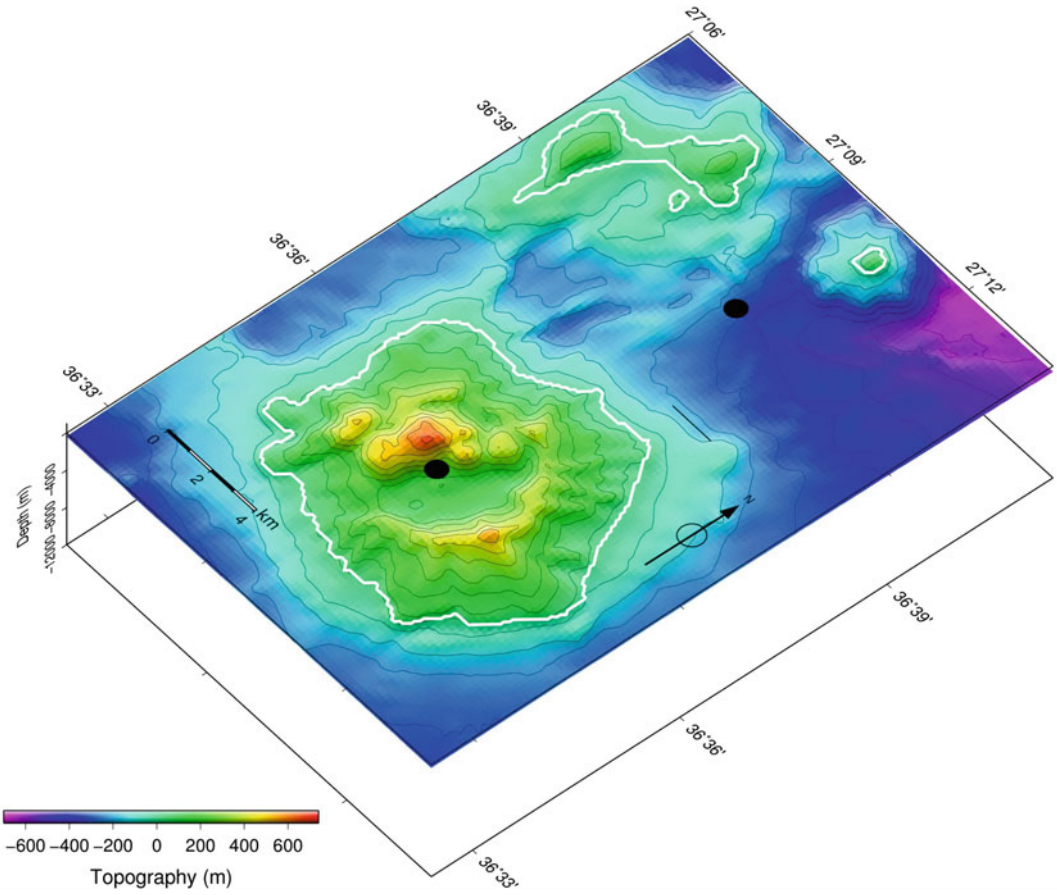

Fig. 10.6 Broader area of Nisyros-Yali volcanic field indicating the location of the two Mogi sources (*black circles*)

the maximum uplift taking place in the caldera. However, these results should be underestimated, because the reference point used in this processing procedure was located approximately 1.5 km SE of Mandraki, at an area that was subjected to a strong uplift, as has been revealed by the GPS data (Lagios et al. 2005).

Based on Differential SAR Interferometry, the observed ground deformation on Nisyros was modelled by Sykioti et al. (2003) as a Mogi point source (Mogi 1958) located at 5(±0.5) km depth beneath the northwestern edge of the island. However, a later study based on combined Differential GPS and SAR Interferometry (Lagios et al. 2005) modelled the observed deformation in the broader area of Nisyros in terms of two Mogi point sources, one onshore and another offshore of Nisyros (Fig. 10.6).

The onshore source is located at the northwestern part of Nisyros Caldera and at a depth of 5.5(±0.5) km. The location of this source coincides with (i) a deeper conductive body (6–9 km) deduced by earlier geophysical (magnetotelluric) measurements that was interpreted as a magma chamber (Dawes and Lagios 1991), and (ii) the junction of the two major faulting zones F1 and F3 at about the centre of the island (Fig. 10.2). It appears that the slightly different location of the two identified onshore Mogi sources is attributed to the different interferometric periods 1995–1997 (Sykioti et al. 2003) and 1996–1999 (Lagios et al. 2005). The offshore source is located about 5 km to the north of Nisyros, to the southeast of Yali, and to the southwest of Strongyli Islet, at a depth of 6.5(±0.5) km. The location of this source coincides with the

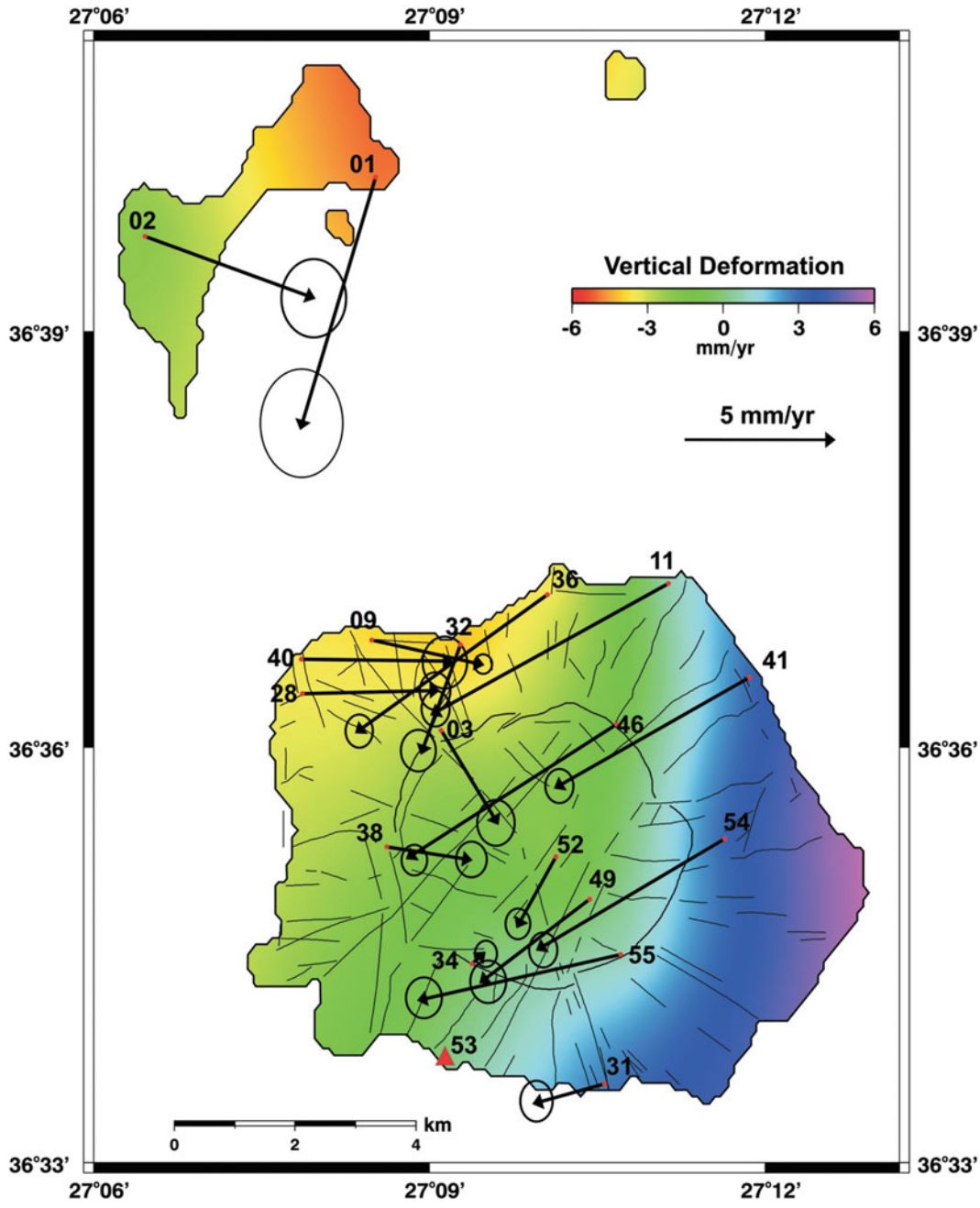

Fig. 10.7 Horizontal and vertical deformation on Yali-Nisyros relative to station 53 (*red triangle*) for the period 2002–2012

intersection of submarine fault zones (Nomikou and Papanikolaou 2011), and is consistent with geophysical (seismological) evidence (Sachpazi et al. 2002) that suggests the presence of an area of low-strength/cohesion volume that may be interpreted as a magma chamber. The two-source approach by Lagios et al. (2005) was based mainly on GPS modelling that subsequently

fitted also the InSAR data. Bearing in mind the ability of the GPS method on accurately defining both the horizontal and vertical deformation component compared to the InSAR technique, which basically provides the deformation only along the LOS direction with its inherent uncertainties, the interpretation by Lagios et al. (2005) may be considered as more justified.

The evolution of the ground deformation relating to GPS results after 2002, as shown in Fig. 10.3, is consistent with the existence of the two Mogi sources (onshore and offshore of Nisyros) as described above. The decrease of pressure inside the magma chambers after 2000 resulted in the observed subsidence of the broader region of Nisyros. This interpretation is supported by both the vertical and horizontal components of the GPS vectors in Nisyros, as well as the displacements that occurred at Yali, as previously described. It is noted that all GPS results refer to the station in northeastern Kos, which did not experience any unexpected motion for the period before or after the seismic crisis in Nisyros. This is evident by an earlier work of Parcharidis et al. (2005), and a more recent one by Sakkas et al. (2014).

Similar to the GPS results for the period after 2002, the SqueeSAR™ analysis indicates that subsidence occurred (Fig. 10.4), which is consistent with the reduction of pressure for the onshore Mogi source. A similar deformational pattern was also observed by Derdelakos et al. (2013) using the Singular Value Decomposition interferometric technique, while their Persistent Scatterers Interferometric (PSI) approach did not yield cogent results for Nisyros, which further validates the effectiveness of the SqueeSAR™ algorithm with its incorporation of DS (non-man-made) targets.

For a direct comparison between the GPS and the interferometric results for the period 2002–2012, an additional analysis of the GPS data was implemented by choosing the same reference point as used for the SqueeSAR™ analysis (Station No. 53). The comparison is presented in Fig. 10.7, which revealed a significant subsidence in the northern part of the island. The horizontal component of the velocity vector emphasizes this subsiding pattern, showing opposite horizontal motion for the stations located across this zone. The uplifted pattern of the southeastern part, although it is extrapolated from only two GPS stations located close to the caldera's rim, coincides with the pattern of motion deduced by the descending data set (Fig. 10.4b). Deformation on Yali also exhibited significant subsidence, with the horizontal component pointing offshore towards the second (offshore) Mogi source (Fig. 10.6). The nature of the subsidence will be better controlled in the future by remeasuring the station at Strongyli (Str), which is to the northeast of this offshore source.

Note that the assumed lower levels of pressure prevailing at the magma chambers after 2000–2002 should have correspondingly an effect on the state of the hydrothermal field associated with the Nisyros Volcano. Gravity measurements on Nisyros between 2003 and 2006 have shown short-term fluctuations of the hydrothermal system and are attributed to shallow fluid flow and degassing processes (Gottsmann et al. 2005, 2007a, b).

Nevertheless, the volcanic hazard from the occurrence of likely hydrothermal explosions is significant and, among other issues, is why Nisyros has been categorized as a "Very High Threat" (Kinvig et al. 2010). This threat is something that should be taken seriously by state and local authorities, and not underestimate the potential danger.

References

Amelung FS, Jonsson S, Zebker H, Segall P (2000) Widespread uplift and 'trapdoor' faulting in Galapagos volcanoes observed with radar Interferometry. Nature 407:993–996. doi:10.1038/35039604

Bonforte A, Guglielmino F, Coltelli M, Ferretti A, Puglisi G (2011) Structural assessment of Mt. Etna Volcano from permanent scatterers analysis. J Geophys Res 12(2):Q02002. doi:10.1029/2010GC003213

Chiodini G, Cioni R, Leonis C, Marini L, Raco B (1993) Fluid geochemistry of Nisyros Island, Dodecanese, Greece. J Volcanol Geotherm Res 56:95–112

Chiodini G, Brombach T, Caliro S, Cardellini C, Marini L, Dietrich V (2002) Geochemical indicators of possible ongoing volcanic unrest at Nisyros Island

(Greece). Geophys Res Lett 29(16). doi:10.1029/2001GL014355
Dach R, Hugentobler U, Fridez P, Meindl M (2007) Bernese GPS Software Version 5.0. Astronomical Institute, University of Bern, Bern
Dawes GJK, Lagios E (1991) A magnetotelluric survey of the Nissyros geothermal field (Greece). Geothermics 20(4):225–235
Derdelakos K, Parcharidis I, Benekos G, Papageorgiou E (2013) Deformation timeseries monitoring of Nisyros Volcano (Greece) during unrest and rest period. In: Proceedings of the ESA living planet symposium 2013, Edinburgh UK 9–13 Sept 2013, ESA SP-722
Di Paola GM (1974) Volcanology and petrology of Nisyros Island (Dodecanese, Greece). Bull Volcanol 38:944–987
Ferretti A, Prati C, Rocca F (1999) Non-uniform motion monitoring using the Permanent Scatterers Technique. In: Proceedings of the 2nd international workshop ERS SAR interferometry, FRINGE, Liège, Belgium, 10–12 Nov, pp 1–6
Ferretti A, Prati C, Rocca F (2000) Analysis of permanent scatterers in SAR interferometry. In: International geoscience and remote sensing symposium (IGARSS), vol 2, pp 761–763
Ferretti A, Prati C, Rocca F (2001) Permanent scatterers in SAR interferometry. IEEE Trans Geosci Remote Sens 39(1):8–20
Ferretti A, Fumagalli A, Novali F, Prati C, Rocca F, Rucci A (2011) A new algorithm for processing interferometric data-stacks: SqueeSAR. IEEE Trans Geosci Remote Sens 49(9):3460–3470
Ganas A, Lagios E (2003) LANDSAT7 night imaging of the Nisyros Volcano, Greece. Int J Remote Sens 24(7):1579–1586
Ganas A, Lagios E, Tzannetos N (2002) An Investigation into the spatial accuracy of the IKONOS 2 Ortho-imagery within an urban environment. Int J Remote Sens 23(17):3513–3519
Ganas A, Lagios E, Petropoulos G, Psiloglou B (2010) Thermal imaging of Nisyros volcano (Aegean Sea) using ASTER data: estimation of radiative heat flux. Int J Remote Sens 31(15):4033–4047
Geotermica Italiana (1983) Nisyros 1 geothermal well. PPC-EEC Report, p 106
Geotermica Italiana (1984) Nisyros 2 geothermal well. PPC-EEC Report, p 44
Gorceix MH (1873a) Sur d'état du volcan de Nisyros au mois de mars 1873. C R Acad Sci (Paris) 77:597–601
Gorceix MH (1873b) Sur la récente éruption de Nisyros. CR Acad Sci Paris 77:1039
Gorceix MH (1873c) Sur l'éruption boueuse de Nisyros. CR Acad Sci Paris 77:1474–1477
Gorceix MH (1874) Phénomènes volcaniques de Nisyros. CR Acad Sci Paris 77:444–446
Gottsmann J, Rymer H, Wooller LK (2005) On the interpretation of gravity variations in the presence of active hydrothermal systems: Insights from the Nisyros Caldera, Greece. Geoph Res Lett 32. doi:10.1029/2005GL024061
Gottsmann J, Carniel R, Coppo N (2007a) Oscillations in hydrothermal systems as a source of periodic unrest at caldera volcanoes: multiparameter insights from Nisyros, Greece. Geophys Res Lett 34:L07307. doi:10.1029/2007GL029594
Gottsmann J, Gamiel R, Coppo N, Wooller LK, Rymer H (2007b) Oscillations in hydrothermal systems as a source of periodic unrest at caldera volcanoes: multiparameter insights from Nisyros, Greece. Geophys Res Lett 34. doi:10.1029/2007GL029594
Hanssen RF (2001) Radar Interferometry: data interpretation and error analysis. Kluwer Academic publishers
Hardimann JC (1999) Deep sea tephra from Nisyros Island, Eastern Aegean Sea, Greece. In: Firth CR, McGuire WJ (eds) Volcanoes in the quaternary, Geological Society (London), Special Publications 161, pp 69–88
Ioannidis K (1998) Nisyros Island: Observed damages to buildings in Mandraki. Newslett Euro Cent Prev Forecast Earthquakes 2:33–35
Kavouridis T, Kuris D, Leonis C, Liberopoulou V, Leontiadis J, Panichi C, La Ruffa G, Caprai A (1999) Isotope and chemical studies for a geothermal assessment of the island of Nisyros (Greece). Geothermics 28:219–239
Keller J, Rehren TH, Stadlbauer E (1990) Explosive volcanism in the Hellenic arc. A summary and review. In: Proceedings of the third scientific congress Thera and the Aegean World III, Earth Science, vol 2, pp 13–26
Kinvig HS, Winson A, Gottsmann J (2010) Analysis of volcanic threat from Nisyros Island, Greece, with implications for aviation and population exposure. Nat Hazards Earth Syst Sci 10:1101–1113
Lagios E (1991) Magnetotelluric study of the structure of the Nisyros geothermal field. Bull Geol Soc Greece 25 (3):393–407
Lagios E (2000) Intense crustal deformation rates on Nisyros Island (Greece), deduced from GPS studies, may foreshadow a forthcoming volcanic event. In: Balassanian S et al (eds) Earthquake hazard and seismic risk reduction, Kluwer Academic Publishers, pp 249–259
Lagios E, Apostolopoulos G (1995) Integrated geophysical study of the geothermal system in the southern part of Nisyros Island, Greece. J Appl Geophys 34:55–61
Lagios E, Chailas S, Giannopoulos J, Sotiropoulos P (1998) Surveillance of Nisyros Volcano: establishment and remeasurement of GPS and Radon networks. Bull Geol Soc Greece 32(4):15–27
Lagios E, Dietrich V, Stavrakakis G, Parcharidis I, Sakkas V, Vassilopoulou S (2001) Will Nisyros Volcano (GR) become active? Seismic unrest and crustal deformation. Euro Geol 12:44–50
Lagios E, Sakkas V, Parcharidis I, Dietrich V (2005) Ground deformation of Nisyros volcano (Greece) for the period 1995–2002: results from DInSAR and DGPS observations. Bull Volc 68(2):201–214
Lagios E, Vassilopoulou S, Sakkas V, Dietrich V, Damiata BN, Ganas A (2007) Testing of satellite

and ground thermal imaging of low-temperature fumarolic fields: The dormant Nisyros Volcano (Greece). ISPRS J Photogram Remote Sens 62 (2):447–460

Lagios E, Papadimitriou P, Novali F, Sakkas V, Fumagalli A, Vlachou K, Del Conte S (2012) Combined seismicity pattern analysis, DGPS and PSInSAR studies in the broader area of Cephalonia (Greece). Tectonophysics 524–525:43–58

Lagios E, Sakkas V, Novali F, Ferretti A, Vlachou K, Dietrich V (2013) SqueeSAR™ and GPS ground deformation monitoring of Santorini Volcano (Greece): tectonic implications. Tectonophysics 594:38–59

Limburg EM, Varekamp JC (1991) Young pumice deposits on Nisyros, Greece. Bull Volcanol 54 (1):68–77

Longchamp C, Bonadonna C, Bachmann O (2011) Characterization of tephra deposits with limited exposure: the example of the two largest explosive eruptions at Nisyros Volcano (Greece). Bull Volcanol 73:1337–1352

Makris J, Chonia T (1999) Active and passive seismic studies of Nisyros volcano - East Aegean Sea. In: Proceedings of 1999 CCSS workshop, Communication of the Dublin Institute for Advance Studies, Geophysical Bulletin, vol 49, pp 9–12

Marini L, Principe C, Chiodini G, Cioni R, Fytikas M, Marinelli G (1993) Hydrothermal eruptions of Nisyros (Dodecanese, Greece). Past events and present hazard. J Volcanol Geotherm Res 56:71–95

Mendrinos D, Choropanitis I, Polyzou O, Karytsas C (2010) Exploring the geothermal resources in Greece. Geothermics 39:124–137

Mogi K (1958) Relations between the eruptions of various volcanoes and the deformations of ground surfaces around them. Bull Earthquake Res Inst Univ Tokyo 36:99–134

Nomikou P, Papanikolaou D (2011) Extension of active fault zones on Nisyros Volcano across the Yali-Nisyros channel based on onshore and offshore data. Mar Geophys Res 32:181–192

Nomikou P, Croff-Bell K, Papanikolaou D, Livanos I, Fero-Martin J (2013a) Exploring the submarine flanks of Yali and Strongyli volcanic islets at the eastern edge of the Aegean Volcanic Arc. Zeitschrift Geomorphol 57(Suppl 3):125–137

Nomikou P, Papanikolaou D, Alexandri M, Sakellariou D, Rousakis G (2013b) Submarine volcanoes along the Aegean Volcanic Arc. Tectonophysics 597–597:123–146

Papadopoulos GA, Sachpazi M, Panopoulou G, Stavrakakis G (1998) The volcano-seismic crisis of 1996–97 in Nisyros, SE Aegean Sea, Greece. Terra Nova 10:151–154

Papanikolaou D, Nomikou P (2001a) Tectonic structure and volcanic centres at the eastern edge of the Aegean volcanic arc around Nisyros Island. Bull Geol Soc Greece 34(1):289–296

Papanikolaou D, Nomikou P (2001b) Tectonic structure and volcanic centres at the eastern edge of the Aegean Volcanic Arc around Nisyros Island. In: Proceedings 9th international congress, Athens, Sept 2001, Bulletin Geological Society Greece, vol XXXIV, pp 1289–1296

Papanikolaou D, Lekkas E, Sakellariou DT (1991) Geological structure and evolution of Nisyros Volcano. Bull Geol Soc Greece 25(1):405–419

Papazachos B, Papazachou C (1989) Earthquakes in Greece. Zitis, Thessaloniki, Greece

Parcharidis I, Lagios E (2001) Deformation in Nisyros Volcano (Greece) using differential interferometry. Bull Geol Soc Greece 34(4):1587–1594

Parcharidis I, Foumelis M, Sakkas V, Lagios E (2005). Deformation monitoring in Kos Island (Hellenic Volcanic Arc, Eastern Greece) using Differential Interferometry. In: Geosciences and remote sensing symposium (IGARSS), vol 4, pp 2899–2902

Peltier A, Bianchi M, Kaminski J, Rucci A, Staudacker T (2010) PSInSAR™ as a new tool to monitor pre-eruptive volcano ground deformation: validation using GPS measurements in Piton. Geophys Res Lett 37:I12301. doi:10.1029/2010GL043846

Sachpazi M, Kontoes Ch, Voulgaris N, Laigle M, Vougioukalakis G, Olga Sikioti G, Stavrakakis G, Baskoutas J, Kalogeras J, Lepine JCl (2002) Seismological and SAR signature of unrest at Nisyros caldera, Greece. J Volcanol Geoth Res 116:19–33

Sakkas V, Novali F, Lagios E, Bellotti F, Vassilopoulou S, Damiata BN, Allievi J (2014) Ground deformation study of Kos Island (SE Greece) based on SqueeSAR™ interferometric technique. In: Geosciences and remote sensing symposium (IGARSS), 2014 IEEE International, Quebec Canada, pp 4319–4322

Stiros SC (2000) Fault pattern of Nisyros Island volcano (Aegean Sea, Greece): structural, coastal and archeological evidence. In: McGuire WJ, Griffiths DR, Hancock PL, Stewart IS (eds) The archeology of geological catastrophes. Geological Society Special Publications, London, vol 171, pp 385–397. doi:10.1144/GSL.SP.2000.171.01.28

Stiros SC, Vougioukalakis G (1996) The 1970 Yali (SE edge of the Aegean volcanic arc) earthquake swarm: surface faulting associated with a small earthquake. Ann Tecton 10:20–30

Sykioti O, Kontoes C, Elias P, Briole P, Sachpazi M, Paradissis D, Kotsis I (2003) Ground deformation at Nisyros Volcano (Greece) detected by ERS-2 SAR differential interferometry. Int J Remote Sens 24:183–188

Tibaldi A, Pasquare FA, Papanikolaou D, Nomikou P (2008) Tectonics of Nisyros Island, Greece, by field and offshore data, and analogue modelling. J Struct Geol 30:1489–1506

Vassilopoulou S, Lagios E (2002) The use of the ortho-images in geo-environmental applications: the ortho-ikonos 2 image of Nisyros Island (Greece). In: Proceedings of the 6th Hellenic geographical congress, vol 2, pp 95–101

Vassilopoulou S, Hurni L, Dietrich V, Baltsavias M, Pateraki M, Lagios E, Parcharidis I (2002) Ortho-photo generation using IKONOS-2 imagery and high resolution DEM: a case study on monitoring the volcanic hazard on Nisyros Island (Greece). ISPRS J Photogram Remote Sens 57:24–38

Vougioukalakis G (1993) Volcanic stratigraphy and evolution of Nisyros Island. Bull Geol Soc Greece 28(2):239–258

Zouzias D, Miliaresis GC, Seymour KS (2011) Probable regional geothermal field reconnaissance in the Aegean region from modern multi-temporal night LST imagery. Environ Earth Sci 62:717–723

Ground Deformation and Gravity Changes of the Kos-Nisyros Volcanic System Between 1995 and 2008

11

Stefanie Hautmann and Joachim Gottsmann

Abstract

With the beginning of unrest of the Kos-Nisyros volcanic system in late 1995, temporal-spatial monitoring of surface deformation and gravity changes was established for the first time on Nisyros island. The collection and analysis of geodetic observables allowed for the identification of two distinctive dynamics associated with the unrest: (i) a major inflation/deflation sequence (1995–2000) affecting the whole of Nisyros island with vertical uplift of up to 140 mm subsequently followed by subsidence of 70 mm and (ii) sinusoidal variations in gravity and ground deformation at periods of tens of minutes to hours with amplitudes of up to 25 μGal and 40 mm, respectively. The major episode of ground uplift has been attributed to pore pressure increase within the hydrothermal aquifer induced by intensified magma degassing, while the switch to surface subsidence in 1998 was probably promoted by seismic induced fault dilation that increased rock permeability and facilitated efficient hydrothermal discharge resulting in fluid volume decrease and ground deflation. The periodic short-term oscillations, first recognized in 2003, predominantly occurred along well-documented fault zones and appear to be driven by episodic degassing of a magma reservoir and release of fluids that interacted with a succession of overlying hydrothermal aquifers and a mechanically heterogeneous and anisotropic shallow crust. Diminution of short-term dynamics in both frequency and amplitude between 2003 and 2008 indicate slow unrest waning and return to background levels of activity of the volcanic/magmatic system by spring 2008.

S. Hautmann (✉)
Institute of Geochemistry and Petrology,
Swiss Federal Institute of Technology, ETH Zurich,
ETH-Zentrum, CH 8092 Zurich, Switzerland
e-mail: stefanie.hautmann@erdw.ethz.ch

J. Gottsmann
School of Earth Sciences, University of Bristol,
Wills Memorial Building, Queens Road,
Bristol BS8 1RJ, UK

11.1 Introduction

Restless volcanic systems are governed by complex magmatic and hydrothermal processes in the underground that can initiate geodetic signals; i.e., crustal deformation and changes in

V.J. Dietrich and E. Lagios (eds.), *Nisyros Volcano*, Active Volcanoes of the World,
DOI 10.1007/978-3-319-55460-0_11

the gravitational acceleration, both measurable at the ground surface. Analysis and modelling of the geodetic observables enable the imaging of active magmatic systems in the ground as well as the assessment of causative subsurface processes related to magma flux (e.g. Nishimura et al. 2001; Marchetti et al. 2009; Lu et al. 2010; Hautmann et al. 2013), gas ascent (Hautmann et al. 2014) and hydrothermal fluid flow (Wicks et al. 1998; Battaglia et al. 2006). The detection and quantification of fluid migration in the underground is vital for the assessment of a volcanic system in terms of its activity state and eruption forecasting. Particularly in caldera systems that repeatedly experience phases of unrest, the identification of subsurface processes and mechanisms that herald a switch from background activity to possible impending eruption is of paramount importance (Troise et al. 2001; Gottsmann et al. 2006; Battaglia et al. 2008; Gottsmann and Battaglia 2008).

The Kos-Nisyros volcanic field (Fig. 11.1) is a caldera system that underwent several episodes of unrest in historical times (e.g., Marini et al. 1993). Today's locus of hydrothermal activity is the 3.8 km wide Nisyros caldera that truncates the centre of Nisyros island. Hydrothermal activity on Nisyros is expressed at the surface by active fumaroles and hydrothermal explosion craters within the caldera as well as by thermal springs in coastal areas (e.g., Lagios et al. 2005). The current subsurface model of the caldera is that it is underlain by a magma reservoir (at unknown depth), which fuels a hydrothermal system that consists of two stacked aquifers located in the upper crust (<1500 m beneath the caldera floor, Fig. 11.2).

The aquifers differ in temperature and geochemical fluid composition, with supercritical fluids above 300 °C in the deep and boiling fluids at ~100 °C in the shallow aquifer (Dawes and Lagios 1991; Chiodini et al. 1993, 2002). A total of 13 phreatic eruptions occurred in Nisyros in historical times (Marini et al. 1993), with the most recent eruptive event being a steam-driven hydrothermal explosion in 1888. The eruption was preceded by increased seismic activity that probably formed a pathway for fluids to transfer from the deep to the shallow aquifer, which finally triggered the eruption (Marini et al. 1993). Since then short episodes of local seismic unrest were reported to be felt in 1953 and 1970 (Sachpazi et al. 2002) but did not culminate in an eruption. The most recent episode of seismic unrest, which was in the same time the first to be instrumentally documented, started at the end of 1995. Thenceforth earthquake activity increased continually and peaked in August 1997. Seismic activity remained at high levels throughout 1998 until it declined to background level activity in early 1999 (Sachpazi et al. 2002). The epicentres of the events were mainly confined to the Yali-Nisyros region (Sachpazi et al. 2002). Increased seismic activity was accompanied by fault reactivation in Yali and the town of Mandraki in NW Nisyros (Vougioukalakis et al. 1998). In 1997 intensified fumarolic activity occurred in the Nisyros caldera (Brombach et al. 2001) but attenuated towards the end of the year.

The onset of high-level seismic activity in the Kos-Nisyros volcanic field raised the awareness for potential hazards posed by the Nisyros caldera in case of a re-awakening of eruptive activity. In consequence, volcanic monitoring, including for the first time geodetic surveillance, was established on Nisyros island. This paper presents a review on geodetic monitoring conducted on Nisyros between 1995 and 2008, i.e., since the beginning of the seismic crisis until a time when the system had reverted to a mode of background activity. We will give a detailed overview on the collection, modelling and interpretation of published ground deformation data enhanced with new data from surface deformation and gravimetric surveys. Finally, we will outline underlying mechanisms of the observed ground deformation/gravitational changes and will compare observations from Nisyros caldera with findings from other caldera settings.

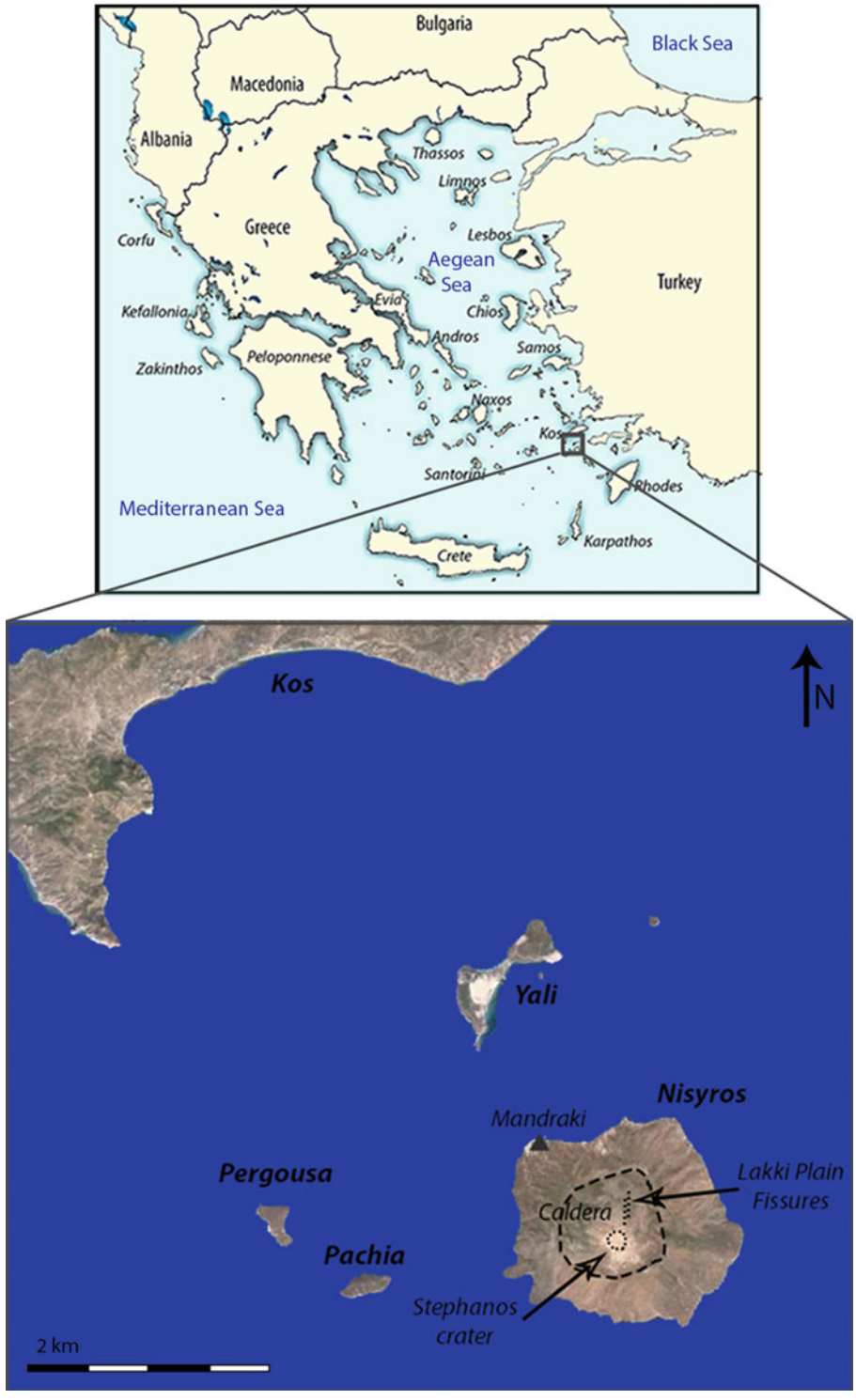

Fig. 11.1 (*Top*) Map of the Aegean region of the Mediterranean displaying the location of the islands of Kos and Nisyros (framed). (*Bottom*) Satellite view of the Kos-Nisyros area with indication of major structural features (Nisyors caldera, Lakki plain, Stephanos crater)

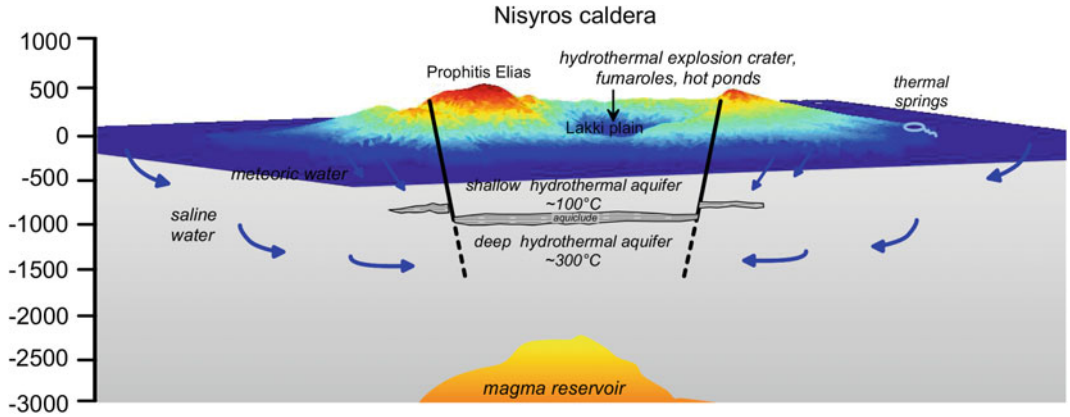

Fig. 11.2 Topography of Nisyros island with a schematic illustration of its subsurface structure (modified after Marini et al. 1993; Lagios et al. 2005). Degassing of a magma reservoir beneath the caldera charges two confined hydrothermal aquifers located in the shallow crust. Hydrothermal explosion crater, fumaroles and hot ponds are the surface expression of hydrothermal activity within the caldera. Major fault systems crossing Nisyros provide pathways for hydrothermal fluid escape across the Lakki plain and to thermal springs along the coast

11.2 Syn- and Post-seismic Deformation 1995–2000

11.2.1 InSAR and GPS Data Collection

Due to a lack of routine geodetic surveillance in the early 1990s the onset of surface uplift that was associated with or even preceded the seismic crisis was not recognized. The collection of geodetic data on Nisyros started in 1995 by means of satellite-based monitoring techniques (Fig. 11.3), more specifically Interferometric Synthetic Aperture Radar (InSAR: Sachpazi et al. 2002; Sykioti et al. 2003; Lagios et al. 2005) and since 1997 also Global Positioning System (GPS: Lagios et al. 2005).

SAR interferograms from Nisyros were generated between May 1995 and September 2000 with a total of six images acquired in the ascending and three images acquired in the descending pass of the satellite sensor (Sachpazi et al. 2002; Sykioti et al. 2003). Due to satellite orbital problems, images from after 2000 are not available (Lagios et al. 2005). Data were acquired from the ERS-2 system and reduced for topography using a DEM generated from a 1:5000 topographic map (Sachpazi et al. 2002; Sykioti et al. 2003). Depending on the sensitivity to the topography of interferometric pairs (expressed by the altitude of ambiguity) the error in inferred ground deformation ranges between 5 and 15% for individual observation periods. Interferometric images from descending passes were only used for qualitative analysis as to their low coherence.

SAR interferometric images were also constructed for the adjacent Kos island from satellite passes on August 1996, July 1999 and September 2000 (Parcharidis et al. 2005). Inferred interferograms, however, lack imaging a clear deformation pattern, due to low coherence of the interferometric pairs.

The first GPS network was installed in June 1997 and re-occupied seven times until July 2002 (Lagios et al. 2005). The network consisted of 18 benchmarks that were distributed across Nisyros and referred to a base site on Kos Island. The data was collected with dual-frequency WILD receivers and post-processed with the Bernese GPS Software Version 4.2 (Rothacher et al. 1993). The achieved accuracy of GPS data is given as between 2–3 mm and 4–6 mm at the horizontal and vertical component, respectively (Lagios et al. 2005).

Both InSAR and GPS data are time-lapse datasets covering distinct observation periods at intervals between 3 and 13 months (Fig. 11.3).

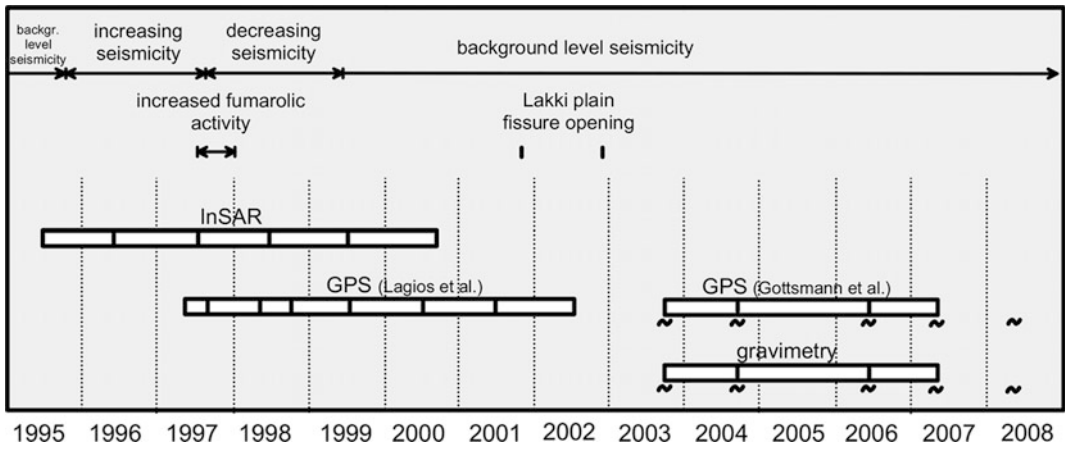

Fig. 11.3 Overview of geodetic surveys performed on Nisyros island between 1995 and 2008. Monitoring intervals of time-lapse observations are indicated by *white boxes* with the times of individual survey campaigns and satellite passes marked by *vertical bars*. Survey campaigns that included continuous occupations within the caldera are marked by a *tilde* (~). Associated seismic activity levels and visually observed changes within the caldera are displayed at the *top*

Note that GPS data were collected in campaign mode, thus continuous deformation data are not available from the early unrest. The radar interferometric images allow documentation of ground deformation only in the slant range direction, which is 23.5° from the vertical, making the technique more sensitive to vertical than to horizontal displacements. In contrast, GPS data resolve surface deformation in vertical and horizontal vectors with a higher accuracy in the horizontal components. As such, the complementary use of both techniques can yield high precision constraints on the absolute magnitude and spatial distribution of surface deformation. On Nisyros, however, SAR images and GPS data were not acquired simultaneously allowing only for a qualitative combination of both datasets.

11.2.2 Inflation/Deflation Sequence

For the time interval between June 1995 and June 1997 SAR interferograms document ground uplift across the entire island of Nisyros with maximum deformation of 140 mm in slant direction. The centre of surface deformation was located on the NW edge of the Nisyros caldera, about 1.5 km south of the town Mandraki (Sachpazi et al. 2002; Sykioti et al. 2003). Interferometric images from the individual observation periods report 84 mm uplift during the first (June 1995–May 1996) and 56 mm uplift during the second year (May 1996–June 1997; Sachpazi et al. 2002; Sykioti et al. 2003). From June 1997 to June 1999 InSAR data then show a deformation of 42 mm into the opposite direction (i.e., ground subsidence), while the records from May 1998 to September 2000 indicate a deflation by 70 mm (Sykioti et al. 2003). Due to incompatibility of interferometric images surface deformation between June 1997 and May 1998 is not quantifiable. All observation intervals show a similar relative displacement pattern with radially symmetric ground deformation around a stationary centre of deformation located on the NW caldera rim.

GPS data document vertical deformation between June 1997 and October 1998 with a maximum upward movement of 140 mm at 3 sites in the NW of Nisyros and uplift between 40 and 60 mm at all other sites on island (Lagios et al. 2005). Horizontal displacements range between 20 and 60 mm and diverge from the NW rim of the Nisyros caldera (i.e. the centre of deformation

inferred from SAR images). For the subsequent observation period (October 1998–June 1999) GPS data indicate further uplift at a maximum of 8 mm, while for the interval between June 1999 and July 2000 a deflation of 20 mm was detected. Associated horizontal displacements indicate 10–20 mm southward movement of all sites during 1998–1999, while during 1999–2000 horizontal deformation was not detected at a significant level (Lagios et al. 2005).

Both InSAR and GPS data document ground uplift of up to 140 mm on Nisyros Island during the seismic crisis. From the combination of both datasets it was inferred that ground inflation ended in mid-1998 (Sykioti et al. 2003). While InSAR data indicate a strong post-crisis deflation, GPS records from after 1998 show variations in uplift/subsidence at amplitudes only within or slightly above the limits of data accuracy.

11.2.3 Modelling of Source Parameters

The most simple and therefore most widely employed approach to model geodetic data is the 'Mogi model' that inverts ground deformation data for a spherical pressure source that is embedded in a isotropic, homogeneous, elastic half-space (Mogi 1958). Although this model is based on a very simplifying assumption—as it neglects others than spherical source geometries as well as effects due to surface topography, crustal discontinuities and variations in mechanical rock properties—Mogi solutions offer a reasonable first approximation to source depth and volume changes associated with the recorded ground deformation. A Mogi point source inversion was performed by Sykioti et al. (2003) on InSAR data for the period June 1995 to June 1997, which is the time interval with the most pronounced surface deformation and therefore the clearest interferogram. The authors inferred a source location 1.5 ± 0.4 km south of Mandraki (i.e., close to the caldera rim), a source depth of 5 ± 0.5 km and a source volume change of 0.026 ± 0.004 km^3.

Lagios et al. (2005) applied GPS recorded deformation data from 1997 to 2001 to Mogi equations assuming a dual-chamber system with one source located in the NW of Nisyros caldera (1 km SE of the source centre inferred by Sykioti et al. 2003) and another source situated about 6 km north of Nisyros. The existence of an additional offshore source was assumed from seismic data (Makris and Chonia 1999; Sachpazi et al. 2002). A best fit of model to GPS data was obtained for a simultaneous inflation of both sources. The offshore source was inferred to be located at 6.5 ± 0.5 km depth with a source volume change of 0.012 ± 0.002 km^3, while the onshore source was found to be centred at 5.5 ± 0.5 km depth and underwent a volume change of 0.007 ± 0.001 km^3. In order to account for the large amplitudes in surface uplift observed at three sites in NW Nisyros, Lagios et al. (2005) considered this region as a separate tectonic block and allowed in their modelling for a right-lateral normal dislocation along the Mandraki fault. Trials to model the observed deformation exclusively with fault activation failed owing to unacceptably large misfits of model to data. Lagios et al. (2005) further apply the source parameters derived from the dual-Mogi model to generate a synthetic interferometric image for qualitative comparisons with collected InSAR data. The results, however, show that although the assumption of a two source model might be justified from GPS and seismic data, the better agreement of synthetic interferograms with InSAR images is achieved for the single source model (compare Sykioti et al. 2003).

11.2.4 Interpretation

Based on the available geodetic data it is not possible to prefer one model over the other in order to determine the source parameters. This reflects the problem of non-uniqueness of model

solutions that can derive from data noise, insufficient network coverage and/or temporal aliasing. Due to the lack of additional geodetic data, such as Electronic Distance Measurements, tilt, strain or gravity, it requires other information derived from seismic, geochemical or petrological monitoring to constrain the causative source(s) for the most active unrest period. Although it remains unclear whether or not pressure changes in an offshore magma chamber contributed to the surface uplift observed on Nisyros, it is widely agreed that ground deformation was generated by mechanisms different than purely elastic crustal response to magma injection and withdrawal (Sachpazi et al. 2002; Sykioti et al. 2003; Caliro et al. 2005). Sykioti et al. (2003) argue that ascribing the surface inflation to magma chamber filling implies that in consequence the subsequently following deflation period must result from the removal of this magma volume. Subsurface migration of magma was not confirmed from geodetic data, although there is the possibility that magma migrated towards a reservoir located offshore Nisyros. Seismic data, however, indicate fluid transport in 1997 from NW Nisyros (the centre of maximum ground deformation) towards the central part of Nisyros caldera rather than in the opposite direction (Sachpazi et al. 2002). Sykioti and co-workers conclude that the sequence of ground uplift and subsidence was mainly a thermodynamically controlled poroelastic response of the shallow crust to magma injection at depth. Caliro et al. (2005) more specifically assume that the observed deformational changes were related to increased subsurface hydrothermal activity due to intensified magma degassing at depth. The authors suggest that the hydrothermal system in the shallow crust was charged by heat and fluids from the deeper-seated magma body causing an overpressure build-up in the shallow crust that resulted in surface uplift. Intensification of activity in the hydrothermal discharge area (fumarolic degassing, thermal springs) observed towards the end of the seismic crisis might have facilitated cooling processes in the shallow crust, which then entailed the reversal of ground deformation. This interpretation is indeed supported by seismic data that indicate fluid transport towards the caldera's centre shortly before the onset of increased hydrothermal surface activity (Sachpazi et al. 2002).

11.3 Fissure Opening in Nisyros Caldera 2001–2002

On 20 November 2001 a shallow fissure opened abruptly in the eastern Nisyros caldera (Fig. 11.4), more specifically the Lakki plain (Lagios et al. 2005). Although seismic and deformational activity was at low level at this time, this event revealed that tensional stressing of the subsurface still persisted. The open rupture was oriented in N-S direction with a length of about 350 m and a depth of 10 m at maximum. Dilation varied between 1 and 5 m along the fissure. About a year later, on 18 December 2002, the rupture extended southwards for another 250 m but did not penetrate deeper into the ground. As to the lack of lateral and vertical dislocations associated with the rupture, the fissure opening is attributed to the accumulation of purely horizontal EW directed tensional stresses (Lagios et al. 2005). GPS records from Lagios et al. (2005) covering the time intervals Sept 2000–June 2001 and June 2001–July 2002 give indeed evidence for a repeated uplift of the caldera floor by a total of 20 mm. In addition, horizontal displacements from the latter observation period indicate E-W extension of the island's centre by approximately 20 mm (Lagios et al. 2005). Modelling the GPS data with a simple Mogi model failed due to a highly disperse pattern in the deformational field. Lagios et al. (2005) therefore assume that crustal weaknesses due to fault structures considerably influenced the deformational field and that fissure opening in Lakki plain was a result of a local accumulation of uncompensated near-surface stresses.

Fig. 11.4 Picture of the Lakki plain fissure in 2006. N-S oriented fissures started to open in 2001 in absence of preceding or accompanying seismic activity. The ruptures most likely result from local accumulation of uncompensated near-surface stresses

11.4 Hydrothermal Background Activity 2003–2008

11.4.1 Time-Lapse Microgravity/GPS Data

Upon the re-occurrence of surface activity expressed by fissure opening in Lakki plain, a new joint gravity-deformation network was established on Nisyros in November 2003 (Fig. 11.5) in order to detect and document long-term mass/density variations in the islands underground. The network was re-occupied in October 2004 and partly re-visited in May 2006 and May 2007 (Gottsmann et al. 2005, 2007). The network comprised a total of 23 benchmarks distributed across the entire island including a N-S directed line through the Nisyros caldera. Collected data was referred to a base site in the NW of Nisyros (shrine base; see Table 11.1), as the installation of an off-island base was due to financial and logistical reasons not feasible. Time-lapse gravity data was sampled using a Lacoste&Romberg gravimeter G-403 and reduced for Earth and Ocean tides, instrumental drift and elevation changes inferred from co-recorded GPS data. The collection of GPS data was conducted with 2 Leica GPS 500 receivers operated at 1 Hz for 60 min at each site. Post-processing was performed using Leica Geosystems SKI-Pro software. The precision of each individual gravimeter reading was within 3 μGal, while accuracy of individual GPS determined sited positions was 10 and 12 mm for the horizontal and vertical component, respectively.

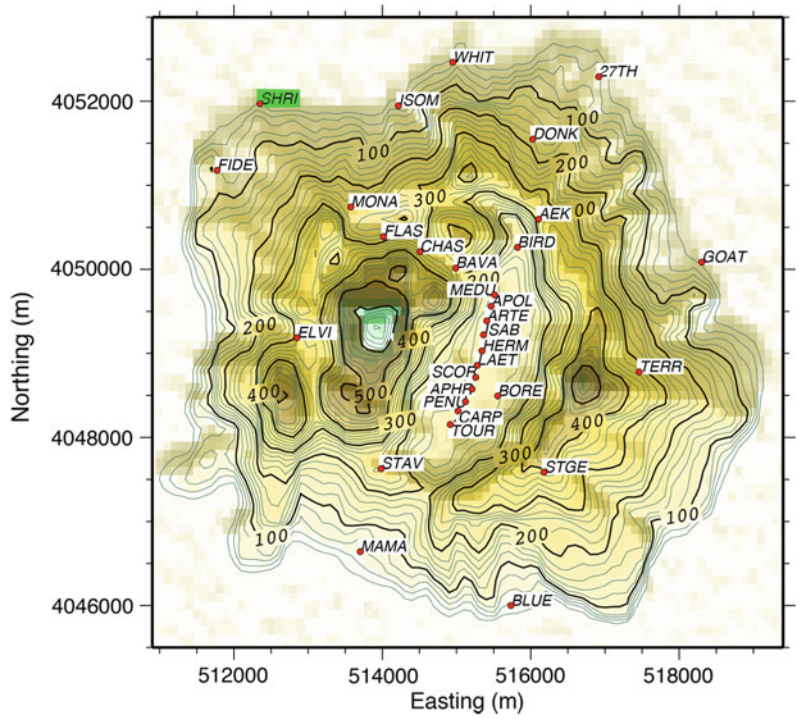

Fig. 11.5 Topographic map of Nisyros with the network for combined GPS and gravity surveillance established in 2003 and re-occupied until 2008. The reference site shrine base (SHRI) is located in the NW of the island and highlighted in *green*

Table 11.1 De-drifted, de-tided and free-air corrected time-lapse gravity data (μGal) and corresponding errors from the observation intervals October 2003–October 2004, October 2003–May 2006 and October 2003–May 2007

BM ID	Easting (m)	Northing (m)	2003/4		2003/6		2003/7	
			dg (μGal)	stdev (μGal)	dg (μGal)	stdev (μGal)	dg (μGal)	stdev (μGal)
AEK	516,103.87	4,050,590.76	−16	15	−18	14	−10	20
White beach	514,949.25	4,052,460.06	−12	11				
Goat beach	518,304.61	4,050,082.37	9	9				
Donkey	516,025.16	4,051,545.80	−15	11	19	10		
Terrace	517,463.82	4,048,773.93	−28	13	0	14	−11	19
St George	516,180.20	4,047,582.32	−32	17	−22	10	−31	14
Isomat	514,216.92	4,051,941.14	5	9	−41	8	34	8
27 October	516,914.71	4,052,288.79	−8	8	10	8	−9	7
Blue bell	515,733.38	4,045,996.45	2	6	4	9		
Bird bath	515,820.07	4,050,253.18	3	14	4	16	−9	14
Carpark	515,019.01	4,048,308.21	0	12	0	13		
Borehole	515,555.43	4,048,487.91	5	10	−12	7	9	7
Monastery	513,576.67	4,050,737.32	−29	15	−14	26	9	18
Fidel	511,773.93	4,051,178.00	−15	13				
Artemis	515,406.02	4,049,381.74	−6	15				
Stavros	513,986.03	4,047,624.77	−41	15	−22	23	5	14

(continued)

Table 11.1 (continued)

BM ID	Easting (m)	Northing (m)	2003/4		2003/6		2003/7	
			dg (μGal)	stdev (μGal)	dg (μGal)	stdev (μGal)	dg (μGal)	stdev (μGal)
Chasm	514,506.23	4,050,205.98	14	23				
Elvis	512,850.84	4,049,181.00	−9	16				
Isabel	515,362.23	4,049,215.49	−7	21				
Bavaria	514,988.85	4,050,010.74	10	14				
Scorchio	515,257.81	4,048,709.38	−9	10				
Mama Nisyros	513,703.95	4,046,636.53	−2	6				
Shrine base	512,349.72	4,051,962.54	Reference					

Time-lapse gravity data from the monitoring intervals 2003–2004 and 2003–2006 document gravity variations between −41 and 14 μGal across the entire island (Fig. 11.6, Table 11.1). However, the uncertainty over multiple readings at individual benchmarks during different survey loops was ±6–26 μGal, leaving only very few sites affected by significant long-term gravity changes. During 2003–2004 significant changes occurred at 5 sites along the caldera rim with a decrease in gravity between −28 and −41 μGal. The spatial correlation of gravity changes with respect to mapped primary and secondary fault systems on the island (Stiros 2000) suggest that the gravity changes may originate from fault-bound dynamics (Fig. 11.6). Hot springs in the northern and southern extension of the major faults (Lagios et al. 2005), lineaments of anomalous CO_2 degassing in the Lakki plain (Caliro et al. 2005) and the alignment of phreatic explosion pits along major NNW-SSE F1 fault systems evidence that the structural discontinuities provide pathways for hydrothermal fluids due to enhanced fracture permeability. We thus assume that the reported gravity variations result from fluid migration along the major fault systems. Gravity residuals measured between 2003 and 2006 are most likely of the same origin since the significant long-term changes align along the NNE-SSW F1 faults that cross the central caldera and extend towards the coast. Gravity changes reported for the period 2003–2007 are only within the standard deviation (see Table 11.1) and therefore insignificant.

Co-recorded GPS data from 2003–2004 document surface subsidence of up to 40 mm and northwestward displacement of up to 30 mm of the entire island relative to the reference site installed near Mandraki harbour (Fig. 11.7). This observation allows for different interpretations: One scenario is that the deformation reflects an uplift and southeastwards displacement of the NW part of the island (including the reference site), which would relate to an inflating shallow seated off-island pressure source positioned NW of the island close to the coast (not identical with the offshore source suggested by Lagios et al. 2005).

Another interpretation is that southeastern Nisyros was undergoing subsidence and northwestward movement. This scenario would require a deflation of a rather oblate source centered below the SE caldera together with a lateral pushing towards the NW from a second source located off-island in the SE of Nisyros. A westward movement of Nisyros relative to Kos was also observed as early as 2001 (Lagios et al. 2005) and might have continued through 2004. However, the absence of off-island reference observations precludes constraints on source location and mechanism and available data only allow us to conclude that deformation on Nisyros after 2003 was largely controlled by off-island sources. A tectonic decoupling of the NW part of the island (including Mandraki) from the rest of Nisyros seems to be likely. Surface deformation between 2003 and 2006 reveals a more diffuse pattern (Fig. 11.7): Northwestward displacements—although less pronounced—are still

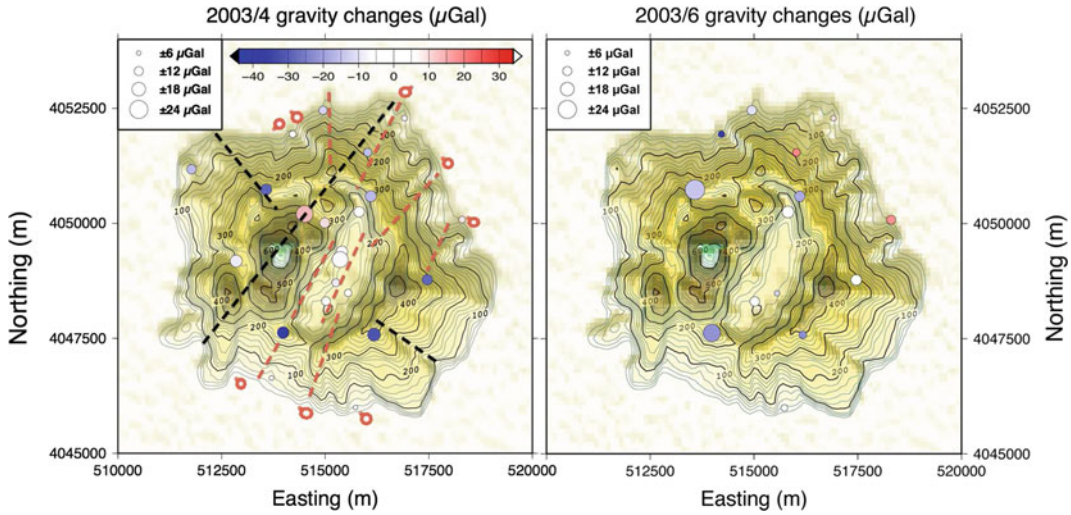

Fig. 11.6 Map of Nisyros with superimposed residual gravity changes (μGal) from the observation intervals October 2003–October 2004 (*left*) and October 2003–May 2006 (*right*). The *circle* size indicates the uncertainty over multiple readings at individual benchmarks with measurement uncertainties of up to ±26 μGal. These uncertainties predominantly result from short-term oscillations of the gravity field as discussed in the text and shown in Figs. 11.8, 11.9 and 11.10. (Multi-) Annual residual gravity change records are thus highly aliased and are only significant at very few sites (coloured *dark blue*). The *left* Fig. 11.6 displays the major faults systems of Nisyros island and location of off-shore thermal springs (*red circles*). Faults that were activated during the volcano-seismic crisis of 1995–2000 are shown in *black*. Additional faults classified in the F1 and F2 fault systems (see Stiros 2000; Lagios et al. 2005) are given in *red*. The F1 fault system is NE-NNW/SW-SSW oriented, while the F2 fault system is directed towards N-NW/S-SE. The locations of benchmarks affected by significant gravity changes coincide with the major faults zones

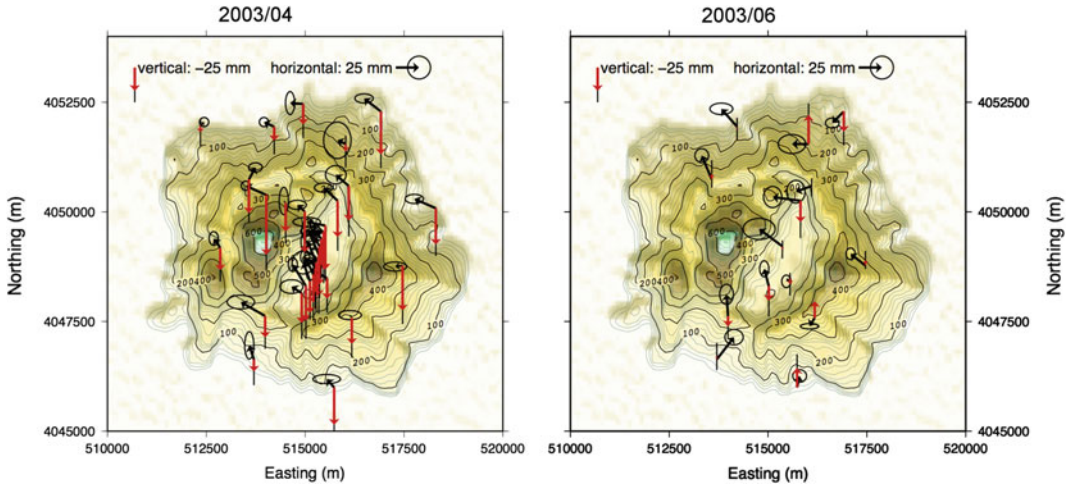

Fig. 11.7 Map of Nisyros showing recorded changes in ground deformation (m) from the observation intervals October 2003–October 2004 (*left*) and October 2003–May 2006 (*right*). The accuracy of site positions is 0.01 and 0.012 m for horizontal and vertical deformation, respectively. Horizontal and vertical changes of the second monitoring interval are given in *black* and *blue* *arrows*, respectively. The overall deformation pattern of the first observation window indicates subsidence and northwestward displacement of the island with respect to a reference located in the NW corner of the island. In contrast, the deformation pattern of the second monitoring period is more diffuse and hints at multiple pressure sources and fault-related anisotropic crustal responses

apparent, while vertical displacements reveal recessive subsidence (with respect to 2003–2004) of the caldera floor and up to 25 mm uplift outside the caldera. This deformation field indicates either a superposition of multiple stress sources or a complex structural architecture that controls the stress and strain relationship in an heterogenous and anisotropic subsurface.

11.4.2 Continuous Multi-parametric Geophysical Data

While the primary aim of the microgravity surveys was to quantify time-lapse mass/density changes in the caldera's subsurface, the surveys in 2003 and 2004 unexpectedly revealed sinusoidal changes in residual gravity data over a period of 45–60 min (Gottsmann et al. 2006). The amplitude of the short-term variations was between 12 and 25 μGal and as such at the same scale than the residual gravity changes observed between the individual measurement campaigns (Gottsmann et al. 2005). The gravity oscillations were confined to regions of known hydrothermally altered deposits and anomalous CO_2 flux within the Lakki plain and along the southern caldera rim. Co-recorded GPS time series data attest that the oscillations in gravity did not emanate from free-air effects initiated by changes in ground elevation.

Survey campaigns conducted in May 2006 and May 2007 consequently focused on the installation of a combined multi-parametric geophysical experiment in order to assess for the first time short-term dynamic background processes in a restless caldera system (Gottsmann et al. 2007). The set-up included continuous geodetic (4 Leica GSP 500 receivers at 1 Hz), gravimetric (Lacoste & Romberg D-41 recording at 1 Hz, Lacoste & Romberg G-403 and G-513 recording at 0.003 Hz for about 30 h), seismic (Lennartz LE-3D/5 s at125 Hz) and electromagnetic (VLF, 15–250 kHz at 4 Hz recording frequency) measurements in the areas earlier identified as being affected by short-term cyclic changes in gravity. In May 2008 only GPS and continuous gravity data (using B-028 gravity meter) were collected. Residual gravity time-series collected during the survey campaigns in 2006, 2007 and 2008 are shown in Figs. 11.8, 11.9 and 11.10.

The multi-parametric data showed oscillatory behaviour of gravity changes, ground deformation, seismicity and electromagnetic perturbations. Positive gravity changes were accompanied by ground uplift and ground subsidence was matched by gravity decrease.

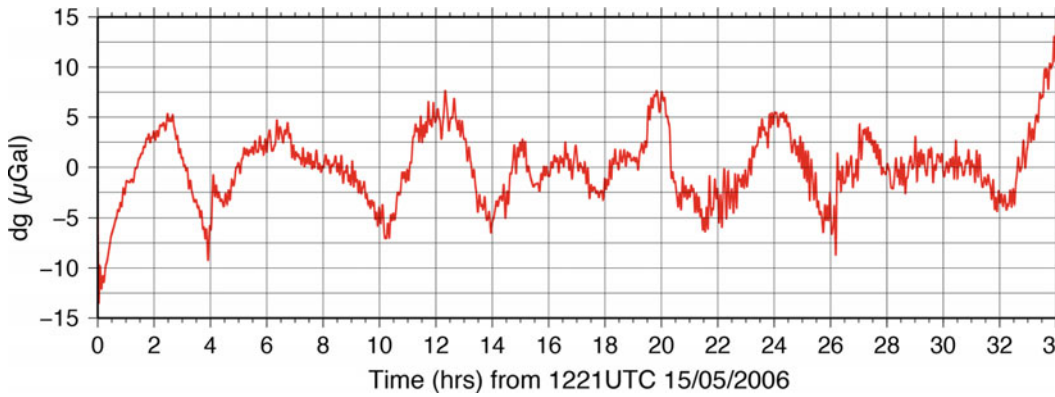

Fig. 11.8 Continuous gravity data recorded at UTM 515,661.50 m Easting and UTM 4,048,567.75 Northing (near BORE) at 1 Hz (Lacoste & Romberg D-41) over a period of 36 h starting on 15 May 2006 12:21 UTC. The time-series is band-pass filtered at cut-off period between 5 min and 7.5 h. Sinusoidal gravity changes of ±10 μGal are attributed to hydrothermal fluid circulation in the shallow subsurface (see text for details)

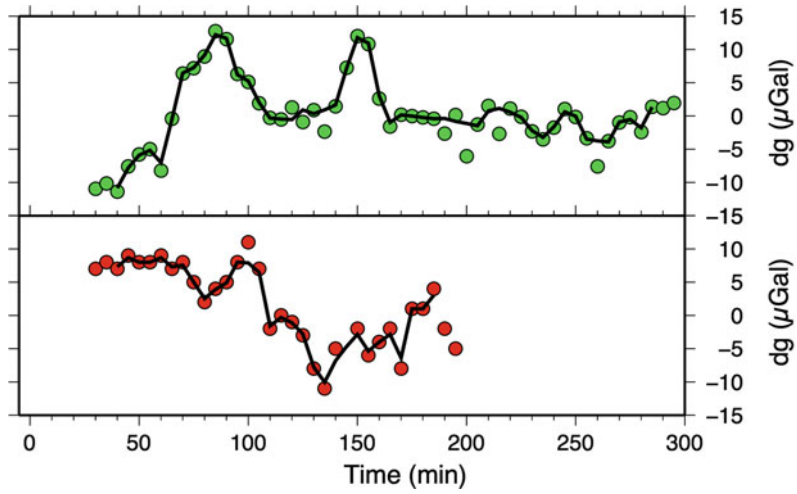

Fig. 11.9 Gravity time-series produced via repeated readings at 0.0033 Hz at two benchmarks in Lakki plain. (*Top* UTM 514,427.20 Easting and UTM 4,048,392.90 Northing, start: 1610 UTC May 20, 2007; *bottom* UTM 515,558.70 Easting and UTM 4,048,489.50 Northing, start: 1302 UTC May 18, 2007) within the caldera (*bottom*) using Lacoste & Romberg G-403. Data have been cleaned for linear instrument drift and tidal effects; the first 30 min of observations during instrument settling have been removed to improve clarity. The data show peak-to-peak variations in gravity of up to 25 μGal at periods of 45–60 min

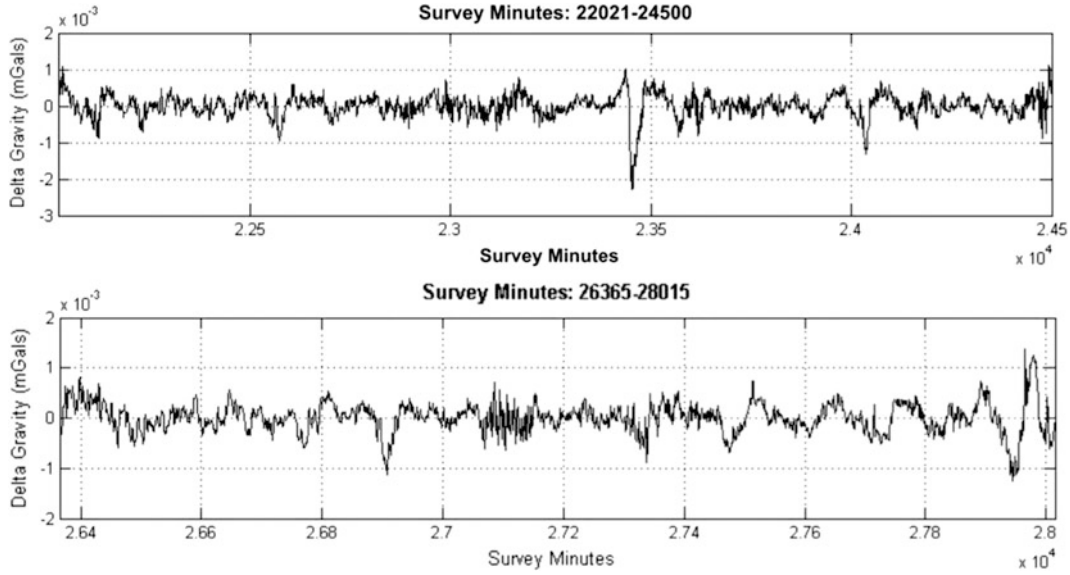

Fig. 11.10 Example of residual continuous gravity data recorded at UTM 515,661.50 m Easting and UTM 4,048,567.75 Northing (near BORE) at 1 Hz (Burris Meter B-028). The data shown in the *top* panel starts June 6, 2008 0700 UTC, while the data shown in the *bottom* panel starts June 9, 2008 0724 UTC. Both time-series are de-tided, de-trended and high-pass filtered at cut-off period of 3 h

Electromagnetic changes were inversely correlated with the gravity/GPS signals. Seismic records displayed repeated bursts in seismic intensity in the character of tremor waveforms. Gravity and ground deformation peaked during bursts of seismic intensity, while the peak

amplitude in the VLF signal was delayed by 18 min.

We applied various band-pass and high-pass filters to continuous gravity time-series recorded in 2006 and 2008 and established power spectra using Fast-Fourier transforms. Results for the seismic, gravity and electromagnetic time series recorded in 2006 indicate peak periods of between 45 and 70 min, matching the timescales of cyclic activity observed by discrete gravity measurements in 2004 (Gottsmann et al. 2005, 2007). Figure 11.8 shows a pass-band filtered (between 5 min and 7.5 h) continuous residual gravity record from May 2006 with peak periods of 64 and 273 min. Residual gravity change amplitudes are ±8 μGal around the mean. Applying the same filter to the May 2008 data (64 h of continuous records) revealed the same peak period (273 min), however, with a much smaller amplitude of ±1.5 μGal in residual gravity (i.e., about an order of magnitude lower). High-pass filtering both datasets below a period of 3 h gives peak periods of 104 and 140 min at ±6 μGal during 2006 and less than ±1 μGal during 2008. It thus appears that between 2004 (first continuous recordings) and 2008 (last continuous recordings) the high-frequency gravity changes decreased in amplitude while they increased in period. However, we lack constraints on the wider frequency contents of the 2004 data, as those records were obtained over less than two hours of manual recording time.

What is the nature of the short-term dynamics displayed in the combined multi-parametric geophysical data? Gottsmann et al. (2007) assume that non-steady degassing of the deep magma reservoir triggers sudden volume expansion of supercritical fluids in the overlying hydrothermal system, which causes pressure increase that finally results in elastic inflation of the upper crust. The seismic tremor relates to degassing activity, while associated gravity changes are explained by the Bouguer effect of deformation resulting from the migration of density boundaries at depth. The ensuing rise of fluids and vapor along a network of fractures and faults results in a source pressure decrease as seen in the associated ground subsidence. The observed time delay of the peak electromagnetic signal with respect to the gravity and seismic signals most likely reflects changes in the secondary induced electromagnetic field below the Lakki Plain at a depth of ca. 35 m given the employed 20.8 kHz observation frequency. The multi-parameter results indicate thermohydromechanical (THM) disturbances that result from episodic degassing of a magma reservoir and re-charge of hot fluids from depth that ascend through a complex network of stacked hydrothermal aquifers and fractured rock. The delay time was used to estimate propagation speeds of the THM waves at 0.4–1.4 m/s.

11.5 Synopsis

Since the beginning of the volcano-seismic crisis on Nisyros in 1995, geodetic observations from Nisyros island were dominated by two dynamic processes occurring over different timescales: (i) a 5-year long sequence of gradual ground uplift and subsequent subsidence with maximum vertical displacements of 140 mm and (ii) oscillating short-term variations in gravity and ground deformation at sub semi-diurnal periods between 45 and 300 min with amplitudes of up to 25 μGal and 40 mm, respectively. Although the spatial and temporal variability of the observed signals is fundamentally different, governing mechanisms in the subsurface are assumed to be similar, with fluid circulation in the shallow crust causing overpressures in the hydrothermal system (Sachpazi et al. 2002; Caliro et al. 2005; Gottsmann et al. 2007). In fact, it is widely acknowledged (e.g. Todesco 2007; Hurwitz et al. 2007; Fournier and Chardot 2012) that repeating episodes of ground uplift/subsidence (bradyseisms) in caldera settings not necessarily reflect changes in the state of the deep magmatic system but result from dynamics in the shallow geothermal system. Bradyseisms at time-scales and magnitudes similar to and larger than those observed on Nisyros are known from several other caldera settings (including Campi Flegrei, Long Valley and Yellowstone) and numerous multi-parametric studies including quantitative models of collected geodetic data have

demonstrated its hydrothermal origin (e.g. Battaglia et al. 2006; Gottsmann et al. 2006; Todesco et al. 2010; Lowenstern and Hurwitz 2008).

The conceptual model for volcano-hydrothermal systems, established by Fournier (1999), suggests that aqueous fluids and gases are expelled from magma due to either crystallization, convection or repeated injection of fresh material into the reservoir. The ascent of high temperature magmatic fluids and its inflow into the shallow hydrothermal system induces fluid overpressures and heating, which causes ground uplift due to poroelastic and thermoelastic expansion of the host rock. Deformation switches back to rock contraction and surface subsidence when either the flux rate of magmatic fluids into the hydrothermal system attenuates and/or pore pressures exceed the yield strength of the host rocks, leading to the formation of pathways for rapid fluid exhalation (Fournier 1999).

Deformational processes due to poroelastic and thermoelastic expansion and its controlling factors were investigated in detail via numerical simulations (Hurwitz et al. 2007; Todesco et al. 2010). Model results revealed that surface deformation (magnitude, rate and pattern) is highly sensitive to material porosity and permeability, but also to host rock rigidity, fluid injection rate and depth. For ground uplift on decadal and shorter timescales fluid volume increase rather than thermal rock expansion appears to be the dominant causative process (Hurwitz et al. 2007). Accounting for H_2O/CO_2-multiphase fluid flow (compared to H_2O-single phase flow) showed that variations in fluid composition affect long-term deformational processes over centennial to millennial timescales (Hutnak et al. 2009).

Numerical simulations and insights from similar caldera settings thus support the assumptions that poroelastic deformation induced by the caldera-hosted hydrothermal system has played a major role in both short-term (tens of minutes—hours) and long-term (annual) geodetic changes on Nisyros (Sachpazi et al. 2002; Caliro et al. 2005; Gottsmann et al. 2007). However, a quantitative model on recorded geodetic data accounting for poroelastic crustal response is as yet missing and should be considered for future research.

Unprecedented insights into subsurface caldera dynamics were gained from the identification of short-periodic changes in gravity and ground deformation that continued on Nisyros for several years after seismicity and hydrothermal discharge in the caldera returned to background level activity. The gathered dataset is the first to document high-frequency gravity oscillations in a volcanic setting, which, however, might be owed to the fact that continuous gravimetric observations are not yet standard in volcano monitoring (Williams-Jones et al. 2008). We consider the attenuation of short-term signals between 2003 and 2008 in both frequency and amplitude as indicator for unrest waning and possible termination. In fact, our results imply that integrated geodetic observations over a broad frequency range (periods of sec to decades) should be regarded an effective tool to better assess the spatio-temporal dynamics of volcanic unrest and to enable early detection of system reactivation as well as unrest waning. The research on Nisyros indicates that unrest may continue for more than a decade after initial volcano reactivation.

References

Battaglia M, Troise C, Obrizzo F, Pingue F, De Natale G (2006) Evidence for fluid migration as the source of deformation at Campi Flegrei caldera (Italy). Geophys Res Lett 33:L01307. doi:10.1029/2005GL024904

Battaglia M, Gottsmann J, Carbone D, Fernandez J (2008) 4D volcano gravimetry. Geophysics 73(6):WA3–WA18. doi:10.1190/1.2977792

Brombach T, Hunziker J, Chiodini G, Cardellini C, Marini L (2001) Soil diffuse degassing and thermal energy fluxes from the southern Lakki plain, Nisyros (Greece). Geophys Res Lett 28:69–72. doi:10.1029/2000GL008543

Caliro S, Chiodini G, Galluzzo D (2005) Recent activity of Nisyros volcano (Greece) inferred from structural, geochemical and seismological data. Bull Volc 67:358–369. doi:10.1007/s00445-004-0381-7

Chiodini G, Cioni R, Leonis C, Marini L, Raco B (1993) Fluid geochemistry of Nisyros Island, Dodecanese, Greece. J Volcanol Geotherm Res 56:95–112

Chiodini G, Brombach T, Caliro S, Cardellini C, Marini L, Dietrich V (2002) Geochemical indicators of possible ongoing volcanic unrest at Nisyros Island (Greece). Geophys. Res. Lett. 29(16). doi: 10.1029/2001GL014355

Dawes GJK, Lagios E (1991) A magnetotelluric survey of the Nissyros geothermal field (Greece). Geothermics 20(4):225–235

Fournier RO (1999) Hydrothermal processes related to movement of fluid from plastic into brittle rock in the magmatic-epithermal environment. Econ Geol 94:1193–1211. doi:10.2113/gsecongeo.94.8.1193

Fournier N, Chardot L (2012) Understanding volcano hydrothermal unrest from geodetic observations: insights from numerical modeling and application to White Island volcano, New Zealand. J Geophys Res 117:B11208. doi:10.1029/2012JB009469

Gottsmann J, Battaglia M (2008) Deciphering causes of unrest at collapse calderas: Recent advances and future challenges of joint gravimetric and ground deformation studies. In: Gottsmann J, Martí J (eds) Caldera Volcanism: analysis, modelling and response, developments in volcanology, vol 10, pp 417–446. doi:10.1016/S1871-644X(07)00012-5

Gottsmann J, Rymer H, Wooller LK (2005) On the interpretation of gravity variations in the presence of active hydrothermal systems: insights from the Nisyros Caldera, Greece. Geophys Res Lett 32. doi: 10.1029/2005GL024061

Gottsmann J, Camacho AG, Tiampo KF, Fernandez J (2006) Spatiotemporal variations in vertical gravity gradients at the Campi Flegrei caldera (Italy): a case for source multiplicity during unrest? Geophys J Int 167(3):1089–1096. doi:10.1111/j.1365-246X.2006.03157.x

Gottsmann J, Carniel R, Coppo N (2007) Oscillations in hydrothermal systems as a source of periodic unrest at caldera volcanoes: multiparameter insights from Nisyros, Greece. Geophys Res Lett 34:L07307. doi:10.1029/2007GL029594

Williams-Jones G, Rymer H, Mauri G, Gottsmann J, Poland M, Carbone D (2008) Towards continuous 4D microgravity monitoring of volcanoes. Geophysics 73: WA19–WA28. doi:10.1190/1.2981185

Hautmann S, Hidayat D, Fournier N, Linde AT, Sacks IS, Williams CP (2013) Pressure changes in the magmatic system during the December 2008/January 2009 extrusion event at Soufrière Hills Volcano, Montserrat (W.I.), derived from strain data analysis. J Volcanol Geoth Res 250:34–41. doi:10.1016/j.jvolgeores.2012.10.006

Hautmann S, Witham F, Christopher T, Cole P, Linde AT, Sacks IS, Sparks SJ (2014) Strain field analysis on Montserrat (W.I.) as tool for assessing permeable flow paths in the magmatic system of Soufrière Hills Volcano. Geochem, Geophys, Geosyst 15. doi:10.1002/2013GC005087

Hurwitz S, Christiansen LB, Hsieh PA (2007) Hydrothermal fluid flow and deformation in large calderas: inferences from numerical simulations. J Geophys Res 112:B02206. doi:10.1029/2006JB004689

Hutnak M, Hurwitz S, Ingebritsen SE (2009) Numerical models of caldera deformation: effects of multiphase and multicomponent hydrothermal fluid flow. J Geophys Res 114:B04411. doi:10.1029/2008JB006151

Lagios E, Sakkas V, Parcharidis I, Dietrich V (2005) Ground deformation of Nisyros volcano (Greece) for the period 1995–2002: results from DInSAR and DGPS observations. Bull Volc 68(2):201–214

Lowenstern JB, Hurwitz S (2008) Monitoring a supervolcano in repose: Heat and volatile flux at the Yellowstone caldera. Elements 4:35–40. doi:10.2113/GSELEMENTS.4.1.35

Makris J, Chonia T (1999) Active and passive seismic studies of Nisyros volcano—East Aegean Sea. Proceedings of 1999 CCSS Workshop, Communication of the Dublin Institute for Advance Studies. Geophys Bull 49:9–12

Marchetti E, Genco R, Ripepe M (2009) Ground deformation and seismicity related to the propagation and drainage of the dyke feeding system during the 2007 effusive eruption at Stromboli volcano (Italy). J Volcanol Geoth Res 182:155–161. doi:10.1016/j.jvolgeores.2008.11.016

Marini L, Principe C, Chiodini G, Cioni R, Fytikas M, Marinelli G (1993) Hydrothermal eruptions of Nisyros (Dodecanese, Greece). Past events and present hazard. J Volcanol Geotherm Res 56:71–95

Mogi K (1958) Relations between the eruptions of various volcanoes and the deformations of ground surfaces around them. Bull Earthquake Res Inst Univ Tokyo 36:99–134

Nishimura T, Ozawa S, Murakami M, Sagiya T, Tada T, Kaidzu M, Ukawa M (2001) Crustal deformation caused by magma migration in the northern Izu Islands, Japan. Geophys Res Lett 28:3745–3748. doi:10.1029/2001GL013051

Parcharidis I, Foumelis M, Sakkas V, Lagios E (2005). Deformation Monitoring in Kos Island (Hellenic Volcanic Arc, Eastern Greece) using Differential Interferometry. In: Geosciences and Remote Sensing Symposium (IGARSS), vol 4, pp 2899–2902

Rothacher M, Beutler G, Gurtner W (1993) Bernese GPS Software Documentation version 3.4. Astronomical Institute, University of Berne, Switzerland

Sachpazi M, Kontoes Ch, Voulgaris N, Laigle M, Vougioukalakis G, Olga Sikioti G, Stavrakakis G, Baskoutas J, Kalogeras J, Lepine JCl (2002) Seismological and SAR signature of unrest at Nisyros caldera, Greece. J Volcanol Geoth Res 116:19–33

Stiros SC (2000) Fault pattern of Nisyros Island volcano (Aegean Sea, Greece): structural, coastal and archeological evidence. In: McGuire WJ, Griffiths DR, Hancock PL, Stewart IS (eds) The archeology of geological catastrophes, vol 171. Geological Society Special Publications, London, pp 385–397. doi:10.1144/GSL.SP.2000.171.01.28

Sykioti O, Kontoes C, Elias P, Briole P, Sachpazi M, Paradissis D, Kotsis I (2003) Ground deformation at Nisyros Volcano (Greece) detected by ERS-2 SAR differential interferometry. Int J Remote Sens 24:183–188

Todesco M (2007) Hydrothermal fluid circulation and its effect on caldera unrest. In: Gottsmann J, Martí J (eds) Caldera volcanism: analysis, modelling and response, developments in volcanology, vol 10, pp 393–416

Todesco M, Rinaldi AP, Bonafede M (2010) Modeling of unrest signals in heterogeneous hydrothermal systems. J Geophys Res 115:B09213

Troise C, Castagnolo D, Peluso F, Gaeta FS, Mastrolorenzo G, De Natale G (2001) A 2D mechanical-thermalfluid-dynamical model for geothermal systems at calderas: an application to Campi Flegrei, Italy. J Volcanol Geoth Res 109(1–3):1–12

Vougioukalakis G, Sachpazi M, Perissoratis K et al (1998) The 1995–1997 seismic crisis and ground deformation on Nisyros volcano, Greece: a volcanic unrest? 6th Int. Meeting on Colima volcano, Abstracts Volume

Lu Z, Dzurisin D, Biggs J, Wicks, C, McNutt S (2010) Ground surface deformation patterns, magma supply, and magma storage at Okmok volcano, Alaska, from InSAR analysis: 1. Intereruption deformation, 1997–2008. J Geophys Res 115:B00B02. doi:10.1029/2009JB006969

Wicks C, Thatcher W, Dzurisin D (1998) Migration of fluids beneath Yellowstone caldera inferred from satellite radar interferometry. Science 282:458–462. doi:10.1126/science.282.5388.458

Epilogue Nisyros Island, the Inaccessible Outpost Between Orient and Occident, Home of a Restless Giant

12

Volker Jörg Dietrich

Abstract

The epilogue is meant to provide a short review of the colourful history of Nisyros Island, found at the crossroads between occidental and oriental cultures. The interesting cultural and historical heritage of the island is a courtesy of its geographical position, in the southeast corner of the Aegean Sea, and of the circular and mountainous volcanic morphology, making it a rather inaccessible island, where values are more easily preserved. Nisyros Island offers not only a unique volcanic history and beauty of its nature, but also the splendour of art and civilization, expressed through prehistoric and historic locations and monuments. In this respect, Nisyros differs from all Dodecanese and Aegean islands. Etymological studies have led to a variety of interpretations regarding the various names of the island: Porphyris, Kisiris and Nisyros. Greek Mythology is present in many legends, which have been preserved in poems by Greek and Roman writers and geographers. Prehistoric witnesses are present from Early Neolithic times, in the form of relicts from the "Cycladic and Minoan" civilizations. Historical records start from the Hellenistic epoch and continue uninterrupted through Roman, Byzantine, Venetian and Ottoman eras, into modern times. Each of these periods has enriched the island with ancient caverns and spas, magnificent castles, churches and monasteries with hagiographic frescoes. We invite the reader to dwell in the wonders of Nisyros island.

The pre-historic development of Nisyros Island can be better understood taking into account the entire history of the southeastern Mediterranean, as well as all natural phenomena, such as the geographical, climatic and volcanological peculiarities and catastrophes. The small circular mountainous island must have been an ideal

V.J. Dietrich (✉)
Institute of Geochemistry and Petrology, Swiss Federal Institute of Technology, ETH Zurich, ETH-Zewntrum, 8092 Zürich, Switzerland
e-mail: volker.dietrich@erdw.ethz.ch

V.J. Dietrich and E. Lagios (eds.), *Nisyros Volcano*, Active Volcanoes of the World,
DOI 10.1007/978-3-319-55460-0_12

Fig. 12.1 Nisyros Island with the main prehistoric and historic locations (Minoan period, Greek Roman period, Mideival period and monasteries). *Photo* Google earth

rescue and hiding place for small groups of early Neolitic settlers, despite the fact of lack of fresh water. There, they were protected from riots of pirats and bandits, not being familiar with such an wilderness island. The pumice cover and soft volcanic rocks allowed simple treatment for constructions of caves and buildings. Although the early inhabitants know the steaming fumaroles in the hydrothermal craters, the intensive smell of sulphur gases and hot springs on the shores, they were not aware about the danger of a possible volcanic eruption, emitting lavas, bombs and ashes covering the total environment. All these phenomena were unknown, since they dated back in the Eastern Mediterranean at least 20,000 years. The catastrophic experience appeared with the Minoan eruption of Santorini around 3620 BC causing total devastation in the South Aegean islands and Crete and breakdown of the blooming Minoan civilization (Fig. 12.1).

12.1 Mythology and Etymology

Already in Hellenistic time, the islands of Kos and Nisyros were well known to the Greeks, based on their colonization from the Peloponnese since Archaic times and their polytheistic believe with the Asclepius sanatoria cult documented in the medical school of Hippocrates from Kos and the daily use of the hot springs in Kos and Nisyros, as well as in their believe of the origin

of the islands, i.e. glorified in the battle between the titans and giants on the Parthenon fries of the Akropolis in Athens. In the "Periplus of Pseudo-Skyllax", a mid-4th century BC circumnavigation, Nisyros Island is placed in Caria.

The first citation of Nisyros can be found in the "Bibliotheca" (Βιβλιοθήκη) of Apollodorus of Athens (A, 6, 2; 2nd century BC), a compendium of myths and legends. Strabo (Στράβων), a Greek geographer, philosopher and historian (c. 64/63 BC–c. AD 24) reported in his "Geographia" (X, 5, 16) the mythological birth of the island of Nisyros as follows: The titan Poseidon, helping Zeus in his battle against the giants, chased the fearful giant Polyvotis over land and seas. When Poseidon reached the island of Kos, Poseidon broke off a piece of the western island with his mighty trident and hurling it at Polyvotis and buried him under it (Fig. 12.2). This broken off piece of Kos became the island of Nisyros. The volcano was created over the mouth of Polyvotis and the constant rumblings and groaning at depth are the chest sighs of the buried giant.

Strabo described Nisyros (X, 5, 16) as follows: "is round and high and rocky, the rock being that of which millstones are made".

Fig. 12.2 Poseidon crushing Polybotis under a huge rock; *black-figure* amphora from the 5th century BC. *Photo* Yorgos Fafalis, © Athens, Museum of Cycladic Art, inv. no. SP 98

According to Plinius (1st century AD, "Nat. Hist." V 36) Nisyros was known as "Porphyris" ("purple") on account of the abundant murex shells from which the Phoenicians produced the famous purple-red color or less plausible from reddish porphyry stones, which do not occur on this island.

Dionysius Periegetes, 2nd century AD, cartographer of the famous world map as a disc and Stefanos Byzantinus (c. 6th century AD), the author of the important geographical dictionary "Ethnica", gave several etymological interpretations to the Name of Nisyros. According to Eustathios of Thessalonike (a Greek bishop and scholar, c. 1115–1195/6) and commenting on Periegetes the name Nisyros originated from the Greek words neo, ("to swim"), and syro, ("to drag"), taking as a reference to Polyvotis who swam the last few moments while dragging the rock, which he had received from Poseidon on his back.

12.2 History and Civilisation

The settlements of Nisyros Island and on Yali reach back to Neolithic times in the order of c. 6000 years BP. First settlers in the Dodecanese islands may have come from the west Anatolian coast and Asia Minor making their way towards south to Crete and west to the Aegean islands (Pendlebury 1965). Early trading is indicated by the findings of obsidian from Yali in the first center of obsidian fabrication on the island of Saliagos between Paros and Antiparos (Renfrew et al. 1965).

During the beginning of the Bronze time, a time span of approximate 600 years between 3000 and 2400 B.C a new wave of settlers from the East introduced the "Cycladic Civilization", which was characterized by a certain social hierarchy, believing in reincarnation and worshipped female deities. The beginning of exchange trading started by the "longboats" during the Kero-Syros culture approx. 2600–2400 B.C., which were built from tall cedar trees in Lebanon (in the pre-Phoenician cities of Ugarit and Byblos), and were paddled by large crews

mainly along the Anatolian coast. These people knew how to mine and smelt bronze and copper, as well as a first sophisticated casting, bringing along domesticated animals, and evolved sophisticated methods of agricultural production. They developed a craftsmanship in stones, carving marble figurines, which they buried with their dead. Settlements on Nisyros Island during this time relate to findings of pottery fragments and of a "folded arm female figurine" (Fig. 12.3), similar to those from the "Chalandriani tombs" on Syros island.

Around the same period an invasion of people from the area Caria opposite to the islands of Kos and Rhodos with ethnic roots close to Lycians and Lydians may have taken place. According to Diodorus Siculus (Bibliotheca Historica; c. 60–30 BC) they may have been the first real inhabitants of Nisyros.

Thousand years later, the first sailing galleys from the Levant coast and Cyprus (originally Egyptian constructions) were able to withstand the open sea and heavy weather. Extensive trading started throughout the Eastern Mediterranean, Cyprus, Rhodes, Kos, Crete, and the Aegean islands, which led to a Cycladic-Minoan thalassocracy, the volcanic ring island Santorini (at that time "Kallisti", the "most beautiful") advancing to central trading point of the Aegean Sea due to its geographic position and secure shelter within the inner Caldera lake (Dietrich 2004).

Cycladic-Minoan settlements have been found along the Anatolian coast between Samos and Rhodes, such as Tigani, Miletus, Iasos, Knidos etc. There is also evidence of remnants in Yali, which definitely served as obsidian raw material supplier (Georgiadis 2008). This is proven by the obsidian vessel (Fig. 12.4) found tin the palace of Zagros, made out of white-speckled obsidian from Yali; Late Neopalatial period (1450 BC, LMII).

Fig. 12.3 Folded arm female figurine (Kero-Syros culture c. 2600–2400 B.C.) found in Nisyros; *Photo* Marcus Cyron, Altes Museum: Antikensammlung Berlin

Fig. 12.4 Ritual vessel with high degree of aesthetics and superb workmanship from the "Sanctuary Treasury" of the palace of Zagros, made out of white-speckled obsidian from Yali; Late Neopalatial period (1450 BC, LMII); *Photo* V.J. Dietrich Archaeological Museum Herakleion Crete

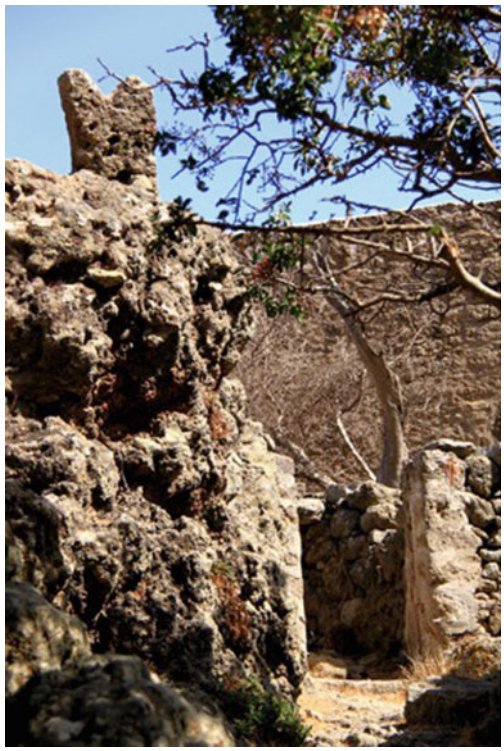

Fig. 12.5 Remnants of a Cycladic-Minoan settlement or outpost represented by a pair of "horns of consecration" at the northern entrance of the little Nymfios valley in the center of the island. *Photo* Barry's Ramblings

Solid evidence for a Cycladic-Minoan settlement or outpost has not been found yet on the island of Nisyros. However, a remarkable indication is represented in a pair of "horns of consecration" (Fig. 12.5) that have been carved out of the solid rhyodacitic rocks at the northern entrance of the little Nymfios valley in the center of the island. In addition, numerous unidentified stone cuttings (Fig. 12.6) and a cave with a carved pillar (Fig. 12.7) have been described on the eastern and northeastern side of the same valley and interpreted by Economakis and de Vries (2001). as a singular sacred Minoan enclave. The circumstance, that these structures were placed in a remote hidden place high up in the mountains also allows the interpretation of refugee constructions of survivors from the Santorini volcanic Minoan eruption c. 1620 BC and tsunami, which devastated the entire coasts of the Cycladic islands, Crete and eastern Mediterranean.

Fig. 12.6 Unidentified stone cuttings on the eastern and northeastern side of the Nymfios valley. *Photo* Barry's Ramblings

With this catastrophe and with subsequent major earthquakes, the Minoan civilization in Crete and definitely in the Cycladic islands came to an end. In the Argolis, the Cycladic and Minoan emigrants formed a new and powerful civilization, the "Mycenae civilization", based on military principles and monumental customs, which lasted for another four hundred years. With the help of seafarers from Cyprus and the Levant the Mycenaean's returned mainly to Crete; little is known about the Dodecanese islands and, i.e. Kos and Rhodes. Several constructions, which can be seen as Mycenaean remains have been detected in Nisyros: the base walls of Paleokastro at the northern part, resembling the classical "cyclopean" tracery of a Mycenaean citadel, relict walls at Tafies south-west of Mandraki, Vathia, and in the foundations of the Stavros monastery. Homer mentioned in the epic poem Iliad, Nisyros provided ships and troops to fight, under the command of the rulers of Kos Pheidippos and Antiphos, children of Thessalos, the son of

Fig. 12.7 Unidentified stone cuttings and a cave with a carved pillar on the eastern and northeastern side of Nymfios valley. *Photo* Barry's Ramblings

Herakles against Troy in 1184 BC. Since no archaeological solid data have been found, the epic poem remains a glamorous phantasy story. There were neither proper ships and sheltered bays nor large populations on the Dodecanese islands to provide troops. The fall of the Mycenaean empire is rather assigned to a time of increase natural catastrophes (Dietrich 2004), such as major earthquakes and flooding accompanied by social unrest and destruction than invasion of the Dorians from north. Despite the fact, that the Phoenicians became dominant traders in the eastern Mediterranean 1200 and 1150 BC, no traces have been found so far on Nisyros Island. The reason may be seen in the lack of harbours for their galleys, which were built with a keel for anchoring in protected bays. The lack of springs (only one known at Pigi) and water supplies, as well as the climatic conditions at these periods might have been responsible avoiding the island.

No archaeological findings can be assigned from the Minoan—Mycenaean period until the Archaic to Classical times from the 7th to 4th century BC, a time gap of more than 400 years (Stampolidis et al. 2011). The classical poets and historians assigned the first inhabitants of the Aegean islands as "Pelasgians" with an origin from Argos in the Peloponnese and the Greek mainland.

The Greek historian Herodotus (c. 485–425 BC, VII, 99) stated that the Dorian population in Kos, Kalymnos, Nisyros, Kasos and Karpathos arrived from Peloponnese, i.e. from Epidaurus and Argos. Indications were found by the German archaeologist Ludwig Ross (1843) ancient foundations in the locality of Argos close to the monastery of Stavros in the southern slopes of the island, which already had been reported by Stephanus Byzantinus, possibly being an important sanctuary of Argive Poseidon. A possible Pelasgian location is the Dracospilia grotto above Cape Korfos.

Nisyros must have reached a certain economic importance during archaic times, proven by the archaeological finds such as steles and vessels from the cemetery of the 8th–5th centuries B.C (Filimonos and Apostolou 2010) and displayed in the Archaeological Museum at Mandraki. The autonomy of the island during the 4th century BC seems to be indicated by its own coinage (Ashton 1999) as witnessed by the inscriptions in several places on the island (Chaviaras 1913; Arafas 2002). In addition, the island was also known at those times for its thermal waters as it is evident from an inscription in the Roman thermal bath at Pali.

During the second part 4th century BC Paleokastro was built as a highly organized defense system (Fig. 12.8), which comprised watchtowers and lighthouses around the island and neighboring islet in order to control the ship routes and naval activity between the Anatolian coast, Crete, Rhodes, Kos and the Cycladic islands.

Several watchtowers ("fryktories") from this period have been found on the islet of Pergousa, on the southwest side of Nisyros, at Drakospilia on Cape Lefkos, at Pyrgoi near Kateros; at Skopi near the municipal baths (Loutra) on the north side of the island. According to the construction of the walls with its precise, tightly-fitting joints

Fig. 12.8 Paleokastro is the Classical and Hellenistic Acropolis that was built during the 4th century BC on an ancient settlement with fortifications and outside cementaries (Filimonos-Tsopotou 2013) and is situated on the hill overlooking the village of Mandraki. The walls consist of *black* accurately formed andesitic basalt from its lava underground. In some cases these cubolds reach 3.5 m and weigh up to 4 tons. Six towers are still standing on the south side along with a wall 230 m long while on the east side there are two towers and 80 m of wall. *Photo* Barry's Ramblings

of the lava blocks this powerful fortification has been as part of a defence system of the Mausolus dynasty of Asia Minor (Karia), who governed the Dodecanese islands of Rhodes, Kos, Tilos, and Nisyros during the period 355–332 BC (Pimouuet-Pédarros 2000; Apostolou 2014).

Another flourishing time of Nisyros started when Alexander the Great claimed the Dodecanese islands around 333 BC including Nisyros after liberating Asia-Minor from the Persians. After Alexander's death the islands split into several independently governed territories until in the 3rd century BC Rhodes took over the control. It seems that Nisyros joined Rhodian Parea c. 200 BC taking part in the Cretan war and winning over King Philip V of Macedon, the Aetolian League and several Cretan cities (Papachristodoulou 1933).

There were defense systems on Nisyros Island, observatories and towers all over the island and communication with the castle was maintained through smoke signals during the day and fire signals during the night. Retaining foundations and cisterns on the hill testify the existence of Hellenistic-Roman settlement. As harbour served the little inlet east of the high cliff, which has been filled up completely by currents with sand and silt, as well as local debris. Many traces of Roman settlements, such as columns, steles, sculptures of white marble and vessels have been found. However, the settlement below and around the Paleokastro site moved gradually towards the sea, overbuilding the ancient inlet harbour, spreading eastward parallell along the coastline and founding the main settlement Mandraki of the island.

A detailed description of the Roman period has been given by Economakis and de Vries (2001). It seems that Nisyros had produced its own silver and copper coins with images of Poseidon, Artemis, Aphrodite, Apollo, and a dolphin with trident (Fig. 12.9).

Strabo (X, 5, 16) mentioned that at the 1st century on Nisyros one city with harbor, a thermal bath (Fig. 12.10), and a Poseidon temple occurred devoted to the principal deity of the island. Two little bays may have given shelter at these time periods, a deeper inlet eastward behind the high cliffs of Mandraki and an analogue bay eastward behind Cape Akrotiri at Pali.

Fig. 12.9 Roman coin: Poseidon on a sitting on a rock with his trident in hand found in Nisyros (Ashton 1999)

During the 4th century the Western Roman Empire went down and with it the naval control of the Mediterranean, which was followed by chaotic raids of pirates and galley fleets of the Vandales. The time between the 7th and 11th century the entire Mediterranean and the Aegean Seas were the scene of continuous naval battles of the Byzantine empire with help of the "Holy Allies" England and Spain against the Muslim conquests. Signs out of the Eastern Roman Empire and Byzantine time exist in Nisyros in several basilicas and Early Christian churches at least in ten places (Economakis and de Vries 2001), i.e. in the church of Faneromeni (Fig. 12.11).

At the end of 11th century the "Holy Roman Empire" started the Crusades, which led to the Kingdom of Jerusalem and the Crusader states along the Levantine coast. These ventures reopened the Mediterranean to trade and travel, enabling the kingdoms of Genua and Venice to flourish.

The Venetians started commercial trading based on political and cultural grounds with the Byzantine Empire and founded a commercial outpost 1082 in Rhodes. During the 13th century Nisyros was dominated by Genoa, that in 1309 sold the island to the Order of the Knights of Saint John from Jerusalem, who built in 1315 the fortified bastion on the top of the cliffs above the village of Mandraki that thrusts northward into the sea (Fig. 12.12); besides four other forts in strategic points around the island, i.e. the fort of Pandenichi overlooking Emborios and a fort on top of the Parletia neck inside the caldera beneath Mt. St. John Theologian.

The localities Mandrachi, Palaiocastro, Pandenichi (Emborios), Nicea and Argos are shown

Fig. 12.10 The vault of the Roman thermal bath of the spring Panagia Thermiani east of Pali. *Photo* community of Nisyros

Fig. 12.11 The domed Byzantine church of Faneromeni (11th century) on the western slopes of the island; in the background the hillside of Paleokastro. *Photo* V.J. Dietrich

Fig. 12.12 The fort the order of the Knights of Saint John from Jerusalem built after 1315 on the pillow lava cliffs of Mandraki. The northwestern part is occupied by the monastery of "Panagia Spiliani" (Virgin of the Grotto), founded at least during early 18th century. *Photo* V.J.Dietrich

Fig. 12.13 Nisyros Island in the book "Liber Insularum Archipelagi", c. 1420, Cristoforo Buondelmonti. It covers the Ionian Islands, Aegean Islands and Constantinople; vellum, 18 × 25 cm; 1 exemplar at National Maritime Museum, Greenwich, London. The map shows an eruption of gases in the central part of the volcanic island; Buondelmonti mentions in his description the commercial explotation of sulphur and millstones

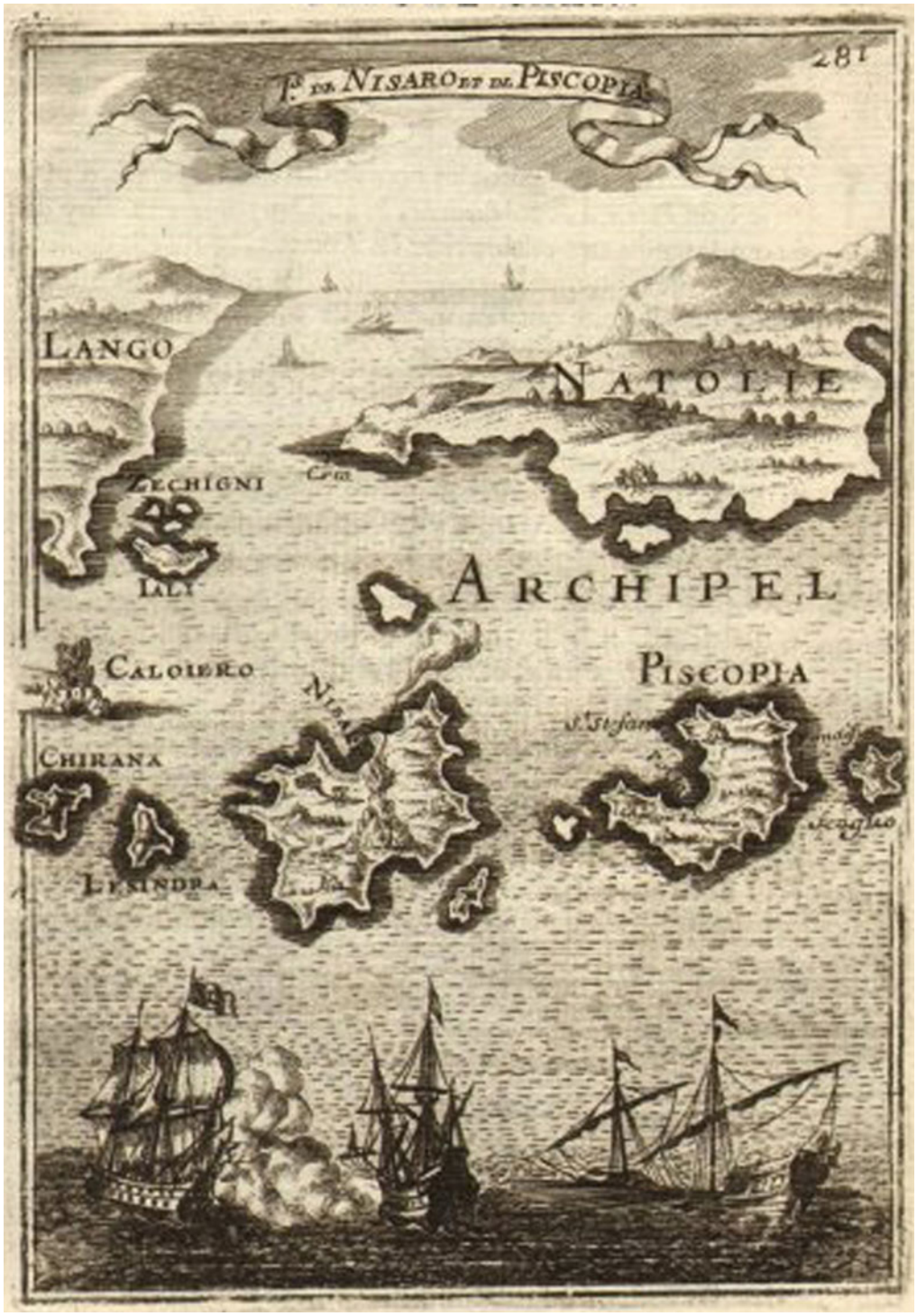

Fig. 12.14 Isla De Nisaro de Piscopia' 1683, Allain Manesson Mallet, copperplate map 10.5 × 14.5 cm. The map depicts the Dodecanese islands of Nisaro (Nisyros), Piscopia (Tilos), Lango (Kos), Iali and Zechigni (Yali western part separated from eastern part), Caloiero (Kefalos peninsula), Chirana (Pergusa, Lesindra (Pachia) and the Datça peninsula (part of the coast of Anatolia)

in the first "precise" map of Nisyros from Christoforo Buondelmonti from 1420/1422 (Fig. 12.13): "*Here* (in the island of Nisyros), *Flaminius consul, coming back from Orient has been predicted to win in the coming fighting against Galics, as actually happened. For this reason the island has been always considered of good omen by Latin people. Also Cleopatra and Antonius passed by Nisyros and razed to the ground the island as its inhabitants refused to obey their orders. The island is eighteen miles in circumference and there are five towns to be seen there: Mandrachi and Paleocastro are the largest; Pandenichi, Nicea and Argos are found elsewhere around the island. In the centre of the island there is a very high mountain which belches out sulfur fire from underground passages day and night, as it happens in the island of Stromboli, near Lipari*".

Despite the conquest of the city of Constantinople and the fall of the Byzantine Empire 1453 by the Ottomans, the Knights of St. John reinforced their forts to defend the outlooks against the Ottoman fleets. However, Nisyros Island got attacked in 1455, 1457 and 1483; many inhabitants were killed or carried away into slavery. After half a century the island was almost deserted, 1522/1523 the Knights of Rhodes and Kos had to capitulate. The twelve islands Ikaria, Patmos, Leros, Kalymnos, Nisyros, Astypalaia, Symi, Tilos, Chalki, Kassos, Karpathos and Kastellorizo, except Kos and Rhodes received a certain autonomy and freedom as a separate Ottoman province, called "Isporad Adisi" (origin of the later name Dodekanese). Despite the Ottoman domination the commercial trading of the Venetian fleets continued till the end of the 17th century. Many geographical maps of the Mediterranean and the Aegean Seas were published during this period (Fig. 12.14). During the second part of the 18th century the island was less controlled due to the destruction of the Ottoman fleet during the Russo-Turkish War. Many Nisyrians could return or leave founding settlements in Odessa, Konstantinople and Izmir. Although many families converted to the Islam, the Christian orthodox and catholic religion was tolerated. Churches and monasteries

Fig. 12.15 Remnants of a hidden chapel in the western hills below Nikia. *Photo* Stavros Osaris

were built or restored during the 18th and 19th century (i.e. Figs. 12.15, 12.16, 12.17, 12.18; for review see Orsaris 2012).

Throughout its long history, Nisyros was a place of intense spirituality and religiosity. Proof of it is the numerous places of worship, as evidenced by

Fig. 12.16 Hidden chappel Agia Marina above the cliffs of the southeast coast. *Photo* Stavros Osaris

Fig. 12.17 The catholic Armas monastery is dedicated to Ioannis Prodromos (John the Baptist) and dated mid 18th century. The abandoned but undisturbed stone buildings around the chapel showing the monastery's original size and still containing in the underground store areas pithoi and lids still intact. *Photo* V.J. Dietrich

Fig. 12.18 The chapel of Armas with ornate iconostasis and apse are completely decorated 18th century frecoes by Neophytos of Symi, meticulously divided into small panels crowded with detail. Behind the simple, rustic wooden screen, the altar and prothesis table are ancient *spolia*. *Photo* V. J. Dietrich

the remains of small churches, the countless temples of Byzantine and post-Byzantine periods and the hidden chapels that are scattered in the countryside.

The monastery Panagia Spiliani ("Virgin Mary of the Grotto") has become the most famous and picturesque monastic complex of the island, which dates back to at least early 18th century, and appears today as the most typical landmark approaching Nisyros from the sea (Fig. 12.12).

According to the legend, people from Mandraki saw a flickering light on the side of a cliff near the hot springs of Loutra. A farmer climed up the cliff and discovered a small icon of the Virgin Mary (Fig. 12.19). He took this icon to the church of Panagia I Potamitissa (the Virgin of the Rivers) for safekeeping.

The next day, the icon was missing. They supposed it to be stolen. A few days later, it was rediscovered by the locals on a hay bale in the castle grotto in the high cliffs above Mandraki. Again they took the icon to the church of Panagia i Potamitissa but again the icon went missing and was rediscovered in this same cave on the rocks. This continued a few times until the locals recognised the mysterious happenings as a divine sign and decided to consecrate this site with a church and to leave the icon in its preferred location. This cave has been called Panagia Spiliani and the monastery was built above this cave, which may be assigned during the 16th century. The Nissyrians dedicate this icon for protection of the island.

During the Greek revolution that began in 1821, the Nisyrians supported the Greek fleet anchoring at Yali prior to the naval battle of Gerontas in the year of 1824 near Leros. However, their liberation did not last very long. According to the "London treaty" the Dodecanese islands were put back under Ottoman and later Turkish Republic rule, which ended on May 12, 1912.

Modern times started in the island at this period with the construction of Mandraki harbour and a long pier (Fig. 12.20), which gave enough shelter from northerly winds for small steamboats and allowed to a certain extend weather indepentend transport to Kos and Rhodes.

Fig. 12.19 The "Virgin Mary of the Grotto" the protector of the island of Nisyros and located in a cave on a 30 m high rock. 170 steps lead to the holy cave of the monastery Panagia i Spiliani. The icon was silver-gilded soon after the Russo-Turkish war in the late 18th century. *Source of picture* Kentris 1993

Fig. 12.20 The reinforced pier at Mandraki harbor 1920. Unknown photographer

According to the Lausanne treatise, the "*Regio Decreto n. 1854*" in 1925, all Dodecanese islands were given to Italy until the collapse of the fascist regime and the country's surrender to the Allies in 1943, followed by a short period of German military occupation. After the surrender May 8, 1945 the islands were put under British military protectorate until they were formally united with Greece 28th October 1947 ending 630 years of foreign rule over the islands.

Although the island of Nisyros had suffered occupations for centuries, the inhabitants developed their own unique dialect, a combination of ancient and modern Greek independent from Latin, Turkish, Italian and other linguistic influences, which proves the island's inaccessible character.

References

Apostolou A (2014) Restoration of the ancient fortification and landscaping of surrounding area of Palaiokastro, Nisyros. Intern Conference on Fortified Heritage: management and sustainable development, Pamplona, 15–17 Oct 2014 Fortius Pamplona-Bayonne, Spain, 11 pp

Arfaras ME (2002) Porphyris of antiquity (in Greek). Kamiros, Athens 111 pp

Ashton R (1999) The coinage of Nisyros. In: Amandry et al (eds), Mélanges Le Rider, pp 15–24

Buondelmonti Cristoforo (c. 1420) Liber Insularum Archipelagi

Chaviaras M (1913) Nisyrou Epigraphai. Archaeologiki Ephemeris, p 16

Dietrich VJ (2004) Die Minoische Katastrophe, ein Vulkan verändert die Welt. Neujahrsblatt Naturf Ges Zürich207 Stück 149:93 S

Economakis R, de Vries C (2001) Nisyros, History and Architecture of an Aegean Island. Publishing House Melissa, Athens, Greece 199 p

Filimonos-Tsopotou M (2013) The Paleokastro von Nisyros (in Greek) Nisyriaka vol 20, pp 149–172

Filimonos-Tsopotou M, Apostolou A (2010) Restoration, arrangement and display of the ancient fortification walls of Nisyros. Europa Nostra Scientific Bulletin 64:75–87

Georgiadis M (2008) The obsidian in the Aegean beyond Melos. Oxf J Archaeol 27:101–117

StI Kentris (1993) Nisyros (in Greek). Roi Brothers ltd Haidari, Athens

Orsaris St (2012) The wallpaintings in Nisyrian Churches (in Greek) University Ecclesiastical Academy of Thessaloniki, AGM 672, Dept of Management and Conservation of Cultural Heritage Objects, 94 pp

Papachristodoulou IChr (1933) The relationship between Nisyros and Rhodes at ancient times (in Greek). Nisyriaka 12:39–52

Pendlebur JD (1965) The archaeology of crete. Norton & Company, Incorporated, W W, 432 pp

Pimouguet-Pédarros I (2000) Archéologie de la Défense Histoire des fortifications antiques de Carie (époques classique et hellénistique). Paris, pp 298–299

Renfrew C, Cann JR, Dixon JE (1965) Obsidian in the Aegean. Ann Br School Athens 60:225–47; and (2008), Oxf J Archaeol 27:101–117

Ross L (1843) Reisen auf den griechischen Inseln II. Stuttgart-Tübingen, pp 70–72

Stampolidis NC, Tassoulas Y, Filimonos-Tsopotou M (2011) Islands off the beaten track. An archaeological journey to the Greek islands of Kastellorizo, Symi, Halki, Tilos and Nisyros. Museum of Cycladic Art (Nicholas and Dolly Goulandris Foundation, Athens, Hellenic Ministry of Culture and Tourism, ISBN-10: 9607064933, 438 pp

Index

V.J. Dietrich and E. Lagios (eds.), *Nisyros Volcano*, Active Volcanoes of the World,
DOI 10.1007/978-3-319-55460-0